Impact of GNSS singular events on the integrity of airport navigation systems

Leslie Montloin

▶ **To cite this version:**

Leslie Montloin. Impact of GNSS singular events on the integrity of airport navigation systems. Signal and Image processing. Toulouse INP, 2014. English. NNT : 2014INPT0051 . tel-01377380v1

HAL Id: tel-01377380

https://theses.hal.science/tel-01377380v1

Submitted on 6 Oct 2016 (v1), last revised 27 Oct 2023 (v2)

HAL is a multi-disciplinary open access archive for the deposit and dissemination of scientific research documents, whether they are published or not. The documents may come from teaching and research institutions in France or abroad, or from public or private research centers.

L'archive ouverte pluridisciplinaire **HAL**, est destinée au dépôt et à la diffusion de documents scientifiques de niveau recherche, publiés ou non, émanant des établissements d'enseignement et de recherche français ou étrangers, des laboratoires publics ou privés.

THÈSE

En vue de l'obtention du

DOCTORAT DE L'UNIVERSITÉ DE TOULOUSE

Délivré par :

Institut National Polytechnique de Toulouse (INP Toulouse)

Discipline ou spécialité :

Signal, Image, Acoustique et Optimisation

Présentée et soutenue par :

Mme LESLIE MONTLOIN

le jeudi 10 juillet 2014

Titre :

IMPACT OF GNSS SINGULAR EVENTS ON THE INTEGRITY OF AIRPORT NAVIGATION SYSTEMS

Ecole doctorale :

Mathématiques, Informatique, Télécommunications de Toulouse (MITT)

Unité de recherche :

Laboratoire de Télécommunications (TELECOM) de l'ENAC

Directeur(s) de Thèse :

M. CHRISTOPHE MACABIAU

MME ANAÏS MARTINEAU

Rapporteurs :

M. BERND EISSFELLER, UNIVERSITE FAF MUNICH

M. MICHAEL BRAASCH, OHIO UNIVERSITY ATHENS

Membre(s) du jury :

M. EMMANUEL DUFLOS, ECOLE CENTRALE DE LILLE, Président

M. CHRISTOPHE MACABIAU, ECOLE NATIONALE DE L'AVIATION CIVILE, Membre

M. LAURENT AZOULAI, AIRBUS FRANCE, Membre

Mme ANAÏS MARTINEAU, ECOLE NATIONALE DE L'AVIATION CIVILE, Membre

ACKNOWLEDGMENTS

This work has been carried out in the GNSS and Signal Processing Group of the TELECOM Lab at the ENAC. I acknowledge ANRT and Airbus for funding this thesis.

I am grateful to Bernd Eissfeller and Michael. S. Braasch for accepting to review the thesis, and to Emmanuel Duflos for accepting to be part of the jury. Thank you for the interest you have shown in my thesis, for your comments and advices on the manuscript, and of course for coming to my Ph.D. defense.

I would like to thank my ENAC thesis directors: Christophe Macabiau, Carl Milner, Anaïs Martineau, Alexandre Chabory for their advices all along this work and for the technical discussions. Thank you to Alexandre for the technical support on EM. I would like to warmly acknowledge Carl for his constant support and enthusiasm during these last two years, for his availability even during the busy days, and for the time he spent on my papers and on my manuscript.

I am also very grateful to Laurent Azoulai, my Airbus supervisor, for his involvement in my project, for the technical and operational advices, and for his constant support all along my thesis. I acknowledge Adrien Chen for the technical support on the multipath error modeling part and Pierre Néri for his help. Thank you also to Sandra Poussin and Geneviève Oudart for the opportunity to do my Ph.D. for Airbus, and to Laetitia Olivier and Michel Bovet for their encouragement and for the interest they showed in the project. I acknowledge the Airbus radio-navigation team EYAN3 for the good atmosphere and for the good time we spent in Ax-les-Thermes.

Several ENAC students have also been involved in the thesis. Thank you to Ma Long for the 3D model of Blagnac airport, Quentin Tessier for his important help concerning the ION GNSS 2012 paper, Christophe Charbonnieras and Thomas Longo for their work on new GPS and Galileo signals, Antoine Plainard for his contribution concerning the simulation results proposed in this manuscript, the Master GNSS 2013 students for their work on the validity of the 3D model of Toulouse Blagnac.

I am very grateful to the ENAC SIGNAV and EMA labs. I would specially thank Jérémy Vézinet for all the technical discussions and for his constant help on the Kalman filtering. I acknowledge Olivier Julien, Anne-Christine Escher, Lina Deambrogio, Daniel Salos, Myriam Foucras, Philippe Brocard for their support on hybridization, integrity, maths, signal processing. Thank you so much to my ENAC/Supaero/ENSICA friends for all the memories in Nashville, for the bowling matches in Balma, for the restaurants in Toulouse, for the “pantagruélique” dinner in Saint Orens, and of course for the moral support during the thesis:

thank you to Myriam, Lina, Amani, Alizé, Philippe, Paulo, Seb Carca, Seb Roche, Jérem, Jérôme, ...

I warmly acknowledge the Imajing team. Thank you to Etienne Lamort de Gail for his support and for the advices concerning the defense, thank you to my new colleagues for the very good atmosphere that helped me to relax for the defense: Yvonnic, Marie-Anne, Bruno, Quentin...

Finally, thank you so much to my parents and to my sisters for their listening and for their moral support all along the thesis. I acknowledge the rest of my family and my friends for the good times we spent together. Thank you to Seb R. for his Patience and constant encouragement and during this last year.

ABSTRACT

Global Navigation Satellite Systems (GNSSs) are currently used in civil aviation to provide aircraft with position and velocity estimates from en-route to Precision Approach (PA) operations. GNSSs are also used during surface operations for the position awareness. The taxi operation consists in three sub-phases: the *taxi on taxiway*, the taxi on *apron taxiway* and the *taxi on taxi lane* (gate phase) sub-phases. The position awareness function requires a visual check of the airport environment by pilots. Extending the use of GNSS to the guidance function during airport surface operations and under zero-visibility conditions remains a challenge. Indeed, during these operations, GNSS measurements may be affected by GNSS singular events, such as multipath or ionosphere anomalies. GNSS singular events may lead to unacceptable position errors in terms of accuracy and integrity for the zero-visibility guidance function. Current GNSS integrity monitoring systems are not designed to totally account for the GNSS singular event effects. The assessment of the GNSS singular event effects on the accuracy and integrity of GNSS-based airport surface navigation systems and the development of GNSS mitigation and integrity monitoring systems designed to properly protect users from the singular event effects are thus essential.

GNSS measurement error and integrity failure models are key inputs in the design of GNSS integrity monitoring systems. In this thesis, work has been mainly focused on the modelling of GNSS multipath measurement errors, on the assessment of the multipath impact on the GNSS-based position error, and on the development of GNSS multipath integrity failure models.

For this matter, the dual frequency GPSL1C+GPSL5 and GalileoE1+GalileoE5a multipath pseudo-range error model adapted to airport navigation has been proposed, when the aircraft is parked or is moving in the airport environment. Three multipath sources are considered in this thesis: the airport surface, the aircraft structure and the airport buildings and gates. The multipath ranging error is modelled as the sum of a deterministic bias (induced by the aircraft structure itself and the airport surface) and of a stochastic error (induced by the airport obstacles).

Next, the analysis of the impact of multipath on the GNSS-based position error has been proposed. The first step consists in choosing a GNSS-based positioning algorithm suitable for the zero-visibility airport guidance application. A double constellation Global Positioning System (GPS)+Galileo/Inertial Reference System (IRS)/Digital Elevation Map (DEM) tight coupling algorithm based on a linearized Kalman filter has been selected. The horizontal position error at the output of this positioning algorithm can be over-bounded by a bi-dimensional Gaussian distribution characterized by a bias vector and by a covariance matrix. Secondly, the theoretical analysis of the impact of the GNSS deterministic multipath ranging errors on the horizontal position bias and of the GNSS multipath stochastic ranging errors on the covariance matrix of the horizontal position error are assessed. The third step is the quantification by simulations of the multipath impact on both horizontal position bias and

covariance matrix along with the assessment of the accuracy performance of the positioning algorithm in the presence of multipath throughout a given taxi procedure path at Toulouse Blagnac airport, France.

The results associated with the proposed position error models are as follows. The deterministic multipath ranging errors are dependent on the elevation mask angles and induce a horizontal position bias equal to a few centimeters up to a few decimeters. Moreover, the presence of a stochastic multipath error on a single GNSS measurement induces an inflation of the covariance matrix of the horizontal position error of a few millimeters up to a few centimeters, depending on the stochastic parameters (standard deviation, correlation time) that characterize the stochastic multipath ranging error. From the accuracy analysis, the positioning algorithm is not suitable for the *taxi on taxi lane* phase (gate operations).

Finally, a GNSS multipath integrity failure model has been proposed for both *taxiway* and *apron* operations along a given procedure path at Blagnac airport. The developed failure model describes the characteristics in terms of standard deviation and correlation time of the GNSS single multipath ranging failures, the occurrence model of the GNSS single multipath ranging failures and their conditions of occurrence. Under the assumptions stated in the thesis, and particularly in the absence of mobile obstacles in the scene, such as other parked aircraft, GNSS single ranging failures do not occur during both *taxiway* and *apron* operations along the considered procedure path at Blagnac airport.

RESUME

Les systèmes de navigation par satellites (GNSS) sont actuellement utilisés en aviation civile pour estimer la position et la vitesse des avions pour les opérations en-route jusqu'aux approches de précison. Les systèmes GNSS sont également utilisés pendant les opérations de surface pour la fonction « position awareness ». Les opérations de surface regroupent trois sous-phases, qui sont la phase de « *taxi on taxiway* », la phase de « *taxi on apron taxiway* » et la phase de « *taxi on taxilane* ». La fonction « position awareness » oblige les pilotes à effectuer une vérification visuelle de l'environnement aéroportuaire. L'utilisation des systèmes GNSS pour guider l'avion pendant les opérations de surface et dans les conditions de zéro-visibilité reste un challenge pour la communauté aviation civile. En effet, durant les opérations de surface, les mesures GNSS peuvent être affectées par des évènements singuliers GNSS, tels que les multi trajets ou les anomalies ionosphériques. Les évènements singuliers GNSS peuvent engendrer des erreurs de positionnement jugées inacceptables en termes de précision et d'intégrité pour la fonction de guidage de l'avion en environnement aéroportuaire et sous les conditions de zéro-visibilité. Les systèmes de contrôle d'intégrité GNSS utilisés actuellement ne sont pas conçus pour prendre en compte les effets de tels évènements singuliers. L'analyse des effets des évènements singuliers sur la précision et sur l'intégrité des systèmes de navigation aéroportuaires basés sur les systèmes GNSS et le développement de systèmes de contrôle d'intégrité GNSS conçus pour protéger les utilisateurs des évènements singuliers GNSS sont donc essentiels.

Les modèles d'erreurs de mesures GNSS et les modèles de pannes sont essentiels pour la conception de systèmes de contrôle d'intégrité GNSS. Dans cette thèse, les travaux se sont principalement focalisés sur la modélisation des erreurs de mesures GNSS dues aux multi trajets, sur l'analyse de l'impact des multi trajets sur l'erreur de positionnement, et sur le développement d'un modèle de pannes multi trajets.

Pour cela, les modèles d'erreurs multi trajets sur les pseudo-distances GNSS bi-fréquence GPSL1C+GPSL5 et GalileoE1OS+GalileoE5a sont proposés. Ces modèles sont adaptées au cas où l'avion est statique dans l'environnement aéroportuaire, et au cas où l'avion se déplace dans l'environnement aéroportuaire. Trois sources de multi trajets sont considérées dans la thèse : la surface de l'aéroport, la structure de l'avion sur lequel est monté l'antenne GNSS, et les bâtiments de l'aéroport. L'erreur multi trajets est modélisée comme la somme d'un biais déterministe (induit par la structure de l'avion et la surface de l'aéroport), et une erreur stochastique (induite par les bâtiments de l'aéroport).

Ensuite, l'analyse de l'impact des multi trajets sur l'erreur de positionnement est proposée. La première étape consiste à choisir l'algorithme de positionnement GNSS adapté à la fonction de guidage des avions dans un environnement aéroportuaire et sous les conditions de zéro-visibilité. Un algorithme double constellations Global Positioning System (GPS) + Galileo / Inertial Référence System (IRS) / Digital Elevation Map (DEM) basé sur un filtrage de Kalman linéarisé a été sélectionné. La deuxième étape consiste à analyser l'impact des multi

trajets sur la position horizontale estimée en sortie du filtre de Kalman. L'erreur de position horizontale en sortie de filtre de Kalman peut être modélisée comme une distribution Gaussienne bidimensionnelle caractérisée par un biais et par une matrice de covariance. L'impact des erreurs multi trajets sur le biais et sur la matrice de covariance de l'erreur de position horizontale est analysé de manière qualitative. La troisième étape est la quantification pas simulations de l'impact des multi trajets sur le biais et sur la matrice de covariance de l'erreur de position horizontale, ainsi que l'étude de la performance de l'algorithme de positionnement en termes de précision le long d'une procédure de taxi sur l'aéroport de Toulouse Blagnac, en France.

Les résultats associés à l'analyse de l'impact des multi trajets sur l'erreur de positionnement sont les suivants. La partie déterministe de l'erreur multi trajets sur les mesures GNSS induit un biais sur la position horizontale estimée par le filtre de Kalman. Ce biais dans le domaine de la position est de quelques centimètres et peut atteindre quelques décimètres. De plus, la partie stochastique de l'erreur multi trajets sur les mesures GNSS induit une inflation de la matrice de covariance de l'erreur de position horizontale en sortie de filtre de Kalman. Cette inflation peut atteindre quelques centimètres en écart type, et dépendant des caractéristiques (écart type, temps de corrélation) de l'erreur stochastique de multi trajets sur les mesures GNSS. Concernant les performances de l'algorithme de positionnement en termes de précision, l'algorithme sélectionné n'est pas adapté à la phase « *taxi on taxi lane* ».

Finalement, un modèle de pannes multi trajets est proposé pour les sous phase de « *taxi on taxiway* » et de « *taxi on apron taxiway* ». Le modèle de pannes développé décrit les caractéristiques des pannes simples multi trajets en termes d'écart type et de temps de corrélation, le modèle d'occurrence des pannes simples multi trajets, ainsi que les conditions d'occurrence de telles pannes. En tenant compte des hypothèses décrites dans la thèse, et particulièrement en l'absence d'obstacles mobiles dans la scène aéroportuaire, les pannes simples multi trajets ne se produisent pas le long des phases de « *taxi on taxiway* » et de « *taxi on apron taxiway* » sur la procédure de taxi sélectionnée dans l'aéroport de Toulouse Blagnac, en France.

TABLE OF CONTENTS

LIST OF FIGURES

LIST OF TABLES

CHAPTER 1

Introduction

1.1. Motivations

The constant growth of the traffic density in airports and the complex architecture of some airports induce operational errors during airport surface operations. As illustrations of operational errors there are runway incursions that may lead to aircraft collisions. The United States Federal Aviation Administration (FAA) has recorded a mean of 20 aircraft collisions a year [FAA, 2013], leading to FAA recommendations to mitigate the collision risks. Hence, there is a need to make the surface operations safer while maintaining the airport capacity under critical conditions that are:

- low visibility conditions,
- high traffic density conditions.

Therefore, advanced capabilities are needed to ensure safety and to maintain aerodrome capacity in all weather conditions. In order to provide these advanced capabilities, Surface Movement Guidance and Control Systems (SMGCSs) are developed. SMGCSs should be capable of assisting aircraft to maneuver safely and efficiently on the airport surface and should support four primary functions that are defined as follows [RTCA, 1999]:

- The **guidance** function provides guidance necessary for movements through clear and continuous indications allowing pilots or autopilots to maintain their positions on the intended routes and for situational awareness.
- The **surveillance** function captures the information on aircraft, vehicles, and objects within the coverage area and updates data needed for guidance and control.
- The **routing** function provides assignment of a route to individual aircraft, which provide safe and efficient movement for its current position to its intended final position.
- The **control** function provides a safe and efficient means of managing movements and planning for requested movements, detects conflicts/incursions and provides solutions.

Estimating the position of aircraft present in airport environments is of primary importance for both guidance and surveillance functions. It is thus required to design navigation systems that estimate aircraft positions during airport surface operations and that meet the performance requirements related to both guidance and surveillance functions in all visibility conditions. Since the guidance function requires higher requirements levels than the surveillance function, the main challenge for the civil aviation community is to develop a

navigation system that meets the performance requirements related to the guidance function in all visibility conditions. This thesis focuses on the guidance function.

Currently, some ASMGCs, such as the Onboard Airport Navigation System (OANS) developed by Thales and deployed on A380 Airbus aircraft, make use of GNSS to provide pilots with guidance information. The airport moving map and the route to follow are displayed on the navigation display during airport surface operations. However, this function, commonly called "position awareness", requires the pilots checking visually the airport environment during the surface operations. Hence, one of the main limitations of the position awareness is that it cannot be used under zero visibility conditions. There is currently a need to extend the use of the guidance function during airport surface operations to zero-visibility conditions. Under zero-visibility conditions, the guidance function will enable to perform automatic airport surface operations without any visual observations of the airport environments by the pilots. The performance requirements levels related to the navigation system for the guidance function under zero-visibility conditions are higher than those for the position awareness function. Indeed, the guidance function under zero-visibility conditions requires sub-meter level accuracy and integrity navigation system performance requirements, as discussed in Chapter 2. In comparison, the navigation system accuracy requirement for the OANS position awareness function is of the order of 20 meters. No integrity requirements are related to the position awareness function since the displayed moving maps will be correlated with an outside visual check. Finally, note that only notional values of the navigation system performance requirements are provided in this thesis for the position awareness function, since these requirements are protected by the Airbus copyrights.

GNSS is an excellent candidate to be part of the navigation system that will meet the stringent performance requirements related to the guidance function under zero-visibility conditions. There are two main reasons for this.

- Firstly, GNSS is currently used in civil aviation from en-route to precision approaches (CAT I). GNSS infrastructures to support en-route to CAT I operations can be used for airport surface operations. In addition, the civil aviation community has collected feedback and information concerning the operations and the performance of Global Positioning System (GPS). For both reasons, it is interesting to assess the feasibility of extending the use of GNSS to airport surface operations.
- Secondly, the Air Navigation Conference (ANC) in [ANC, 2003] underlines that one of the challenge of the civil aviation community is to use GNSS "from gate to gate". This implies extending the use of GNSS to surface operations. Regarding this guideline, extensive efforts concerning the enhancement of GNSS constellations, augmentation systems and signals used in civil aviation have been conducted during the last years. The improved constellations, augmentation systems and signals will be available by 2025. These improvements are expected to result in significant operational benefits [ANC, 2012]. Hence, it is interesting to assess the feasibility of extending the use of current and future GNSSs to airport surface operations.

The use of GNSS during airport surface operations under zero-visibility conditions raises issues since GNSS measurements may be affected by GNSS singular events during these operations. In this thesis, GNSS singular events are defined as events which effects on the GNSS measurements have not been totally taken into account in the design of current GNSS augmentation systems and that may lead to unacceptable position errors for the zero-visibility guidance function. Two main reasons explain why some singular events present in airport environments have not been totally taken into account in the design of current GNSS augmentation systems.

- Firstly, there is a lack of knowledge concerning some singular events that may affect GNSS measurements in airport environments. There are two reasons for this.
  - Some singular events occur rarely. A limited number of available observations concerning a singular event have been collected. In addition, the occurrence of some events, such as ionosphere anomalies, is difficult to predict since the physical phenomena inducing these events are not well-understood.
  - Some singular events, such as multipath inducing large measurement biases, are specific to the airport environments and are local phenomena. Their causes, occurrence and effects on the GNSS measurements and on the GNSS-based positioning errors have not been fully assessed since these singular events do not affect GNSS measurements for the operations that are currently covered by GNSS.
- Secondly, some singular events present in airport environments have not been totally taken into account in the design of current GNSS augmentation systems since they induce errors that are considered to be sufficiently low not to be considered for phases of flight currently covered by GNSS. However, these errors are significant for the guidance function during airport surface operations under zero-visibility conditions.

Six GNSS singular events are identified in airport environments:

- Space and ground segments failures inducing multiple GNSS ranging failures,
- Space and ground segments errors inducing nominal biases. Nominal biases on the GNSS measurements are nearly constant errors over the duration of the surface operation and are systematic errors. These biases are therefore addressed in the fault-free case and are not be assimilated to ranging failures.
- Group delay and phase center variations of the GNSS airborne antenna,
- Ionosphere anomalies,
- Intentional and unintentional interference,
- Multipath.

Among the singular events listed above, this thesis mainly focuses on multipath. Multipath is the reception of reflected or diffracted replicas of the desired signal [Kaplan *et al*., 2006] by the GNSS airborne antenna. For en-route to approach operations, the structure of the aircraft itself is the dominant source of multipath error. However, during surface operations, additional sources of multipath errors, such as other aircraft and buildings surrounding the GNSS airborne antenna, may affect the pseudo-range measurements [Chen, 2010]. This results in two main consequences. Firstly multipath replicas are one of the dominant contributors of errors for surface operations [Enge *et al*., 2010]. They may have a significant impact on the accuracy of the GNSS-based airport surface navigation system. Indeed, multipath may result in horizontal positioning errors of the order of a few meters [Braasch *et al*., 2000]. Secondly the standardized model used in current GNSS integrity monitoring algorithms from en-route to approach operations is not valid for taxi and parking operations. No multipath error model compliant with airport environments is currently standardized. Indeed, multipath errors during surface operations have not been fully assessed since this singular event does not affect GNSS measurements for the operations that are currently covered by GNSS. Hence, multipath in airport environments may affect the integrity of pseudo-range estimates.

In order to extend the use of GNSS to the guidance function under zero-visibility conditions during airport surface operations, it is necessary to assess the effects of multipath on the accuracy and integrity of GNSS-based airport surface navigation systems.

1.2. Objectives

The overall objective of this Ph.D. is to address the effects of singular events on the accuracy and integrity of GNSS-based airport surface navigation systems through modelling, with a special attention to multipath. The following research goals are distinguished:

1/ To review the causes, the effects and the occurrence of GNSS singular events in airport environments.

2/ To develop GNSS multipath measurement error models in an airport environment.

- To propose criteria for a representation of the 3D airport model that is suitable for the development of the GNSS multipath measurement error models.
- To assess the influence of the input parameters on the error models.

3/ To choose a GNSS-based positioning algorithm for the guidance function under zero-visibility conditions.

4/ To model the GNSS-based position error in the presence of multipath in airport environments.

- To model the impact of multipath on the GNSS-based position errors by taking into account the selected GNSS-based positioning algorithm.
- To assess the accuracy of the GNSS-based position error.

5/ To propose a methodology to identify:

- the GNSS multipath single ranging failures in airport environments,
- the occurence of such GNSS multipath ranging errors in airport environments.

1.3. Contributions

The contributions of this Ph.D. thesis are presented in this subsection.

1/ The impact of the six GNSS singular events identified in Section 1.1 on the accuracy and integrity of the GNSS-based airport surface navigation systems has been reviewed by means of a bibliographic study. Based on this study, the following singular events may have a significant impact on both accuracy and integrity of GNSS-based navigation systems for the zero-visibility airport surface guidance function:

- The space and ground segments errors inducing nominal biases as well as the group delay and phase center variations of the GNSS airborne antenna. Future Aircraft Based Augmentation System (ABAS) integrity monitoring systems will be designed to provide sufficient protection against these biases. Note that ABAS system is presented in Section 3.3.
- The space and ground segments failures inducing multiple GNSS ranging failures when Aircraft Based Augmentation System (ABAS) is used as the GNSS augmentation system.
- The Continuous Wave (CW) unintentional interference and the intentional interference.
- The ionosphere anomalies in the single frequency mode.
- The multipath.

Future multi-frequency GNSS navigation systems will mitigate the effects of the ionosphere anomalies. CW interference, intentional interference and multipath represent a threat in terms of accuracy and integrity for the application, regardless of the frequency mode and of the GNSS augmentation system. Multipath effects are further investigated in this Ph.D. thesis.

2/ GNSS multipath measurement error models have been developed for airport surface operations considering that the multipath sources in the airport environments are the airport

buildings and gates, the ground and the structure of the aircraft on which the GNSS antenna and receiver are mounted. The GNSS multipath measurement error can be modelled as the sum of:

- A deterministic error induced by multipath from the ground and from the aircraft structure.
- A zero-mean stochastic error induced by multipath from the airport buildings and gates. The stochastic nature of this error term comes from the uncertainties in the true aircraft positions along the procedure path followed by the aircraft during the surface operation. Simplifications can be done when representing the 3D model of the airport buildings and gates for the estimation of the stochastic error model parameters:
  - Isolated objects of size below 0.8m can be neglected [Chen, 2010].
  - Details in the range of the wavelength do not have to be represented [Ait Ighli, 2013].
  - Concrete sub-meter recesses and overhangs on concrete facades do not have to be represented.

3/ GNSS position error models have been developed for airport surface operations in the presence of multipath. For this analysis:

- A positioning algorithm based on a GNSS/IRS/DEM tight coupling linearized Kalman filter has been chosen to support the zero-visibility guidance function during surface operations.
- The analytical expressions of the impact of multipath on the bias and covariance matrix of the horizontal position error at the output of the positioning algorithm have been derived.

4/ The accuracy performance of the GNSS/IRS/DEM positioning algorithm during the *taxi on taxiway*, *taxi on apron taxiway*, and *taxi on taxi lane* sub-phases of a specific procedure path at Toulouse Blagnac airport, France, has been assessed. More specifically, *taxi on taxi lane* sub-phases is performed when the aircraft is moving under its own power in the gate area. At this occasion, it has been shown that:

- GPS/Galileo elevation mask angle of 15°/15° improves the accuracy performance compared to the standard elevation mask angle of 5°/10°
- The positioning algorithm does not meet the accuracy performance requirement for the zero-visibility guidance function during the *taxi on taxi lane* sub-phase.
- A positioning algorithm based on a GNSS/IRS/DEM/Wheel Speed Sensor (WSS) tight coupling Kalman filter has been implemented to test if this implementation enables meeting the accuracy requirements of the *taxi lane* sub-phase. This implementation does not account for the WSS correlation modes in the time domain and between the wheels. The aid of WSS measurements reduces the standard deviation of the horizontal position error in the longitudinal direction. However, this aid is insufficient to reach the accuracy requirements of the *taxi lane* sub-phase.

5/ A methodology to model the characteristics (standard deviation, correlation time) and the occurrence of GNSS single multipath ranging failures in a given airport environments and over a given procedure path has been developed.

1.4. Thesis outline

This sub-section presents the general organization of this thesis.

Chapter 2 is an overview of the different navigation performance requirements developed in civil aviation. Firstly, it defines the different phases of flight with a special attention to the taxi operation. The taxi operation consists in several sub-phases. Each taxi sub-phase is presented and defined. Secondly, the navigation performance requirements allocation is described. Thirdly, the navigation system performance requirements for the guidance function

under zero-visibility conditions and for the taxi sub-phases are presented and discussed. These requirements are compared to the Signal-In-Space (SIS) navigation performance requirements that have been standardized for en-route to PA operations.

Chapter 3 presents the current and future GNSS constellations, signals and augmentation systems as well as the different GNSS measurements errors in both nominal and faulty conditions. GNSS signals and constellations are firstly reviewed. The GNSS constellations and signals suitable for the application are selected by taken into account the civil aviation context and the performance requirements for the application. Next, the GNSS nominal and faulty measurement error models are presented and discussed. The choice to treat multipath as a priority is justified. Finally, GNSS augmentation systems are reviewed. The choice of ABAS as the augmentation system that will support the guidance function is also justified.

Chapter 4 presents the impact of multipath on the GNSS measurements. Firstly, the different stages of the transmission channel model are defined and described. The impact of multipath on the GNSS signals received by the GNSS airborne antenna is analyzed. Secondly, the impact of multipath on the code tracking loops of the GNSS receiver and on the GNSS code measurements are assessed.

Chapter 5 proposes GNSS multipath measurement error models for the *taxi on taxiway*, *taxi on apron taxiway* and *taxi on taxi lane* sub-phases. Firstly, the GNSS multipath ranging error simulator used to derive the error models is presented. The assumptions and simplifications that have been done when developing the GNSS multipath error models are presented and discussed. Secondly, the static and dynamic configurations concepts are defined. Thirdly, the GNSS multipath error models are developed in both static and dynamic configurations. The impact of the input parameters on the error models is discussed.

Chapter 6 proposes a GNSS-based positioning algorithm suitable for the guidance function application during surface operations. Firstly, the Position Velocity Time (PVT) estimation techniques are reviewed. A PVT technique based on the integration of GNSS with other sensors is chosen based on the performance requirements for the application. Drawbacks and advantages of several navigation sensors and signals of opportunity are discussed. The navigation sensors that are integrated with GNSS are identified. After that, the coupling strategies are briefly reviewed and the open-loop GNSS/IRS/DEM tight coupling linearized Kalman filter architecture is selected. Finally, the architecture of the software that simulates the GNSS-based position error at the output of this tight coupling Kalman filter is presented. Limitations of this software are underlined.

Chapter 7 analyses the impact of multipath on the GNSS-based position error and assesses the accuracy performance of the positioning algorithm during surface operations. Firstly, the impact of the GNSS multipath measurement errors on the bias and on the covariance matrix of the horizontal GNSS-based positioning error at the output of the positioning algorithm described in Chapter 6 is assessed through a theoretical analysis. Next, the position bias induced by multipath and the increase of the covariance matrix induced by multipath are quantified by simulations. Finally, the horizontal position error model adapted to surface operations is proposed and the accuracy of the positioning algorithm presented in Chapter 6 is assessed. The impact of the satellite elevation mask angle on the accuracy performance is discussed.

Chapter 8 proposes a methodology to develop a GNSS multipath integrity failure model in airport environments. Firstly, the importance to develop integrity failure models for the design of a GNSS integrity monitoring system is shown. Secondly, GNSS multipath single ranging failures are defined. A methodology to identify the characteristics (standard deviation,

correlation time) of the GNSS multipath single ranging failures in a given airport is developed. Thirdly, a methodology to model the occurrence of such failures is proposed.

Chapter 9 presents the main results and the conclusions of this thesis. Recommendations for future work are also presented.

CHAPTER 2

Civil aviation requirements

GNSS can be used as a Navigation aid (Navaid) if GNSS can support the operational requirements established by the standardization bodies for both in-flight and surface operations. The highest global authority on aviation standardization is the International Civil Aviation Organization (ICAO), an agency of the United Nations, whose aim is to develop a global civil aviation system that consistently and uniformly operates at peak efficiency and provides optimum safety, security and sustainability [ICAO, 2013]. ICAO is responsible for establishing the Standards And Recommended Practices (SARPs) concerning air navigation. In particular, Volume 1 of Annex 10 defines the standards and the SIS navigation performance requirements for radio-navigation aids, including GNSS [ICAO, 2006].

The Minimum Operational Performance Standards (MOPSs) for GPS and Galileo airborne receivers are developed by the Radio Technical Commission for Aeronautics (RTCA) and by the European Organization for Civil Aviation Equipment (EUROCAE) bodies, respectively. RTCA and EUROCAE gather together administrations, aircraft manufacturers, equipment manufacturers and service providers. The RTCA SC-159 working group develops minimum standards that form the basis for FAA approval of equipment using GPS as a primary means of civil aircraft navigation. In Europe, EUROCAE WG-62 working group is responsible for the preparation of minimum standards for the first generation of Galileo airborne receivers. The use of dual constellation (Galileo+GPS) receivers will be standardized jointly by EUROCAE and RTCA in a future MOPS.

The main intent of this chapter is to present and to discuss the navigation system performance criteria for the zero-visibility guidance function during taxi operations. This chapter firstly defines the different phases of flight with a special attention to taxi phases, the navigation system performance concept and the navigation system performance criteria. Next, the chapter presents and discusses the navigation system performance requirements for the taxi operations proposed in [Schuster *et al*., 2011]. It also compares the requirements to the signal-in-space performance requirements for En-route to CAT I operations established in the ICAO SARPs. Finally, the accuracy and integrity requirements proposed in [Schuster *et al*., 2011] are modified and relaxed to account for les flight technical error budget guaranteed by Airbus.

2.1. Phases of flight definitions

A flight begins when any person boards the aircraft with the intention of flight and continues until such time as all such persons have disembarked [ICAO, 2001]. A flight consists of several phases of flight. In this document, a phase of flight refers to a period within a flight. This section presents and defines the different phases of flight.

2.1.1. Definitions

The ICAO and the Commercial Aviation Safety Team (CAST) have jointly defined the different phases of flight [ICAO-CAST, 2010]. The CAST body is independent of ICAO and includes experts from several air carriers, aircraft manufacturers, engine manufacturers, pilot associations, regulatory authorities, transportation safety boards. The different phases of flight are listed and defined below:

- **Standing:** "Prior to pushback or taxi, or after arrival, at the gate, ramp, or parking area, while the aircraft is stationary".
- **Pushback/Towing:** "Aircraft is moving in the gate, ramp, or parking area, assisted by a tow vehicle".
- **Taxi:** "The aircraft is moving on the aerodrome surface under its own power prior to takeoff or after landing". The taxi phase includes the following sub-phases:
  - Power Back (for departure): "Takes place when the aircraft, under its own power, reverses from the stand or parking position".
  - Taxi to Runway (for departure): "Commences when the aircraft begins to move under its own power leaving the gate, ramp, apron, or parking area, and terminates upon reaching the runway".
  - Taxi to Takeoff Position (for departure): "From entering the runway until reaching the takeoff position".
  - Taxi from Runway (for arrival): "Begins upon exiting the landing runway and terminates upon arrival at the gate, ramp, apron, or parking area, when the aircraft ceases to move under its own power".
- **Takeoff:** "From the application of takeoff power, through rotation and to an altitude of 35 feet above runway elevation".
- **Departure (or initial climb):** "From the end of the takeoff sub-phase to the first prescribed power reduction, or until reaching 1000 feet above runway elevation or the Visual Flight Rules (VFR) pattern, whichever comes first".
- **En-route.** En-route operations are classified as follows:
  - The oceanic en-route phase covers operations over ocean areas generally characterized by low traffic density.
  - The continental en-route phase covers operations typically characterized by moderate to high traffic densities.
- **Approach.** The instrument approach phase includes the following sub-phases:
  - Initial approach: "That part of an instrument approach procedure between the initial approach fix and the intermediate approach fix",
  - Intermediate approach: "That part of an approach procedure between the intermediate approach fix and the final approach fix or point",
  - Final approach: "from the final approach fix to the beginning of the landing flare".
- **Landing:** "From the beginning of the landing flare until aircraft exits the landing runway, comes to a stop on the runway, or when power is applied for takeoff in the case of a touch-and-go landing".

Further details about approaches categories and taxi operations phases are presented in the next two sections.

2.1.2. Approach and landing operations categories

Instrument approach and landing operations are classified as follows [ICAO, 2010]:

- **Non-Precision Approach** (NPA) and landing operations: "An instrument approach and landing which utilizes lateral guidance but does not utilize vertical guidance".
- **Precision Approach** (PA) and landing operations: "An instrument approach and landing using precision lateral and vertical guidance with minima as determined by the category of operation". Three categories of precision approach and landing operations have been defined by the ICAO in [ICAO, 2010] and are denoted by CAT I, CAT II and CAT III operations.
- **Approach and landing Procedures with Vertical guidance** (APV): "An instrument approach and landing which utilizes lateral and vertical guidance but does not meet the requirements established for precision approach and landing operations". Two different classes of APV approaches can be identified depending on the method utilized to provide the vertical guidance [Escher, 2003]:
  - The first class is characterized by a GNSS lateral guidance and by a barometric vertical guidance. This approach is called APV Barometric Vertical Navigation (BARO-VNAV).
  - The second class is characterized by a GNSS lateral and vertical guidance. This class was introduced to avoid the limitations presented by the barometric vertical guidance in terms of accuracy and integrity failures. The terms APV-I and APV-II refer to two levels of GNSS approach and landing operations with vertical guidance [ICAO, 2006].

Categories of approach and landing operations are defined according to the level of confidence that can be placed by the pilot into the system he is using to help him land the plane safely. Approach and landing operations are divided in two main segments: the aircraft first follows the indication provided by the landing system, and then secondly the pilot takes over in the final part and controls the aircraft using visual outside information. When the reliability of the landing system increases, the height of the aircraft over the ground at which the pilot takes over the final part of the landing can be decreased [Macabiau, 1997]. Approach and landing operations are specified by a decision height and two visual requirements, the visibility and the runway visual range. The decision height, the visibility and the runway visual range are defined as follows:

- **Decision Height** (DH): A specified height in the precision approach or approach with vertical guidance at which a missed approach must be initiated if the required visual reference to continue the approach has not been established [ICAO, 2010b].
- **Visibility**: Visibility for aeronautical purposes is the greater of [ICAO, 2005]:
  - the greatest distance at which a black object of suitable dimensions, situated near the ground, can be seen and recognized when observed against a bright background,
  - the greatest distance at which lights of approximately 1000 candelas can be seen and identified against an unlit background.
- **Runway visual range** (RVR): The range over which the pilot of an aircraft on the centre line of a runway can see the runway surface markings or the lights delineating the runway or identifying its center line [ICAO, 2010b].

Table 2-1 presents the minimum values of the DH, the visibility and the RVR required for each type of approach and landing operations.

The DH for APV operations is set to 76m (250ft), except for Localizer Performance with Vertical Guidance – 200 (LPV-200) operations. LPV-200 is an instrument approach procedure in which guidance is provided down to a minimum DH as low as 200ft height above touchdown [Lee *et al.*, 2007].

Operation		DH requirement	Visual requirement
NPA		DH > 107m	Depending on the airport equipment
APV		DH > 76m (except for LPV-200)	
CAT I		DH > 60m	Visibility > 800m or RVR > 550m
CAT II		30m < DH < 60m	RVR > 300m
CAT III	**CAT IIIA**	0m < DH < 30m	RVR > 175m
	CAT IIIB	0m < DH < 15m	175m > RVR > 50m
	CAT IIIC	DH = 0m	RVR = 0m

Table 2-1: Minimum values of DH, visibility and RVR for approach and landing operations [ICAO, 2006]

2.1.3. Taxi operation and related functions

This section provides further details about the different phases of a taxi operation and presents the different functions that have been elaborated in order to help pilots maneuvering on the airport surface.

2.1.3.1. Airport areas, taxiways and runway

The different areas of an airport are detailed in this section. Taxi operations take place in the **movement area** of the aerodrome. The movement area is the part of an aerodrome to be used for the take-off, landing and taxiing of aircraft, consisting of [ICAO, 2009]:

- The **apron(s)** are the areas intended to accommodate aircraft for purposes of loading or unloading passengers, mail or cargo, fuelling, parking or maintenance. The **gate** is a designated area on an apron intended to be used for parking an aircraft.
- The **maneuvering area** is the part of an aerodrome to be used for the take-off, landing and taxiing of aircraft, excluding aprons.

During the push back, taxi to runway and taxi from runway sub-phases defined in Section 2.1.1, the aircraft is moving on **taxiways**. The taxiway is a defined path on a land aerodrome established for the taxiing of aircraft and intended to provide a link between one part of the aerodrome and another, including:

- The **taxi lane** is a portion of an apron intended to provide access to gates only [ICAO, 2009].
- The **apron taxiway** is a portion of a taxiway system located on an apron [ICAO, 2009].
- The **rapid exit taxiway** is a taxiway connected to a runway and designed to allow landing aeroplanes to turn off at higher speeds than are achieved on other exit taxiways thereby minimizing runway occupancy times [ICAO, 2009].
- The **normal taxiway**, also called **taxiway** in the following, is a portion of a taxiway system located in the maneuvering area and provides a link between the rapid exit taxiway or the runway and the apron taxiway.

During the taxi to takeoff position sub-phase defined in Section 2.1.1, the aircraft is moving on the **runway**. The runway a defined rectangular area on a land aerodrome prepared for the landing and take-off of aircraft [ICAO, 2009]. Parts of the aprons and the maneuvering area at Toulouse Blagnac airport, France, are depicted in Figure 2-1.

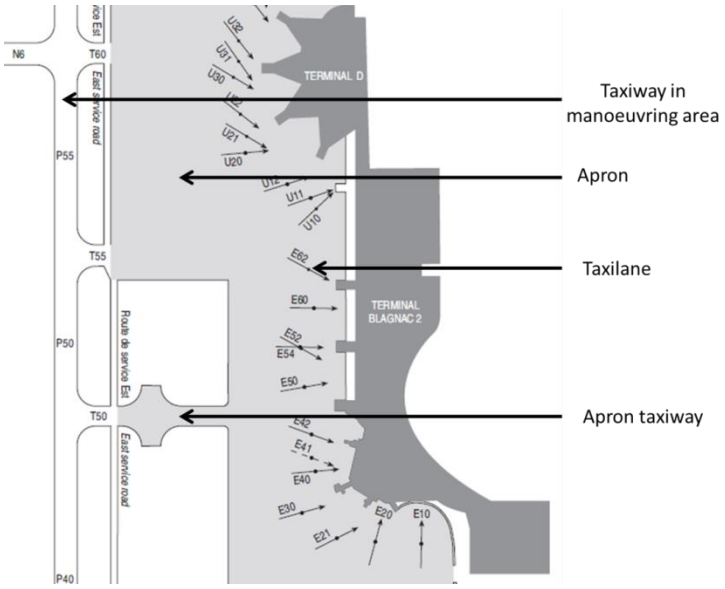

Figure 2-1 : Apron and maneuvering areas at Toulouse Blagnac airport [SIA, 2013]

2.1.3.2. Sub-phases

The taxi operation consists of the following sub-phases:

- The ***push back*** defined in Section 2.1.1,
- The ***taxi on taxi lane*** is performed when the aircraft is moving under its own power in the gate area on taxi lanes.
- The ***taxi on apron taxiway*** is performed when the aircraft is moving under its own power in the apron area on apron taxiways.
- The ***taxi on taxiway*** is performed when the aircraft is moving in the maneuvering area on taxiways.
- The ***taxi on runway*** is performed when the aircraft is moving in the maneuvering area on the runway.

Figure 2-2 represents the departure and arrival scenarios.

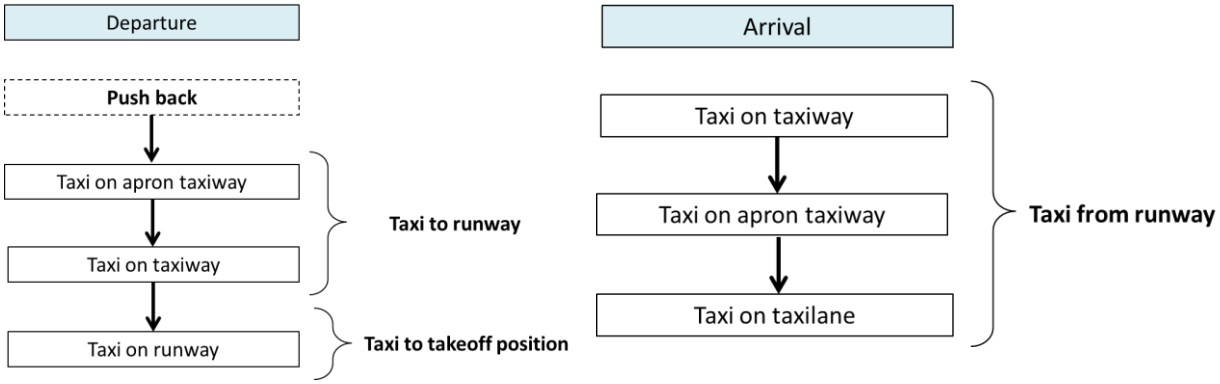

Figure 2-2: Departure and arrival taxi sub-phases

2.1.3.3. Functions

The different functions elaborated in order to help pilots maneuvering during surface movements are presented in this section. The number of accidents and incidents during taxi operations, including runway incursions, is increasing [ICAO, 2004]. Contributing factors include the increasing number of operations that take place in low visibility conditions and the progressive increase in traffic [ICAO, 2004]. Therefore, advanced capabilities are needed to ensure safety and to maintain aerodrome capacity in all weather conditions. In order to provide these advanced capabilities, SMGCSs are being developed. SMGCSs should be capable of assisting aircraft to maneuver safely and efficiently on the airport surface and should support four primary functions that are defined in Chapter 1.

In their simplest form, current SMGCSs rely on the "see and be seen" principle for supporting the surveillance and guidance functions. It means that the information necessary for the surveillance and the guidance functions are provided by the Air Traffic Control (ATC) based on a visual observation of the aircraft, vehicles and objects on the airport maneuvering and apron areas. The routing and control functions are facilitated through voice and data communications [RTCA, 1999].

Visual means are not adequate to maintain aerodrome capacity in low visibility conditions. Similarly, in high traffic density conditions, visual means lead to low capacity and delays since they require a human intervention to support the surveillance, routing, guidance and control functions. Since SMGCSs based on visual means are poor operationally, Advanced-SMGCSs (A-SMGCSs) are under development. As justified in Chapter 1, such advanced systems are intended to use technologies, such as GNSS, that will enable to maintain the aerodrome capacity in all visibility conditions. In addition, A-SMGCSs will limit the human intervention and will enable to limit the low capacity and delay issues encountered with SMGCSs based on visual means.

2.2. Requirements presentation

This section provides an overview of the different types of civil aviation requirements.

2.2.1. Total system performance requirements

In order to present the concept of total system performance requirements, it is firstly necessary to present the concepts of Area Navigation (RNAV) and of Performance Based Navigation (PBN).

The concept of Area Navigation (RNAV) is a method of navigation which permits aircraft operation on any desired flight path within the coverage of station-referenced navigation aids or within the limits of the capability of self-contained navigation aids, or a combination of these [RTCA, 2003]. RNAV procedures are not restricted to the location of ground-based navigation aids. RNAV operations are specified using one of the following approaches [Azoulai, 2009]:

- The sensor based approach. In this case, RNAV operations are based on a particular means of navigation, and it is mandatory to use this one.
- The performance based approach. In this case, RNAV operations are based on a set of performance requirements to be met. These requirements have not been developed for a specific navigation means. This approach refers to the Performance Based Navigation (PBN) concept. The PBN concept represents a shift from sensor-based to performance-based navigation.

PBN offers a number of advantages over sensor based approach [ICAO, 2008]. As an illustration, performance based approach avoids the need for developing sensor-specific operations with each new evolution of navigation systems, which would be cost-prohibitive.

According to [ICAO, 2008], the navigation performance requirements for RNAV operations specified by a performance based approach are defined in terms of accuracy, integrity, availability and continuity. These total system navigation requirements are specified for the Total System Error (TSE). TSE is represented in Figure 2-3.

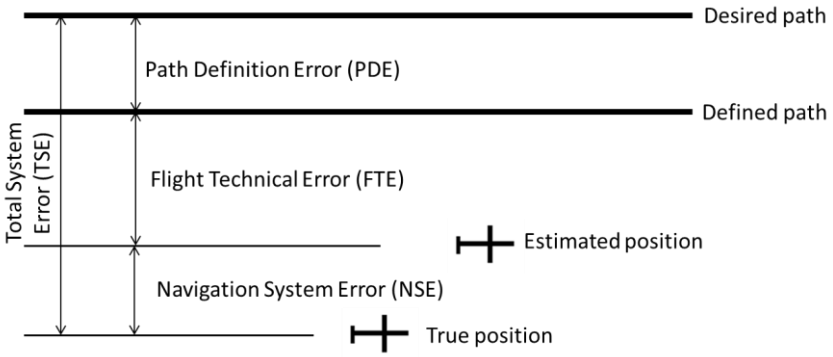

Figure 2-3 : Total System Error [ICAO, 2008]

The TSE is the difference between the true position and the desired position. This error is equal to the vector sum of [ICAO, 2008]:

- The **Path Definition Error** (PDE) PDE occurs when the path defined in the system does not correspond to the desired path, that is the path expected to be flown over the ground.
- The **Fight Technical Error** (FTE) relates to the air crew or autopilot's ability (steering system) to follow the defined path or track, including any display error.
- The **Navigation System Error** (NSE) refers to the difference between the aircraft's estimated position and actual position.

2.2.2. Navigation system performance requirements

The total system performance requirements on the TSE are allocated to the path definition unit, to the navigation system, and to the steering system. The overall strategy for this allocation is depicted in Figure 2-4. The navigation system performance requirements are defined as the total system performance requirements allocated to the navigation system and are expressed in terms of NSE. These requirements are defined by means of four criteria that are the accuracy, integrity, availability and continuity. Section 2.2.4 defines these four criteria.

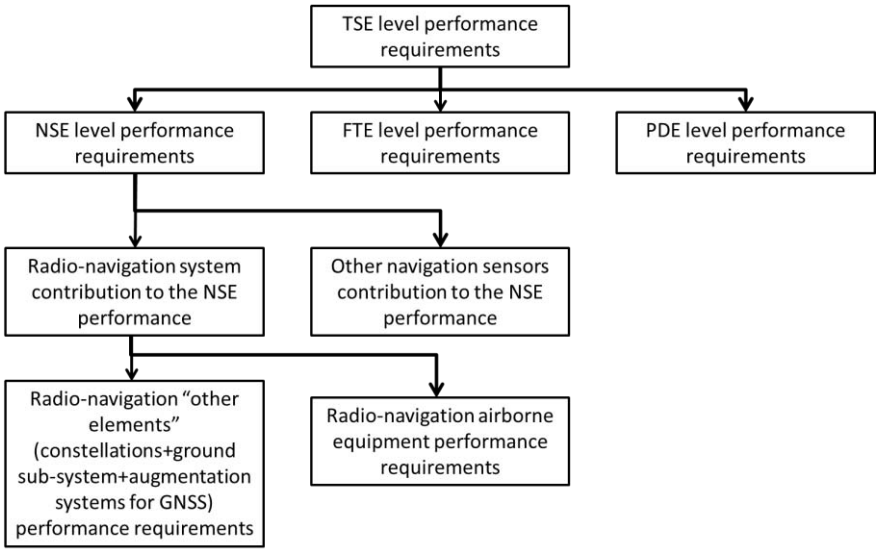

Figure 2-4: TSE requirements allocation

2.2.3. SIS navigation performance requirements

The navigation system used to support the operations that are currently standardized, that are the en-route to CAT I operations, may consist solely of a radio navigation system, or it may also include other aircraft sensors. The navigation system performance requirement is allocated to the radio-navigation system and to the other navigation sensors. As depicted in Figure 2-4, the radio-navigation system contribution to the NSE performance depends on:

- the airborne radio-navigation receiver,
- the other elements, defined in the case of GNSS as the GNSS constellation(s), the GNSS ground sub-system and augmentation system(s) used to estimate the aircraft position.

In the case of GNSS, the MOPS for GPS and Galileo airborne receivers are developed by the RTCA and by EUROCAE bodies, respectively.

ICAO develops SARPs for the other elements. More specifically, Volume 1 of ICAO Annex 10 [ICAO, 2006] defines the SIS navigation performance requirements for the radio-navigation aids, including GNSS. In the case of GNSS, GNSS can be used during a given operation if the GNSS constellation(s), the GNSS ground sub-system(s) and the augmentation system(s) combined with a fault-free receiver meets the SIS navigation performance requirements for that operation. The fault-free receiver is assumed to be a receiver with nominal accuracy and time-to-alert performance. Such a receiver is assumed to have no failures that affect the integrity, availability and continuity performance [ICAO, 2006].

Navigation system performance requirements and SIS navigation performance requirements are defined by means of four criteria that are the accuracy, integrity, availability and continuity. In the next section, the position error is the difference between the aircraft's estimated position and actual position.

2.2.4. Criteria

2.2.4.1. Accuracy

Accuracy characterizes the degree of conformance between the estimated or measured position and/or velocity of a platform at a given time and its true position and/or velocity [RTCA, 1991]. ICAO defines a 95% confidence level in order to characterize the accuracy of

the system. For an estimated position at a specific location, the probability that the position error is within the 95% confidence level should be at least 95% [ICAO, 2006].

Note that the accuracy of the position estimated by means of GNSS is impacted by the constellation configuration. Hence, this accuracy cannot be correctly assessed by averaging the position errors over different constellation configurations. In comparison, if the considered navigation system is the Instrument Landing System (ILS), the distribution of the position error can be considered to be the same over the time.

2.2.4.2. Integrity

Integrity is a measure of the trust that can be placed in the correctness of the information supplied by the total system. Integrity includes the ability of a system to provide timely and valid warnings to the user (alerts) when the system must not be used for the intended operation [ICAO, 2006]. Integrity is defined by three parameters:

- The **Integrity Risk** (IR) is the allowed probability of providing a position that is out of tolerance without warning the user within the time-to-alert [ICAO, 2006].
- The **Alert Limit** (AL) has been defined to ensure that the GNSS position error is acceptable and represents the largest position error allowable for a safe operation [ICAO, 2006]:
  - The Horizontal Alert Limit (HAL) is the radius of a circle in the horizontal plane (the local plane tangent to the WGS-84 ellipsoid), with its center being at the true position, that describes the region that is required to contain the indicated horizontal position with the required probability for a particular navigation mode,
  - The Vertical Alert Limit (VAL) is half the length of a segment on the vertical axis (perpendicular to the horizontal plane of WGS-84 ellipsoid), with its center being at the true position, that describes the region that is required to contain the indicated vertical position with the required probability for a particular navigation mode. Note that VALs are only defined for PA and APV operations.
- The **Time-To-Alert** (TTA) is the maximum allowable elapsed time from the onset of a positioning failure until the equipment annunciates the alert [RTCA, 2006].

In order to fully define the TTA, the definition of positioning failure is required. If the equipment is aware of the navigation mode/alert limit, a positioning failure is defined to occur whenever the difference between the true position and the estimated position exceeds the applicable AL (HAL Lateral Alert Limit (LAL) or VAL). Note that the concept of LAL is not detailed in this thesis. This concept is further developed in [RTCA, 2008c]. If the equipment is not aware of the navigation mode/alert limit, a positioning failure is defined to occur whenever the difference between the true position and the estimated position exceeds the applicable protection limit [RTCA, 2006].

2.2.4.3. Continuity

Continuity is defined as the ability of the total system (comprising all elements necessary to maintain aircraft position within the defined airspace) to perform its function without interruption during the intended operation. More specifically, continuity is the probability that the specified system performance will be maintained for the duration of a phase of operation, presuming that the system was available at the beginning of that phase of operation and was predicted to operate throughout the operation [RTCA, 2009].

2.2.4.4. Availability

The availability of a navigation system is defined as the ability of the system to provide the required function and performance at the initiation of the intended operation [RTCA, 2009]. The availability of GNSS is characterized by the portion of time the system is to be used for

navigation during which reliable navigation information is presented to the crew, autopilot, or other system managing the flight of the aircraft.

2.3. Navigation performance requirements

Section 2.2.2 has defined the concept of navigation system performance requirements and of SIS navigation performance requirement. This section provides the SIS navigation performance requirements that have been standardized by ICAO and the navigation system performance requirements that are currently under development.

2.3.1. ICAO SIS navigation performance requirements

Even if GNSS is expected to be used for all phases of flight, current SARPs established by ICAO provide SIS navigation performance requirements only for en-route, terminal, departure as well as for approach and landing operations down to Category I precision approach. In addition:

- GNSS SIS performance requirements for CAT II and III precision approach operations are under standardization. These requirements are not included in this document.
- Navigation system performance requirements for taxi operations are under review. Parts of the requirements that have been proposed in the literature are presented in Section 2.3.2.

Standardized GNSS SIS performance requirements are provided in Table 2-2.

From the Table 2-2, ranges of values are given for the continuity requirement for en-route, terminal, initial approach, NPA and departure operations. This requirement is dependent upon several factors including the intended operation, traffic density, complexity of airspace [ICAO, 2006]. The lower value is the minimum requirement for areas with low traffic density and airspace complexity. The higher value given is appropriate for areas with high traffic density and airspace complexity. A range of values is also given for the availability requirements as these requirements are dependent upon the operational need which is based upon several factors including the frequency of operations, weather environments, the size and duration of the outages. Further details about the use of availability requirements are developed in [ICAO, 2006].

	Accuracy		**Integrity**				**Continuity**	**Availability**
	Horizontal 95% confidence level	Vertical 95% confidence level	TTA	AL		IR		
				Horizontal	Vertical			
En-route	3.7 km	N/A	5 min	7.4km (*) 3.7km (**)	N/A	$1 - 1.10^{-7}$/h	$1\text{-}1.10^{-4}$/h to $1\text{-}1.10^{-8}$/h	0.99 to 0.99999
En-route, terminal	0.74 km	N/A	15 s	1.85 km	N/A	$1 - 1.10^{-7}$/h	$1\text{-}1.10^{-4}$/h to $1\text{-}1.10^{-8}$/h	0.99 to 0.99999
Initial approach, intermediate approach, NPA, departure	220.0 m	N/A	10 s	556.0 m	N/A	$1 - 1.10^{-7}$/h	$1\text{-}1.10^{-4}$/h to $1\text{-}1.10^{-8}$/h	0.99 to 0.99999
APV I	16.0 m	20.0m	10 s	40.0 m	50.0 m	$1 - 2.10^{-7}$/approach	$1\text{-}8.10^{-6}$ in any 15 s	0.99 to 0.99999
APV II	16.0 m	8.0m	6 s	40.0 m	20.0 m	$1 - 2.10^{-7}$/approach	$1\text{-}8.10^{-6}$ in any 15 s	0.99 to 0.99999
CAT I	16.0 m	6.0m to 4.0m	6 s	40.0 m	35.0m to 10.0m	$1 - 2.10^{-7}$/approach	$1\text{-}8.10^{-6}$ in any 15 s	0.99 to 0.99999

Table 2-2: SIS performance requirements [ICAO, 2006]

(*) for oceanic en-route or continental low density en-route

(**) for continental en-route

2.3.2. Navigation system performance requirements for taxi operation

As stated in Chapter 1, one of the objectives of this thesis is to define a navigation algorithm capable to provide an aircraft position estimate that is used by the aircraft infrastructure for the guidance purpose in all visibility conditions. Hence, this section focuses on the navigation performance requirements for the guidance function.

2.3.2.1. Existing requirements

Navigation system performance requirements for taxi operation and for the guidance function are under review. Among the publications dealing with these requirements, [RTCA, 1999] develops total system performance requirements in terms of accuracy, continuity, availability and integrity under all visibility conditions. This document also provides the navigation system performance requirements in terms of integrity, continuity and availability for the guidance function. The performance requirements in terms of accuracy for the *taxi on taxiway* and for the *taxi on apron taxiway* are also provided. However, the performance requirements in terms of accuracy for the *taxi on the taxi lane* sub-phase are to be determined. [Guilloton *et al*., 2011] provides navigation system performance requirements for the guidance function using the Functional Hazard Assessment (FHA) method [Wilkinson *et al*., 1998].

Schuster in [Schuster *et al*., 2011] uses the methodology developed in [RTCA, 1999] to elaborate the tolerable TSE for the guidance function and for the *taxi on the taxiway*, *taxi on the apron taxiway* and *taxi on the taxi lane* sub-phases. Next, Schuster in [Schuster *et al*., 2011] presents a complete set of navigation system performance requirements for each sub-phase in terms of accuracy, continuity, availability and integrity. Requirements proposed in this publication are adapted to the zero visibility conditions. The methodology to develop such requirements is presented in the next section.

2.3.2.2. Navigation system performance requirements for guidance

In this section, a requirements derivation methodology for the guidance function's NSE performance is presented [Schuster *et al*., 2011]. Requirements derived using this methodology and proposed in [Schuster *et al*., 2011] are also provided.

Navigation system performance requirements for taxi operation and for the guidance function requirements are derived for each airport category. Indeed, navigation performance requirements depend on the airport layouts [RTCA, 2009] [Schuster *et al*., 2011], such as the taxiway width or the distance between taxiway centerlines and any obstacle. Airports are classified into six categories, namely categories A to F [ICAO, 2009]. Airport categories are defined according to the size of the aircraft allowed to circulate on the airport. In this document, requirements for category F airports are presented. Category F airports corresponds to commercial airports and can support all types of aircraft, including A380 and B747.

Figure 2-5 depicts the general approach used for the derivation of the navigation system performance requirements in terms of accuracy and integrity. Further details about the derivation of continuity and availability requirements are provided in [Schuster *et al*., 2011].

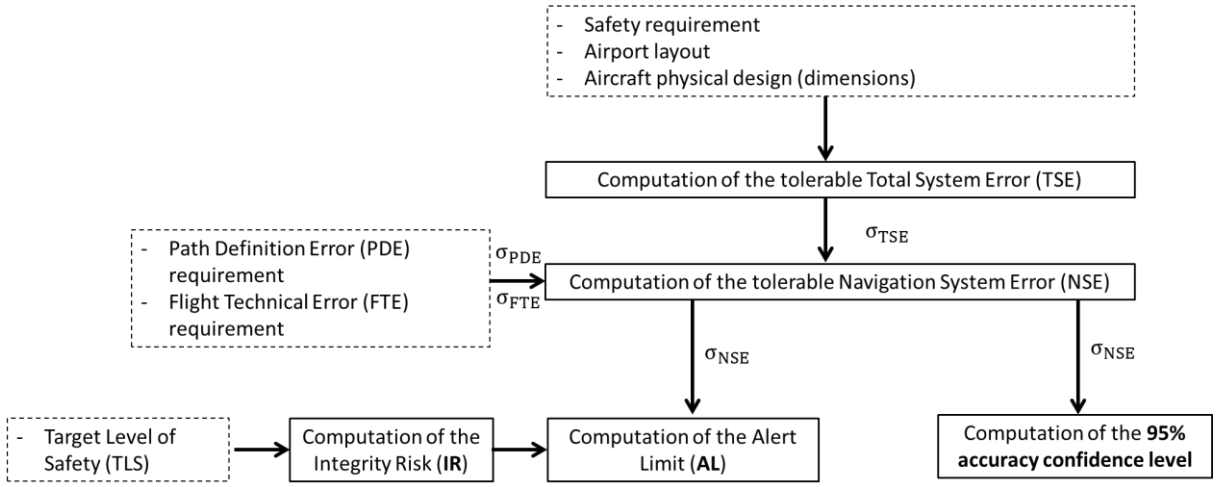

Figure 2-5 : Derivation of the navigation system performance requirements [Schuster *et al.*, 2011]

The approach used to develop accuracy and integrity navigation system performance requirements is based on basic safety considerations that are extrapolated from those for CAT IIIC precision approaches. From Section 2.1.2, both RVR and DH for CAT IIIC are set to 0m, corresponding to zero visibility conditions. For taxi phases, safety is expressed as the probability that the aircraft will accidently exceed the airport surface boundaries and/or collide with an airport obstacle. The safety requirement is set to 10^{-6} for each sub-phase, which corresponds to the maximum allowed probability of exceeding the lateral limits of the runway for the CAT IIIC operation [FAA, 1999].

The safety requirement is used in combination with the airport layout and aircraft dimensions to derive the tolerable TSE, which is considered as a Gaussian error with a standard deviation σ_{TSE}. The TSE is composed of the NSE, the PDE and the FTE which are considered as Gaussian errors in [Schuster *et al.*, 2011]. The tolerable NSE standard deviation σ_{NSE} is isolated based on:

- Assumptions on the PDE standard deviation denoted as σ_{PDE}. It is assumed that the overall system includes a map relating the position from the navigation unit to the physical position on the airport. The map uncertainties induce the PDE which is characterized by a standard deviation $\sigma_{PDE} = 0.25\text{m}$ [ICAO, 2009].
- Assumptions on the FTE standard deviation denoted as σ_{FTE} . The FTE relates to the air crew or autopilot's ability to follow the defined path or track, including any display error. An analysis based on real data during sub-phases leads to the σ_{FTE} values provided in Table 2-3.

	Taxi on taxiway	***Taxi on apron taxiway***	***Taxi on taxi lane***
σ_{FTE}	70cm	50cm	15cm

Table 2-3: FTE standard deviation values [Schuster *et al.*, 2011]

The IR for the specific sub-phase is then computed from the Target Level of Safety (TLS), which is the risk of fatal accident during the entire operation of an aircraft from the point it leaves the gate until it arrives at its destination. [Schuster *et al.*, 2011] allocates the total TLS attributed to the taxi operation to each taxi sub-phase. This allocation is made proportionally to the exposure time of each sub-phase. The exposure time is defined as the duration of a particular operation over which the integrity and continuity requirements are evaluated. These

are determined by computing the typical time the aircraft spent in each phase over several airports (see Table 2-5). This approach leads to an integrity risk for each sub-phase that is proportional to the exposure time of that sub-phase. Another approach would be to allocate the TLS regarding the statistics on the number of fatal accidents per sub-phase. Such statistics are provided by some organisms, such as the Flight Safety Foundation. Finally, the AL is computed based on the IR and on the tolerable NSE. In line with the most stringent requirements for Cat IIIC operations, a TTA of 1s is adopted.

The navigation system performance requirements for the guidance function under zero-visibility conditions for category F airports and during the *taxi on taxiway,* the *taxi on apron taxiway* and the *taxi on taxi lane* are provided in Table 2-4.

	Horizontal accuracy 95% confidence level	**Integrity**			**Continuity [/op]**	**Availability**
		TTA	IR [/op]	HAL		
Taxi on taxiway	1.3m	1s	$2.9.10^{-8}$	3.6m	$2.9.10^{-4}$	0.999 to 0.99999
Taxi on apron	0.5m	1s	$7.25.10^{-9}$	1.4m	$7.25.10^{-5}$	0.999 to 0.99999
Taxi on taxi lane	0.5m	1s	$7.25.10^{-9}$	1.4m	$7.25.10^{-5}$	0.999 to 0.99999

Table 2-4: Navigation system performance requirements – guidance function – category F airports [Schuster *et al*., 2011]

In Table 2-4, the risk of integrity or of continuity failure is evaluated over the duration of a particular operation. Exposure times for each sub-phase are provided in Table 2-5.

	Taxi on taxi lane	***Taxi on apron taxiway***	***Taxi on taxiway***
Exposure time	360s	90s	90s

Table 2-5: Surface exposure times [Schuster *et al*., 2011]

2.3.2.3. Performance requirements analysis

This section analyses the navigation system performance requirements presented in Section 2.3.2.2. These requirements are firstly compared to the most stringent requirements which are currently standardized, that are the requirements for CAT I operation. Secondly, the navigation system performance requirements related to the taxi operation are discussed and modifications concerning these requirements are proposed.

Firstly, the navigation system performance requirements for the guidance function under zero visibility are compared to SIS navigation performance requirements for CAT I operation presented in Section 2.3.1. In terms of accuracy, the horizontal 95% confidence levels range from a few decimeters to a few meters during the taxi operation, while confidence levels are few tens of meters during CAT I operation. In terms of integrity, the same conclusion can be made for HAL. The IR is roughly 100 times lower for taxi operation phases than for CAT I operation. To conclude, surface movement operations are much more stringent in terms of accuracy and integrity than CAT I operation. In terms of continuity, the requirements are relaxed compared to the CAT I approach. The requirement for the taxi phases is roughly 10

times less stringent for the taxi phases than for CAT I approach. Indeed, and unlike in precision approaches, there is a reduced safety risk associated by a loss of continuity in taxi operations. If a loss of continuity occurs, the aircraft will stop in the airport, and the collision risk can be mitigated by the Air Traffic Control (ATC). Even is a loss of continuity does not lead to a safety issue, it has been chosen to conserve a relatively stringent continuity requirement for taxi operations, since a loss of continuity can lead to Air Traffic Management (ATM) issues, such as a limitation of the airport capacity during several hours.

Secondly, assumptions made to derive performance requirements for the guidance function under zero visibility are discussed. The FTE values used in the computation of the accuracy requirements and of the HAL seem to be conservative. Indeed, under low visibility conditions, the autopilot is likely to be used to pilot the aircraft. When the autopilot is used to pilot the aircraft, the FTE can be neglected during straight lines and $\sigma_{FTE} = 25\text{cm}$ during turns for *taxi and taxiway* and *taxi on apron taxiway* sub-phases [Airbus, 2014]. In order to be conservative, a value of $\sigma_{FTE} = 25\text{cm}$ is assumed *for taxi and taxiway* and *taxi on apron taxiway* sub-phases. This value is adopted in this thesis since it is assumed that the autopilot is used for the taxi operation. Note that, if the pilot is assumed to drive the aircraft, the FTE shall be increased, leading to reduce the HAL and the accuracy confidence level related to the navigation system performance requirements. The FTE value of the *taxi on taxi lane* is retained. It appears also likely that the FTE value is reduced when the aircraft speed is reduced. The methodology presented in Section 2.3.2.2 is reused in Table 2-6 to derive the accuracy navigation system performance requirements and the HAL for both *taxi on taxiway* and *taxi on apron taxiway* sub-phases with the updated values of σ_{FTE}.

	Horizontal accuracy 95% confidence level	**HAL**
Taxi on taxiway	1.9m	5.2m
Taxi on apron	1.0m	2.9m

Table 2-6: Updated navigation system performance requirements – guidance function – category F airports

From Table 2-6, using a slightly less conservative value of FTE compared to the values presented in Section 2.3.2.2 allows increasing the horizontal 95% confidence level and the HAL. This is because the maximal allowable σ_{NSE} value is increased when σ_{FTE} is decreased. As an example, for the apron sub-phase, both accuracy level and HAL are multiplied by a factor 2 with the reduced σ_{FTE}.

Other requirement parameters are not modified by adopting a reduced σ_{FTE}. The TTA and the IR are stringent compared to the TTA and IR standardized for the other in-flight operations. The IR is of the order of $10^{-9}/\text{op}$ for every sub-phase. Considering this values, the produced effect of an integrity loss (undetected positioning failure within the TTA) is considered as catastrophic regardless of the sub-phase. This means that the integrity loss may lead to the aircraft loss. Some modifications can be suggested in order to review, and possibly to decrease, the proposed IR values. Indeed, the IR values stated in Table 2-4 have not been designed to take into account the produced effects of an integrity loss during each sub-phase. The produced effects of a loss of integrity depend on the aircraft speed, on the type of obstacles in which the aircraft may collide [Guilloton *et al*., 2011]. Hence, the effects depend on the sub-phase. Approaches, such as the FHA based approaches, allows deriving IR that depends on the safety criticality (minor, major, hazardous, and catastrophic) associated to

each integrity loss. Hence, it can be suggested to review the IR level by taken into account the produced effects of the integrity loss for each sub-phase. Nevertheless, in this thesis, the requirements stated in Table 2-4 (values in brackets for the accuracy requirements and for the HAL values) are adopted. They appear to be stringent compared to the values that would have been obtained with the FHA approach.

2.4. Conclusions

This chapter has provided the definition of each in-flight and surface operation. More specifically, this chapter has focused on taxi operations that include three sub-phases as defined by ICAO [ICAO, 2009]: the *taxi on taxiway*, the *taxi on apron taxiway* and the *taxi on taxi lane*. In order to ensure safety and to maintain aerodrome capacity in all weather conditions, A-SMGCSs are developed to support four primary functions that are surveillance, routing, guidance and control. Publications presenting the guidance navigation performance requirements under zero-visibility conditions for *taxi on taxiway*, *taxi on apron taxiway* and *taxi on taxi lane* have been reviewed. New accuracy and integrity performance requirements for *taxi on taxiway* and *taxi on apron taxiway* have been derived by accounting for less conservative assumptions on the FTE than the values used in the existing publications. Finally, further modifications that have not been done in this thesis concerning these new requirements are advised.

CHAPTER 3

GNSS signals, measurement models and augmentation systems

As described in Chapter 1, one of the challenges for the civil aviation community is to support the guidance function navigation system performance requirements during the taxi operation under low visibility conditions. In this context, A-SMGCSs are under development and are intended to use technologies that enable to maintain aerodrome capacity under high traffic density conditions and/or under low visibility conditions. GNSS appears to be an adequate technology to be used in A-SMGCSs.

One objective of the thesis is to develop a GNSS-based navigation algorithm capable of supporting the guidance function navigation system performance requirements during the taxi operation under low visibility conditions. The structure of this algorithm is presented in Chapter 6. In order to develop such an algorithm and to assess the performance of the algorithm, it is firstly essential to:

- select the GNSS constellation(s), the GNSS signal(s) and the GNSS augmentation system that will be considered for the design of the algorithm.
- review the models of the GNSS errors that may affect GNSS pseudo-range measurements during taxi operations in both nominal and degraded conditions.

This chapter is organized as follows. Section 3.1 reviews the GNSS constellations and the GNSS signals and selects the constellations and signals retained for the application. Section 3.2 presents the GNSS measurement error models in both nominal and degraded conditions. Section 3.3 reviews the GNSS augmentation systems and selects the augmentation system retained for the application.

3.1. GNSS constellations and GNSS signals

3.1.1. GNSS constellations

3.1.1.1. GNSS constellations review

This section reviews the different GNSS constellations that are currently operational or under development. Next, the GNSS constellations considered in this project are selected.

For each GNSS constellation, Table 3-1 provides the status, the number of GNSS satellites that have been already launched and that are currently operational, the targeted number of GNSS satellites, and the coverage of the GNSS constellation.

GNSS constellation	Status	Number of operational satellites	Targeted number of operational satellites	Coverage
GPS (American system)	Operational	31 (US Air Force ensures availability of at least 24 satellites 95% of the time) [GPS, 2013]	At least 24 satellites 95% of the time	Worldwide
Galileo (European system)	Under development	4 [EC, 2013]	27 by 2020 [EC, 2013]	Worldwide
GLONASS (Russian system)	Operational	24 [FSA, 2013]	24 [FSA, 2013]	Worldwide
BeiDou/Compass (Chinese system)	Under development	15 (geostationary and non-geostationary satellites) [IGS, 2013]	35 (geostationary and non-geostationary satellites) by 2020 [BeiDou, 2013]	China and the neighboring regions in 2012, worldwide by 2020
QZSS (Japanese system)	Under development	4 (geostationary and quasi-zenith orbit satellites)	7 (geostationary and quasi-zenith orbit satellites) by 2018 [JAXA, 2012]	East Asia, and Oceania
IRNSS (Indian system)	Under development	1 [GPS world, 2013]	7 (geostationary and non-geostationary satellites) by 2015 [Navipedia, 2013]	India and the neighboring areas

Table 3-1: Current and future GNSS constellations

In Table 3-1, QZSS stands for Quasi Zenith Satellite System. IRNSS stands for Indian Regional Navigation Satellite System. Unlike GPS, Galileo, GLONASS, Beidou and IRNSS, QZSS cannot operate independently and is developed to enhance the availability of GNSS over Japan.

3.1.1.2. Case of study

The GNSS constellation choice has been based on four criteria that are:

- The **system coverage**. The GNSS(s) chosen in this project must have a global coverage at any time. Since QZSS and IRNSS do not have a global coverage, these systems are not considered in this project.

- The **current and future use of the system in civil aviation**. The GNSS(s) chosen in this project must be currently used in civil aviation or will be most likely used in civil aviation in the coming years. Information concerning the use of the global coverage systems in civil aviation are provided as follows:
  - GPS is currently used in civil aviation and in Airbus aircraft,
  - Galileo is likely to be used in civil aviation when Galileo will be fully operational. More precisely, MOPSs for airborne double constellation GPS/Galileo receivers have been elaborated [EUROCAE, 2010]. These MOPSs have not been finalized and are not currently mature enough to be certified.
  - GLONASS is not currently used in Airbus aircraft and no GLONASS MOPSs have been elaborated. However, GLONASS MOPSs might be developed in the coming years.
  - BeiDou is not currently used in Airbus aircraft. Beidou MOPSs have not been finalized and no formal plans to develop such MOPSs have been established. For this reason, BeiDou system is not considered in this project.

At this stage of the selection, it can be envisaged to use GPS, Galileo and/or GLONASS in this project.

- The **number of operational satellites** in the system. The number of satellites will determine if a single GNSS constellation can be used in the navigation algorithm or if a multi-constellation navigation system has to be envisaged for the intended application. According to the development plans, GPS, Galileo and GLONASS will have up to 27 operational satellites by 2020. From Section 2.3.2.3, the accuracy and integrity GNSS SIS requirements for the guidance function during the taxi operation under low visibility conditions are stringent. The horizontal accuracy 95% confidence levels and the HALs are few meters. Hence, in order to improve the GNSS performance in terms of accuracy and integrity, GNSS pseudo range redundancy is needed and at least two GNSS constellations are considered in this thesis. More specifically, in order to limit the avionics complexity it is proposed to consider two GNSS constellations in the thesis.
- The **available information concerning the SIS errors**. The SIS error is the error of the SIS in the range domain caused by the satellite, the satellite payload, and the navigation message (ephemeris data, clock, ect.) [ESA, 2005]. In this project, qualitative analyses of the nominal SIS errors for each selected GNSS are required. As an example, they are needed to assess the GNSS-based navigation algorithm performance in terms of accuracy.

As explained herein, two GNSS constellations are considered in this project in order to meet the stringent SIS performance requirements in terms of accuracy and integrity. One of the selected systems is GPS. Indeed, GPS is already fully operational and used in civil aviation. In addition, GPS ground and space segments performances, such as nominal SIS error accuracy, have been evaluated in the literature [Kovach, 2008] [Lee *et al*., 2007]. The other selected system is Galileo as a result of the advanced civil aviation MOPS standardization development [EUROCAE, 2010]. Even if Galileo is not yet fully operational, preliminary assumptions concerning the Galileo ground and space segments performances, such as nominal SIS error accuracy, are available [EUROCAE, 2010]. These assumptions have not be validated. Finally, public information on the accuracy and integrity of GLONASS ground and space segments induced errors is limited. GLONASS is thus not considered in this thesis.

3.1.2. GNSS signals

This section identifies the current and future GPS and Galileo signals that will be available for civil aviation applications with the GPS modernization and the Galileo development.

GPS and Galileo signals are located in the Radio Navigation Satellite Services (RNSS) frequency bands. The current and future GPS and Galileo signals that will be available for civil aviation applications are located in the Aeronautical Radio Navigation Services (ARNS) frequency bands. ARNS bands are reserved for aeronautical systems and are protected from in-band interference by regulation authorities. RNSS frequency bands, ARNS frequency bands and GPS and Galileo frequency bands are represented in Figure 3-1.

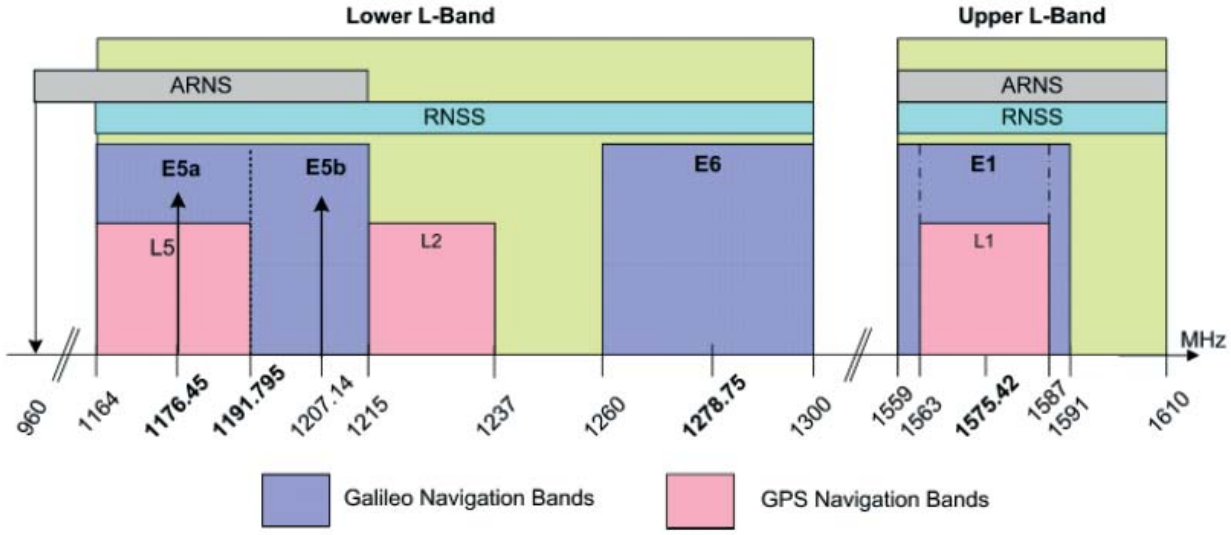

Figure 3-1: GPS and Galileo frequency bands [ICD, 2010]

The current and future GPS and Galileo signals that will be available for civil aviation applications are:

- GPSL1 signals. There are two types of GPSL1 signals: GPSL1C/A and GPSL1C signals,
- GalileoE1 signal,
- GPSL5 signal,
- GalileoE5a signal,
- GalileoE5b signal.

These GNSS signals are described in the next section.

3.1.2.1. Modulations and structure

GPS and Galileo signals are the sum of a data and a pilot component, except for GPSL1C/A. On each component, waveforms are combined and the resulting signal is multiplied by a Radio Frequency (RF) carrier. The combination of the waveforms is a baseband signal. The modulation of the waveforms by the RF carrier leads to center the signal about the carrier frequency. On the data component, the waveforms that are multiplied by the RF carrier are:

- the navigation waveform. The navigation message, which is a binary signal. It contains the different types of data needed to perform positioning [ICD, 2010]. Included in the navigation message are ephemeris parameters, ionosphere model parameters, time and clock correction parameters, satellite health status, navigation data validity and SIS accuracy information.
- a spreading waveform, also called PseudoRandom Noise (PRN) waveform or primary code waveform, which is similar to the data waveform, but with a much higher symbol rate. The symbol rate of the spreading waveform is called chip rate and is referred to as f_c in the following. The duration of each chip is $T_c = \frac{1}{f_c}$, where T_c is called chip period. The

spreading waveform is periodic and the finite sequence of bits needed to generate the spreading waveform is referred to the PRN code.
- For GPSL5, GalileoE5a and GalileoE5b, a secondary code waveform.

On the pilot component, the waveforms that are multiplied by the RF carrier are:

- a PRN waveform,
- a secondary code waveform.

Omitting the noise term, the expression of the GPS or Galileo signal broadcast by a satellite j at time t is:

$$s^j(t) = A_{D,j}c_{D,j}(t)\cos\left(2\pi f_L t + \theta_{D,j}\right) + A_{P,j}c_{P,j}(t)\cos\left(2\pi f_L t + \theta_{P,j}\right) \quad \text{Eq - 3-1}$$

where:

- $A_{D,j}$ is the amplitude of the data component,
- $A_{P,j}$ is the amplitude of the pilot component. $A_{P,j}$ is null for GPSL1C/A.
- $c_{D,j}(t)$ is the baseband signal that modulates the carrier component on the data channel,
- $c_{P,j}(t)$ is the baseband signal that modulates the carrier component on the pilot channel,
- f_L is the carrier frequency,
- $\theta_{D,j}$ is the phase of the data carrier,
- $\theta_{P,j}$ is the phase of the pilot carrier. Some of the considered signals, such as GalileoE1, are characterized by a data component that is in-phase with the pilot component. In this case, $\theta_{D,j} = \theta_{P,j}$. Other GNSS signals, such as GalileoE5a, are characterized by a data component that is in-quadrature with the pilot component. In this case, $\theta_{P,j} = \theta_{D,j} + \frac{\pi}{2}$.

Table 3-2 provides the carrier frequency and the modulation technique relating to each GPS and Galileo signal. The code length and the chip rate of the PRN codes on each data and pilot component are indicated in Table 3-2. The code length and the chip rate of the secondary codes on each data and pilot component are also indicated. Table 3-2 also provides the navigation data rate.

In the Table 3-2, “cps” stands for chip per second and “bps” stands for bit per second. GPS and Galileo signals use four types of modulation techniques: Binary Phase Shift Keying (BPSK), Time Multiplexed Binary Offset Carrier (TMBOC), Quadrature Phase Shift Keying (QPSK) and Composite Binary Offset Carrier (CBOC). The next section provides a brief background on the BOC modulation.

GNSS signal	Central frequency [MHz]	Data/ pilot power sharing	Modulation	PRN code length / chip rate f_c	Navigation data rate	Secondary code length / Secondary code rate
GPSL1C/A	1575.42	NA	BPSK(1)	1ms 1.023Mcps	50bps	NA
GPSL1C-I (data)	1575.42	25%	BOC(1,1)	10ms 1.023Mcps	100bps	NA
GPSL1C-Q (pilot)		75%	TMBOC(6,1,4/33)	10ms 1.023Mcps	NA	18s 100bps
GPSL5-I	1176.45	50%	BPSK(10)	1ms 10.23Mcps	1000bps	10ms 1Mbps
GPSL5-Q		50%	BPSK(10)	1ms 10.23Mcps	NA	20ms 1Mbps
GalileoE1-B (data)	1575.42	50%	CBOC(6,1,1/11,+)	4ms 1.023Mcps	250bps	NA
GalileoE1-C (pilot)		50%	CBOC(6,1,1/11,-)	4ms 1.023Mcps	NA	100ms 250bps
GalileoE5a-I	1176.45	50%	BPSK(10)	1ms 1.023Mcps	50bps	20ms 1Mbps
GalileoE5a-Q		50%	BPSK(10)	1ms 10.23Mcps	NA	100ms 1Mbps
GalileoE5b-I	1207.14	50%	BPSK(10)	1ms 10.23Mcps	250bps	4ms 1Mbps

Table 3-2: Characteristics of the GPS and Galileo signals [GPS Wing, 2008] [ICD, 2010]

Note that the different modulation techniques and code rates are detailed in the next section.

3.1.2.2. GPS and Galileo autocorrelations and power spectral densities

This section provides the models of the GPS and Galileo autocorrelation functions and Power Spectral Densities (PSD) functions.

3.1.2.2.1. GPSL1C/A signal

GPS satellites currently broadcast the GPSL1 signal. The GPSL1 signal consists of two carrier components which are in phase quadrature with each other. One carrier component is multiplied by the modulo-2 sum of the civilian spreading code, referred to as Coarse/Acquisition (C/A) code, and the GPS navigation message. The other carrier component is multiplied by the modulo-2 sum of the military Precise (P(Y)) code and the GPS navigation message. Civilian users have no access to the military code. In the following, GPSL1C/A denotes the C/A component of the GPSL1 signal.

GPSL1C/A is a BPSK(1) signal. The notation BPSK(n) is used to denote a BPSK signal with a chip rate equal to: $n \times 1.023$ Mcps. Further details on the BPSK modulation are provided in [Kaplan *et al*., 2006]. Without considering the repetition of the spreading code, and assuming an infinite front-end bandwidth and to autocorrelation side lobes, the expression of the autocorrelation of the GPSL1C/A spreading waveform is:

$$R_{BPSK}(\tau) = \begin{cases} 1 - \frac{|\tau|}{Tc}, |\tau| \leq Tc \\ 0, \text{elsewhere} \end{cases} \quad \text{Eq - 3-2}$$

where Tc is the PRN chip duration of the spreading code.

The PSD function is defined as the Fourier transform of the autocorrelation function. The normalized PSD function (specified without the effect of band-limiting filters and payload imperfections) of the spreading waveform is:

$$G_{BPSK}(f) = T_c \mathrm{sinc}^2(\pi f T_c) \qquad \text{Eq - 3-3}$$

where $\mathrm{sinc}(.)$ denotes the sinc function.

3.1.2.2.2. GPSL1C signal

The modernization program of the GPS constellation will allow the emission of a new civil GPS signal on the L1 frequency band, which is GPSL1C. The first launch of a modernized GPS block-III satellite is planned for 2014 [Lockheed Martin, 2012]. The full operation of GPSL1C signal is planned by the International Committee GNSS to occur in 2021 [ICGNSS, 2010].

The data bit stream is modulated using BOC(1,1) modulation [GPS Wing, 2008]. The pilot bit stream is envisaged to be modulated using a TMBOC(6,1,4/33) modulation technique. TMBOC(6,1,4/33) technique uses a mixture of BOC(1,1) symbols and BOC(6,1) symbols. All the bits of the pilot component are modulated using BOC(1,1) modulation, except 4 bits every 33 bit sequences which are modulated using BOC(6,1) modulation technique. Further details about the BOC modulation are provided in [Kaplan *et al*., 2006]. The model of the autocorrelation of the baseband signals of the GPSL1C data component and pilot component are given by, respectively:

$$\begin{aligned} R_{L1C-I}(\tau) &= R_{BOC(1,1),\sin}(\tau) \\ R_{L1C-Q}(\tau) &= \frac{29}{33} R_{BOC(1,1),\sin}(\tau) + \frac{4}{33} R_{BOC(6,1),\sin}(\tau) \end{aligned} \qquad \text{Eq - 3-4}$$

where $R_{BOC(1,1),\sin}$ is the autocorrelation function of a spreading waveform modulated by a BOC(1,1) sine-phased signal and $R_{BOC(6,1),\sin}$ is the autocorrelation function of a spreading waveform modulated by a BOC(6,1) sine-phased signal.

The normalized PSD function of the total (data+pilot) GPSL1C signal (specified without the effect of band-limiting filters and payload imperfections) is:

$$G_{L1C}(f) = \frac{3}{4} G_{L1C-Q}(f) + \frac{1}{4} G_{L1C-I}(f) = \frac{10}{11} G_{BOC(1,1),\sin}(f) + \frac{1}{11} G_{BOC(6,1),\sin}(f) \qquad \text{Eq - 3-5}$$

where:

- G_{L1C-D} is the PSD function of the baseband signal of the GPSL1C data component,
- G_{L1C-P} is the PSD function of the baseband signal of the GPSL1C pilot component,
- $G_{BOC(1,1),\sin}$ is the PSD function of a spreading waveform modulated by a BOC(1,1) sine-phased signal and $G_{BOC(6,1),\sin}$ is the PSD function of a spreading waveform modulated by a BOC(6,1) sine-phased signal. The analytical expressions of both functions are provided in [Avila Rodriguez, 2008].

3.1.2.2.3. GalileoE1 signal

The GalileoE1 data bit stream is modulated using CBOC(6,1,1/11,+) modulation. The pilot bit stream is modulated using CBOC(6,1,1/11,-) modulation. CBOC(6,1,1/11) linearly combines BOC(1,1) and BOC(6,1) sub-carriers [ICD, 2010][Macabiau *et al*., 2007]. Further details about the combination of BOC(1,1) and BOC(6,1) sub-carriers in the CBOC

modulation technique are provided in [ICD, 2010][Foucras *et al*., 2013][Julien *et al*., 2007]. The model of the autocorrelation of the baseband signals of the GalileoE1 data component and pilot component are given by, respectively:

$$\begin{aligned} R_{E1-B}(\tau) &= \frac{10}{11}R_{BOC(1,1),sin}(\tau) + \frac{1}{11}R_{BOC(6,1),sin}(\tau) \\ &\quad + \frac{20}{121}R_{BOC(1,1)BOC(6,1),sin}(\tau) \\ R_{E1-C}(\tau) &= \frac{10}{11}R_{BOC(1,1),sin}(\tau) + \frac{1}{11}R_{BOC(6,1),sin}(\tau) \\ &\quad - \frac{20}{121}R_{BOC(1,1)BOC(6,1),sin}(\tau) \end{aligned} \qquad \text{Eq - 3-6}$$

where $R_{BOC(1,1)BOC(6,1),sin}$ is the cross correlation function between $R_{BOC(1,1),sin}$ and $R_{BOC(6,1),sin}$.

The normalized PSD (specified without the effect of band-limiting filters and payload imperfections) of the GalileoE1 baseband signal has the same expression as the normalized PSD of GPSL1C baseband signal. This PSD is called the Multiplexed BOC (MBOC) PSD in the following [Julien *et al*., 2007].

3.1.2.2.4. GPSL5 and GalileoE5 signals

For civil aviation users, L5 is the second ARNS frequency band. The utilization of two frequency bands, L1 and L5 bands, will enable airborne estimation of the dispersive ionospheric delay. The ionosphere is one of the main error sources that affect the pseudo-range measurements [Enge, 2003]. GPS-L5 should be fully operational by 2020 [Gruber, 2011].

GPSL5 and GalileoE5a share the same frequency band. Consequently, the same GNSS airborne antenna can be implemented to process both GPSL5 and GalileoE5a signals. The use of GPSL5 and GalileoE5b signals would increase the complexity of the GNSS antenna to be used since these signals do not share the same frequency band. For this reason, GalileoE5b is not further studied.

Both GPSL5 and GalileoE5a data and pilot bit streams are modulated using a BPSK(10) modulation. The expressions of the autocorrelations of the baseband signals on the data component and on the pilot component are given by Eq -3-4. Similarly, the normalized PSD functions (specified without the effect of band-limiting filters and payload imperfections) of the GPSL5 and GalileoE5a baseband signals on the data component and on the pilot component are given by Table 3-2.

3.1.2.2.5. Autocorrelation functions and PSD functions representation

In this section, the GPS and Galileo autocorrelation functions and PSD functions are represented and compared.

Future typical airborne GNSS receivers will use the pilot components of GPSL1C, GPSL5, GalileoE1 and/or GalileoE5a to estimate the pseudo range measurements between airborne GNSS antenna and visible GNSS satellites. For this reason, the autocorrelation functions (Figure 3-2) of the baseband signals of the pilot components of GPSL1C, GPSL5, GalileoE1 and GalileoE5a are depicted. The autocorrelation function of the baseband signal of GPSL1C/A is also represented. In this Figure, the effects of band-limiting filters are not taken into account.

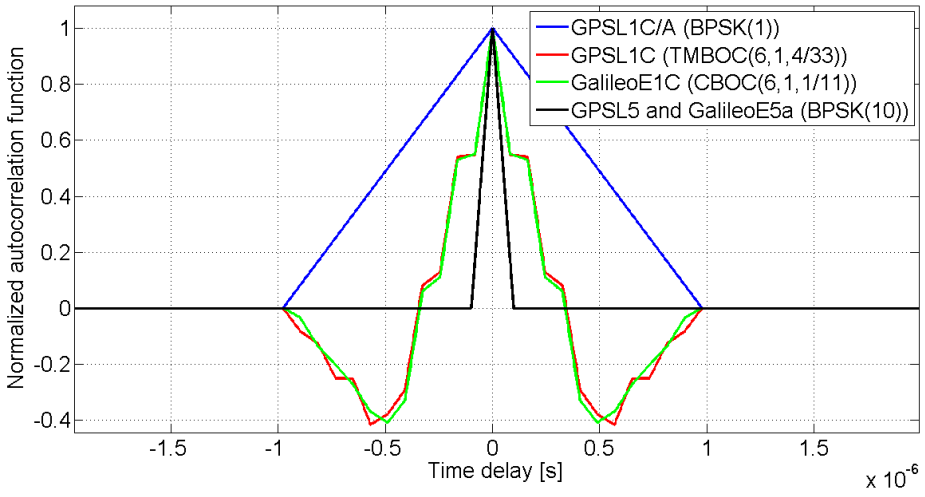

Figure 3-2: Autocorrelation functions of GPS and Galileo signals

GPSL1C/A, GPSL1C and GalileoE1 autocorrelation functions are null for a time delay higher than 1 chip duration, corresponding to $9.78.10^{-7}$s from Table 3-2. Note also that the similarities in the autocorrelation of the GPSL1C and GalieloE1 are discussed later in this thesis (see Chapter 4). GPSL5 and GalileoE5a autocorrelation functions are null for a time delay higher than 1 chip duration, corresponding to $9.78.10^{-8}$s, that is 10 times lower than for signals on the L1 frequency band.

Figure 3-3 presents the PDFs of the baseband signals of the GPS and Galileo signals. In this Figure, the effects of band-limiting filters are not taken into account.

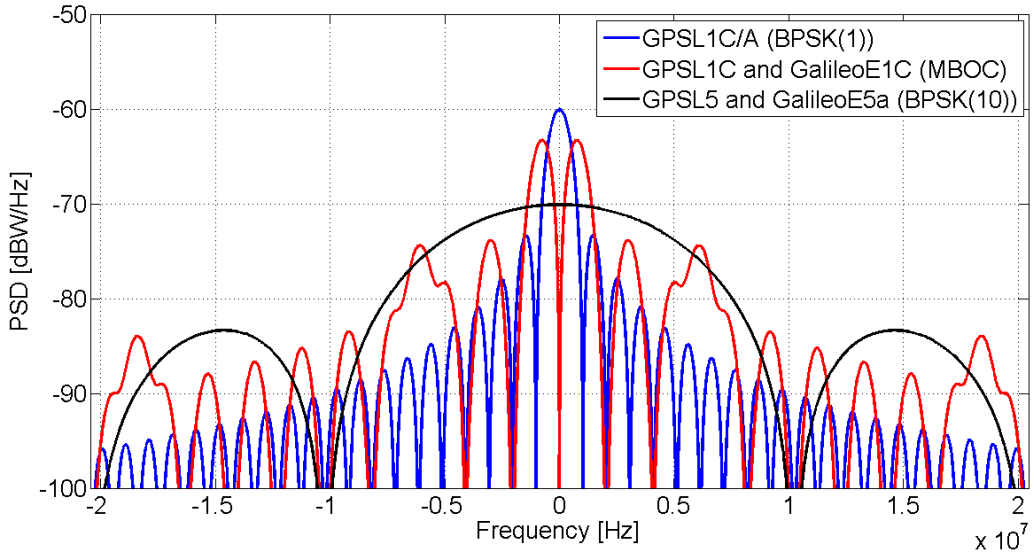

Figure 3-3: PSD functions of GPS and Galileo signals

The GPSL1C and GalieoE1C spectrum is split on each side of the central frequency. This allows putting a fraction of the power away from the central frequency and improving the tracking performance in the presence of thermal noise and multipath [Julien *et al.*, 2007]. The main lobes of the BPSK are placed in between the lobes of the BOC, allowing a good spectral separation. The PSD functions of the baseband signals of the pilot components of GPSL5 and GalileoE5a have the shape of the BPSK spectrum represented in Figure 3-3. The width of the

main lobe of the GPSL5 and GalileoE5a PDFs is ten times higher for GPSL5 than for GPSL1C/A, leading to improve the noise performance of the GPS receiver and to reduce the tracking error.

3.2. GNSS pseudo-range measurement model

This section presents the error models affecting GNSS code pseudo-range measurements in airport environments. The pseudo-range errors can be classified as follows:

- The **nominal ranging errors** affect GNSS measurements when all GNSS segments are working according to their specifications and the magnitudes of other external error sources are within their typical range [Salos, 2012].
- The **ranging failures** are due to an anomaly of the satellite itself or to environmental effects on the GNSS ranging signal [Lee, 2004].

Nominal ranging errors are systematic errors which are always present while ranging failures affect punctually GNSS measurements. Assuming that $N\,(N \in \mathbb{N}^*)$ GNSS pseudo-range measurements are used by the GNSS receiver to estimate the aircraft position at a given time t, the GNSS code pseudo-range measurement error vector at time t is:

$$\mathbf{E}(t) = \boldsymbol{\varepsilon}(t) + \mathbf{B}(t) \qquad \text{Eq - 3-7}$$

where:

- $\boldsymbol{\varepsilon}(t)$ is the nominal ranging error vector at time t,
- $\mathbf{B}(t)$ is the ranging failure vector at time t.

The nominal ranging errors are presented in 3.2.1. The GNSS ranging failures are described in section 3.2.2.

3.2.1. GNSS nominal ranging errors

3.2.1.1. Identification

The nominal ranging error vector is the result of various error sources. The error sources can be considered as independent [RTCA, 2006] and they cause nominal ranging errors that can be analyzed separately. Seven error sources have been identified in airport environments:

- Control and space segments,
- Ionosphere delay,
- Troposphere delay,
- Multipath,
- GNSS airborne antenna group delay and phase center variations,
- GNSS receiver thermal noise.

Among the nominal errors induced by the control and space segments there are the errors induced by the inaccuracy of the broadcast satellite clock corrections and ephemeris and the nominal biases induced by other error sources, such as GNSS ground antenna group delay and phase center variations.

The effects of the inaccuracy of the broadcast satellite clock corrections and ephemeris, of the ionosphere delay and of the troposphere delay on the GNSS raw code measurements during taxi operations may be modeled as zero-mean Gaussian distributions. These models have been standardized [RTCA, 2009] and are used as inputs in civil aviation integrity monitoring

systems. The standardized GNSS nominal ranging error models presented in this chapter are residual error models after correction of the GNSS measurements by airborne mitigation techniques recommended in [RTCA, 2009] [EUROCAE, 2010]. Standardized residual error models after Ground Based Augmentation System (GBAS) and Satellite Based Augmentation System (SBAS) corrections are not presented in this chapter. The effects of the GNSS receiver thermal noise on the GNSS raw code measurements during taxi operations have also been modeled as zero-mean Gaussian distributions [Betz *et al*., 2009].

The models of the multipath errors adapted in in flight-operations have also been standardized [RTCA, 2009]. However, the multipath error models adapted to surface operation has not been standardized. Similarly, models of the GNSS airborne antenna group delay and phase center variations errors and of the nominal biases induced by the control and space segments are not standardized for airport environments. Current civil aviation integrity monitoring systems do not provide sufficient protection against these effects in airport environments. However, future integrity monitoring systems are proposed to protect users from parts of these effects, and more specifically from nominal biases induced by GNSS antenna group delay and phase center variations and by the control and space segments [GEAS, 2010] [WG-C ARAIM, 2012]. In this thesis, the GNSS error sources, such as multipath in airport environments, that are not taken into account as part of the error model assumed for the existing integrity monitoring applications and that may lead to positioning failures for the guidance function under zero-visibility conditions are referred to as "GNSS singular events".

3.2.1.2. Time correlation of GNSS nominal ranging errors

The nominal code ranging errors induced by the inaccuracy of the broadcast satellite clock corrections and ephemeris errors, the ionosphere delay, the troposphere delay and the GNSS receiver thermal noise are correlated in time. These errors are modelled in the time domain with an autoregressive model derived from a first-order Gauss-Markov process [RTCA, 2009]. In the GNSS receiver, the code pseudo-range measurement estimated with a sampling period T_e. The nominal code ranging error due to an error source "err source" at a given epoch time t_i is given by:

$$\varepsilon_{\text{err source}}(t_i) = a\varepsilon_{\text{err source}}(t_{i-1}) + \sqrt{1-a^2}\eta_{\text{err source}}(t_i) \qquad \text{Eq - 3-8}$$

where:

- $\varepsilon_{\text{err source}}$ represents the satellite clock and ephemeris nominal code ranging error $\varepsilon_{\text{Sat\&Eph}}$, the ionosphere nominal code ranging error $\varepsilon_{\text{iono}}$, the troposphere nominal code ranging error $\varepsilon_{\text{tropo}}$ or the thermal noise nominal code ranging error $\varepsilon_{\text{noise}}$,
- $a = e^{-\frac{T_e}{T_{\text{err source}}}}$,
- $T_{\text{err source}}$ is the nominal raw code ranging error correlation time,
- $t_i - t_{i-1} = T_e$,
- $\eta_{\text{err source}}(t_i)$ is modeled as a stationary, zero-mean Normal distribution, $\eta_{\text{err source}}(t_i) \sim N(0, {\sigma_{\text{err source}}}^2)$.
- $\sigma_{\text{err source}}$ is the standard deviation of the nominal raw code ranging error Gauss-Markov process.

The standard deviations and correlation times related to the Gauss-Markov processes modelling the satellite clock and ephemeris nominal code ranging error $\varepsilon_{\text{Sat\&Eph}}$, the ionosphere nominal code ranging error $\varepsilon_{\text{iono}}$, the troposphere nominal code ranging error $\varepsilon_{\text{tropo}}$ and the thermal noise nominal code ranging error $\varepsilon_{\text{noise}}$ are provided in the four next sections.

3.2.1.3. Satellite clock and ephemeris error

Inaccuracies in the data broadcast in the navigation message induce nominal ranging errors. The inaccuracies include inaccurate ephemeris data used to compute the GNSS satellite trajectories. Moreover, satellite clock corrections for clock drifts are inexact. Both ephemeris data inaccuracies and satellite clock correction inaccuracies generate a residual nominal ranging error $\varepsilon_{\mathrm{Sat\&Eph}}$. Furthermore, $\varepsilon_{\mathrm{Sat\&Eph}}$ depends on the performance of the GNSS ground segment and space segment that compute the ephemeris and satellite clock corrections.

For GPS, the standard deviation of $\varepsilon_{\mathrm{Sat\&Eph}}$ is included in the User Range Accuracy (URA). URA is a statistical measure (1 sigma value) of the GPS range errors for which the space and control segments are responsible, excluding errors due to the user equipment and transmission media [ARINC, 2006]. Several URA values are proposed in the literature. The modernized GPS III program (including the emission of GPSL5 and GPSL1C signals) will allow reaching a URA value of 0.3m to 1.0m [Lee *et al*., 2007].

For Galileo, the standard deviation of $\varepsilon_{\mathrm{Sat\&Eph}}$ is included in the Galileo Signal In Space Accuracy (SISA). The SISA is the predicted minimum standard deviation of the normal distribution that overbounds the faut-free SIS error. The SISA nominal value is set to 0.85m in [EUROCAE, 2010].

In this thesis, it is assumed that modernized GPS and Galileo performance will be equivalent. Hence, the standard deviation of both GPS and Galileo raw code ranging errors due to satellite clock and ephemeris inaccuracies is given by:

$$\sigma_{\mathrm{Sat\&Eph}} = 0.85\mathrm{m} \qquad \text{Eq - 3-9}$$

The correlation time of the raw code ranging errors due to satellite clock and ephemeris inaccuracies is set to 2 hours [RTCA, 2009] [EUROCAE, 2010]. The correlation time is relatively long. This mainly because the orbital errors as well as the ranging errors due to inaccuracies in the clock drift corrections are re-initialized via uploads every few hours [RTCA, 2009] and vary slowly between resets via uploads. In the following, a correlation time of $T_{\mathrm{Sat\&Eph}} = 1\,\mathrm{hour}$, based on the average period of time satellites are visible to the user, will be used [Martineau, 2008].

3.2.1.4. Ionosphere error

The ionosphere covers the region between approximately 50 and 1500 km above the earth and is characterized by the presence of free (negatively charged) electrons and positively charged ions. The free electrons induce a delay on GNSS code sequence and a phase advance on the carrier phase. The ionosphere is a dispersive medium, meaning that the ionosphere code delay and phase advance are function of the carrier frequency [Leick, 1995]. In addition, the code delay and phase advance are function of the Total Electron Content (TEC) $[\mathrm{el/m^2}]$ that represents the number of free electrons in a 1-square meter column along the path satellite-receiver. The ionosphere code delay generates an error on the raw code pseudo-range measurement between the satellite and the receiver that is a function of the central frequency f_L of the GNSS signal and of the TEC [Leick, 1995]:

$$\varepsilon_{\mathrm{iono}} = \frac{40.30}{{f_L}^2}\mathrm{TEC} \qquad \text{Eq - 3-10}$$

In nominal conditions, and in the time domain, the TEC presents strong diurnal variations. The TEC also depends on the season and on the solar cycle. In nominal conditions, and in the

spatial domain, the TEC presents strong spatial variations. Indeed, the world can be divided into three regions: the low-latitude regions which include the equatorial regions, the mid-latitude regions and the high-latitude regions which include the polar cap regions. The ionization of a region may be stronger than others [Eurocontrol, 2010]. Hence, electron content differences can be observed between regions.

Under nominal conditions, both temporal and spatial TEC variations induce temporal and spatial regular TEC gradients, respectively:

- The regular **temporal TEC gradients** refer to variations of the TEC in the time domain and under nominal ionosphere conditions. More precisely, temporal TEC gradients refer to the variation of the TEC value (and thus of the ionospheric code delay) that is observed by a single static receiver which processes the signal coming from a single satellite during a period of time Δt.
- The **spatial TEC gradients** refer to variations of the TEC in the horizontal space domain and under nominal ionosphere conditions. More precisely, spatial TEC gradient refers to the difference of the TEC values (and thus of the ionospheric code delays) that are observed by different receivers having different positions in the horizontal domain and processing the signals coming from a single satellite at the same time.

3.2.1.4.1. GPS single frequency mode

GPS civil receivers apply the Klobuchar ionospheric model to correct the ionospheric code delay, which is estimated to reduce at least 50% of the root-mean-square raw code ranging error due to the ionosphere delay [Klobuchar, 1987]. The standardized model of the standard deviation of the residual raw code ionosphere ranging error for GPSL1C/A and GPSL1C signals and is given by [RTCA, 2009]:

$$\sigma_{iono,L1} = \max\left\{\frac{cX_{iono}}{5}, F\tau_v\right\} \text{ with } F = \left(1 - \left(\frac{R_E \cos(El)}{R_E + h_I}\right)^2\right)^{-1/2} \qquad \text{Eq - 3-11}$$

where:

- X_{iono} is the Klobuchar ionosphere code delay corrections [s],
- c is the speed of light in vacuum [m/s],
- F is the obliquity factor:
- $R_E = 6378136.0\text{m}$,
- $h_I = 350000.0\text{m}$,
- El is the satellite elevation angle,
- $\tau_v = \begin{cases} 9\text{m for } 0 \leq |\phi_m| \leq 20 \\ 4.5\text{m for } 20 < |\phi_m| \leq 55 \\ 6\text{m for } 55 > |\phi_m| \end{cases}$
- ϕ_m is the geomagnitude latitude [°].

Simulations proposed in [Salos, 2012] compare the term $F\tau_v$ to 20% of the Klobuchar ionosphere correction term between 1994 and 2009. Simulations results found that, during the studied time period, $F\tau_v$ always exceeded $\frac{cX_{iono}}{5}$. Hence, it is reasonable to set:

$$\sigma_{iono,L1} = F\tau_v \qquad \text{Eq - 3-12}$$

The ionospheric residual error of GPSL5 signals is obtained as follows:

$$\sigma_{iono,L5} = \left(\frac{f_{L1}}{f_{L5}}\right)^2 \sigma_{iono,L1} \qquad \text{Eq - 3-13}$$

3.2.1.4.2. Galileo single frequency mode

Galileo civil receivers apply the NeQuick ionospheric model to correct at least 70% of the ionospheric code delay [Arbesser, 2006]. The raw code ionospheric residual error model for single-frequency Galileo receivers is not yet standardized. [Arbesser, 2006] specifies that the residual error standard deviation of single-frequency receivers must not exceed 30% of the correction magnitude, or the equivalent first order delay of a 20-TECu slant TEC, whichever is larger [Arbesser, 2006]. Based on this specification and on the IGS (International GNSS Service) TEC database, [Salos, 2012] proposes a model of the residual error standard deviation that would have been obtained in the previous years. More specifically, the historical data used to set up the model have been taken from 1998 to 2010 because this period covers the 11-year solar period. The model of the residual error standard deviation on the L1 frequency band is as follows:

$$\sigma_{iono,E1} = F\sigma_{iono,v} \qquad \text{Eq - 3-14}$$

where:

- F is defined in the previous paragraph,
- $\sigma_{iono,v}$ is the standard deviation of the GalileoE1 residual ionosphere ranging error at zenith. $\sigma_{iono,v}$ decreases when the geomagnetic latitude of the receiver (ϕ_m) increases. $\sigma_{iono,v}$ is in the range
- 7.5m ; 3.9m], where 7.5m corresponds to $\phi_m = 0°$ and 3.9m corresponds to $\phi_m = 75°$. The value of $\sigma_{iono,v}$ at the geomagnetic latitude of Toulouse airport, France, is 4.5m.

The ionospheric residual error of GalieoE5a signals is obtained using Eq - 3-13. The correlation time of the raw code residual ionospheric ranging errors is set to $T_{iono} = 1800s$ in [RTCA, 2009] [EUROCAE, 2010].

3.2.1.4.3. GPS and Galileo dual frequency mode

Since the ionosphere is a dispersive medium, the residual raw code ionosphere ranging errors after Klobuchar and NeQuick corrections are carrier frequency-dependent. Hence, dual frequency civil receivers can measure the pseudo-range to each satellite at two different frequencies and may combine them to form an iono-free pseudo-range measurement unaffected by the first order ionospheric delay.

By denoting $\varepsilon_{iono,L1}$ the first-order residual raw code ionosphere ranging error on L1 GNSS signals, the first-order residual raw code ionosphere ranging error on L5 GNSS signals $\varepsilon_{iono,L5}$ is given by:

$$\varepsilon_{iono,L5} = \left(\frac{f_{L1}}{f_{L5}}\right)^2 \varepsilon_{iono,L1} \qquad \text{Eq - 3-15}$$

The iono-free GPSL1C/A-GPSL5 or GPSL1C-GPSL5 and GalileoE1-GalileE5a code pseudo-range measurements are given by, respectively:

$$\begin{aligned} \rho_{L1C-L5} &= k_a\,\rho_{L1C} + k_b\,\rho_{L5} \\ \rho_{E1-E5a} &= k_a\,\rho_{E1} + k_b\,\rho_{E5a} \end{aligned} \qquad \text{Eq - 3-16}$$

where:

- ρ_{L1C} and ρ_{L5} are the code pseudo-range measurements on GPSL1C/A or GPSL1C and GPSL5, respectively,
- ρ_{E1} and ρ_{E5a} are the code pseudo-range measurements on GalileoE1and GalileE5a, respectively,
- $k_a = \frac{{f_{L1}}^2}{{f_{L1}}^2 - {f_{L5}}^2} \cong 2.261$
- $k_b = \frac{{f_{L5}}^2}{{f_{L5}}^2 - {f_{L1}}^2} \cong -1.261$
- f_{L1} is the L1 central frequency and f_{L5} is the L5 central frequency.

Iono-free pseudorange combinations remove the first order ionospheric delay, but higher order errors remain. Nevertheless, their magnitude is insignificant compared to other error sources [Salos, 2012]. Thus, the standard deviations of the GPS and Galileo iono-free residual raw code ionosphere ranging error are assumed to be:

$$\begin{aligned} \sigma_{iono,L1-L5} &= 0\text{m} \\ \sigma_{iono,E1-E5a} &= 0\text{m} \end{aligned} \qquad \text{Eq - 3-17}$$

3.2.1.5. Troposphere error

The troposphere covers the region between the Earth surface and approximately 40 km above the earth and is characterized by the presence of neutral atoms and molecules. The troposphere induces a delay on GNSS code sequence and a phase delay on the carrier phase. The troposphere is a non-dispersive medium, meaning that the code and phase delays are carrier frequency-independent [Leick, 1995].

The tropospheric model to correct the troposphere code delay in aviation receivers is specified in [RTCA, 2006]. The standardized model of the standard deviation of the residual raw code troposphere ranging error after troposphere error correction is given by [RTCA, 2009] [EUROCAE, 2010]:

$$\sigma_{tropo} = \begin{cases} 0.12 \times \dfrac{1.001}{\sqrt{0.002001 + \sin^2(\text{El})}} & \text{for El} \geq 4° \\ 0.12 \times \dfrac{1.001}{\sqrt{0.002001 + \sin^2(\text{El})}} (1 + 0.015(4° - \text{El})^2) & \text{for } 2° < \text{El} \leq 4° \end{cases} \qquad \text{Eq - 3-18}$$

The anomalous troposphere ranging errors induced by the troposphere storms are as part of the nominal troposphere error model. There are two reasons for this:

- troposphere storms, are considered to occur often enough to be part of the nominal operation [ICAO, 2009b],
- the residual anomalous troposphere errors have a low magnitude and can be considered to be part of the nominal error model.

The correlation time of the raw code residual troposphere ranging errors is set to $T_{tropo} = 1800\text{s}$ in [RTCA, 2009] [EUROCAE, 2010]. A correlation time of 30 minutes is applied to represent the correlation time of the residual troposphere error when the system passes a troposphere storm [RTCA, 2009].

3.2.1.6. GNSS receiver thermal noise error

In order to precisely estimate the code pseudo-range measurements, the GNSS receiver first filters, pre-amplifies down-converts and samples the incoming GNSS signals in the front-end block. The code delays of each incoming signal are thus roughly estimated in the acquisition block. The signal tracking block and more precisely the Delay Locked Loop (DLL) refines the estimation of the code delay and provides a dynamic estimation of this parameter. A DLL is a feedback system that synchronizes its own local PRN replica with the incoming PRN signal, so that code delay estimate can be derived from estimate of the local PRN code. For the synchronization process, the DLL uses a discriminator that compares the Early, Late and Prompt correlator outputs. A detailed presentation of the DLL operation is presented later in this thesis (Chapter 4). The code delay estimate is then converted in meters to provide the code pseudo-range measurement estimate.

Thermal noise present at the receiver front-end perturbs the tracking process and causes nominal thermal noise errors on the code pseudo-range measurement estimates [Kaplan *et al*., 2006]. The standard deviation of the nominal thermal noise code ranging errors depends on the DLL discriminator. The Early Minus late Power (EMLP) discriminator is widely used in civil aviation applications. Assuming:

- the EMLP DLL discriminator is used,
- the receiver's front end filter is approximated by a rectangular band-pass filter centered at zero frequency and having two-sided bandwidth. B_{fe} is the two-sided front-end bandwidth [Hz],
- the thermal noise is white with power spectral density. N_0 is the constant noise PSD of the thermal noise [W/Hz],

the standard deviation of the nominal thermal noise code ranging error is given by [Betz *et al*., 2009]:

$$\sigma^2{}_{noise} = c^2 \frac{B_n(1-0.5B_nT_I)\int_{-B_{fe}/2}^{B_{fe}/2} G_s(f)\sin^2(\pi f\Delta)df}{(2\pi)^2\frac{C}{N_0}\left(\int_{-B_{fe}/2}^{B_{fe}/2} fG_s(f)\sin(\pi f\Delta)df\right)^2}\left[1 + \frac{\int_{-\frac{B_{fe}}{2}}^{\frac{B_{fe}}{2}} G_s(f)\cos^2(\pi f\Delta)df}{T_I\frac{C}{N_0}\left(\int_{-\frac{B_{fe}}{2}}^{\frac{B_{fe}}{2}} G_s(f)\cos(\pi f\Delta)df\right)^2}\right] \quad \text{Eq - 3-19}$$

where:

- $G_s(f)$ is the normalized signal power spectral density [/Hz],
- C is the signal carrier power [W],
- B_n is the loop bandwidth [Hz],
- T_I is the integration time [s]
- Δ is the two-sided early-late spacing [s]

Typical values of DLL parameters used in civil aviation applications are provided in the next Table. A 1-Hz loop bandwidth is typically chosen for aviation applications [Chen, 2010] [Neri, 2011]. With higher values of loop bandwidths, the DLL could follow higher level of dynamics. A narrower loop bandwidth enables decreasing the noise error magnitude. B_{fe} is set to 20MHz for GPSL1C/A and GPSL5 and GalileoE5a in order to process the main and

secondary lobes (for L1C/A) and the main lobe of L5 and E5a signals. B_{fe} is set to 14MHz for GPSL1C and GalileoE1 to process up to the main lobe of the BOC(6,1) component of the received pilot component. The chip spacing is set to 1/12 for GPSL1C and GalileoE1 since it is the maximal possible value for an EMLP discriminator, as fully explained in [Julien, 2007]. Other values of chip spacing are recommended in [Salos, 2012] and [Chen, 2010]. The presence of the secondary code on the pilot component for Galileo signals and for the GPSL1C signals allows increasing the integration time up to 100ms.

GNSS signal	Modulation	T_I [ms]	Δ [chip]	B_{fe} [MHz]	B_n [Hz]
GPSL1C/A	BPSK-R(1)	20	1/2	20	1
GPSL1C-P	TMBOC(6,1,4/33)	20 to 100	1/12	14	1
GPSL5-P	BPSK(10)	20	1/4	20	1
GalileoE1-C	CBOC(6,1,1/11,-)	20 to 100	1/12	14	1
GalileoE5a -P	BPSK(10)	20 to 100	1/4	20	1

Table 3-3: GNSS receiver parameters

3.2.1.6.1. GPS and Galileo single frequency mode

Figure 3-4 shows the values of the standard deviations of the GPS and Galileo raw code ranging errors due to receiver thermal noise as a function of the C/N0 ratio. Curves are plotted based on Eq - 3-19 with the DLL parameters indicated in Table 3-3.

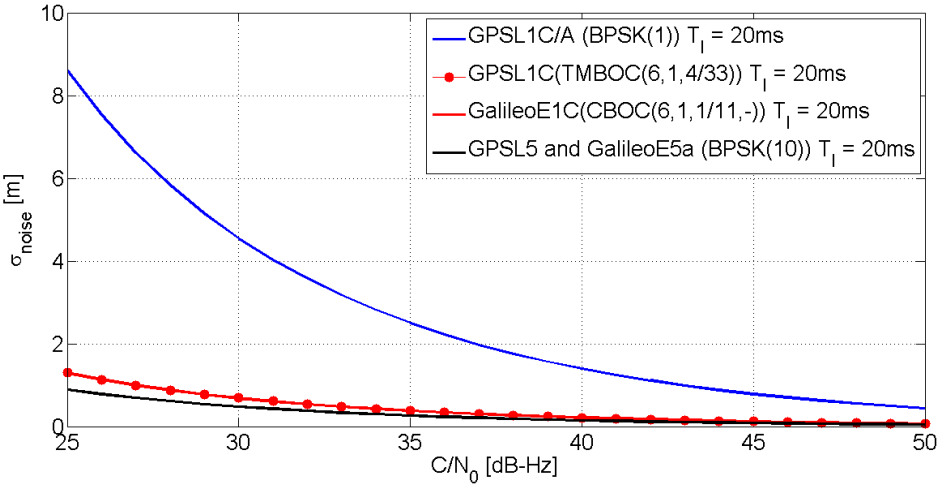

Figure 3-4: Standard deviation of the code thermal noise ranging error - $T_i = 20ms$

BPSK(10) signals are the most robust against thermal noise effects since part of their power is spread away from the central frequency. Then, TMBOC and CBOC signal standard deviations are roughly 30% higher than BPSK(10) standard deviations. Finally, BPSK(1) signals have the poorest robustness in terms of noise effects. Note that the results provided in Figure 3-4 have been obtained for an integration time of 20ms for GPSL1C, GalileoE1 and GalileoE5a. If an integration time of 100ms is adopted for these signals, simulations show that the receiver noise standard deviations are decreased of roughly 10cm at low C/N0 ratios (25dB-Hz to 30dB-Hz), and are roughly equal to the values obtained with an integration time of 20ms at higher C/N0 ratios. As justified in Section 6.2.2, the C/N0 ratios for the application are likely to be higher than 30dB-Hz. Hence, increasing the integration time to 100ms does not provide

a significant benefit in terms of thermal noise reduction. It has been chosen to set the value of T_I to 20ms in the rest of the thesis.

3.2.1.6.2. GPS and Galileo dual frequency mode

Iono-free pseudorange combinations increase the standard deviation of the code thermal noise ranging error. Indeed, the standard deviation of the GPS and Galileo iono-free residual raw code thermal noise ranging error is:

$$\sigma_{noise,L1-L5} = \sqrt{{k_a}^2 \, {\sigma_{noise,L1}}^2 + {k_b}^2 \, {\sigma_{noise,L5}}^2}$$
$$\sigma_{noise,E1-E5a} = \sqrt{{k_a}^2 \, {\sigma_{noise,E1}}^2 + {k_b}^2 \, {\sigma_{noise,E5a}}^2} \qquad \text{Eq - 3-20}$$

where:

- $\sigma_{noise,L1}$ and $\sigma_{noise,L5}$ are the thermal noise error standard deviations on GPSL1C/A or GPSL1C and GPSL5, respectively.
- $\sigma_{noise,E1}$ and $\sigma_{noise,E5a}$ are the thermal noise error standard deviations on GalileoE1 and GalileoE5a, respectively,
- k_a and k_b are detailed in section 3.2.1.4.3.

The receiver noise error correlation time is driven by the DLL bandwidth [Martineau, 2008]. Hence, the correlation time of the single-frequency and iono-free raw code ranging errors due to receiver noise is $T_{noise} = 1/B_{DLL}$.

3.2.1.7. Multipath error

In an airport environment, signal transmission follows not only the direct path, but also a number of distinct propagation paths [Pagani *et al*., 2008]. At the output of the GNSS airborne antenna, the observed signal corresponds to the combination of different signals, each of them presenting a different attenuation, a different phase rotation, and a different code delay. These signal distortions may cause significant errors on the GNSS code pseudo-range measurements. The main phenomena responsible for the multipath propagation are as follows [Pagani *et al*., 2008][Kaplan *et al*., 2006]:

- **Reflection** takes place on obstacles of large dimensions with respect to the wavelength.
- **Transmission** occurs when the medium where the reflection takes place is not perfectly opaque. This causes part of the incident wave travelling through the material.
- **Diffraction** takes place on the edges of large sized obstacles with respect to the wavelength.
- **Diffusion** occurs when an ElectroMagnetic (EM) wave travels towards a group of obstacles of small dimensions with respect to the wavelength.
- **Shadowing** is excess attenuation of the direct path, typically introduced when the direct path propagates through a structure.

In the following, all these phenomena are included in the electromagnetic (EM) scattering phenomenon. Scattering is the re-radiation of EM field on an obstacle that is illuminated by an incoming EM field. Few models can be proposed to predict raw code multipath ranging errors in airport environments:

- **Statistical models** (either purely or partially) which are based on extensive measurement campaigns in **urban environments**. [Park *et al*., 2010] uses the Jahn statistical transmission channel model [Jahn *et al*., 1996] to over-bound the multipath ranging errors in urban environments by a zero-mean Normal distribution. The main advantage of this kind of models is that they are independent of the considered airport. They are thus easy to

embed since they do not require an airport database on-board. However, some characteristics of the urban and airport environments are different. As an example, terminals are generally located on one side of the taxiways in airports while buildings are present in both sides of the roads in urban environments. Hence urban statistical multipath ranging errors models are not well-adapted to precisely model the multipath errors affecting the pseudo-range measurements in airport environments.

- **Statistical models** (either purely or partially) which are based on extensive measurement campaigns during **in-flight operations**. As an example, the "high resolution aeronautical multipath navigation Channel" developed for European Space Agency (ESA) statistically predicts the characteristics of the multipath signals that are scattered or reflected by the aircraft structure (aircraft fuselage) or by the ground during aircraft approaches [Steingass *et al*., 2004]. This publication shows that the multipath error is mainly induced by the aircraft fuselage during the approach phase. This model has been set up by means of a measurement campaign carried out in 2002 by DLR, Joanneum Research, and the University of Vigo for ESA. This model has been coupled to a generic receiver simulator in [Macabiau *et al*., 2006] to present the estimated standard deviation of a zero-mean Normal distribution that over bounds the 100s smoothed GNSS code ranging error due to multipath for a landing aircraft on the GPSL1C/A, GPSL5, GalileoE5a GalileoE5b signals. These error models are also compared to the 100s smoothed GPSL1C/A error model standardized for en-route to CAT I operations [ICAO, 2006] and validated in [Murphy *et al*., 2000]. The standard model appears to be conservative regarding to the error model for GPSL1C/A developed based on the "high resolution aeronautical multipath navigation Channel". However, these models are not adapted to surface operations. Firstly, they do not take into account the effects of scattered signals from airport obstacles, such as terminals, on the raw code multipath ranging errors. Secondly, the ground echo signals that affect the GNSS signals during in-flight operations may have larger code delays and larger attenuation regarding to the ground echo signals affecting the GNSS signals during taxi operations.
- **Mainly or purely deterministic models** which are based on an electromagnetic description of multipath. [Chen, 2010] provides a prediction of the multipath ranging error knowing a description of the 3D airport environment, the GNSS airborne antenna position and the satellite position. The main advantage of these models is the precision of the error prediction. The main limitation being the complexity of implementation requiring a realistic 3D representation of the airport environment.

No raw code multipath ranging error model is currently standardized. However, EM prediction tools and real data analyses allow quantifying the raw code multipath ranging errors and the errors in the GNSS-based position estimates in airport environments. Causes of multipath errors and order of magnitudes of multipath errors in airport environments are presented in Table 3-4.

From Table 3-4, multipath may lead to code ranging errors of up to few meters, which is high relative to the magnitude of code ranging errors caused by the other sources of errors. Multipath is considered to be one of the dominant sources of errors for GNSS during surface movements [Park *et al*., 2010].

Singular event	Multipath
Cause	EM scattering phenomenon, including reflection, transmission, diffraction, diffusion, shadowing, of the incoming EM wave on the aircraft structure itself, on the airport surface and on other obstacles on the airport such as terminals or other aircraft.
Magnitude of code ranging errors	Up to few dozens of meters close to (few meters from) large metallic terminals or to another aircraft on GPSL1C/A [Chen, 2010]. *Note*: for in-flight operations, the smoothed multipath ranging errors are over-bounded by a zero-mean Normal distribution which standard deviation is up to few dozens of decimeters for GPSL1C/A signal [RTCA, 2009] and for Galileo signals [EUROCAE, 2010].
Magnitude of positioning errors	Up to few meters for a GPSL1C/A mono-constellation [Braasch *et al*., 2000], assuming that GNSS measurements estimates are corrected by Ground Based Augmentation System (GBAS) corrections.

Table 3-4: Causes and magnitude of GNSS multipath induced errors

3.2.1.8. Control and space segment induced biases and GNSS airborne antenna induced biases

As shown in the previous paragraphs, most of the GNSS nominal code ranging errors can be modeled by a zero-mean Gaussian distribution. However, some phenomena induce nominal biases on the code pseudo-range measurements. Nominal biases on the GNSS measurements account for both near-constant uncorrected errors and non-Gaussian behavior. Nominal biases include errors that remain essentially constant throughout the duration of an approach and therefore cannot be treated as purely random [GEAS, 2010]. Among the contributors there are mainly the GNSS airborne antenna and both control and space segments. The causes of the nominal biases are further detailed in sections 3.2.1.8.1 and 3.2.1.8.2.

3.2.1.8.1. GNSS airborne antenna induced bias

The GNSS airborne antenna introduces three main effects on the processed GNSS signals. It modifies the received power of the GNSS signals, it introduces an antenna phase offset on the GNSS signals and it introduces an antenna group delay on the GNSS signals. Since airborne antennas are not isotropic, these effects depend on the angle of arrival of the incoming EM waves.

Antenna phase center variations as a function of the EM wave angles of arrival can be a source of error on the GNSS phase measurements [Kunysz, 2010]. Since this chapter focuses on raw code error sources, antenna phase variation induced errors are not detailed in this chapter.

Group delay variations as a function of the EM wave angle of arrival can be a source of error on the GNSS raw code pseudo-range measurements. Indeed, group delays initiated by the GNSS antenna on the processed signals are different toward each satellite, since each satellite is characterized by its own angle of arrival with respect to the GNSS airborne antenna. These antenna group delays induce biases on the GNSS raw code pseudo-range measurements. Since these biases are different for each satellite, they cannot be removed by the user clock bias estimate. In addition, no correction algorithm is currently standardized to remove the effects of such biases. No raw code ranging error model representing the effects of GNSS antenna group delay variations is currently standardized. The causes of multipath errors and order of magnitude of GNSS airborne antenna group delay variations and antenna group delay variations induced errors are presented in Table 3-5.

Singular event	GNSS airborne antenna group delay variations
Cause	Antenna group delays on processed GNSS signals which depend on the angle of arrival of the processed GNSS signals
Magnitude of antenna group delay variations	Group delay variations as a function of the angle of arrival are up to 2 nanoseconds [Murphy *et al*., 2007]. Highest variations are for different satellite azimuth angles at low satellite elevation angles.
Magnitude of code ranging errors	From a few millimeters up to a few decimeters on GPSL1C/A [Murphy *et al*., 2007]. Few decimeters errors occur at low satellite elevation angles for particular satellite azimuth angles. The bias due to the antenna group delay variations has a variation of up to $\mp$40cm around the average value [Macabiau *et al*., 2014].

Table 3-5: Causes and magnitude of errors induced by GNSS airborne antenna group delay variations

Differentiating the contribution of the antenna and the contribution of multipath to the group delay estimate is complex since multipath from the ground plane on which the antenna is located influences the antenna transfer function estimate. Group delay estimates presented in Table 3-5 are initiated by the antenna group delays and by the multipath from the ground plane on which the antenna is located. The ground plane is generally modeled as an infinite metallic plane or by a finite plane with curved edges to avoid the edge diffraction phenomenon [Murphy *et al*., 2007].

3.2.1.8.2. Control and space segments induced bias

GPS ground station antennae present phase center variations and group delay variations as a function of the angle of arrival. These variations induce nominal biases on the GPS code pseudo-range measurements [Shallberg *et al*., 2002]. GPS nominal deformations also induce nominal biases on the GPS code pseudo-range measurements [Mitelman *et al*., 2004] [Phelts, 2001].

3.2.1.8.3. Conclusion

Future GNSS integrity monitoring systems will be designed to protect users from the effects of nominal biases. [GEAS, 2010] assumes that the magnitude of nominal biases is between 10cm and 75cm. The nominal biases proposed in [Murphy *et al.,* 2007] and in [Mitelman *et al*., 2004] [Phelts, 2001] are of the order of a few centimeters up to a few decimeters. Hence, the magnitude of the nominal biases used in [GEAS, 2010] is reasonable.

3.2.1.9. Conclusion

The multipath GNSS code ranging error model is not available for surface operations. In the absence of multipath, the GNSS nominal code pseudo-range measurement error vector at time t is:

$$\boldsymbol{\varepsilon}(t) = \boldsymbol{\varepsilon}_{\text{Sat\&Eph}}(t) + \boldsymbol{\varepsilon}_{\text{iono}}(t) + \boldsymbol{\varepsilon}_{\text{tropo}}(t) + \boldsymbol{\varepsilon}_{\text{noise}}(t) + \mathbf{b}(t) \qquad \text{Eq - 3-21}$$

where:

- $\mathbf{b}(t)$ is the ranging nominal bias vector at time t,
- $\boldsymbol{\varepsilon}_{\text{Sat\&Eph}}(t) + \boldsymbol{\varepsilon}_{\text{iono}}(t) + \boldsymbol{\varepsilon}_{\text{tropo}}(t) + \boldsymbol{\varepsilon}_{\text{noise}}(t)$ is the stochastic nominal ranging error vector at time t. The standard deviation of the stochastic nominal ranging error in the absence of multipath is given by:

$$\sigma_{w/o\ mp} = \sqrt{\sigma^2{}_{Sat\&Eph} + \sigma^2{}_{iono} + \sigma^2{}_{tropo} + \sigma^2{}_{noise}} \qquad \text{Eq - 3-22}$$

$\sigma_{w/o\ mp}$ is plotted as a function of the satellite elevation angle in the single frequency mode and in the dual frequency mode in Figure 3-5. For this Figure, the DLL discriminator is assumed to be a EMLP discriminator, regardless of the tracked signal. The DLL chip spacing and the other DLL characteristics are stated in Table 3-3.

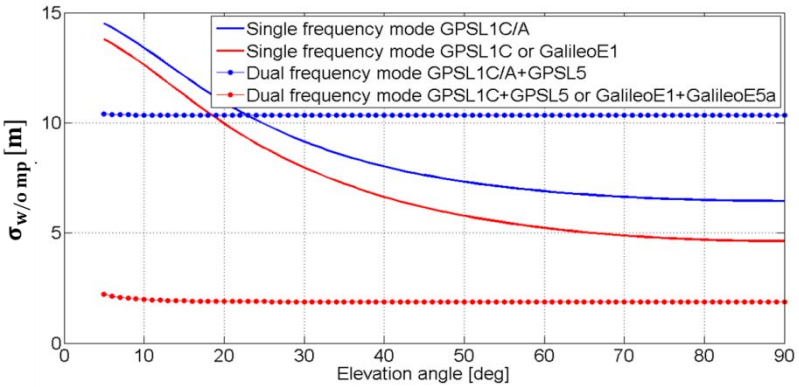

Figure 3-5 : Standard deviation of the nominal code ranging error in the absence of multipath, $C/N0 = 30dB - Hz$, Toulouse (France) latitude

In single frequency mode, the code ranging error standard deviation is lower for GPSL1C and GalileoE1 signals than for GPSL1C/A. This is due to the poor robustness of GPSL1C/A against thermal noise. The dual frequency mode allows eliminating the ionosphere error component. Thanks to this elimination, the code ranging error standard deviation is lower for the dual-frequency mode GPSL1C+GPSL5 signals than for the single-frequency mode GPSL1C. The dual-frequency mode also induces an inflation of the thermal noise code ranging error standard deviation compared to the single-frequency mode. This explains why, at high elevation angle, the code ranging error standard deviation is higher for the dual-frequency mode GPSL1C/A+GPSL5 signals than for the single-frequency mode GPSL1C/A. Due to the poor robustness of GPSL1C/A against thermal noise, and considering the sub-meter level navigation system performance requirements in terms of accuracy and integrity for the application (guidance function under low visibility conditions during taxi operations), the GPSL1C/A signal is not considered in the rest of this thesis.

3.2.2. GNSS ranging failures

3.2.2.1. Identification

Four sources of GNSS ranging failures have been identified for airport environments:

- Control and space segment events,
- Ionosphere anomalies,
- Unintentional and intentional interference,
- Multipath.

As discussed in Section 3.2.1.5, the anomalous troposphere ranging errors induced by the troposphere storms are as part of the nominal troposphere error model. For this reason,

anomalous troposphere ranging errors induced by troposphere anomalies are not presented in this section.

In order to properly identify which failure sources may represent a threat in terms integrity for taxi operations, the magnitude and the probability of occurrence of each failure mode must be assessed. This is the goal of the following sub-sections.

3.2.2.2. Control and space segment events generating GNSS satellite ranging failures

3.2.2.2.1. Major Service Failure

A Major Service Failure (MSF) is defined to occur whenever a healthy SIS's instantaneous User Ranging Error (URE) exceeds the SIS not-to-exceed tolerance without a timely alert (alarm or warning) being provided. The not-to-exceed tolerance is defined to be 4.42 times the upper bound of the currently transmitted URA. This definition is valid for the GPS constellation [GPS SPS, 2008] and can be extended to the Galileo constellation [EUROCAE, 2010]. The instantaneous URE includes only the pseudo-range set error budget components assigned to the control and space segments.

[GPS SPS, 2008] contains the assurance that the probability of occurrence an individual GPS major service failure does not exceed:

$$p_{MSF,GPS} \leq 1.0.10^{-5}/\mathrm{SV/hr} \qquad \text{Eq - 3-23}$$

[GPS SPS, 2008] assumes a maximum duration of the MSFs of 6 hours, but this duration is expected to be shortened to 1 hour for Galileo and for the modernized GPS constellation [Martineau, 2008].

[EUROCAE, 2010] contains the assurance that the probability of occurrence an individual Galileo major service failure will be on average 3 major failures per year for a 27 Galileo satellites constellation. This corresponds to a probability of occurrence an individual Galileo major service failure of:

$$p_{MSF,Galileo} \leq 1.3.10^{-5}/\mathrm{SV/hr} \qquad \text{Eq - 3-24}$$

GPS MSF events are sufficiently characterized and some current integrity monitoring systems implemented onboard, such as Receiver Autonomous Integrity Monitoring (RAIM) systems, are designed to detect MSF with a probability of missed detection that depends on the targeted operation. However, some control and space segments events may generate smaller single ranging failures not considered as MSF. Current RAIM systems are not designed to protect users from these smaller single ranging failures which are presented in the next paragraph.

3.2.2.2.2. Other GNSS single satellite ranging failures

Some of the control and space segment ranging failures characterized by a size below the not-to-exceed tolerance bound defined in the previous paragraph are currently not fully characterized in terms of magnitude, error shape and probability of occurrence. Elements extracted from the literature to characterize these GNSS single satellite ranging failures are recapped in Table 3-6.

From Table 3-6, control and space segment events induced failures are due to several ranging failure sources. The effects of each failure source on the ranging measurements in terms of magnitude, error shape and probability of occurrence have not been fully characterized. The magnitude, error shape and probability of occurrence of GNSS single ranging failures highly

depend on their cause(s). In addition, no information on the duration of control and space segments failures inducing small ranging errors has been found.

Singular event	Control and space segment events inducing GNSS single ranging failures
Causes	Mainly failures in the space segment (i.e. clock frequency shift, navigation message aberration, modulation imperfections, ect)
Magnitude of ranging failures	Example 1: errors induced by clock frequency shift: slow ramp errors [1.0m/hr ; 2.0m/hr]
	Example 2: errors induced by navigation message aberration: magnitude to be determined
Probability of occurrence of ranging failures	Example 1: Clock frequency shift: $2.5.10^{-9}/\mathrm{SV}/150\mathrm{s}$
	Example 2: Navigation message aberration: occurrence to be determined

Table 3-6: Causes and magnitude of single ranging failures caused by control and space segment events [GPS SPS, 2008] [Boeing, 2005]

3.2.2.2.3. GNSS multiple satellite ranging failures

On-board integrity monitoring systems implemented onboard (such as RAIM), are not designed to detect satellite ranging failures occurring simultaneously on multiple satellite with a sufficiently high probability [Lee, 2004]. However, some control and space segment events may generate multiple satellite ranging failures and are classified as follows:

- **Multiple independent control and space segment failure modes** may occur simultaneously and generate ranging failures on multiple pseudo-range measurements at the same time. An independent control and space segment failure mode represents a failure in the control or space segment that induces a satellite ranging failure on a single pseudo-range measurement. Independent control and space segment failure modes mainly originate from anomalies in the space segment and are presented in Section 3.2.2.2.2. The computation of the probability of occurrence of simultaneous multiple independent control and space segment failures requires knowing the probabilities of occurrence each independent control and space segment failure [Martineau, 2008]. From Section 3.2.2.2.2, the probability of occurrence of the MSF is known. The probability of occurrence of two MSFs on two visible satellites at the same time is $1.3 \times 10^{-8}/150\mathrm{s}$ given 12 satellites in view. However, the probability of occurrence of multiple control and space failures inducing small ranging errors occurring simultaneously is complex to determine since the occurrence of control and space failures inducing small ranging errors is not sufficiently characterized.
- A **common control and space segment failure mode** generates ranging failures on multiple pseudo-range measurements at the same time when they occur. These faults are called “correlated faults” in the literature [WG-C ARAIM, 2012]. Elements extracted from the literature to characterize the GNSS multiple satellite ranging failures caused by the common control and space segment failure modes are recapped in Table 3-7.

Singular event	Control and space segment events inducing GNSS multiple ranging failures	
Causes	Failures in the control segment: - Curve fit errors in the ground segment, - Wrong data used in MCS:: ✓ Erroneous values of various constants used by the GPS MCS to estimate satellite orbits and clocks could. ✓ Biased satellite tracking data into MCS. - Software or hardware errors in the MCS or in one or more ground stations which perform measurements to estimate satellite orbits and clocks.	Anomalies in the information supplied to the control segment by an external source: - Bad Earth Orientation Parameters (EOPs) and Earth Rotation Rate Parameters (EOPPs) predictions upload due to two types of events: ✓ Change in Earth motion since the upload of EOPs and EOPPs predictions because of geological phenomena, such as earthquakes. ✓ Faulty process to generate EOPs and EOPPs. - Bad solar flux observations which imply bad ionospheric correction data upload. - Bad reference orbit used, - Bad UTC offset data.
Magnitude of ranging failures	Bad upload from control segment caused by wrong data used ion the MCS: ramp error of $[0\text{km.hr}^{-1}, 3\text{km.hr}^{-1}]$	Bad upload from erroneous EOPs or ERRPs upload: ramp error of up to $1.1\ \text{cm.hr}^{-1}$
	Bad upload from MCS hardware or software failure: to be determined	Bad upload from erroneous solar flux observations: to be determined
Probability of occurrence of ranging failures	Bad upload from control segment caused by wrong data used in the MCS: $1.0 \times 10^{-8}/\text{upload}$	Bad upload from erroneous EOPs or ERRPs upload: $6 \times 10^{-12}/150\text{s}$ [Boeing, 2005]. However, GPS wing claims values of $1.0 \times 10^{-5} - 1.0 \times 10^{-7}/\text{hr/SV}$ for GPS II and $1.0 \times 10^{-9}/\text{hr/SV}$ for GPS III
	Bad upload from MCS hardware or software failure: to be determined	Bad upload from erroneous solar flux observations: to be determined

Table 3-7: Causes and magnitude of multiple ranging failures caused by common control and space segment failure modes [GPS SPS, 2008] [Boeing, 2005] [Pervan, 2011] [GEAS, 2010] [WG-C ARAIM, 2012]

Among the threats listed in Table 3-7, erroneous EOP and EOPP parameters are explicitly listed as a potential integrity fault mode in the current GPS Standard Positioning Service Performance Standard [GPS SPS, 2008]. For multiple satellite ranging failures due to erroneous EOPs and ERPPs, the predicted induced ranging error is a ramp error of a few centimeters per hour [Boeing, 2005] while other publications predict that the induced horizontal positioning error will grow to a few tens of meters per seconds [Pervan, 2011] [GEAS, 2010]. Similarly, different publications propose different values of probability of occurrence of erroneous EOPs and ERPPs [Boeing, 2005] [Pervan, 2011]. In addition, no information on the duration of control and space segments failures inducing small ranging errors has been found.

From Table 3-7, the effects of other common control and space segment failure modes on the ranging measurements in terms of magnitude, error shape and probability of occurrence have not been fully characterized.

The assumed probability of occurrence of common failure modes causing multiple satellite ranging failures is 1.3×10^{-8}/150s for RAIM LPV-200 approaches [Lee *et al*., 2007] for the modernized GPS constellation. It appears to be comparable to the probability of two simultaneous independent GPS ranging failures, given that about 12 satellites are in view, and that the mean duration of a single anomaly is 1 hour [Fernow, 2011].

3.2.2.3. Ionosphere anomalies

Observations have shown that the ionosphere electron content can be temporally and locally strongly modified compared to the ionosphere electron content in nominal conditions [Jakowski]. These strong modifications in the nominal ionosphere electron content are designated as "ionosphere anomalies" in this thesis and are listed below. Note that ionosphere anomalies are induced by causes called "ionosphere events" in this thesis. Both ionosphere anomalies and ionosphere events concepts are thus distinct in the following. Some current integrity monitoring systems, such as RAIM, are not designed to detect the ranging failures induced by the ionosphere anomalies with the related and targeted level of detection performance.

3.2.2.3.1. Scintillations

The scintillations are dynamic effects due to irregularities in the electron concentration causing fast variations in the ionized particles concentration. Irregular zones in the ionosphere produce diffraction of the GNSS signals going through these zones [Humphreys *et al*., 2009]. Diffraction of the radio signals causes fluctuations in the signal amplitude and phase. Hence, scintillations are characterized as a rapid change in the amplitude (amplitude scintillation) and phase (phase scintillation). Phase scintillation effects on the code tracking are negligible and can be ignored [Hegarty *et al*., 2000]. Hence, this section focuses on amplitude scintillations. Elements extracted from the literature to characterize the GNSS raw code ranging errors caused by the amplitude scintillations are recapped in Table 3-8.

The ionosphere events causing the ionosphere anomalies are fully described in the literature [Eurcontrol, 2010]. The effects of scintillations in a region can last from 30 minutes up to several hours. The probability of occurrence of strong amplitude scintillations has been evaluated in some low latitude regions [Béniguel, 2005]. In mid-latitude regions, the occurrence has been sufficiently characterized to consider that scintillations have a minimal impact in terms of integrity, continuity and availability.

Singular event	Amplitude scintillations
Causes (ionosphere events)	- Auroras - Ionosphere storms - Plume effects - Travelling Ionosphere Disturbances (TIDs) - Sporadic E-layers - Ionosphere blobs - Ionosphere bubbles - Ionosphere bays
Magnitude of ranging failures	Impact of amplitude scintillations on code ranging errors equivalent to an increase of the standard deviation of the GNSS receiver thermal noise ranging error σ_{noise} [Hegarty *et al*., 2000] σ_{noise} is increased from a few decimeters to a few meters at low C/N0 ratio Note: amplitude scintillations may result in a complete loss of lock of GNSS signals, leading to a reduced number of available satellites of at most 4 satellites in low latitude regions
Occurrence of singular event	Daily in equatorial regions

Table 3-8: Causes and magnitude of ranging failures caused by amplitude scintillations [Hegarty *et al*., 2000] [Groves, 2004] [Eurocontrol, 2010] [ICAO, 2006b]

3.2.2.3.2. Irregular TEC values

The TEC [el/m²] represents the number of free electrons in a 1-square meter column along the path satellite-receiver. Elements extracted from the literature to characterize the GNSS raw code ranging errors caused by the irregular TEC values are recapped in the next Table.

Singular event	Irregular TEC values
Causes (ionosphere events)	Ionosphere storms
Magnitude of ranging failures	Large ionospheric raw code ranging errors up to few dozen of meters observed in October 2003 over North America.
Occurrence of singular event	0.00442/day over North America. This value is obtained from geomagnetic activity observation over the half solar cycle duration following the solar peak of 1999 and is likely to be conservative since ionosphere anomalies occur more likely in the years following the solar peaks.

Table 3-9: Causes and magnitude of ranging failures caused by irregular TEC values [Pullen *et al*., 2006] [Datta-Barua, 2008]

A conservative bound of the probability of occurrence of extreme ionosphere storms has been evaluated over North America [Pullen *et al.*, 2006]. Such a bound is not publically known over Europe.

3.2.2.3.3. Irregular TEC gradients

The concept of spatial and temporal TEC gradients under nominal conditions has been introduced in Section 3.2.1.4. Let's introduce the concept of irregular TEC gradients.

Irregularities in the ionosphere composition induced by ionosphere events may generate irregular values of spatial and temporal TEC gradients that are not modeled by the Klobuchar and NeQuick models. Elements extracted from the literature to characterize the GNSS raw code ranging errors caused by the irregular TEC gradients are recapped in Table 3-10.

Singular event	Irregular TEC gradients
Causes (ionosphere events)	- Ionosphere storms - TIDs - Ionosphere blobs - Ionosphere bubbles
Magnitude of ranging failures	Large ionospheric raw code ranging error variations in the time domain. Error variations up to 150mm/s on L1 GNSS signals observed in October 2003 over North America for a static receiver. Large ionospheric raw code ranging error variations in the horizontal space domain. Error variations up to 425mm/km on L1 GNSS signals observed in October 2003 over North America.
Occurrence of singular event	0.00442/day over North America. This value is obtained from geomagnetic activity observation over the half solar cycle duration following the solar peak of 1999 and is likely to be conservative since ionosphere anomalies occur more likely in the years following the solar peaks.

Table 3-10: Causes and magnitude of ranging failures caused by irregular TEC gradients [Datta-Barua *et al*., 2010] [Pullen *et al*., 2006]

A conservative bound of the probability of occurrence of severe ionosphere storms inducing irregular spatial and temporal TEC gradients has been evaluated over North America [Pullen et al, 2006]. Such a bound is not publically known over Europe.

3.2.2.4. Interferences

3.2.2.4.1. Unintentional interference

Radio-frequency signals may interfere unintentionally with GNSS signals. Radio-frequency signals are generated by:

- Equipment that intentionally generates and emits radio-frequency signals in the GNSS frequency bands to operate and not for hostile purpose. As an example, Distance Measurement Equipment (DME) station transponders emit radio-frequency signals in the GNSS L5 frequency band.
- Equipment that unintentionally emits RF signals. Unintentional emissions in the GNSS frequency bands are essentially due to the non-linearity of some RF emitters that generates harmonics in the GNSS frequency bands.

Radio-frequency interfering signals can be classified as follows:

- Pulsed signals are concentrated in the temporal domain. Examples of these signals are Ultra Wide Band (UWB) [Pagani *et al*., 2008] signals that are used for indoor localization and for short range communications are DME, TACtical Air Navigation (TACAN), Joint Tactical Information Distribution System (JTIDS) signals [Raimondi, 2008] [Bastide, 2004].

- Carrier Wave (CW) signals that are characterized in the frequency domain as a single tone in the GNSS frequency bands and that are modeled in the temporal domain as a pure sinusoid [Borio, 2008].
- Wideband signals that are characterized in the frequency domain by a wide bandwidth relative to the GNSS signal bandwidths and narrowband signals that are characterized in the frequency domain by a narrow bandwidth relative to the GNSS signal bandwidths [Kaplan *et al*., 2006].

Elements extracted from the literature to characterize the GNSS raw code ranging errors caused by unintentional interference are recapped in Table 3-11, in Table 3-12 and in Table 3-13.

The effects of unintentional pulsed, narrowband and wideband interferences on a particular GNSS signal can be modelled as the effect of additional white noise at the receiver input on this signal, or, equivalently, as a decrease of the C/N0 ratio related to the affected signal. The effects of these interferences on the code ranging errors can be included in the GNSS receiver thermal noise ranging error model that is a function of the C/N0 ratio. Hence, any positioning failure due to the combination of nominal errors and pulsed, narrowband or wideband interferences is detected by the current integrity monitoring systems with the same level of integrity performance as the detection performance level related to the detection of positioning failures induced by the GNSS receiver thermal noise errors.

Unintentional CW interferences may generate biases on one or several code pseudo-range measurements that may not be properly detected by GNSS integrity monitoring systems. Some current integrity monitoring systems, such as RAIM, are not designed to detect the ranging failures induced by the CW interference with the related and targeted level of detection performance.

Singular event	Unintentional interference with pulsed signals
Cause	Unintentional and intentional emission of pulsed interfering signals in the GNSS frequency bands
Magnitude of ranging failures	Civil aviation receivers are equipped with pulsed interference mitigation techniques, such as pulse blanker [Bastide, 2004] in order to comply with civil aviation performance requirements under strong pulsed interference conditions [Tran *et al*., 2001]. Equivalent to a decrease of the C/N0 ratio. Impact of pulsed interference on code ranging errors equivalent to an increase of the standard deviation of the GNSS receiver thermal noise ranging error σ_{noise} . σ_{noise} is increased a few decimeters on GPSL5 under the worst case DME/TACAN/JTIDS scenario in the United States and in the presence of a pulse blanker [Tran *et al*., 2001].
Occurrence of singular event	Unknown in airport environments

Table 3-11: Causes and magnitude of ranging failures caused by pulsed interfering signals

Singular event	Unintentional interference with CW signals
Cause	Unintentional emission of CW interfering signals in the GNSS frequency bands
Magnitude of ranging failures	Impact of CW interference on code ranging errors: - Introduction of biases on one or several raw code pseudo-range estimates. Interference biases mainly depend on Early-Late correlator spacing of the DLL, the power, the phase, the frequency and the Doppler frequency rate of the interfering signal with respect to the GNSS signal spectrum [RTCA, 2008]. The bias magnitude on GPSL1C/A is up to 20m in the presence of a CW interfering signal 5dBm below the GPSL1C/A RFI mask [Ouzeau, 2009]. - Increase of the standard deviation of the GNSS raw code ranging error on one or several raw code pseudo-range estimates. Standard deviation increase of few decimeters up to few meters for powerful CW interfering signals. This augmentation has not a significant impact on the positioning error since only few pseudo-ranges measurements are affected by CW interference [Martineau, 2008].
Occurrence of singular event	Unknown in airport environments

Table 3-12: Causes and magnitude of ranging failures caused by CW interfering signals

Singular event	Unintentional interference with wideband and narrowband signals
Cause	Unintentional emission of wideband and narrowband interfering signals in the GNSS frequency bands
Magnitude of ranging failures	Equivalent to a decrease of the C/N0 ratio Impact of narrowband and wideband interference on code ranging errors equivalent to an increase of the standard deviation of the GNSS receiver thermal noise ranging error σ_{noise} .
Occurrence of singular event	Unknown in airport environments

Table 3-13: Causes and magnitude of ranging failures caused by wideband and narrowband interfering signals [Betz *et al*., 2009]

3.2.2.4.2. Intentional interference

The intentional interference threat models may be classified as follows:

- **Jamming** is the most likely form of intentional attack and is defined as the broadcast of radio-frequency power that interferes with a receiver's ability to track the GNSS genuine signals, resulting in denial of service [Lo *et al*., 2009]. A GNSS jammer is a device that emits powerful signals in the GNSS frequency bands [Papadimitratos *et al*., 2008]. Examples of jamming events are described in the literature [Ochieng] [PNT, 2010]. GNSS signals are particularly vulnerable to jamming mainly because of the relative low power of GNSS signals at the surface of the Earth.

- **Spoofing** is the more anecdotal form of intentional attack and is defined as the broadcast of competing signals that make the position estimated by the user receiver incorrect [Lo *et al*., 2009]. GNSS signals used tracked by GNSS airborne receivers are particularly vulnerable to spoofing mainly because of the absence of encryption on these open-service GNSS signals. Competing signals may be generated [Papadimitratos *et al*., 2008]:
  - Based on previously received GNSS signals: the spoofer records navigation messages and re-transmits them. This is called "replay" attacks.
  - Based on signal generators that are able to generate GNSS signals with falsified navigation parameters with respect to the parameters contained in the genuine GNSS signals [Motella *et al*., 2010] [Enge *et al*., 2009] [Humphreys *et al*., 2008].

Elements extracted from the literature to characterize the GNSS raw code ranging errors caused by intentional interference are recapped in Table 3-14.

Singular event	**Intentional interference**	
Causes	**Jamming attack**	**Spoofing attack**
Magnitude of ranging failures	Impact of jamming on code ranging errors: - Complete loss of lock of a GNSS signals and deny of service - Same effects as a CW unintentional interference if the jamming attack is the emission of a CW signal. Note: a 100W jammer source can make an airborne receiver lose track of the GPSL1C/A signals in a zone of up to several hundreds of kilometers around the jamming source.	Raw code ranging error depends on the tracked competing signals. For replay attacks: raw code ranging errors generally modeled as a drift with a rate that depends on the attack.
Occurrence of singular event	Precise occurrence unknown in airport environments. Jamming is frequent in or near airports, but jamming events do not have always an impact on the GNSS signals used in civil aviation.	Unknown in airport environments

Table 3-14: Causes and magnitude of ranging failures caused by intentional interfering signals

Since the error magnitude, the error shape and the occurrence of interference, and more specifically of intentional interference, is not fully characterized, some current integrity monitoring systems, such as RAIM, used in aviation applications are not designed to detect the ranging failures induced by the intentional interference with the related and targeted level of detection performance.

3.2.2.5. Multipath

The concept of GNSS ranging failures due to multipath and of probability of occurrence of multipath ranging failures will be further developed in Chapter 8 of this thesis.

3.2.3. Case of study

In Chapter 2, it is established that the alert limits and integrity risks for the guidance application during surface operations under low visibility conditions are small compared to those for en-route to APV operations. Hence, designing integrity monitoring systems for surface operations requires taking into account the effects of multipath in airport environment and the effects of several error sources that were neglected for en-route to APV operations and that include:

- Nominal ranging biases due to the space and control segments and due to the GNSS airborne antenna,
- Single satellite ranging failures that have magnitude below the MSF not-to-exceed threshold,
- Multiple satellite ranging failures,
- Ranging failures due to ionosphere anomalies,
- Ranging failures due to intentional and unintentional interference.

Investigating the impact of nominal ranging biases on the accuracy and on the integrity for surface operations is not considered as a priority since the magnitude of nominal ranging biases is low compared to the magnitude of ranging errors as a result of multipath or ionosphere anomalies.

Similarly, small single satellite ranging failures and multiple satellite ranging failures are not assessed in this thesis. The error magnitude, the error shape and the occurrence of such failures have not been sufficiently characterized to properly analyze the impact of these failures on the accuracy and integrity. In addition, two of the three implemented augmentation systems (GBAS and SBAS) are designed to detect such failures. GBAS and SBAS are presented in Section 3.3.

As justified in Section 3.2.2.4.1, any positioning failure due to the combination of nominal errors and pulsed, narrowband or wideband interferences is detected by the current integrity monitoring systems with the same level of detection performance as the detection performance level related to the detection of positioning failures induced by the GNSS receiver thermal noise errors. For this reason, pulsed, narrowband and wideband interferences are not treated in this thesis.

GNSS ranging failures induced by CW interferences may not be detected by GNSS integrity monitoring systems with the related and targeted level of detection performance. Biases induced by CW interferences occur when a powerful CW interfering signals is emitted at a frequency in the spectrum of a GNSS signal during few seconds. The occurrence of the emission of such CW interfering signals is considered as negligible in the literature. Hence, CW interferences are not treated in this thesis.

Intentional interference effects may not be detected by the current integrity monitoring algorithms used in civil aviation and intentional interference effects may be especially dangerous for surface operations and low altitude in-flight operations. Nevertheless:

- Occurrence and error amplitudes are unpredictable since they depend on the activity of the spoofers/jammers. The threat has not been sufficiently characterized to properly analyze the impact of these failures on the accuracy and integrity. In addition, in the absence of occurrence information and impact analysis of intentional interference on ranging measurements, there is still a doubt concerning the real necessity to consider this threat for the application.
- The nature of all possible existing attacks is relatively unknown and as the nature of future attacks remains unpredictable. There is a risk that the analyses or/and detection techniques

that would be proposed in this project are adapted to attacks that are or will become marginal.
- Since intentional interference emissions in the L1 and L5 bands are illegal, one could argue that any potential threat induced by intentional interference needs to be addressed by law enforcement and not by the airborne system architecture.

For these three last reasons, this thesis does not deal with intentional interference.

Ionosphere anomalies and multipath generate the largest code ranging errors during surface operations. The standard deviation of the residual ionosphere code ranging error after corrections by the ionosphere models recommended in [RTCA, 2009] [EUROCAE, 2010] of after GBAS or SBAS differential ionosphere corrections may be inappropriate in the presence of ionosphere anomalies since:

- The recommended ionosphere models [RTCA, 2009] [EUROCAE, 2010] assumes a nominal ionization of the ionosphere,
- SBAS and GBAS ground subsystem and airborne receivers may experience significantly different ionospheric errors [Datta-Barua, 2008] in the presence of scintillations or irregular TEC gradients.

In the single frequency mode, ionosphere anomalies detection techniques during operations supported by SBAS are implemented [Walter *et al*., 2000] [Sparks *et al*., 2005]. Recently, new techniques able to maintain the integrity and availability of the position solution under irregular ionosphere conditions have been developed and are expected to be implemented in the future SBAS versions [Sparks *et al*., 2011] [FAA, 2011]. Ground and airborne TEC gradients detection and mitigation techniques during operations supported by GBAS are under standardization [ICAO, 2010] [RTCA, 2008b] [EUROCAE, 2010].

The Iono-free (Ifree) smoothing technique combines dual-frequency carrier and code measurements to eliminate the ionosphere component at the expense of an inflation of the ground and airborne thermal noise errors [Konno *et al.*, 2006]. IFree technique is standardized in the drafts Galileo EUROCAE MOPSs [EUROCAE, 2010] and is expected to be standardized in the future GPSL1-L5 RTCA MOPSs.

To conclude, even if current integrity monitoring systems are not designed to detect the effects of the ionosphere anomalies with the related and targeted level of detection performance, single frequency detection and mitigation techniques are under standardization and the Ifree technique will eliminate the ionosphere component. However, no multipath detection and mitigation technique exists which is able to maintain the integrity and availability of the position solution during surface operations is under standardization. The multipath error will not be eliminated by dual-frequency techniques. It is thus essential to design integrity monitoring systems that take into account the effects on multipath in airport environments. The multipath error modelling and the multipath failure analysis are addressed in the following chapters.

3.3. GNSS augmentation systems

3.3.1. Systems presentation

In order to meet the civil aviation operational requirements in terms of accuracy, integrity, availability and continuity, the aviation community has standardized augmentation systems to

correct the GNSS pseudo-range measurements and to monitor the received SIS. Three kinds of GNSS augmentation systems are described below.

SBASs are wide coverage augmentation system in which the user receives augmentation information from a satellite-based transmitter [ICAO, 2006]. SBAS consists of the satellite subsystems, the ground subsystem and the airborne subsystem. The ground subsystem collects measurements from the core constellation satellites and the SBAS geostationary satellites and computes differential corrections and SIS integrity data. It transmits these data to the airborne subsystem via the geostationary satellites. SBAS allows correcting each pseudo-range measurements by a satellite clock correction term, an ephemeris correction term and an ionospheric correction term [RTCA, 2006].

GBASs provide locally relevant pseudo-range corrections and integrity monitoring for GNSS ranging sources [ICAO, 2006]. GBAS consists of the satellite subsystems, the ground subsystem and the airborne subsystem. The ground subsystem consists of GNSS reference receivers and a GBAS ground facility close to the airport and provides ephemeris and satellite clock errors, tropospheric errors and ionospheric errors differential corrections to the airborne receiver. The tropospheric and ionospheric delays are partially mitigated by the differential corrections since the spatial de-correlation between the reference receivers and the airborne receivers is responsible for small residual troposphere and ionosphere errors. The ground subsystem also monitors the integrity of the space and ground systems and provides differential correction integrity data to the airborne receiver.

ABAS is an augmentation system that augments and/or integrates the information obtained from the other GNSS elements with information available on board the aircraft [ICAO, 2006]. ABAS monitors the integrity of the position solution using:

- redundant information from GNSS information (multiple range measurements) through RAIM algorithms,
- redundant information from additional on-board sensors (e.g. barometric altimeter, clock and inertial navigation system (INS)) through Aircraft Autonomous Integrity Monitoring (AAIM) algorithms.

In addition, improvements of the accuracy, availability and continuity can be obtained in the case of AAIM thanks to the integration of GNSS measurements with external sensor measurements [Néri, 2011].

3.3.2. Case of study

In Section 3.2.3, it is established that this thesis focuses on multipath error modelling and multipath failure modes analysis in airport environments. In order to analyze the multipath failure modes, the impact of multipath on the positioning error must be assessed. For this assessment, models of the residual ranging errors are required and depend on the GNSS augmentation system that is used. Three GNSS augmentation systems can be proposed to support surface operations:

- SBAS. In obstructed areas, such as in airport environments, the visibility of the SBAS geostationary satellites may be degraded. Hence, the data link between the geo satellites and the airborne antenna may not be optimal. For this reason, SBAS is not retained in the context of this thesis.
- GBAS. In order to meet the meter level SIS accuracy and integrity operational requirements for surface operations presented in Table 2-4, GBAS double-constellation GPS+Galileo and dual-frequency L1+L5 must be considered.
- ABAS. As for GBAS, ABAS double-constellation GPS+Galileo and dual-frequency L1+L5 must be considered in this thesis.

GBAS double-constellation dual-frequency will not support surface operations before 2023. ABAS double constellations and dual frequency is likely to be used before the GBAS double-constellation dual-frequency operation, that is to say by 2021. In addition, ABAS is of particular interest as they do not need the support of external infrastructures. Hence, this thesis assumes that surface operations will be supported by a double-constellation and dual-frequency ABAS.

3.4. Conclusions

In this chapter, nominal ranging errors and ranging failures affecting GNSS measurements during surface operations are presented. Multipath is one of the main error contributors in the airport environment and may significantly degrade both accuracy and integrity of the position solution. It is thus essential to maintain the integrity of the position solution by designing integrity monitoring systems able to properly detect multipath failures. This thesis models the multipath error and analyzes multipath failures in the airport environment.

The multipath error modelling and the multipath failure analysis require identifying first the GNSS constellations, the GNSS signals and the GNSS augmentation system that will support future surface operations under low visibility conditions. GPS and Galileo will be likely to be used in aviation applications by 2020 and are retained in this thesis. The L1 and L5 signals that are considered are: GPSL1C, GPSL5, GalileoE1 and GalileoE5a. Finally, ABAS double-constellation multi-frequency is chosen to support the guidance function during surface operations under low visibility conditions.

CHAPTER 4

Impact of multipath on GNSS measurements

This chapter presents the theoretical impact of multipath on:

- the GNSS signals received by the GNSS airborne antenna,
- the code delay estimated by the GNSS airborne receiver,
- the code pseudo-range measurements estimated by the GNSS airborne receiver.

In Section 4.1, this chapter introduces the transmission channel models in the presence of multipath. In Section 4.2, the signal processing blocks of the GNSS airborne receiver are described. In Section 4.3, the theoretical impact of multipath on the code tracking loop and on the code pseudo-range measurements is assessed.

4.1. Transmission channel modeling

4.1.1. Definition

The transmission channel includes any media and device inside which the signal travels between the transmitter and the receiver [Pagani *et al*., 2008]. It includes:

- the transmitter antenna,
- the propagation channel,
- the receiver antenna.

The propagation channel represents the transformation of the electromagnetic waves throughout their propagation in the physical medium that is used to send the signal from transmitter to the receiver [Pagani *et al*., 2008] [Proakis, 2001]. In the literature, some publications assimilate the propagation channel and the transmission channel. In this thesis, both concepts are distinct. The transmitter, the transmission channel and the receiver are presented in Figure 4-1.

Each part of the transmission channel can be mathematically represented by its own model. In the following, each transmission channel stage is presented separately.

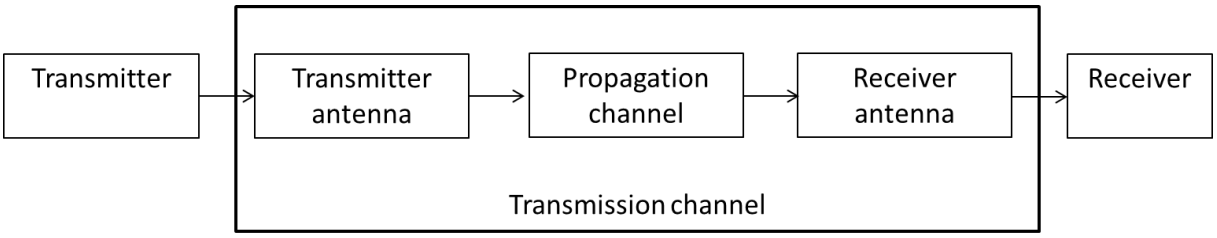

Figure 4-1: Propagation channel and transmission channel

4.1.2. Transmitter antenna

The transmitter antenna is the satellite antenna which radiates GNSS signals with a Right-Hand Circular Polarization (RHCP).

4.1.3. Multipath propagation channels

Throughout their propagation between the transmitter antenna and the receiver antenna, GNSS electromagnetic waves are affected by:

- atmospheric perturbations,
- interference perturbations,
- multipath perturbations.

The atmospheric perturbations occur in the ionosphere and troposphere. Atmospheric and interference perturbations are presented in Sections 3.2.1.4, 3.2.1.5 and 3.2.2.4.

Multipath perturbations are due to EM scattering, defined as the re-radiation of EM field on an obstacle that is illuminated by an incoming EM field. EM scattering includes reflection, transmission, diffraction and shadowing perturbations. These perturbations are defined in Section 3.2.1.7. As a result of EM scattering, the received GNSS signal can be modelled as the combination of different signals, that is to say as a number of superimposed replicas of the signal emitted by the transmitter antenna. In this document, the echo signals, also called multipath, are the different GNSS signals resulting from the EM scattering phenomena. Each echo signal presents an attenuation, a phase rotation and a code delay with respect to the direct signal.

In this chapter, both direct and echo signals are assumed to be affected by the same atmospheric perturbations. Indeed, at the local scale of the airport, it can be considered that the scattered signals are affected by the same ionospheric and tropospheric effects. In addition, it is assumed that the direct signal and the echo signals are not affected by interference. Multipath perturbations and other perturbations can thus be treated separately. The rest of this chapter focuses on the propagation channel modelling in the presence of multipath perturbations only.

The parameters of the propagation channel can be predicted based on three types of models [Chen *et al*., 2010] that are described as follows:

- The **deterministic models** use electromagnetic multipath prediction methods and require a description of the 3D scene to predict multipath parameters [Ercek *et al*., 2005] [Chen *et al*., 2009].
- The **statistical models** estimate the channel parameters as random variables by means of a statistical description of the environment based on extensive experimental data [Jahn *et al*., 1996].
- The **hybrid deterministic-statistical models** are based on both deterministic and statistical predictions [Steingaß *et al*., 2004] [Chen *et al*., 2010].

4.1.4. Receiver antenna

The receiver antenna induces two effects on the received GNSS signals [Chen, 2010] that are described as follows:

- The receiver antenna introduces a group delay and a phase shift on the GNSS signals.
- The receiver antenna influences the power of the received GNSS signals and introduces polarization losses due to polarization mismatch between the receiver antenna and the incoming GNSS EM waves.

GNSS receiver antennas are not isotropic. This implies a variation of the induced group delay and phase shift as a function of the angle of arrival of the incoming GNSS EM waves. This variation may lead to errors on the GNSS measurements, as detailed in Section 3.2.1.8.1. The power of the received signals and the polarization losses also depend on the angle of arrival of the incoming GNSS EM waves. For example, signals coming from the ground are strongly attenuated by the antenna pattern. The group delay, the phase shift, and the power distortions induced by the GNSS receiver antennas also depend on the frequency of the received signal. The variations of the induced group delay and phase shift as a function of the frequency are further detailed in [Murphy *et al.*, 2007].

From Chapter 3, this Ph.D. thesis assumes that the GNSS receiver will use GNSS signals on both L1 and L5 frequency bands to estimate the GNSS airborne antenna position. Hence, the GNSS receiver antenna is assumed to be a dual-band L1+L5 antenna. Dual-band antennas are generally represented by their antenna gain pattern or by their effective height on both L1 and L5 frequency bands. For the L1 frequency band, the antenna gain and effective height representations are detailed and compared in [Chen, 2010]. Since the effective height representation allows taking into account the impact of the antenna on the carrier phase of the received GNSS signal, this representation is chosen in this thesis.

4.1.5. Transfer function of the transmission channel

The received GNSS signal can be modelled as a number multipath, each of them presenting an attenuation, a phase rotation, and a code delay. The transmission channel can thus be represented like a linear filter [Pagani *et al.*, 2008] characterized by a transfer function. Three techniques can be used to compute the transfer function of the transmission channel [Chen, 2010].

4.1.5.1. Narrowband model

The narrowband model is based on assumptions on the mathematical expression of the transfer function. Narrowband transmission channel models consider that the transfer function is constant over the channel bandwidth. Both baseband impulse response and frequency responses related to the narrowband transmission channel models are given by Eq - 4-1. Both models apply to GNSS signals that are converted to baseband.

$$h(t) = \alpha\delta(t-\tau)e^{j\theta}$$
$$H(f) = \alpha e^{-j2\pi f\tau}e^{j\theta} \qquad \text{Eq - 4-1}$$

where:

- α is the attenuation of the signal at the receiver antenna output,
- δ is the Dirac distribution,
- τ is the code delay of the signal at the receiver antenna output,
- θ is the phase shift of the signal at the receiver antenna output.

The narrowband models do not differentiate the direct signal to the echo signals since the excess code delay and phase diversity of multipath are neglected in the impulse response and frequency response related to the narrowband transmission channel models. The narrowband models only take into account the amplitude attenuation induced by the multipath, that is to say the fading effect induced by multipath.

Narrowband models imply that the channel is sufficiently narrow so that its response can be considered as constant across the channel bandwidth. GNSS signals are characterized by relatively wide bandwidth, that is to say of few MHz up to few dozens of MHz [Parkinson *et al*., 1996]. The frequency response of the multipath transmission channel cannot be considered to be constant over the channel bandwidth. The narrowband models are not adapted to represent the multipath transmission channel for GNSS signals, and they are thus not adapted to predict GNSS multipath errors.

4.1.5.2. Wideband model

The wideband model is based on assumptions on the mathematical expression of the transfer function. Wideband models consider that the direct signal and each echo signal are affected by their own attenuation, phase rotation and code delay over the frequency band. The channel impulse response is characterized by the presence of multiple paths which code delays are spread over a time delay range [Chen, 2010]. Both baseband impulse response and frequency responses related to the wideband transmission channel models are, respectively:

$$h(t) = \sum_{k=0}^{K} \alpha_k \delta(t - \tau_k) e^{j2\pi f_{D,k} t + j\theta_k}$$
$$H(f) = \sum_{k=0}^{K} \alpha_k e^{-(j2\pi f - f_{D,k})\tau_k + j\theta_k} \qquad \text{Eq - 4-2}$$

where:

- K is the number of multipath,
- $\alpha_k = \frac{A_k}{A_0}$ is the ratio between the amplitude A_k of the k^{th} multipath at the receiver antenna output and the amplitude A_0. A_0 is the amplitude of the signal at the receiver antenna output that would have been obtained if no multipath sources would be present in the scene,
- δ is the Dirac distribution,
- τ_k is the code delay of the k^{th} multipath at the receiver antenna output. For the direct signal, τ_k is denoted as τ_0 and is the geometric delay between the satellite and the GNSS receiver antenna.
- $f_{D,k}$ is the Doppler-shift of the k^{th} multipath at the receiver antenna output,
- θ_k is the phase shift of the k^{th} multipath at the receiver antenna output.

4.1.5.3. Exact model

In the absence of assumption on the mathematical expression of the transfer function, the exact channel model technique requires computing the frequency response of the channel on the whole spectrum of each GNSS signal. Chen [Chen, 2010] has demonstrated that both exact and wideband models lead to similar transfer functions. Since the exact model development is time-consuming, the wideband transmission channel model is adopted.

4.1.5.4. Received signal

The expression of the GNSS signals broadcast by a satellite j at time t is given by Eq - 3-1. Omitting index j, and using the baseband impulse response of the wideband model from Eq - 4-2, the total L1+L5 received signal at the receiver antenna output in the absence of noise is modeled as:

$$s_1(t) = s_{1,D,L1}(t) + s_{1,P,L1}(t) + s_{1,D,L5}(t) + s_{1,P,L5}(t) \qquad \text{Eq - 4-3}$$

where:

- $s_{1,D,L1}(t)$ and $s_{1,D,L5}(t)$ are the data components on the L1 and L5 frequency bands, respectively,
- $s_{1,P,L1}(t)$ and $s_{1,P,L5}(t)$ are the pilot components on the L1 and L5 frequency bands, respectively.

The rest of this chapter focuses on the impact of multipath on the GNSS receiver with a special attention on the impact of multipath on the DLL code delay estimate. Since the L1C, L5, E1 and E5a signals have a data and a pilot channel, several DLL architectures exist. Among the tracking options, some use only the data or the pilot component, and other use both channels. Both approaches are further discussed in [Bastide, 2004]. It is shown that the absence of navigation data on the pilot component allows integrating longer. Tracking the pilot component leads to reduce the noise at the correlator output and to lower the tracking threshold. Hence, this tracking option is retained in the following and the DLL is assumed to use only the pilot components to estimate the code delay. For this reason, it is chosen to develop the expression of the received pilot components $s(t)_{1,P,L1}$ and $s(t)_{1,P,L5}$ in this paragraph:

$$\begin{aligned} s_{1,P,L1}(t) &= \sum_{k=0}^{K} A_{k,L1} c_{P,L1}(t - \tau_{k,L1}) \cos\left(2\pi(f_{L1} + f_{D,k,L1})t + \theta_{k,L1}\right) \\ s_{1,P,L5}(t) &= \sum_{k=0}^{K} A_{k,L5} c_{P,L5}(t - \tau_{k,L5}) \cos\left(2\pi(f_{L5} + f_{D,k,L5})t + \theta_{k,L5}\right) \end{aligned} \qquad \text{Eq - 4-4}$$

where:

- The indexes L1 and L5 indicates multipath parameters on the L1 and L5 frequency bands, respectively,
- $c_{P,L1}(.)$ and $c_{P,L5}(.)$ are the pilot waveforms on the L1 and L5 signals, respectively,
- $\tau_{k,L1} = \tau_{k,L5} = \tau_k$ since the code delay of the k^{th} multipath is independent of the frequency band.

4.1.6. Multipath parameters definition and computation

From Section 4.1.5, each multipath k is characterized by four multipath parameters $(\alpha_k, \tau_k, f_{D,k}, \theta_k)$ at the GNSS receiver antenna output. The amplitude a_k and the phase θ_k depend on the characteristics of both the propagation channel and the receiver antenna. They can be computed as in [Chen, 2010]:

$$\begin{aligned} a_{k,L1} &= \frac{\mathbf{E}_{L1}(\mathbf{e}_{r,k}).\mathbf{l}_{L1}(\mathbf{e}_{r,k})}{V_0} \quad \text{and} \quad a_{k,L5} = \frac{\mathbf{E}_{L5}(\mathbf{e}_{r,k}).\mathbf{l}_{L5}(\mathbf{e}_{r,k})}{V_0} \\ \theta_{k,L1} &= \mathrm{Arg}\left(\mathbf{E}_{L1}(\mathbf{e}_{r,k}).\mathbf{l}_{L1}(\mathbf{e}_{r,k})\right) \quad \text{and} \quad \theta_{k,L5} = \mathrm{Arg}\left(\mathbf{E}_{L5}(\mathbf{e}_{r,k}).\mathbf{l}_{L5}(\mathbf{e}_{r,k})\right) \end{aligned} \qquad \text{Eq - 4-5}$$

where:

- $\mathbf{e}_{r,k}$ is the unit vector of direction of arrival for the k^{th} multipath.
- $\mathbf{E}_{L1}(\mathbf{e}_{r,k})$ and $\mathbf{E}_{L5}(\mathbf{e}_{r,k})$are the electric fields of the k^{th} multipath on the L1 and L5 frequency bands, respectively.
- $\mathbf{l}_{L1}(\mathbf{e}_{r,k})$ and $\mathbf{l}_{L5}(\mathbf{e}_{r,k})$ are the vectorial effective heights of the GNSS receiver antenna on the L1 and L5 frequency bands, respectively.
- V_0 is the open-circuit voltage at the output of the antenna obtained for an ideal configuration in which the antenna is perfect and the scene is empty.

The code delay τ_k and the Doppler-shift $f_{D,k}$ depend on the characteristics of the propagation channel. Assuming a stationary satellite and a stationary 3D scene, $f_{D,k}$ is:

$$f_{D,k,L1} = \frac{f_{L1}}{c} v_{r,k} \text{ and } f_{D,k,L5} = \frac{f_{L5}}{c} v_{r,k} \qquad \text{Eq - 4-6}$$

where:

- c is the speed of light in vacuum,
- $v_{r,k}$ is given by $v_{r,k} = -\mathbf{v}.\mathbf{e}_{r,k}$,
- $\mathbf{v}$ is the receiver speed vector.

The multipath ranging error simulator presented in Section 5.1 has been developed in the framework of an Airbus-ENAC PhD thesis [Chen, 2010]. This software allows computing the multipath parameters presented in this section in a given 3D scene. Each illuminated facet of the 3D scene generates a multipath. In order to reduce the computation load and the number of multipath that can become important in case of a complex 3D scene, adjacent multipath in terms of delay are grouped in the simulator and multipath parameters are computed for each group of multipath. The multipath reduction process is further detailed in [Chen, 2010]. This process is used in the rest of this thesis.

4.2. GNSS receiver

Section 4.1 provides the expression of the GNSS signal at the GNSS receiver antenna output in the presence of multipath. The GNSS signal is then processed by the GNSS Radio-Frequency (RF) front-end and by the Intermediate-Frequency (IF) signal processing block of the GNSS receiver. This processing allows providing both phase and code delay estimates of the received GNSS signal. This section presents the operation of the front-end and of the IF signal processing block for only one satellite signal.

4.2.1. GNSS receiver architecture

A generic GNSS receiver block diagram is provided in Figure 4-2.

The signal parameters estimation is performed by the RF front-end and by the IF signal processing blocks. A brief overview of the RF front-end is provided in the next section. Further details on the front-end processing are given in [Kaplan *et al*., 2006].

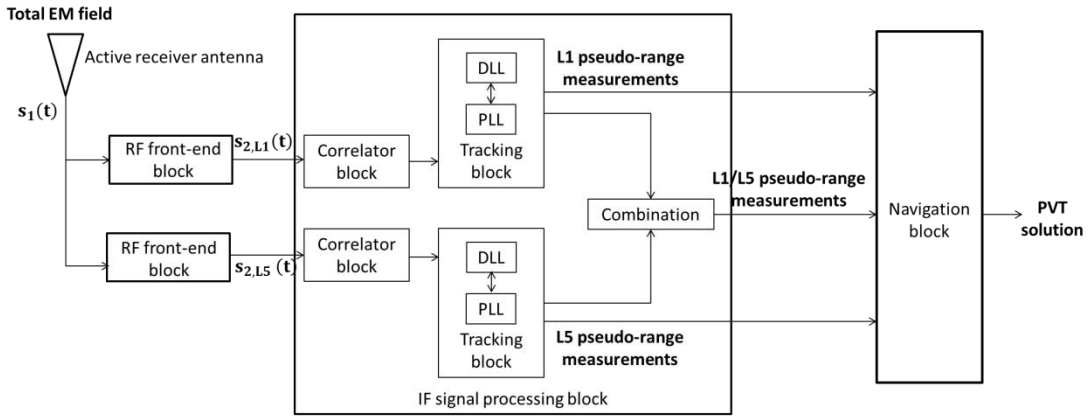

Figure 4-2: GNSS receiver architecture

4.2.2. Radio-Frequency front-end

The RF front end allows:

- Amplifying the signal by means of Low Noise Amplifier (LNA) and input filters.
- Down-converting the signal to the IF. The down-conversion is performed by mixing the incoming signal with a local carrier and by low-pass filtering the result. The local carrier is generated using a reference oscillator by a frequency synthesizer.
- Pass-band filtering the IF signal. This filtering allows extracting the frequency band of interest. The bandwidth of the IF filter is denoted as B_{fe} in the following.
- Sampling and quantifying the IF signal.

Omitting the noise term, the expression of the pilot component of the GNSS signal after amplification, down-conversion, sampling and quantization on L1 and L5 frequency bands are given by Eq - 4-7. Note that, in this equation, the time t represents the sampled time. For sake of clarity, the notation $\mathtt{t}$ is kept to designate the sampled time.

$$s_{2,P,L1}(t) = \sum_{k=0}^{K} a_{k,L1} c_{P,L1}(t-\tau_k)\cos\left(2\pi\left(f_{L1,IF}+f_{D,k,L1}\right)\mathtt{t}+\theta_{k,L1}\right)$$
$$s_{2,P,L5}(t) = \sum_{k=0}^{K} a_{k,L5} c_{P,L5}(t-\tau_k)\cos\left(2\pi\left(f_{L5,IF}+f_{D,k,L5}\right)\mathtt{t}+\theta_{k,L5}\right) \qquad \text{Eq - 4-7}$$

where:

- $f_{L1,IF}$ and $f_{L5,IF}$ are the intermediate frequencies of the L1 and L5 GNSS signals, respectively.

An overview of the IF processing block is provided in the next section.

4.2.3. Intermediate frequency processing

4.2.3.1. Acquisition block

The IF signal is firstly processed by the acquisition block, also called the correlator block, in the IF processing block. The goals of the acquisition stage are to decide either the presence or the absence of a GNSS signal and to provide a rough estimation of the propagation time and the Doppler frequency of the incoming signal. Different acquisition strategies specific to civil aviation applications are proposed in the literature [RTCA, 2008].

4.2.3.2. Tracking blocks

The signal tracking block refines the estimation of the code delay and Doppler frequency. It also estimates the carrier phase. By maintaining continuously updated estimates of the signals parameters, the signal tracking block provides a dynamic estimation of these parameters. Two separate locked loops are used.

- The DLL aims to precisely estimate the code delay and its changes over time.
- The Phase Locked Loop (PLL) aims to precisely estimate the Doppler frequency and the carrier phase and their changes over time.

It will be further explained in chapter 6 of this thesis that only raw code pseudo-range measurements are used to estimate the aircraft position. Indeed, the smoothing of the code measurements by the carrier phase measurements is not considered in the framework of this thesis. Hence, this chapter focuses on the multipath error on the code pseudo-range measurements. From Figure 4-2, the multipath phase tracking error induces an error on the code tracking estimate. However, the phase tracking error is small with respect to the code tracking error [Kaplan *et al*., 2006]. For this reason, in the analytical expressions of the multipath code tracking error proposed in this chapter, the effect of the phase tracking error on the code delay estimate is neglected. In the GNSS receiver simulator presented in Chapter 5 and used to derive the multipath error mode, the phase tracking error is taken into account. An overview of the DLL is provided herein. Further details on the PLL are given in [Kaplan *et al*., 2006].

A DLL is a feedback system that is able to track the delay of a GNSS signal. DLL is able to synchronize its own local code replica with the incoming code signal, so that code delay estimate can be derived from estimate of the local code. Figure 4-3 depicts the general structure of the DLL. The DLL processing architecture is the same for both L1 and L5 GNSS signals. Hence, the expressions of the code replicas, carrier replicas, correlator outputs and discriminator outputs presented in this section can be applied to both L1 and L5 GNSS signals. In the next Figure, $\hat{f}_D$ is the Doppler-shift estimated by the PLL at sampled time t and $\hat{\theta}$ is the carrier phase estimated by the PLL at the sampled time t.

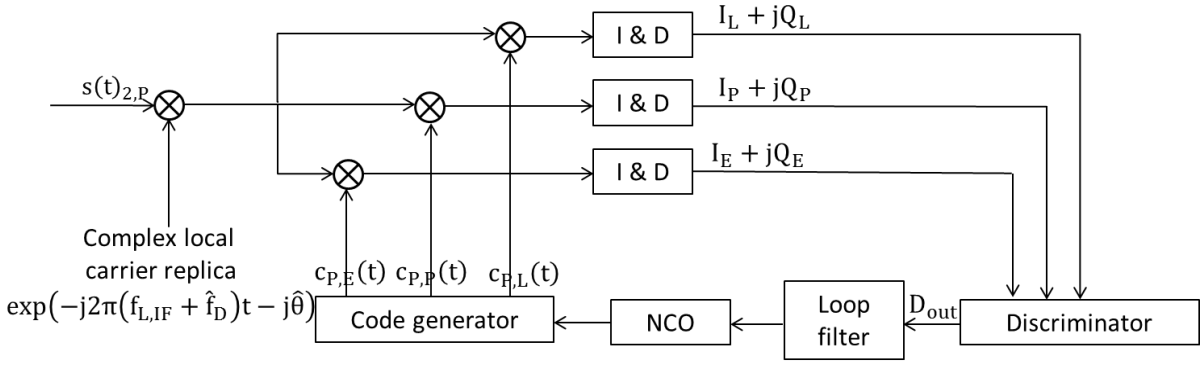

Figure 4-3: General structure of a DLL

The DLL is an iterative process: at iteration $n, n \in \mathbb{N}^*$, the loop updates the code delay estimate by adding the code delay estimated by the loop at iteration $n-1$ and the estimated code delay error provided by the loop during iteration n. The code delay estimate at iteration 0 (first iteration) is deduced from the acquisition stage. Several steps are needed to estimate the code delay error at iteration n and are presented in the following.

The pilot component of the incoming GNSS signal is multiplied by the in-phase and the quadrature-phase components of a local carrier in order to convert the incoming signal to baseband. In this document, the DLL architecture only uses the pilot component to estimate the signal parameters because this architecture is usually used in civil aviation. However, some implementations of tracking loops use both data and pilot channels [Muthuraman, 2010]. The baseband signal is correlated by three copies of a local code replica, each with a different delay. At sampled time t, the Early, Prompt and Late copies are:

$$\begin{aligned} c_{P,E}(t) &= c_P\left(t - \hat{\tau} + \frac{\Delta}{2}\right) \\ c_{P,P}(t) &= c_P(t - \hat{\tau}) \\ c_{P,L}(t) &= c_P\left(t - \hat{\tau} - \frac{\Delta}{2}\right) \end{aligned} \qquad \text{Eq - 4-8}$$

where $\hat{\tau}$ is the delay estimated by the DLL during iteration $n-1$,

Integrate and Dump (I&D) filters are used to correlate the local code replica to the in-phase and quadrature-phase components of the incoming baseband signal. In the digital domain, this integration is performed by adding together N samples of signals obtained after the multiplication with the three local codes. The integration time is denoted as T_I in this thesis. The I&D filter outputs are called "correlator outputs" in the following. They consist in an in-phase component (I) and in a quadrature-phase component(Q). In order to group both in-phase and quadrature phase components in a single term, the complex notation $(I + jQ)$ is used to represent the correlator outputs.

Omitting the noise term, and assuming that the code delays τ_k and carrier phases θ_k of the k^{th} multipath is considered to be constant during the integration time, the correlator outputs can be expressed as [Van Dierendonck *et al*., 1992]:

$$\begin{aligned} I_E + jQ_E &= \sum_{k=0}^{K} \frac{a_k}{2} R_{c,P}\left(\varepsilon_\tau + \Delta\tau_k - \frac{\Delta}{2}\right) \frac{\sin\left(\pi(\varepsilon_{f,D} + \Delta f_{D,k})T_I\right)}{\pi(\varepsilon_{f,D} + \Delta f_{D,k})T_I} \exp(j\varepsilon_\theta + j\Delta\theta_k) \\ I_P + jQ_P &= \sum_{k=0}^{K} \frac{a_k}{2} R_{c,P}(\varepsilon_\tau + \Delta\tau_k) \frac{\sin\left(\pi(\varepsilon_{f,D} + \Delta f_{D,k})T_I\right)}{\pi(\varepsilon_{f,D} + \Delta f_{D,k})T_I} \exp(j\varepsilon_\theta + j\Delta\theta_k) \\ I_L + jQ_L &= \sum_{k=0}^{K} \frac{a_k}{2} R_{c,P}\left(\varepsilon_\tau + \Delta\tau_k + \frac{\Delta}{2}\right) \frac{\sin\left(\pi(\varepsilon_{f,D} + \Delta f_{D,k})T_I\right)}{\pi(\varepsilon_{f,D} + \Delta f_{D,k})T_I} \exp(j\varepsilon_\theta + j\Delta\theta_k) \end{aligned} \qquad \text{Eq - 4-9}$$

where:

- $R_{c,P}(.)$is the auto-correlation function of the pilot waveform.
- $\varepsilon_\tau = \tau_0 - \hat{\tau}$ is the code delay error. It is the code delay difference between the code delay of the direct signal and the code delay estimated by the DLL at the iteration $n-1$.
- $\Delta\tau_k = \tau_k - \tau_0$ is the code delay difference between the k^{th} multipath and the direct signal.
- $\varepsilon_\theta = \theta_0 - \hat{\theta}$ is the carrier phase error. It is the carrier phase difference between the phase of the direct signal and the phase estimated by the PLL.
- $\Delta\theta_k = \theta_k - \theta_0$ is the carrier phase difference between the phase of the k^{th} multipath and the phase of the direct signal.
- $\Delta f_{D,k} = f_{D,k} - f_{D,0}$ is the Doppler-shift difference between the k^{th} multipath and the direct signal.

- $\varepsilon_{f,D} = f_{D,0} - \hat{f}_D$ is the Doppler-shift error. It is the Doppler-shift difference between the Doppler-shift of the direct signal and the Doppler-shift estimated by the PLL.

In the absence of echo signals, only the direct signal is tracked by the DLL. The direct signal is mentioned by index $k = 0$. Eq - 4-9 can be simplified as:

$$\begin{aligned} I_E + jQ_E &= \frac{a_0}{2} R_{c,P}\left(\varepsilon_\tau - \frac{\Delta}{2}\right) \exp(j\varepsilon_\theta) \frac{\sin(\pi\varepsilon_{f,D} T_I)}{\pi\varepsilon_{f,D} T_I} \\ I_P + jQ_P &= \frac{a_0}{2} R_{c,P}(\varepsilon_\tau) \exp(j\varepsilon_\theta) \frac{\sin(\pi\varepsilon_{f,D} T_I)}{\pi\varepsilon_{f,D} T_I} \\ I_L + jQ_L &= \frac{a_0}{2} R_{c,P}\left(\varepsilon_\tau + \frac{\Delta}{2}\right) \exp(j\varepsilon_\theta) \frac{\sin(\pi\varepsilon_{f,D} T_I)}{\pi\varepsilon_{f,D} T_I} \end{aligned} \qquad \text{Eq - 4-10}$$

The correlator outputs are processed by the DLL discriminator which aims to extract the code delay error ε_τ. The discriminator output is a signal that is proportional to the code delay error. Different DLL discriminators can be implemented. Their advantages and disadvantages are discussed in [Betz *et al*., 2009] [Kaplan *et al*., 2006]. The non-coherent EMLP discriminator is usually implemented in civil aviation receivers and the discriminator output signal is:

$$D_{out} = \left(I_E{}^2 + Q_E{}^2\right) - \left(I_L{}^2 + Q_L{}^2\right) \qquad \text{Eq - 4-11}$$

The DLL is locked when:

$$D_{out} = 0 \quad \text{or, equivalently,} \quad \left(I_E{}^2 + Q_E{}^2\right) = \left(I_L{}^2 + Q_L{}^2\right) \qquad \text{Eq - 4-12}$$

The discriminator output signal is processed by the loop filter that aims to reduce the noise present at the discriminator output and to respond effectively to the signal dynamic. The loop filter is characterized by two parameters:

- The loop filter order which determines the ability of the loop filter to respond to different types of signal dynamics,
- The loop bandwidth denoted as B_n in this thesis. It determines the ability of the loop filter to reduce the noise present at the discriminator output.

Finally, the Numerically Controlled Oscillator (NCO) is used to generate the local signal replicas.

4.2.4. GNSS receiver settings

Table 4-1 presents the GNSS receiver parameter values that are adopted to compute the multipath errors in the rest of the chapter. The choice of these values is further justified in Section 3.2.1.6. From Figure 4-2, the carrier-aiding technique is used by the code tracking loop. A first-order DLL is used in the rest of the thesis. Note that, without carrier-aiding, the DLL needs to be at least second-order to accommodate vehicle dynamics.

GNSS signal	B_{fe} [MHz]	T_I [ms]	Δ [chip]	B_n [Hz]	DLL loop filter order
GPSL1C-Q	14	20	1/12	1	1
GPSL5-Q	20	20	1/4	1	1
GalileoE1-C	14	20	1/12	1	1
GalileoE5a-Q	20	20	1/4	1	1

Table 4-1: GNSS receiver parameters setting

4.3. Impact of multipath on GNSS code pseudo-range measurements

This section assesses the impact of multipath on the code delay estimation and on GNSS code pseudo-range measurements.

4.3.1. Impact of multipath on the code delay estimate

In order to understand the impact of multipath on the code delay estimate error, the case where no echo signal affects the received GNSS signal is firstly considered. In the absence of multipath, and from Eq - 4-10 and Eq - 4-12, the stability point is achieved when:

$$\left|R_{c,P}\left(\varepsilon_\tau + \frac{\Delta}{2}\right)\right| = \left|R_{c,P}\left(\varepsilon_\tau - \frac{\Delta}{2}\right)\right| \qquad \text{Eq - 4-13}$$

The symmetry of auto-correlation function of the pilot code $R_{c,P}(.)$ with respect to the ordinate axis is underlined in Section 3.1.2.2.5. Due to this symmetry, the stability point is achieved when $\varepsilon_\tau = 0$. As an illustration, Figure 4-4 shows the evolution of $\left|R_{c,P}\left(\varepsilon_\tau + \frac{\Delta}{2}\right)\right|$ and $\left|R_{c,P}\left(\varepsilon_\tau - \frac{\Delta}{2}\right)\right|$ as a function of ε_τ for GPSL5-P and for $\Delta = 0.25$ chip. The stability point corresponds to a null error on the code delay estimate.

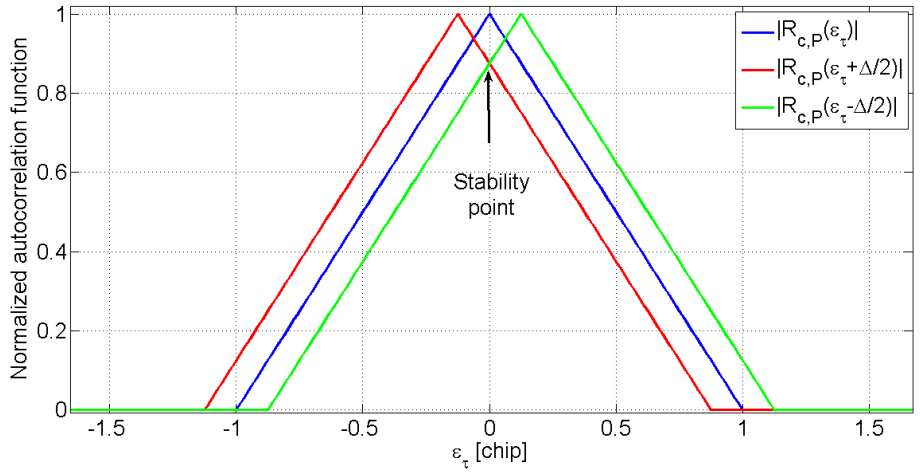

Figure 4-4: Normalized correlator outputs for GPSL5 – absence of multipath

In order to understand the impact of multipath on the code delay estimate error, the case where the direct signal and a single echo signal are received by the receiver antenna is secondly considered. In the following, the direct signal is mentioned by index $k = 0$ and the echo signal is mentioned by index $k = 1$. From Eq - 4-10 and Eq - 4-12, the stability point is achieved when:

$$\left|\frac{a_0}{2}R_{c,P}\left(\varepsilon_\tau - \frac{\Delta}{2}\right)\frac{\sin(\pi\varepsilon_{f,D}T_I)}{\pi\varepsilon_{f,D}T_I}\exp(j\varepsilon_\theta) + \frac{a_1}{2}R_{c,P}\left(\varepsilon_\tau + \Delta\tau_1 - \frac{\Delta}{2}\right)\frac{\sin(\pi(\varepsilon_{f,D}+\Delta f_{D,1})T_I)}{\pi(\varepsilon_{f,D}+\Delta f_{D,1})T_I}\exp(j\varepsilon_\theta + j\Delta\theta_1)\right|$$
$$= \left|\frac{a_0}{2}R_{c,P}\left(\varepsilon_\tau + \frac{\Delta}{2}\right)\frac{\sin(\pi\varepsilon_{f,D}T_I)}{\pi\varepsilon_{f,D}T_I}\exp(j\varepsilon_\theta) + \frac{a_1}{2}R_{c,P}\left(\varepsilon_\tau + \Delta\tau_1 + \frac{\Delta}{2}\right)\frac{\sin(\pi(\varepsilon_{f,D}+\Delta f_{D,1})T_I)}{\pi(\varepsilon_{f,D}+\Delta f_{D,1})T_I}\exp(j\varepsilon_\theta + j\Delta\theta_1)\right|$$

Eq - 4-14

As an illustration, Figure 4-5 shows the evolution of $\left|a_0 R_{c,P}\left(\varepsilon_\tau - \frac{\Delta}{2}\right) + a_1 R_{c,P}\left(\varepsilon_\tau + \Delta\tau_1 - \frac{\Delta}{2}\right)\right|$ and $\left|a_0 R_{c,P}\left(\varepsilon_\tau + \frac{\Delta}{2}\right) + a_1 R_{c,P}\left(\varepsilon_\tau + \Delta\tau_1 + \frac{\Delta}{2}\right)\right|$ as a function of ε_τ for GPSL5-P and for $\Delta =$ 0.25 chip. In this Figure, it is assumed that $a_0 = 1$, $a_1 = 0.5$, $\Delta\tau_1 = 0.3$chip, $\Delta\theta_1 = 0$ rad, $\Delta f_{D,1} = 0$Hz, and it is assumed that the tracking loops perfectly track the phase and the Doppler frequency of the direct signal. Hence, $\varepsilon_\theta = 0$ rad and $\varepsilon_{f,D} = 0$Hz.

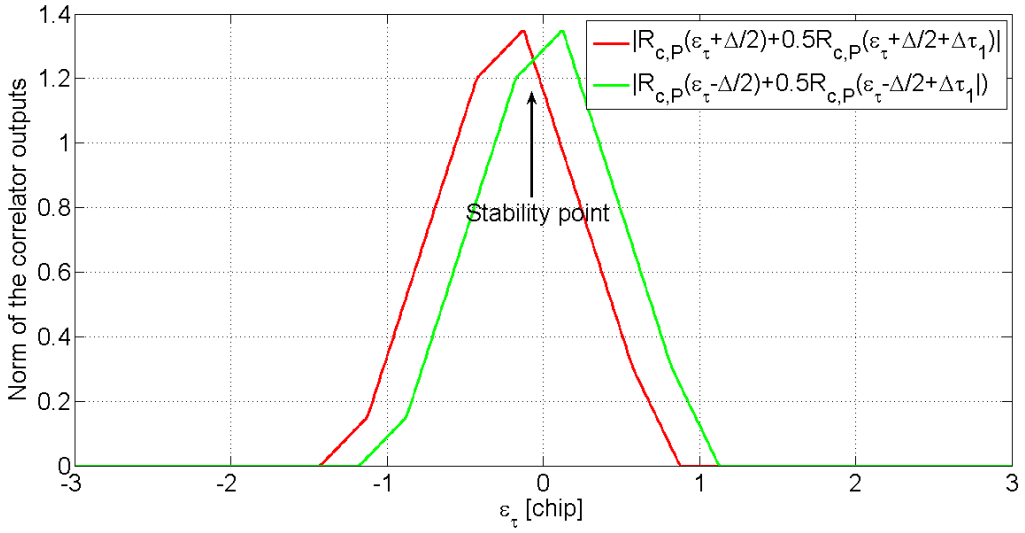

Figure 4-5: Normalized correlator outputs for GPSL5 – presence of a single echo signal

From the last Figure, in the presence of multipath, correlator outputs are affected by a distortion. This distortion depends on the amplitude, code delay and carrier phase of the echo signals. Because of this distortion, when the discriminator output is null and the stability point is reached, the code delay estimate is affected by an error ε_τ. $\varepsilon_\tau < 0$ in Figure 4-5. ε_τ is called multipath code tracking error in the following.

4.3.2. Impact of multipath on the code pseudo-range measurements

4.3.2.1. Raw code multipath ranging error definition

The DLL code delay estimates are converted to code pseudo-range measurements in the GNSS receiver. The multipath code delay error induces an error on the code pseudo-range measurements that is called "raw code multipath ranging error" in the following and that is given by:

$$\varepsilon_{mp} = c\varepsilon_\tau \qquad \text{Eq - 4-15}$$

Three different kinds of raw code multipath ranging errors are distinguished in this thesis.

- The multipath errors that affect the L1 code pseudo-range measurements. They are denoted $\varepsilon_{mp,L1C}$ and $\varepsilon_{mp,E1}$ for the GPSL1C and GalileoE1 signals, respectively.
- The multipath errors that affect the L5 code pseudo-range measurements. They are denoted $\varepsilon_{mp,L5}$ and $\varepsilon_{mp,E5a}$ for GPSL5 and GalileoE5a signals, respectively.

- The multipath errors that affect the iono-free L1+L5 code pseudo-range measurements. They are denoted $\varepsilon_{mp,L1C-L5}$ and $\varepsilon_{mp,E1-E5a}$ for the GPSL1C+GPSL5 and GalileoE1+GalileoE5a code pseudo-range measurements, respectively.

From Section 3.2.1.4.3, the dual-frequency raw code multipath ranging errors are related to single-frequency raw code multipath ranging errors as follows:

$$\varepsilon_{mp,L1C-L5} = k_a\, \varepsilon_{mp,L1C} + k_b\, \varepsilon_{mp,L5}$$
$$\varepsilon_{mp,E1-E5a} = k_a\, \varepsilon_{mp,E1} + k_b\, \varepsilon_{mp,E5a} \qquad \text{Eq - 4-16}$$

4.3.2.2. Raw code multipath ranging errors in the presence of a single echo signal

In the case where the direct signal and a single echo signal are received by the receiver antenna, the minimal and maximal code tracking errors can be represented by multipath error envelopes. Multipath errors envelopes for the GPSL1C, GPSL5, GalileoE1 and GalileoE5a are presented in Section 4.3.2.2.1. In addition, the GPSL1C, GPSL5, GalileoE1 and GalileoE5a code tracking errors as a function of the amplitude, code delay and phase of the echo signal are represented and discussed in Section 4.3.2.2.2.

4.3.2.2.1. Multipath error envelope

The minimal and maximal multipath code tracking errors are commonly illustrated by the multipath error envelopes that provide the raw code multipath ranging error values as a function of the code delay between the direct and the echo signal $\Delta\tau_1$. Minimal and maximal multipath errors are achieved for $\Delta\theta_1 = 0$ and $\Delta\theta_1 = \pi$, respectively. Multipath error envelopes presented in this section have been simulated with the Airbus-ENAC GNSS correlator outputs simulator assuming that:

- The ratio between the direct signal amplitude and a single echo amplitude is $\alpha = 0.5$.
- The tracking loops perfectly track the phase and the Doppler frequency of the direct signal: $\varepsilon_\theta = 0\text{rad}$ and $\varepsilon_{f,D} = 0\text{Hz}$.
- The satellite, the multipath sources and the receiver are static, meaning that $\Delta f_{D,1} = f_{D,1} = f_{D,0} = 0\text{Hz}$.
- The DLL discriminator is a EMLP discriminator.
- The IF filter is a rectangular band-pass filter.
- The DLL chip spacing and the IF filter bandwidth values are indicated in Table 4-1.

Figure 4-6 represents the multipath errors envelope for GPSL5 and GalileoE5a signals that are both BPSK-modulated signals.

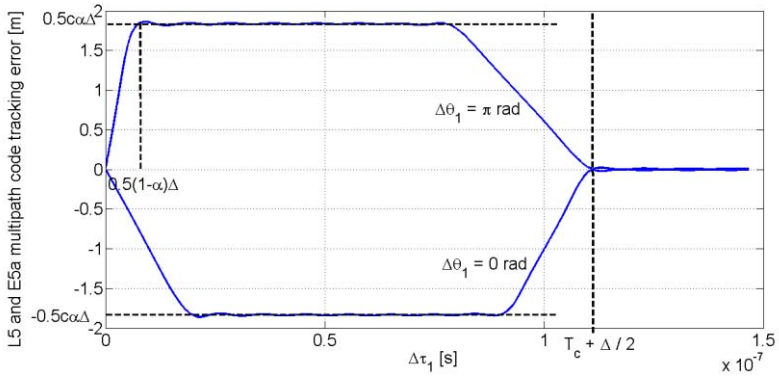

Figure 4-6 : Multipath errors envelope for GPSL5 and GalileoE5a signals

The analytical expressions of the maximal and minimal multipath errors for an unlimited IF filter bandwidth are indicated in the Figure and are $\mp c\alpha\frac{\Delta}{2}$ [Macabiau, 2004]. The maximal multipath error is reached when $\Delta\tau_1 = (1-\alpha)\frac{\Delta}{2}$ for an unlimited IF filter bandwidth.

Section 3.1.2.2.5 underlines the differences in the autocorrelation function of the pilot waveform $R_{c,P}(\varepsilon_\tau)$ for the L5 and the L1 signals. Due to these differences, the error envelopes for the L5 signals are different than the multipath error envelopes obtained for GPSL1C and GalileoE1 signals. Figure 4-7 represents the multipath errors envelope for GPSL1C and GalileoE1 signals.

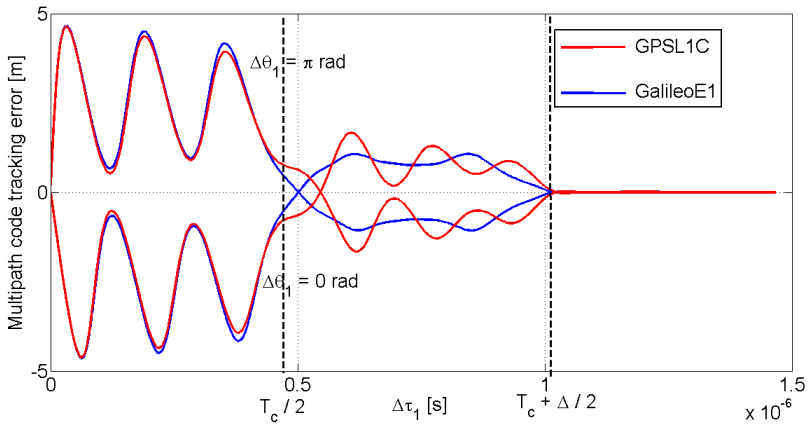

Figure 4-7 : Multipath errors envelope for GPSL1C and GalileoE1 signals

The high similarities in the shape of the autocorrelation function of the pilot waveform between GPSL1C and GalileoE1 is underlined in Section 3.1.2.2.5. These similarities explain the high correlation between the multipath error envelopes of both GPSL1C and GalileoE1 signals. The deviation between both errors envelope tends to increase with $\Delta\tau_1$. At low $\Delta\tau_1$ values, that is to say for $\Delta\tau_1 < \frac{T_c}{2}$, the deviation is not significant since the CBOC(6,1,1/11,-) and TMBOC(6,1,4/33) autocorrelation functions are quasi-identic around the correlation peak. At high $\Delta\tau_1$,the maximal difference between both errors envelopes is 73cm, when the GalileoE1 error is roughly 80cm.

For GPSL1C, GPSL5, GalileoE1 and GalileoE5a signals, the maximal amplitude of the multipath errors depend on the relative amplitude of the echo signal. The maximal error for GPSL1C and GalileoE1 is roughly twice the maximal error for GPSL5 and GalileoE5a given the relative amplitude of the echo signal $\alpha = 0.5$ and given the chip spacing values indicated in Table 4-1. Multipath characterized by a relative code delay $\Delta\tau_1$ higher than $T_c + \frac{\Delta}{2}$ are filtered out by the receiver [Kaplan *et al.*, 2006] and their impact on the raw code multipath ranging error is considered to be negligible. In the ranging domain, this means that when the difference between the distance travelled by an echo signal and by the direct signal is higher than 329.7m for L1 signals, the echo signal has a no influence on the L1 multipath error. Similarly, when the difference is higher than 33.0m for L5 signals, the echo signal has a no influence on the L5 multipath error. Hence, compared to GPSL1C and GalileoE1, GPSL5 and GalileoE5a enable filtering out more multipath than GPSL1C and GalileoE1 signals, since all multipath characterized by a relative code delay above 33.0m (in the ranging domain) are filtered out by L5 signals.

4.3.2.2.2. Multipath error models and representations

The multipath error values are represented in the previous paragraph for $\Delta\theta_1 = 0$ and $\Delta\theta_1 = \pi$. For the case of BPSK-modulated signals, and in the presence of a single echo signal, Appendix A, Section A.3, derives the analytical expression of the multipath code tracking error as a function of the relative amplitude α, of the relative code delay $\Delta\tau_1$ and of the relative carrier phase $\Delta\theta_1$ of the echo signal under the following assumptions:

- The tracking loops perfectly track the phase and the Doppler frequency of the direct signal: $\varepsilon_\theta = 0\text{rad}$ and $\varepsilon_{f,D} = 0\text{Hz}$.
- The satellite, the multipath sources and the receiver are static, meaning that $\Delta f_{D,1} = f_{D,1} = f_{D,0} = 0\text{Hz}$.
- The front-end filtering effects on the Early and Late correlator outputs are not taken into account, or, equivalently, the front-end low-pass filter is assumed to have an infinite bandwidth,
- the DLL discriminator is a EMLP discriminator.
- The relative code delay $\Delta\tau_1$ is below $(1-\alpha)\frac{\Delta}{2}$.

The multipath code tracking error can be expressed as:

$$c\varepsilon_\tau = -c\Delta\tau_1 \frac{\alpha^2 + \alpha\cos(\Delta\theta_1)}{1 + \alpha^2 + 2\alpha\cos(\Delta\theta_1)} \qquad \text{Eq - 4-17}$$

Assuming a stationary satellite, a stationary 3D scene and a stationary GNSS receiver antenna:

$$\Delta\theta_1 = -2\pi f_{L5}\Delta\tau_1 + \Delta\phi_1 \qquad \text{Eq - 4-18}$$

where $\Delta\phi_1$ is the phase shift difference between the phase shift of the first echo signal and the phase shift of the direct signal.

Figure 4-8 represents the evolution of the code tracking errors on L5 and E5a given by Eq – 4-17 as a function of $\Delta\tau_1$ for different values of α and for $\Delta\phi_1 = 0$ rad. If a different value of $\Delta\phi_1$ is taken to represent the evolution of the errors, the error shape would remain similar, but the position of the peaks along the $\Delta\tau_1$ axis would change. The error envelope presented in Figure 4-6 for $\alpha = 0.5$ is also represented in Figure 4-8.

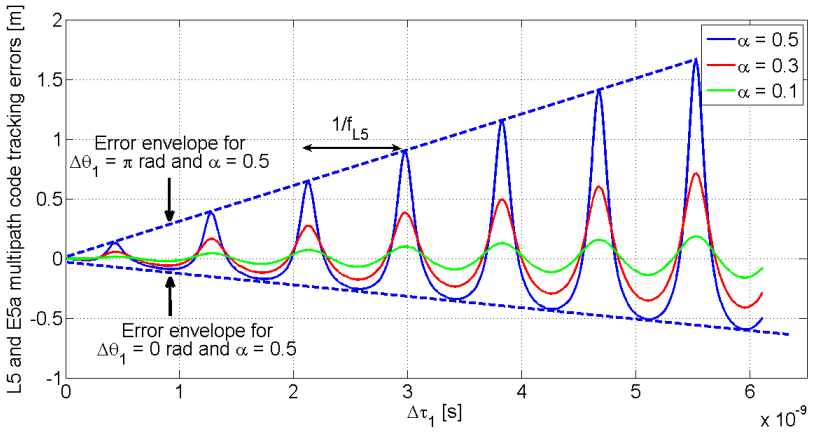

Figure 4-8 : Multipath code tracking errors for GPSL5 and GalileoE5a signals

From Figure 4-8, the code tracking errors present high variations along the $\Delta\tau_1$ axis. The period of the oscillations is $\frac{1}{f_{L5}}$. Indeed, from Eq - 4-18, if the difference between the relative code delays $\Delta\tau_1$ of two multipath is $\frac{1}{f_{L5}}$, both multipath have the same relative carrier phase $\Delta\theta_1$. In addition, the amplitude of the oscillations of the raw code multipath ranging errors is proportional to the relative amplitude α.

Due to the complexity of the autocorrelation function of the CBOC(6,1,1/11,-) and TMBOC(6,1,4/33) waveforms, the related analytical expressions of the raw code multipath ranging error is not provided in this thesis. However, multipath errors have been simulated with the ENAC GNSS correlator outputs simulator assuming:

- The tracking loops perfectly track the phase and the Doppler frequency of the direct signal: $\varepsilon_\theta = 0\text{rad}$ and $\varepsilon_{f,D} = 0\text{Hz}$.
- The satellite, the multipath sources and the receiver are static, meaning that $\Delta f_{D,1} = f_{D,1} = f_{D,0} = 0\text{Hz}$.
- The DLL discriminator is a EMLP discriminator.
- The DLL chip spacing and the IF filter bandwidth values are indicated in Table 4-1.
- $\Delta\theta_1 = -2\pi f_{L1}\Delta\tau_1 + \Delta\phi_1$.

Figure 4-9 represents the evolution of the simulated code tracking errors on L1C and E1 as a function of $\Delta\tau_1$ for different values of α and for $\Delta\phi_1 = 0$ rad. The error envelopes presented in Figure 4-7 for $\alpha = 0.5$ and for GPSL1C and GalileoE1 is also represented in Figure 4-9.

For the same reasons as for the L5 signals, the period of the oscillations is $\frac{1}{f_{L1}}$. In addition, the amplitude of the oscillations of the errors is proportional to the relative amplitude α. Finally, since the values of $\Delta\tau_1$ are low with respect to the chip period in Figure 4-9, the difference between the GPSL1C and GalileoE1 multipath errors is not significant. Further details about the difference between the GPSL1C and GalileoE1 multipath errors are provided in Section 4.3.2.2.1.

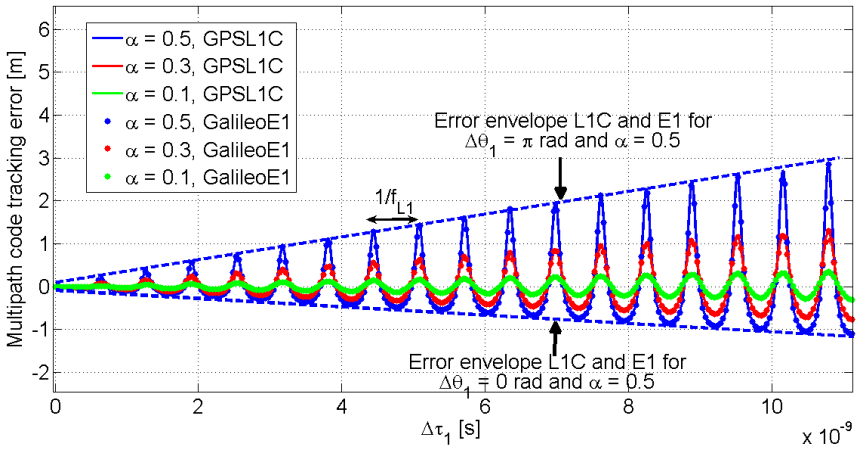

Figure 4-9: Multipath code tracking errors for GPSL1C and GalileoE1 signals as a function of the relative code delay

4.4. Conclusions

This chapter has reviewed the definition of the transmission channel. The transfer function of the transmission channel can be represented by different models. In the presence of multipath perturbations, the wideband model has been adopted to represent the transmission channel transfer function. Based on this transfer function, the received GNSS signal at the receiver antenna output has been modelled as the sum of the direct signal and of the echo signals. The presence of the echo signals in the expression of the total received signal induces code delay estimate errors and raw code multipath ranging errors. Three kinds of parameters influence the raw code ranging errors: the parameters of the GNSS signals, the parameters of the GNSS receiver and the multipath parameters. The influence of the multipath parameters on the raw code multipath ranging error values has been discussed. The analytical expression of the GPSL5 and GalileoE5a multipath code tracking errors as a function of the multipath parameters has been established.

CHAPTER 5

GNSS multipath ranging error models

As explained in Section 3.2.3, there is a need to develop a GNSS integrity monitoring system capable of protecting users from the effects of multipath in airport environments. The design of such a system requires modelling the impact of multipath on the GNSS pseudo-range measurements and on the GNSS-based position estimate.

This chapter analyzes the shape of multipath errors that may affect GNSS raw code pseudo-range measurements during the taxi operation. From Chapter 2, the taxi operation includes three sub-phases: the *taxi on the taxiway*, the *taxi on the apron taxiway* and the *taxi on the taxi lane*. Based on an error shape analysis, GNSS raw code ranging error models adapted to surface operations are proposed for the taxi sub-phases. Parameters influencing the error models are identified. In order to illustrate the multipath error shapes and the multipath error models, simulation results are presented based on a simple 3D modeling of Toulouse Blagnac airport, France. Nevertheless, the way to model raw code multipath ranging errors proposed in this chapter could be used for any airport.

This chapter is organized as follows. The GNSS multipath error generator used to analyze the multipath errors and to develop the multipath ranging error models is presented in Section 5.1. The assumptions made to simulate the multipath errors are discussed. The simulation scenario is presented in Section 5.2. Next, both static and dynamic configurations are defined in Section 5.3. Finally, the error models in both static and dynamic configurations are derived Sections 5.4 and 5.5. The values of the error model outputs are discussed.

5.1. GNSS multipath ranging error computation

5.1.1. GNSS multipath ranging error simulator architecture

In this chapter, GNSS multipath raw code ranging errors are computed by means of a prediction simulator that estimates the GNSS multipath ranging errors in an airport environment in a deterministic way. This simulator has been mainly developed in the framework of a previous ENAC-Airbus PhD thesis and is fully described in [Chen *et al.*, 2009].

Figure 5-1 presents the architecture of the simulator.

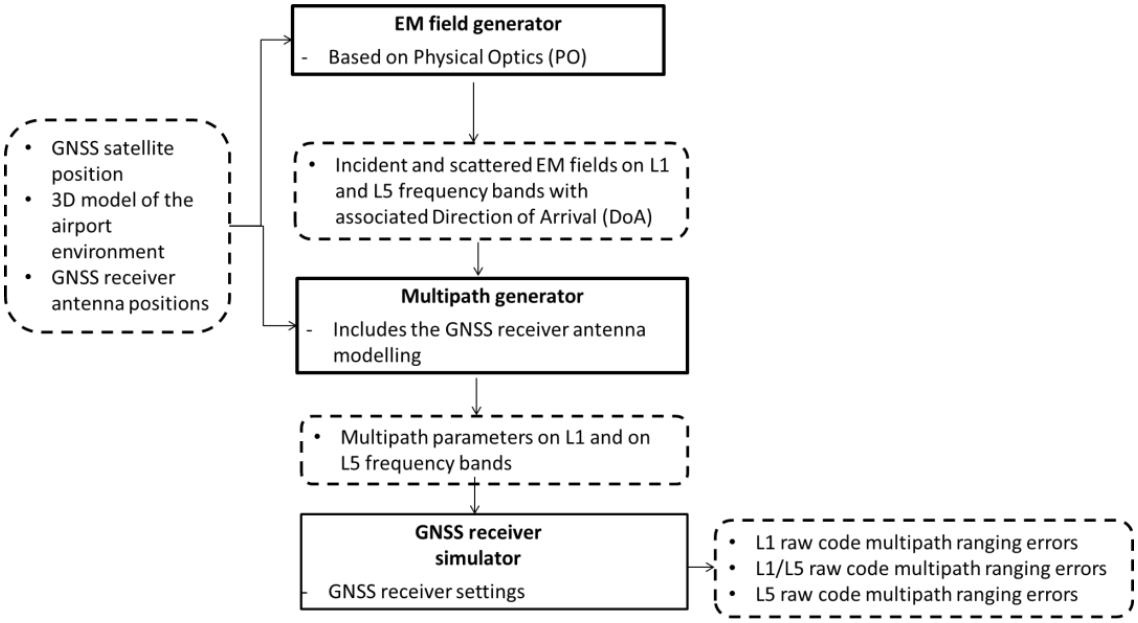

Figure 5-1 : Architecture of the deterministic GNSS multipath ranging error simulator

The EM fields associated with the direct signal and with each echo signal arriving at the GNSS receiver antenna input are predicted by the EM field generator. This prediction uses Physical Optics (PO) method, Geometrical Optics (GO) and an adaptation of the generalized image theorem to take into account a dielectric ground. It computes the scattered EM field at the GNSS receiver input. The EM field prediction is fully described in [Chen *et al*., 2009]. The simulator can compute multiple interactions up to order 2 for metallic and dielectric multilayer facets. When modeled as dielectric, a facet is modeled as a multilayer slab of constant thickness. Each layer is characterized by its thickness and its dielectric coefficient. The first and second order interactions are presented in Section 5.1.3.

The input parameters of the EM field generator are the GNSS satellite position, a 3D modeling of the airport environment and the GNSS receiver antenna positions. These input parameters and the computed EM fields are used by the multipath generator to predict the transmission channel parameters, that are the multipath parameters presented in Section 4.1.6. The multipath parameters prediction depends on the GNSS receiver antenna model implemented in the software. It is underlined in Section 5.5 that the multipath parameters present small scale variations in the space domain. The variations are of the order of the wavelength of the GNSS signals, that is to say of the order of 20cm. Hence, due to the Shannon criterion, the maximal possible spatial sampling period is 10cm. Assuming an aircraft speed of 10m.s^{-1}, the maximal time sampling period is 10ms, leading to a minimal sampling period of 100Hz. In this Chapter, it is chosen to compute the multipath parameters with a temporal sampling period of 4ms, leading to a sampling frequency of 250Hz. The multipath parameters are then processed by the GNSS receiver simulator that predicts the raw code multipath ranging errors for the GPSL1C, GalileoE1, GPSL5, GalileoE5a and dual-frequency GPSL1C+GPSL5 and GalileoE1+GalileoE5a measurements. The multipath error prediction depends on the GNSS receiver settings implemented in the software.

The following section presents the main input parameters that have been used to present the simulation results proposed in this chapter, that are the GNSS satellite position, the 3D model of the airport environment, the GNSS receiver antenna model and the GNSS receiver settings.

5.1.2. Input parameters of the GNSS multipath ranging error simulator

5.1.2.1. GNSS satellite position

Table 2-5 reveals that the mean duration of the *taxi on the taxiway*, the *taxi on the apron taxiway* and the *taxi on the taxi lane* sub-phases is between 90 seconds and 360 seconds. The taxi operation duration is thus up to few minutes. The angular variation of the elevation and azimuth angles of the GNSS satellite is few tenths of degrees during trajectories of few minutes. These angular variations are not significant and the satellite is assumed to be stationary during the taxi operation. The stationary position of the GNSS satellite is an input parameter of the software.

5.1.2.2. 3D model of the airport environment

The simulator presented in Section 5.1.1 is designed to predict the multipath errors affecting the GNSS receiver of an aircraft A319. In order to clearly distinguish this A319 aircraft to other aircraft potentially present in the airport environment, the A319 aircraft is called the "assessed aircraft" and the other aircraft are named as "surrounding aircraft" in the following. The elements of the airport environment that may have an impact on the multipath errors are called "multipath sources" and can be classified into three types of elements:

- The **structure of the A319 assessed aircraft** itself, including its fuselage, wings and empennage,
- The **airport surface**, also called ground in the following,
- The **obstacles** that are defined as any element of the airport environment other than the airport surface and the A319 assessed aircraft structure. Obstacles can be classified as follows:
  - Fixed obstacles that mainly include terminal buildings, terminal gates and warning signs,
  - Mobile obstacles that mainly include surrounding aircraft, buses, cars, trucks, footbridges and containers.

The model of each type of multipath sources is described in the three next sections.

5.1.2.2.1. Structure of the assessed aircraft

The structure of the assessed aircraft induces echo signals characterized by relative code delays $\Delta\tau_k$ of roughly $1\text{ns} \leq \Delta\tau_k \leq 2\text{ns}$ [Steingass *et al*., 2004]. k represents the index of the echo signal. Hence, for GPSL1C and GalileoE1 signals, we get:

$$\begin{aligned} 10^{-3}T_c \leq \Delta\tau_k \leq 2.10^{-3}T_c \quad & \text{for GPSL1C and GalileoE1 signals} \\ 10^{-2}T_c \leq \Delta\tau_k \leq 2.10^{-2}T_c \quad & \text{for GPSL5 and GalileoE5a signals} \end{aligned} \qquad \text{Eq - 5-1}$$

The aircraft structure is not a significant source of multipath. As an example, Macabiau in [Macabiau *et al*., 2006] shows that the multipath ranging errors during the approach phase is essentially induced by the structure of the assessed aircraft. The standard deviation of this error has been obtained by combining the statistical multipath propagation channel model called the High Resolution Aeronautical channel and described in [Steingaß *et al.*, 2004] with a GNSS receiver simulator. Regardless of the elevation angle, the standard deviation of the raw (unsmoothed) multipath code tracking error is several centimeters up to a few decimeters for the GPSL1C, the GalileoE1 BOC(1,1), the GPSL5 and the GalileoE5a signals.
The excess code delays of the echo signals are non-significant with respect to the chip period of the GNSS signals. The transmission channel model does not take into account the excess code delays of the multipath from the structure of the assessed aircraft. It only takes into

account the amplitude attenuation induced by the multipath from the structure of the assessed aircraft, that is the fading effect induced by these multipath. The assessed aircraft structure is not modelled in the 3D airport environment model. However, the aircraft structure is integrated in the model of the GNSS receiver antenna, as detailed in Section 5.1.2.3.

5.1.2.2.2. Airport surface

The airport surface is supposed to be flat, flawless and homogeneous at the scale of the airport. The airport surface is assumed to be dry tar. Dry tar is characterized by a permittivity of $2 - j0.12$ in the L1 and L5 frequency bands [Von Hippel, 1961]. The imaginary part of the permittivity represents losses. Concrete has a similar permittivity as dry tar. Lawn or metallic parts of the airport surface are also represented by dry tar. In addition, the airport surface can be considered as an infinite plane if the airport surface can be considered to be flat over few hundreds of meters. This hypothesis is valid for most of the airports, including Toulouse Blagnac airport. It is considered that Toulouse Blagnac airport surface can be represented by an infinite plane.

5.1.2.2.3. Obstacles

5.1.2.2.3.1. Fixed obstacles

Figure 5-2 is a representation of the 3D modeling of the terminal buildings and terminal gates of Toulouse Blagnac airport. The positions of the terminal buildings and terminal gates are expressed in the direct and orthogonal reference frame $(O, \mathbf{x}, \mathbf{y}, \mathbf{z})$. The horizontal plane $(O, \mathbf{x}, \mathbf{y})$ represents the airport surface. The $\mathbf{z}$ axis is the local vertical vector pointing upwards. O is the center of the semi cylinder that represents Blagnac airport Hall D. The A319 assessed aircraft is also represented in Figure 5-2.

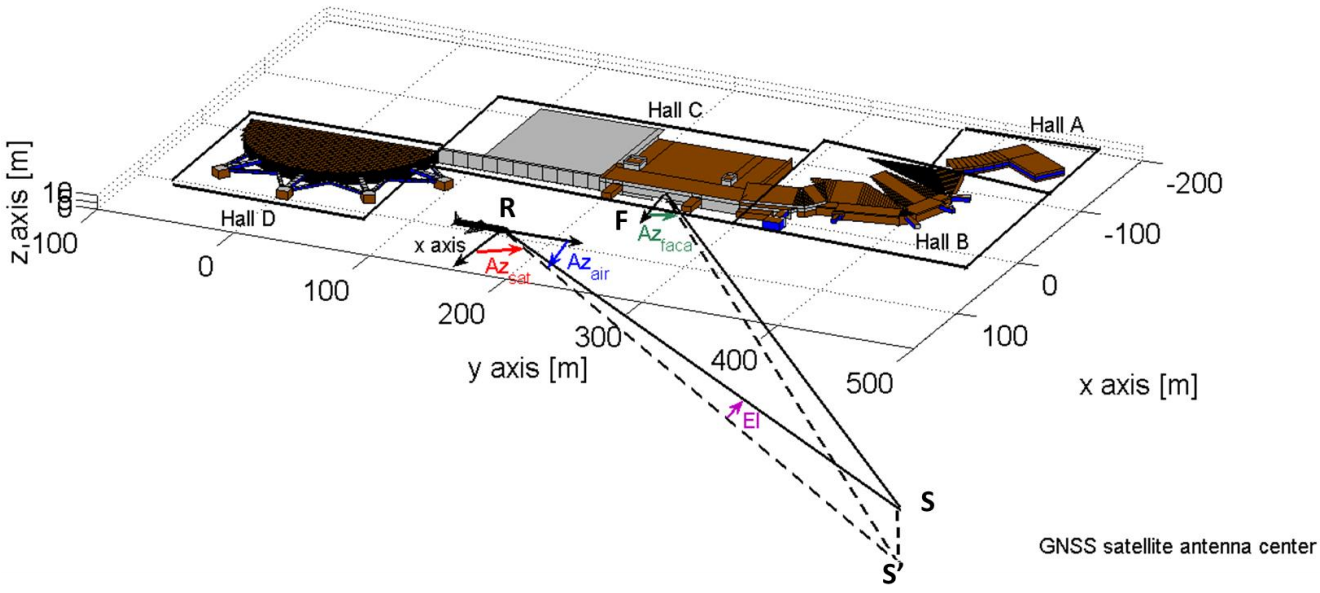

Figure 5-2: 3D modeling of the terminal buildings and terminal gates of Toulouse Blagnac airport, France

Let's denote $\mathbf{R}, \mathbf{S}$ and $\mathbf{F}$ the positions of the airborne antenna, of the satellite antenna and of the center of a facade in $(O, \mathbf{x}, \mathbf{y}, \mathbf{z})$, respectively. Let's denote $\mathbf{S}'$ the position of the projection of point $\mathbf{S}$ in the horizontal horizontal plane $(O, \mathbf{x}, \mathbf{y})$. $\mathbf{S}'$ is expressed in $(O, \mathbf{x}, \mathbf{y}, \mathbf{z})$. The

following angles are presented in Figure 5-2. The satellite elevation angle El is the angle between the vector **RS′** and the vector **RS**.

- The azimuth angle Az_{sat} is the angle between the **x** axis and the vector **RS′**.
- The aircraft azimuth angle Az_{air} is the angle between the vector parallel to the aircraft centerline pointing towards the aircraft nose and the vector **RS′.**
- The facade azimuth angle Az_{faca} (defined for plane facades only) is the angle between the normal vector of the facade and pointing towards the exterior of the façade and the vector **FS′**.

Blagnac airport consists in four different halls called Hall A to Hall D. Each hall is made of concrete (brown facets), glass (blue facets) or/and metallic (grey facets) rectangular facades. The assumed dielectric permittivity and thickness of concrete and glass walls are provided in Table 5-1. The imaginary part of the relative permittivity represents losses. The assumed permittivity and thickness of concrete facades correspond to realistic values that typically represent the permittivity and thickness of hardened concrete walls [Von Hippel, 1961]. The assumed permittivity and thickness of glass walls also correspond to realistic values.

Material	Assumed permittivity in the L1 and L5 frequency bands	Assumed thickness
Concrete	$6.5 - j0.4$	30cm
Glass	$5 - j0.025$	5mm

Table 5-1: Assumed characteristics of the concrete and glass facades

In addition, the terminal and gate façades of each hall are represented by simple 3D modeling. More specifically, five types of simplifications have been done when designing the 3D modeling of the terminal buildings and terminal gates of the airport.

- **Simplification 1**: Details characterized by a size below the wavelength, are not represented. Amongst these details there are:
  - Bricks
  - Windows frames
  - Metallic armatures on the glass walls characterized by a width of a few centimeters. Glass facades with such metallic armatures are represented by homogeneous and flawless glass facades.
  - Glass horizontal sticks on metallic walls (such as for the metallic façade of Hall C of Toulouse Blagnac airport) characterized by a width of a few centimeters. Metallic facades with such glass parts are represented by homogeneous and flawless metallic facades.
- **Simplification 2**: Sub-meter level concrete details on concrete walls such as concrete overhangs and recesses on are not represented.
- **Simplification 3**: The roughness of the building and gate walls, that are the millimeter to centimeter level asperities on the walls (such as small asperities on rendering) are not represented.
- **Simplification 4**: the GNSS multipath errors are computed by only considering the EM field reflected over the ground and scattered by the facades of the airport buildings and gates. The EM field that penetrates in the buildings and gates, that is scattered by obstacles in buildings such as walls, and that reaches the GNSS airborne antenna, is not considered in the multipath error computation. Hence, the interior parts of the buildings and gates are not represented.

- **Simplification 5**: The dielectric permittivity and thickness of concrete and glass walls are constant in the airport.

The impact of simplifications 1 and 2 on the multipath ranging error models and the validity of these simplifications will be further discussed in Appendix B, Section B.1. The analysis of the validity of simplifications 3 to 5 for the derivation of the multipath error models presented in this Chapter remains as future work.

Other fixed obstacles at Toulouse Blagnac airport environment are small-size (sub-meter level) obstacles such as panels. Isolated small-size obstacles induce ranging errors that are negligible with respect to larger objects (meter level) since [Chen, 2010] has shown that the power scattered by small objects is negligible compared to the power scattered by larger objects. Hence, fixed sub-meter level obstacles are not represented in the 3D model of Toulouse Blagnac airport environment.

5.1.2.2.3.2. Mobile obstacles

The presence of some mobile obstacles in the scene, such as parked surrounding aircraft, may considerably influence the magnitude of the GNSS multipath ranging errors [Chen, 2010]. However, this Ph.D. remains a first step in the development of a multipath threat model adapted to surface operations. It appears to be judicious in a first step to develop multipath error models in the presence of fixed obstacles only. For this reason, mobile obstacles are thus not represented in the 3D modeling of the airport environment. It can be proposed in a second step to develop models of prediction of the positions of the mobile obstacles in a specific airport environment. These position models could be used to develop multipath error models that are valid in the presence of both fixed and mobile obstacles.

5.1.2.3. GNSS receiver antenna

In the simulations, the GNSS receiver antenna is mounted on a A319 aircraft. In Section 5.1.2.2.1, it is explained that the structure of the assessed A319 aircraft is not a significant source of multipath. However, the presence of this aircraft structure impacts the GNSS receiver antenna pattern. For this reason, the model of the airborne antenna integrates the presence of the structure of the A319 assessed aircraft. Right and left circular polarization gains have been measured on the L1 frequency band by Airbus on a GPS antenna mounted on a model of a A319 aircraft. The data have been interpolated in the framework of a previous Ph.D. thesis [Chen, 2010] on a grid of 5 degrees in azimuth and elevation. The antenna gain pattern in both RHCP and Left Hand Circular Polarization (LHCP) is provided in Figure 5-3 on a grid of 5 degrees in azimuth and elevation.

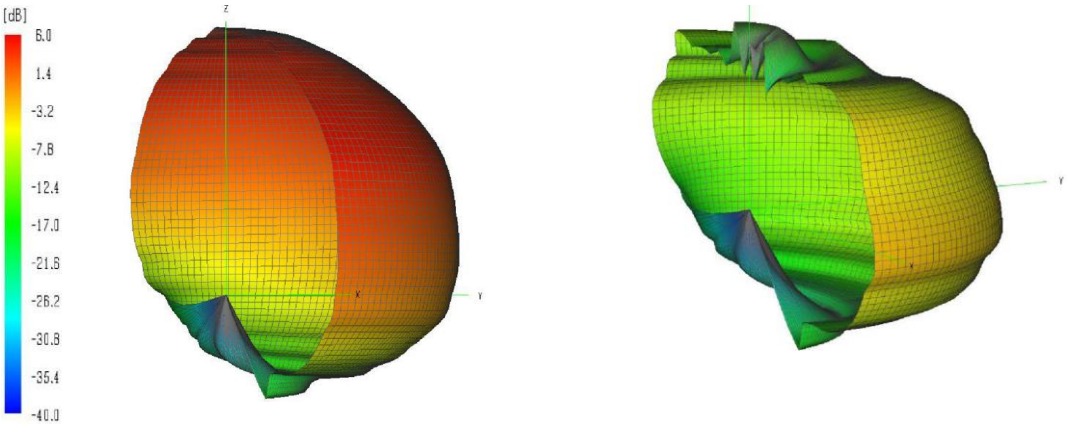

RHCP gain pattern [dB] LHCP gain pattern [dB]

Figure 5-3: 3D L1 gain pattern of the GPS antenna mounted on a A319 aircraft [Chen, 2010]

The interpolated RHCP and LHCP gains are plotted in Figure 5-4 when the signal arrives orthogonally to the aircraft fuselage and for different elevation angles. In this Figure, 0° corresponds to zenith and 180° corresponds to the ground direction.

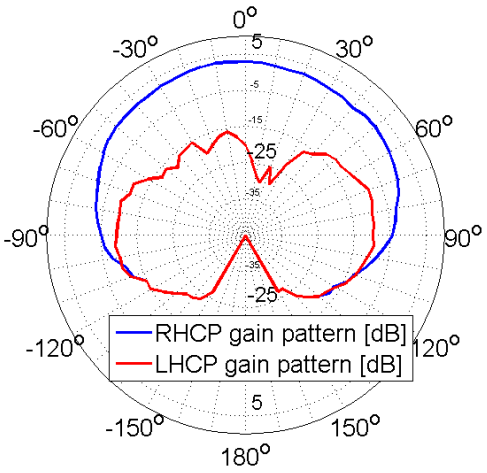

Figure 5-4: 2D L1 gain pattern of the GPS antenna mounted on a A319 aircraft

The radiation pattern is designed to reject the impact of signals coming from the ground and is oriented towards the sky.

In this thesis, the antenna gains, initially measured on an A319 model for the L1 frequency band, have been used for both L1 and L5 GPS and Galileo signals. Indeed, the gain patterns of the future dual-band L1+L5 antennas that will be used in civil aviation are not currently publically known. In addition, it is expected that the difference between the gain patterns on the L1 and L5 frequency bands will not be significant for three reasons. Firstly, both L1 and L5 antennas will be located at the same position on the aircraft fuselage. Secondly, both L1 and L5 frequency bands are closed. Thirdly, the same type of antenna (patch antennas) will be used to design both L1 and L5 frequency band antennas.

The antenna model does not take into account the group delays and phase delays induced by the antenna and by the multipath from the structure of the assessed A319 aircraft. The design of an antenna model that takes into account these delays remains as future work.

5.1.2.4. GNSS receiver settings

The GNSS receiver settings are discussed and provided in Section 4.2.4.

5.1.3. First and second-order interactions

The simulator can compute multiple interactions up to order 2 for metallic and dielectric multilayer facets. Indeed, [Chen, 2010] has shown that the prediction of the interactions with the scene up to order 2 is sufficient to predict the multipath ranging errors. First-order interactions are classified as follows:

- **Ground first-order reflections** correspond to the field coming from the satellite, reflected by the airport surface and reaching the antenna.
- **Obstacle first-order interactions** correspond to the field coming from the satellite, scattered by an obstacle and reaching the antenna.

Second-order interactions are classified as follows:

- **Ground/obstacle second-order interactions** correspond to the field coming from the satellite, reflected by the ground, then scattered by an obstacle, and finally reaching the antenna.
- **Obstacle/Ground second-order interactions** correspond to the field coming from the satellite, scattered by an obstacle, then reflected by the ground, and finally reaching the antenna.
- **Obstacle/Obstacle second-order interactions** correspond to the field coming from the satellite, scattered by an obstacle, then scattered by another obstacle, and finally reaching the antenna.

First and second-order interactions that include the assessed aircraft structure (such as obstacle/aircraft interactions) are partially taken into account in the software since the impact of the multipath from the aircraft structure is included in the radiation pattern of the GNSS receiver antenna. The excess code delays and phase shifts that affect the multipath scattered by the structure of the assessed aircraft structure are not taken into account.

5.1.4. Limitations

This section summarizes the main assumptions that have been made when computing the multipath errors in the airport environment by means of the simulator described in Section 5.1.1. The assumptions can be classified into three categories that are listed below.

- The first category includes assumptions that have been demonstrated as being valid. Among these assumptions, the GNSS satellites are considered to be stationary. Isolated obstacles of size below 80cm are not represented in the 3D modeling of the airport environment.
- The second category includes the simulation assumptions that have been made in the simulations presented in this chapter:
  - A simplified 3D modeling of the terminal buildings and terminal gates is implemented.
  - The ground is an infinite plane made of dry tar.
  - The same antenna gain pattern is used to compute both L1 and L5 antenna gains. The antenna group delay and phase delay are not included in the antenna model.

  The assumptions are relative to the values of the parameters used in the simulations for the computation of the multipath errors. A modification in these assumptions would result in changes in the values of the computed errors, but would not modify the way to model multipath errors in the airport environment.
- The third category includes the simplification assumptions. Indeed, this project constitutes a first step in the design of a multipath threat model adapted to airport environments. Some of the phenomena influencing the multipath ranging errors in the airport environment are not treated. More specifically, the impact of mobile obstacles on the multipath error is notably not assessed in this thesis. The error models presented in this chapter are valid in the absence of mobile obstacles.

5.2. Simulations scenario

In order to illustrate and analyze the shape of raw code multipath ranging errors in an airport environment, the multipath errors that affect the GNSS receiver of the assessed A319 aircraft that performs an arrival taxi operation at Toulouse Blagnac airport are considered. The aircraft will follow an assigned path in the airport during the operation, and this path is defined in the next section.

5.2.1. Low Visibility Procedure path

Under low visibility conditions, aircraft must follow specific paths from the runway to the gates. These paths are referred to as the Low Visibility Procedure (LVP) paths in the following. It is assumed that the assessed aircraft must perform an arrival taxi operation under low visibility conditions and that the assessed aircraft wants to reach the gate referred to as "Arrival gate" in Figure 5-5. From the Air Traffic Control (ATC) procedures, it must follow the LVP path indicated by red arrows in Figure 5-5 [SIA, 2013]. This path is constituted by 4 segments, referred to as Segment 1 to 4.

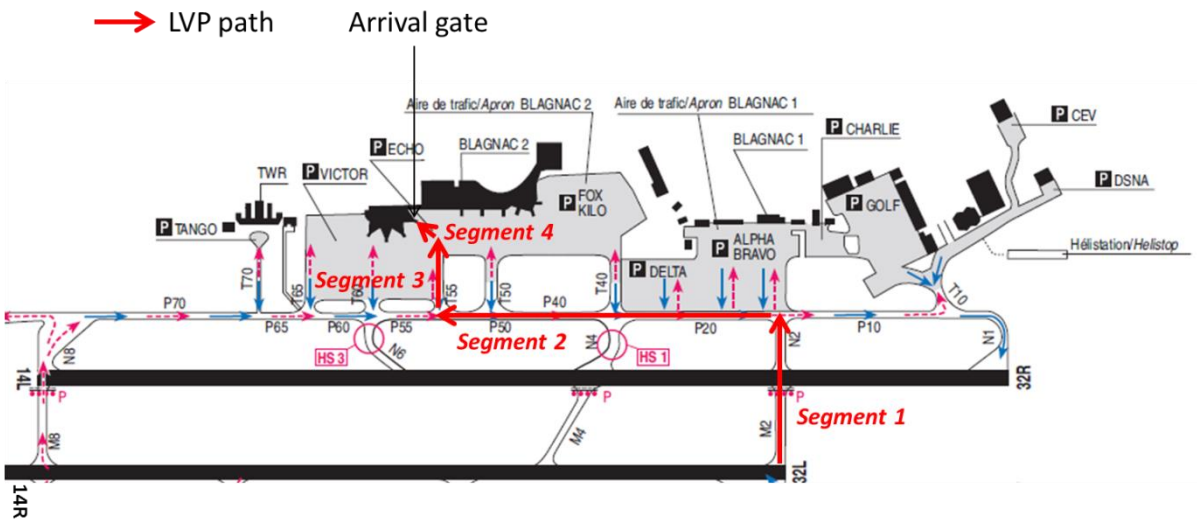

Figure 5-5: LVP path at Toulouse Blagnac airport, France

It can be easily demonstrated that, if the difference between the height of the assessed A319 antenna and the height of a building is above a given threshold Δh_{min}, the obstacle may mask the reception of the direct GNSS signal from the satellite, and the GNSS antenna may not receive the Line Of Sight (LOS) signal. This is represented in Figure 5-6.

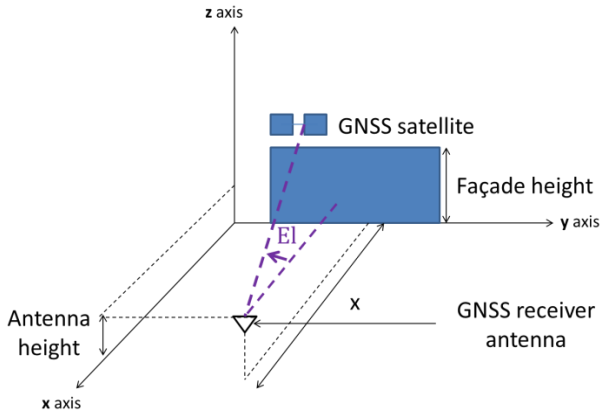

Figure 5-6: GNSS receiver antenna height and façade height representation

Δh_{min} is:

$$\Delta h_{min} = \tan(El)x \qquad \text{Eq - 5-2}$$

where:

- x is the horizontal distance between the obstacle and the GNSS antenna,
- El is the satellite elevation angle.

An analysis based on the height of each airport building and on the distance of the antenna to each building along the LVP procedure shows that the LOS is always present in the considered scenario along segments 1, 2 and 3, even with a satellite elevation as low as 5°. However, when the antenna is on segment 4, on the last 15m of the segment before arriving at the gate, the difference between the height of the assessed A319 antenna and the height of Hall C is below the threshold Δh_{min} for El in the range $[5°; 7.4°]$. Hence, on this segment portion, and if the satellite azimuth angle $Az_{sat} \in [90°; 270°]$, the antenna may only receive Non Line Of Sight (NLOS) signals.

5.2.2. Aircraft dynamic

This section presents the typical speed of the assessed aircraft along the LVP path presented in the last paragraph. The taxi operation at the arrival can be divided into three sub-phases: the *taxi on taxiway* is performed along segments 1 and 2, *taxi on apron taxiway* is performed along segments 3, and the *taxi on taxi lane* is performed on segment 4. Each phase is further detailed in Chapter 2. The typical aircraft is indicated in Table 5-2..

	Taxi on taxiway **Segments 1 and 2**	***Taxi on apron taxiway*** **Segment 3**	***Taxi on taxi lane*** **Segment 4**
Aircraft speed	$5 - 26\ \mathrm{m.s^{-1}}$	$0 - 5\ \mathrm{m.s^{-1}}$	$0 - 5\ \mathrm{m.s^{-1}}$

Table 5-2: Taxi speeds [RTCA, 1999]

5.3. Static and dynamic configurations

5.3.1. Static configuration and steady-state

The static configuration is defined as the configuration in which the assessed A319 aircraft is static in the airport environment. Since only fixed obstacles are considered in the scene, and since the GNSS satellite is assumed to be stationary, the transmission channel in the static configuration is stationary. The impulse response of the transmission channel is represented in Eq - 4-2.

Let's analyze the DLL response to the multipath in the static configuration. It is assumed that the static GNSS receiver antenna of the assessed aircraft receives a GNSS signal emitted by the GNSS stationary satellite. At time $t < 0s$, the received GNSS signal only consists of the direct signal. From time $t = 0s$, the received signal is the aggregate of the direct signal and of the echo signals scattered by the scene. Simulation parameters are recapped in Table 5-3.

	Parameter description	**Parameter value**
Satellite position	Satellite elevation angle El	20°
	Satellite azimuth angle Az_{sat}	0°
GNSS airborne antenna position	Coordinates in $(0, \mathbf{x}, \mathbf{y}, \mathbf{z})$	[35.83,132.4,5.88]
	Aircraft azimuth angle Az_{air}	90°

Table 5-3: Simulation parameters used for Figure 5-7

Figure 5-7 represents the evolution of the raw code multipath ranging errors in the time domain before and after the apparition of the echo signals.

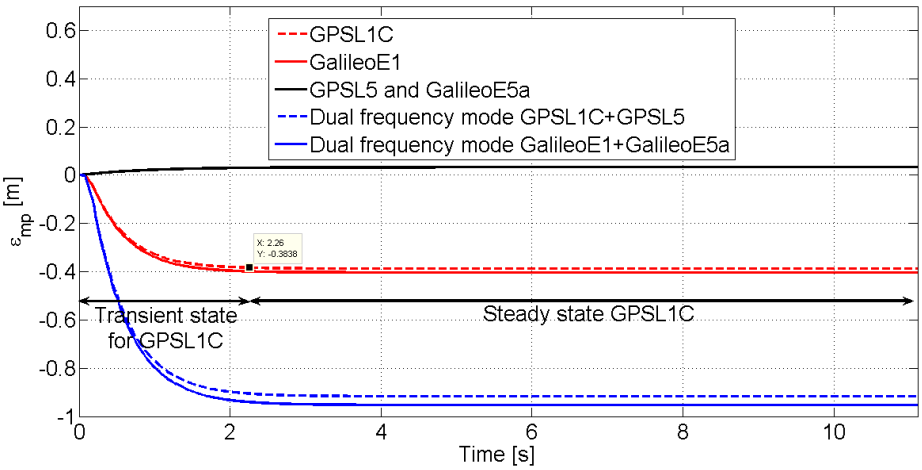

Figure 5-7: Raw code multipath ranging error in the static configuration

The evolution of the multipath error in the time domain can be viewed as the response of a first-order filter to a step input. This is because the DLL order 1 one. Hence, the DLL can be viewed as a first-order low-pass filter [Borre *et al.*, 2006]. After the apparition of the echo signal, the multipath error converges in the time domain until a time-constant value that is referred to as "raw code multipath ranging error in steady-state" in the following. This convergence period is called "transient state" and lasts few seconds. This is shown in Table 5-4 that provides the 99% response time related to the evolution of the raw code multipath ranging errors plotted in Figure 5-7.

	GPSL1C	GalileoE1	GPSL5 and GalileoE5a	GPSL1C+ GPSL5	GalileoE1+ GalileoE5a
99% response time	2.22s	2.26s	3.96s	2.38s	2.38s

Table 5-4: 99% response time related to the evolution of the raw code multipath ranging error

It is also shown in Table 5-4 that the values of the multipath parameters and the modulation technique influence the duration of the transient state. This is because the transfer function of the DLL discriminator depends on the modulation of the GNSS signal that is processed [Julien, 2005] and on the power of the received signal. After the transient state, the multipath error remains constant since the multipath parameters are constant. This time interval is called "steady-state".

5.3.2. Dynamic configuration

When the assessed aircraft is moving in the airport, the relative position of the GNSS receiver antenna with respect to the position of the obstacles of the scene and with respect to the position of the GNSS satellite is varying. The parameters of the transmission channel change in the time domain. The rate of change of the channel parameters depends on the aircraft dynamic. Fast variations of the parameters change the way the DLL responds to the multipath.

When the parameters variations are fast, the DLL cannot converge to the static multipath error in steady-state at each point of a given trajectory. The aircraft is said to be in the "dynamic configuration" or "dynamic regime". As an illustration, Figure 5-8 plots the GPSL1C multipath error along a segment parallel to the **y** axis assuming that the assessed aircraft has a constant speed of $1\mathrm{m.s}^{-1}$. These errors are compared to the static GPSL1C raw code multipath ranging errors in steady-state obtained when the assessed aircraft is in the static configuration on the segment. Other parameters of the simulation are stated in Table 5-3.

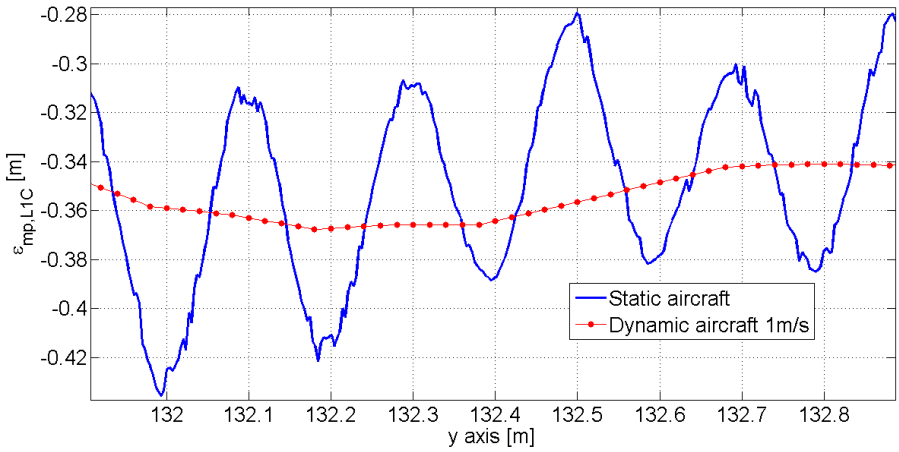

Figure 5-8: Raw code multipath ranging error in the static and dynamic configurations

From Figure 5-8, when the aircraft speed is as low as $1\mathrm{ms}^{-1}$, the variations of the transmission channel parameters are fast enough to change the way the DLL responds to the multipath compared to the static configuration. As long as the aircraft moves with a speed higher than $1\mathrm{ms}^{-1}$, the aircraft is said to be in the dynamic configuration. The magnitude of the error is reduced in the dynamic configuration, as further detailed in Section 5.5.2. In this Ph.D. thesis, the multipath errors are analyzed when the assessed aircraft performs uniform and rectilinear trajectories. The aircraft speed is assumed to be at least $1\mathrm{ms}^{-1}$ during uniform and rectilinear trajectories. Hence, in this thesis, when the aircraft performs uniform and rectilinear trajectories, the aircraft is said to be in the dynamic configuration.

5.4. Multipath error models in static configuration

This section analyzes the multipath errors that affect raw code pseudo-range measurements in the static configuration in an airport environment. The evolution of the raw code multipath ranging error as a function of the time in the static configuration is assessed in Section 5.3.1. This section aims to investigate the evolution of the steady-state raw code multipath ranging error in the space domain and to propose models of the steady-state raw code multipath ranging errors adapted to the static configuration in airport environments.

As an illustration of the space dependence of the multipath errors at the scale of the airport, Figure 5-9 presents the map of the dual-frequency GPSL1C+GPSL5 multipath ranging error in steady- state. This simulation has been obtained based on the simplified 3D model of Toulouse Blagnac airport presented in Section 5.1.2.2.3.1. The parameters used for this simulation are presented in Table 5-5.

	Parameter description	Parameter value
Satellite position	Satellite elevation angle El	20°
	Satellite azimuth angle Az_{sat}	0°
GNSS airborne antenna position	Antenna height h_{ant}	5.88m
	Aircraft azimuth angle Az_{air}	0°

Table 5-5: Simulation parameters used for Figure 5-9

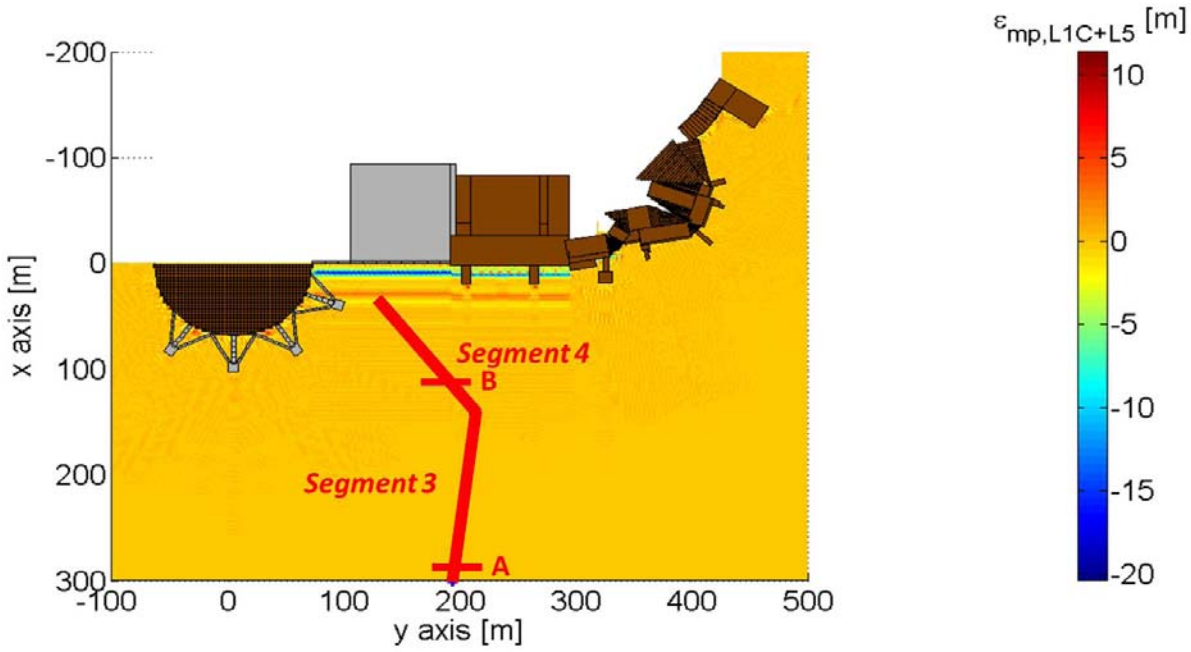

Figure 5-9: Simulated multipath ranging error GPSL1C+GPSL5 in steady state at Toulouse Blagnac airport, France

Depending on the relative positions of the GNSS airborne antenna, the GNSS satellite, and the obstacles in the scene, two scenarios can be distinguished.

- In the **first scenario**, the GNSS airborne antenna only receives echo signals reflected from the ground and scattered from the structure of the assessed aircraft. This configuration also includes the situation where the antenna also receives weak echo signals that have been scattered by one or several fixed obstacles, but the presence of these weak signals does not influence the raw code multipath ranging error at the DLL output. This is the case in point A of segment 3.
- In the **second scenario**, the GNSS airborne antenna also receives echo signals scattered by one or several obstacles. This is the case in point B of segment 4.

The next section investigates the spatial evolution of the steady-state raw code multipath errors due to echo signals from the airport surface and from the structure of the assessed aircraft (first scenario) and provides a model of such an error.

5.4.1. Error due to the ground and the aircraft structure

5.4.1.1. Multipath parameters and multipath error variation in the space domain

The spatial variations of the multipath errors depend on the spatial variations of the multipath parameters. Hence, in the following paragraph, the spatial variation of the multipath parameters is firstly investigated.

The impact of the structure of the assessed aircraft is included in the GNSS airborne antenna radiation pattern. Hence, at the receiver antenna output, the signal can be modelled as the sum of the direct signal and the echo signals due to the reflection on the airport surface. Since, from Section 5.1.2.2.2, the ground is assumed to be an infinite plane and made of dry tar, the reflection of the incident GNSS EM wave on the ground results in a single echo signal [Chen, 2010] that is represented by index "1" in this paragraph. It can be easily demonstrated that the relative code delay between the echo signal from the ground and the direct signal is given by:

$$\Delta\tau_1 = \tau_1 - \tau_0 = \frac{2h_{ant}\sin(El)}{c} \qquad \text{Eq - 5-3}$$

where h_{ant} [m] is the antenna height with respect to the airport surface.

A realistic GNSS airborne antenna induces group delays on both direct and reflected signals. These group delays are not taken into account in Eq - 5-3. From Eq - 5-3, it can be already expected that $\Delta\tau_1$ will remain roughly constant over the airport scale since the angular variations of the elevation angle El at the scale of the airport is roughly 0 degree. Table 5-6 quantifies the maximal variations of $\Delta\tau_1$, $\Delta\theta_1$, and α_1 along a 1 kilometer long segment on the **x** axis at Toulouse Blagnac airport.

	Difference between the minimal and maximal value along the 1km segment	
GNSS signal	**GPSL1C and GalileoE1**	**GPSL5 and GalileoE5a**
$\boldsymbol{\Delta\tau_1 = \tau_1 - \tau_0}$	$5.52.10^{-7}$ T_c	$5.52.10^{-6}$ T_c
$\boldsymbol{\Delta\theta_1 = \theta_1 - \theta_0}$	$5.3.10^{-3}$ rad	$4.0.10^{-3}$ rad
$\boldsymbol{\alpha = a_1/a_0}$	$9.3.10^{-3}$	$9.3.10^{-3}$
$\boldsymbol{\varepsilon_{mp}}$	$2.3.10^{-5}$ m	$2.24.10^{-4}$ m

Table 5-6: Maximal variations of the multipath parameters and error from the ground echo signal along a 1km segment

$\Delta\tau_1$ is roughly constant along the segment since the satellite elevation angle remains roughly constant over the 1 kilometer segment. Similarly, $\Delta\theta_1$ is roughly constant along the segment. Indeed, $\Delta\tau_1$ is roughly constant along the segment. In addition, the phase shift on echo signal "1" is roughly constant along the segment since the ground is assumed to be an infinite plane and made of dry tar.

The group delays and phase shifts induced by the GNSS antenna are not taken into account in the simulation results presented in Table 5-6. It can be expected that $\Delta\tau_1$ and $\Delta\theta_1$ are roughly constant along the segment even if the group delays and phase shifts induced by the GNSS antenna would be taken into account in the simulation results. Indeed, the group delays and phase shifts induced by the GNSS antenna on both direct and echo signals would remain constant over the segment since both satellite elevation angle and aircraft azimuth angle remain roughly constant over the segment.

Finally, α is roughly constant along the segment. This is because:

- The power of the EM wave scattered by the ground is roughly constant along the segment. Indeed, the ground is assumed to be planar and infinite tar ground and the dielectric permittivity of the ground is thus considered to be constant at the scale of the airport.
- The GNSS airborne antenna gains on both direct and echo signals remain constant over the segment since both satellite elevation angle and aircraft azimuth angle remain roughly constant over the segment.

As a conclusion, for a fixed satellite elevation angle, for a fixed aircraft azimuth angle, and for a planar and infinite ground made of dry tar, the multipath parameters of the echo signal from the ground are roughly constant at the scale of the airport.

The multipath parameters determine the value of the multipath ranging error in steady-state. Hence, it can be expected that the multipath ranging error induced by the airport surface and by the structure of the assessed aircraft is roughly constant at the scale of the airport for a fixed satellite elevation angle and a fixed aircraft azimuth angle. The maximal variations of the multipath ranging error over the 1 kilometer segment are quantified in Table 5-6 and are few hundredths of millimeters up to few tenths of millimeters, depending on the GNSS signal.

The multipath errors at the scale of a realistic airport would show higher variations. Indeed, the airport surface is in reality frequently inhomogeneous and may contain lawn or metallic parts. It may also contain snow, water or ice layers. Hence, the permittivity of the ground may in reality not be constant at the scale of the airport. Hence, the phase and the amplitude of the echo signal from the ground may present relatively high variations compared to the variations obtained under the planar and infinite ground made of dry tar hypothesis.

5.4.1.2. Multipath error model

Figure 5-10 provides the values of the GPSL1C+GPSL5 multipath ranging errors in steady-state due to the airport surface and the structure of the assessed aircraft for a wide range of pairs $\{\text{satellite elevation El}, \text{aircraft azimuth } Az_{air}\}$ and for a planar and infinite ground made of dry tar. El and Az_{air} are sampled with a step of size 5° each. El is in the range [0°, 90°] and Az_{air} is in the range [0°, 360°]. The GNSS receiver antenna height is $h_{ant} = 5.88\text{m}$.

From Eq - 5-3, and denoting T_c the chip period of GPSL1C and GalileoE1, $\Delta\tau_1$ is between $3.5.10^{-3}\ T_c$ for $El = 5°$ and $4.0.10^{-2}\ T_c$ for $El = 90°$. From Section 4.3.2.2.1, and taken into account the low values of $\Delta\tau_1$, the multipath ranging error on GPSL1C is roughly equal to the multipath ranging error on GalileoE1. Hence, the errors values shown in Figure 5-10 also represent the GalileoE1+GalileoE5a multipath ranging errors in steady-state due to the airport surface and the structure of the assessed aircraft.

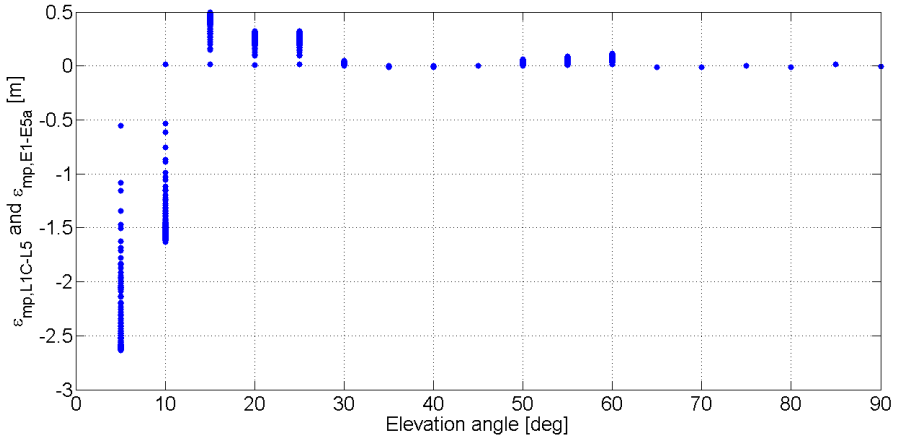

Figure 5-10: Dual-frequency multipath ranging error due to the airport surface and the aircraft structure

From Figure 5-10, three main observations can be made:

- For a fixed aircraft azimuth angle, the amplitude of the multipath errors tends to decrease when the elevation angle increases. The radiation pattern is designed to reject the impact of signals coming from the ground and is oriented towards the sky. At high elevation angles, the echo signal is coming downwards and is thus strongly rejected by the antenna. The amplitude of the multipath error is low (millimeter level). At low elevation angles, both direct and echo signals have roughly the same direction of arrival that is parallel to the airport surface. The reflected EM wave from the ground, which is mainly LHCP, is not strongly rejected since the antenna polarization is roughly linear at low elevation angles. The amplitude of the multipath error is large (decimeter up to meter level).
- For a fixed elevation angle, the error varies from a few millimeters up to a few decimeters with respect to the relative aircraft orientation. This is due to the GNSS airborne antenna pattern that is not-omnidirectional. At low elevation angles, the antenna gains depend significantly on the direction of arrival of the incoming EM waves, as represented in Figure 5-3. The error varies of a few decimeters with respect to the relative aircraft orientation. At high elevation angles, the direction of arrival of the incoming EM waves does not significantly change with respect to the aircraft azimuth angle. The antenna gains do not depend significantly on the azimuth angle of the incoming EM waves, as represented in Figure 5-3. The error varies of a few millimeters with respect to the relative aircraft orientation.

At low elevation angle and for $Az_{air} = 0°$, the GPSL1C+GPSL5 multipath ranging errors in steady-state due to the airport surface and the structure of the assessed aircraft is significantly different from the error values when $Az_{air} \neq 0°$. An interpretation of this observation is proposed in Appendix A, Section A.4.

The next section investigates the spatial evolution of the multipath errors in steady-state due to echo signals from the airport surface, from the structure of the assessed aircraft and from obstacles in the airport environment (second scenario) and provides a model of such an error.

5.4.2. Error due to the ground, the aircraft structure and the obstacle(s)

5.4.2.1. Static impact zone

The multipath ranging errors due to the airport surface, the structure of the assessed aircraft and obstacle(s) are analyzed in the impact zones of the airport. This section defines the concept of the impact zone.

Figure 5-9 shows that the steady-state raw code multipath ranging error presents spatial variations in the horizontal plane of the scene located at $h_{ant} = 5.88\text{m}$ above the ground. Closed to the obstacles, that is to say a few meters far from the obstacles, the echo signals reaching the GNSS receiver antenna are characterized by high relative amplitudes. At fixed satellite elevation and aircraft azimuth angles, this leads to relatively high variations of the multipath error (variations up to few meters) around a central value, which is the multipath error that would be obtained if the ground and the aircraft structure were the only multipath sources in the scene. Far from the obstacles, the error variations are low for two possible reasons:

- Firstly, the relative amplitude of the echo signals scattered from the obstacles is reduced, leading to relatively weak variations of the multipath error (variations of up to few centimeters) around the central value.
- Secondly, the relative code delay of the echo signals scattered from the obstacles become high and thus may not affect the multipath error. Indeed, from Section 4.3.2.2.1, any echo signal characterized by a relative code delay above $\Delta\tau = T_c + \frac{\Delta}{2}$ does not impact the multipath ranging error.

As an illustration of the relative amplitude of the echo signals, the histograms of the relative amplitudes in the L1 frequency band for the direct and echo signals are presented in Figure 5-11. In scenario 1, 10 true receiver antenna positions are equally distributed in an inner grid in zone 1 which is closed to the obstacles, and the relative amplitudes are simulated over all antenna positions. In scenario 2, 10 true receiver antenna positions are equally distributed in an inner grid in zone 2 which is far from the obstacles, and the relative amplitudes are simulated over all antenna positions. The simulation parameters are recapped in Table 5-7.

	Parameter description	Parameter value
Satellite position	Satellite elevation angle El	20°
	Satellite azimuth angle Az_{sat}	0°
GNSS airborne antenna positions	Aircraft azimuth angle Az_{air}	0°
	Scenario 1: antenna positions in zone 1 (closed to the airport buildings)	x range: [25.0,27.0] y range: [150.0,152.0] $z = 5.88$
	Scenario 2: antenna positions in zone 2 (far from the airport buildings)	x range: [140.0,142.0] y range: [150.0,152.0] $z = 5.88$

Table 5-7: Simulation parameters used for Figure 5-11

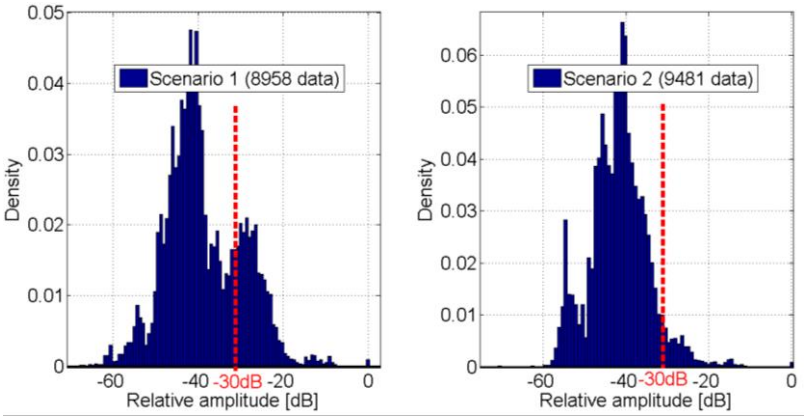

Figure 5-11: Histograms of the L1 relative amplitude of the echo signals

In Figure 5-11 it is shown that the number of echo signals arriving in zone 1 and characterized by a relative high amplitude (relative amplitude above 30dB) represents 20.7% of the total number of echo signals arriving in this zone. In comparison, the number of echo signals arriving in zone 2 and characterized by a relative high amplitude (relative amplitude above 30dB) represents 5.1% of the total number of echo signals arriving in this zone. Hence, Far from the obstacles, the relative amplitude of the echo signals scattered from the obstacles is reduced.

In this document, the static impact zone is defined as the horizontal area of the airport located at $h_{ant} = 5.88\text{m}$ above the ground where the variations of the raw code multipath ranging error in steady-state are significant with respect to the other sources of ranging errors. Section 3.2.1.9 reveals that, in dual frequency mode, the standard deviation of the stochastic ranging error due to the troposphere, the ionosphere, the satellite clock and ephemeris inaccuracies, and the receiver thermal noise is few decimeters. The impact zone is the area where the amplitude variations of the multipath error around the central value are higher than 10% of 10cm, that is to say 1cm.

The impact zone location depends on the satellite elevation and azimuth angles since both angles influence the amplitude of the multipath ranging errors closed to the obstacles. In order to determine the location of the impact zone related to a given satellite position, the multipath ranging errors are computed in the scene with a spatial period of 5cm for that satellite position. The spatial period must be small enough with respect to the wavelength to clearly observe the variations of the multipath error around the central value. The impact zone is then determined by considering the zone of the airport where the amplitude variations of the multipath error around the central value are higher than 1cm. As an example, Figure 5-12 represents the evolution of the multipath ranging errors along a 30 meter long sub-segment of segment 3 represented in Figure 5-9 for a satellite elevation of 5° and for a satellite azimuth of 0°. Note that, in this simulation, the elevation angle has been voluntary decreased to 5° in order to clearly distinguish the high amplitude variations of the errors inside the impact zone to the low amplitude variations of the errors outside the impact zone. It is shown in this plot that all antenna positions characterized by an **x** coordinate above 170.3m are considered to be out of the impact zone for a satellite elevation of 5° and for a satellite azimuth of 0°.

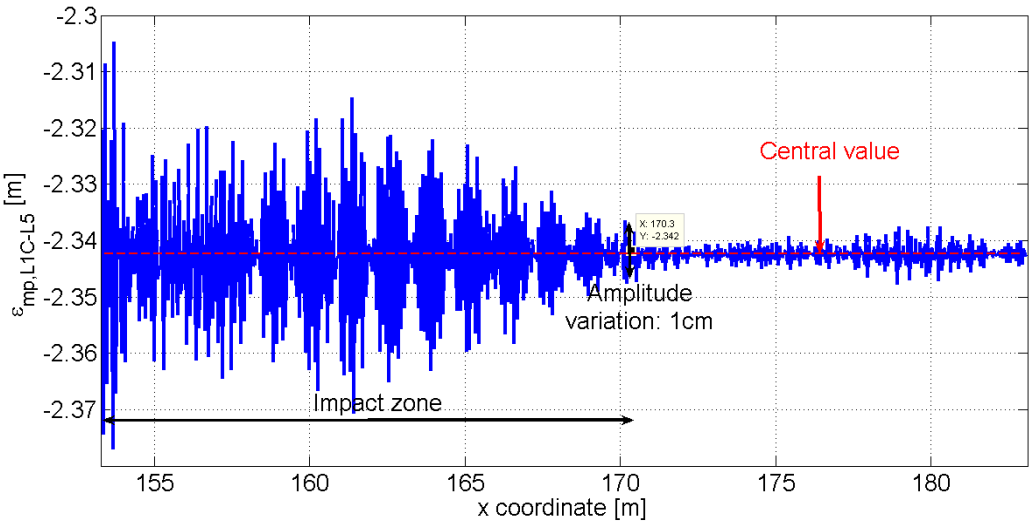

Figure 5-12: Evolution of the multipath ranging error in steady-state over segment 3

The next two sections investigate the spatial evolution of the multipath parameters and of the multipath errors in steady-state and in the impact zone.

5.4.2.2. Multipath parameter variations in the impact zone

The spatial variation of the multipath parameters in the impact zone is investigated in this section. In the impact zone, the signal received by the GNSS antenna can be modelled as the sum of the direct signal, the echo signal from the airport surface and the echo signals that have been scattered by at least one obstacle. The multipath parameters of the echo signal reflected from the ground and reaching the GNSS receiver antenna have been analyzed in Section 5.4.1.1. The multipath parameters of the echo signals that have been scattered by at least one obstacle are investigated in this paragraph.

For this analysis, a static assessed aircraft on segment 4 depicted in Figure 5-9 is considered. The error is computed over segment 4 that is located closed to the airport obstacles. This allows clearly visualizing the amplitude variations of the errors induced by the airport obstacles. On segment 4, the aircraft is in the impact zone related to the GNSS satellite characterized by a satellite elevation angle of 20° and by a satellite azimuth angle of 0°. The airborne antenna receives a large number of multipath from airport obstacles along the segment 4. The evolutions of the multipath parameters of any echo signals are not represented in this section. It is preferred to illustrate the multipath parameter evolution of a single echo signal, referred to as echo signal "2". Echo signal "2" is scattered from Hall C and received by the airborne antenna along segment 4. Estimating the multipath ranging error in the impact zone by considering only one single echo signal from the airport buildings is not valid. However, in this section, a single echo signal is considered since it allows going even further in the multipath parameter analysis. The conclusions proposed in this section concerning the spatial evolution of the multipath parameters of echo signal "2" can be applied to any echo signals scattered by at least one airport obstacle and received by the GNSS antenna.

The evolution of the multipath parameters of an echo signal, referred to as index "2", that is emitted by the satellite, scattered by the metallic façade of Hall C, and that arrives at the GNSS receiver antenna, is plotted in Figure 5-13 over the 116 meter long segment 4 [CD] for the relative amplitude and relative code delay parameters and over a 1 meter long portion of segment 4 [ED] for the relative phase shift. Simulation parameters are provided in Table 5-8.

	Parameter description	Parameter value
Satellite position	Satellite elevation angle El	20°
	Satellite azimuth angle Az_{sat}	0°
GNSS airborne antenna position	Aircraft azimuth angle on segment 4 Az_{air}	218.29°
	Between points E and D for the relative phase shift plot	E[36.61; 133.02; 5.88] D[35.83; 132.4; 5.88]
	Between points C and D for the relative amplitude and for the relative code delay plots	C[126.9; 204.3; 5.88] D[35.83; 132.4; 5.88]

Table 5-8: Simulation parameters used for Figure 5-13

The spatial variation of the multipath parameters related to echo signal "2" are analyzed as follows.

The relative code delay evolution is quasi linear. Appendix A, Section A.1.1, proposes the analytical expression of the relative code delay $\Delta\tau_2$ of an echo signal that is emitted by the satellite, scattered by a reflector and that reaches the receiver antenna. The expression is provided along a segment located in the specular direction.

The relative phase shift is quasi periodic. Spatial periods of 13cm for L1 signals and 17cm for L5 signals are observed. The spatial period of $\Delta\theta_2$ is of the order of λ_L. As demonstrated in Appendix A, Section A.1.2, the spatial period of the phase shift $\Delta\theta_2$ depends on the orientation of the segment in the impact zone, on the satellite elevation and azimuth angles and on the central frequency of the GNSS signal f_L.

The relative amplitude presents large scale variations on the assessed segment. The small discontinuities of α are due to the antenna gains interpolation in the software. The amplitude of α depends on the orientation of the facade on which echo signal "2" is scattered, and thus on the satellite azimuth angles. This phenomena is underlined in Figure 5-13 by comparing the values of α for GPSL1C, $Az_{sat} = 0°$ and $El = 20°$ to the values of α for $Az_{sat} = 20°$ and $El = 20°$. In addition, the amplitude of α depends on the satellite elevation angle. The amplitudes of the echo signals from the façade of Hall C are high for low elevation angles and tend to decrease for high elevation angles. This phenomena is underlined in Figure 5-13 by comparing the values of α for GPSL1C, $Az_{sat} = 0°$ and $El = 20°$ to the values of α for GPSL1C, $Az_{sat} = 0°$ and $El = 5°$.

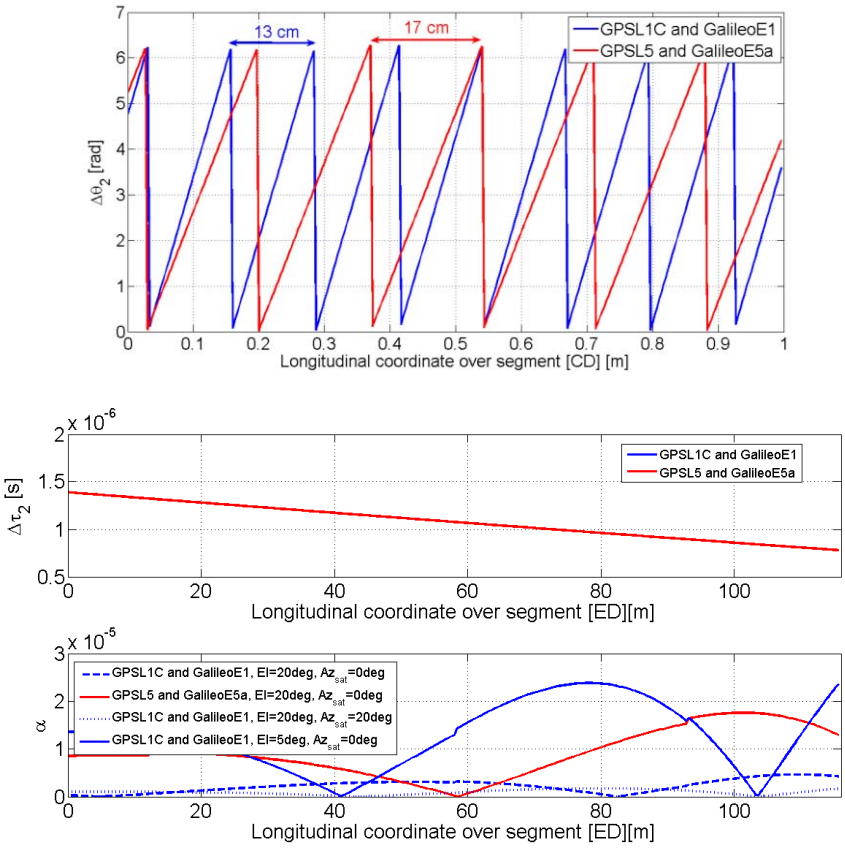

Figure 5-13: Evolution of the multipath parameters of echo signal "2" over segments [CD] and [ED]

5.4.2.3. Multipath ranging error variations in the impact zone

The spatial variation of the multipath ranging errors in the impact zone is investigated in this section. The multipath parameters determine the value of the raw code multipath ranging error in steady-state. Hence, it can be expected that the variations of the multipath parameters, and more specifically the small scale variations of the relative phase shift, cause variations of the multipath error in the impact zone. This is validated as follows. The evolution of the dual frequency GPSL1C+GPSL5 steady-state raw code multipath ranging errors and over segments [CD] and [ED] are plotted in Figure 5-14.

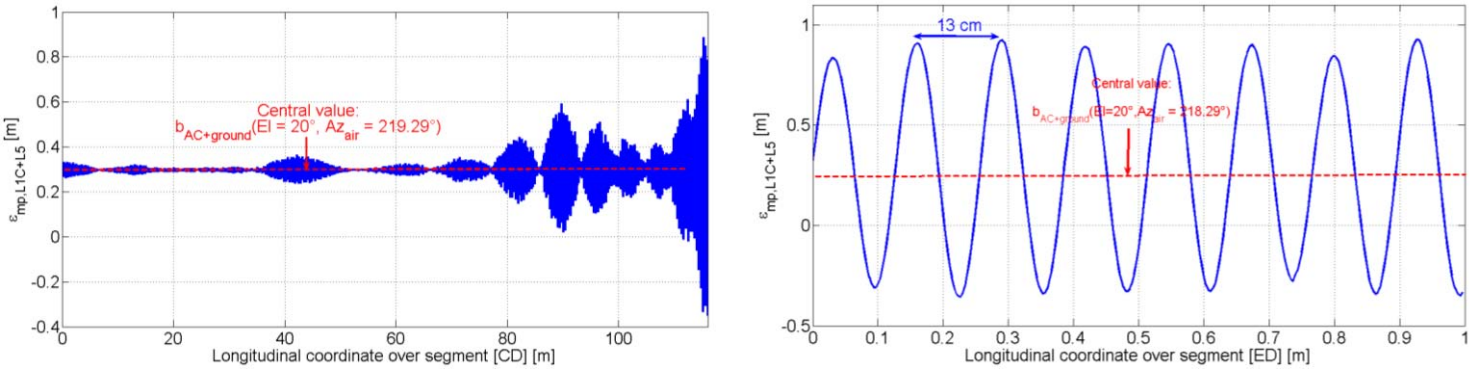

Figure 5-14: Evolution of the GPSL1C+GPSL5 multipath ranging error over segments [CD] and [ED]

5.4.2.3.1. Analysis of the spatial variations of the multipath errors

The small-scale spatial variations of the errors along segment [ED] is discussed in this section. The spatial variations of multipath errors along [ED] are due to the small scale variations of the relative phase shift $\Delta\theta_2$ on GPSL1C and on GPSL5 along segment [ED]. The spatial period of $\Delta\theta_2$ and thus the spatial period of the oscillations of the multipath errors depend on the orientation of the segment in the impact zone and on the satellite elevation and azimuth angles. The spatial period of the multipath ranging error is of the order of λ_L.

5.4.2.3.2. Analysis of the amplitude of the multipath errors

The values of the errors along segment 4 are discussed in this section.

Firstly, both plots of Figure 5-14 reveal that the multipath errors oscillate on segment 4 around a central value. This central value corresponds to the multipath error that would be obtained if the ground and the aircraft structure were the only multipath source. The multipath error due to the ground and the aircraft structure is fully analyzed in Section 5.4.1.2. In this section, this error is denoted as $b_{AC+ground}(El, Az_{air})$. This error depends on both the satellite elevation angle and the aircraft azimuth along the segment.

Secondly, the amplitude of the oscillations of the multipath errors along segment 4 is driven by the amplitude of the multipath at the GNSS receiver antenna output. The evolution of the multipath error along segment [CD] reveals that the amplitude of the oscillations of the multipath errors tend to decrease when the distance to the obstacles increases. This is because the amplitude of the echo signals tends to decrease when the distance to the obstacles increases. The amplitude of the error oscillations also depends on the satellite azimuth angles. This is because the echo signal amplitude depends on the satellite azimuth angle with respect to the scene (see Figure 5-13). As an illustration, the maximal peak-to-peak amplitudes of the multipath errors along segment [ED] are indicated in Table 5-9 for different satellite azimuth

angles. Finally, from Table 5-9, and for a constant satellite azimuth angle of 0°, the peak-to-peak amplitude for El = 5° is roughly 5 times the peak-to-peak amplitude for El = 20°. This is because low elevation angles cause relatively high echo signal amplitudes (see Figure 5-13) and high multipath error amplitudes.

	$\mathbf{El = 20°}$ $\mathbf{Az_{sat} = 0°}$	$\mathbf{El = 20°}$ $\mathbf{Az_{sat} = 40°}$	$\mathbf{El = 5°}$ $\mathbf{Az_{sat} = 0°}$
Maximal peak-to-peak amplitude over segment [ED]	1.27m	94.5cm	7.46m

Table 5-9: Peak-to-peak amplitude of the GPSL1C+GPSL5 multipath ranging error over segment [ED]

This section has investigated the spatial evolution and the amplitude of the multipath errors in steady-state and in the impact zone. The next section provides a model of the multipath errors in the impact zone.

5.4.2.4. Over-bounding Gaussian multipath error model

5.4.2.4.1. Methodology

It is established in Section 5.4.2.3 that the multipath ranging error at a given location in the impact zone can be decomposed as follows:

$$\varepsilon_{mp,L1C+L5} = b_{AC+ground}(El, Az_{air}) + b_{obs} \qquad \text{Eq - 5-4}$$

where:

- $b_{AC+ground}(El, Az_{air})$ is the multipath ranging error that would have been obtained if the ground and the aircraft structure were the only multipath sources present at that given location. This term is induced by the ground first-order reflection.
- b_{obs} represents the oscillations of the multipath ranging error $\varepsilon_{mp,L1C+L5}$ around the central value $b_{AC+ground}(El, Az_{air})$ in the impact zone. b_{obs} is induced by the scattering of the EM field on the airport obstacles. This term is induced by the obstacle first and second-order interactions.

The component $b_{AC+ground}(El, Az_{air})$ depends on:

- the GNSS receiver antenna radiation pattern and the GNSS receiver settings,
- the airborne antenna height h_{ant},
- the satellite elevation El and aircraft azimuth Az_{air} angles.

Both angles can be predicted or measured. In addition, assuming a planar and infinite ground made of dry tar, the values of $b_{AC+ground}(El, Az_{air})$ can be predicted and are provided in Section 5.4.1.2 for the antenna pattern and for the receiver settings considered in this thesis and presented in Section 5.1.2. For this reason, it can be considered that the component $b_{AC+ground}(El, Az_{air})$ can be determined in a deterministic way.

The component b_{obs} depends on:

- the satellite position (the satellite elevation El and azimuth Az_{sat} angles),
- the 3D model of the airport environment,
- the GNSS receiver antenna radiation pattern and the GNSS receiver settings,

- the true position of the GNSS receiver antenna and the aircraft azimuth angle Az_{air}.

Determining the component b_{obs} in the impact zone in a deterministic way is complex as it would require knowing the position of the airborne antenna in the impact zone with a high level of precision (centimeter precision level since the spatial period of the multipath error is of the order of 10 centimeters). It is thus proposed to provide a statistical model of the error component b_{obs} in the impact zone that is independent of the true position of the GNSS receiver antenna in the impact zone. Since a model independent of the aircraft azimuth angle will be simpler to use, it is proposed to set up a statistical model of the error component b_{obs} that is also independent of the aircraft azimuth angle Az_{air}. The methodology used to obtain the error models is sketched in Figure 5-15.

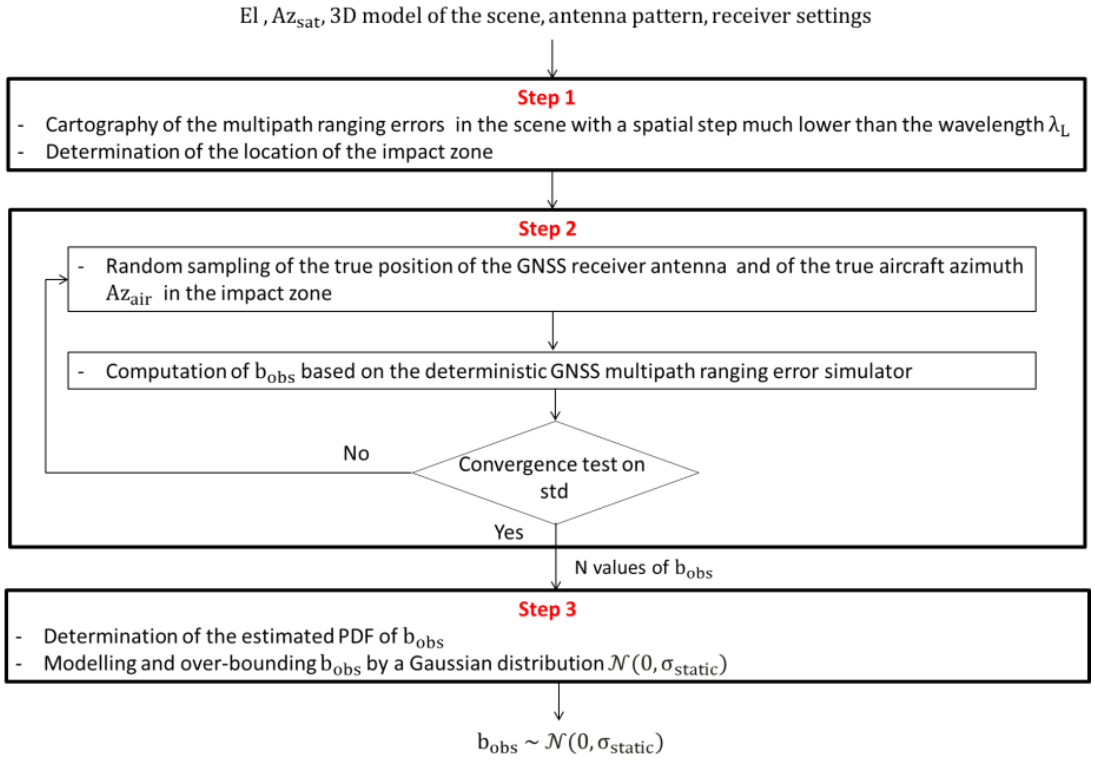

Figure 5-15: Methodology to model of b_{obs} in the impact zone

In order to illustrate this methodology, the dual-frequency GPSL1C+GPSL5 over-bounding Gaussian multipath error model is derived in an impact zone on segment 4. The satellite elevation and azimuth angles are $El = 20°$ and $Az_{sat} = 0°$, respectively.

Step 1

Figure 5-14 shows the evolution of the multipath ranging error over segment 4 (segment [CD]) for $El = 20°$ and $Az_{sat} = 0°$. The amplitude of the oscillations b_{obs} around the central value is above 1cm on the entire segment 4. Hence, the entire segment 4 is included in the impact zone. Figure 5-16 depicts segment 4.

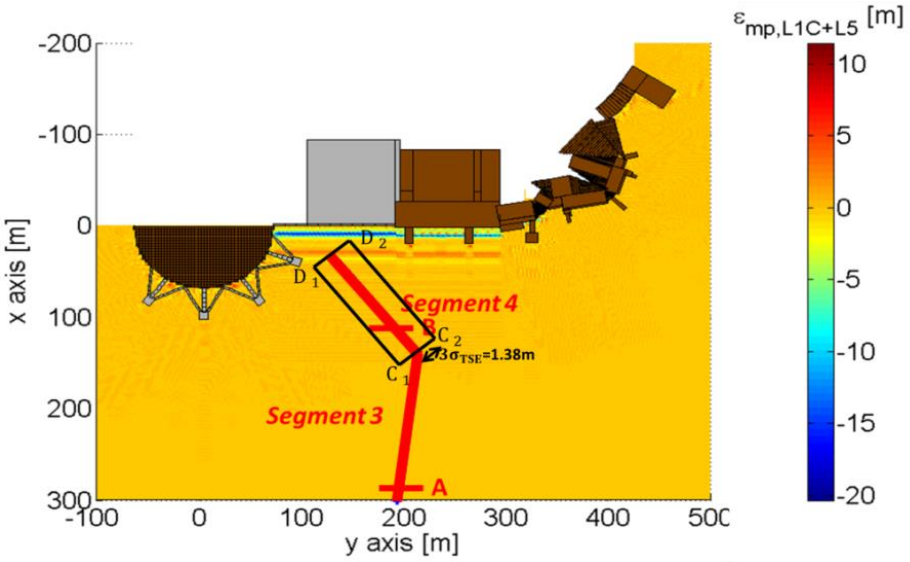

Figure 5-16: Random position of the GNSS receiver antenna in the impact zone

Step 2

In order to estimate the Probability Density Function (PDF) of the components b_{obs} along segment 4 and in the impact zone, a Monte Carlo simulation is performed. For each Monte Carlo iteration, two input variables are randomly generated: the aircraft position in the impact zone along segment 4 and the aircraft azimuth angle. The probability distributions attached to each variable are detailed below.

From Chapter 2, the lateral distance between the desired path and the true position shall be lower than $3\sqrt{\sigma_{NSE}^2 + \sigma_{PDE}^2 + \sigma_{FTE}^2} = 3\sigma_{TSE}$ 99.6% of the time. In this thesis, it is assumes that a system monitors the accuracy of the GNSS horizontal position estimate and that the lateral distance between the desired path and the true position is lower than $3\sqrt{\sigma_{NSE}^2 + \sigma_{PDE}^2 + \sigma_{FTE}^2} = 3\sigma_{TSE}$ 99.6% of the time. From the values of the required σ_{NSE}, σ_{PDE} and σ_{FTE} presented in Chapter 2, the maximal allowed value of σ_{TSE} is set to 46cm for the *taxi on taxi lane* sub-phase, 61cm for the *taxi on apron taxiway* sub-phase, and 1.01m for the *taxi on taxiway* sub-phase. At each iteration, it is chosen to select uniformly the true horizontal GNSS receiver antenna position in the rectangular zone depicted in Figure 5-16. An important remark is that the error model along segment 4 is developed by simulating multipath errors along the whole segment 4. A single error model is developed along segment 4. However, the error amplitude along segment 4 is not constant. Hence, it is recommended as future work:

- either to define and distinguish the parts on the segment on which the error amplitude is roughly constant and then to develop an error model for each of these parts.
- or to determine the segment part where the error amplitude is maximal and to estimate the standard deviation parameter on this part. Note that this suggestion is more conservative than the suggestion stated above, but is easier to manipulate since only one error model is developed for the segment.

The aircraft azimuth angle follows a Gaussian distribution that is centered on the aircraft azimuth angle on segment 4 (218.29°) and that is characterized by a standard deviation equal to $\sigma_{az,air} = 30$. Hence, 99.6% of the simulated aircraft azimuth angles will be in the interval $[218.29° - 3\sigma_{az,air}; 218.29 + 3\sigma_{az,air}] = [218.29° - 90 ; 218.29 + 90]$.

The multipath ranging error is then computed for each Monte Carlo iteration. The convergence test is performed and the simulation is stopped at the first iteration for which the convergence test is passed. The convergence test is detailed in Appendix B, Section B.2. As shown in Appendix B, Section B.2, $N = 2454$ is the minimal number of samples required to correctly estimate the model parameters in the simulation scenario considered in this section. A rigorous approach to quantify the quality of the parameter estimators is to use confidence interval [Papoulis, 1991]. The computation of the confidence intervals is not presented in this thesis.

Step 3

The estimated Probability Density Function (PDF) based on the $N = 2454$ simulated GPSL1C+GPSL5 multipath ranging errors is plotted in Figure 5-17, blue curve. The estimated mean and standard deviation of the error when the simulation stops are denoted as μ_{est} and σ_{est} , respectively. μ_{est} and σ_{est} are indicated in Table 5-10.

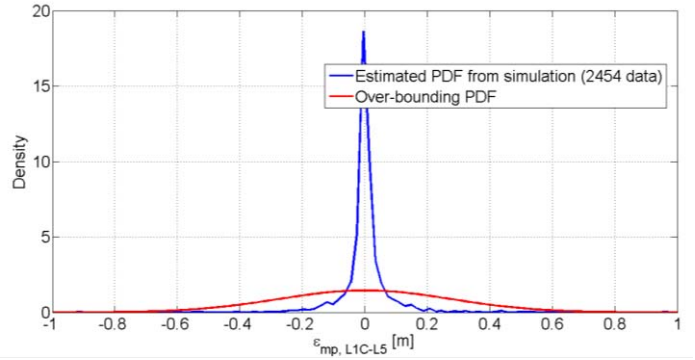

Figure 5-17 : Estimated and over-bounding Gaussian PDFs of b_{obs} in the impact zone

Estimated statistical moments of the distribution of b_{obs}	
$\mu_{est} = 1.7\text{mm}$	$\sigma_{est} = 9.0\text{cm}$

Table 5-10 : Standard deviation and mean of the distribution of b_{obs}

The distribution of b_{obs} in the impact zone can be considered as centered. This is because b_{obs} represents the oscillation term of the multipath error around the central value $b_{AC+ground}(El, Az_{air})$.

The multipath ranging error model proposed in this document is intended to be included within GNSS integrity monitoring algorithms for airport operations. For this reason, the priority is to model the estimated distribution by a distribution that over-bounds the tails of the estimated distribution. In addition, it has been chosen to over-bound the estimated distribution by a Gaussian distribution since the stochastic measurement error models used in the ABS integrity monitoring algorithms to check GNSS measurements consistency and compute protection levels are over-bounded Gaussian distributions. The feasibility to over-bound the estimated PDF by a distribution that best fits the estimated distribution and to design integrity monitoring algorithms that use non-Gaussian distribution as expected measurement error models is not discussed in this thesis and remains asfuture work.

DeCleene's Cumulative Density Function (CDF) algorithm is used [DeCleene, 2000] to compute the standard deviation of the over-bounding Gaussian distribution. Note that the CDF over-bounding method requires the estimated distributions to be symmetric and

unimodal. The estimated distributions do not exactly fulfil these conditions, but approximately do. In the application, it is always possible to find a Gaussian distribution that over-bounds the tails of the distribution of the multipath ranging error in the impact zone. This is because the PDF of the multipath ranging errors in the impact zone is a positive and bounded function. Indeed, as shown in Section 4.3.2.2.1, the maximal amplitude of the multipath ranging errors in the impact zone is driven by the amplitude of the multipath. Since the multipath amplitude is bounded in the scene, the amplitude of the multipath errors is also bounded in the impact zone. Hence, the PDF is a bounded function.

The multipath ranging error at a given location in the impact zone can be modelled as follows:

$$\varepsilon_{mp,L1C+L5} = b_{AC+ground}(El, Az_{air}) + b_{obs} \quad \text{Eq - 5-5}$$

where:

$$b_{obs} \sim \mathcal{N}(0, \sigma_{static}) \quad \text{Eq - 5-6}$$

The PDF of the over bounding Gaussian distribution is represented in red in Figure 5-17. The standard deviation of the DeCleene distribution is 27.5cm and is roughly 3 times higher than the standard deviation of the multipath errors obtained by simulations. The values of the over-bounding Gaussian distribution parameter σ_{static} is further discussed in the next paragraph.

5.4.2.4.2. Simulation results

The sensitivity of the over-bounding Gaussian distribution parameter σ_{static} to the satellite elevation El and to the satellite azimuth Az_{sat} angles is analyzed in this section. The simulation results presented in this paragraph have been obtained by simulating the GPSL1C+GPSL5 multipath ranging errors b_{obs} in the impact zone. However, it is shown in Appendix B, Section B.3, that the modulation difference between GPSL1C and GalileoE1 signals does not significantly impact the values ofσ_{static}. Hence the simulation results provided in this section are also valid for the GalileoE1+GalileoE5a case.

The evolution of σ_{static} as a function of El in the impact zones located along segments 3 and 4 is represented in Figure 5-18. The over-bounding Gaussian error model is not developed for elevation angles above 35 degrees and for segment 3 since segment 3 does not cross any impact zone for these elevation angles.

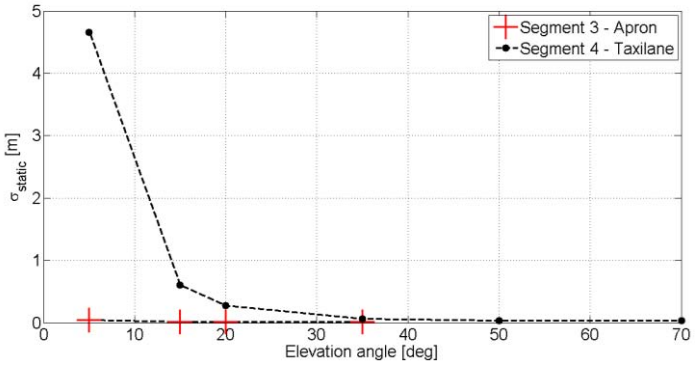

Figure 5-18: σ_{static} as a function of the satellite elevation angle $Az_{sat} = 0°$

For segment 4, σ_{static} tends to decrease when El increases. The amplitude ratios of the echo signals are relatively high at low elevation angles, and tend to decrease when the elevation angle increases. This phenomenon is underlined in Section 5.4.2.2. The amplitude of the

oscillations of the multipath ranging errors in the impact zone increases with the amplitude ratios of the received echo signals, as illustrated in Table 5-9. This explains why the estimated PDF of the multipath error in the impact zone is characterized by a standard deviation σ_{static} that is significant at low elevation angles. For segment 3, σ_{static} is roughly constant as a function of El. Indeed, segment 3 is relatively far from the airport obstacles (few dozens of meters up to few hundred of meters), and the amplitude of the variations of the multipath error in the impact zone along segment 3 are low (few centimeters level) regardless of the satellite elevation angle.

Note that other parameters influence the echo signal amplitude ratios, and thus the values of σ_{static}. The characteristics of the obstacles inducing echo signals in the impact zone and the relative location of the impact zone with respect to these obstacles also determine the amplitude of the echo signals. Points located in the impact zone of segment 3 are further away from the large metallic Hall C facade than points located in the impact zone of segment 4. Hence, at fixed elevation angles, the values of σ_{static} are lower for the impact zone along segment 3 than for the impact zone along segment 4. As an illustration, σ_{static} reaches few meters over segment 4 at low elevation angles while σ_{static} reaches few decimeters over segment 3 at low elevation angles.

The evolution of σ_{static} as a function of Az_{sat} in the impact zones located along segments 3 and 4 are represented in Figure 5-19.

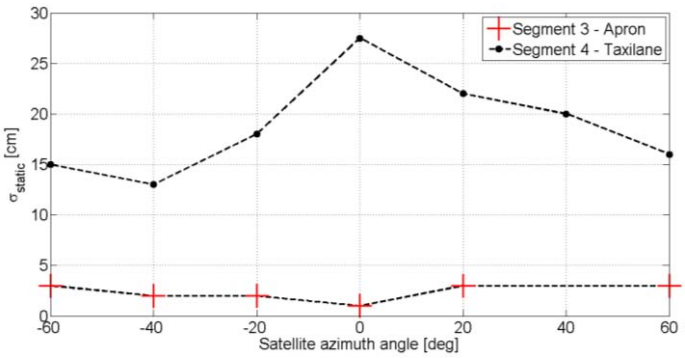

Figure 5-19: σ_{static} as a function of the satellite azimuth angle, El = 20°

For segment 3, σ_{static} is roughly constant as a function of Az_{sat}. Indeed, segment 3 is relatively far from the airport obstacles, and the amplitude of the variations of the multipath error in the impact zone along segment 3 at an elevation angle of El = 20° are low regardless of the satellite azimuth angle. Hence, σ_{static} is roughly constant and low (few centimeter level) as a function of Az_{sat}. For segment 4, σ_{static} varies as a function of Az_{sat}. Indeed, the error amplitude on segment 4 varies as a function of Az_{sat}. This phenomenon is further discussed in Section 5.4.2.2.

5.5. Multipath error models in dynamic configuration

This section analyzes and proposes models of the multipath errors that affect raw code pseudo-range measurements in dynamic configurations in an airport environment. In this thesis, the dynamic multipath error models are developed for uniform and rectilinear trajectories. The error models are not developed for non-constant speed trajectories or/and

curved trajectories. The minimal aircraft speed along a uniform and rectilinear trajectory is assumed to be $1\mathrm{m.\,s^{-1}}$.

5.5.1. Error due ground and aircraft structure

5.5.1.1. Multipath parameters and multipath error variation in the space domain

This subsection analyzes the multipath parameters evolution and the raw code multipath ranging error evolution throughout a uniform and rectilinear trajectory that is outside of any impact zone. Throughout such a trajectory, the ranging measurement between the satellite and the GNSS airborne antenna is mostly affected by multipath errors due to the reception of the echo signal transmitted by the GNSS satellite and reflected over the ground and over the aircraft structure. This echo signal is indicated by index "1" in this section.

Throughout the trajectory, and at time t, the echo signal from the ground is characterized by three multipath parameters: the relative code delay $\Delta\tau_1(t)$, the amplitude ratio $\alpha(t)$ and the relative phase shift $\Delta\theta_1(t)$. Assuming that the airport surface is modelled as an infinite and planar ground made of dry tar, and as explained in Section 5.4.1.1, the relative code delay and the relative phase are roughly constant throughout the trajectory. In the dynamic configuration, the phase shift at time t of both direct and echo signal "1" induced by the transmission channel are, respectively:

$$\begin{aligned}\theta_{0,L}(t) &= -2\pi\left(f_L + f_{D,0,L}(t)\right)\tau_0(t) + \phi_0(t)\\ \theta_{1,L}(t) &= -2\pi\left(f_L + f_{D,1,L}(t)\right)\tau_1(t) + \phi_1(t)\end{aligned} \qquad \text{Eq - 5-7}$$

where:

- $f_{D,0,L}$ and $f_{D,1,L}$ are the Doppler frequency shifts of the direct and echo signals, respectively,
- ϕ_0 and ϕ_1 are the phase shifts induced by the propagation channel and by the GNSS receiver antenna on the direct and echo signals, respectively.

The relative phase shift of echo signal "1" is:

$$\begin{aligned}\Delta\theta_1(t) &= \theta_{1,L}(t) - \theta_{0,L}(t)\\ &= -2\pi\left(f_L + f_{D,1,L}(t)\right)\tau_1(t) + 2\pi\left(f_L + f_{D,0,L}(t)\right)\tau_0(t) + \phi_1(t)\\ &\quad - \phi_0(t)\end{aligned} \qquad \text{Eq - 5-8}$$

$\Delta\theta_1(t)$ is roughly constant throughout the trajectory. There are three reasons for this:

- As explained in Section 5.4.1.1, the relative phase shift $\phi_1(t) - \phi_0(t)$ induced by the propagation channel and by the GNSS receiver antenna is roughly constant throughout the trajectory.
- It is demonstrated in Appendix A, Section A.2.1, that the Doppler frequency shifts of both direct and echo signals are roughly equal and constant throughout the trajectory.
- The relative code delay $\Delta\tau_1(t) = \tau_1(t) - \tau_0(t)$ is roughly constant throughout the trajectory.

For a planar and infinite ground made of dry tar, the multipath parameters of the echo signal from the ground are roughly constant at the scale of the airport throughout an uniform and rectilinear trajectory. It can be expected that the multipath ranging error induced by the airport surface and by the structure of the assessed aircraft is roughly constant throughout a rectilinear trajectory outside from any impact zone. This hypothesis is validated in Table 5-11

that shows the maximal variation of the error throughout a constant speed straight line trajectory on 30m long portion of segment 3 [FG].

	Parameter description	Parameter value
Satellite position	Satellite elevation angle El	20°
	Satellite azimuth angle Az_{sat}	0°
GNSS airborne antenna position	Aircraft azimuth angle on segment 3 Az_{air}	172.85°
	Between points F and G	F[320.0; 191.6; 5.88] G[290.2; 195.3; 5.88]
GNSS airborne antenna speed	Aircraft speed v	1m.s^{-1}
Maximal variation of $\varepsilon_{mp,L1C-L5}$ and $\varepsilon_{mp,E1-E5a}$		1.1×10^{-4}m

Table 5-11: Maximal variation of the dual-frequency raw code multipath ranging errors in the dynamic configuration over a 30 meter long portion

The maximal variations of the raw code multipath ranging error over the trajectory are few tenths of millimeters. Note that the multipath error induced by the ground and the aircraft structure is varying throughout curved trajectories. Indeed, in this case, the aircraft azimuth angle is changing throughout the trajectory, and this would result in the variation of the ranging bias $b_{AC+ground}$ throughout the trajectory. Note also that, as mentioned in Section 5.4.1, the phase and the amplitude of the echo signal from the ground may present relatively high variations over a segment in realistic airport since the airport surface is in reality frequently inhomogeneous and may contain lawn or metallic parts.

5.5.1.2. Multipath error model

The multipath parameters of the echo signal from the airport surface reflection throughout a uniform and rectilinear trajectory do not strongly depend on the aircraft speed on that trajectory. There are two reasons for this:

- Firstly, the amplitude ratio and the relative code delay do not depend on the aircraft dynamic and are the same in both static and dynamic configurations for a fixed satellite elevation angle and for a fixed aircraft azimuth angle.
- Secondly, the relative phase shifts throughout the trajectory do not strongly depend on the aircraft dynamic on a straight line trajectory. Indeed, it can be easily demonstrated that the relative phase shift in the dynamic configuration ($\Delta\theta_{1,dyn}$) and in the static configuration ($\Delta\theta_{1,static}$) throughout a given segment are related by:

$$\Delta\theta_{1,dyn}(t) = \Delta\theta_{1,static}(t) + 2\pi\left(f_{D,0,L}(t) - f_{D,1,L}(t)\right)\tau_0(t) - 2\pi f_{D,1,L}(t)\Delta\tau_1(t) \qquad \text{Eq - 5-9}$$

It is demonstrated in Appendix A, Section A.2.2, that both terms $2\pi\left(f_{D,0,L}(t) - f_{D,1,L}(t)\right)\tau_0(t)$ and $2\pi f_{D,1,L}(t)\Delta\tau_1(t)$ are low regarding $\Delta\theta_{1,static}(t)$. Hence, it can be considered that $\Delta\theta_{1,dyn}(t) \approx \Delta\theta_{1,static}(t)$ over a segment. To conclude, for fixed elevation and aircraft azimuth angles, both static and dynamic aircraft receive an echo signal from the ground characterized by roughly the same multipath parameters. Hence, the multipath ranging error induced by the airport surface and by the structure of the assessed aircraft is roughly constant throughout a trajectory outside from any impact zone, and is equal to:

$$\varepsilon_{mp}(t) = b_{AC+ground}(El, Az_{air}) \qquad \text{Eq - 5-10}$$

where:

- The bias values $b_{AC+ground}$ can be extracted from the static configuration. $b_{AC+ground}$ values are provided in Section 5.4.1.2 for the dual-frequency GPSL1C+GPSL5 and GalileoE1+GalileoE5a measurements.
- El and Az_{air} are the satellite elevation angle and the aircraft azimuth angle of the aircraft when the aircraft performs the straight line trajectory.

The next section investigates the evolution of the multipath ranging errors due to echo signals from the airport surface, from the structure of the assessed aircraft and from obstacles throughout a uniform and rectilinear trajectory. It also provides a model of such an error.

5.5.2. Error due to ground, aircraft structure and obstacle(s)

5.5.2.1. Dynamic impact zone

The multipath ranging errors due to the airport surface, the structure of the assessed aircraft and obstacle(s) in the dynamic configuration are analyzed in the dynamic impact zones of the airport. The goal of this section is to define the concept of dynamic impact zone.

In order to illustrate the concept of dynamic impact zone, let's consider the case where an aircraft performs a uniform and rectilinear trajectory along segment 3. Throughout the trajectory, the aircraft crosses the static impact zone related to one satellite. The portion of segment 3 in the static impact zone related to a satellite characterized by a satellite elevation angle of 20° and by a satellite azimuth angle of 0° is represented in Figure 5-20. More details about the determination of the location of the static impact zone are provided in Section 5.4.2.1.

Two cases can be distinguished:

- In case 1, the aircraft will park at the gate and arrives from segment 2. The multipath error due to the aircraft structure, the ground and the obstacles must be modelled between the instant the aircraft reaches point H until the end of the segment located in point C. In this case, the locations of both static and dynamic impact zones are identical.
- In case 2, the aircraft will leave the airport and arrives from segment 4. The multipath error must be modelled between point C until the moment the aircraft has left the static impact zone for 1s, that is to say when the aircraft reaches point I. Indeed, as underlined in Section 5.3, the DLL behaves as a first-order low pass filter characterized by a response time of roughly 1s, that is the inverse of the DLL bandwidth. Hence, along a trajectory, the multipath ranging errors are time-correlated. Denoting t_0 the time instant when the aircraft reaches point H, the multipath error at time t_0 depends on the multipath error in the interval $[t_0 - 1s, t_0]$. Hence, the multipath errors between points H and I may still be affected by the obstacle effects, even if the airborne antenna is physically outside the static impact zone. In this case, the portion of segment 3 located in the dynamic impact zone is [CI], while the portion of segment 3 located in the static impact zone is [CH].

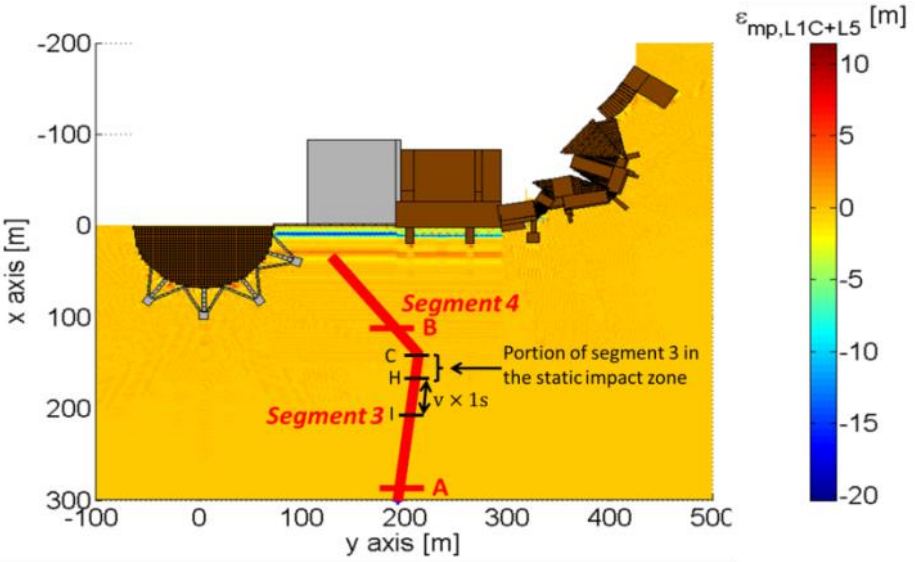

Figure 5-20: Static and dynamic impact zones

To conclude, along a uniform and rectilinear trajectory, the aircraft is said to be in the dynamic impact zone:

- from the instant the aircraft enters in the static impact zone, or from the beginning of the trajectory if the first point of the trajectory is in the static impact zone,
- until the instant the aircraft hast left the static impact zone for $1s$, or until the end of the trajectory if the last point of the trajectory is in the static impact zone.

5.5.2.2. Multipath parameters variation in the impact zone

The multipath parameters of the echo signals that have been scattered by at least one obstacle are analyzed in this section.

For this analysis, the aircraft performs a rectilinear and uniform trajectory along segment 4, that is to say along segment [CD] (dynamic configuration). The coordinates of C and D and the aircraft azimuth angle along [CD] are provided in Table 5-8. On segment 4, the aircraft is in the dynamic impact zone related to the GNSS satellite characterized by a satellite elevation angle of 20° and by a satellite azimuth angle of 0°. For the same reasons as those presented in Section 5.4.2.2, the multipath parameters evolution is illustrated in this section for a single echo signal, referred to as echo signal "2". Echo signal "2" is scattered from Hall C and received by the airborne antenna along segment 4.

Both relative amplitude and relative code delay parameters are not affected by the dynamic of the aircraft along segment 4. The evolutions of the relative amplitude and code delay of echo signal "2" have been plotted in Figure 5-13 over segment [CD] in the static configuration. Conclusions provided in Section 5.4.2.2 concerning the evolution of these parameters along a segment of the impact zone in the static configuration can be applied to the dynamic configuration.

The relative phase shift related to echo signal "2" over segment [CD] is different in the static and dynamic configurations because both direct signal and echo signal "2" are affected by a Doppler frequency in the dynamic configuration. For this reason, the relative phase shift is specifically investigated in this section. Figure 5-21 represents the evolution of the relative phase shift $\Delta\theta_2$ along the 1 meter long portion [DE] of segment 4 in the dynamic impact zone for different aircraft speeds. Simulation parameters are provided in Table 5-8.

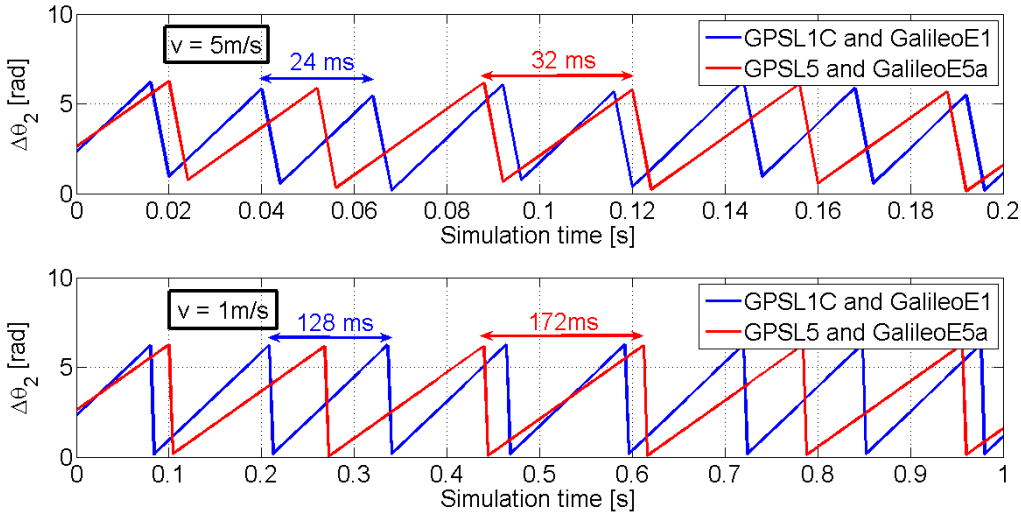

Figure 5-21: L1 and L5 dynamic relative phase shifts over segment [DE] on segment 4

From Section 5.4.2.2, the spatial period of the relative phase shifts in the static configuration depends on the central frequency of the assessed signal, the trajectory orientation in the scene and the satellite elevation and azimuth angles. In the dynamic configuration, the temporal period of the oscillations of the phase also depends on the aircraft speed. Figure 5-21 shows that the relative phase shift $\Delta\theta_2$ of echo signal "2" present fast variations along segment [DE] characterized by a temporal period that is roughly 24ms for an aircraft speed of $5\mathrm{m.s^{-1}}$ on the L1 frequency band. The temporal period is increased to roughly 128ms for an aircraft speed of $1\mathrm{m.s^{-1}}$. This is mainly due to the fact that, in the high speed scenario, the quasi-linear evolution of the relative code delay $\Delta\tau_2$ is fast compared to the evolution in the low aircraft speed scenario. The fast relative code delay evolution in the high speed scenario induces fast variations of the relative phase shift.

5.5.2.3. Multipath ranging error variation in the impact zone

The spatial variation of the multipath ranging errors in the impact zone is investigated in this section. The evolution of the dual frequency GPSL1C+GPSL5 multipath ranging errors over segment [ED] described in Table 5-8 are plotted in Figure 5-22.

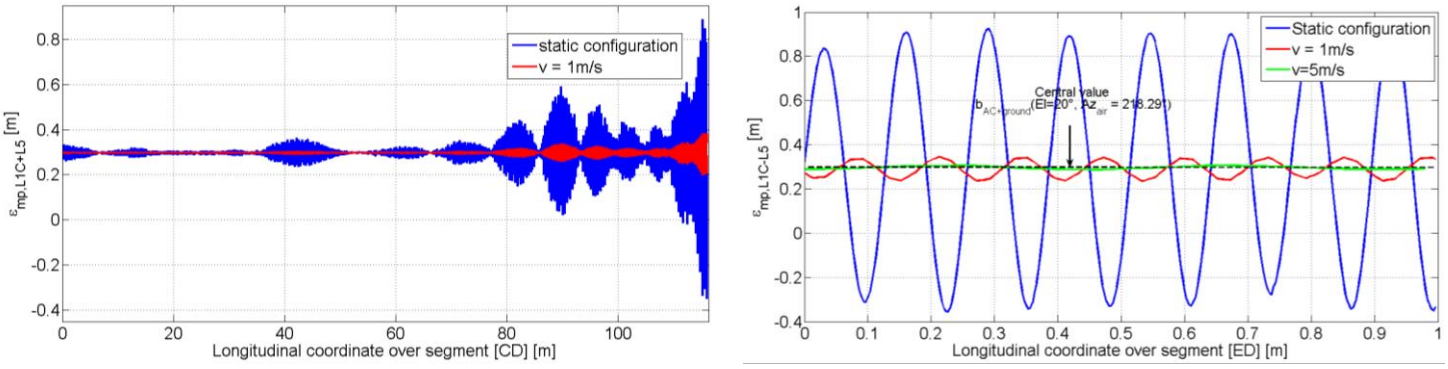

Figure 5-22: GPSL1C+GPSL5 multipath ranging errors over segment [CD] and [ED]

5.5.2.3.1. Analysis of the temporal period of the multipath errors

The time period of the errors along segment [ED] is discussed in this section. Two observations can be made from Sections 5.5.2.2 and 5.5.2.3:

- From Figure 5-22, the period of the oscillations of the error is roughly 140ms for an aircraft speed of 1m.s^{-1}. This roughly corresponds to the period of the relative phase shift on L1, as shown in Figure 5-21.
- From Figure 5-22, the period of the oscillations of the error is roughly 80ms for an aircraft speed of 5m.s^{-1}. However, the period of the oscillations of the error for an aircraft speed of 5m.s^{-1} is roughly much lower and is 30ms.

To conclude, in the dynamic configuration, the DLL induces a smoothing of the multipath errors compared to the static configuration. The DLL impacts the time period of the error along the segment, especially for relatively high aircraft speeds such as for 5m.s^{-1}. As a consequence, the time period of the error along the segment is higher than the time period of the relative phase shifts over the same segment.

5.5.2.3.2. Analysis of the amplitude of the multipath errors

The values of the errors along segment 4 are discussed in this section.

Firstly, from Figure 5-22, the error presents oscillations around a central value that corresponds to the multipath error that would have affected the pseudo-range measurement if the multipath sources were the airport surface and the structure of the assessed aircraft only. This error is denoted as $b(\text{El}, \text{Az}_{\text{air}})$ and is fully described in Section 5.5.1.2.

Secondly, from Figure 5-22, the amplitude ratio of the echo signals is not the only parameters influencing the multipath error amplitude over the trajectory. In the dynamic configuration, the DLL induces a smoothing of the multipath errors induced by the airport obstacles compared to the static configuration. The amplitude of the error oscillations tends to decrease when the aircraft speed increases. Hence the aircraft speed is the second parameter influencing the multipath error amplitude over the trajectory.

5.5.2.4. First-order Gauss-Markov process multipath error model

5.5.2.4.1. Methodology

It is established in Section 5.5.2.3 that the multipath ranging error in the dynamic configuration and in the impact zone can be decomposed as follows:

$$\varepsilon_{\text{mp,L1C+L5}}(t) = b_{\text{AC+ground}}(\text{El}, \text{Az}_{\text{air}}) + u_{\text{obs}}(t) \qquad \text{Eq - 5-11}$$

where:

- $b_{\text{AC+ground}}(\text{El}, \text{Az}_{\text{air}})$ is the multipath ranging error that would have been obtained if the ground and the aircraft structure were the only multipath sources present at that given location. This error is induced by the ground first-order reflections. As explained in Section 5.4.2.4.1, $b_{\text{AC+ground}}(\text{El}, \text{Az}_{\text{air}})$ is considered as a deterministic bias in the thesis.
- $u_{\text{obs}}(t)$ is a zero-mean time-dependent error that represents the oscillation of $\varepsilon_{\text{mp,L1C+L5}}(t)$ around $b_{\text{AC+ground}}(\text{El}, \text{Az}_{\text{air}})$. u_{obs} is induced by obstacles first and second-order interactions. This oscillation term depends on:
  - The satellite position (the satellite elevation El and azimuth Az_{sat} angles).
  - The 3D model of the airport environment.
  - The GNSS receiver antenna radiation pattern and the GNSS receiver settings.
  - The true trajectory location and orientation.
  - The aircraft speed over the trajectory v.

Determining the component $u_{\text{obs}}(t)$ in the impact zone in a deterministic way is complex as it would require knowing the trajectory location and orientation of the airborne antenna in the

impact zone with a high level of precision (centimeter precision level since the spatial period of the multipath error is of the order of 10 centimeters). It is thus proposed to provide a stochastic model of the error component $u_{obs}(t)$ in the impact zone that is independent of the true trajectory of the GNSS receiver antenna in the impact zone. The true trajectory is modelled by its own statistical distribution. The parameters of the stochastic ranging error model are obtained by doing Monte Carlo simulations. The methodology used to obtain the stochastic error models is sketched in Figure 5-23.

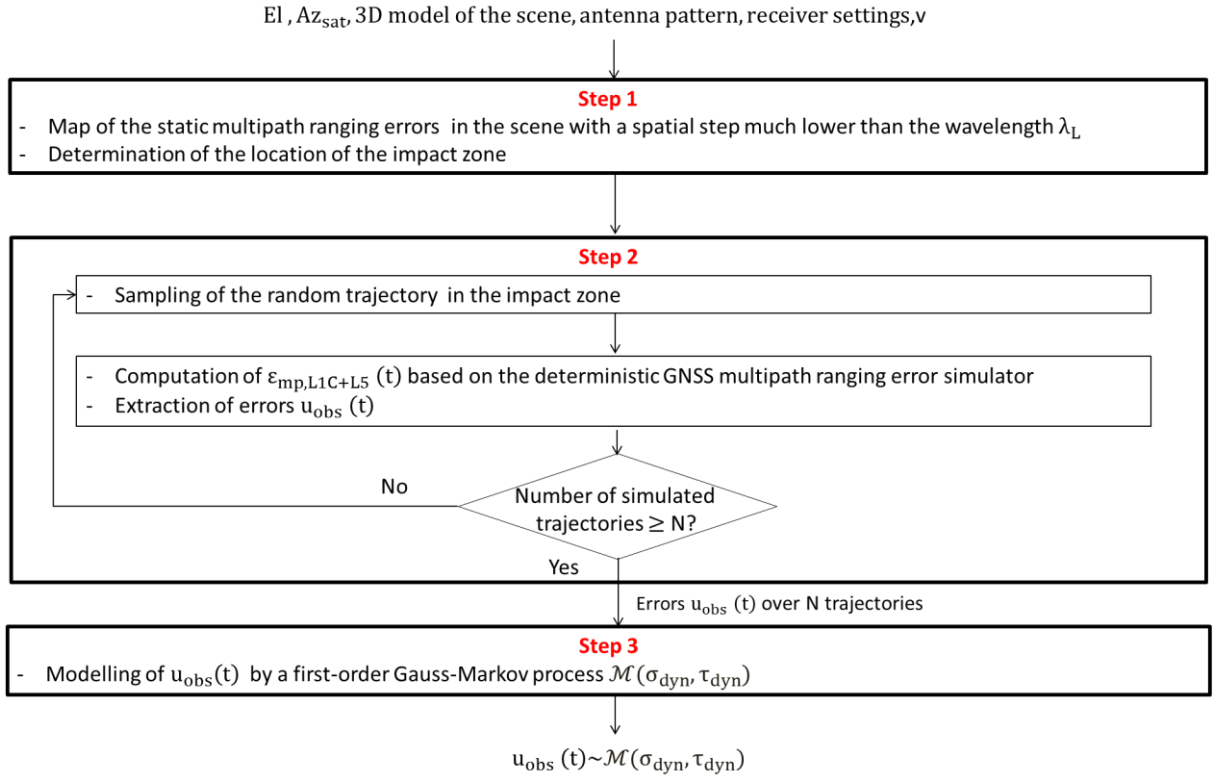

Figure 5-23: Methodology to derive the multipath error model in the impact zone – dynamic configuration

In order to illustrate this methodology, the dual-frequency GPSL1C+GPSL5 error model of $u_{obs}(t)$ is derived in an impact zone on segment 4. In this simulation, it is assumed that the aircraft performs a uniform and rectilinear trajectory over the whole segment 4. The aircraft comes from segment 3 and will park at the gate. The aircraft speed is $v = 1\text{m.s}^{-1}$. The satellite elevation and azimuth angles are $El = 20°$ and $Az_{sat} = 0°$, respectively.

Step 1

Figure 5-14 shows that the amplitude of the oscillations of the multipath ranging error in steady state around the central value is above 1cm on the entire segment 4. Hence, the entire segment 4 is included in the dynamic impact zone.

Step 2

In order to estimate the Power Spectral Density (PSD) of the components u_{obs} along a segment 4 and in the impact zone, a Monte Carlo simulation is performed. For each Monte Carlo iteration, an aircraft trajectory in the impact zone along segment 4 is randomly generated. The probability distribution attached to this variable is detailed as follows. The coordinates of the entrance point in the impact zone are uniformly chosen on segment $[C_1C_2]$ represented in Figure 5-16. The trajectory orientation is randomly selected in such a way that

the final point of the trajectory is uniformly distributed on segment $[D_1D_2]$ represented in Figure 5-16. The multipath ranging errors are then computed along each simulated trajectory, and the errors $u_{obs}(t)$ are extracted from the computed multipath ranging errors along each trajectory. Since the multipath errors in the dynamic impact zone depend on the multipath errors affecting the pseudo-range measurements up to 1s before entering in the impact zone, the multipath errors are also computed along the trajectory up to 1s before the entrance in the impact zone. Note finally that, in the simulations, only N=5 trajectories are randomly chosen in the impact zone. Indeed, Appendix B, Section B.4, shows that the PSD functions of the components u_{obs} over two distinct trajectories in the impact zone are almost the same. For this reason, it is acceptable to develop the error model of the component u_{obs} based on a limited number of Monte Carlo iterations along segment 4.

An important remark is that the error model along segment 4 is developed by simulating multipath errors along the whole segment 4, and by processing and over-bounding the PSD of the simulated errors along the whole segment 4. A single error model is developed along segment 4. However, the error amplitude along segment 4 is not constant, as underlined in Figure 5-22. Hence, it is recommended as future work:

- to sub-divide the trajectory into parts where the error amplitude is roughly constant and to develop a time-varying (non-stationary) error model throughout the trajectory.
- or to determine the trajectory part where the error amplitude is maximal and to estimate the model parameters on this part. Note that this suggestion is more conservative than the suggestion stated above, but is easier to manipulate since only one stationary error model is developed for the trajectory.

Step 3

The multipath ranging error model related to the zero-mean component $u_{obs}(t)$ proposed in this document is intended to be included within GNSS integrity monitoring algorithms for airport operations. For this reason, the priority is to model the estimated PSD of $u_{obs}(t)$ over segment 4 by the PSD of a stochastic process that over-bounds the estimated PSD of $u_{obs}(t)$. In addition, it has been chosen to over-bound the estimated PSD by the PSD of a stationary zero-mean first-order Gauss-Markov process $\mathcal{M}(\tau_{dyn}, \sigma_{dyn})$ characterized by a correlation time τ_{dyn} and by a standard deviation σ_{dyn}. Indeed, as underlined in Section 5.4.2.4.1, the stochastic measurement error models used in the ABAS integrity monitoring algorithms are Gaussian models. Figure 5-24 illustrates the estimated PSD of the errors $u_{obs}(t)$ along the segment 4 and the PSD of the Gauss-Markov process for different values of τ_{dyn}, σ_{dyn}. It is clearly shown in this figure that the estimated PSD cannot be assimilated to the first-order Gauss-Markov PSD shape. However, the first-order Gauss-Markov is retained for the application since judicious choices of the parameters $(\tau_{dyn}, \sigma_{dyn})$ enable the Gauss-Markov PSD to over-bound the estimated PSD. Combinations of multiple first-order Gauss-Markov processes or second-order low-pass filters are sometimes used to obtain slightly better modelling of correlated processes [Xing, 2010][Kubrak, 2008] at the expense of increasing the complexity of the model. The feasibility to over-bound the estimated PSD by a PSD that best fits the estimated PSD and to design integrity monitoring algorithms that use non-Gaussian error models as expected measurement error models is not discussed in this thesis and remains as future work. In this Ph.D. thesis, it is this proposed to model the multipath ranging error in the dynamic configuration and in the impact zone as follows:

$$\varepsilon_{mp,L1C+L5}(t) = b_{AC+ground}(El, Az_{air}) + u_{obs}(t) \qquad \text{Eq - 5-12}$$

where $u_{obs}(t)$ is a zero-mean correlated error that is modelled as a stationary first-order Gauss-Markov process $\mathcal{M}(\tau_{dyn}, \sigma_{dyn})$.

The methodology used to determine the parameters τ_{dyn}, σ_{dyn} is presented as follows. The normalized PSD of the first-order Gauss-Markov process is provided below:

$$PSD_{GM}(f) = \frac{2{\sigma_{dyn}}^2}{\tau_{dyn}\left((2\pi f)^2 + \frac{1}{{\tau_{dyn}}^2}\right)} \quad \text{Eq - 5-13}$$

For any given value of τ_{dyn}, it is possible to find the minimal value of σ_{dyn} for which the PSD of the Gauss-Markov process over-bounds the estimated PSD. Similarly, for any given value of σ_{dyn}, it is possible to find the minimal value of τ_{dyn} for which the PSD of the Gauss-Markov process over-bounds the estimated PSD. Hence, there is an infinite number of pairs $(\tau_{dyn}, \sigma_{dyn})$ that lead to over-bound the estimated PSD. In this thesis, it has been chosen to set τ_{dyn} to a fixed value and to compute the minimal value of σ_{dyn} for which the PSD of the Gauss-Markov process over-bounds the estimated PSD. Note that this is a first approach. An advanced methodology that is recommended as future work consists in determining the pair $(\tau_{dyn,optim}, \sigma_{dyn,optim})$ that meets the two following criteria:

- The PSD of the first-order Gauss-Markov process $\mathcal{M}(\tau_{dyn,optim}, \sigma_{dyn,optim})$ over-bounds the estimated PSD of $u_{obs}(t)$,
- The pair $\mathcal{M}(\tau_{dyn,optim}, \sigma_{dyn,optim})$ leads to minimize the effects of the multipath ranging error $u_{obs}(t)$ modelled as a Gauss-Markov process on the covariance of the horizontal position error. The impact of a stochastic error modelled as a first-order Gauss-Markov process $\mathcal{M}(\tau_{dyn}, \sigma_{dyn})$ on the covariance of the horizontal position error is analyzed in Chapter 7.

Let's detail the methodology used to compute the parameter σ_{dyn} when the parameter τ_{dyn} is fixed. Figure 5-24, left hand side, illustrates the estimated PSD over one of the simulated trajectory over segment 4, namely trajectory 1. It also illustrates the Gauss-Markov process PSD for different values of σ_{dyn} and for $\tau_{dyn} = 10\text{ms}$. It can be observed in this figure that the PSD of the Gauss-Markov process under-estimates the estimated PSD when $\sigma_{dyn} < 41.5\text{cm}$. The PSD of the Gauss-Markov process over-estimates the estimated PSD when $\sigma_{dyn} > 41.5\text{cm}$. σ_{dyn} is chosen to be the lowest standard deviation of the Gauss-Markov process that over-bounds the estimated PSD of the error along all simulated trajectories in the impact zone. In the example treated in this section, σ_{dyn} is 41.5cm for the trajectory 1, and is the highest standard deviation obtained over all simulated trajectories.

Let's detail the methodology used to choose the value of τ_{dyn}. Figure 5-24, right hand side, illustrates the PSD of the Gauss-Markov process for different values of $\tau_{dyn}(1\text{ms}, 10\text{ms}, 100\text{ms})$. For each value of τ_{dyn}, σ_{dyn} has been calculated *via* the methodology illustrated in Figure 5-24, left hand side and is called optimal σ_{dyn}.

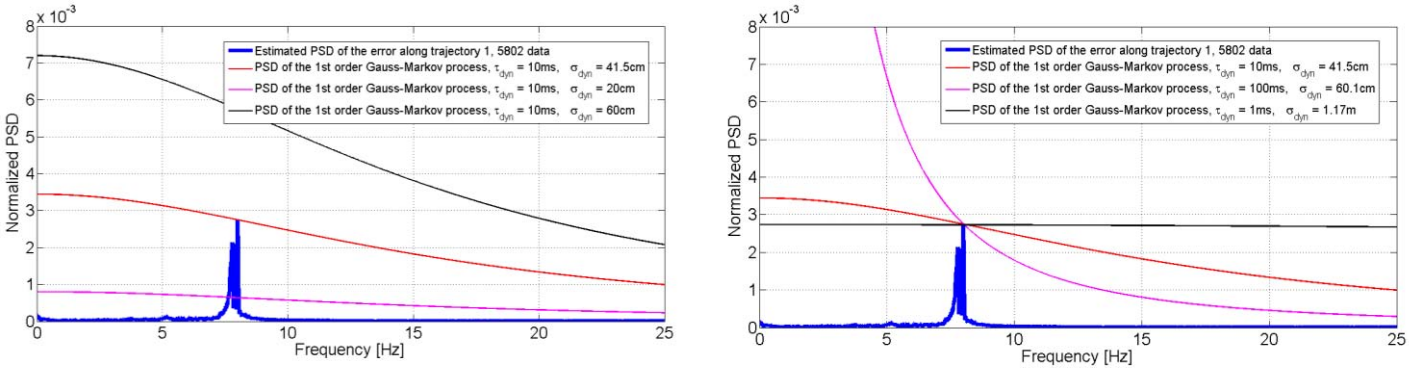

Figure 5-24 : First-order Gauss-Markov process PSDs and estimated PSD of u_{obs} in the impact zone on segment

High values of τ_{dyn} ($\tau_{dyn} = 100\text{ms}$) concentrate the power of the Gauss-Markov process in the low frequencies. The value of the optimal σ_{dyn} for $\tau_{dyn} = 100\text{ms}$ is roughly 60cm, which is larger than the value of σ_{dyn} obtained for $\tau_{dyn} = 10\text{ms}$, that is 41.5cm. The analysis proposed in Section 7.1 on the covariance of the horizontal position error shows that this covariance is proportional to both τ_{dyn} and σ_{dyn} parameters. The choice of $\tau_{dyn} = 100\text{ms}$ leads to inflate both correlation time and standard deviation compared to the choice $\tau_{dyn} = 10\text{ms}$. Since it is suitable to adopt a value of τ_{dyn} that reasonably inflates the covariance of the position error, the choice of $\tau_{dyn} = 100\text{ms}$ is discarded for the application.

A low value of τ_{dyn} ($\tau_{dyn} = 1\text{ms}$) leads to over-bound the high-frequency components. The optimal value of σ_{dyn} for $\tau_{dyn} = 1\text{ms}$ is roughly 1.2m, which is larger than the value of σ_{dyn} obtained for $\tau_{dyn} = 10\text{ms}$, that is 41.5cm. The analysis proposed in Section 7.1 on the covariance of the horizontal position error shows that this covariance is very sensitive to the value of σ_{dyn}. As an illustration, it is shown that when σ_{dyn} is increased of roughly 50cm, the variance of the position error in both North and East directions is increased of a few centimeters. However, the error position variances only vary by a few millimeters when τ_{dyn} vary in the time interval $[1\text{ms}, 100\text{ms}]$. The choice of $\tau_{dyn} = 1\text{ms}$ is discarded for the application. It is chosen to adopt the value of τ_{dyn} that minimizes the value of the optimal σ_{dyn}, that is to say 10ms.

In order to show that $\tau_{dyn} = 10\text{ms}$ is a reasonable choice for other simulation scenarios, the optimal σ_{dyn} has been calculated for different values of τ_{dyn} $(1\text{ms}, 10\text{ms}, 100\text{ms})$ under different simulation scenarios described in Table 5-12.

For the same reasons as those exposed for the simulation scenario 1 ($v = 1\text{m/s}$,$El = 20°$, $Az_{sat} = 0°$), $\tau_{dyn} = 10\text{ms}$ is a reasonable choice for other simulation scenarios and is adopted in the rest of the thesis.

	Scenario 1 $\mathbf{v = 1m/s}$ $\mathbf{El = 20°}$ $\mathbf{Az_{sat} = 0°}$	**Scenario 2** $\mathbf{v = 5m/s}$ $\mathbf{El = 20°}$ $\mathbf{Az_{sat} = 0°}$	**Scenario 3** $\mathbf{v = 1m/s}$ $\mathbf{El = 70°}$ $\mathbf{Az_{sat} = 0°}$	**Scenario 4** $\mathbf{v = 1m/s}$ $\mathbf{El = 20°}$ $\mathbf{Az_{sat} = 20°}$
$\mathbf{\tau_{dyn} = 1ms}$	1.17m	40.3cm	83.6cm	1.31m
$\mathbf{\tau_{dyn} = 10ms}$	41.5cm	15.2cm	28cm	45.9cm
$\mathbf{\tau_{dyn} = 100ms}$	60.1cm	27.2cm	41.2cm	63.6cm

Table 5-12 : Optimal σ_{dyn} for different simulation scenarios

5.5.2.4.2. Simulation results

The sensitivity of the first-order Gauss-Markov process parameter σ_{dyn} to the aircraft speed v, to the satellite elevation angle El, and to the satellite azimuth angle Az_{sat} is analyzed in this section.

The simulation results presented in this paragraph have been obtained by simulating the GPSL1C+GPSL5 multipath ranging errors u_{obs} in the impact zone. However, it is shown in Appendix B, Section B.3, that the modulation difference between GPSL1C and GalileoE1 signals does not significantly impact the values of the multipath ranging errors in the impact zone. Hence the simulation results can be extended to the GalileoE1+GalileoE5a case.

The evolution of σ_{dyn} as a function of v in the impact zones located along segments 3 and 4 is represented in Figure 5-25.

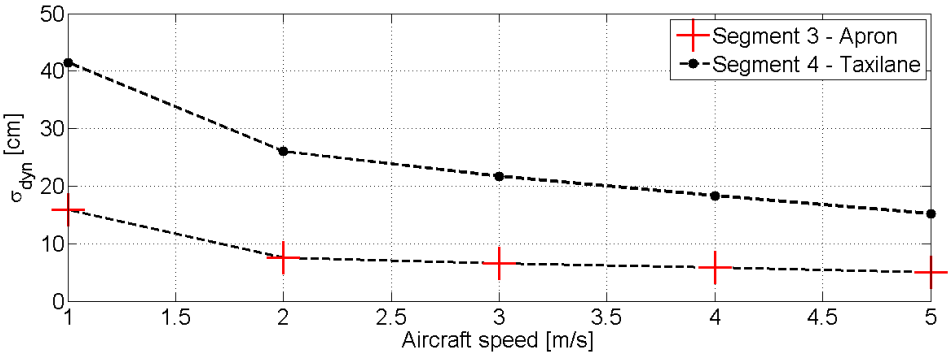

Figure 5-25: σ_{dyn} as a function of the aircraft speed, $El = 20°$, $Az_{sat} = 0°$

σ_{dyn} tends to decrease when v increases. Indeed, the aircraft speed induces a smoothing of the multipath ranging error along the trajectory. This phenomenon is underlined in Section 5.5.2.3. The characteristics of the obstacles inducing echo signals in the impact zone and the relative location of the impact zone with respect to these obstacles also determine the amplitude of the echo signals. Points located in the impact zone of segment 3 are further away from the large metallic Hall C facade than points located in the impact zone of segment 4. Hence, at fixed aircraft speed, the values of σ_{dyn} are lower for the impact zone along segment 3 than for the impact zone along segment 4.

The evolution of σ_{dyn} as a function of El in the impact zones located along segments 3 and 4 is represented in Figure 5-26.

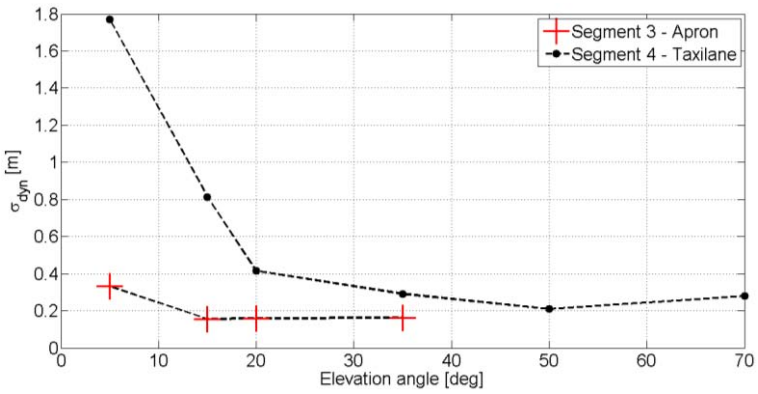

Figure 5-26: σ_{dyn} as a function of the satellite elevation angle, $v = 1m/s$, $Az_{sat} = 0°$

For segment 3, σ_{static} decreases with the elevation angle when the elevation angle is between 5° and 20°. For elevation angles equal or higher than 20°, σ_{static} is roughly constant and is relatively low (centimeter level) regardless the satellite elevation angle. For segment 4, σ_{static} tends to decrease when El increases and may reach few meters at low elevation angles. An interpretation of this observation is detailed in Section 5.4.2.4.2.

The evolution of σ_{dyn} as a function of Az_{sat} in the impact zones located along segments 3 and 4 are represented in Figure 5-27.

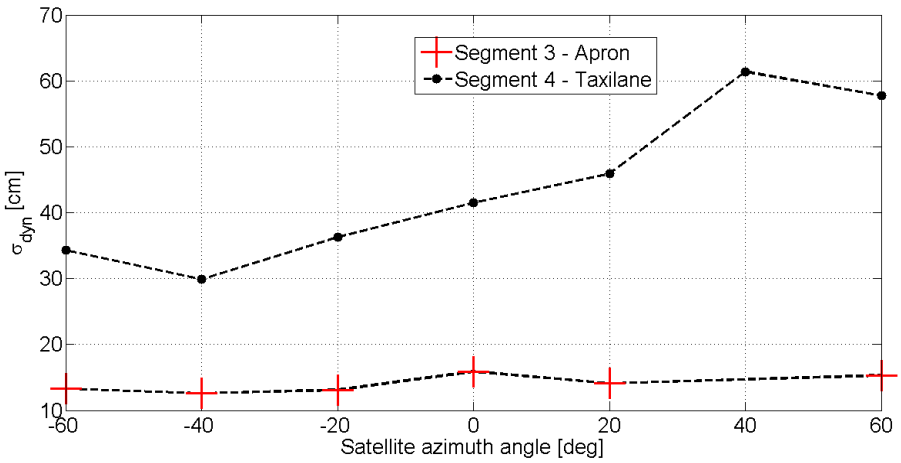

Figure 5-27: σ_{dyn} as a function of the satellite azimuth angle, $v = 1m/s$, $El = 20°$

For segment 3, σ_{static} is low (centimeter level) roughly constant as a function of Az_{sat}. For segment 4, σ_{static} is of the order of a few decimeters and varies with Az_{sat} increases. An interpretation of this observation is detailed in Section 5.4.2.4.2.

5.6. Conclusions

This chapter has proposed multipath ranging error models adapted to surface operations. Three multipath sources are considered: the structure of the assessed A319 aircraft, the airport surface modelled as an infinite and planar ground made of dry tar, and fixed airport obstacles that are the airport buildings and the airport gates.

The model parameter values proposed in this chapter have been obtained using a simple 3D model of Toulouse Blagnac airport, France. The types of simplification that have been done when modelling the 3D model of this airport have been exposed. The validity of two simplifications for multipath error models derivation has been discussed and demonstrated. Firstly, details characterized by a size below the wavelength do not have to be represented. Secondly, sub-meter level concrete details on concrete walls such as concrete overhangs and recesses on are not represented. The analysis of the validity of other simplifications for the application remains as future work. Even if parameter values provided in this chapter are specific to an airport and to an antenna model, the way to model the multipath error is intended to be used in other airports and for other antenna models.

In the static configuration, the multipath ranging error induced by the airport surface, the structure of the assessed aircraft and the obstacle(s) is modelled as the sum of:

- a deterministic bias $b_{AC+ground}$ induced by the ground first-order reflections and that depends on the antenna height, on the elevation angle, and on the relative aircraft azimuth angle. This bias reaches several decimeters at low elevation angles. The values of the biases $b_{AC+ground}$ provided in the thesis are independent of the 3D model of the airport buildings and gates.
- a bias b_{obs} induced by obstacles first and second-order interactions. Due to the uncertainties in the aircraft position in the impact zone, $b_{obs}$is considered as a random variable. b_{obs} has been over-bounded by a zero-mean Gaussian distribution characterized by a standard deviation σ_{static}. σ_{static} depends on the elevation angle, on the satellite azimuth angle, and on the position and characteristics of the obstacles inducing echo signals in the impact zone. Highest values of σ_{static} are obtained at low elevation angles and closed to the airport obstacles. As an illustration, the worth case values of σ_{static} along the LVP procedure of Toulouse airport are obtained along the taxi lane and are a few meters.

In the dynamic configuration, only uniform and rectilinear trajectories are considered. The multipath ranging error induced by the airport surface, the structure of the assessed aircraft and the obstacle(s) in a dynamic impact zone is modelled as the sum of:

- a stationary bias $b_{AC+ground}$,
- a zero-mean oscillation term $u_{obs}(t)$. Due to the uncertainties in the aircraft trajectory around the procedure path in the impact zone, u_{obs} is considered as a stochastic correlated process. The correlated process u_{obs} has been over-bounded by a stationary first-order Gauss-Markov process over the trajectory. The correlation time τ_{dyn} of this Markov process has been set to a fixed value of 10ms. This choice has been justified and illustrated by simulations. The standard deviation σ_{dyn} of this process depends on the elevation angle, on the satellite azimuth angle, on the position and characteristics of the obstacles inducing echo signals in the impact zone, and on the aircraft speed. Highest values of are obtained at low elevation angle, close to the airport buildings, and at low aircraft speed. As an illustration, the worth case values of σ_{dyn} along the LVP procedure of Toulouse airport are obtained along the taxi lane and are a few meters. It is also recommended as future work to validate the developed multipath ranging error models by real data.

CHAPTER 6

GNSS-based positioning algorithm

As explained in Chapter 1, there is a need to develop a GNSS-based navigation system capable to support the required navigation performance relating to the guidance function for use during taxi operations under low visibility conditions. The first step in the design of this navigation system is the development of the GNSS-based positioning algorithm capable of estimating the GNSS receiver antenna position with an accuracy that is compliant with the navigation system accuracy performance requirements. From Chapter 3, two GNSS constellations are considered in this thesis: GPS and Galileo. GPS and Galileo satellites broadcast both L1 (GPSL1C and GalileoE1) and L5 (GPSL5 and GalileoE5a) signals.

This chapter describes the architecture of a GNSS-based positioning algorithm suitable for the application. The reasons behind this choice of architecture are explained in Section 6.1. The algorithm architecture is further detailed in Section 6.2. The accuracy performance of the algorithm will be quantified in Chapter 7.

6.1. Choice of the positioning algorithm architecture

6.1.1. Review of Position Velocity Time estimation techniques

Position Velocity Time (PVT) estimation techniques are classified as follows:

- **"Stand alone" PVT techniques** use a set of GNSS pseudo-range measurements and possibly initial estimates of the user position and clock. The GNSS measurements are not corrected by any differential corrections and are not integrated with other information sources. However, the initial user position and clock may be estimated by means of external sensor(s). The Least-Squares (LS) and Weight Least-Squares (WLS) solutions [Kaplan *et al*., 2006] use GNSS measurements at one snapshot in time to estimate the PVT solution. It is also possible to incorporate the past GNSS measurements into the position estimator by the means of algorithms such as the Kalman filter. This algorithm will be further detailed in the second part of this chapter. Since some applications require high navigation performance in terms of accuracy, integrity, continuity and availability, two classes of augmented PVT techniques have been developed and are listed below.
- **Differential PVT techniques** improve the positioning performance using one or more reference stations at known locations, each equipped with at least one GNSS receiver. The reference station(s) provides GNSS pseudo-range corrections to the user via a data link. GBAS and SBAS are used in civil aviation applications to bring differential corrections. Both systems are briefly presented in Section 3.3.1.

- **PVT techniques based on the integration of GNSS with other sensors** or information sources may be used to define a system whose performance exceeds that of the individual sensors [Kaplan *et al*., 2006]. The method most widely used for this integration is the Kalman filter.

Among the PVT estimation techniques listed in the previous paragraph, differential PVT techniques are not considered in this project since the use of GBAS and SBAS are out of the scope of this thesis, as explained in Section 3.3.2.

Concerning the "stand alone" PVT techniques, [Néri, 2011] shows that, under the following conditions:

- A double constellation GPS (24 satellites constellation) and Galileo (27 satellites constellation) is considered. Iono-free GPSL1C/A+GPSL5 and GalileoE1+GalileoE5a smoothed code pseudo-range measurements are used to estimate the user position. The code carrier smoothing technique is implemented as presented in [RTCA, 2009] with a smoothing time constant of $T_{smooth} = 100s$.
- The nominal GNSS pseudo range measurement errors are induced by the inaccurate satellite clock correction and ephemeris information, by the residual ionosphere and troposphere delay, by the receiver thermal noise and by the multipath. Except for multipath, nominal error models related to these error sources are developed in Section 3.2.1. The nominal multipath ranging error model standardized for in-flight operations [RTCA, 2009] is used.
- The user position is estimated by means of a combined GPS/Galileo WLS algorithm fully described in [Néri, 2011]. The position solution is computed during 270 seconds approaches, over around three days, with a time step of 10 minutes, and over 16 different airport locations around the world.

the worst case standard deviation of the vertical NSE under nominal conditions, computed over each 270 second approach, is 1.2m. It is assumed that the standard deviation of the horizontal NSE will have the same order of magnitude than the standard deviation of the vertical NSE.

From Table 2-4, the maximal acceptable standard deviation of the horizontal NSE required to meet the accuracy requirement is 95cm for the *taxi on taxiway* phase, 50cm for the *taxi on apron taxiway* phase and 25cm for the *taxi on taxi lane* phase.

By comparing the order of magnitude of the standard deviation of the horizontal NSE obtained with WLS in the dual-frequency double constellation mode to the maximal acceptable standard deviation needed to meet the accuracy requirement, it is concluded that an augmented PVT technique must be used to reach the navigation performance requirements. A PVT technique based on the integration of GNSS with other sensors and other information sources is thus considered in the rest of this thesis. In the next section, a review of possible navigation sensors and signals of opportunity that could be integrated with GNSS is provided.

6.1.2. Review of navigation sensors/signals of opportunity

Inertial sensors are good candidates to be integrated with GNSS due to the complementary of their characteristics with respect to GNSS. GNSS can be used to compensate for slow inertial position drifts. In return, inertial sensors may ensure coasting during GNSS outage due to intentional or non-intentional interference for example. In addition, inertial sensors have been used on commercial aircraft for several decades [Diesel, 1995] and their error models are fully described in the literature [Kayton *et al*., 1996]. Inertial Reference System (IRS) is thus considered to be a suitable technology for the application.

Other navigation sensors and signals of opportunity which may be integrated with GNSS and inertial sensors are listed below:

- Distance Measuring Equipment (DME)
- Instrument Landing System (ILS)
- Secondary Surveillance Radar (SSR)
- Wheel Speed Sensor (WSS) and odometer
- Wi-Fi or Worldwide Interoperability for Microwave Access (WiMAX)
- Ultra Wide Band (UWB)
- Light Detection and Ranging (LIDAR)
- Radio Frequency IDentification (RFID)
- Ultrasound sensors and infrared sensors
- Video camera

The main drawbacks and advantages related to each technology are indicated in Appendix C. By means of the elements provided in Appendix C concerning each technology, the navigation sensors and signals of opportunity can be classified into three categories:

- Technologies which are not sufficiently mature to have a known level of accuracy performance or technologies not sufficiently accurate regarding the application. DME, SSR, RFID, ultrasound and infrared sensors and video camera are included in this category. Since this project does not aim to derive the performance of navigation sensors, but rather to investigate the impact of multipath on multi-sensors positioning algorithms, these navigation sensors are not considered in this thesis. They are thus not yet suitable technologies.
- Technologies not well-adapted to airport navigation since they are sensitive to topologic changes, they are adapted to small scale environments (indoor applications), they cannot be used in the entire maneuvering and apron area and/or they require equipment installation over the airport surface. ILS, Wi-Fi and WiMAX and UWB are included in this category and are not suitable technologies.
- Technologies that use external and expensive database to be fully operational, or sensors that are installed onboard but their use increases the complexity of the positioning algorithm. LIDAR and WSS/odometers are included in this category. These technologies are envisaged to be part of the PVT solution if the PVT solution based on the coupling GNSS/inertial sensors is not enough accurate to meet the accuracy requirement.

To conclude, the proposed PVT solution is a GNSS/IRS coupling architecture. Three other sensors are identified to potentially enhance the performance of the GNSS/IRS solution in terms of accuracy: WSS, odometers and LIDAR.

6.1.3. Review of GNSS/IRS coupling techniques

This section presents the different existing GNSS/IRS coupling techniques and selects the coupling techniques used in the PVT solution considered in this thesis. Three main coupling architectures can be considered:

- Ultra-tight coupling techniques wherein, for example, IRS estimates are used to aid the GPS receiver delay and phase lock loops [Li, 2009].
- Tight coupling techniques that use GNSS pseudo-range measurements to estimate the slow time varying growth of the inertial position error vector by means of a Kalman filter [Diesel, 1995].
- Loose coupling techniques where GNSS position and velocity are used to estimate the IRS position errors [Kubrak, 2008].

Ultra-tight techniques generally require complex modifications in the signal processing blocks of the GNSS receiver. In the framework of this project, it is preferred to propose a positioning algorithm that does not require modifying the core of the GNSS receiver and the tracking loops. For this reason, ultra-tight techniques are not retained for the application.

Conversely, loose coupling techniques are simple to implement but present several drawbacks. Firstly, they cannot be used when the number of visible satellites falls under five satellites since the GNSS estimated position velocity and time are used as measurements in the fusion Kalman filter. However, this does not represent a significant drawback for the application since two separate satellite constellations are considered and airport environments are not obstructive environments. Secondly, they generally present suboptimal performance in terms of accuracy compared to the tight-coupling techniques [Farrell *et al*., 1999] [Kubrak, 2008]. Among the reasons that explain this sub-optimality, the GPS position error components are correlated to each other. The cross covariance must be implemented in the Kalman filter but are generally unknown by the user [Farrell *et al*., 1999]. This may lead to relatively poor accuracy performance of the loose coupling techniques.

Tight coupling techniques are commonly used in commercial aircraft [Diesel, 1995]. They generally present better performance than loose coupling techniques but at the expense of a higher complexity. Tight coupling techniques are selected for the application. There is no limitation on the number of satellites in visibility with this coupling strategy. Nonlinear pseudo-range information are used as measurements.

In addition, tight coupling algorithms can operate in open-loop or closed-loop modes. In the open-loop mode, the INS operates independently of the GNSS measurements. Hence, there is no risk of propagating error modes from one senor to the other. The main drawback of the open-loop mode is that no compensation or calibration of the inertial sensor or altitude error sources are performed by a GNSS feedback. Hence, due to the inertial drift, the inertial mechanization model implemented in the Kalman filter can suffer from non-linearities during long flights, and the filter may potentially diverge.
In the closed-loop mode, a feedback loop is used to correct the inertial sensor outputs using the error estimates obtained from the Kalman filter. The main advantage of the close-loop mode is that the inertial position, attitude angles and velocity errors do not grow rapidly in the time domain, as it can be observed with the open-loop mode. The linearization of the inertial error model is more accurate when the inertial position, velocity and attitude angles are small. The main disadvantage is that, in case of large GNSS measurement errors, the calibration of the inertial sensors by the GNSS feedback in the closed-loop scheme is degraded until the end of the flight. There is thus a risk of propagating error modes from one sensor to the other.
In the application considered in the thesis, the inertial errors will remain relatively small during the operation. Indeed, the exposure time of the taxi operations is only few minutes, and the inertial sensors used to estimate the aircraft position have good performance. As an illustration, the horizontal inertial position errors after a taxi operation with the inertial sensors considered in the thesis will be several decimeters. Hence, even in the open-loop mode, the linearity of the inertial error model implemented in the Kalman filter will be maintained for the application. For this reason, a tight-coupling algorithm that operates in open-loop mode can be considered in this thesis.

6.1.4. Synthesis

In this thesis, a GNSS/IRS tight coupling technique is considered. It operates in the open-loop mode. The GNSS pseudo-range measurements are used to estimate the slow varying growing inertial position error vector. This position error vector estimate is performed by means of a

Kalman filter. The inertial position estimate is then corrected by the inertial position error vector estimate, and this corrected position estimate is called "GNSS/IRS position estimate".

6.2. GNSS/IRS/DEM position error computation

It is shown in Section 6.1.3 that the proposed GNSS-based positioning technique is a GNSS/IRS tight coupling technique. In order to investigate the performance of such an algorithm, a Matlab software aiming to compute the positioning error vector at the output the coupling algorithm has been implemented. The general structure of this software is provided in Figure 6-1.

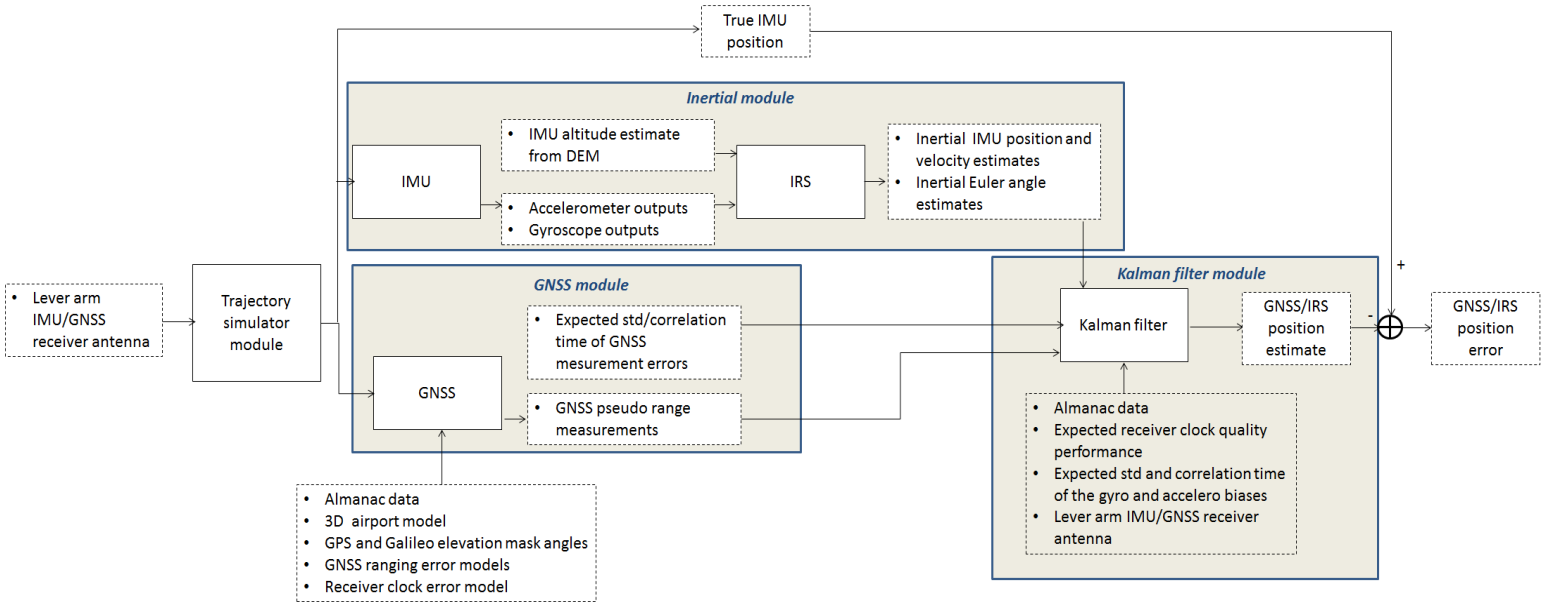

Figure 6-1: Architecture of the GNSS/IRS/DEM positioning error simulator

As depicted in the Figure 6-1, five main modules are implemented in the software, namely the trajectory simulator module, the GNSS module, the inertial module, the Digital Elevation Map (DEM) module and the Kalman filter module. A brief description of each module is provided below.

6.2.1. Trajectory simulator module

A trajectory simulator is implemented in order to compute:

- The true Inertial Measurement Unit (IMU) position and the true IMU velocity vector,
- The true aircraft attitude angles,
- The true GNSS receiver antenna position,

along a specific taxi operation in a given airport. The true IMU position and velocity vectors are firstly computed in the North East Down (NED) coordinate frame centered on the first point of the trajectory and presented in Appendix F. Since the airport surface is considered as a horizontal plane (see Section 5.1.2.2.2), both pitch and roll angles are considered as zero along the operation. Raised cosine functions are used to represent the continuous evolution of the yaw angle and of the aircraft speed along the operation. The true IMU position is then converted to geodetic coordinates (the Latitude Longitude Altitude-LLA) reference frame. The true IMU position in LLA, the yaw angle and the relative position of the IMU with

respect to the GNSS receiver antenna allow computing the true GNSS receiver antenna position in LLA along the operation. The true IMU and GNSS receiver antenna positions, the true IMU velocity vector and the true yaw angle are computed with a sampling frequency of 5Hz, that is a typical sampling frequency used in GNSS/IRS tight coupling Kalman filters in commercial aircraft.

6.2.2. GNSS module

A GNSS module is implemented so as to compute the GNSS pseudo-range measurements injected in the Kalman filter in order to determine the GNSS/IRS position estimate. The GNSS pseudo-range measurements used in commercial aircraft to be hybridized with the IRS outputs are not smoothed by the code-carrier smoothing filter since the Kalman filter itself induces a smoothing on the position estimate. Hence raw code GNSS pseudo-range measurements are generated by the GNSS module. The GNSS measurements are computed with a sampling frequency of 5Hz. The methodology used to simulate these GNSS measurements is sketched in Figure 6-2.

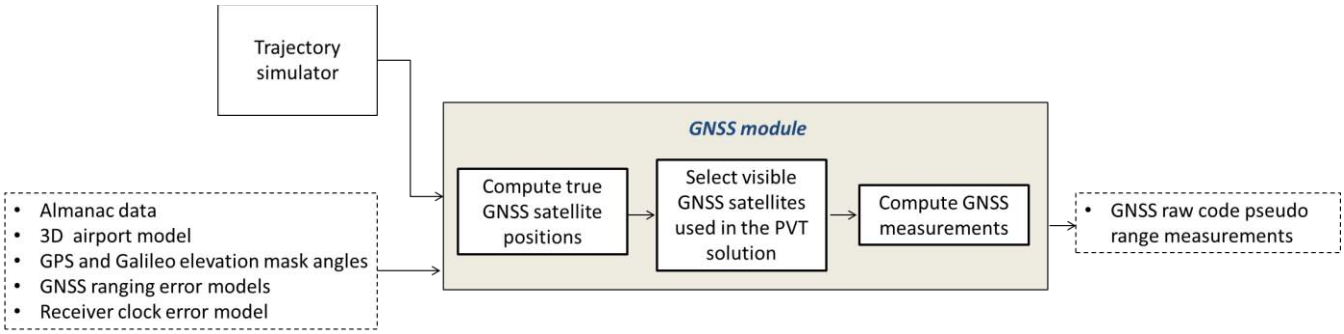

Figure 6-2: General architecture of the GNSS module

6.2.2.1. GNSS satellite position computation

The first step consists in computing the GPS and Galileo satellite positions based on the almanac data. An optimized 24 satellite GPS constellation [RTCA, 2006] and a 27 satellite Galileo constellation [EUROCAE, 2010] are considered in the simulator. The GNSS satellites are considered to be stationary during the trajectory, as justified in Section 5.1.2.1. By denoting t_0 and t_{end} the first and last time instants of the considered trajectory respectively, the GNSS satellite positions are computed at epoch t_0 and are considered to be constant in the time interval $[t_0; t_{end}]$, that is to say during the trajectory.

6.2.2.2. GNSS satellites used in the PVT solution

The second step consists in selecting the GNSS pseudo-range measurements that will be used in the PVT solution at each time epoch $t_i \in [t_0; t_{end}]$. t_i is a discrete time instant sampled at 5Hz. A GNSS satellite j is used in the PVT solution at time epoch t_i if the three following conditions are met:

- The visibility test is passed, that is to say the elevation angle of satellite j is above the elevation mask angle t_i. The minimal mask angle set to 5° in [RTCA, 2006] for GPS satellites and is set to 10° for Galileo satellites [EUROCAE, 2010]. These mask angles can be easily increased in the software since they are considered to be software inputs. The effect of the satellite elevation mask angle on the accuracy of the horizontal position error is further discussed in Chapter 7.

- The GNSS receiver antenna receives the LOS signal from satellite j at t_i. Three situations can be distinguished, depending on the nature of the GNSS signals from satellite j reaching the GNSS receiver antenna. In the first situation, the LOS and the NLOS are received by the GNSS receiver antenna. In second situation, the LOS and NLOS signals are not received by the GNSS receiver antenna. The satellite is not used in the PVT solution. In third situation, NLOS signals are received by the GNSS receiver antenna and the LOS signal is not received. The satellite is not used in the PVT solution. Indeed, in this thesis, it is considered that detection techniques are implemented in the GNSS receiver in order to detect the reception of NLOS signals in the absence of the LOS signal. It is assumed that NLOS GNSS measurements are detected and excluded from the PVT solution. Among the existing detection techniques, some solutions are based on the monitoring of the received signal-to-noise ratio [Groves *et al*., 2013], some solutions use an antenna array to measure the angle of arrival of the received signals [Xiong, 1998], some techniques use a 3D model of the environment to detect NLOS signals [Bourdeau *et al.*, 2012] [Peyraud *et al*., 2013] [Wang *et al*., 2013].
- The C/N0 ratio of the total (pilot+data) GPSL1C signal (or GalileoE1 signal) received from satellite j at t_i is above the GPSL1C (or GalileoE1) minimal C/N0 ratio required for the demodulation, acquisition and tracking steps and detailed in [Julien 2010]. If it is the case, and if the C/N0 ratio of the total (pilot+data) GPSL5 signal (or GalileoE5a signal) received from satellite j at t_i is above the GPSL5 (or GalileoE5a) minimal C/N0 ratio required for the demodulation, acquisition and tracking steps and detailed in [RTCA, 2004] [EUROCAE, 2010], the dual-frequency L1/L5 GNSS pseudo-range measurement from satellite j is used in the PVT solution. If the C/N0 test is passed only by the L1 signal received from the visible satellite j, the single-frequency L1 GNSS pseudo-range measurement from satellite j is used in the PVT solution. The C/N0 ratios of the signals received from each visible GNSS satellite at t_i are obtained considering that the GNSS receiver antenna only receives the LOS signal. The link budget used to derive the C/N0 ratios is fully described in Appendix D.

One of the main limitations relating to the GNSS/IRS position generator is that the impact of multipath on the C/N0 ratios is not taken into account in the link budget used to compute the C/N0 ratios and developed in Appendix D. This has two main consequences.

- Firstly, the potential loss of track of L1 and/or L5 signals due to the effects of multipath is not considered in this thesis.
- Secondly, the increase of the standard deviation of the receiver noise error σ_{noise} of a GNSS measurement induced by a reduction of the C/N0 ratio due to multipath on that GNSS measurement is not considered in this thesis. A preliminary analysis reveals that C/N0 reductions induced by multipath are not expected to have a significant impact on the standard deviation of the receiver noise ranging errors and on the standard deviation of the UERE. There are two reasons for this.
  - Firstly, a preliminary analysis shows that most of the C/N0 ratios computed based on Appendix D are comprised in the interval [40dB-Hz;45dB-Hz] If multipath induces a reduction of the C/N0 of few dB-Hz, the C/N0 ratios will be mostly comprised in the interval [35dB-Hz;45dB-Hz]. The function that relates σ_{noise} to C/N0 is roughly constant (centimetre-level variations) for $C/N0 \in$ [35dB-Hz;45dB-Hz], regardless of the GNSS signals considered in this Chapter (GPSL1C, GPSL5, GalileoE1 and GalileoE5a). This can be observed in Figure 3-4. Hence, the σ_{noise} is not expected to be significantly affected by multipath.
  - Secondly, σ_{noise} for $C/N0 \in$ [35dB-Hz;45dB-Hz] are few centimeters, regardless of the GNSS signals considered in this Chapter. In comparison, the standard deviation of the

ranging error induced by the satellite clock and ephemeris inaccuracies is $\sigma_{sat\&eph} = 85\text{cm}$. Consequently, the standard deviation of the UERE is not dominated by the receiver noise effects.

To conclude, a first analysis reveals that the impact of the multipath on the C/N0 ratios is not expected to have a significant impact on the standard deviation of the UERE. However, further investigations are required to assess the reduction of the C/N0 and to validate this first analysis.

6.2.2.3. GNSS measurement computation

The third step consists in generating GNSS raw code pseudo range measurements at each time epoch $t_i \in [t_0; t_{end}]$. GNSS measurements are generated based on the true GNSS receiver antenna position at t_i, on the GNSS satellite positions during the trajectory and on the GNSS raw code pseudo range measurement error models described in Section 3.2.1 and in Chapter 5. Assuming that N GNSS raw code pseudo range measurements are used in the Kalman filter at time t_i, the GNSS measurement vector generated at time t_i by the GNSS module is:

$$\boldsymbol{\rho}_{GNSS}(t_i) = \begin{bmatrix} \rho_{GNSS\,1}(t_i) \\ \vdots \\ \rho_{GNSS\,j}(t_i) \\ \vdots \\ \rho_{GNSS\,N}(t_i) \end{bmatrix}$$

$$\begin{aligned} \rho_{GNSS\,j}(t_i) &= r_{GNSS\,j}(t_i) + b(t_i) + \varepsilon_{iono\,j}(t_i) + \varepsilon_{tropo\,j}(t_i) \\ &+ \varepsilon_{Sat\&Eph\,j}(t_i) + \varepsilon_{noise\,j}(t_i) + \varepsilon_{mp\,j}(t_i) \end{aligned} \qquad \text{Eq - 6-1}$$

where:

- $r_{GNSS\,j}(t_i)$ is the true range between satellite "j" and the GNSS airborne antenna at time t_i,
- $b(t_i)$ is the receiver clock offset at time t_i. The receiver clock offsets are generated assuming that the airborne GNSS receiver is equipped with a TCXO clock. Clock errors are generated from the differential technique developed in [Winkel, 2000].
- $\varepsilon_{iono\,j}(t_i)$, $\varepsilon_{tropo\,j}(t_i)$, $\varepsilon_{Sat\&Eph\,j}(t_i)$, $\varepsilon_{noise\,j}(t_i)$ are the raw code nominal ionosphere, troposphere, satellite clock and ephemeris, receiver thermal noise errors between satellite j and the GNSS airborne antenna at time t_i,
- $\varepsilon_{mp\,j}(t_i)$ is the raw code multipath error between satellite j and the GNSS airborne antenna at time t_i.

The impact of multipath on the C/N0 ratios is not taken into account in the link budget used to compute the C/N0 ratios. Hence, the increase of the standard deviation of the thermal noise code ranging error due to the effects of multipath is not considered in this thesis.

6.2.3. Inertial module

An inertial module is implemented so as to compute:

- The IRS position and velocity estimates of the IMU in LLA and in the NED navigation frame,
- The IRS Euler angle estimates.

6.2.3.1. IMU module

The first step consists in computing the accelerometer and gyroscope measurements through the IMU module. This module has been implemented in the framework of a PhD project [Vézinet, 2013]. The accelerometer measurements are defined as the absolute non-gravitational acceleration of the aircraft expressed in the aircraft body frame (b) presented in Appendix F. The gyroscope measurements are defined as the absolute angular velocity of the aircraft expressed in the aircraft body frame (b). The IMU module firstly computes the ideal accelerometer and gyroscope measurements from the true IMU position and velocity as well as from the true aircraft Euler angles computed in the trajectory simulator module. The IMU mechanization is not detailed in this document and further details about these computations are provided in [Farrell *et al*., 1999] and [Escher, 2003]. Since typical sampling frequencies of the IMU and IRS modules are few hundreds of Hz in commercial aircraft, the trajectory simulator outputs are oversampled at 100Hz at the IMU module input. Secondly, The IMU module computes the non-ideal accelerometer and gyroscope measurements by considering several typical sources of errors affecting the accelerometer and gyroscope measurements that are [Kayton *et al*., 1996]:

- The measurement noise. The white random noise error vector is denoted as $\boldsymbol{\eta}_{\text{IMU}}$ in the following.
- The measurement bias on the measured acceleration or angular rate. This bias can be caused by an error in the initial bias estimation and/or uncompensated temperature fluctuations. The measurement bias is denoted as $\mathbf{b}_{\text{IMU}}$ in the following.
- The misalignment error due to the alignment of the measurement axes from the orthogonal platform axes. The misalignment matrix is denoted as $\mathbf{misa}$ in the following.
- The error in the calibrated gyroscope or accelerometer scale factor. The scale factor error matrix is denoted as $\mathbf{k}_{1,\text{IMU}}$ in the following.

The inertial measurement error models used in the described IMU module have been extracted from the outputs of another ENAC/Airbus PhD project that partly focuses on the accelerometer and gyroscope measurement error models [Vézinet, 2013]. The measured absolute non-gravitational acceleration or angular velocity of the aircraft expressed in the body frame at time t_i is:

$$\mathbf{x}_{\text{meas}}(t_i) = \boldsymbol{\eta}_{\text{IMU}}(t_i) + \mathbf{b}_{\text{IMU}}(t_i) + \mathbf{misa}\left(\mathbf{I}_{3\times3} + \mathbf{k}_{1,\text{IMU}}\right)\mathbf{x}_{\text{true}}(t_i) \qquad \text{Eq - 6-2}$$

where:

- $\mathbf{x}_{\text{true}}$ represents the ideal acceleration or the ideal angular velocity of the aircraft at t_i. $\mathbf{x}_{\text{meas}}$ represents the non-ideal acceleration or angular velocity measurements at t_i.
- $\boldsymbol{\eta}_{\text{IMU}}(t_i)$ is modelled as a zero-mean three dimensional Gaussian distribution [Vézinet, 2013]: $\boldsymbol{\eta}_{\text{IMU}}(t_i) \sim \mathcal{N}\left(\begin{bmatrix}0\\0\\0\end{bmatrix}, \begin{bmatrix}{\sigma_\eta}^2 & 0 & 0\\ 0 & {\sigma_\eta}^2 & 0\\ 0 & 0 & {\sigma_\eta}^2\end{bmatrix}\right)$,
- $\mathbf{b}_{\text{IMU}}(t_i)$ is modeled by a three dimensional first-order Gauss-Markov process [Vézinet, 2013]:

$$\mathbf{b}_{\text{IMU}}(t_i) = a\mathbf{b}_{\text{IMU}}(t_{i-1}) + \sqrt{1-a^2}\boldsymbol{\eta}_{0,\text{IMU}}(t_i) \text{ for } t_i > t_0 \qquad \text{Eq - 6-3}$$
$$\mathbf{b}_{\text{IMU}}(t_i) = \boldsymbol{\eta}_{0,\text{IMU}}(t_i) \text{ for } t_i = t_0$$

where:

- t_0 is the initial time epoch of the simulation,
- $a = \exp(-\frac{Te}{T_{IMU}})$
- T_{IMU} is the correlation time related to the Gauss-Markov process,
- Te is the sampling period of the inertial sensor measurements,
- $\boldsymbol{\eta}_{0,IMU}(t_i)$ is modelled as a zero-mean three dimensional Gaussian distribution [Vézinet, 2013]: $\boldsymbol{\eta}_{0,IMU}(t_i) \sim \mathcal{N}\left(\begin{bmatrix}0\\0\\0\end{bmatrix}, \begin{bmatrix}{\sigma_0}^2 & 0 & 0\\ 0 & {\sigma_0}^2 & 0\\ 0 & 0 & {\sigma_0}^2\end{bmatrix}\right)$.
- $\mathbf{misa} = \sin\begin{bmatrix}\frac{\pi}{2} - w_\theta & -w'_\psi & w_\varphi{}' \\ w'_\psi & \frac{\pi}{2} - w_\varphi & -w'_\theta \\ -w'_\varphi & w'_\theta & \frac{\pi}{2} - w_\psi\end{bmatrix}$. $w_\theta, w'_\theta, w_\varphi, w'_\varphi, w_\psi$ and w'_ψ are modelled as uniform distributions [Vézinet, 2013] in the misalignment interval I_{misa},
- $\mathbf{k}_{1,IMU} = \begin{bmatrix}\eta_{1,IMU,x} & 0 & 0\\ 0 & \eta_{1,IMU,y} & 0\\ 0 & 0 & \eta_{1,IMU,z}\end{bmatrix}$. $\eta_{1,IMU,x}$, $\eta_{1,IMU,y}$ and $\eta_{1,IMU,z}$ are modelled as uniform distribution [Vézinet, 2013] in the scale factor uncertainty interval I_1.

The values of the parameters describing the error terms used in the simulator cannot be published in this thesis since these values come from an Airbus supplier and are protected by copyright.

6.2.3.2. IRS module

The second step consists in computing the inertial position and velocity estimates of the IMU and the inertial Euler angle estimates based on the accelerometer and gyroscope measurements through the IRS module. This module has been implemented in the framework of another Ph.D. thesis [Escher, 2003]. The IRS mechanization is not detailed in this document and further details about these computations are provided in [Escher, 2003].

An important remark is that, when the IRS estimates the IMU position based in the inertial measurements, the vertical position error may grow in the time domain. This phenomenon is frequently referred to as "vertical channel divergence" in the literature. The vertical channel of the IRS platform may be stabilized by means of a baro-aiding technique that use both inertial measurements and baro-altimeter measurements to bound the vertical channel error within limits [Kayton *et al*., 1996] [Dadu *et al*., 2007]. Due to the relatively poor performance of baro-altimeters (0.06% full scale, or, equivalently, few meters accuracy [Honeywell, 2010]) compared to the navigation solution accuracy performance required for the application, a Digital Elevation Map (DEM) is used in the navigation algorithm to estimate the terrain altitude. The inertial vertical channel is bounded by a third-order loop described in [Vézinet, 2013]. The DEM module is presented in the next section.

The inertial position, velocity and attitude angle estimates are finally under sampled to reach a sampling frequency of 5Hz that is the sampling frequency adopted in the GNSS/IRS/DEM tight coupling Kalman filter.

6.2.4. Digital Elevation Map module

The terrain altitude estimated by the DEM at time t_i is generated as follows:

$$Al_{meas}(t_i) = Al_{true}(t_i) + \eta_{DEM}(t_i) \qquad \text{Eq - 6-4}$$

where:

- Al_{true} represents the ideal IMU altitude at t_i.
- $\eta_{DEM}(t_i)$ is the altitude noise error at time t_i and is assumed to be over bounded by a zero-mean Gaussian distribution [Salos, 2012].

The distribution of the altitude error at the scale of the airport is complex to assess. The altitude error will vary smoothly at the scale of the airport, meaning that the altitude error is spatially correlated at the scale of the airport. In addition, altitude errors can be biased. In order to represent the error by a simple and conservative model, the altitude error distribution at the scale of the airport can be over-bounded by a zero-mean normal distribution characterized by a standard deviation σ_{DEM}. The values of σ_{DEM} are further discussed below.

The accuracy of DEM depends on production steps from the photogrammetric or LIDAR-generated mass points to the DEM generation. The vertical accuracy of elevation models is also a function of horizontal resolution [NDEP, 2004]. By denoting σ_{DEM} the standard deviation of the altitude noise error, $\sigma_{DEM} = 9.1\text{cm}$ for a horizontal contour interval of 1ft and reaches 7.5m for a horizontal contour interval of 80ft [NDEP, 2004]. It is chosen to take a medium vertical accuracy of $\sigma_{DEM} = 2\text{m}$. This corresponds to a commercialized DEM [Intermap, 2012].

6.2.5. Kalman filter module

A Kalman filter module is implemented so as to estimate the slowly varying inertial estimation errors. GNSS raw code pseudo range measurements are used to estimate the inertial estimation errors. The coupling technique is a tight coupling, wherein INS outputs are integrated with GNSS measurements in a Kalman filter. The IMU position and velocity as well as the aircraft Euler angle estimated by the INS module are then corrected by the inertial error estimates. This section presents the Kalman filter architecture used to estimate the inertial estimation errors.

6.2.5.1. Nonlinear to linearized system model

The Kalman filter model consists in two subsystems: a dynamics subsystem and a measurement subsystem. Let's denote $\mathbf{x}(t)$ the vector comprised of the position, velocity and attitude as well as sensor measurements at time t, as if they were provided by an ideal IRS platform. The dynamics model relates $\mathbf{x}(t)$ to $\dot{\mathbf{x}}(t)$ and this describes the time evolution of $\mathbf{x}(t)$. Let's denote $\mathbf{y}(t)$ the vector made of the GNSS pseudo-range measurements at time t:

$$\mathbf{y}(t) = \begin{bmatrix} \rho_{GNSS\,1}(t) \\ \vdots \\ \rho_{GNSS\,j}(t) \\ \vdots \\ \rho_{GNSS\,N}(t) \end{bmatrix} \qquad \text{Eq - 6-5}$$

The measurement model relates $\mathbf{y}(t)$ to $\mathbf{x}(t)$. Both dynamic and measurement models are given as follows:

$$\begin{aligned} \dot{\mathbf{x}}(t) &= f(\mathbf{x}(t), t) + \mathbf{w_s}(t) \\ \mathbf{y}(t) &= h(\mathbf{x}(t), t) + \mathbf{w_o}(t) \end{aligned} \qquad \text{Eq - 6-6}$$

where:

- $\mathbf{w_s}$ is the state noise vector.
- $\mathbf{w_o}$ is the observation noise vector.

Both dynamic and measurement models are nonlinear models [Farrell *et al*., 1999]. In order to use the Kalman filter to estimate the position, it is firstly necessary to linearize the system model. As done in [Farrell *et al*., 1999], let's define a reference trajectory $\bar{\mathbf{x}}$ satisfying:

$$\begin{aligned}\dot{\bar{\mathbf{x}}}(t) &= f(\bar{\mathbf{x}}(t), t)\\ \bar{\mathbf{y}}(t) &= h(\bar{\mathbf{x}}(t), t)\end{aligned} \qquad \text{Eq - 6-7}$$

Let's state:

$$\begin{aligned}\mathbf{x}(t) &= \bar{\mathbf{x}}(t) + d\mathbf{x}(t)\\ \mathbf{y}(t) &= \bar{\mathbf{y}}(t) + d\mathbf{y}(t)\end{aligned} \qquad \text{Eq - 6-8}$$

$d\mathbf{x}(t)$ is expected to be small during the operation. It is demonstrated in [Farrell *et al*., 1999] that the system model can be defined by the following linear continuous model:

$$\begin{aligned}\dot{d\mathbf{x}}(t) &= \mathbf{F}(t)d\mathbf{x}(t) + \mathbf{w_s}(t)\\ d\mathbf{y}(t) &= \mathbf{H}(t)d\mathbf{x}(t) + \mathbf{w_o}(t)\end{aligned} \qquad \text{Eq - 6-9}$$

where:

$$\begin{aligned}\mathbf{F}(t) &= \left.\frac{\partial f}{\partial \mathbf{x}}\right|_{\mathbf{x}(t)=\bar{\mathbf{x}}(t)}\\ \mathbf{H}(t) &= \left.\frac{\partial h}{\partial \mathbf{x}}\right|_{\mathbf{x}(t)=\bar{\mathbf{x}}(t)}\end{aligned} \qquad \text{Eq - 6-10}$$

After discretization, the dynamics model equation and the measurement model equation are, respectively:

$$\begin{aligned}\dot{d\mathbf{x}}(t_i) &= \mathbf{F}(t_{i-1})d\mathbf{x}(t_{i-1}) + \mathbf{w_s}(t_i)\\ d\mathbf{y}(t_i) &= \mathbf{H}(t_i)d\mathbf{x}(t_i) + \mathbf{w_o}(t_i)\end{aligned} \qquad \text{Eq - 6-11}$$

where:

- $d\mathbf{y}(t_i)$ is the observation vector defined as the difference between the GNSS pseudo-range measurements $\mathbf{y}$ and ranges calculated between the reference trajectory position and the tracked satellites position $\bar{\mathbf{y}}$**.**
- **F** is the linearized transition matrix in discrete time.
- **H** is the linearized observation matrix also known as design matrix in discrete time.
- $d\mathbf{x}(t_i)$ is the state vector in discrete time. It consists in the inertial position errors, the inertial velocity errors, the inertial attitude errors and sensors measurement errors. Three types of states are also added to the state vector: the receiver clock bias, the receiver clock drift, and the long term GNSS correlated ranging errors.

The state vector is further detailed in the next section.

6.2.5.2. State vector

The errors estimated in the Kalman filter are classified as follows:

- The inertial navigation errors, that are the inertial position error, the inertial velocity error, and the inertial Euler angle errors,
- The inertial measurement errors, that are the accelerometer and gyroscope errors,
- The errors affecting GNSS measurements, that are GNSS receiver clock bias and drift and the long term correlated errors. From Section 3.2.1, in the dual frequency configuration, the GNSS ranging errors are affected by two kinds of long-term correlated errors: the troposphere errors and the errors due to inaccuracies in the broadcast satellite clock corrections and ephemeris. In nominal conditions, the inaccuracies in the broadcast satellite clock corrections and ephemeris are the dominant source of long-term correlated errors since the standard deviation of the satellite clock and ephemeris errors is higher than the standard deviation of the troposphere errors. Further details about the standard deviation of the nominal satellite clock and ephemeris errors and of the nominal troposphere errors are provided in Section 3.2.1. For this reason, the Kalman filter is calibrated so as to estimate long term correlated ranging errors due to inaccuracies in the broadcast satellite clock corrections and ephemeris. Note that a more optimal approach would be to design the filter so as to estimate also the troposphere residual errors in the correlated ranging errors states. The design of such as filter remains as future work.

Let's assume that N raw code GNSS pseudo range measurements are used by the Kalman filter at time t to estimate the inertial estimation errors. The state vector at time t is formed by the quantities to estimate and is:

$$d\mathbf{x}(t_i) = [d\mathbf{p}(t_i) \quad d\mathbf{v}(t_i) \quad d\boldsymbol{\Phi}(t_i) \quad \mathbf{b_g}(t_i) \quad \mathbf{b_a}(t_i) \quad b(t_i) \quad d(t_i) \quad \boldsymbol{\varepsilon}_{\mathrm{Sat\&Eph}}(t_i)]^T \qquad \text{Eq - 6-12}$$

where:

- $d\mathbf{p}(t_i) = [dp_{x,w}(t) \quad dp_{y,w}(t)]^T$ is the IRS horizontal position error vector in the wander azimuth navigation reference frame at time t_i,
- $d\mathbf{v}(t_i) = [dv_{x,w}(t_i) \quad dv_{y,w}(t_i)]^T$ is the IRS horizontal velocity error vector in the wander azimuth navigation reference frame at time t_i,
- $d\boldsymbol{\Phi}(t_i) = \left[d\phi_{x,w}(t_i) \quad d\phi_{y,w}(t_i) \quad d\phi_{z,w}(t_i)\right]^T$ is the IRS alignment errors vector in the wander azimuth navigation reference frame at time t,
- $\mathbf{b}_g(t_i) = \left[b_{g,x,b}(t_i) \quad b_{g,y,b}(t_i) \quad b_{g,z,b}(t_i)\right]^T$ is the gyrsoscope error vector in the aircraft body reference frame at time t,
- $\mathbf{b}_a(t_i) = \left[b_{a,x,b}(t_i) \quad b_{a,y,b}(t_i)\right]^T$ is the horizontal accelerometer error vector in the aircraft body reference frame at time t
- $b(t_i)$ and $d(t_i)$ are the GNSS receiver clock bias and drift at time t_i. In this thesis, it is assumed that the inter-system time shift between the GPS and Galileo times is known in the dual-constellation GPS/Galileo receiver. Hence, the receiver clock bias and drift are estimated for both GPS and Galileo measurements. If the inter-system time shift were unknown, a clock bias and a clock drift would have been evaluated separately for the GPS measurements and for the Galileo measurements.
- $\boldsymbol{\varepsilon}_{\mathrm{Sat\&Eph}}(t_i) = \left[\varepsilon_{\mathrm{Sat\&Eph}\,1}(t_i), \ldots, \varepsilon_{\mathrm{Sat\&Eph}\,j}(t_i), \ldots, \varepsilon_{\mathrm{Sat\&Eph}\,N}(t_i)\right]^T$ is the long term correlated raw code GNSS ranging errors vector due to inaccuracies in the broadcast satellite clock corrections and ephemeris at time t_i.

The inertial position, velocity and attitude angle error estimates are expressed in the wander azimuth reference frame that is defined in Appendix F. The aircraft body reference frame is

also presented in Appendix F. The next section explains how the state vector is estimated by means of a Kalman filter.

6.2.5.3. State vector estimation

The Kalman filter computes the estimated state vector components by taking into account:

- The *a priori* dynamics of the unknown states,
- Information provided by the GNSS measurements.

The system is thus characterized by two models: a dynamic model, also called the state transition model and a measurement model. Both models are presented in Eq - 6-11. The Kalman filter computes at each time epoch t_i the estimate of the state vector from all GNSS measurements from t_0 to t_i. The state vector estimate is denoted as:

$$d\hat{\mathbf{x}}^+(t_i) = E[d\mathbf{x}(t_i) \mid d\mathbf{y}(t_0) \dots d\mathbf{y}(t_i)] \quad \text{Eq - 6-13}$$

The Kalman filter computes $d\hat{\mathbf{x}}^+(t_i)$ in two steps:

- The **prediction** step determines the state vector at time t_i knowing all the observations from time t_0 to time t_{i-1} by means of the state transition model equation. This prediction is the *a priori* state vector estimate and is denoted as:

$$d\hat{\mathbf{x}}^-(t_i) = E[d\mathbf{x}(t_i) \mid d\mathbf{y}(t_0) \dots d\mathbf{y}(t_{i-1})] \quad \text{Eq - 6-14}$$

- The **estimation** step determines the state vector at time t_i by correcting the former prediction by taking into account the information provided by the observation $d\mathbf{y}(t_i)$.

The Kalman filter extension to nonlinear system models is provided in Table 6-1. The following notations are used:

- $\mathbf{P}^-(t_i)$ represents the predicted covariance matrix of the a priori estimation error.
- $\mathbf{P}^+(t_i)$ represents the estimated covariance matrix of the estimation error.
- $\mathbf{Q}(t_i)$ represents the predicted covariance matrix of the state noise vector at time t_i:

$$\mathbf{Q}(t_i) = \text{cov}[\mathbf{w_s}(t_i)] \quad \text{Eq - 6-15}$$

- $\mathbf{R}(t_i)$ represents the predicted covariance matrix of the measurement noise vector at time t_i:

$$\mathbf{R}(t_i) = \text{cov}[\mathbf{w_o}(t_i)] \quad \text{Eq - 6-16}$$

- $\mathbf{I}(t_i)$ and $\mathbf{K}(t_i)$ are the innovation vector and the Kalman gain matrix at time t_i.

The equations provided in Table 6-1 are implemented using one of the following techniques [Farrell *et al.*, 1999].

- In the linearized Kalman filter implementation, $\bar{\mathbf{x}}(t)$ is a predetermined trajectory. The GNSS measurements do not affect the calculations of **F, H, P** or **K**.
- In the Extended Kalman Filter (EKF) implementation, $\bar{\mathbf{x}}(t)$ is the estimated trajectory that is the predetermined trajectory corrected by the state vector estimated by the Kalman filter. The design matrix **H** is linearized around the estimated trajectory and does depend on the GNSS measurements. The GNSS measurements also affect the calculations of **P** and **K**.

In the EKF implementation, and if the estimated trajectory is near the actual trajectory, the linearization of the Kalman matrices will be good and the state estimate will be good. In this case, the EKF may produce better performance than the linearized Kalman filter. If the estimated trajectory is far from the actual trajectory, the linearization of the Kalman matrices

will be inaccurate and the state estimate will be degraded. The EKF is thus riskier than the linearized Kalman filter when large GNSS ranging errors make the state estimation inaccurate. In this case, the EKF may produce worse performance than the linearized Kalman filter.

In the application, the aircraft may be affected by severe multipath ranging errors (few tens of meters amplitude), specifically during the *taxi on taxi lane* operation. This is underlined in Chapter 5. Hence, the linearized Kalman filter implementation is chosen for this thesis. The possibility of using an EKF and the comparison between both linearized and EKF implementations remains as future work.

Initialization	• Initial estimates of $d\hat{\mathbf{x}}^+(t_0)$, $\mathbf{P}^+(t_0)$
Measurement update	• $\mathbf{K}(t_i) = \mathbf{P}^-(t_i)\mathbf{H}(t_i)^T[\mathbf{H}(t_i)\mathbf{P}^-(t_i)\mathbf{H}(t_i)^T + \mathbf{R}(t_i)]^{-1}$ • $d\mathbf{y}(t_i) = \mathbf{y}(t) - \bar{\mathbf{y}}(t)$ • $\mathbf{I}(t_i) = d\mathbf{y}(t_i) - \mathbf{H}(t_i)d\hat{\mathbf{x}}^-(t_i)$ • $d\hat{\mathbf{x}}^+(t_i) = d\hat{\mathbf{x}}^-(t_i) + \mathbf{K}(t_i)\mathbf{I}(t_i)$ • $P^+(t_i) = [1 - \mathbf{K}(t_i)\mathbf{H}(t_i)]\mathbf{P}^-(t_i)$
Time propagation	• $d\hat{\mathbf{x}}^-(t_{i+1}) = \mathbf{F}(t_i)d\hat{\mathbf{x}}^+(t_i)$ • $\mathbf{P}^-(t_{i+1}) = \mathbf{F}(t_i)\mathbf{P}^+(t_i)\mathbf{F}(t_i) + \mathbf{Q}(t_{i+1})$
Definitions	• $\bar{\mathbf{x}}$ is the reference trajectory around which the transition and design matrix are linearized • $\bar{\mathbf{y}}(t) = h(\bar{\mathbf{x}}(t), t)$ • $\mathbf{F}(t_i)$ is the linearized transition matrix in discrete time. The linearized continuous transition matrix is: $\mathbf{F}(t) = \left.\frac{\partial f}{\partial \mathbf{x}}\right\|_{\mathbf{x}(t)=\bar{\mathbf{x}}(t)}$ • $\mathbf{H}(t_i)$ is the linearized design matrix in discrete time. The linearized design transition matrix is: $\mathbf{H}(t) = \left.\frac{\partial h}{\partial \mathbf{x}}\right\|_{\mathbf{x}(t)=\bar{\mathbf{x}}(t)}$

Table 6-1: Extension of Kalman filter equations to non-linear systems [Farrell *et al.*, 1999]

The next paragraph presents the implementation of the state transition model matrices.

6.2.5.4. State transition model matrices

Since it is assumed that the GNSS measurement errors, the receiver clock/drift, and the inertial errors are independent of each other, the state transition matrix and the predicted state noise covariance matrix are implemented as follows:

$$\mathbf{F} = \begin{bmatrix} \mathbf{F_1} & 0 & 0 \\ 0 & \mathbf{F_2} & 0 \\ 0 & 0 & \mathbf{F_3} \end{bmatrix}$$
$$\mathbf{Q} = \begin{bmatrix} \mathbf{Q_1} & 0 & 0 \\ 0 & \mathbf{Q_2} & 0 \\ 0 & 0 & \mathbf{Q_3} \end{bmatrix} \qquad \text{Eq - 6-17}$$

Presentation of F_1 and Q_1

$\mathbf{F_1}$ is the 13×13 sub state transition matrix that represents the a priori dynamics of the first 12 components of d$\mathbf{x}$ that are the inertial navigation errors, the inertial measurement errors. The model of the continuous $\mathbf{F_1}$ matrix is as follows [Farrell *et al.*, 1999] [Diesel, 1995]:

$$\begin{bmatrix} \dot{\mathbf{dp}} \\ \dot{\mathbf{dv}} \\ \dot{\mathbf{d\Phi}} \\ \dot{\mathbf{b}}_g \\ \dot{\mathbf{b}}_a \end{bmatrix} = \underbrace{\begin{bmatrix} 0 & \mathbf{F}_{pv} & 0 & 0 & 0 \\ 0 & 0 & \mathbf{F}_{v\Phi} & 0 & \mathbf{F}_{vacc} \\ \mathbf{F}_{\Phi p} & \mathbf{F}_{\Phi v} & \mathbf{F}_{\Phi\Phi} & \mathbf{F}_{\Phi gyro} & 0 \\ 0 & 0 & 0 & \mathbf{F}_{gyro\ gyro} & 0 \\ 0 & 0 & 0 & 0 & \mathbf{F}_{accel\ accel} \end{bmatrix}}_{\mathbf{F_1}} \begin{bmatrix} \mathbf{dp} \\ \mathbf{dv} \\ \mathbf{d\Phi} \\ \mathbf{b}_g \\ \mathbf{b}_a \end{bmatrix} + \underbrace{\begin{bmatrix} \boldsymbol{\eta}_p \\ \boldsymbol{\eta}_v + \boldsymbol{\eta}_{noise,a} \\ \boldsymbol{\eta}_\Phi + \boldsymbol{\eta}_{noise,b} \\ \boldsymbol{\eta}_{b,g} \\ \boldsymbol{\eta}_{b,a} \end{bmatrix}}_{\mathbf{w_{s,1}}} \quad \text{Eq - 6-18}$$

The wander azimuth mechanization used to compute the sub-matrices of $\mathbf{F_1}$ is described in [Diesel, 1995]. $\mathbf{F}_{gyro\ gyro}$ and $\mathbf{F}_{accel\ accel}$ represent the a-priori dynamics of the gyroscope and accelerometer measurement biases. The correlation times of the gyroscope and accelerometer biases used in the Kalman filter for the implementation of $\mathbf{F}_{gyro\ gyro}$ and $\mathbf{F}_{accel\ accel}$ are the correlation times used to generate the gyroscope and accelerometer biases. $\mathbf{F_1}$ is then discretized. The discretization process is based on Taylor series approximations and is if fully described in [Escher, 2003].

$\mathbf{Q_1}$ is the 12×12 sub state noise covariance matrix that represents the predicted covariance of the first 12 components of the state noise vector denoted as $\mathbf{w_{s,1}}$. More specifically, $\mathbf{Q_1}$ is the predicted covariance matrix of the error made in the prediction of the first 12 lines of the state vector. The prediction errors may come from two main error sources. Firstly, there are the linearization and integration processes used in the prediction mechanization of the error state. Secondly, there are the inertial sensor measurement errors that are not estimated by the Kalman filter and that affect the prediction of the state vector. In the continuous domain, $\mathbf{Q_1}$ is given by:

$$\mathbf{Q}_1 = \begin{bmatrix} \mathbf{C}_p & 0 & 0 & 0 & 0 \\ 0 & \mathbf{C}_{va} & 0 & 0 & 0 \\ 0 & 0 & \mathbf{C}_{\Phi g} & 0 & 0 \\ 0 & 0 & 0 & \mathbf{C}_{bg} & 0 \\ 0 & 0 & 0 & 0 & \mathbf{C}_{ba} \end{bmatrix} \quad \text{Eq - 6-19}$$

$\mathbf{Q_1}$ is then discretized. The discretization process is based on Taylor series approximations and is if fully described in [Escher, 2003]. In Eq - 6-19:

- $\mathbf{C}_p$ is the predicted covariance matrix of the error $\boldsymbol{\eta}_p$ made in the prediction of the horizontal positioning error. Since the predicted horizontal positioning error is a linear function of the horizontal velocity error, the prediction of the horizontal positioning error is not affected by any linearization effects. Hence, $\mathbf{C}_p = 0$.
- $\mathbf{C}_{va}$ is the predicted covariance matrix of the error $\boldsymbol{\eta}_v + \boldsymbol{\eta}_{noise,a}$ made in the prediction of the horizontal velocity error. $\boldsymbol{\eta}_v$ represents the error in the prediction of the horizontal velocity error due to the linearization and integration processes used in the prediction of the velocity error. In addition, $\boldsymbol{\eta}_{noise,a}$ represents the error in the prediction of the horizontal velocity error due to the integration of the accelerometer measurement noise. $\mathbf{C}_{va}$ has been implemented by using the covariance matrix of the accelerometer measurement noise error developed in Eq - 6-2. This covariance matrix has been voluntarily inflated by a factor 10^6 in order to include the errors in the velocity error

prediction due to the integration of the residual accelerometer measurement biases that have not been estimated by the Kalman filter.

- $\mathbf{C}_{\Phi g}$ is the predicted covariance matrix of the error $\boldsymbol{\eta}_{\Phi} + \boldsymbol{\eta}_{\text{noise,b}}$ made in the prediction of the attitude angle errors. As done for $\mathbf{C}_{\text{va}}$, $\mathbf{C}_{\Phi g}$ has been implemented by using the covariance matrix of the gyroscope measurement noise error developed in Eq - 6-2. This covariance matrix has been voluntarily inflated by a factor 10^4 in order to include the errors in the attitude angle error prediction due to the integration of the residual gyroscope measurement biases that have not been estimated by the Kalman filter.
- $\mathbf{C}_{\text{bg}}$ is the predicted covariance matrix of the error $\boldsymbol{\eta}_{\text{b,g}}$ made in the prediction of the gyroscope bias. $\mathbf{C}_{\text{bg}}$ has been implemented by using the covariance matrix of the same order of magnitude than the covariance matrix of the gyroscope measurement bias developed in Eq - 6-3.
- $\mathbf{C}_{\text{ba}}$ is the predicted covariance matrix of the error $\boldsymbol{\eta}_{\text{b,a}}$ made in the prediction of the accelerometer bias. $\mathbf{C}_{\text{ba}}$ has been implemented by using the covariance matrix of the same order of magnitude than the covariance matrix of the accelerometer measurement bias developed in Eq - 6-3.

Presentation of F_2 and Q_2

$\mathbf{F}_2$ is the 2×2 sub state transition matrix that represents the a priori dynamics of the GNSS receiver clock bias and drift. The model of the continuous F_2 matrix is as follows:

$$\begin{bmatrix} \dot{b} \\ \dot{d} \end{bmatrix} = \underbrace{\begin{bmatrix} 0 & F_{pv} \\ 0 & 0 \end{bmatrix}}_{\mathbf{F_2}} \begin{bmatrix} b \\ d \end{bmatrix} + \underbrace{\begin{bmatrix} \eta_{b,clock} \\ \eta_{d,clock} \end{bmatrix}}_{\mathbf{w_{s,2}}} \quad \text{Eq - 6-20}$$

$\mathbf{Q}_2$ is the predicted covariance matrix of the error vector $\mathbf{w}_{\text{s,2}}$ that corresponds to the errors made in the prediction of receiver clock bias and drift. The discrete covariance matrix $\mathbf{Q}_2$ is as follows:

$$\mathbf{Q}_2 = \begin{bmatrix} q_{11} & q_{12} \\ q_{21} & q_{22} \end{bmatrix} \quad \text{Eq - 6-21}$$

where q_{11} , q_{12} , q_{21} , q_{22} are developed in [Brown *et al.*, 1994]. q_{11} , q_{12} , q_{21} , q_{22} depend on the quality of the local oscillator that is characterized by the Allan constants. The Allan constants for the TCXO receiver clocks are provided in [Winkel, 2000].

Presentation of F_3 and Q_3

$\mathbf{F}_3$ is the $N \times N$ sub state transition matrix that represents the *a priori* dynamics of the last N raw code pseudo-range measurement errors due to inaccuracies in the satellite clock corrections and ephemeris. Assuming that the Kalman filter perfectly knows the dynamics of correlated long-term ranging errors due to inaccuracies in the satellite clock corrections and ephemeris, the discrete F_3 matrix is as follows:

$$\begin{bmatrix} \varepsilon_{\text{Sat\&Eph 1}}(t_{i+1}) \\ \vdots \\ \varepsilon_{\text{Sat\&Eph N}}(t_{i+1}) \end{bmatrix} \quad \text{Eq - 6-22}$$

$$= \underbrace{\begin{bmatrix} e^{-\frac{Te}{T_{Sat\&Eph}}} & 0 & 0 \\ 0 & \ddots & 0 \\ 0 & 0 & e^{-\frac{Te}{T_{Sat\&Eph}}} \end{bmatrix}}_{\mathbf{F_3}(t_i)} \begin{bmatrix} \varepsilon_{Sat\&Eph\ 1}(t_i) \\ \vdots \\ \varepsilon_{Sat\&Eph\ N}(t_i) \end{bmatrix} + \underbrace{\begin{bmatrix} \eta_{Sat\&Eph\ 1}(t_i) \\ \vdots \\ \eta_{Sat\&Eph\ N}(t_i) \end{bmatrix}}_{\mathbf{w}_{S,3}}$$

where:

- $Te = 200ms$ is the sampling period of the discretized Kalman filter,
- A correlation time $T_{sat\&eph} = 3600s$ is implemented.

$\mathbf{Q}_3$ is the predicted covariance matrix of the error vector $\mathbf{w_3}$ that corresponds to the errors made in the prediction of long-term GNSS ranging errors. The discrete covariance matrix is as follows $\mathbf{Q}_3$:

$$\mathbf{Q}_3 = \begin{bmatrix} (1-a^2)\sigma_{Sat\&Eph}{}^2 & 0 & 0 \\ 0 & \ddots & 0 \\ 0 & 0 & (1-a^2)\sigma_{Sat\&Eph}{}^2 \end{bmatrix} \qquad \text{Eq - 6-23}$$

where:

- a and $\sigma_{Sat\&Eph}$ are defined in Section 3.2.1.3.

The next paragraph presents the implementation of the observation model matrices.

6.2.5.5. Measurement model matrices

The design matrix implementation is described in [Diesel, 1995]. The measurement noise covariance matrix at time t_i is implemented by assuming that the sources of raw code ranging errors are independent to each other at time t_i:

$$\mathbf{R}(t_i) = \begin{bmatrix} \sigma_1(t_i)^2 & 0 & \cdots & \cdots & 0 \\ 0 & \ddots & & & \vdots \\ \vdots & & \sigma_j(t_i)^2 & & \vdots \\ \vdots & & & \ddots & 0 \\ 0 & \cdots & \cdots & 0 & \sigma_N(t_i)^2 \end{bmatrix} \qquad \text{Eq - 6-24}$$

where:

- $\sigma_{sat\,j}(t_i)^2$ is the expected variance of the raw code pseudo range measurement error on satellite j at time t_i. It is assumed that the Kalman filter perfectly knows the standard deviation of the troposphere, ionosphere, satellite clock and ephemeris and thermal receiver noise errors affecting the pseudo-range measurement from satellite "j" to the GNSS receiver antenna at time t_i. It is also assumed that the Kalman filter has no information on the multipath ranging error standard deviation during surface operations. Hence, the measurement noise variance on satellite "j" at t_i is implemented as:
- $\sigma_j(t_i)^2 = \sigma_{iono\,j}(t_i)^2 + \sigma_{tropo\,j}(t_i)^2 + \sigma_{Sat\&Eph\,j}{}^2 + \sigma_{noise\,j}(t_i)^2$
- $\sigma_{iono\,j}(t_i)$ is the standard deviation of the nominal ionosphere raw code ranging error used to generate the ionosphere ranging error on satellite j at time t_i,
- $\sigma_{tropo\,j}(t_i)$ is the standard deviation of the nominal troposphere raw code ranging error used to generate the troposphere ranging error on satellite j at time t_i,
- $\sigma_{Sat\&Eph\,j}{}^2 = 0.85^2 m^2$,

- $\sigma_{noise\,j}(t_i)^2$ is the standard deviation of the nominal receiver thermal noise raw code ranging error used to generate the noise ranging error on satellite j at time t_i.

Note that it has been decided to include the standard deviation of the ranging errors induced by the satellite clock and ephemeris inaccuracies in the matrix **R.** This is because these ranging errors are not entirely estimated by the filter and removed from the ranging measurements. Hence, **R** a conservative model of the actual covariance matrix of the code ranging error vector.

6.3. Conclusions

This chapter has selected the architecture of a GNSS-based positioning algorithm suitable to support the navigation performance requirements related to the guidance function during taxi operations under low visibility conditions. The selected PVT solution is a GNSS/IRS/DEM tight coupling algorithm wherein GNSS raw code pseudo range measurements are used in a Kalman filter to estimate the inertial position estimate errors. In order to analyze the performance of this coupling algorithm in terms of accuracy and to provide a model of the positioning error at the output of this PVT solution, a Matlab software is implemented. This software simulates the positioning errors at the PVT solution output and is composed of four main modules:

- The **trajectory module** simulates the true aircraft trajectory, velocity and attitude during taxi operations,
- The **GNSS module** directly generates the GNSS measurements used by the Kalman filter to estimate the inertial position errors. The GNSS pseudo-range measurements are affected by errors whose models are provided in Chapters 3 and 5 of this thesis. The main limitation of the implemented software is that the effects of multipath on the C/N0 of the tracked GNSS signals are not taken into account in the code. This has two consequences. Firstly, the potential loss of tracking of GNSS signals due to multipath in airport environments are not taken into account in the GNSS module. Secondly, the degradation of the receiver thermal noise ranging error standard deviation due to multipath is not taken into account in the GNSS module.
- The **inertial module** simulates the accelerometers, gyroscopes measurements and estimates the aircraft position, velocity and attitude angles by means of these measurements and by means of the terrain altitude estimated by the DEM.
- The **Kalman filter module** simulates the inertial position error estimates and the GNSS/IRS position estimates. The Kalman filter state transition matrices and measurement matrices are implemented assuming that the Kalman filter knows perfectly the correlation times of the GNSS ranging errors induced by the satellite clock and ephemeris inaccuracies and the correlation times of the gyroscope and accelerometer biases. Note that this is another limitation related to the software since real Kalman filters do not have perfect knowledge on the system dynamics. The Kalman filter is also supposed to know the variances of the ionosphere, troposphere, satellite clock and ephemeris, and thermal noise ranging errors. The Kalman filter is supposed to have no information on the multipath ranging errors.

CHAPTER 7

Impact of multipath on the position error

In order to develop a GNSS-based navigation system capable to support the required navigation performance related to the guidance function during the taxi operation under low visibility conditions, a GNSS/IRS/DEM tight coupling positioning algorithm is selected for the application and is presented in Chapter 6.

This chapter analyses the impact of the multipath ranging errors on the GNSS/IRS/DEM position estimate errors. The multipath ranging errors are modelled using the multipath ranging error models adapted to surface operations and presented in Chapter 5. This chapter is organized as follows. Section 7.1 recalls the GNSS multipath ranging error models and the GNSS measurement error models adapted to airport surface operations and extracted from Chapter 3 and Chapter 5. The theoretical impact of the multipath ranging errors on the GNSS/IRS position estimate error is derived. Section 7.2 re-uses this theoretical analysis to quantify the impact of the GNSS multipath ranging errors on the GNSS/IRS/DEM position error. Section 7.3 analyses the GNSS/IRS/DEM position errors induced by GNSS multipath from the airport surface and from the aircraft structure and evaluates the performance of the GNSS/IRS position estimate in terms of horizontal accuracy.

7.1. Theoretical multipath impact on the position error

7.1.1. Notations

This section presents the notations that will be used in the rest of the chapter. The navigation performance requirements presented in Section 2.3.2.3 for taxi operations are provided in the horizontal domain. For this reason, the impact of multipath on the GNSS/IRS/DEM horizontal position estimate error is investigated. The general architecture of the GNSS/IRS/DEM tight coupling positioning algorithm is given in Figure 7-1.

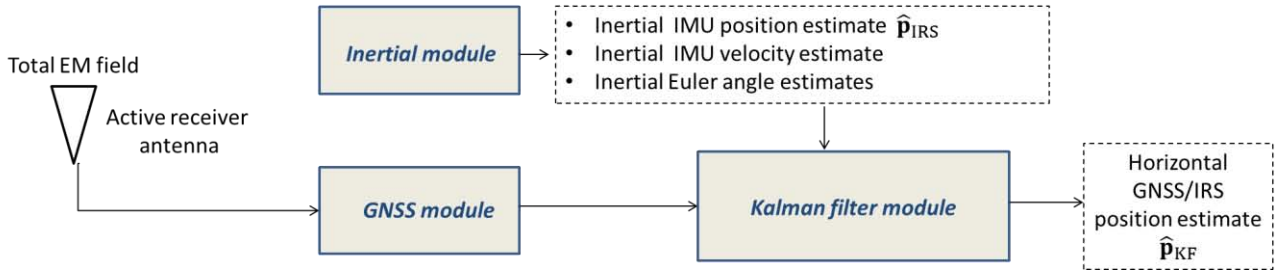

Figure 7-1: Architecture of the GNSS/IRS/DEM tight coupling positioning algorithm

Denote $\hat{\mathbf{p}}_{KF}(t_i)$ the GNSS/IRS/DEM horizontal position estimate of the IMU at time epoch t_i and $\mathbf{p}(t_i)$ the true horizontal position of the IMU at time epoch t_i:

$$\mathbf{p}(t_i) = \hat{\mathbf{p}}_{KF}(t_i) + \boldsymbol{\varepsilon}_p(t_i) \qquad \text{Eq - 7-1}$$

where $\boldsymbol{\varepsilon}_p(t_i)$ is the (2×1) horizontal GNSS/IRS position estimate error at time epoch t_i.

Section 7.1 derives the theoretical impact of the multipath ranging errors on the GNSS/IRS/DEM horizontal position estimate error $\boldsymbol{\varepsilon}_p$. The methodology used to analyze this impact is developed in the next section.

7.1.2. Methodology

Let's state:

- $\hat{\mathbf{p}}_{IRS}(t_i)$ the horizontal position estimated by the inertial module at time t_i,
- $d\hat{\mathbf{p}}^+(t_i)$ the inertial horizontal position error that is estimated by the Kalman filter at time t_i,
- $d\mathbf{p}(t_i)$the true inertial horizontal position error at time t_i.

Using these notations, we get:

$$\begin{aligned} \hat{\mathbf{p}}_{KF}(t_i) &= \hat{\mathbf{p}}_{IRS}(t_i) + d\hat{\mathbf{p}}^+(t_i) \\ \mathbf{p}(t_i) &= \hat{\mathbf{p}}_{IRS}(t_i) + d\mathbf{p}(t_i) \end{aligned} \qquad \text{Eq - 7-2}$$

From Eq - 7-1, the GNSS/IRS/DEM horizontal position error at time t_i is:

$$\boldsymbol{\varepsilon}_p(t_i) = \mathbf{p}(t_i) - \hat{\mathbf{p}}_{KF}(t_i) \qquad \text{Eq - 7-3}$$

Eq - 7-2 and Eq - 7-3 lead to:

$$\boldsymbol{\varepsilon}_p(t_i) = d\mathbf{p}(t_i) - d\hat{\mathbf{p}}^+(t_i) \qquad \text{Eq - 7-4}$$

From Eq - 7-4, $\boldsymbol{\varepsilon}_p(t_i)$ can be written as:

$$\boldsymbol{\varepsilon}_p(t_i) = [d\mathbf{x}(t_i)]_{1:2} - [d\hat{\mathbf{x}}^+(t_i)]_{1:2} = [d\mathbf{x}(t_i) - d\hat{\mathbf{x}}^+(t_i)]_{1:2} \qquad \text{Eq - 7-5}$$

where:

- $d\mathbf{x}(t_i)$is the true state vector at time t_i,
- $d\hat{\mathbf{x}}^+(t_i)$ is the state vector estimated by the Kalman filter at time t_i,
- $[\cdot]_{1:2}$ is the (2×1) sub-vector of vector $[\cdot]$ composed of the first two elements of $[\cdot]$.

From Eq - 7-5, and in order to investigate the theoretical impact of multipath on the horizontal GNSS/IRS position estimate error, it is proposed to assess the impact of multipath on the state vector estimate error $d\mathbf{x}(t_i) - d\hat{\mathbf{x}}^+(t_i)$. Based on the following analysis, the multipath impact on the expectation and on the covariance of the GNSS/IRS/DEM horizontal position estimate error is derived. Note that the position estimate error is Gaussian in this chapter since the measurement errors are modelled by over-bounding Gaussian distributions and since the Kalman filter is a linear filter. Hence, the position estimate error is fully characterized by a mean vector and a covariance matrix. For this reason, it is sufficient to analyze the multipath impact on the mean vector and on the covariance matrix of the position error in order to assess the multipath impact on the position error.

7.1.3. Multipath impact on the state vector estimate error

In order to analyze the multipath impact on the state vector estimate error, it is proposed to compare:

- The state vector estimate error that would have been obtained assuming that the GNSS pseudo-range measurements at any time t_i are affected by all error sources (ionosphere effects, troposphere effects, receiver noise effects, satellite clock and ephemeris inaccuracies, and multipath effects),
- The state vector estimate error that would have been obtained assuming that the GNSS pseudo-range measurements at any time t_i are only affected by the other error sources (ionosphere effects, troposphere effects, receiver noise effects and satellite clock and ephemeris inaccuracies) whilst in the absence of multipath effects.

For this analysis, we state:

- $d\hat{\mathbf{x}}^+(t_i)$ the state vector estimate at time t_i assuming that the GNSS pseudo-range measurement vector at any time t_i is:

$$\mathbf{w_o}(t_i) = \mathbf{z}(t_i) + \mathbf{b}(t_i) + \mathbf{u}(t_i) \qquad \text{Eq - 7-6}$$

  $d\hat{\mathbf{x}}^+(t_i)$ is the estimate of the true state vector $d\mathbf{x}(t_i)$. The GNSS linearized measurement model that links $d\mathbf{x}(t_i)$ to $\mathbf{w_o}(t_i)$ is:

$$d\mathbf{y}(t_i) = \mathbf{H}(t_i)d\mathbf{x}(t_i) + \mathbf{w_o}(t_i) \qquad \text{Eq - 7-7}$$

  In Eq - 7-6 and Eq - 7-7:

  - $\mathbf{z}(t_i)$ is the zero-mean stochastic GNSS measurement error vector induced by the ionosphere effects, the troposphere effects, the receiver noise effects, the satellite clock and ephemeris inaccuracies.
  - $\mathbf{b}(t_i)$ is the deterministic GNSS measurement error vector induced by multipath. As discussed in Chapter 5, $\mathbf{b}(t_i)$ is the multipath error component induced by the ground first-order interactions.
  - $\mathbf{u}(t_i)$ is the stochastic GNSS measurement error vector induced by multipath. As discussed in Chapter 5, $\mathbf{u}(t_i)$ is the multipath error component induced by the obstacles first and second-order interactions. $\mathbf{u}(t_i)$ is a zero-mean error vector.
  - $d\mathbf{y}(t_i)$ is the observation vector obtained when the GNSS measurements are affected by all error sources, including multipath.

  In Eq - 7-6, the total ranging error is assumed to be the sum of the ranging errors due to all error contributors. Eq - 7-6 is true if it is considered that the tracking loops can be approximated by linear models. This assumption is valid since the ranging errors standard

deviations of the different contributors of errors are sufficiently low regarding the parameters of the tracking loops.

- $d\hat{\mathbf{x}}^{+}_{w/o\ mp}(t_i)$ the state vector estimate at time t_i that would have been estimated by the Kalman filter if the GNSS pseudo-range measurement vector at any time t_i were only affected by the stochastic term due to the receiver noise, the satellite clock and ephemeris errors, the troposphere and the ionosphere. $d\hat{\mathbf{x}}^{+}_{w/o\ mp}(t_i)$ the state vector estimate at time t_i assuming that the GNSS pseudo-range measurement vector at any time t_i is:

$$\mathbf{w}_{o,w/o\ mp}(t_i) = \mathbf{z}(t_i) \qquad \text{Eq - 7-8}$$

$d\hat{\mathbf{x}}^{+}_{w/o\ mp}(t_i)$ is the estimate of the true state vector $d\mathbf{x}_{w/o\ mp}(t_i)$. The GNSS linearized measurement model that links $d\mathbf{x}_{w/o\ mp}(t_i)$ to $\mathbf{w}_{o,w/o\ mp}(t_i)$ is:

$$d\mathbf{y}_{w/o\ mp}(t_i) = \mathbf{H}(t_i)d\mathbf{x}_{w/o\ mp}(t_i) + \mathbf{w}_{o,w/o\ mp}(t_i) \qquad \text{Eq - 7-9}$$

In Eq - 7-9, $d\mathbf{y}_{w/o\ mp}(t_i)$ is the observation vector obtained when the GNSS measurements are affected by all error sources, excluding multipath.

Let's state the following hypotheses (*):

- At any time t_i, the GNSS measurement error vectors $\mathbf{z}(t_i), \mathbf{b}(t_i) + \mathbf{u}(t_i)$ and the process noise vector $\mathbf{w_s}(t_i)$ are independent of each other. This assumption is considered to be valid since they are due to error sources that are independent.
- The initial predictions of the covariance matrix $\mathbf{P}^{+}(t_0)$ and of the state vector $d\hat{\mathbf{x}}^{+}(t_0)$ are independent of the multipath ranging error vector $\mathbf{b}(t_i) + \mathbf{u}(t_i)$.
- The state vector $d\mathbf{x}$ is estimated by a linearized Kalman filter, meaning that the Kalman filter matrices $\mathbf{H}, \mathbf{F}$ are independent of the GNSS measurements. In addition, it is assumed that the Kalman filter contains the exact models of the transition state matrix $\mathbf{F}$ and of the design matrix $\mathbf{H}$. The potential non-linearities in the propagation model (matrix $\mathbf{F}$) are not accounted for. In other words, the horizontal position error models developed in the thesis do not consider the effects of the potential non-linearities in the propagation model implemented in the Kalman filter. This is because, for the application, the linearity of the propagation model is maintained, as justified in Section 6.1.3.
- The Kalman filter matrix $\mathbf{R}$ is independent of the GNSS multipath measurement errors.

It is demonstrated in Appendix E, Section E.1, that, under the hypotheses stated above (*), the error in the state vector estimated in the presence of multipath $d\mathbf{x}(t_i) - d\hat{\mathbf{x}}^{+}(t_i)$ and the error in the state vector that would have been estimated in the absence of multipath $\left(d\mathbf{x}(t_i) - d\hat{\mathbf{x}}^{+}_{w/o\ mp}(t_i)\right)$ can be related by:

$$d\mathbf{x}(t_i) - d\hat{\mathbf{x}}^{+}(t_i) = \left(d\mathbf{x}(t_i) - d\hat{\mathbf{x}}^{+}_{w/o\ mp}(t_i)\right) + \boldsymbol{\phi}(t_i) \qquad \text{Eq - 7-10}$$

where $\boldsymbol{\phi}(t_i)$ represents the impact of the multipath on the error in the state vector estimate error at time t_i and can be expressed as:

$$\boldsymbol{\phi}(t_i) = \left(\mathrm{I} - \mathbf{K}(t_i)\mathbf{H}(t_i)\right)\mathbf{F}(t_{i-1})\boldsymbol{\phi}(t_{i-1}) - \mathbf{K}(t_i)\left(\mathbf{b}(t_i) + \mathbf{u}(t_i)\right) \qquad \text{Eq - 7-11}$$

where $\boldsymbol{\phi}(t_0) = \mathbf{0}$. From Eq - 7-11, the impact of the multipath on the state vector estimate error at time t_i is due to:

- The propagation of the multipath error from time t_{i-1} to time t_i. This propagation is represented by the first term of the right part of Eq - 7-11.
- The multipath error vectors at time t_i. This impact is represented by the second term of the right part of Eq - 7-11.

In this section, the theoretical impact of multipath on the state vector estimate error has been analyzed. In the next section, this analysis is re-used to assess the theoretical impact of multipath on the expectation of the GNSS/IRS/DEM horizontal position estimate error.

7.1.4. Multipath impact on the expectation of the position error

From Eq - 7-5, the GNSS/IRS horizontal position error at time t_i can be expressed as:

$$\boldsymbol{\varepsilon}_p(t_i) = [d\mathbf{x}(t_i) - d\hat{\mathbf{x}}^+(t_i)]_{\mathbf{1:2}} \qquad \text{Eq - 7-12}$$

Let's compute the expectation of the GNSS/IRS horizontal position error at time t_i:

$$E\left[\boldsymbol{\varepsilon}_p(t_i)\right] = E[d\mathbf{x}(t_i) - d\hat{\mathbf{x}}^+(t_i)]_{1:2} \qquad \text{Eq - 7-13}$$

From Eq - 7-10 we get:

$$E\left[\boldsymbol{\varepsilon}_p(t_i)\right] = E\left[\left(d\mathbf{x}(t_i) - d\hat{\mathbf{x}}^+{}_{w/o\,mp}(t_i)\right) + \boldsymbol{\phi}(t_i)\right]_{1:2} \qquad \text{Eq - 7-14}$$

At any time t_i, the GNSS measurement error vectors $\mathbf{z}(t_i), \mathbf{u}(t_i)$ and the process noise vector $\mathbf{w_s}(t_i)$ are zero-mean stochastic error vectors. It is demonstrated in Appendix E, Section E-2, that, under this assumption, and using Eq – 7-10, the expectation of the GNSS/IRS/DEM horizontal position error at time t_i is:

$$\begin{aligned} E\left[\boldsymbol{\varepsilon}_p(t_i)\right] &= \left[E[\boldsymbol{\phi}(t_i)]\right]_{1:2} \\ &= \left[\left(I - \mathbf{K}(t_i)\mathbf{H}(t_i)\right)\mathbf{F}(t_{i-1})E[\boldsymbol{\phi}(t_{i-1})] - \mathbf{K}(t_i)\mathbf{b}(t_i)\right]_{1:2} \end{aligned} \qquad \text{Eq - 7-15}$$

where $E[\boldsymbol{\phi}(t_0)] = \mathbf{0}$. Note that, if the following matrices or vectors are known at any time t_k, $t_k \leq t_i$:

- The Kalman filter matrices $\mathbf{K}(t_k)$, $\mathbf{H}(t_k)$ and $\mathbf{F}(t_{k-1})$,
- The deterministic multipath ranging error $\mathbf{b}(t_k)$,

then it is possible to predict the expectation of the GNSS/IRS/DEM horizontal position error at time t_i by means of Eq - 7-15. From Eq - 7-15, the expectation of the GNSS/IRS/DEM horizontal position error at time t_i is due to:

- The propagation of expectation of the GNSS/IRS/DEM horizontal position error from time t_{i-1} to time t_i. This propagation is represented by the first term of the right part of Eq - 7-15.
- The deterministic multipath ranging error vector $\mathbf{b}(t_i)$ at time t_i. This impact is represented by the second term of the right part of Eq - 7-15.

In this section, the theoretical impact of multipath on the expectation of the GNSS/IRS/DEM horizontal position estimate error has been analyzed. In the next section, the theoretical impact of multipath on the covariance of the GNSS/IRS/DEM horizontal position estimate error is assessed.

7.1.5. Multipath impact on the covariance of the position error

From Eq – 7-5, the GNSS/IRS horizontal position error at time t_i can be expressed as:

$$\boldsymbol{\varepsilon}_p(t_i) = [d\mathbf{x}(t_i) - d\hat{\mathbf{x}}^+(t_i)]_{\mathbf{1:2}} \quad \text{Eq - 7-16}$$

Let's compute the covariance of the GNSS/IRS horizontal position error at time t_i:

$$\text{cov}\left[\boldsymbol{\varepsilon}_p(t_i)\right] = \text{cov}[d\mathbf{x}(t_i) - d\hat{\mathbf{x}}^+(t_i)]_{1:2} \quad \text{Eq - 7-17}$$

From Eq - 7-8 we obtain:

$$\text{cov}\left[\boldsymbol{\varepsilon}_p(t_i)\right] = \text{cov}\left[\left(d\mathbf{x}(t_i) - d\hat{\mathbf{x}}^+_{\text{w/o mp}}(t_i)\right) + \boldsymbol{\phi}(t_i)\right]_{1:2} \quad \text{Eq - 7-18}$$

From Chapter 5, the correlated process $\mathbf{u}(t_i)$ can be modeled as zero-mean first-order Gauss-Markov process. From Eq – 3-14, $\mathbf{u}(t_i)$ can be expressed as:

$$\mathbf{u}(t_i) = \begin{bmatrix} u_{\text{sat }1}(t_i) \\ \vdots \\ u_{\text{sat N}}(t_i) \end{bmatrix} = \underbrace{\begin{bmatrix} e^{-\frac{T_e}{\tau_{\text{dyn }1}(t_i)}} & 0 & 0 \\ 0 & \ddots & 0 \\ 0 & 0 & e^{-\frac{T_e}{\tau_{\text{dyn N}}(t_i)}} \end{bmatrix}}_{\mathbf{C}(t_i)} \underbrace{\begin{bmatrix} u_{\text{sat }1}(t_{i-1}) \\ \vdots \\ u_{\text{sat N}}(t_{i-1}) \end{bmatrix}}_{\mathbf{u}(t_{i-1})} + \underbrace{\begin{bmatrix} \eta_{\text{sat }1}(t_i) \\ \vdots \\ \eta_{\text{sat N}}(t_i) \end{bmatrix}}_{\boldsymbol{\eta}(t_i)} \quad \text{Eq - 7-19}$$

where:

- T_e is the sampling period of the GNSS pseudo-range measurements at the Kalman filter input.
- $\tau_{\text{dyn j}}(t_i)$ and $\sigma_{\text{dyn j}}(t_i)$ are the correlation time and the standard deviation associated with the Gauss-Markov process that models the multipath ranging error on satellite j at time t_i. Let's denote $R_{mp}(t_i)$ the covariance matrix of the stochastic multipath ranging error vector $\mathbf{u}(t_i)$:

$$\mathbf{R}_{mp}(t_i) = \begin{bmatrix} \sigma_{\text{dyn }1}(t_i)^2 & 0 & 0 \\ 0 & \ddots & 0 \\ 0 & 0 & \sigma_{\text{dyn N}}(t_i)^2 \end{bmatrix} \quad \text{Eq - 7-20}$$

It is demonstrated in Appendix E, Section E-3, that, if $\mathbf{u}(t_i)$ can be modeled as zero-mean first-order Gauss-Markov process, and under the assumptions stated above (*), the covariance of the GNSS/IRS horizontal position error at time t_i is:

$$\text{cov}\left[\boldsymbol{\varepsilon}_p(t_i)\right] = \mathbf{C}_{p,\text{w/o mp}}(t_i) + \mathbf{C}_{p,mp}(t_i) \quad \text{Eq - 7-21}$$

where:

- $\mathbf{C}_{p,\text{w/o mp}}(t_i) = \text{cov}\left[d\mathbf{x}(t_i) - d\hat{\mathbf{x}}^+_{\text{w/o mp}}(t_i)\right]_{1:2,1:2}$ represents the covariance matrix of the GNSS/IRS/DEM horizontal position estimate error at time t_i in the absence of multipath affecting the GNSS pseudo-range measurements.
- $[\cdot]_{1:2,1:2}$ represents the (2×2) sub-matrix of $[\cdot]$ composed of the first two lines and of the first two columns of $[\cdot]$.

- $\mathbf{C}_{p,mp}(t_i) = \text{cov}[\boldsymbol{\phi}(t_i)]_{1:2,1:2}$ represents the increase of the covariance of the GNSS/IRS/DEM horizontal position estimate error induced by the presence of multipath stochastic ranging errors on the GNSS pseudo-range measurements:

$$\begin{aligned}\mathbf{C}_{p,mp}(t_i) = \text{cov}[\boldsymbol{\phi}(t_i)]_{1:2,1:2} = [&\mathbf{A}(t_i)\text{cov}[\boldsymbol{\phi}(t_{i-1})]\mathbf{A}(t_i)^T \\ &+\mathbf{K}(t_i)\mathbf{R}_{mp}(t_i)\mathbf{K}(t_i)^T \\ &-\mathbf{A}(t_i)\text{E}[\boldsymbol{\phi}(t_{i-1})\mathbf{u}^T(t_{i-1})]\mathbf{C}^T(t_i)\mathbf{K}^T(t_i) \\ &-\left(\mathbf{A}(t_i)\text{E}[\boldsymbol{\phi}(t_{i-1})\mathbf{u}^T(t_{i-1})]\mathbf{C}^T(t_i)\mathbf{K}^T(t_i)\right)^T]_{1:2,1:2}\end{aligned} \quad \text{Eq - 7-22}$$

where:

- $\mathbf{A}(t_i) = \left(I - \mathbf{K}(t_i)\mathbf{H}(t_i)\right)\mathbf{F}(t_{i-1})$
- $\mathbf{R_{mp}}(t_i)$ and $\mathbf{C}(t_i)$ are detailed in Eq - 7-19,
- $\text{cov}[\boldsymbol{\phi}(t_0)] = \mathbf{0}$
- $\text{E}[\boldsymbol{\phi}(t_{i-1})\mathbf{u}(t_{i-1})^T]$ can be expressed as :

$$\text{E}[\boldsymbol{\phi}(t_{i-1})\mathbf{u}(t_{i-1})^T] = \mathbf{A}(t_{i-1})\text{E}[\boldsymbol{\phi}(t_{i-2})\mathbf{u}(t_{i-2})^T]\mathbf{C}(t_{i-1})^T - \mathbf{K}(t_{i-1})\mathbf{R}_{mp}(t_{i-1}) \quad \text{Eq - 7-23}$$

where $\text{E}[\boldsymbol{\phi}(t_0)\mathbf{u}(t_0)^T] = \mathbf{0}$.

Note that, if the following matrices or vectors are known at any time t_k, $t_k \leq t_i$:

- The Kalman filter matrices $\mathbf{K}(t_k)$, $\mathbf{H}(t_k)$ and $\mathbf{F}(t_{k-1})$,
- The covariance matrix of the stochastic multipath ranging error vector $\mathbf{R}_{mp}(t_k)$ and the correlation time matrix of the stochastic multipath ranging error vector $\mathbf{C}(t_k)$,

then it is possible to predict the term $\mathbf{C}_{p,mp}(t_i)$. From Eq - 7-22, the covariance of the GNSS/IRS/DEM horizontal position error at time t_i is due to:

- The propagation of the covariance matrix induced by multipath from time t_{i-1} to time t_i. This propagation is represented by the first term of the right part of Eq - 7-22.
- The covariance matrix of the stochastic multipath ranging errors at time t_i. This impact is represented by the second term of the right part of Eq - 7-22.
- The time correlation of the stochastic multipath ranging errors at time t_i. This impact is represented by the last two terms of the right part of Eq - 7-22.

7.2. Quantification of the multipath impact on the position error

One of the objectives of this thesis is to identify the GNSS multipath ranging failures, which are the multipath ranging errors that may lead to a horizontal position error larger than the HAL for the guidance function under low visibility conditions. For this identification, it is firstly required to quantify the impact of the GNSS multipath ranging errors on the horizontal position error.

This section provides a quantitative analysis of the horizontal position bias $\text{E}[\boldsymbol{\varepsilon}_p(t_i)]$ induced by multipath and of the covariance increase of the horizontal position error $\mathbf{C}_{p,mp}(t_i)$ induced by multipath.

7.2.1. Multipath impact on the expectation of the position error

This section is organized as follows. The simulation scenario used to quantify the position bias $\text{E}[\boldsymbol{\varepsilon}_p(t_i)]$ is presented in Section 7.2.1.1. Next, the deterministic GNSS multipath ranging error vector $\mathbf{b}(t_i)$ inducing the position bias $\text{E}[\boldsymbol{\varepsilon}_p(t_i)]$ throughout the simulated trajectory is

presented in Section 7.2.1.2. Finally, the deterministic GNSS multipath ranging errors and the position bias $E[\boldsymbol{\varepsilon}_p(t_i)]$ are quantified throughout the simulated trajectory in Section 7.2.1.3.

7.2.1.1. Simulation scenario

The expectation of the horizontal position error induced by the GNSS multipath ranging biases is evaluated using the following simulation scenario. An aircraft arrives at Toulouse Blagnac airport, France. The followed procedure is the LVP path that is fully described in Section 5.2.1. The considered LVP path is depicted in Figure 7-2.

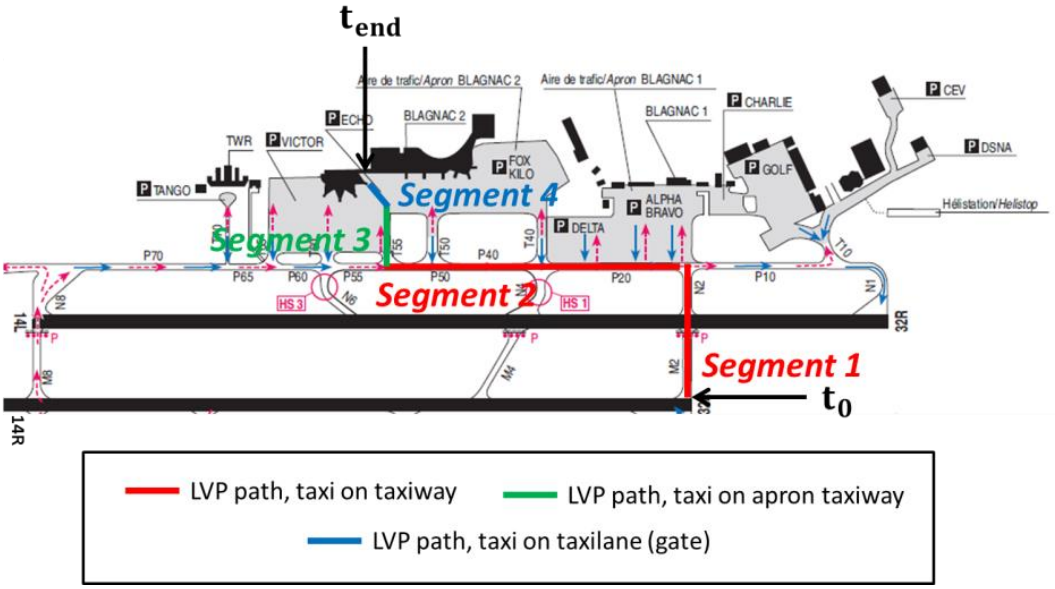

Figure 7-2: LVP path at Toulouse Blagnac airport, France

The LVP path consists in four segments.

- Segment 1 and 2 that correspond to the *taxi on taxiway* sub-phase.
- Segment 3 that corresponds to the *taxi on apron taxiway* sub-phase.
- Segment 4 that corresponds to the *taxi on taxi lane* sub-phase.

In this scenario, the aircraft is moving on segments 1, 2, 3 and 4. The case where the aircraft stops during the operation is not considered. The speed of the aircraft along each segment is constant and is indicated in Table 7-1. The aircraft velocity may change during turns. The velocity variation during turns follows the shape of a raised cosine function, as detailed in Section 6.2.1.

	Taxi on taxiway	***Taxi on apron taxiway***	***Taxi on taxi lane***
	Segments 1 and 2	**Segment 3**	**Segment 4**
Typical aircraft speed [RTCA, 1999]	$5 - 26\ \mathrm{m.s^{-1}}$	$0 - 5\ \mathrm{m.s^{-1}}$	$0 - 5\ \mathrm{m.s^{-1}}$
Aircraft speed used for the simulation	$10\ \mathrm{m.s^{-1}}$	$2\ \mathrm{m.s^{-1}}$	$2\ \mathrm{m.s^{-1}}$

Table 7-1: Taxi speeds used along the LVP path

Denoting t_0 the epoch time when the operation begins, that is to say when the aircraft starts to move on segment 1 after having left the runway. As justified in Section 5.1.2.1, the satellite geometry is considered to be frozen during the taxi operation. Hence, from time instant t_0 until the moment the aircraft reaches the arrival gate t_{end}, the satellite positions are considered to be stationary. Both t_0 and t_{end} are indicated in Figure 7-2.

In order to quantify $E[\boldsymbol{\varepsilon}_p(t_i)]$ for each time epoch $t_i \in [t_0, t_{end}]$ of the trajectory, the LVP trajectory is simulated by the trajectory simulator presented in Section 6.2.1. Next, a particular satellite geometry indicated by time epoch t_0 is considered and the position error simulator presented in Section 6.2 is used to simulate the Kalman filter matrices $\mathbf{K}(t_i)$, $\mathbf{H}(t_i)$ and $\mathbf{F}(t_{i-1})$ at each time epoch t_i of the simulated trajectory. The deterministic multipath ranging error vector $\mathbf{b}(t_i)$ is computed for each time epoch $t_i \in [t_0, t_{end}]$ using the error models developed in Section 7.2.1.2. Finally, the horizontal position bias $E[\boldsymbol{\varepsilon}_p(t_i)]$ is computed for each time epoch t_i using the model established in Section 7.1.4. Note that, in the following, the 2D position bias $E[\boldsymbol{\varepsilon}_p(t_i)]$ in the horizontal domain induced by the deterministic multipath ranging errors in the dynamic configuration is denoted as $\mathbf{b}_{p,mp}(t_i)$.

The next section reminds the models of the GNSS deterministic multipath ranging error vectors $\mathbf{b}(t_i)$ in both static and dynamic configurations.

7.2.1.2. GNSS multipath ranging error models

As established in Section 5.5.1 and in Appendix A, Section A.5, the multipath ranging errors that affects the GNSS pseudo-range measurement related to satellite j at time $t_i \in [t_0, t_{end}]$ throughout the LVP trajectory is:

$$\varepsilon_{mp\,j}(t_i) = b_{AC+ground}\left(El_j(t_0), Az_{air\,j}(t_i)\right) + u_{obs\,j}(t_i) \qquad \text{Eq - 7-24}$$

where:

- $u_{obs\,j}(t_i)$ is the stochastic multipath ranging error,
- $b_{AC+ground}\left(El_j(t_0), Az_{air\,j}(t_i)\right)$ is a deterministic multipath ranging error.
- $El_j(t_0)$ is the satellite j elevation angle along the trajectory. El_j is considered to be constant throughout the trajectory,
- $Az_{air\,j}(t_i)$ is the aircraft azimuth angle with respect to the satellite j at time t_i. Note that the angle $Az_{air\,j}$ is defined in Section 5.1.2.2.3.1.

Let's denote N the number of GNSS measurements used in the Kalman filter to estimate the PVT solution at time t_i. The deterministic GNSS multipath ranging error vector $\mathbf{b}(t_i)$ at time t_i in the dynamic configuration is:

$$\forall\, t_i \in [t_0, t_{end}], \mathbf{b}(t_i) = \begin{bmatrix} b_{AC+ground}\left(El_1(t_0), Az_{air\,1}(t_i)\right) \\ \vdots \\ b_{AC+ground}\left(El_N(t_0), Az_{air\,N}(t_i)\right) \end{bmatrix} \qquad \text{Eq - 7-25}$$

7.2.1.3. Simulation results

GNSS deterministic multipath ranging errors

This sub-section illustrates the evolution of the GNSS deterministic multipath ranging error vector $\mathbf{b}(t_i)$ in the time interval $[t_0, t_{end}]$ throughout the LVP trajectory presented in Section 7.2.1.1.

For this illustration, the evolution of the aircraft azimuth angle $Az_{air\,j}(t_i)$ and of the deterministic multipath ranging error $b_{AC+ground}\left(El_j(t_0), Az_{air\,j}(t_i)\right)$ throughout the simulated trajectory is shown in Figure 7-3 for two satellites: a Galileo satellite identified by PRN 62 and a GPS satellite identified by PRN 4. Both PRN 4 and PRN 62 satellites are visible satellites for the considered satellite geometry and are used in the Kalman filter to estimate the PVT solution throughout the whole LVP trajectory. Both satellite elevation angle and satellite azimuth angle are indicated in Table 7-2.

	Satellite elevation angle El	**Satellite azimuth angle Az_{sat}**
PRN 4 satellite	$34.98°$	$-47.78°$
PRN 62 satellite	$10.15°$	$-27.33°$

Table 7-2: Satellite elevation and azimuth angles for PRN 4 and PRN 62 satellites

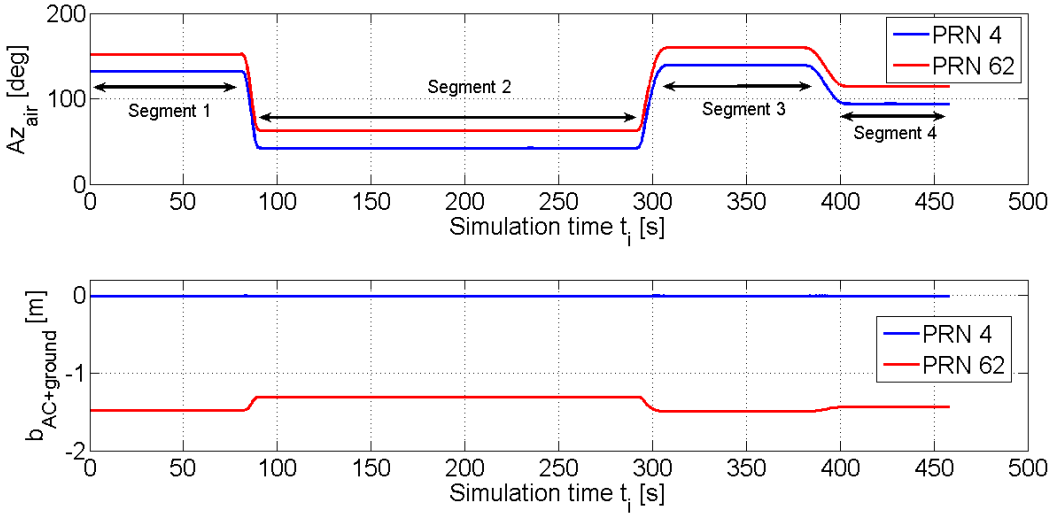

Figure 7-3: Aircraft azimuth angle and of the multipath ranging error $b_{AC+ground}$ for PRN 4 and PRN 62 satellites

As expected from Section 5.4.1.2, the GNSS multipath ranging error $b_{AC+ground}$ induced by the aircraft structure and by the airport surface is roughly zero for PRN 4 since the satellite elevation angle related to this satellite is relatively high, that is to say almost 35°. The magnitude of the GNSS multipath ranging error $b_{AC+ground}$ for PRN 62 is much higher, that is to say roughly -1.5m, since the satellite elevation angle related to PRN 62 is roughly 10°. The value of $b_{AC+ground}$ varies by a few decimeters when the direction of the aircraft fuselage characterized by the angle Az_{air} changes in the airport scene.

Horizontal position bias

The evolution of the position bias $\mathbf{b}_{p,mp}(t_i)$ induced by the deterministic multipath ranging error vector $\mathbf{b}(t_i)$ throughout the LVP trajectory is detailed in this sub-section. For this presentation, the evolution of the North $\mathbf{b}_{p,mp,N}(t_i)$ and East $\mathbf{b}_{p,mp,E}(t_i)$ components of $\mathbf{b}_{p,mp}(t_i)$ throughout the simulated trajectory is shown in Figure 7-4 for the considered satellite geometry.

The evolution of $\mathbf{b}_{p,mp}(t_i)$ is computed in two configurations (configurations 1 and 2) characterized by different elevation mask angles. The elevation mask angles for each configuration are provided in Table 7-3. Table 7-3 also indicates the number of satellites used in the Kalman filter to estimate the position solution. In both configurations, and for the considered satellite geometry, simulations have shown that this number of satellites is fixed throughout the trajectory.

	Elevation mask angle GPS constellation	**Elevation mask angle Galileo constellation**	**Number of satellites used to estimate the position**
Configuration 1	5° [RTCA, 2006]	10° [EUROCAE, 2010]	15
Configuration 2	15°	15°	12

Table 7-3: Elevation mask angles for configurations 1 and 2

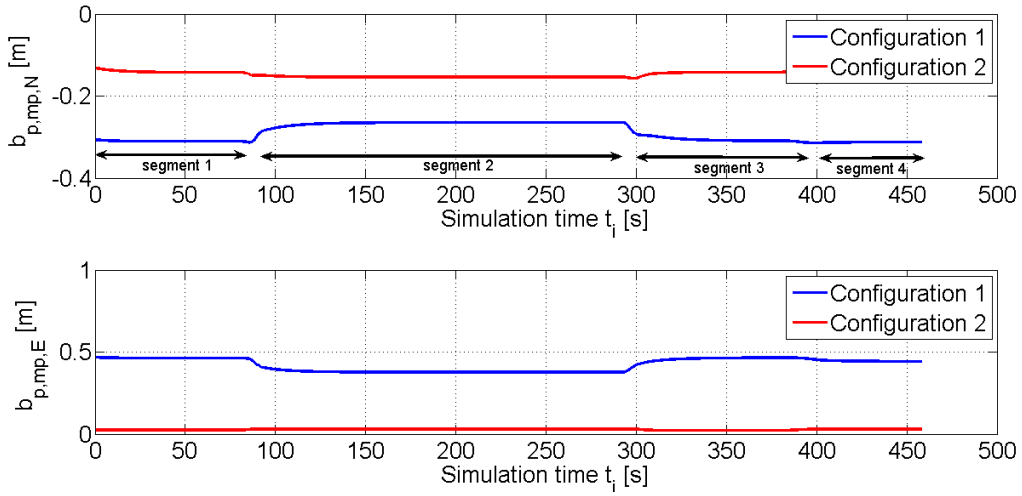

Figure 7-4: Expectation of the horizontal position error $\mathbf{b}_{p,mp}$

In configuration 1, three satellites used throughout the trajectory to estimate the PVT solution have a satellite elevation below 15°. From Section 5.4.1.2, the GNSS multipath ranging errors $b_{AC+ground}$ that affect the pseudo-range measurements associated to low elevation satellites are characterized by high amplitudes (several decimeters). These high amplitude ranging errors $b_{AC+ground}$ induce relatively high horizontal position biases in both North and East directions. The position biases are of the order of few decimeters in the North and East directions.

In configuration 2, the satellites characterized by an elevation below 15° are not used in the estimation of the PVT solution, reducing the number of satellites used by the Kalman filter from 15 for configuration 1 to 12 for configuration 2. These high amplitude ranging errors $b_{AC+ground}$ do not impact anymore the horizontal position biases in both North and East directions. The position biases are of the order of a few centimeters in the North and East directions.

In configurations 1 and 2, the horizontal position biases in both North and East directions vary by a few centimeters throughout the simulated trajectory. This is due to the variations of the aircraft azimuth angles Az_{air} throughout the trajectory that induces variations of the

deterministic ranging errors $b_{AC+ground}$ due to the multipath from the aircraft structure and the airport surface.

7.2.2. Multipath impact on the covariance of the position error

It has been underlined in Chapter 5 that, in the dynamic configuration, and when the GNSS airborne antenna is in the impact zone related to satellite j at time epoch t_i, the GNSS pseudo-range measurement from the GNSS airborne antenna to the satellite j is affected by the sum of:

- a GNSS ranging error $u_{obs\,j}(t_i)$ induced by the airport obstacles,
- a GNSS multipath deterministic error $b_{AC+ground}\left(El_j(t_0), Az_{air\,j}(t_i)\right)$ induced by the aircraft structure and the airport surface.

In this document, the impact zone is defined as the horizontal area of the airport located at $h_{ant} = 5.88m$ above the ground where the amplitude variations of the multipath error $u_{obs\,j}$ around the multipath bias $b_{AC+ground}$ are higher than 1cm. Since the true trajectory of the airborne antenna around the procedure path in the impact zone is considered as a random parameter, and since the error term $u_{obs\,j}$ depends on this parameter, $u_{obs\,j}(t_i)$ has been modelled by a stochastic correlated process. This process is a zero-mean first-order Gauss-Markov process $\mathcal{M}(\tau_{dyn\,j}, \sigma_{dyn\,j})$ characterized by a correlation time $\tau_{dyn\,j}$ and a standard deviation $\sigma_{dyn\,j}$. The GNSS multipath stochastic error $u_{obs\,j}$ induces an increase of the position error covariance matrix assessed in this section. This section provides a quantitative analysis of the augmentation of the covariance of the horizontal position error $\mathbf{C}_{p,mp}$ induced by the GNSS stochastic multipath ranging errors during airport surface operations.

7.2.2.1. Simulation scenario

In order to quantify the term $\mathbf{C}_{p,mp}(t_i)$ induced by the GNSS stochastic multipath ranging errors, the simulation scenario described in Section 7.2.1.1 is considered. The stochastic multipath ranging error vector $\mathbf{u}(t_i)$ is computed for each time epoch t_i using the error models developed in Section 7.2.2.2. Finally, the augmentation of the covariance of the horizontal position error $\mathbf{C}_{p,mp}(t_i)$ induced by the GNSS stochastic multipath ranging errors is computed for each time epoch t_i using the model established in Section 7.1.4.

The next section reminds the models of the GNSS stochastic multipath ranging error vectors $\mathbf{u}(t_i)$ in the dynamic configuration.

7.2.2.2. GNSS multipath ranging error models

By keeping the same notations as in Section 7.2.1.1, denote t_0 and t_{end} the initial and final instants of the trajectory, respectively. In the time interval $[t_0; t_{end}]$, the multipath ranging errors that affect the GNSS pseudo-range measurement related to satellite j at time t_i is:

$$\varepsilon_{mp\,j}(t_i) = b_{AC+ground}\left(El_j(t_0), Az_{air\,j}(t_i)\right) + u_{obs\,j}(t_i) \qquad \text{Eq - 7-26}$$

where:

- $b_{AC+ground}$ is a deterministic multipath ranging error.
- $u_{obs\,j}(t_i)$ is the stochastic multipath ranging error. The model of $u_{obs\,j}(t_i)$ is developed in this section.

As explained in Chapter 5, $u_{obs\,j}$ represents the oscillations of the multipath ranging error $\varepsilon_{mp,sat\,j}$ around the multipath ranging deterministic error $b_{AC+ground}$ induced by multipath from the aircraft structure and by the airport surface. Two cases can be distinguished:

- If the GNSS airborne antenna is outside the impact zone related to satellite j at time epoch t_i, the ranging error $\varepsilon_{mp\,j}$ is equal to the deterministic ranging error induced by the aircraft structure and by the airport surface.
- If the GNSS airborne antenna is inside the impact zone related to satellite j at time epoch t_i, the correlated process $u_{obs\,j}(t_i)$ can be over bounded by a first-order Gauss Markov process characterized by a standard deviation $\sigma_{dyn\,j}$ and by a correlation time $\tau_{dyn\,j}$.

An important remark is that this project aims to quantify the impact of a single multipath ranging error induced by the airport surface, the aircraft structure, and the airport obstacles. For this reason, it is assumed in this part that only one satellite is affected by multipath from the airport obstacles. The quantification of the covariance of the horizontal position error in the presence of multipath ranging errors induced by the airport obstacles on multiple satellites at the same time remains as future work.

A preliminary analysis shows that, for the considered satellite geometry, when the elevation mask is set to 5° for GPS and 10° for Galileo, and when the aircraft is on segment 3, the GNSS airborne antenna is in the impact zone related to satellite PRN 62. Let's note Z the point on segment 3 where the GNSS airborne antenna enters in the impact zone related to satellite PRN 62. The coordinates of point Z have been determined by means of the methodology established in Section 5.4.2.1. Let's note t_Z the epoch time for which the airborne antenna reaches point Z.

Both satellite elevation angle and satellite azimuth angle of PRN 62 are indicated in Table 7-4. The methodology presented in Section 5.5.2.4 is re-used to compute the standard deviation σ_{dyn62} and correlation time τ_{dyn62} that characterize the Gauss-Markov process that over-bounds the correlated process $u_{obs\,62}(t_i)$ in the impact zone and along segment 3. The obtained values of $\sigma_{dyn\,62}$ and $\tau_{dyn\,62}$ are indicated in in Table 7-4.

	Satellite elevation angle El_{62}	**Satellite azimuth angle Az_{62}**	**$\sigma_{dyn\,62}$**	**$\tau_{dyn\,62}$**
PRN 62 satellite	10.15°	−27.33°	19.5cm	10.0ms

Table 7-4: Characteristics of the Gauss-Markov process for PRN 62 satellite

As explained above, it is assumed that, on segment 3, and from epoch time t_Z, PRN 62 is the only satellite affected by multipath from the airport obstacles. The GNSS multipath ranging errors on the other satellites are assumed to be due to the aircraft structure and to the airport surface. In the simulation, $\mathbf{u}(t_i)$ can thus be modelled as follows:

$$\forall t_i \in [t_k; t_Z[, \mathbf{u}(t_i) = \begin{bmatrix} 0 \\ \vdots \\ 0 \\ \vdots \\ 0 \end{bmatrix} \text{ and } \forall t_i \in \left[t_Z; t_{end,seg3}\right], \mathbf{u}(t_i) = \begin{bmatrix} 0 \\ \vdots \\ u_{obs\,62}(t_i) \\ \vdots \\ 0 \end{bmatrix} \qquad \text{Eq - 7-27}$$

where:

- $\mathbf{u}(t_i)$ is a (15x1) vector since, when the elevation mask is set to 5° for GPS and 10° for Galileo, Section 7.2.1 reveals that the number of satellites used in the PVT solution estimation is constant throughout the LVP procedure and is 15 satellites.
- $u_{sat\,62}(t_i)$ is modelled as a first-order Gauss Markov process characterized by a standard deviation $\sigma_{dyn\,62} = 19.5\text{cm}$ and by a correlation time $\tau_{dyn\,62} = 10.0\text{ms}$.
- $t_{end,seg3}$ is the epoch time for which the aircraft reaches segment 4.

The covariance term $\mathbf{C}_{p,mp}$ of the horizontal position error induced by the GNSS stochastic multipath ranging error $u_{obs\,62}$ is analyzed in the next section.

7.2.2.3. Simulation results

Temporal evolution of $\mathbf{C_{p,mp}(t_i)}$

The evolution of the horizontal position error covariance induced by multipath $\mathbf{C}_{p,mp}(t_i)$ along the segment 3 is presented in this section. For this analysis, the evolution of the standard deviations of the North and East position errors induced by multipath is shown in Figure 7-5. The variance of the position error induced by multipath in the North and East directions at time t_i are denoted as $C_{p,mp,N}(t_i)$ and $C_{p,mp,E}(t_i)$, respectively.

$C_{p,mp,N}(t_i)$ and $C_{p,mp,E}(t_i)$ are related to $\mathbf{C}_{p,mp}(t_i)$ as follows:

$$\mathbf{C}_{p,mp}(t_i) = \begin{bmatrix} C_{p,mp,N}(t_i) & C_{p,mp,E-N}(t_i) \\ C_{p,mp,E-N}(t_i) & C_{p,mp,E}(t_i) \end{bmatrix} \qquad \text{Eq - 7-28}$$

where $C_{p,mp,E-N}(t_i)$is the cross-covariance of the position errors in the North and East directions.

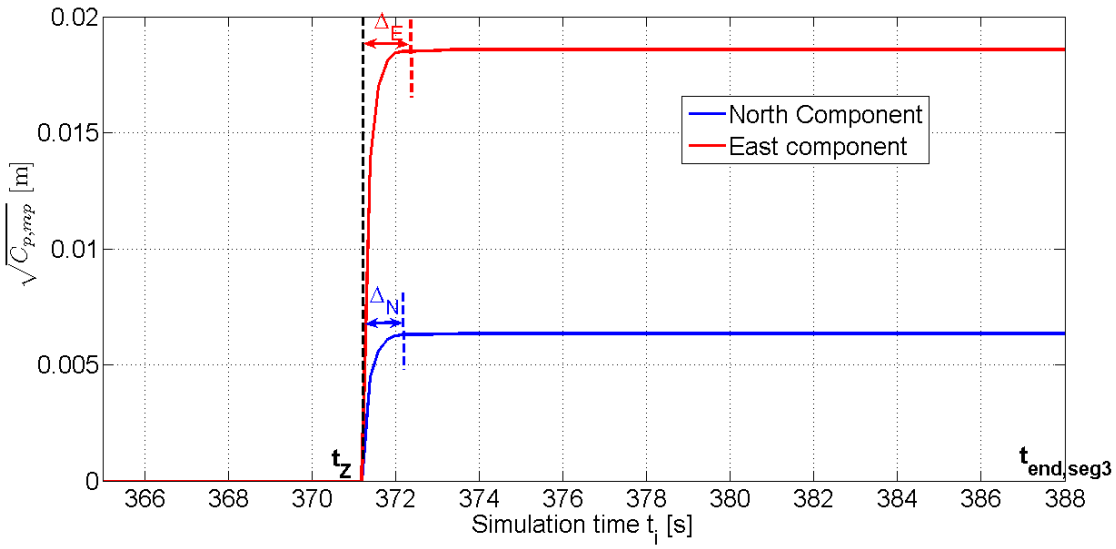

Figure 7-5 : Standard deviations of the North and East position errors induced by the multipath stochastic ranging error on PRN 62

As depicted in Figure 7-5, the error variances in the North and East directions converge to a final constant value after a transient state that follows the apparition of the stochastic ranging error on the PRN 62 satellite. The evolution of the terms $C_{p,mp,N}$ and $C_{p,mp,E}$ in the time domain are interpreted as follows. From Eq - 7-22, $\mathbf{C}_{p,mp}(t_i)$ can be considered as the

response of an equivalent filter to the stochastic multipath ranging error vector $\mathbf{u}(t_i)$. The coefficients of the equivalent filter depend on the Kalman matrices $\mathbf{K}, \mathbf{H}$ and $\mathbf{F}$. During the considered trajectory, the coefficients of the equivalent filter remain roughly constant. There are three reasons for this.

- Firstly, the GNSS satellites are considered to be stationary during the operation and the impact of the multipath on the C/N0 of the GNSS signals used in the PVT solution is not taken into account. Hence, the satellite elevation angles and the C/N0 ratios are roughly constant over the trajectory. Hence, the predicted covariance of the GNSS measurement errors **R** is roughly constant throughout the trajectory.
- Secondly, due to the relatively low dynamic of the aircraft throughout the trajectory, the design matrix **H** and the state transition matrix **F** are roughly constant throughout the trajectory.
- Thirdly, the Kalman filter is assumed to have converged at the epoch at which the *taxi on taxiway* operation starts. Hence, and from the two previous remarks, the Kalman gain matrix **K** is roughly constant throughout the trajectory.

Hence, the error variances in the North and East directions converge to constant values. Moreover, the convergence time lasts roughly several tens of milliseconds. As an example, Table 7-5 provides the 99% response time of the filter observed in Figure 7-5.

99% response time, North direction: Δ_N	**99% response time, East direction: Δ_E**
80ms	90ms

Table 7-5: 99% response time related to the the position error variances

This transient time highly depends on the expected values of the raw code pseudo range measurement errors standard deviations that are given to the Kalman filter. In the simulation, the expected standard deviation of the GNSS measurement errors is dominated by the expected standard deviation of the ranging error induced by inaccuracies in the satellite clock corrections and in the ephemeris, which is relatively high at 85cm. The Kalman filter mainly "relies on" the dynamic model, the Kalman gain is thus relatively low, and the transient period is thus relatively short.

Sensitivity of $\mathbf{C}_{p,mp}(t_i)$ to the characteristics of the stochastic multipath ranging error

The influence of the characteristics of the stochastic multipath ranging error $(\sigma_{dyn\,62}, \tau_{dyn\,62})$ on the covariance of the horizontal position error covariance induced by multipath $\mathbf{C}_{p,mp}(t_i)$ is presented in this section. In Chapter 5, a value of $\tau_{dyn} = 10.0\text{ms}$ has been adopted to model the stochastic multipath ranging errors along segments 3 and 4, regardless of the satellite position and of the aircraft speed in the impact zone. However, it is mentioned in Section 5.5.2.4 that the choice of the first-order Gauss-Markov model parameters $(\sigma_{dyn}, \tau_{dyn})$ can be refined. In this case, the value of τ_{dyn} will depend on the satellite position and on the aircraft speed in the impact zone. Hence, even if the value of τ_{dyn} is fixed in the simulation results proposed in Chapter 5, it is proposed in this section to investigate the impact of $\tau_{dyn\,62}$ on $\mathbf{C}_{p,mp}(t_i)$.

It has been shown in the last subsection that the components of $\mathbf{C}_{p,mp}(t_i)$ converge to constant values in steady state after the apparition of the stochastic multipath ranging error on PRN 62. The evolution of the steady state values of $\mathbf{C}_{p,mp}(t_i)$ as a function of $\sigma_{dyn\,62}$ and for a fixed $\tau_{dyn\,62} = 10.0\text{ms}$ is depicted in Figure 7-6. Note that, in this Figure, $\sigma_{dyn\,62}$ varies

between 0m and 5m. Indeed, it has been established in Chapter 5 that the values of σ_{dyn62} may reach several meters.

As depicted in Figure 7-6, for a fixed $\tau_{dyn\ 62} = 10.0$ms, the steady state standard deviations of the North and East position errors induced by multipath increase quasi linearly with respect to the standard deviation of the stochastic multipath ranging error on PRN 62 $\sigma_{dyn\ 62}$. The standard deviations of the position errors are up to few centimeters when $\sigma_{dyn\ 62}$ is below 1m. The standard deviations of the position errors are up to few decimeters when $\sigma_{dyn\ 62}$ reaches few meters.

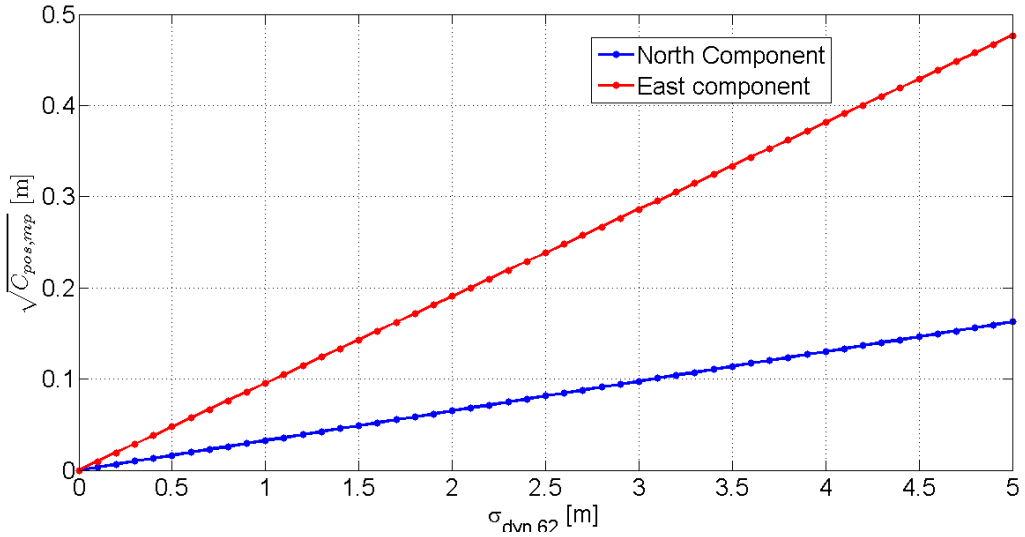

Figure 7-6: Steady state standard deviations of position errors induced by multipath as a function of $\sigma_{dyn\ 62}$

The evolution of the steady state standard deviations of the position error induced by multipath as a function of $\tau_{dyn\ 62}$ is depicted in Figure 7-7 for $\sigma_{dyn\ 62} = 19.5$cm (left hand side) and for $\sigma_{dyn\ 62} = 5.0$m (right hand side). The evolution of the standard deviations as a function of $\tau_{dyn\ 62}$ are plotted for a low and a high value of $\sigma_{dyn\ 62}$ in order to show that the shape of this evolution does not depend on the value of $\sigma_{dyn\ 62}$.

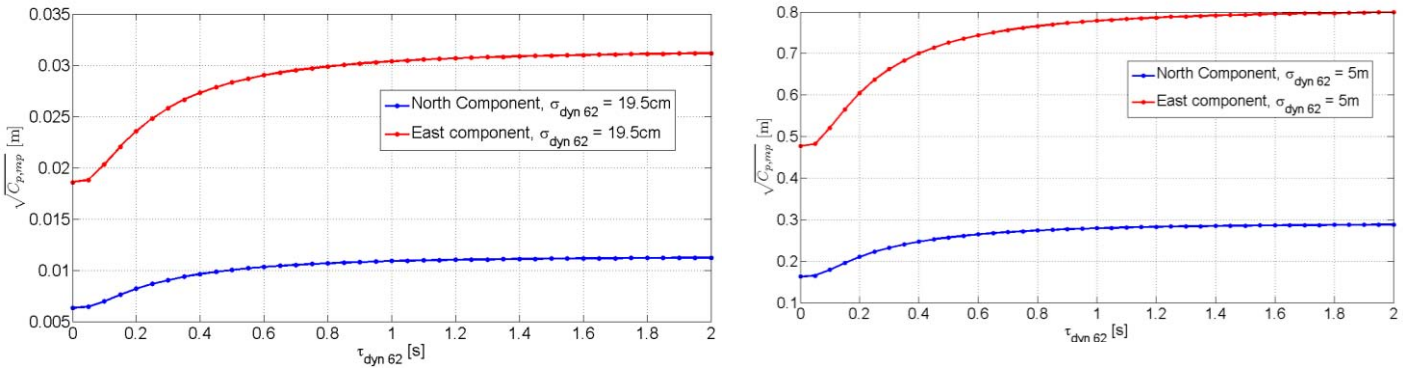

$\sigma_{dyn\ 62} = 19.5$cm $\sigma_{dyn\ 62} = 5.0$m

Figure 7-7: Steady state standard deviations of position errors induced by multipath as a function of $\tau_{dyn\ 62}$

The Kalman filter behaves as a low pass filter. This implies that the high-frequency (low correlation time $\tau_{dyn\,62}$) multipath stochastic errors are filtered out by the Kalman filter. The minimal steady state standard deviations of the North and East position errors are thus obtained for multipath stochastic ranging errors almost uncorrelated in the time domain, that is to say for $\tau_{dyn\,62}$ closed to 0s. When $\tau_{dyn\,62}$ reaches few seconds, that is to say when $\tau_{dyn\,62}$ is around 2s, the steady state standard deviations of the North and East position errors are almost twice the steady state standard deviations obtained when $\tau_{dyn\,62}$ is few milliseconds. Note finally that the shape of the evolution of the position error standard deviations as a function of $\tau_{dyn\,62}$ is similar to the shape of the evolution of $e^{-\frac{\alpha}{x}}$ as a function of x. Indeed, as shown in Eq - 7-22, the covariance matrix $\mathbf{C}_{p,mp}(t_i)$ is proportional to the correlation time matrix:

$$\mathbf{C}(t_i) = \begin{bmatrix} 0 & 0 & \cdots & \cdots & 0 \\ 0 & \ddots & & & \vdots \\ \vdots & & e^{-\frac{T_e}{\tau_{dyn\,62}(t_i)}} & & \vdots \\ \vdots & & & \ddots & 0 \\ 0 & \cdots & \cdots & 0 & 0 \end{bmatrix} \qquad \text{Eq - 7-29}$$

7.3. Evaluation of accuracy performance

Section 7.1 proposes analytical models of the impact of GNSS multipath ranging errors on the horizontal position error at the GNSS/IRS tight coupling positioning algorithm output during the taxi operation. This section re-uses these models to assess the accuracy of the horizontal position error in the presence of multipath throughout the LVP procedure path at Toulouse Blagnac airport, France.

The objective of this section and the error models used in this section are detailed in Section 7.3.1. The simulation scenario and the methodology used to assess the accuracy are presented in Section 7.3.2. The simulation results are presented in Section 7.3.3 for different elevation mask angles. In the same section, these performances are discussed and compared to the accuracy system navigation performance requirements presented in Section 2.3.2.3.

7.3.1. Objective and limitations

The objective of this section is to evaluate the accuracy of the horizontal position estimated by the tight coupling GNSS/IRS/DEM Kalman filter during the *taxi on taxiway*, *taxi on apron taxiway*, and *taxi on taxi lane* sub-phases related to the LVP procedure path at Toulouse Blagnac airport, France. For this accuracy analysis, it is considered that the GNSS pseudo-range measurements and the inertial sensors are affected by the following error models:

- The inertial sensors are affected by the nominal error model detailed in Section 6.2.3.
- The GNSS pseudo-range measurements are affected by the stochastic nominal errors detailed in Section 3.2.1 for the ionosphere, troposphere, satellite clock and ephemeris inaccuracies, and receiver noise error sources.
- The GNSS pseudo-range measurements are affected by the deterministic multipath ranging induced by the ground first-order reflections.

The results presented in this section do not take into account the effects of multipath from airport obstacles on the horizontal position errors. A rigorous analysis of the accuracy

performance during the surface operations would require taking into account the impact of multipath from the airport obstacles on the position error. Indeed, multipath from the airport obstacles affect GNSS measurements during the LVP *taxi on apron taxiway* and the LVP *taxi on taxi lane* sub phase, as underlined in Chapter 5. However, it is chosen not to consider the effects of multipath from airport obstacles in this section for the following reasons.

- It is acceptable not to take into account the effects of multipath from the airport obstacles when evaluating the accuracy performance during both *taxi on taxiway* and *taxi on apron taxiway* sub-phases throughout the LVP procedure path at Toulouse Blagnac airport. Using the methodology developed in Section 5.4.2.1, it can be shown that, for the satellite geometry used in Section 7.2.2 and for an elevation mask angle of 5° for GPS and 10° for Galileo, the airborne antenna does not cross any impact zone throughout the LVP *taxi on taxiway* sub-phase and is in the impact zone related to six different visible satellites during the *taxi on apron taxiway* sub-phase. In other words, six GNSS measurements are affected by GNSS stochastic multipath ranging errors induced by the airport obstacles during the *taxi on apron taxiway* sub-phase. From Chapter 5, the standard deviation of the multipath stochastic ranging errors induced by the airport obstacles during the *taxi on apron taxiway* are at most few decimeters. By using the methodology used in Section 7.2.2, it has been calculated that, if the six GNSS measurements are simultaneously affected by a stochastic error modelled as a zero-mean first-order Gauss Markov process characterized by a correlation time of 10ms and a standard deviation of 20cm, these multipath errors will result in an increase of the standard deviation of the position errors of 3cm in the East direction and of 5cm in the North direction. This remains insignificant regarding the standard deviations of the North and East position errors induced by the troposphere, satellite clock corrections and ephemeris inaccuracies, and receiver noise stochastic errors. These standard deviations are of the order of a several decimeters, as underlined in Appendix E, Section E.4. Hence, even if several measurements are affected by multipath from the airport obstacles, it is acceptable not to take into account the effects of multipath from the airport obstacles when evaluating the accuracy performance during both *taxi on taxiway* and *taxi on apron taxiway* sub-phases throughout the LVP procedure path at Toulouse Blagnac airport.
- The standard deviation of the multipath stochastic ranging errors induced by the airport obstacles during *taxi on taxi lane* may reach several decimeters up to few meters. Section 7.2.2 shows that these errors will result in an increase of the standard deviation of the North and East position errors of few centimeters up to few decimeters. Hence, it is unacceptable not to take into account the effects of multipath from the airport obstacles when evaluating the accuracy performance during the *taxi on taxi lane* sub-phase. However, the motivation for this section is to have a first overview of the capacity of the positioning algorithm to maintain the accuracy navigation requirements in the presence of multipath errors from the airport surface and from the aircraft structure during the *taxi on taxi lane* sub-phase.

For both reasons, it is proposed not to take into account the effects of multipath from the airport obstacles in the accuracy assessment presented in this section.

7.3.2. Methodology

In order to properly explain the methodology that has been adopted to assess the accuracy of the horizontal position estimate, it is important to define firstly the concept of surface operation.

7.3.2.1. Surface operation definition

In the context of airport surface navigation, an operation is defined based on three parameters:

- the time epoch t_0 of the beginning of the operation,
- the sub-phase length Δt,
- the procedure (desired path) that is indicated by the Air Traffic Control (ATC) staff and that must be followed by the aircraft. When the aircraft performs a *taxi on taxiway* sub-phase, the procedure path is on the taxiway network. When the aircraft performs a *taxi on apron taxiway* sub-phase, the procedure path is on the apron taxiway network. When the aircraft performs a *taxi on taxi lane* sub-phase, the procedure path is on the taxi lane network.

t_0, Δt and the procedure path are sketched Figure 7-8.

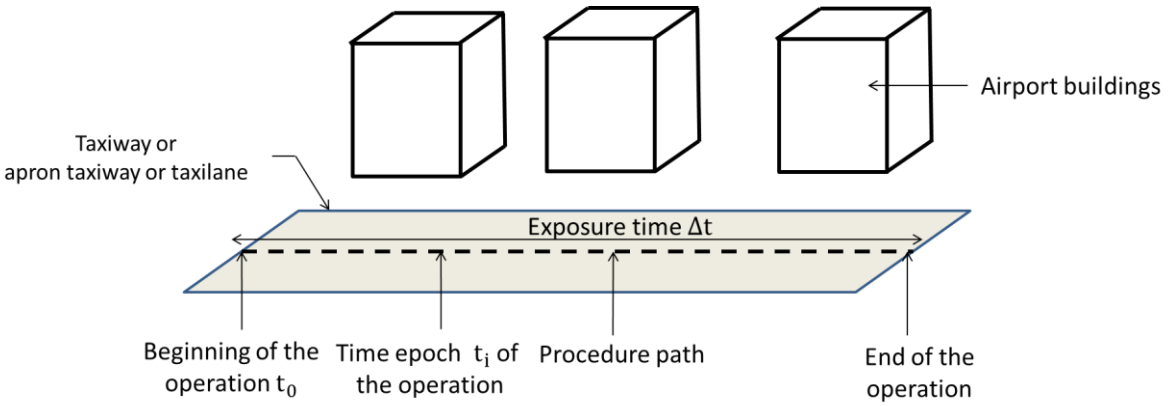

Figure 7-8: Representation of a surface operation

Since the satellite geometry is considered to be frozen throughout the operation from time t_0, t_0 is also used in the following to indicate the satellite geometry.

7.3.2.2. General methodology for accuracy assessment

The accuracy of the position estimate over a given sub-phase must be evaluated along every operation related to the sub-phase, and at every time epoch t_i of each operation. The accuracy navigation system performance requirement at time epoch t_i of an operation starting at epoch time t_0 is met if the following constraint is met:

$$P_{|\boldsymbol{\varepsilon}_p|<Acc_{95\%}}(t_i) > 0.95 \qquad \text{Eq - 7-30}$$

where:

- $Acc_{95\%}$ represents the required horizontal 95% confidence level for the considered sub-phase and is presented in Section 2.3.2.3 for the different taxi sub-phases.
- $|\boldsymbol{\varepsilon}_p|$ is the norm of the horizontal position error in nominal conditions,
- $P_{|\boldsymbol{\varepsilon}_p|<Acc_{95\%}}(t_i)$ is the probability that $|\boldsymbol{\varepsilon}_p|$ exceeds $Acc_{95\%}$ at time epoch t_i of the operation and with the satellite geometry at t_0.

Meeting the accuracy requirement presented in Eq - 7-30 is a condition for the availability of service for each geometry [Lee *et al.*, 2007] and for each time epoch of the taxi operation.

7.3.2.3. Adopted methodology

7.3.2.3.1. Horizontal position error model

In order to correctly estimate the probability $P_{|\boldsymbol{\varepsilon}_p|<Acc_{95\%}}(t_i)$ for a given satellite geometry t_0 at time t_i, it is essential to provide a model of the horizontal position error $\boldsymbol{\varepsilon}_p$ over the segment and for the satellite geometry at t_0. The Kalman filter described in Chapter 6 is a linear estimator. Since the measurement errors are normally distributed and since the position estimator is linear, the horizontal position error distribution at epoch time t_i and for the satellite geometry t_0 can be modelled by a bi-dimensional Gaussian distribution [Younes, 2000][Ober, 2003]:

$$\boldsymbol{\varepsilon}_p(t_i) \sim \mathcal{N}\left(\mathbf{b}_{p,mp}(t_i), \mathbf{C}_{p,w/o\ mp}(t_i)\right) \qquad \text{Eq - 7-31}$$

where:

- $\mathbf{C}_{p,w/o\ mp}(t_i)$ is the covariance matrix of the horizontal position at epoch time t_i and for the satellite geometry t_0.
- $\mathbf{b}_{p,mp}(t_i)$ is the horizontal position bias at epoch time t_i and for the satellite geometry t_0.

Recall that, since the GNSS measurement errors that have been applied to the GNSS pseudo-range measurements in the position error simulator described in Section 6.2 over-bounds the true GNSS measurement error distributions, the bi-dimensional Gaussian distribution that models the horizontal position error at the Kalman filter output over-bounds the true horizontal position error distribution.

7.3.2.3.2. Methodology description

Considering a satellite geometry at t_0, the accuracy of the position estimate at every time epoch t_i of a given segment is roughly constant. Indeed, over a given segment, both covariance $\mathbf{C}_{p,w/o\ mp}$ and bias $\mathbf{b}_{p,mp}$ of the horizontal position error can be considered as constant in the (NED) reference frame for a satellite geometry at t_0. This is explained as follows.

For a given satellite geometry at t_0, and considering the error sources listed in Section 7.3.1, the covariance of the horizontal position error over a given segment at epoch time t_i depends on the inertial sensor errors and on the stochastic nominal ionosphere, troposphere, satellite clock and ephemeris, and receiver noise ranging errors. This covariance $\mathbf{C}_{p,w/o\ mp}(t_i)$ is roughly constant over a given segment since:

- the inertial sensor error parameters (covariance matrix of the measurement noise $\boldsymbol{\eta}_{IMU}$, covariance matrix and correlation time of the measurement bias $\mathbf{b}_{IMU}$, the misalignment matrix misa and the scale factor error matrix $\mathbf{k}_{1,IMU}$) are considered to be constant during the taxi operation.
- the standard deviations related to the stochastic nominal ionosphere, troposphere, satellite clock and ephemeris, and receiver noise ranging errors only depend on the satellite geometry in this thesis. Hence, these standard deviations are considered to be constant during the taxi operation.

For a given satellite geometry at t_0, and considering the error sources listed in Section 7.3.1, the bias on the horizontal position error over a given segment at epoch time t_i depends on the GNSS deterministic multipath ranging errors induced by the airport surface and the aircraft structure. This position bias $\mathbf{b}_{p,mp}(t_i)$ is roughly constant over a given segment. Indeed, it is

established in Section 7.2.1 that, for a given constellation configuration, the horizontal position bias $\mathbf{b}_{p,mp}(t_i)$ on a segment depends on the aircraft azimuth angle on that segment. Along a given segment, the aircraft may not perfectly follow the procedure path. The aircraft azimuth angle and the horizontal position bias $\mathbf{b}_{p,mp}(t_i)$ may vary along the segment. However, it is shown in Section 7.2.1.3 that, when the aircraft azimuth angle variations are a few dozens of degrees, the resulting position bias variations is at most a few centimeters. This remains low regarding the magnitude of the horizontal position bias $\mathbf{b}_{p,mp}(t_i)$ that is a few decimeters in magnitude for a GPS elevation mask of 5° and for a Galileo elevation mask of 10°. In addition, the expected aircraft angle variations along a segment are of the order of few degrees, so the horizontal bias variations along a segment will be less than the few centimeters observed in Figure 7-4. It is considered that the horizontal position bias $\mathbf{b}_{p,mp}(t_i)$ that affects the antenna position estimate on a given segment of the airport is the position bias $\mathbf{b}_{p,mp}(t_i)$ that would have affected the position estimate if the aircraft would have perfectly followed the straight line trajectory path along the segment. This horizontal position bias is constant over the segment.

To conclude, for a given satellite geometry, the covariance $\mathbf{C}_{p,w/o\ mp}(t_i)$ and the bias $\mathbf{b}_{p,mp}(t_i)$ of the horizontal position error can be considered as roughly constant over a given segment. Since the horizontal position error at each epoch time t_i on the segment can be modelled by a bi-dimensional Gaussian distribution and since this error can be considered as a second-order stationary random process over the segment, $P_{|\boldsymbol{\varepsilon}_p|<Acc_{95\%}}(t_i)$ is constant over the segment. Hence, a single probability $P_{|\boldsymbol{\varepsilon}_p|<Acc_{95\%}}(t_i)$ is evaluated per segment and for each satellite geometry t_0.

The methodology to compute $\mathbf{b}_{p,mp}(t_i)$ over a segment is developed in Section 7.2.1 for a given satellite geometry at t_0. Appendix E, Section E.4, develops the methodology to compute $\mathbf{C}_{p,w/o\ mp}(t_i)$ over a segment for a given satellite geometry at t_0. The methodology used to compute $P_{|\boldsymbol{\varepsilon}_p|<Acc_{95\%}}(t_i)$ based on the model of the 2D position error model is explained in the next section.

7.3.2.3.3. Probability of exceeding the 95% accuracy confidence bound

It is shown in Section 7.3.2.3.1 that the 2D horizontal position error $\boldsymbol{\varepsilon}_p(t_i)$ over a segment of the airport is over-bounded by a bi-dimensional Gaussian distribution. Different techniques have been elaborated in the literature to compute the probability that the 2D horizontal position error stays within a circle of radius $Acc_{95\%}$. In this thesis, it is chosen to use a model of $P_{|\boldsymbol{\varepsilon}_p|<Acc_{95\%}}$ to evaluate this probability. Indeed, no analytical solution has been founded to compute this probability and numerical computations are complex and time-consuming.

Among the existing techniques to model $P_{|\boldsymbol{\varepsilon}_p|<Acc_{95\%}}$, [Lee, 1995] [Kelly, 1997] [Milner *et al.*, 2010] propose methodologies that may lead to underestimate $P_{|\boldsymbol{\varepsilon}_p|<Acc_{95\%}}$, which is undesirable when evaluating the accuracy performance. It is preferred in this thesis to use the methodology developed in Appendix B of [Ober, 2003] and in [ICAO, 2006]. Indeed, this methodology always leads to over-bound $P_{|\boldsymbol{\varepsilon}_p|<Acc_{95\%}}$.

7.3.3. Simulation results

7.3.3.1. Limitations

Before presenting the simulation results, it is important to state the main assumptions that have been made when evaluating the accuracy of the horizontal position error at Toulouse Blagnac airport. The assumptions can be classified into three categories that are listed below.

- Assumptions have been made concerning the **sources of multipath** affecting the GNSS measurements during the LVP procedure path at Toulouse Blagnac airport. More specifically, results proposed in this section do not take into multipath from airport obstacles. The reasons of this assumption have been detailed in Section 7.3.1.
- Assumptions have been made concerning the computation of the **GNSS deterministic multipath ranging errors from the aircraft structure and from the airport surface**:
  - The airport surface is an infinite and planar ground made of dry tar.
  - The same antenna gain pattern is used to compute both L1 and L5 antenna gains. The antenna group delay and phase delay are not included in the antenna model.
- A simplification has been made in the evaluation of **standard deviations of the GNSS receiver noise ranging errors**. The impact of multipath on the C/N0 ratios, and hence on the standard deviation of the receiver thermal noise ranging errors, has not been taken into account. The validity of this simplification is discussed in Section 6.2.2.3.

7.3.3.2. Simulation settings

Based on the methodology explained in Section 7.3.2.3, $P_{|\boldsymbol{\varepsilon}_p|<Acc_{95\%}}(t_i)$ is computed over each segment of the LVP procedure path for different satellite geometries t_0. The number of simulated satellite geometries is indicated below.

Most of the constellation configurations are represented by simulating the GPS and Galileo constellations over three days. Due to the limited simulation capacity, it is choosen to simulate the constellations with a time step of 10 minutes over three days. This leads to simulate $N_{const} = 433$ different constellation configurations over a three day time interval.

The $P_{|\boldsymbol{\varepsilon}_p|<Acc_{95\%}}(t_i)$ over each segment of the LVP procedure path and for a given satellite geometry are computed using the horizontal bias $\mathbf{b}_{p,mp}$ and the covariance matrix $\mathbf{C}_{p,w/o\ mp}$ of the horizontal postion error. The position bias has been computed based on the analytical expression developed in Eq - 7-15. The covariance matrix has been estimated using the simulation scenario presented in Appendix E, Section E-4. As detailed in this Appendix, a total number of 80 position error samples has been used to estimate the covariance matrix $\mathbf{C}_{p,w/o\ mp}$ over each segment of the LVP procedure path and for a given satellite geometry.

The $P_{|\boldsymbol{\varepsilon}_p|<Acc_{95\%}}(t_i)$ over each segment of the LVP procedure path are computed in two configurations (configurations 1 and 2) characterized by different elevation mask angles. The elevation mask angles for each configuration are provided in Table 7-3.

7.3.3.3. Results

Figure 7-9 presents the probability that the 2D horizontal position error $\boldsymbol{\varepsilon}_p$ is lower than the 95% accuracy confidence bound on the *taxi on taxiway* segment (segment 1), on the *taxi on apron taxiway* segment (segment 3) and on the *taxi on taxi lane* segment (segment 4). For sake of clarity, $P_{|\boldsymbol{\varepsilon}_p|<Acc_{95\%}}(t_i)$ is not represented for segment 2 (*taxi on taxiway* segment). The evolution of $P_{|\boldsymbol{\varepsilon}_p|<Acc_{95\%}}(t_i)$ as a function of the satellite geometry t_0 for segment 2 is similar to the evolution of $P_{|\boldsymbol{\varepsilon}_p|<Acc_{95\%}}(t_i)$ for segment 1. This is because:

- The horizontal bias $\mathbf{b_{p,mp}}$ varies of at most few centimeters when the segment orientation changes,
- The covariance matrix $\mathbf{C_{p,w/o\ mp}}$ in the (NED) reference frame is considered to be independent of the trajectory orientation in the scene.

The ratio of the number of satellite configurations for which $P_{|\boldsymbol{\varepsilon}_p|<Acc_{95\%}}(t_i) > 0.95$ over the total number of simulated trajectories $N_{const} = 433$ is quantified Table 7-6. Table 7-6 also presents the mean $P_{|\boldsymbol{\varepsilon}_p|<Acc_{95\%}}(t_i)$ computed over the $N_{const} = 433$ satellite geometries simulated over three days.

In the presence of multipath from the airport surface and from the aircraft structure only:

- The accuracy navigation system performance requirement is met for the *taxi on taxiway* sub-phase for all satellite constellations on segment 1.
- The accuracy navigation system performance requirement is not met for the *taxi on taxi lane* sub-phase, regardless the satellite elevation mask angle and the satellite geometry.
- The accuracy navigation system performance requirement is met for the *taxi on apron taxiway* sub-phase for 95.85% of the satellite configurations when the GPS and Galileo mask angles are 15°. The accuracy requirement is met for the *taxi on apron* taxiway sub-phase for 50.81% of the satellite configurations when the GPS mask angle is 5° and when the GPS mask angle is 10°. An interpretation of this result is provided in the next section.

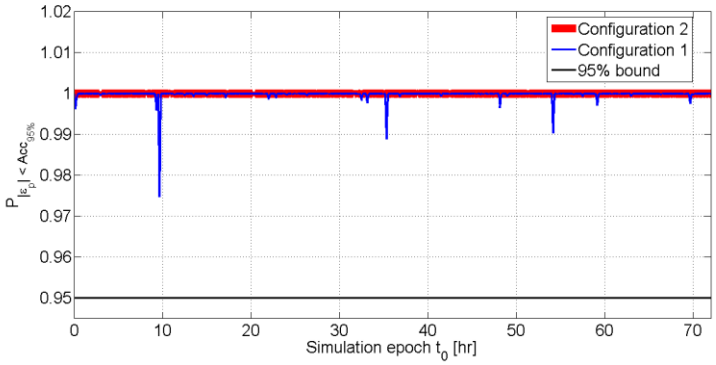

Taxi on taxiway (segment 1)

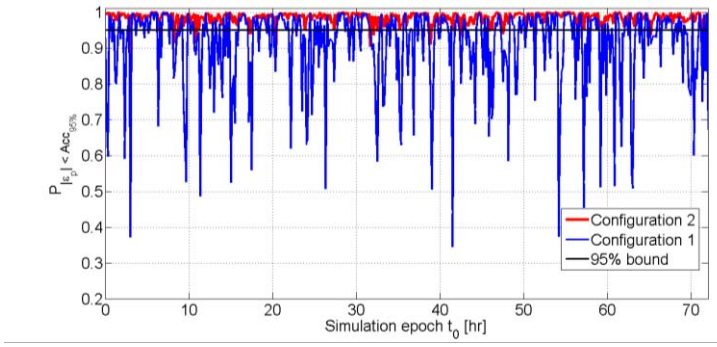

Taxi on apron taxiway (segment 3)

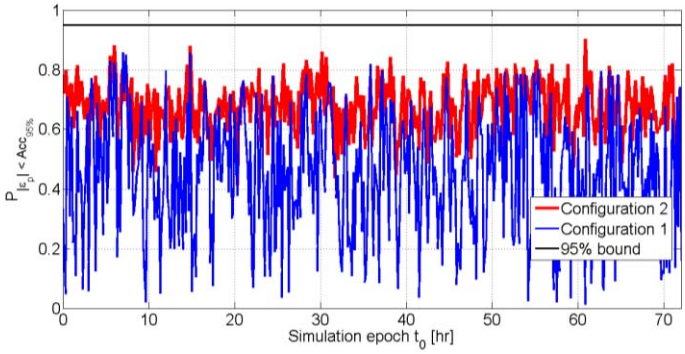

Taxi on taxi lane (segment 4)

Figure 7-9: $P_{|\varepsilon_p|<Acc_{95\%}}$ over three days on segments 1, 3 and 4

	$Acc_{95\%}$	Percentage of satellite geometries for which $P_{|\varepsilon_p|<Acc_{95\%}} > 0.95$		Mean probability $P_{|\varepsilon_p|<Acc_{95\%}}$ calculated over three days	
		Configu-ration 1	Configu-ration 2	Configu-ration 1	Configu-ration 2
Taxi on taxiway	1.9m	100%	100%	99.98%	100%
Taxi on apron taxiway	1.0m	50.81%	95.85%	90.46%	98.41%
Taxi on taxi lane	0.50m	0%	0%	44.02%	67.40%

Table 7-6 : Percentage of satellite geometries for which $P_{|\varepsilon_p|<Acc_{95\%}} > 0.95$ and mean $P_{|\varepsilon_p|<Acc_{95\%}}$ over all simulated satellite configurations

7.3.3.4. Interpretations of the accuracy performance over segment 3

Figure 7-10 shows the mean number of satellites used along segment 3 (*apron* segment) for both mask angle configurations and for each constellation configuration over 72 hours. In configuration 2, approximately three satellites are excluded from the PVT solution estimation compared to configuration 1. Indeed, the elevation mask angles related to configuration 1 are lower than those related to configuration 2.

Due to this reduction in the number of satellites, the mean Horizontal Dilution of Precision (HDOP) over segment 3 is higher for configuration 2 than for configuration 1, as depicted in Figure 7-10. The HDOP is a function of the satellite/user geometry [Kaplan *et al*., 2006] and represents the amplification of the standard deviation of the measurement errors onto the horizontal position error. However, the HDOP values for both elevation mask configurations remain excellent since they are below 1 most of the time. Indeed, the reception conditions are close to the open-sky conditions. The GNSS signals are not blocked by any obstacles along segment 3, as underlined in Section 5.2.1. In addition, a double satellite constellation is considered in this thesis, and the number of satellites in view is thus relatively high.

Figure 7-11 shows the norm of the horizontal position bias $\left|\mathbf{b}_{p,mp}(t_i)\right|$ induced by multipath from the airport surface and from the aircraft structure along segment 3 for each constellation configuration over 72 hours. The elevation mask configuration 2 reduces the amplitude of the positioning biases compared to the elevation mask configuration 1. The horizontal position biases are roughly 10 centimeters for configuration 1, while they may reach 70 centimeters for configuration 2. This phenomenon is interpreted and discussed in Section 7.2.1. The position

bias reduction is significant regarding the 95% accuracy confidence bound for the *taxi on apron taxiway* sub-phase, that is 1.0 meter.

To conclude, the increase in elevation mask angles from configuration 1 to configuration 2 has two main effects. On the one hand, it leads to increase the HDOP factor. Even in the configuration 2, the HDOP factors remain very good and are below 1. On the other hand, it significantly reduces the horizontal position biases induced by multipath.

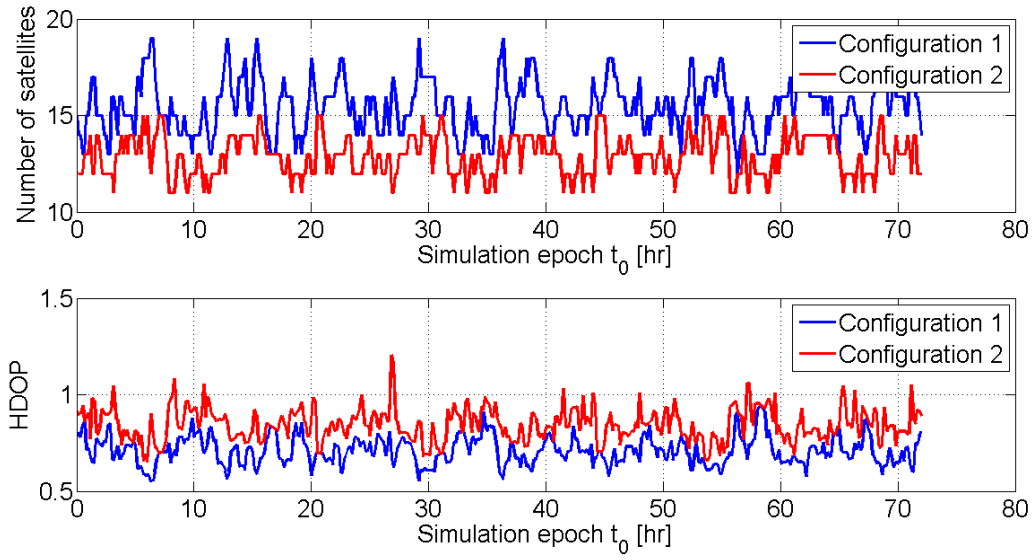

Figure 7-10: Mean number of satellites and mean PDOP along segment 3 for each constellation configuration

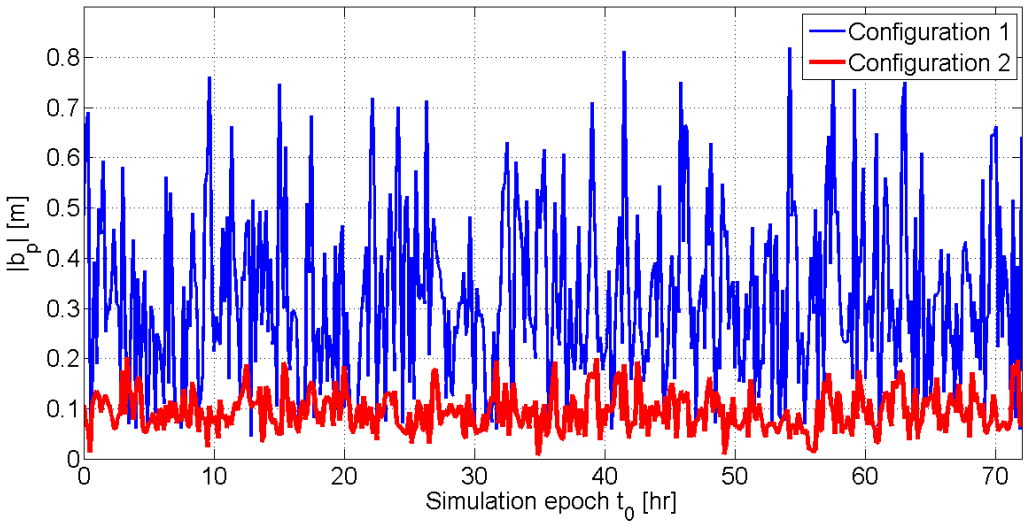

Figure 7-11: Norm of the horizontal position bias along segment 3 for each constellation configuration

Adopting a satellite elevation mask angle of 15° for both GPS and Galileo constellations significantly reduces the position biases while maintaining a good HDOP. In the absence of multipath ranging errors from the airport obstacles, this mask angle allows meeting the accuracy requirement for 95.85% of the simulated satellite configurations. In comparison,

adopting a standard mask angle of 5° for GPS and 10° for Galileo leads to meet the accuracy requirement for 50.81% of the simulated satellite configurations. The identification of the optimum mask angle in terms of accuracy, that is the mask angle that maximizes the availability of the navigation system in terms of accuracy, remains as future work.

7.3.3.5. Synthesis

It has been underlined in this section that, with the satellite elevation mask angle of 15° for GPS and Galileo, the positioning algorithm presented in Chapter 6 leads to meet the accuracy performance requirements for:

- 100% of the satellite geometries and for the *taxi on taxiway* sub-phase.
- 95.85% of the satellite geometries and for the *taxi on apron taxiway* sub-phase.
- 0% of the satellite geometries and for the *taxi on taxi lane* sub-phase.

In order to improve the availability of the accuracy function during both *apron* and *taxi lane* sub-phases, a tight coupling GNSS/IRS/DEM/WSS algorithm has been developed in Appendix G. Simulations presented in this appendix have shown that the accuracy performance for a given satellite geometry is improved by the aid of WSS in the Kalman filter. However, this improvement is relatively weak and the availability of the accuracy function is unchanged by the WSS aid.

In the rest of the thesis, it has been decided to discard the *taxi lane* sub-phase since the considered algorithm does not enable meeting the accuracy requirements for this sub-phase. Designing a navigation system that enables the surface movement guidance function under low visibility conditions for the *taxi on taxiway* and for the *taxi on apron taxiway* presents several operational benefits. Amongst these benefits there is the improvement of the airport capacity under low visibility conditions. To propose a navigation algorithm that enables the guidance function during the *taxi on taxi lane* sub-phase remains as future work. In this Ph.D. thesis, the development of such a system is not considered as a priority since the aircraft can be assisted by a tow vehicle under low visibility conditions to perform the *taxi on taxi lane* sub-phase.

Note finally that it has been decided to keep considering the GNSS/IRS/DEM positioning algorithm for the *taxiway* and *apron* sub-phase, even if the accuracy function availability reaches roughly 96% for the *apron* sub-phase, and not the required 99.9% level. There are three main reasons for this.

- Firstly, the 96% availability is not far from the required 99.9% required availability level. Several possible solutions can be envisaged to potentially improve the availability performance for the apron sub-phase and are listed below :
  - To find the optimal elevation mask angle, that is the mask angle that leads to maximize the accuracy function availability during the *apron* sub-phase.
  - To check if the FTE standard deviation in the future aircraft will be improved compared to the current FTE budgets, and to relax the accuracy navigation system performance requirements if the FTE budget can be lower.
  - To compute the availability using real constellations and not baseline constellations. Indeed, performance obtained with real constellations will likely to be better since real constellations contain more satellites in the sky than baseline constellations.
- Secondly, this GNSS/IRS/DEM has a simple architecture and can be considered as a relatively low-cost solution without external infrastructure. Hence, even if this solution cannot be considered as a full-availability solution for the apron sub-phase, it constitutes an interesting and low cost back up that meets the accuracy requirements for nearly 96% of the satellite geometries.

- Thirdly, this GNSS/IRS/DEM architecture is likely to be the basis for an improved algorithm that would show better performance in the future. The list of the navigation sensors that can be integrated to this GNSS/IRS/DEM architecture is further detailed in Section 6.1.3.

To conclude, for these three reasons, it appears reasonable to continue considering the GNSS/IRS/DEM architecture in the following and for both *taxiway* and *apron* sub-phases.

7.4. Conclusions

In this chapter, the impact of the GNSS multipath ranging errors in the dynamic configuration on the horizontal position error at the output of the GNSS/IRS tight coupling position algorithm has been analyzed. The GNSS multipath ranging error in the dynamic configuration can be modelled as the sum of a GNSS deterministic multipath ranging error and a GNSS stochastic multipath ranging error.

The GNSS deterministic multipath ranging errors are due to the ground first-order reflections. They continually affect the GNSS pseudo-range measurements. These deterministic ranging errors induce horizontal biases of the order of few centimeters with a 15° elevation mask angle, regardless of the 3D model of the airport buildings and gates.

The GNSS stochastic multipath ranging errors are due to the obstacles first and second-order interactions. They may temporally or continually affect one or several GNSS measurements throughout the taxi operation, depending on the relative position of the GNSS antenna, the GNSS satellites and the airport obstacles during the operation. It is reasonable to indicate that, in airport environments such as at Toulouse Blagnac airport, only few (3 to 5 satellites) satellites are simultaneously affected by multipath from obstacle interactions. Obstacles first and second-order interactions induce an increase in the covariance of the horizontal position error. Since only few of the satellites are affected by multipath from obstacles at a time, there is a significantly dilution of the effects of multipath from obstacles in the positioning domain. As an illustration, when the standard deviations of the obstacle multipath ranging errors are a few decimeters (such as along the LVP *apron-taxiway* at Blagnac airport), the standard deviation of the horizontal position error is increased by a few centimeters. When the standard deviations of obstacle multipath ranging errors are a few meters (such as along the LVP *taxi-lane* at Blagnac airport), the standard deviation of the horizontal position error is increased by a few decimeters.

In this chapter, the accuracy of the horizontal position error has also been evaluated assuming that the GNSS measurements are not affected by multipath from the airport obstacles. It has been established that the use of the 15° elevation mask angle for both GPS and Galileo constellations leads to significantly improve the accuracy performance. This result is valid regardless of the 3D model of the airport buildings and gates. Even in the absence of multipath from the airport obstacles, the GNSS/IRS/DEM tight coupling algorithm does not allow meeting the accuracy navigation system performance requirement for the *taxi on taxi lane* sub-phase. For this reason, the rest of this thesis focuses on the *taxi on taxiway* and *on the taxi on apron taxiway* sub-phases. Even if the accuracy function availability for the *apron* sub-phase with the GNSS/IRS/DEM tight coupling algorithm is slightly lower than the required 99.9% availability level, it has been decided to keep considering this algorithm for the rest of this thesis. The reasons of this choice have been further discussed.

CHAPTER 8

GNSS multipath integrity failure model

Current GNSS integrity monitoring systems are not designed to protect against the effects of multipath during surface operations. In order to maintain the integrity of the position solution during surface operations, it is necessary to design integrity monitoring systems that are able to properly detect multipath ranging failures. The design of such systems requires identifying the GNSS multipath integrity failure model. The multipath integrity failure model is defined as the model that describes:

- The factors influencing the characteristics (correlation time, standard deviation) of the GNSS multipath integrity failures,
- The characteristics of the GNSS multipath integrity failures,
- The conditions of occurrence of the GNSS multipath integrity failures,
- The model of the occurrence of the GNSS multipath integrity failures.

The chapter is organized as follows. Section 8.1 details the concept of aviation integrity requirements and of HMI. It explains how the failure models drive the GNSS integrity monitoring system design. Section 8.2 assesses the characteristics of the multipath ranging failures. Simulation results are presented for Toulouse Blagnac airport, France. Section 8.3 proposes a methodology to develop an occurrence model of GNSS multipath ranging failures in a given airport. It evaluates the presence of multipath ranging failures at Toulouse Blagnac airport, France.

Simulation results proposed in this chapter are presented for both *taxi on taxiway* and *taxi on apron taxiway* sub-phases. The multipath failure model is not developed for the *taxi on taxi lane* sub-phase, as fully explained in Section 7.4.

8.1. Integrity concept

Section 8.1.1 recalls and discusses the integrity navigation system performance requirements adapted to the taxi operation. It defines the concepts of HMI and of GNSS ranging failures. Next, Section 8.1.2 explains how the GNSS integrity failure models drive the design of the GNSS integrity monitoring systems. The two main strategies used in civil aviation to develop occurrence models of GNSS ranging failures are also exposed in this section.

8.1.1. Integrity navigation system performance requirements

8.1.1.1. Requirements

As explained in Section 2.2, the navigation system performance requirements are defined using four criteria that are accuracy, availability, continuity and integrity. The integrity navigation system performance requirements are recalled in Table 8-1 for both *taxi on taxiway* and *taxi on apron taxiway* sub-phases.

Sub-phase	TTA	P_{IR}	HAL
Taxi on taxiway	1s	2.9×10^{-8}/op	5.2m
Taxi on apron taxiway	1s	7.25×10^{-9}/op	2.9m

Table 8-1 : Integrity navigation system performance requirements – guidance function – category F airports

8.1.1.2. Interpretation

The previous section provides the integrity navigation system performance requirements for the guidance function under low visibility conditions. This section details the concept of integrity requirements and provides explanations in terms of integrity requirement parameters (TTA, P_{IR}, HAL).

As indicated in Table 8-1, the integrity requirements are given "per operation" [/op]. Section 7.3.2.1 provides the definition of "surface operation" used in the rest of this chapter. The integrity requirement is a "per operation" requirement. This means that the integrity performance requirement must be met individually for every operation [Walter *et al.*, 2003]. In addition, the integrity requirement must be met for every epoch t_i of each operation. In other words, for every epoch t_i, the probability of loss of integrity must be below the allowable integrity risk P_{IR}.

The loss of integrity, or HMI, occurs when a position error is larger than the alert limit, or the current protection level, without any indication of the error within the TTA for the applicable phase of flight [RTCA, 2009]. The TTA is the maximum allowable elapsed time from the onset of a positioning failure until the equipment annunciates the alert [RTCA, 2009] [ICAO, 2006]. A positioning failure is said to occur whenever the position error exceeds the applicable alert limit [ICAO, 2006]. By means the HMI definition, the probability of loss of integrity at time epoch t_i of an operation can be formulated as:

$$P_{HMI,t_i} = P\left[\underbrace{\underbrace{\left(\left|\boldsymbol{\varepsilon}_p(t_i)\right| > HAL\right)}_{\text{Positioning failure}} \&(\text{no detection within TTA})}_{\text{HMI}}\right] \qquad \text{Eq - 8-1}$$

where $\left|\boldsymbol{\varepsilon}_p(t_i)\right|$ represents the norm of the horizontal position error at t_i. For every time epoch t_i of every operation, the integrity monitoring system must be designed to meet the following constraint:

$$P_{IR} \geq P_{HMI,t_i} \qquad \text{Eq - 8-2}$$

where P_{IR} is the allowed probability of providing a position that is out of tolerance without warning the user within the TTA.

8.1.1.3. Fault-free mode and failure modes

8.1.1.3.1. Presentation

An HMI at the time epoch t_i of an operation may be induced by:

- The fault-free mode. This mode covers the causes of HMI that are due to large random errors that can occur with small probability in the normal operation of the system [Lee, 2004].
- A failure mode. This mode covers the causes of HMI that are due to:
  - A **GNSS single ranging failure** on a GNSS pseudo-range measurement. A ranging failure is said to occur when a significantly large error in the range measurement (whether that error is due to an anomaly of the satellite itself or to environmental effects on the satellite ranging signal such as multipath) may potentially cause an HMI event [Lee *et al*., 2007].
  - A **GNSS multiple ranging failure** on multiple GNSS pseudo-range measurements. A multiple ranging failure is said to occur when significantly large errors affect simultaneously multiple ranging measurements and this combination may potentially cause an HMI event. Note also that each multipath ranging error taken separately may not lead to a HMI event.

In the following, the failure mode k is said to occur when a ranging failure induced by a given threat affect a given subset of GNSS satellite measurements. A failure mode k is defined by the particular threat that induces the failure and by the subset of satellites that are affected by the failure. In this chapter, a threat describes the nature of the event that may lead to a ranging failure. As an example, ionosphere anomalies or multipath are GNSS threats for the zero-visibility guidance application during airport surface operations.

8.1.1.3.2. Integrity risk allocation

As underlined in Section 8.1.1.3.1, both fault-free mode and failure modes may lead to a loss of integrity. The total allowed integrity risk P_{IR} can be sub-allocated among the fault-free mode and different failure modes as follows:

$$P_{IR} = P_{IR,FF} + \sum_{k} P_{IR,k} \qquad \text{Eq - 8-3}$$

where:

- $P_{IR,FF}$ is the integrity risk allocated to the fault-free mode.
- $P_{IR,k}$ is the integrity risk allocated to the failure mode k.

The integrity risk allocation drives the design of the GNSS integrity monitoring algorithms. For ABAS, this allocation impacts the required probability of missed detection related to each failure mode, and it also impacts the protection level computation. Several allocation schemes are proposed in the literature so as to improve the integrity function availability. Amongst these publications, allocation schemes to improve the RAIM availability are discussed in [Lee, 2004] [GEAS, 2010].

From Section 8.1.1.2, for every time epoch t_i of every operation, the integrity monitoring system must be designed to meet the following constraint:

$$P_{IR,k} \geq P_{HMI,t_i \,\&\, k} \qquad \text{Eq - 8-4}$$

where $P_{HMI,t_i \,\&\, k}$ is the probability of HMI at time t_i induced by the failure mode k.

8.1.1.3.3. Probability of occurrence of failure modes

This section presents the concept of the probability of occurrence model of a failure mode and explains how the occurrence model drives the design of the GNSS integrity monitoring systems. Eq - 8-4 is equivalent to:

$$P_{IR,k} \geq P_{HMI,t_i \mid k} P_{k,t_i} \qquad \text{Eq - 8-5}$$

where:

- $P_{HMI,t_i \mid k}$ is the probability of HMI at time t_i given that the failure mode k is present at time t_i.
- P_{k,t_i} is the probability of occurrence of the failure mode k at time t_i.

The model of the probability of occurrence of the failure mode k drives the requirements on the GNSS integrity monitoring system. Indeed, From Eq - 8-5, the lower the probability of occurrence model is, the less demanding the requirement is on the probability of missed detection related to the failure mode k. The required probability of missed detection related to a failure mode k is the maximal allowable probability of undetected positioning failure within the TTA in the presence of the failure mode k. For this reason, it is essential to derive a suitable occurrence model of the GNSS ranging failures.

8.1.2. GNSS integrity failure model and GNSS integrity monitoring system design

This section explains how the GNSS integrity failure models influence the design of the GNSS integrity monitoring algorithm. Section 8.1.2.1 shows how the conditions of occurrence of a failure mode influence the way to develop the model of the probability of occurrence of this failure mode. Section 8.1.2.2 shows how the description of the factors influencing the characteristics of the failure mode impacts the protection level computations.

8.1.2.1. Failure mode occurrence models

It is underlined in Section 8.1.1.3.3 that the probability of occurrence model of a failure mode is essential to compute the required probability of missed detection related to this failure mode. Hence, the occurrence models drive the design of the GNSS integrity monitoring systems. This section presents the different strategies that are adopted to derive the models of the probability of occurrence of a failure mode.

The strategy that must be adopted to properly model the occurrence of a failure mode depends on the conditions of occurrence of that failure mode. The conditions of occurrence can be classified into three categories:

- The conditions that are **known**.
- The conditions that are **considered as random**. Two types of random conditions can be distinguished:
  - The conditions that cannot be known in practice, but which may be characterized by known probability distributions.
  - The conditions that could be known in practice, but that are considered as random. These conditions can be considered as random since they depend on environmental

parameters that are difficult to obtain, and since sufficient amount of data and understanding concerning the occurrence of the fault mode is available to consider the probability distribution of these conditions as well-known conditions [Walter *et al*., 2003][Pullen, 2014].

- The conditions that may not be known in practice but that are **considered as deterministic**. These conditions are assigned to their worst case values, that is to say the value that lead to maximize the probability of HMI induced by the failure mode. Conditions that may not be known in practice are considered as deterministic when:
  - these conditions are knowable or potentially foreseeable by means of the installation of measurement equipment or detection and monitoring techniques. More precisely, these conditions can be known or foreseen if there exist a reasonable technique or equipment to predict, detect, observe or measure the value of this factor. It means that such a technique or equipment requires a reasonable financial investment and does not require the installation of a complex and costly system architecture.
  - or the probability distribution of these conditions is not well-known. This can be due to a limited amount of data available to characterize this distribution or/and limited knowledge and understanding concerning these conditions.

Examples of conditions that are considered to be random and conditions that are considered to be deterministic are further developed in the next two sections. Two methodologies are used in civil aviation to derive the occurrence model of a failure mode. These approaches are referred to as "average risk strategy" and "specific risk strategy". Both approaches are developed in Sections 8.1.2.1.1 and 8.1.2.1.2.

8.1.2.1.1. Average risk strategy

In the average risk strategy, all conditions that are unknown in practice are considered as random. The probability distributions of all conditions that are unknown in practice are derived. The probability distributions of all unknown parameters are convolved to create an overall probability of occurrence as a function of the known conditions. The derived probability of occurrence is referred to as the "prior probability of occurrence" in the literature [Pullen *et al*., 2006]. The average risk strategy does not necessarily imply that the mean operator is used to compute the prior probability of occurrence. The average risk strategy is used to model the probability of occurrence of the GNSS ranging failures if the following criteria are met:

- The conditions of occurrence of the failure mode that are unknown in practice have known probability distributions [Pullen, 2014] and can thus be considered as random. More specifically, the civil aviation community has sufficient understanding on the failure mode and has collected enough data in past observations to accurately estimate the probability distributions of the conditions of occurrence of the failure mode unknown in practice. Based on this knowledge, the aviation community is convinced that the estimated probability distributions of conditions of occurrence used to build the prior probability model are conservative.
- The GNSS threat that induces the failure is infrequent [Walter *et al*., 2003], meaning that the *a priori* likelihood of the GNSS threat is well below 1 per operation. Indeed, the main benefit of the average risk strategy is to reduce the probability of occurrence model of the failure mode compared to the model obtained by the "specific risk strategy" presented in the next section. This is because the occurrence model is obtained by averaging the failure mode occurrence over all unknown conditions of occurrence. Using a reduced probability of occurrence bound related to a failure mode allows increasing the probability of missed detection related to this failure mode. If the threat inducing the failure mode occurs relatively frequently, the probability of occurrence model related to the failure mode will

not be well below 1 by using the average risk strategy. The related probability of missed detection will be comparable to the one obtained by means of the specific risk strategy. Hence, using the average risk strategy is not useful when the *a priori* likelihood of the GNSS threat is not well below 1 per operation.

As an example of the use of prior probability models in civil aviation, the average risk strategy is used to model the probability of occurrence of the GNSS single ranging failures induced by a Major Service Failures (MSF) on a given GNSS measurement. This example is briefly presented below.

The satellite j is affected by a GNSS single ranging failure at time t_i if a MSF occurs at that time and if the MSF impacts the satellite j. In order to compute the probability that one of the satellite that is used in the PVT solution is affected by a MSF at time t_i of an operation, the probability that at least one MSF occurs in one hour is required [Martineau, 2008]. This paragraph explains why the average risk can be used to model the probability of occurrence of a MSF in one hour. This probability can be obtained by averaging the occurrences of the MSF over all times. There are two reasons for this. Firstly, the onset time of the MSF is considered as unpredictable and unobservable parameters. Secondly, sufficient knowledge and data concerning the MSF are available to get a conservative model of the prior probability of occurrence model of the MSF per hour and per satellite [Pullen, 2014]. For both reasons, it is acceptable to compute a bound on the probability of occurrence of a MSF per hour by averaging the MSF occurrences over all times. The bound of this probability is set to 10^{-4} / hr / sat [Pervan, 2011]. The complete methodology used to derive this probability is developed in [Pervan, 2011].

8.1.2.1.2. Specific risk strategy

In the specific risk strategy, the failure mode k is treated as always present. Equivalently, the model of the probability of occurrence of the failure mode k is set to 1. The specific risk strategy is used if at least one of the following criteria is met:

- The *a priori* likelihood of the threat inducing the failure mode is relatively frequent,
- The failure mode is driven by conditions of occurrence that are knowable or potentially foreseeable by means of the installation of measurement equipment or detection and monitoring techniques. More precisely, these conditions can be known or foreseen if there exist a reasonable technique or equipment to predict, detect, observe or measure the value of this factor.
- The civil aviation community has no sufficient understanding and data to estimate the probability distributions of the unknown parameters that drive the failure mode.

As an example, the specific risk is used in civil aviation to model the occurrence of GNSS integrity failures induced by the ionosphere anomalies threat. One of the conditions of occurrence of a failure mode induced by an abnormal TEC gradient is the onset of the abnormal TEC gradient over the airport. No conservative models of occurrence probability of abnormal TEC gradients have been retained by the safety community. This is due to the limited understanding and data concerning the onset time of such ionosphere events [Pullen, 2014]. In addition, a networked GBAS or SBAS architecture would help detecting quickly the abnormal ionosphere conditions [Datta-Barua *et al.*, 2010]. Consequently, the onset of abnormal TEC gradients over a given airport can be considered as an observable parameter. Since the onset time of the ionosphere event is considered as an observable parameter and since not enough data are currently available to provide a conservative probability distribution of this parameter, the failure modes induced by the ionosphere event must be treated as always present.

To conclude, Section 8.1.2.1 has shown that it is essential to distinguish the conditions of occurrence of a failure mode to derive a suitable occurrence model of this failure mode and to properly design the GNSS integrity monitoring system. The next section explains how the GNSS integrity failure models also impact the computation of the protection levels by the GNSS integrity monitoring systems.

8.1.2.2. Protection levels

8.1.2.2.1. Protection level concept

In order to properly detect HMI events within the TTA, integrity monitoring algorithms are implemented. The integrity algorithms employed within ABAS consist of functions to check measurement consistency of the sensors and to compute Protection Levels (PLs). During surface operations only Horizontal Protection Levels (HPLs) are computed. Hence, the concept of HPLs is further detailed in this section.

The HPL is the radius of a circle in the horizontal plane [...] with its center being at the true position that describes the region assured to contain the indicated horizontal position [RTCA, 2006]. The HPL under the failure mode k is a statistical bound on the horizontal position error in the presence of this failure mode k. When ABAS is used, the HPL under the failure mode k is a function of the user geometry, of the expected error characteristics in the presence of the failure mode k as well as of the probability of the failure mode k allocated to the responsibility of ABAS.

Different techniques can be used to compute the HPL, depending on the integrity monitoring algorithm that is used to detect and exclude failures. Integrity monitoring algorithms can be classified into two groups, depending on whether the history of data is taken into account or not:

- **Sequential methods** exploit instantaneous and past measurements. As an example, some sequential methods cumulate the norm of the least-square solution residuals, and detect any change in the mean of these residuals [Younes, 2000], [Souteyrat, 1997].
- **Snapshot methods** calculate a test statistic from the instantaneous measurement redundancy. Thus they do not take into account either the correlation of measurements with time or the consistency of the constellation geometry between two instants [Diesel *et al.*, 1995].

8.1.2.2.2. HPL computation

In order to properly derive the HPL under the failure mode k, it is important to identify the factors influencing the signature of the failure mode k. Let's firstly discuss the concept of failure mode signature. Sequential methods take into account information on the history of the measurements to compute the HPL. Hence, the signature of the failure mode for sequential methods is the shape (step, ramp, drift) and the magnitude of the errors induced by the failure mode. Snapshot methods take into account instantaneous expected performance of GNSS measurements to compute the HPL. Hence, the signature of the failure mode for snapshot methods is the instantaneous magnitude of the errors induced by the failure mode.

By using the same classification as the one expressed in Section 8.1.2.1, the factors influencing the signature of a failure mode are classified as follows:

- the factors that are **known**,
- the factors that are **considered as random**. Two random factor types can be distinguished:
  - The factors that cannot be known in practice, but which may be characterized by known statistical distributions whose parameters can be predicted or measured. As an example,

the receiver noise errors have a known distribution that depends on the received signal strength.

- The factors that could be known in practice, but since they depend on environmental parameters that are difficult to obtain, and since their statistical distribution is well-known, they are considered as stochastic factors [Walter *et al*., 2003]. As an example, the nominal ionosphere ranging error is considered as a noise-like distribution which is driven by parameters, such as the elevation angle, that are known. Another example is the multipath ranging error induced by airport obstacles. This error depends on the true airborne antenna position in the airport which is difficult to obtain with a high (centimeter level) accuracy level. Hence, it has been chosen in this thesis to model the error by a statistical distribution which parameters can be obtained by means of a GNSS multipath ranging error simulator that uses a 3D model of the airport building.

- the factors that may not be known in practice but that are **considered as deterministic**. Parameters that may not be known in practice are considered as deterministic when:
  - these factors are knowable or potentially foreseeable by means of the installation of "reasonable" measurement equipment or detection and monitoring techniques. More details about what "reasonable" means in this context are provided in Section 8.1.2.1.
  - or the statistical distribution of these parameters is not well-known. This can be due to a limited amount of data available to characterize this distribution or/and limited knowledge and understanding concerning these parameters.

In civil aviation, the HPL under failure mode k must be computed under the worst case scenario [Pullen *et al*., 2011]. This means that the HPL under failure mode k must be computed by considering that all factors influencing the signature of the failure mode and that are considered to be deterministic take the values that maximize the probability of HMI.

As an example, let's consider the Major Service Failure (MSF) as the fault mode k. The magnitude of the ranging error induced by the MSF has not been sufficiently characterized and its statistical distribution is considered as unknown. Hence, current ABAS snapshot integrity monitoring algorithms, such as AIME [Diesel *et al*., 1995], compute the HPL under the MSF by considering that the ranging error magnitude of the MSF is the highest bias that is not detected with the required missed detection probability. The affected PRN is the PRN that leads to maximize the HPL under the MSF condition. Note that another approach has been retained for the computation of the PLs in the presence of a MSF in future RAIM algorithms, such as ARAIM algorithms. This approach is further described in [WG-C ARAIM, 2012].

Another example concerns the GBAS integrity monitoring algorithm. The signature of the ionosphere failure modes affecting a single or multiple GNSS measurement depends on the characteristics of the ionosphere anomaly. The PLs under abnormal TEC gradient conditions are computed by the GBAS integrity monitoring algorithms using the worst case ionosphere front parameters [Pullen *et al*., 2011]. These parameters are described by the ionosphere threat models published in [ICAO, 2009b]. Indeed, the ionosphere anomaly parameters, such as the spatial and temporal gradients of an ionosphere front, cannot be considered as purely random parameters. This is because:

- The ionosphere anomaly parameters can be considered as observable parameters [Pullen, 2014]. Indeed, a networked GBAS or SBAS architecture would provide indications on the ionosphere conditions and on the ionosphere anomaly parameters.
- Not enough data have been collected to correctly characterize the statistical distribution of the ionosphere anomaly parameters. For this reason, the ionosphere anomaly parameters, such as the spatial and temporal gradients of an ionosphere front, cannot be considered as purely random parameters.

In other applications, it is acceptable to consider the factors that are knowable or potentially foreseeable as purely random if their statistical distributions are known [Pullen *et al*., 2011]. Hence, the HPL are computed by using the statistical distributions of all factors that are not known in practice, even for the factors that could be known by means of additional investment. This approach is referred to as the "average risk" approach in the literature. It differs from the "specific risk strategy" approach that uses the worst case value of the factors that could be known in practice to evaluate the PLs. The main advantage of the average risk approach is that it leads to lower PLs and thus improves system availability. Both approaches to compute the PLs are further compared in [Pullen *et al*., 2011].

8.1.2.3. Synthesis

It has been underlined in Section 8.1.2 that the probability of missed detection related to a specific failure mode and the computation of the PLs under the failure mode are driven by the GNSS integrity failure model associated to the failure mode. The GNSS integrity failure model includes the factors influencing the signature of the failures and the signature of the failures as well as the conditions of occurrence of the failures and the occurrence models of the failures.

8.2. GNSS multipath integrity failures

As discussed in Section 8.1, the development of the GNSS multipath integrity failure models is essential to design a GNSS integrity monitoring that is able to properly detect and exclude multipath failures. The first step in the development of the integrity failure model is to identify the characteristics of the GNSS multipath integrity failures. The second step in the development of such a model is to identify the conditions of occurrence of the multipath failure modes, and to model the occurrence of such failure modes.

This section proposes a methodology to identify the characteristics of the GNSS multipath integrity failures in a given airport environment. An important remark is that this section does not quantify the size of the GNSS multipath ranging errors that affect GNSS measurements in a given airport environment. Instead, this section identifies the multipath ranging errors that would represent a threat in terms of integrity if they were present in the airport environment. The identification of the multipath ranging errors that may represent a threat in terms of accuracy is also essential to maintain the accuracy requirements during surface operations. However, this thesis focuses on the development of integrity failure models and this identification remains as future work.

Section 8.2.1 details the concept of GNSS multipath integrity ranging failures. Section 8.2.2 states which kinds of GNSS failures are identified in this section. Section 8.2.3 elaborates a methodology to identify the GNSS single multipath integrity ranging failures in a given airport environment. Section 8.2.4 re-uses this methodology to identify the GNSS single multipath ranging failures at Toulouse Blagnac airport, France, during both *taxi on taxiway* and *taxi on apron taxiway* sub-phases.

8.2.1. Definitions

Based on the general definition of the GNSS ranging failures provided in Section 8.1.1 the GNSS single and multiple multipath integrity ranging failure are defined as follows.

A **GNSS single multipath ranging failure** occurs when a significantly large error in the range measurement due to multipath may potentially cause a HMI event.

A **GNSS multiple multipath ranging failure** occurs when significantly large errors due to multipath affect simultaneously multiple ranging measurements and this combination may potentially cause a HMI event. Note also that each multipath ranging error taken separately may not lead to a HMI event.

8.2.2. Case of study

As explained in Chapter 5, during a surface operation, all GNSS measurements used in the PVT estimation are affected by a multipath error induced by the airport surface and the aircraft structure. This error is denoted as $b_{AC+ground}$ in this thesis. During the operation, some of the GNSS measurements used in the PVT estimation may also be temporarily or continually affected by multipath from airport obstacles. These measurements are affected by an additional multipath ranging error that represents the impact of multipath from airport obstacles on the GNSS measurement.

This thesis constitutes a first step in the development of a GNSS multipath integrity failure models. The focus is then on the identification of GNSS single multipath ranging failures. The identification of the GNSS multiple multipath ranging failures remains a future work. Hence, in this chapter, it is assumed that only one GNSS measurement can be affected by GNSS multipath from the airport obstacles at each time t_i of the operation. The situation where multiple GNSS measurements are simultaneously affected by multipath from airport obstacles is not considered in this chapter. If the GNSS measurement j is affected by obstacle multipath at time t_i, the GNSS measurement j is affected by an additional multipath ranging error $u_{obs\,j}(t_i)$ induced by the airport obstacles. The multipath ranging errors $u_{obs\,j}$ that may potentially cause an HMI event are identified in this section.

8.2.3. Methodology for GNSS multipath single failure identification

This section develops a methodology to identify the GNSS single multipath ranging failures in a given airport environment.

8.2.3.1. Criterion

This section establishes a mathematical criterion to identify which GNSS multipath ranging errors $u_{obs\,j}$ can be classified as GNSS single multipath ranging failures. Let $P_{IR,mp\,j}$ be the integrity risk allocated to the GNSS single multipath ranging failure affecting the GNSS measurement j. From Section 8.2.1, the GNSS multipath ranging error $u_{obs\,j}$ on the GNSS measurement j is a GNSS single ranging failure if this ranging error may potentially cause an HMI event. In this chapter, $u_{obs\,j}$ is not modelled as a deterministic ranging bias characterized by a given amplitude. Instead, $u_{obs\,j}$ is a correlated process over the trajectory in the impact zone and is modelled by a first-order Gauss-Markov process characterized by two statistical parameters, namely the correlation time $\tau_{dyn\,j}$ and the standard deviation $\sigma_{dyn\,j}$. As shown in Section 8.3.1.2.2, both parameters $\tau_{dyn\,j}$ and $\sigma_{dyn\,j}$ can be known in a deterministic way by means of the methodology presented in Section 5.5. It is proposed to identify the values of the parameters $\tau_{dyn\,j}$ and $\sigma_{dyn\,j}$ for which the GNSS multipath ranging error $u_{obs\,j}$ may potentially cause an HMI event. In addition, $u_{obs\,j}$ is modelled as a Gauss-Markov process. Hence, it is always possible to find a realization of $u_{obs\,j}$ that lead to an HMI event, regardless the values of $\tau_{dyn\,j}$ and $\sigma_{dyn\,j}$ in $\mathbb{R}^{+*}$. For this reason, it is proposed to identify the parameters $\tau_{dyn\,j}$ and $\sigma_{dyn\,j}$ that may cause an HMI event with a probability that is higher than $P_{IR,mp\,j}$. Mathematically, the GNSS multipath ranging error $u_{obs\,j}$ characterized by the parameters $\tau_{dyn\,j}$ and $\sigma_{dyn\,j}$ is classified as a GNSS single multipath integrity failure if:

$$P_{HMI\ \&\ \mathcal{M}(\tau_{dyn\,j},\sigma_{dyn\,j})} \geq P_{IR,mp\,j} \qquad \text{Eq - 8-6}$$

where $P_{HMI\ \&\ \mathcal{M}(\tau_{dyn\,j},\sigma_{dyn\,j})}$ is the probability of HMI induced by the GNSS multipath ranging error $u_{obs\,j}$ modelled by the Gauss-Markov process $\mathcal{M}(\tau_{dyn\,j},\sigma_{dyn\,j})$ on the GNSS measurement j. Eq - 8-6 is equivalent to:

$$P_{HMI\ |\ \mathcal{M}(\tau_{dyn\,j},\sigma_{dyn\,j})}\, P_{\mathcal{M}(\tau_{dyn\,j},\sigma_{dyn\,j})} \geq P_{IR,mp\,j} \qquad \text{Eq - 8-7}$$

where:

- $P_{HMI\ |\ \mathcal{M}(\tau_{dyn\,j},\sigma_{dyn\,j})}$ is the probability of HMI given that a GNSS multipath ranging error $u_{obs\,j}$ modelled by the Gauss-Markov process $\mathcal{M}(\tau_{dyn\,j},\sigma_{dyn\,j})$ is present on the GNSS measurement j.
- $P_{\mathcal{M}(\tau_{dyn\,j},\sigma_{dyn\,j})}$ is the probability of occurrence of the GNSS multipath ranging error $u_{obs\,j}$ modelled by the Gauss-Markov process $\mathcal{M}(\tau_{dyn\,j},\sigma_{dyn\,j})$ on the GNSS measurement j. In this thesis, the event "the Gauss-Markov process $\mathcal{M}(\tau_{dyn\,j},\sigma_{dyn\,j})$ models the ranging error $u_{obs\,j}$ affecting the GNSS measurement j" is a deterministic event. In this chapter, the abusive notation $P_{[\cdot]}$ is used to represent the probabilities of deterministic events [·]. The value of the probability of a deterministic event is assigned to 1 if the event occurs and is assigned to 0 if the event does not occur.

Let's consider the two following conservative assumptions.

- $P_{\mathcal{M}(\tau_{dyn\,j},\sigma_{dyn\,j})}$ is not available at this stage of the multipath integrity failure model development. Hence, it is assumed that the error is always present on the satellite j:

$$P_{\mathcal{M}(\tau_{dyn\,j},\sigma_{dyn\,j})} \equiv 1 \qquad \text{Eq - 8-8}$$

- It is assumed that no detection algorithms are used by the system in order to detect within the TTA the potential positioning failures induced by the the GNSS multipath ranging error $u_{obs\,j}$ modelled by the Gauss-Markov process $\mathcal{M}(\tau_{dyn\,j},\sigma_{dyn\,j})$.

Under the previous two assumptions, Eq - 8-7 is equivalent to:

$$P_{|\varepsilon_p|>HAL\ |\ \mathcal{M}(\tau_{dyn\,j},\sigma_{dyn\,j})} \geq P_{IR,mp\,j} \qquad \text{Eq - 8-9}$$

where $P_{|\varepsilon_p|>HAL\ |\ \mathcal{M}(\tau_{dyn\,j},\sigma_{dyn\,j})}$ is the probability of positioning failure given that the GNSS multipath ranging error $u_{obs\,j}$ modelled by the Gauss-Markov process $\mathcal{M}(\tau_{dyn\,j},\sigma_{dyn\,j})$ is present on the GNSS measurement j.

The next section develops a methodology to assess the pairs $(\tau_{dyn\,j},\sigma_{dyn\,j})$ modelling the GNSS multipath ranging errors $u_{obs\,j}$ on satellite j that may lead to probability of positioning failure higher than the allocated integrity risk $P_{IR,mp\,j}$ for a given sub-phase.

8.2.3.2. Methodology

8.2.3.2.1. General description

This section develops a methodology to assess the pairs $(\tau_{dyn\,j},\sigma_{dyn\,j})$ characterizing the GNSS multipath single ranging failures on satellite j. The methodology consists firstly in

computing the worst-case probability of positioning failure in the presence of a GNSS multipath ranging error modelled by the Gauss-Markov process $\mathcal{M}(\tau_{dyn\,j}, \sigma_{dyn\,j})$ on satellite j. Secondly, the pairs $(\tau_{dyn\,j}, \sigma_{dyn\,j})$ that lead to a worst-case probability of positioning failure higher than the allocated integrity risk $P_{IR,mp\,j}$ are identified. Figure 8-1 represents the general methodology to identify the GNSS multipath single ranging failures for a given sub-phase.

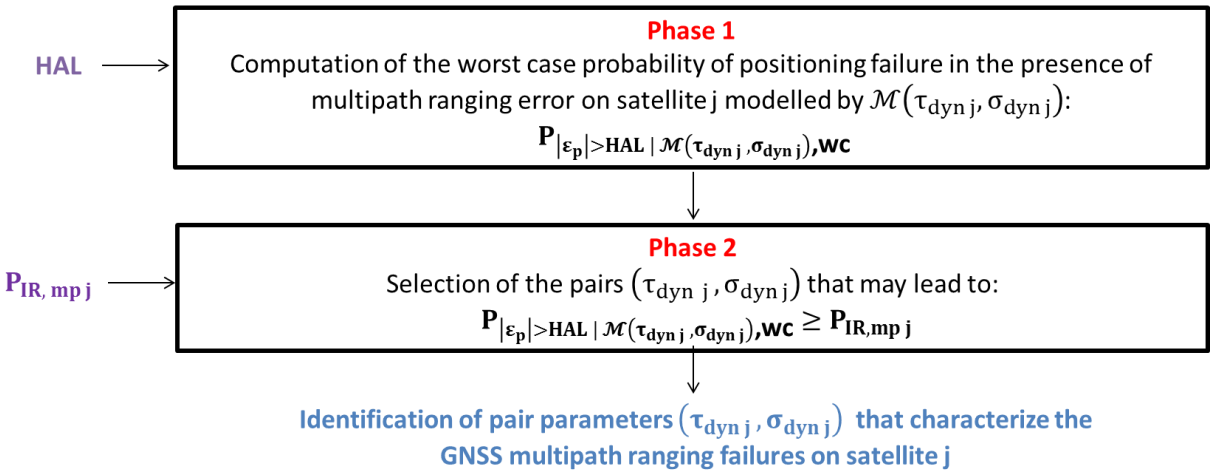

Figure 8-1 : Methodology to identify the GNSS multipath single ranging failures

Section 8.2.3.2.2 presents the methodology to compute the worst-case probability of positioning failure in the presence of a GNSS multipath ranging error $u_{obs\,j}$ modelled by the Gauss-Markov process $\mathcal{M}(\tau_{dyn\,j}, \sigma_{dyn\,j})$ on satellite j (**Phase 1**). Section 8.2.3.2.3 presents the methodology used to identify the GNSS multipath single ranging failures on satellite j (**Phase 2**).

8.2.3.2.2. Worst case probability of positioning failure

From Chapter 5, in the dynamic configuration, and in the impact zone, the GNSS multipath ranging error on satellite j can be modelled as:

$$\varepsilon_{mp\,j}(t_i) = b_{AC+ground}\left(El_j(t_0), Az_{air\,j}(t_i)\right) + u_{obs\,j}(t_i) \qquad \text{Eq - 8-10}$$

This section elaborates a methodology to quantify the worst case probability of positioning failure in the presence of the correlated error process $u_{obs\,j}$ on satellite j modelled by the Gauss-Markov process $\mathcal{M}(\tau_{dyn\,j}, \sigma_{dyn\,j})$. For this quantification, the following scenario has been used. An aircraft performs a given taxi sub-phase. Let's note t_0 the starting time of the operation and t_{end} the final time instant of the operation. The multipath ranging error is injected on satellite j during the sub-phase for each constellation configuration. If the satellite j is not visible for a given satellite geometry, the probability of positioning failure induced by the GNSS multipath ranging error on satellite j is not computed.

As justified in Section 5.1.2.1, the satellite geometry is considered to be frozen during the sub-phase. In addition, the apparition or the disappearance of GNSS satellites during the sub-phase induced by the signal masking are not considered. Indeed, during the *taxi on taxiway* and during the *taxi on apron taxiway* sub-phases, the GNSS signals are not likely to be masked by airport buildings. As an example, it is shown in Section 5.2.1 that the GNSS signals are not masked at Toulouse Blagnac airport during these sub-phases, even when the elevation mask angle is as low as 5°.

At time t_{mp}, the GNSS multipath ranging error $u_{obs\,j}$ is assumed to affect satellite j until the end of the operation t_{end}. Equivalently, the GNSS airborne antenna is assumed to enter in the impact zone related to satellite j at t_{mp}. t_0, t_{mp} and t_{end} are depicted in Figure 8-2.

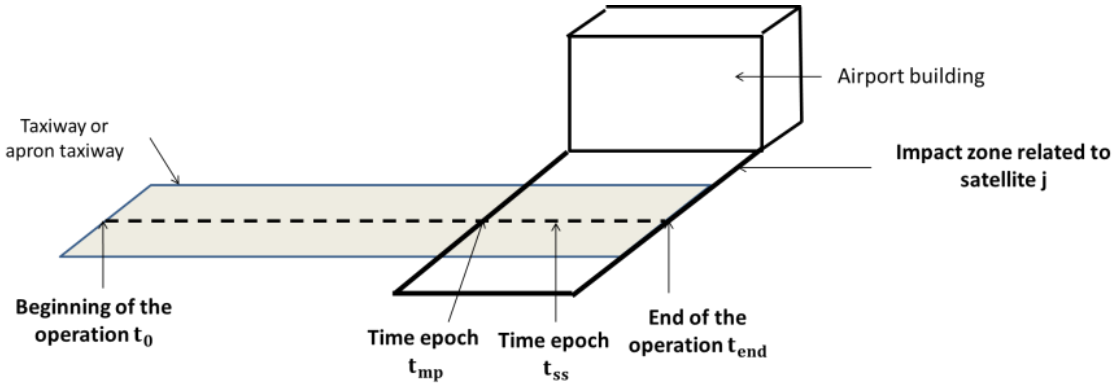

Figure 8-2: Scenario to identify the worst case probability of positioning failure

As explained in Section 7.2.2, the presence of the GNSS multipath ranging error $u_{obs\,j}$ on satellite j from time t_{mp} induces an inflation of the covariance matrix of the horizontal position error. This covariance matrix is progressively inflated from t_{mp} to t_{ss}. t_{ss} is represented in Figure 8-2. At time t_{ss}, this covariance matrix reaches its steady-state value and remains roughly constant until t_{end}. The time t_{mp} is chosen over the operation so that the covariance matrix reaches its steady state value before t_{end}. In other words, t_{end} is chosen such as:

$$t_{ss} \leq t_{end} \qquad \text{Eq - 8-11}$$

From Chapters 5 and 7, the stochastic ($\mathbf{u}$) multipath ranging error vectors during the time interval $[t_0, t_{end}]$ of the sub-phase are:

$$\forall\, t_i \in [t_0, t_{mp}], \mathbf{u}(t_i) = \begin{bmatrix} 0 \\ \vdots \\ 0 \\ \vdots \\ 0 \end{bmatrix} \forall\, t_i \in [t_{mp}, t_{end}], \mathbf{u}(t_i) = \begin{bmatrix} 0 \\ \vdots \\ u_{obs\,j}(t_i) \\ \vdots \\ 0 \end{bmatrix} \qquad \text{Eq - 8-12}$$

From Chapter 7, the horizontal position error in the time interval $[t_{mp}, t_{end}]$ can be modelled as:

$$\forall\, t_i \in [t_{mp}, t_{end}],\ \boldsymbol{\varepsilon}_p(t_i) \sim \mathcal{N}\left(\mathbf{b}_{p,mp}(t_i), \mathbf{C}_{p,w/o\,mp}(t_i) + \mathbf{C}_{p,mp}(t_i)\right) \qquad \text{Eq - 8-13}$$

where:

- $\mathbf{b}_{p,mp}(t_i)$ is the horizontal position bias induced by the GNSS deterministic multipath ranging error vector. $\mathbf{b}_p(t_i)$ is evaluated using Eq - 7-15.
- $\mathbf{C}_{p,w/o\,mp}(t_i)$ is the covariance matrix of the horizontal position error that would be obtained in the absence of stochastic multipath ranging errors. $\mathbf{C}_{p,w/o\,mp}(t_i)$ is evaluated using the methodology developed in Appendix E, Section E.4.
- $\mathbf{C}_{p,mp}(t_i)$ represents the impact of the stochastic multipath error on satellite j on the covariance of the horizontal position error. $\mathbf{C}_{p,mp}(t_i)$ is evaluated using Eq - 7-22.

Based on the horizontal position error model provided in Eq - 8-13 in the presence of the GNSS multipath ranging error on satellite j, the probability of positioning failure is estimated:

- for every time epoch t_i in the time interval $[t_{mp}, t_{end}]$,
- for every satellite configurations. The satellite configurations are represented by index t_0.

The probability of positioning failure in the presence the multipath ranging error process $u_{obs\,j}$ modelled by $\mathcal{M}(\tau_{dyn\,j}, \sigma_{dyn\,j})$ at a given time epoch t_i and for a given satellite configuration t_0 is denoted as $P_{|\varepsilon_p|>HAL \mid \mathcal{M}(\tau_{dyn\,j},\sigma_{dyn\,j})}(t_i, t_0)$. As justified in Section 7.3, the algorithm developed in [Ober, 2003] is used to estimate $P_{|\varepsilon_p|>HAL \mid \mathcal{M}(\tau_{dyn\,j},\sigma_{dyn\,j})}(t_i, t_0)$. The worst case probability of positioning failure in the presence of the multipath error modelled by $\mathcal{M}(\tau_{dyn\,j}, \sigma_{dyn\,j})$ on satellite j is then obtained as follows:

$$P_{|\varepsilon_p|>HAL \mid \mathcal{M}(\tau_{dyn\,j},\sigma_{dyn\,j}),wc} = \max_{\substack{t_i \in [t_{mp}, t_{end}] \\ t_0 \in [t_1, t_{N_{const}}]}} \left(P_{|\varepsilon_p|>HAL \mid \mathcal{M}(\tau_{dyn\,j},\sigma_{dyn\,j})}(t_i, t_0) \right) \quad \text{Eq - 8-14}$$

where N_{const} is the total number of simulated satellite configurations.

8.2.3.2.3. Integrity risk allocated to GNSS multipath single ranging failures

This section presents the methodology used to identify the pairs $(\tau_{dyn\,j}, \sigma_{dyn\,j})$ that characterize the GNSS multipath single ranging failures on satellite j based on the worst case probabilities of positioning failure $P_{|\varepsilon_p|>HAL \mid \mathcal{M}(\tau_{dyn\,j},\sigma_{dyn\,j}),wc}$ (**Phase 2**).

As justified in Section 8.2.3.1, the pairs $(\tau_{dyn\,j}, \sigma_{dyn\,j})$ that characterize the GNSS multipath single ranging failures are the pairs for which:

$$P_{|\varepsilon_p|>HAL \mid \mathcal{M}(\tau_{dyn\,j},\sigma_{dyn\,j}),wc} \geq P_{IR,mp\,j} \quad \text{Eq - 8-15}$$

where $P_{IR,mp\ j}$ is the integrity risk allocated to the GNSS single multipath ranging failure affecting the GNSS measurement j.

The integrity risk allocation among the fault-free mode and the failure modes has not been established at this stage of the project. In the following, it is assumed that the integrity risk allocated to the GNSS single multipath ranging failure $P_{IR,mp\,j}$ represents 10% of the total integrity risk P_{IR}. Note that the impact of the choice of $P_{IR,mp\,j}$ on the identification of the GNSS multipath single ranging failures is further discussed in the next section. $P_{IR,mp\,j}$ is not sub-allocated among the different satellites in view during an operation. There are two reasons for this. Firstly, it is assumed in this chapter that at most one GNSS measurement can be affected by an abnormal multipath ranging error induced by the airport obstacle at each time epoch t_i of the operation. Secondly, the factors that determine which satellite is faulty are known, as fully explained in Section 8.3. Hence, in the following, the index j is omitted in $P_{IR,mp\,j}$. $P_{IR,mp}$ is the integrity risk allocated to the GNSS single multipath ranging failure.

8.2.4. GNSS multipath failure identification at Toulouse Blagnac airport

This section identifies the pairs $(\tau_{dyn\,j}, \sigma_{dyn\,j})$ that characterize of the GNSS multipath integrity ranging failures for the following sub-phases:

- the *taxi on taxiway* sub-phase of the LVP procedure,

- the *taxi on apron taxiway* sub-phase of the LVP procedure.

For this identification, the methodology presented in Section 8.2.3 is re-used. From Section 7.3.2.3, the worst case probability of positioning failure in the presence of the error $u_{obs\,j}$, can be considered as independent of the orientation of the segment when the elevation mask angle of 15° for both GPS and Galileo constellations is chosen. Hence, the failures identified in this section are valid over the entire *taxi on taxiway* sub-phase (segments 1 and 2) of the LVP procedure path.

The methodology established in Section 8.2.3 aims to identify the characteristics of the GNSS single multipath ranging failures related to each satellite j. Since proposing an identification of the GNSS single multipath ranging failure that depends on the satellite PRN may not be simple to manipulate, it is chosen in this section to provide an identification of the GNSS single multipath ranging failures that is independent of the satellite PRN. To do so, the worst case probability of positioning failure in the presence of a GNSS stochastic multipath ranging error $u_{sat\,j}$ is computed over the time epochs $t_i \in [t_{mp}, t_{end}]$, over the satellite constellations t_0 for which the navigation system accuracy performance requirement is met, and over the satellite PRN j of the GPS+Galileo double constellation. This probability is denoted as $P_{|\varepsilon_p|>HAL\,|\,\mathcal{M}(\tau_{dyn},\sigma_{dyn}),\,wc}$ in this section. Figure 8-3 represents the estimated $P_{|\varepsilon_p|>HAL\,|\,\mathcal{M}(\tau_{dyn},\sigma_{dyn}),\,wc}$ as a function of each pair $(\tau_{dyn}, \sigma_{dyn})$ for the *taxi on taxiway* sub-phase (left part) and for the *taxi on apron taxiway* sub-phase (right part).

The simulation settings used for Figure 8-3 are recapped in Table 8-2.

Number of simulated satellite geometries	Satellite geometries simulated over 72hr with a time step of 10 minutes => 433 satellite geometries	
Number of satellites in the constellation	GPS	24 satellites
	Galileo	27 satellites
Elevation mask angle	GPS	15°
	Galileo	15°
GNSS signals	GPS	Dual frequency GPSL1C+GPSL5
	Galileo	Dual frequency GalileoE1+GalileoE5a
GNSS receiver settings	As described in Section 4.2.4	
GNSS measurement error models	**Error source**	**Error model**
	• Troposphere • Ionosphere • Satellite clock and ephemeris inaccuracies • Receiver thermal noise	Stochastic error models described in Section 3.2.1
	Multipath induced by the aircraft structure and the airport surface	Deterministic error model described in Section 7.2.1.2
	Multipath induced by aircraft structure, ground and airport obstacles	Stochastic error model described in Section 5.5.2.4
Inertial sensor error models	Stochastic error models described in Section 6.2.3	

Table 8-2: Simulation settings for Figure 8-3 and Figure 8-4

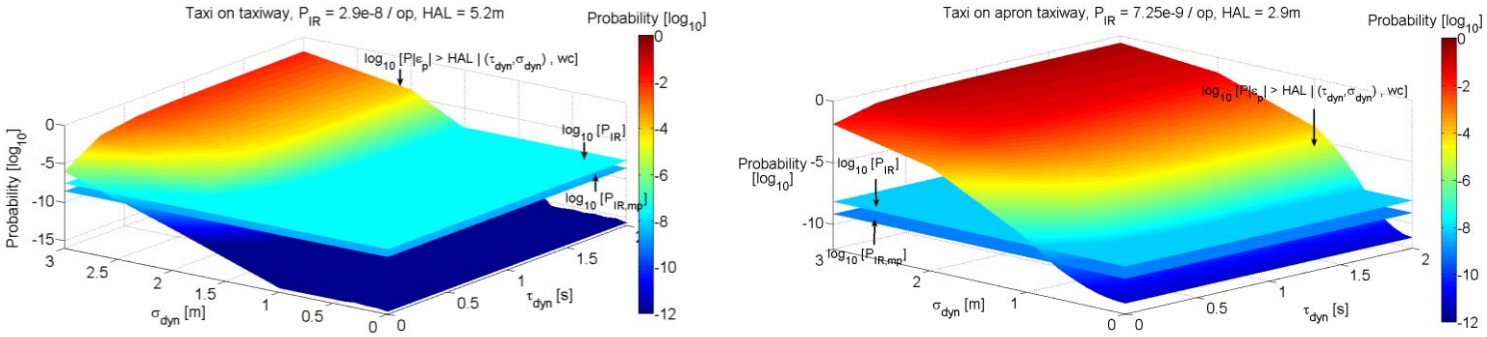

Taxi on taxiway ***Taxi on apron taxiway***

Figure 8-3: Worst case probability of positioning failure in the presence of a stochastic multipath ranging error on a single GNSS pseudo-range measurement

The following remarks can be made from Figure 8-3.

- For a fixed value of τ_{dyn}, $P_{|\varepsilon_p|>HAL \mid \mathcal{M}(\tau_{dyn},\sigma_{dyn}),wc}$ tends to increase when σ_{dyn} increases. This is because the covariance matrix $\mathbf{C}_{p,mp}$ of the 2D horizontal position error induced by the presence of the stochastic multipath ranging error is inflated when σ_{dyn} increases, as underlined in Section 7.2.2.
- For a fixed value of σ_{dyn}, $P_{|\varepsilon_p|>HAL \mid \mathcal{M}(\tau_{dyn},\sigma_{dyn}),wc}$ tends to increase when τ_{dyn} increases in the interval $[0s, 1s]$. This is because the covariance matrix $\mathbf{C}_{p,mp}$ rapidly grows with τ_{dyn} when τ_{dyn} is in the interval $[0s, 1s]$. This is underlined in Section 7.2.2. When τ_{dyn} is above 1s, $\mathbf{C}_{p,mp}$ grows less rapidly as a function of τ_{dyn}, and $P_{|\varepsilon_p|>HAL \mid \mathcal{M}(\tau_{dyn},\sigma_{dyn}),wc}$ remains roughly constant as a function of τ_{dyn}.
- For a fixed pair $(\tau_{dyn}, \sigma_{dyn})$, $P_{|\varepsilon_p|>HAL \mid \mathcal{M}(\tau_{dyn},\sigma_{dyn}),wc}$ is roughly 10^{-3} to 10^{-4} times lower for the *taxi on taxiway* sub-phase than for the *taxi on apron taxiway* sub-phase. Indeed, the HAL for than *taxi on taxiway* sub-phase is roughly twice the HAL for the *taxi on apron taxiway* sub-phase.
- When all GNSS measurements used in the PVT solution are only affected by multipath from the airport surface and form the aircraft structure, that is to say when $\tau_{dyn} = 0s$ and $\sigma_{dyn} = 0m$, $P_{|\varepsilon_p|>HAL \mid \mathcal{M}(\tau_{dyn},\sigma_{dyn}),wc}$ can be neglected regarding the integrity risk. This means the probability of loss of integrity induced by GNSS nominal errors, the inertial nominal errors, and GNSS multipath errors due to the airport surface and the aircraft structure, can be neglected for the application. The values of $P_{|\varepsilon_p|>HAL \mid \mathcal{M}(\tau_{dyn},\sigma_{dyn}),wc}$ when $\tau_{dyn} = 0s$ and $\sigma_{dyn} = 0m$ are recapped in Table 8-3.

	$P_{\|\varepsilon_p\|>HAL \mid \mathcal{M}(\tau_{dyn=0s},\sigma_{dyn=0m}),wc}$	P_{IR}
Taxi on taxiway	3.9×10^{-16}	2.9×10^{-8}/op
Taxi on apron taxiway	7.4×10^{-12}	7.25×10^{-9}/op

Table 8-3: Worst case probability of positioning failure in the absence of a multipath from airport obstacles

Next, the pairs $(\tau_{dyn}, \sigma_{dyn})$ for which the worst case probability of positioning failure is equal to the allowed integrity risk $P_{IR,mp}$ are identified by a blue line in Figure 8-4 for the *taxi on taxiway* sub-phase (left part) and for the *taxi on apron taxiway* sub-phase (right part). Simulation settings for Figure 8-4 are recapped in Table 8-2. As discussed in Section 8.2.3.2.3, it is considered that the integrity risk allocated to GNSS multipath single ranging failures is:

$$P_{IR,mp} = 0.1P_{IR} \qquad \text{Eq - 8-16}$$

The analysis of Figure 8-3 shows that, if another value of $P_{IR,mp}$ is chosen in the interval $[0.1P_{IR}, P_{IR}]$, the values of the $(\tau_{dyn}, \sigma_{dyn})$ represented in the next Figure will only be changed of few millimeters up to few centimeters.

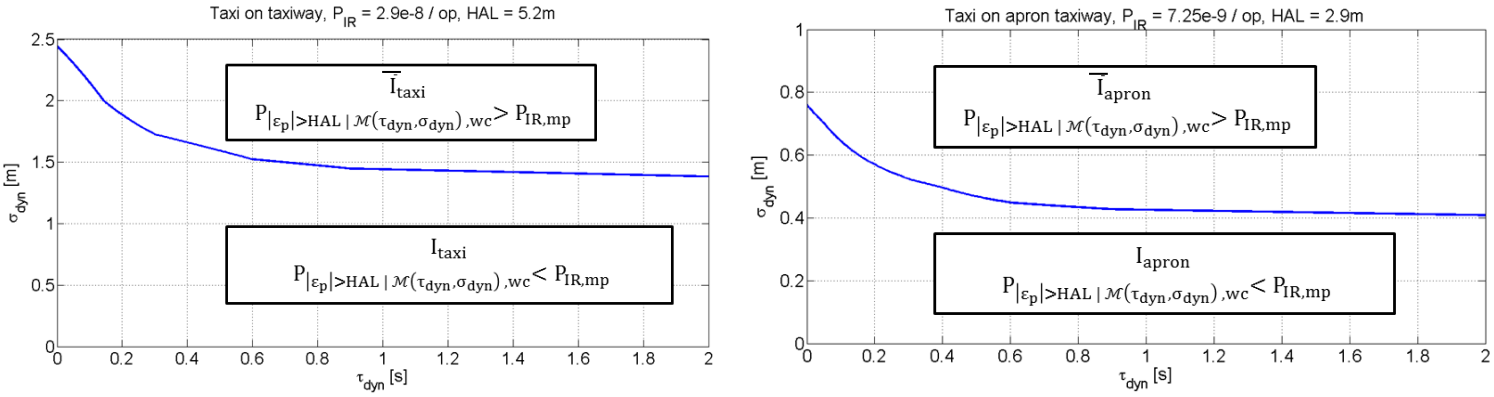

Taxi on taxiway ***Taxi on apron taxiway***

Figure 8-4: Pairs $(\tau_{dyn}, \sigma_{dyn})$ characterizing the GNSS single multipath ranging failures

In Figure 8-4, two regions can be distinguished.

- The regions I_{taxi} and I_{apron} represent the pairs $(\tau_{dyn}, \sigma_{dyn})$ characterizing the multipath ranging errors from the airport obstacles that are not identified as GNSS single multipath ranging failures. Indeed, the worst case probability of positioning failure in the presence of these errors is below $P_{IR,mp}$.
- The regions $\bar{I}_{taxi}$ and $\bar{I}_{apron}$ represent the pairs $(\tau_{dyn}, \sigma_{dyn})$ characterizing the multipath ranging errors from the airport obstacles that are identified as GNSS single multipath ranging failures. Indeed, the worst case probability of positioning failure in the presence of these errors is above $P_{IR,mp}$.

Quantitatively, let's consider a stochastic multipath ranging error that is modelled by a first order Markov process $\mathcal{M}(\tau_{dyn}, \sigma_{dyn})$. If $\tau_{dyn} = 0s$, the minimal value of σ_{dyn} for which the stochastic multipath ranging error is considered to be a single failure is set to 2.4m for the *taxi on taxiway* and 76cm for the *apron* sub-phase. If $\tau_{dyn} > 1s$, the minimal value of σ_{dyn} for which the stochastic multipath ranging error is considered to be a single failure is roughly to 1.4m for the *taxi on taxiway* and 40cm for the *apron* sub-phase.

8.3. Presence of GNSS multipath ranging failures

The development of the GNSS multipath integrity failure models is essential to design a GNSS integrity monitoring that is able to properly detect and exclude multipath failures. The first step in the development of the integrity failure model is to identify the characteristics of the GNSS multipath integrity failures. This has been done in Section 8.2 for the GNSS single multipath failures. The second step, which is the main objective of this section, is to identify the conditions of occurrence of the multipath failures and to model the occurrence of such failures.

Section 8.3.1 proposes a methodology to model the occurrence of such GNSS single ranging failures in a given airport and along a given procedure path. Section 8.3.2 assesses the presence of GNSS multipath ranging failures over the taxi and apron sub-phases of the LVP procedure at Blagnac airport.

8.3.1. Occurrence model for GNSS multipath failure

It is underlined in Section 8.1.2.1 that identifying the conditions inducing the GNSS ranging failures is essential in order to elaborate a suitable strategy to develop the probability of occurrence models. Section 8.3.1.1 presents the conditions leading to multipath single ranging failures during *taxi on taxiway* and *taxi on apron taxiway* phases. Section 8.3.1.2 proposes a methodology to model the occurrence of such GNSS single ranging failures.

8.3.1.1. Conditions of occurrence

Considering a given operation (starting time t_0 + sub-phase length Δt + procedure path) in a given airport, a GNSS multipath single ranging failure on the GNSS measurement j at epoch time t_i is said to occur if the following conditions are met.

- Firstly, the GNSS receiver antenna is located in an impact zone related to the satellite j at epoch time t_i. From Chapter 5, this implies that the GNSS measurement *j* is affected by a correlated process $u_{obs\,j}(t_i)$ modelled as a first-order Gauss-Markov process $\mathcal{M}(\tau_{dyn\,j}, \sigma_{dyn\,j})$ at this time epoch.
- Secondly, the pair $(\tau_{dyn\,j}, \sigma_{dyn\,j})$ that characterizes the multipath error $u_{obs\,j}(t_i)$ is such that: $(\tau_{dyn\,j}, \sigma_{dyn\,j}) \in \bar{I}$, where $\bar{I}$ represents the pairs $(\tau_{dyn}, \sigma_{dyn})$ that characterize the GNSS single multipath ranging failures. $\bar{I}$ is indicated in Figure 8-4 for the *taxi on taxiway* and for the *taxi on apron taxiway* sub-phases of the LVP procedure path at Toulouse Blagnac airport.

8.3.1.2. Occurrence model development

Based on Section 8.3.1.1**,** and considering a given operation in a given airport, the probability of occurrence of a GNSS single multipath ranging failure on the measurement j at epoch time t_i is formulated as follows:

$$P_{mp\,j,t_i} = P_{AC\ in\ IZ,t_i}\, P_{(\tau_{dyn\,j},\sigma_{dyn\,j})\in\bar{I}\,|AC\ in\ IZ,t_i} \qquad \text{Eq - 8-17}$$

where:

- $P_{AC\ in\ IZ,t_i}$ is the probability that the GNSS receiver antenna is in the impact zone related to satellite j at time t_i,
- $P_{(\tau_{dyn\,j},\sigma_{dyn\,j})\in\bar{I}\,|AC\ in\ IZ,t_i}$ is the probability that $(\tau_{dyn\,j}, \sigma_{dyn\,j}) \in \bar{I}$, given that the GNSS receiver antenna is in the impact zone related to satellite j at time t_i.

The strategy to compute $P_{AC\ in\ IZ,t_i}$ is expressed in Section 8.3.1.2.1. The strategy to develop $P_{(\tau_{dyn\ j},\sigma_{dyn\ j})\in\bar{I}\ |AC\ in\ IZ,t_i}$ is thus developed in Section 8.3.1.2.2. Finally, the strategy to evaluate $P_{mp\ j,t_i}$ is recapped and discussed in Section 8.3.1.2.3.

8.3.1.2.1. Computation of $P_{AC\ in\ IZ}$

The condition "GNSS receiver antenna is located in an impact zone related to the satellite j at epoch time t_i and given the satellite configuration t_0" is driven by the following parameters:

- the airport obstacle positions and characteristics as well as the satellite position (elevation and azimuth angles) for the satellite configuration t_0. These parameters determine the location of the impact zone(s) related to satellite j for the satellite configuration t_0.
- the true GNSS receiver antenna position at epoch time t_i.

In this thesis, the obstacle positions and characteristics and the satellite elevation and azimuth angles are supposed to be known in a deterministic way. This thesis does not take into account the uncertainty on the predicted true airport building positions and characteristics as well as on the satellite elevation and azimuth angles. Deterministic multipath ranging error simulators [Chen, 2010] allow predicting the impact zone locations as a function of these parameters. As a consequence, the impact zone locations related to satellite j for the satellite configuration t_0 are considered to be known in a deterministic way. The impact zone related to satellite j for the satellite constellation t_0 is also sketched in Figure 8-5 and is denoted as IZ in the following.

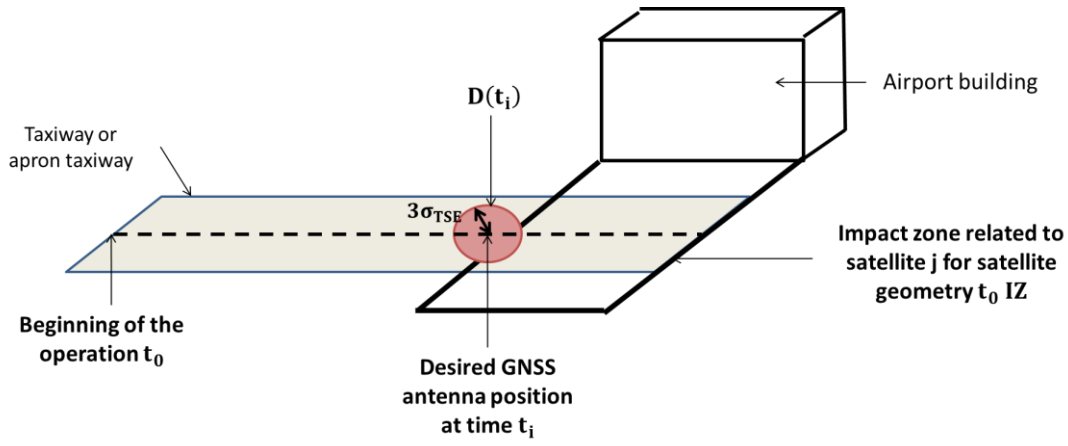

Figure 8-5: Impact zone related to satellite j and positions of the GNSS airborne antenna

The true GNSS antenna position at epoch time t_i cannot be predicted nor precisely measured in practice. One possible strategy to evaluate $P_{AC\ in\ IZ,t_i}$ is to use the statistical distribution of the true GNSS airborne antenna positions at time t_i in order to derive the probability that the GNSS airborne antenna is in the impact zone related to satellite j by means of the average risk strategy. However, using the average risk strategy to evaluate $P_{AC\ in\ IZ,t_i}$ has limited interest. Indeed, and particularly during the *apron* sub-phase and close to the airport obstacles, the probability $P_{AC\ in\ IZ,t_i}$ may be close to 1. For this reason, using the average risk strategy instead of the specific risk strategy does not reduce significantly the model of $P_{AC\ in\ IZ,t_i}$. For this reason, the specific risk strategy is used in this thesis to evaluate $P_{AC\ in\ IZ,t_i}$. This means that the airborne antenna is treated as always in the impact zone related to satellite j at time t_i if the airborne antenna may be located in the impact zone at time t_i. From Chapter 2, the horizontal distance between the desired GNSS airborne antenna position and the true GNSS

airborne antenna position is the TSE. Assuming that the TSE follows a zero-mean Gaussian distribution characterized by a standard deviation σ_{TSE} [Shuster *et al.*, 2011], 99.6% of the true antenna positions at time t_i are in a disk centered on the desired position at time t_i and characterized by a radius of $3\sigma_{TSE}$. This disk is represented in red in Figure 5-8 and is denoted as $D(t_i)$ in the following. The maximal allowed value of σ_{FTE} is discussed in Section 5.4.2.4 and is set to 1.01m for the *taxi on taxiway* sub-phase and to 61cm for the *taxi on apron taxiway* sub-phase. The true antenna positions at time t_i are considered in the disk $D(t_i)$. Using the specific risk strategy, the $P_{AC\ in\ IZ,t_i}$ can thus be evaluated as follows:

$$P_{AC\ in\ IZ,t_i} = \begin{cases} 1 \text{ if } D(t_i) \cap IZ \neq \emptyset \\ 0 \text{ if } D(t_i) \cap IZ = \emptyset \end{cases} \quad \text{Eq - 8-18}$$

8.3.1.2.2. Computation $P_{(\tau_{dyn\,j},\sigma_{dyn\,j})\in\bar{I}\,|AC\ in\ IZ}$

From Section 5.5, the values of the Gauss-Markov parameters $(\tau_{dyn\,j}, \sigma_{dyn\,j})$ in the impact zone are driven by the following parameters:

- the satellite position (elevation and azimuth angles),
- the airport obstacle positions and characteristics,
- the GNSS receiver antenna radiation pattern and the GNSS receiver settings,
- the aircraft speed over the trajectory.

As underlined in Section 8.3.1.2.1, in this thesis, the obstacle positions and characteristics and the satellite elevation and azimuth angles are supposed to be known in a deterministic way. Similarly, the aircraft speed is considered to be measurable and is considered to be known in a deterministic way. This thesis does not take into account the uncertainty on the measured speed that is inherent to the measurement process.

To conclude, both $\tau_{dyn\,j}$ and $\sigma_{dyn\,j}$ depend on a set of parameters that are considered to be observable or predictable. $\tau_{dyn\,j}$ and $\sigma_{dyn\,j}$ can be predicted by means of multipath ranging error simulators [Chen, 2010]. As a consequence, the characteristics of the multipath ranging error in the impact zone $\tau_{dyn\,j}$ and $\sigma_{dyn\,j}$ are supposed to be known in a deterministic way. $P_{(\tau_{dyn\,j},\sigma_{dyn\,j})\in\bar{I}\,|AC\ in\ IZ,t_i}$ can thus be evaluated as follows:

$$P_{(\tau_{dyn\,j},\sigma_{dyn\,j})\in\bar{I}\,|AC\ in\ IZ,t_i} = \begin{cases} 1 \text{ if} (\tau_{dyn\,j}, \sigma_{dyn\,j}) \in \bar{I} \\ 0 \text{ if } (\tau_{dyn\,j}, \sigma_{dyn\,j}) \notin \bar{I} \end{cases} \quad \text{Eq - 8-19}$$

8.3.1.2.3. Synthesis

Considering a given operation in a given airport, the probability of occurrence of a GNSS single multipath ranging failure on the satellite j at epoch time t_i $P_{mp\,j,t_i}$ is the product of two sub probabilities:

- The probability that the GNSS airborne antenna is in the impact zone related to satellite j at t_i.
- The probability that the multipath ranging error $u_{obs\,j}$ on the satellite j at epoch time t_i is a GNSS single multipath ranging failure knowing that the GNSS airborne antenna is in the impact zone related to satellite j at t_i.

Remark that $P_{mp\,j,t_i}$ represents the probability of occurrence of GNSS single multipath ranging failure for:

- a given operation (starting time t_0 + sub-phase length Δt + procedure path) in a given airport,
- a given time epoch t_i along the given operation,
- a given satellite PRN j.

In order to provide a model of the probability of occurrence of GNSS single multipath ranging failure that is easier to manipulate and that is conservative, it is proposed to remove the dependency of the probability on the epoch time t_i of the operation starting at t_0 by using the following model:

$$P_{mp\,j} = \max_{t_i}\left(P_{mp\,j,t_i}\right) \qquad \text{Eq - 8-20}$$

It can also be envisaged to maximize the probability over the satellite PRNs and over the satellite geometries t_0. The resulting probability would be only dependent on the procedure path, and would be simple to manipulate. However, this probability of occurrence model would be extremely conservative. This would decrease the required probability of missed detection of GNSS single multipath ranging failures and this would potentially lead to degrade the availability of the navigation system. For this reason, it can be advised to investigate the effect of maximizing the probability of occurrence over the PRN and the satellite geometries on the availability of the system in order to analyze the real benefits and drawbacks of proposing an occurrence model that is independent of the PRNs and of the satellite geometries.

The occurrence model developed in this section depends on the obstacles positions and characteristics and on the GNSS aircraft positions along the procedure path. Hence, the occurrence model depends on the 3D representation of the airport buildings and on the surface procedure. However, the 3D models of all airports and the procedures paths of all airports are not known. As a consequence, the development of an occurrence model that is common to all procedure paths and all airports is not feasible. The occurrence model is thus specific to an airport and to a procedure path. The next section evaluates the presence of the GNSS single multipath ranging failures along the LVP procedure path of Toulouse Blagnac airport, France.

8.3.2. Presence of GNSS multipath failure at Toulouse Blagnac airport

Section 8.3.1 elaborates a strategy to develop the model of GNSS multipath single ranging failures along a given taxi operation. This section re-uses this methodology to provide the presence model of GNSS multipath single ranging failures at Toulouse Blagnac airport, France *over taxi on taxiway* and *taxi on apron taxiway* sub-phases of the LVP procedure path. The *taxi on taxiway* and the *taxi on apron taxiway* segments along the LVP procedure path are depicted in Figure 8-6.

This section is organized as follows. Section 8.3.2.1 summarizes the assumptions and the simplifications that have been made in this thesis to evaluate the presence of GNSS single multipath ranging failures at Toulouse Blagnac airport, France. Section 8.3.2.2 presents the presence model during the *taxi on taxiway* sub-phase of the LVP procedure path. Section 8.3.2.3 presents the presence model during the *taxi on apron taxiway* sub-phase of the LVP procedure path.

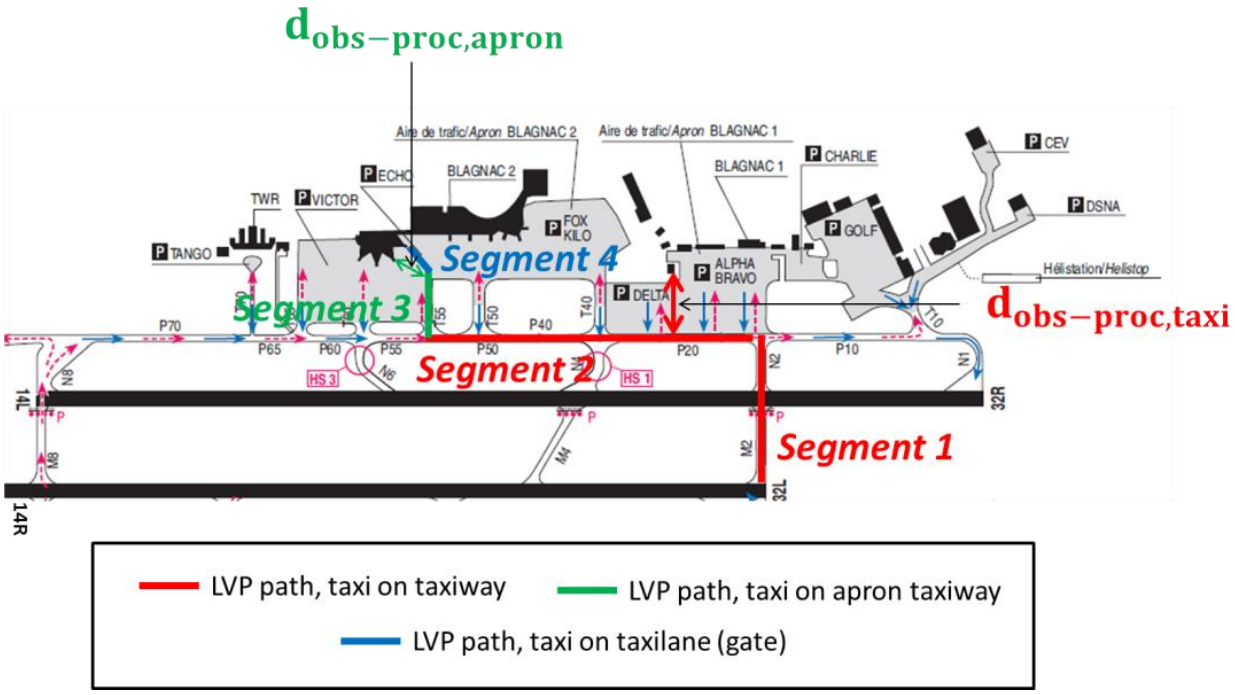

Figure 8-6: *Taxi on taxiway* and *taxi on apron taxiway* segments along the LVP procedure path

8.3.2.1. Limitations

This section summarizes the main assumptions that have been made when evaluating the presence model of GNSS single multipath ranging failures at Toulouse Blagnac airport. The assumptions can be classified into two categories that are listed below.

- Assumptions and simplifications have been made in the evaluation of the Gauss-Markov process parameters $(\tau_{dyn\,j}, \sigma_{dyn\,j})$ that characterize the multipath ranging errors induced by the airport obstacles at Toulouse Blagnac airport, France:
  - $(\tau_{dyn\,j}, \sigma_{dyn\,j})$ have been evaluated using the following parameters and models :
    - The 3D model of the airport is a simplified 3D model. The validity of this model is further discussed in Appendix B, Section B.1. The airport obstacles represented in the scene are the airport buildings and the airport gates. The mobile and movable obstacles, such as other aircraft, footbridges or trucks, are not represented in the scene.
    - The airport surface is an infinite and planar ground made of dry tar.
    - The same antenna gain pattern is used to compute both L1 and L5 antenna gains. The antenna group delay and phase delay are not included in the antenna model.
  - $(\tau_{dyn\,j}, \sigma_{dyn\,j})$ have been evaluated assuming that the variance of the GNSS multipath ranging error induced by the airport obstacles when the aircraft crosses the impact zone is stationary throughout the trajectory in the impact zone.
- Assumptions and simplifications have been made in the evaluation of the Gauss-Markov process parameters $(\tau_{dyn\,j}, \sigma_{dyn\,j})$ that characterize the GNSS multipath single ranging failures. The values of these parameters are presented in Section 8.2.4:
  - The impact of multipath on the C/N0 ratios, and hence on the standard deviation of the receiver thermal noise ranging errors, has not been taken into account. The validity of this simplification is discussed in Section 6.2.2.3.

- An algorithm is assumed to be implemented in the navigation system to set the navigation system "unavailable" when the navigation accuracy performance does not meet the accuracy navigation performance requirement stated in Section 2.3.2.3.

8.3.2.2. Taxi on taxiway

This section presents the presence model of the GNSS single multipath ranging failures over the *taxi on taxiway* procedure represented by red lines in Figure 8-6. An analysis based on the 2D model of Toulouse Blagnac airport represented in Figure 8-6 shows that the minimal horizontal distance between the procedure path and the airport obstacles is:

$$d_{obs-proc,taxi} = 250\text{m} \qquad \text{Eq - 8-21}$$

$d_{obs-proc,taxi}$ is represented in Figure 8-6. As discussed in Section 8.3.1.2.1, the maximal distance between the procedure path and the true aircraft path is $3\sigma_{PDE} = 3 \times 1.01\text{m} = 3.03\text{m}$. Hence, the minimal horizontal distance between the true aircraft path and the airport obstacles is:

$$d_{obs-AC,taxi} = 250\text{m} - 3.03\text{m} = 246.97\text{m} \qquad \text{Eq - 8-22}$$

The methodology developed in Section 5.4.2.1 has been used to estimate the impact zone locations over segment 3 and in the presence of Halls A to D when the satellite elevation is above the mask angle of 15°. This analysis shows that, if the horizontal distance between the GNSS receiver antenna and the façade of an airport obstacle is roughly above 200m, the influence of the echo signals of satellite j received from this obstacle on the multipath ranging error related to satellite j is not significant for the application. It is concluded that, along the considered *taxi on taxiway* procedure path, the GNSS receiver antenna does not go through any impact zone along this procedure path. As a result, regardless the satellite PRN, the time instant t_i and the operation starting time t_0, we obtain:

$$P_{AC\ in\ IZ,t_i} = 0 \qquad \text{Eq - 8-23}$$

This leads to:

$$\forall t_0\ \forall t_i\ \forall\ sat\ j, P_{mp\ j,t_i} = 0 \qquad \text{Eq - 8-24}$$

To conclude, considering the assumptions and simplifications stated in Section 8.3.2.1, it can be considered that GNSS multipath single ranging failures are not present on the *taxi on taxiway* sub-phase of the LVP procedure path at Toulouse Blagnac airport.

8.3.2.3. Taxi on apron taxiway

This section presents the presence model of the GNSS multipath single ranging failures over the *taxi on apron taxiway* procedure represented by a green line in Figure 8-6.

8.3.2.3.1. Analysis of $P_{AC\ in\ IZ}$

The minimal horizontal distance between the procedure path and the airport obstacles is:

$$d_{obs-proc,apron} = 117\text{m} \qquad \text{Eq - 8-25}$$

$d_{obs-proc,apron}$ is represented in Figure 8-6. A portion of segment 3 can be included in the impact zone, depending on the satellite elevation and azimuth angles. It is underlined in Section 5.4 that aircraft does not cross the impact zone related to satellite j on segment 3 when the elevation of satellite j is above 35°. It but may cross the impact zone when the elevation of satellite j is below 35°, regarding the azimuth angle of satellite j. The identification of the pairs satellite elevation/satellite azimuth for which the impact zone covers the segment 3 remains as future work.

To conclude, the GNSS airborne antenna may potentially cross the impact zone along the *apron* segment of the LVP procedure. In order to evaluate the presence model of the GNSS multipath single ranging failures along the apron sub-phase, the probability $P_{(\tau_{dyn\,j},\sigma_{dyn\,j})\in\bar{I}\,|AC\text{ in }IZ}$ along the apron segment are presented in the next section.

8.3.2.3.2. Analysis of $P_{(\tau_{dyn\,j},\sigma_{dyn\,j})\in\bar{I}\,|AC\ in\ IZ\ of\ sat\ j}$

In this section, the model parameters $(\tau_{dyn}, \sigma_{dyn})$ characterizing the multipath ranging errors induced by the airport obstacles in the impact zone along the apron segment are presented and compared to the pairs $(\tau_{dyn}, \sigma_{dyn}) \in \bar{I}_{apron}$ that characterize the multipath ranging errors considered as GNSS single ranging failures.

Figure 8-7 presents:

- The pairs $(\tau_{dyn}, \sigma_{dyn})$ that characterize the multipath ranging errors considered as GNSS single ranging failures for the apron sub-phase and that are above the blue line depicted on each Figure. These pairs are further discussed in Section 8.2.4 and are located in the region denoted as $\bar{I}_{apron}$.
- The multipath error model parameters $(\tau_{dyn}, \sigma_{dyn})$ that characterize the multipath ranging error induced by the airport obstacles along segment 3. These pairs are represented by the dots. These parameters have been obtained by means of the GNSS multipath ranging error simulator described in Chapter 5. The simulation methodology to obtain these pairs is fully described in Section 5.5. The parameters $(\tau_{dyn}, \sigma_{dyn})$ along segment 3 are driven by:
  - the satellite position (elevation and azimuth angles),
  - the airport obstacle positions and characteristics,
  - the GNSS receiver antenna radiation pattern and the GNSS receiver settings,
  - the aircraft speed over the trajectory.

For this reason, multipath error model parameters $(\tau_{dyn}, \sigma_{dyn})$ are plotted for :

- different aircraft speeds in the range $[1\text{m.s}^{-1}, 5\text{m.s}^{-1}]$ (left part of Figure 8-7),
- different satellite elevation angles in the range $[15°, 35°]$ (middle part of Figure 8-7),
- different satellite azimuth angles in the range $[-60°, 60°]$ (right part of Figure 8-7).

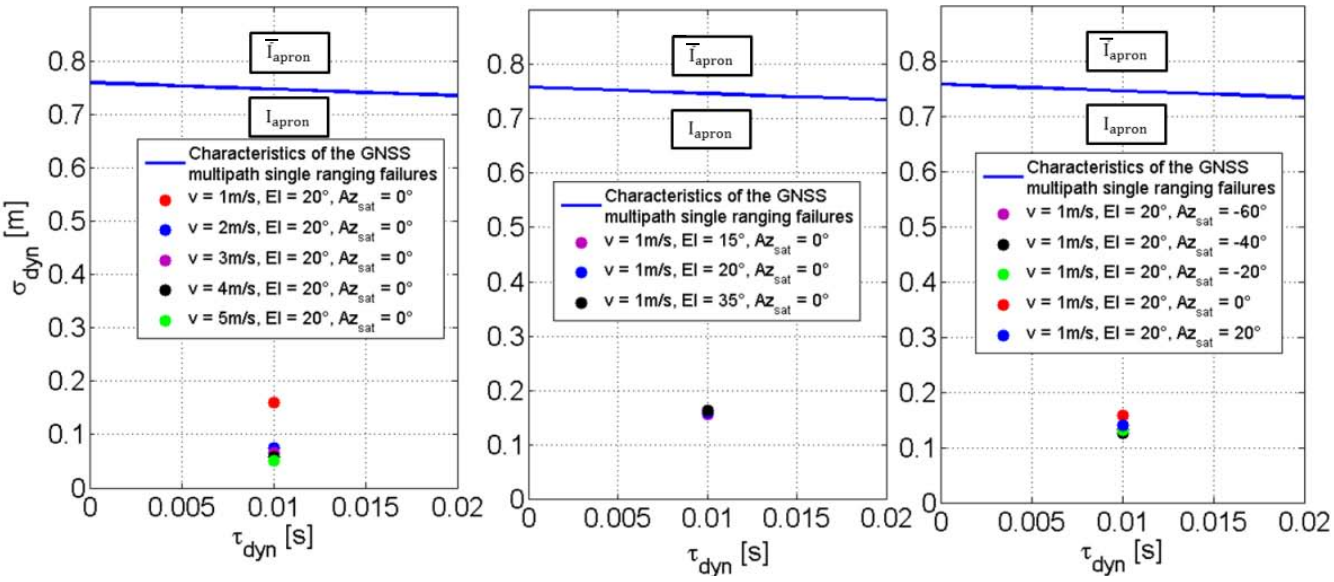

Figure 8-7 : First-order Gauss-Markov process parameters $(\tau_{dyn}, \sigma_{dyn})$ for different aircraft speeds, satellite elevation angles and satellite azimuth angles

The following remarks can be made from Figure 8-7.

- Firstly, for fixed satellite elevation and azimuth angles, the highest value of σ_{dyn} is obtained for the lowest aircraft speed, that is set to 1m.s^{-1} in this thesis. An interpretation of this observation is provided in Section 5.5.
- Secondly, for a fixed satellite azimuth angle and for a fixed aircraft speed, σ_{dyn} is roughly constant as a function of the satellite elevation angle.
- Thirdly, for a fixed satellite elevation angle and for a fixed aircraft speed, σ_{dyn} is roughly constant as a function of the satellite azimuth angle.

Following these remarks, the highest value σ_{dyn} is obtained for an aircraft speed of 1m.s^{-1}, and is below 20cm regardless of the satellite elevation angle or the satellite azimuth angle. The correlation time parameter τ_{dyn} is set to 10ms regardless of the aircraft speed and of the satellite position, as justified in Section 5.5. Hence, regardless of the satellite elevation and azimuth angles, and regardless the aircraft speed on segment 3:

$$(\tau_{dyn}, \sigma_{dyn}) \in I_{apron} \qquad \text{Eq - 8-26}$$

It can be concluded that:

$$\forall t_0\ \forall t_i, \forall \text{sat j}, P_{(\tau_{dyn\,j}, \sigma_{dyn\,j}) \in \bar{I}_{apron}\ |\text{AC in IZ},t_i} = 0 \qquad \text{Eq - 8-27}$$

8.3.2.3.3. Analysis of $P_{mp\,j}$

Eq - 8-27 leads to:

$$\forall t_0\ \forall t_i\ \forall \text{ sat j}, P_{mp\,j,t_i} = 0 \qquad \text{Eq - 8-28}$$

To conclude, considering the assumptions and simplifications stated in Section 8.3.2.1, it can be considered that GNSS multipath single ranging failures are not present on the *taxi on apron taxiway* sub-phase of the LVP procedure path at Toulouse Blagnac airport.

8.4. Conclusions

The navigation system integrity performance requirements for the guidance function during the taxi operation and under low visibility conditions have been recalled and discussed in this chapter. The concept of GNSS integrity failure model has been defined and the importance of the GNSS integrity failure models in the design of the GNSS integrity monitoring systems has been underlined.

Since this project represents a first step in the development of the GNSS multipath integrity failure model, it is proposed to focus on the identification and on the occurrence model of GNSS single multipath ranging failures in the airport environment. This chapter has proposed a methodology to identify the characteristics of the GNSS multipath single ranging failures in a given airport.

Next, this chapter has proposed a methodology to model the occurrence of GNSS multipath single ranging failures in a given airport environment. Since the occurrence model is driven by the airport obstacle characteristics and by the procedure path location relative to the airport obstacles location, the proposed methodology is specific to a procedure path in a given airport. Extending the occurrence models to all procedure paths in a given and to all airports has been discussed. This methodology has been used to model the presence of the GNSS multipath ranging failures during the *taxi on taxiway* and during the *taxi on apron taxiway* sub-phases along the LVP procedure path at Toulouse Blagnac airport. By considering that the airport buildings and the airport gates are the only airport obstacles present in this airport, the occurrence of GNSS multipath ranging failures during the *taxi on taxiway* and during the *taxi on apron taxiway* sub-phases along the LVP procedure path can be considered as null. The occurrence model in the presence of mobile airport obstacles, such as other moving or parked aircraft, has to be assessed. This part remains as future work.

CHAPTER 9

Conclusions

The conclusions relative to each chapter of the thesis are summarized in Section 9.1. Section 9.2 presents the recommendations for future work.

9.1. Summary

In order to make the surface operations safer and to maintain the airport capacity under critical conditions (under low-visibility conditions or high traffic density conditions), advanced surface movement systems are being developed. These systems should support the guidance function under all visibility conditions. Using GNSS for the zero-visibility surface guidance function raises issues since GNSS measurements may be affected by GNSS singular events in airport environments. GNSS singular events may lead to unacceptable position errors in terms of accuracy and integrity for the zero-visibility guidance function. Current GNSS integrity monitoring systems are not designed to totally account for the GNSS singular event effects. Hence, GNSS singular events may represent a threat in terms of accuracy and integrity for the zero-visibility surface guidance function.

The overall objective of this Ph.D. was to address the effects of singular events on the accuracy and integrity of GNSS-based navigation systems for the zero-visibility guidance function application, with a special attention to multipath. More specifically, GNSS measurement error and integrity failure models are key inputs in the design of GNSS integrity monitoring systems. In this thesis, work has been mainly focused on the modelling of GNSS multipath measurement errors, on the assessment of the multipath impact on the GNSS-based position error, and on the development of GNSS multipath integrity failure models for airport navigation.

For this matter, the navigation system performance requirements adapted to the surface guidance function under zero-visibility conditions have been firstly identified in **Chapter 2**. The taxi operation is part of the surface operations and includes three sub-phases: the *taxi on taxiway*, the *taxi on apron taxiway* and the *taxi on taxi lane*. The navigation system performance requirements for the three sub-phases are presented and discussed. New and less stringent accuracy and integrity requirements are proposed to account for a less conservative FTE budget.

Next, the GNSS constellations (GPS and Galileo) and the GNSS signals (GPSL1C, GPSL5, GalileoE1 and GalileoE5a) used in the development of the multipath ranging error and position error models have been selected in **Chapter 3**. ABAS has also been chosen as the augmentation system that will support the application. The choice of these constellations, signals and augmentations system have been discussed and justified. After that, a bibliographic study has been conducted to review the shape, the magnitude and the occurrence of GNSS error measurements with a specific attention to the errors induced by singular events. The capacity of current and future GNSS integrity monitoring systems to provide sufficient protection against the effects of the singular events has been assessed. Based on this assessment, it has been chosen to focus the rest of the thesis on multipath.

Chapter 4 proposes a general analysis of the multipath impact on the GNSS signals and measurements. A wideband model has been chosen to represent the transmission channel. Based on this representation, the analytical expressions of the GNSS signals at the receiver antenna output are presented. Next, the chapter analyzes the multipath impact on the GNSS code delay estimate. For this analysis, a brief description of the DLL has been provided. Finally, the evolution of the multipath code ranging error in the presence of a single multipath and as a function of the relative code delay between the direct and the echo signal has been discussed. The analytical expression of this error for both GPSL5 and GalileoE5a signals has been proposed.

Chapter 5 has proposed the model of the GNSS multipath measurement errors adapted to taxi sub-phases. The error models account for the presence of three types of multipath sources: the airport surface, the aircraft structure, and the airport buildings and gates. Multipath error models have been developed at Toulouse Blagnac airport, France by means of a GNSS multipath ranging error simulator. This software uses a simple 3D model of the airport buildings and gates. The simplifications done to build this 3D model have been presented. It has been identified from the literature that sub-wavelength level details and isolated obstacles of size below 80cm do not have to be modelled in order to properly estimate the GNSS ranging errors. In addition, concrete meter level details on concrete façade do not have to be modelled in order to properly estimate the GNSS ranging error model parameters. Other simplifications, such as on the assumed dielectric permittivity of the glass and concrete walls, have been identified and their analysis is recommended as future work.

Chapter 5 has also proposed multipath ranging error models when the aircraft is parked or is moving in the airport scene. In the dynamic configuration (rectilinear and uniform trajectories with an aircraft speed of 1m/s or higher), the multipath ranging error can be modelled as the sum of two error components. The time-constant deterministic error component throughout the rectilinear trajectory is induced by the ground first-order reflections. It reaches a few decimetres up to a few meters at low satellite elevation angles (that is to say below 15°). Hence, few measurements experience significant ground reflections at a time. The zero-mean time-varying error component throughout the rectilinear trajectory is induced by the obstacles first and second-order interactions. This time-correlated error highly depends on the aircraft trajectory in the scene. Since the aircraft trajectory cannot be known deterministically with a high accuracy level (centimetre level), the time-varying error has been considered as a stochastic correlated process modelled as a zero-mean first-order Gauss-Markov process characterized by a standard deviation and by a correlation time. The sensitivity of the standard deviation to the satellite elevation angle, to the satellite azimuth angle and to the aircraft speed has been assessed. The highest values of the standard deviation are obtained at low aircraft speed, low satellite elevation angles, and close to the airport buildings. As an example, the standard deviation reaches a few meters at Blagnac airport in the gate area, for an aircraft speed of 1m/s and for a satellite elevation angle of 5°.

Next, the effects of the GNSS multipath measurement errors on the horizontal position error has been modelled and quantified. **Chapter 6** has focused on the identification of a positioning algorithm suitable for the application. An open-loop double constellation GPS+Galileo/IRS/DEM tight coupling positioning algorithm has been chosen. The coupling technique is based on a linearized Kalman filter. The reasons that have justified these choices are discussed in the chapter. After having chosen the positioning algorithm, the implementation of the software that simulates the horizontal position error at the output of the positioning algorithm has been presented.

Once the GNSS-based navigation algorithm has been detailed, the impact of multipath on the GNSS-based horizontal position error at the output of the selected positioning algorithm has been assessed in the dynamic configuration and in **Chapter 7**. It has been firstly justified that the position error in the 2D horizontal plane and during surface operations can be over-bounded by a bi-dimensional Gaussian distribution characterized by a 2D bias vector and by a covariance matrix. Next, the multipath impact on both position bias and positioning error covariance matrix has been assessed. It has been concluded that:

- The GNSS deterministic multipath ranging error vector induced by the airport surface and by the aircraft structure generates a bias on the horizontal position error. The analytical expression of this position bias as a function of the Kalman filter matrices and of the deterministic multipath ranging error vector has been provided. The norm of the induced horizontal position bias is a few decimetres for standard satellite elevation mask angles (5° for GPS and 10° for Galileo) and is significantly reduced to a few centimetres for satellite elevation mask angles of 15° for both GPS and Galileo constellations.
- The stochastic multipath ranging error vector induced by the airport buildings and airport gates and modelled as a first-order Gauss-Markov process vector generates an increase of the covariance matrix of the position error in the 2D horizontal plane. The analytical expression of the additional covariance matrix of the position error induced by multipath as a function of the Kalman filter matrices and of the first-order Gauss-Markov process vector has been provided. When only few of the satellites are affected by multipath from the airport buildings and gates at a time, a significant dilution of the obstacle multipath in the positioning domain is observed. In airport environments such as at Toulouse Blagnac airport, it is reasonable to say that few satellites are simultaneously affected by obstacles (3 to 5 satellites at Blagnac airport). As an illustration, the worst case inflation of the standard deviation of the horizontal position error induced by multipath at Blagnac airport is a few decimeters and is experienced in the gate area (*taxi-lane* operation).

Once the position error models adapted to surface operations have been set up, the accuracy of the positioning algorithm has been assessed along the three taxi sub-phases related to a specific procedure path at Blagnac airport. It has been concluded that the elevation mask angle of 15° for both GPS and Galileo constellations improves the accuracy and availability of the system compared to the standard mask angles of 5° for GPS and 10° for Galileo. It is also shown that the accuracy requirement is not met for the *taxi on taxi lane* sub-phase, is met for nearly 96% of the satellite geometries for the *apron* sub-phase and is met for 100% of the satellite geometries for the *taxiway* sub-phase. An open-loop GNSS/IRS/DEM/WSS tight coupling positioning algorithm has been implemented to evaluate the benefit of using WSS measurements in the coupling algorithm to improve the accuracy performance. Even if the WSS aid reduces the standard deviation of the horizontal position error of a few centimeters, this aid is not sufficient to meet the accuracy requirement for the *taxi on taxi lane* sub-phase and does not improve the accuracy function availability for the *apron* sub-phase. The operational benefits of developing a navigation system only for the *taxiway* and *apron* sub-phases have been underlined. Even if the GNSS/IRS/DEM solution is not a full-availability

solution for the apron sub-phase, the benefits of proposing this solution for both taxiway and apron sub-phases have been discussed.

Finally, **Chapter 8** has detailed a methodology to develop the GNSS multipath integrity failure model for single multipath ranging failures in a given airport for the *taxiway* and *apron* sub-phases. The developed failure model describes the characteristics in terms of standard deviation and correlation time of the GNSS single multipath ranging failures, the factors influencing these characteristics as well as the occurrence model of the GNSS single multipath ranging failures and their conditions of occurrence. Under the assumptions stated in the thesis, and particularly in the absence of mobile obstacles in the scene, such as other parked aircraft, GNSS single ranging failures do not occur during both *taxiway* and *apron* operations along the considered procedure path at Blagnac airport.

9.2. Future work

The different recommendations for future work have been discussed in the different chapters of this thesis and are summarized as follows.

Navigation system requirement performance

Concerning the development of integrity navigation system requirement performance for the zero-visibility guidance function, the integrity risk used in this thesis is proportional to the exposure time related to that sub-phase. It would be valuable to account also for the produced effects of the integrity loss for that sub-phase. The produced effects of a loss of integrity depend on the aircraft speed and on the type of obstacles in which the aircraft may collide.

GNSS multipath ranging error models

Concerning the simulation parameters employed by the GNSS multipath ranging error simulator for the estimation of the error model parameters, it is proposed to enhance the model of the GNSS airborne antenna by implementing a dual-band L1+L5 antenna that take into account the group delays and phase delays induced by the antenna and by multipath from the structure of the assessed A319 aircraft.

Concerning the development of the 3D airport models suitable for the estimation of the GNSS multipath ranging error model parameters, further analyses are recommended for future work:

- It is proposed to develop error models that account for more realistic ground surfaces, such as ground surfaces made of tar and grass parts. It would be also valuable to investigate the impact of rain or snow on the error models.
- In order to fully demonstrate the validity of the 3D model of Toulouse Blagnac for the estimation of the multipath error model parameters, it would be valuable to investigate:
  - The impact of the roughness of the building and gate walls on the error models.
  - The necessity to model the interior parts of the buildings and gates in order to estimate the error model parameters.
  - The impact of the dielectric permittivity and thickness of concrete and glass walls on the error models. It would also be valuable to propose recommendations on the values of thickness and permittivity that can be adopted in the 3D airport models to estimate the error model parameters.
- Finally, it is useful to develop a general methodology to develop the 3D airport models suitable for the error model development. In this thesis, the error models have been developed at Blagnac airport. Developing the error models in a given airport is possible if a precise 3D model of the environment is available for that airport. If such data bases are not available, it can be envisaged to build a simple 3D model of the airport environment by classifying each airport façade into clusters. Each cluster gathers together realistic facades

that can be represented by a simple façade in the 3D model. The identification of all façade clusters is required to extend the error models to other airports and is recommended as future work.

Concerning the development of the GNSS multipath ranging error models, recommendations to enhance the models proposed in this thesis are listed as follows:

- The dynamic error model can be enhanced by extending this dynamic model to curved and/or non-uniform trajectories.
- The GNSS multipath ranging errors induced by the airport obstacles in the dynamic configuration are modelled by a first-order Gauss-Markov process characterized by a standard deviation and by a correlation time. In this Ph.D. thesis, the correlation time is set to a fixed value and the standard deviation of the model is calculated in a way that the PSD of the Gauss-Markov process over-bounds the PSD of the time-varying correlated error process throughout the trajectory. It is proposed as a future work to develop an algorithm that estimates the correlation time and the standard deviation of the Gauss-Markov model that lead to over-bound the PSD of the correlated process obtained by simulations while minimizing the covariance matrix of the position error induced by these time-varying multipath errors.
- The static and dynamic models of the GNSS multipath ranging error induced by the airport obstacles along a segment located in the impact zone are characterized by a standard deviation parameter. This parameter is estimated by simulation assuming that the amplitude variations of the error induced by the airport obstacles are constant along the segment. However, along the taxi lane segments particularly, the amplitude of the error induced by the airport obstacles is not constant. Hence, it would be valuable to determine the segment part where the error amplitude is maximal and to estimate the standard deviation parameter on this part.
- The models of the GNSS multipath ranging error are not adapted to the presence of mobile obstacles. In order to account for the presence of mobile obstacles in the scene, it can be proposed to estimate the positions and orientations of the mobile obstacles in the scene by using Automatic Dependent Surveillance – Broadcast (ADS-B) systems. It can also be proposed to develop models of prediction of the positions and orientations of the mobile obstacles in the scene. After that, error models valid in the presence of both fixed and mobile obstacles have to be developed.
- The error component induced by the airport buildings has been modelled by a Gaussian distribution in the static configuration and by a first-order Gauss-Markov process in the dynamic configuration. It is recommended to investigate the feasibility to model the error by over-bounding models that best fits the estimated error. The design of integrity monitoring algorithms that use non-Gaussian error models as expected measurement error models has also to be assessed.
- It is also recommended as future work to validate the developed multipath ranging error models by real data.

Horizontal position error models

Concerning the simulation parameters and the type of Kalman filter employed by the GNSS/IRS/DEM simulator to compute the horizontal position errors, further analyses are recommended:

- It is recommended to analyze the impact of multipath on the C/N0 ratios, on the standard deviations of the receiver thermal noise ranging errors during surface operations, and on the loss of tracking of the GNSS signals. If the multipath impact on the noise error

standard deviations and on the loss of tracking is significant, it is recommended to develop a C/N0 link budget that accounts for the multipath effects.
- It has been underlined that the satellite elevation mask angles for both GPS and Galileo constellations significantly impact the horizontal position bias and the horizontal position error covariance matrix. It would be valuable to determine the optimal satellite elevation mask angle. The optimal mask angle is the angle value for which the accuracy performance of the position algorithm is optimal.
- It is further recommended to analyze and compare the performance of both EKF and linearized Kalman filters during sub-phases where the GNSS measurements are mainly affected by low multipath errors (such as during the *taxi on taxiway* sub-phase) and during sub-phases where the GNSS measurements may be affected by severe multipath errors (such as during the *taxi on taxi lane* sub-phase). If the EKF presents better performance for some of the sub-phases, it is recommended to assess the multipath impact on the position error at the output of the EKF GNSS/IRS positioning algorithm.

It has been shown that the proposed GNSS/IRS and the GNSS/IRS/WSS coupling algorithms do not meet the accuracy navigation system performance requirement related to the *taxi on taxi lane* sub-phase. It is recommended as future work to identify the WSS correlation modes in the time domain and between the wheels by real data analysis and to propose a Kalman filter implementation that accounts for these correlation modes. It is also recommended to integrate an extra sensor in the GNSS/IRS/WSS algorithm in order to meet the accuracy requirement for the *taxi on taxi lane* sub-phase. Among the proposed technologies that could be used for this sub-phase, it has been recommended in this thesis to consider LIDAR. Note also that, since the gate area is a relatively small-scale environment, it can be envisaged to integrate GNSS and IRS with technologies adapted to small-scale environments on taxi lanes. Among these technologies, UWB is of particular interest due to its centimeter level accuracy.

GNSS multipath integrity failure model

Concerning the development of the GNSS multipath integrity failure models for surface operations, further analyses are recommended:

- It is recommended to develop the GNSS multipath multiple failure models for both *taxiway* and *apron* sub-phases.
- Once the GNSS-based positioning adapted to the *taxi on taxi lane* sub-phase will be developed, it is recommended to develop the GNSS multipath single and multiple failure models for this sub-phase.
- Since the aircraft cannot respond instantaneously to the navigation system, a given positioning failure must persist for several seconds before the aircraft position will significantly deviate. Indeed, the aircraft and its control system behaves as a low-pass filter on the NSE. Hence, it is recommended as future work to analyze the minimal duration of a positioning failure required before the aircraft position significantly deviates.

General recommendations and perspectives

As underlined in Chapter 1, extending the use of GNSS to the zero-visibility guidance function requires analyzing the multipath impact on both accuracy and integrity of GNSS-based airport surface navigation systems. This thesis has mainly focused on the identification of GNSS integrity failures. One of the main perspectives is to address the effects of multipath on the accuracy of the positioning algorithm and to identify which GNSS multipath ranging failures may represent a threat in terms of accuracy.

The second main perspective related to this thesis is to develop a GNSS integrity monitoring systems designed to protect users from the effects of multipath during the taxi sub-phases. The designed integrity monitoring systems must be capable of detecting GNSS multipath

failures with required probabilities of missed detection. The following methodology can be suggested concerning the development of a real-time GNSS multipath failure detection technique in airport environments.

- The first step consists in developing a technique to estimate in real-time the multipath error models on the GNSS. The following suggestions can be made for the development of the estimation technique:
  - Firstly, a data-base that pre-defines the signature of each airport obstacle in terms of multipath ranging error models by means of a GNSS multipath ranging error simulator can be developed. Note that it is recommended in this thesis to develop a data-base of error models for two reasons. The first reason is that determining the error models requires a relatively high computation load. Hence, the error models can be difficult to estimate onboard and in real-time. The second reason is that the number of facades and obstacles present in airport environments is limited. In addition, some facades and obstacles may have similar signature in terms of multipath errors.
  - Secondly, it is proposed to develop an algorithm that estimates the localization of the impact zones in real-time from the GNSS satellites positions estimates and from a simplified 3D airport model.
  - Thirdly, it is proposed to develop an algorithm that estimates the GNSS multipath ranging error models on the GNSS measurements in real-time from the estimated impact zone locations, from the GNSS airborne antenna position estimates, and from the pre-defined data base that includes the obstacle signatures in terms of multipath error models.
- The second step consists in detecting and excluding the GNSS measurements that are affected by GNSS multipath failures. Note that the technique that estimates the GNSS multipath ranging error models in real-time can also be used to estimate the accuracy of the horizontal position estimate in real-time and to detect and exclude the GNSS measurements that represent a threat in terms of accuracy.

REFERENCES

[Ait Ighil, 2013] "Ph.D. dissertation: Enhanced physical-statistical simulator of the land mobile satellite channel for multipath modelling applied to satellite navigation systems", M. Ait Ighil, Institit Supérieur de l'Aéronautique et de l'Espace, January 2013

[Airbus, 2014] Personal discussion with Airbus experts on GNSS landing systems and flight dynamics, 2014

[ANC, 2003] "Eleventh Air Navigation Conference, report of committee B to the conference on Agenda Item 6", Montreal, October 2003

[ANC, 2012] "Twelfth Air Navigation Conference, report of the committee to the conference on Agenda Item 6", Montreal, November 2012

[Arbesser, 2006] "Presentation on The Galileo single frequency ionospheric correction algorithm", B. Arbesser-Rastburg, ESA-ESTEC, November 2006

[ARINC, 2006] "GPS Space Segment/Navigation User Interfaces, ARINC Engineering Services, LLC, Interface Specification, IS-GPS-200", Revision D, 7 March 2006

[Azoulai, 2009] "Lecture notes on Navigation Systems for Mastere Aviation Safety – Aircraft Airworthiness", L. Azoulai, October 2009

[Bahl *et al*., 2000] "RADAR: An In-Building RF-based User Location and Tracking System", P. Bahl and V. N. Padmanabhan, Microsoft Research, INFOCOM, 2000

[Bastide, 2004] "Ph.D. dissertation: Analysis of the Feasibility and Interests of Galileo E5a/E5b and GPS L5 Signals for Use with Civil Aviation", F. Bastide, Institut National Polytechnique de Toulouse, 2004

[BeiDou, 2013] "BeiDou Navigation Satellite System website", October 2013

[Béniguel, 2005] "Effects of ionospheric scintillations on GNSS operation", Y. Béniguel, IEEA, 2005

[Betz *et al*., 2009] "Generalized Theory of Code Tracking with an Early-Late Discriminator Part II: Non Coherent Processing and Numerical Results", J.W.Betz, K.R. Kolodziejski, IEEE transactions on aerospace and electronic systems, Vol. 45, No 4, October 2009

[Boeing, 2005] "Volume V – Characterization of the GBAS System Output", Boeing, 2005

[Borio, 2008] "A Statistical Theory for GNSS Signal Acquisition. PhD dissertation", D. Borio, Politecnico di Torino, March 2008

[Borre *et al*., 2006] "A Software-Defined GPS and Galileo Receiver: A Single-Frequency Approach (Applied and Numerical Harmonic Analysis)", K. Borre, D. A. Akos, N. Bertelsen, P. Rinder, S. H. Jensen, 2006

[Bourdeau *et al.*, 2012] "Tight Integration of GNSS and a 3D City Model for Robust Positioning in Urban Canyons", A. Bourdeau, M. Sahmoudi, J-Y. Tourneret, ION GNSS 2012, Nashville, TN, September 2012

[Braasch *et al*., 2000] "LAAS operations in support of airport surface movement, guidance, control and surveillance: initial test results", M. Braasch, M. DiBenedetto, S. Braasch, R. Thomas, Ohio University, IEEE 2000

[Brown *et al*., 1994] "Introduction to Random Signals and Applied Kalman Filtering", R. G. Brown, P. Y. C. Hwang, Wiley, 3rd Edition, 1994

[Byrne, 2013] "AeroMACS – A Global Standard for Airport Surface Communications", D. Byrne, WiMAX forum, 2013

[Campbell *et al*., 2003] "Light Detection and Ranging-Based Terrain Navigation – A Concept Exploration", J. Campbell, M. Uijt de Haag, F. Van Graas, S. Young, ION GNSS 2003, September 2003

[Chen *et al*., 2009] "Development of a GPS Deterministic Multipath Simulator for an Efficient Computation of the Positioning Errors", A. Chen, A. Chabory, A.C. Escher, C. Macabiau, ION GNSS 2009, September 2009

[Chen, 2010] "Development of a Hybrid Deterministic-Statistical GPS Multipath Simulator for Airport Navigation", PhD dissertation, A. Chen, Université de Toulouse, 2010

[Clipp, 2006] "GPS, Inertial Navigation and LIDAR Sensors, Urban 3D Modeling, PPT presentation", B. Clipp, September 2006

[Czopek *et al*., 1993] "Description and performance of the GPS BlockI and II L-band antenna and Link Budget", F. Czopek, Lt. S. Shollenberger, ION GPS 1993

[Dadu *et al*., 2007] "Baro-INS Integration with Kalman Filter", V. Daduc, B.Venugopal Reddya, B. Sitaraa, R.S.Chandrasekhara, G.Satheesh Reddya, 2007

[Datta-Barua et al., 2010] "Ionospheric Threat Parameterization for Local Area Global-Positioning-System-Based Aircraft Landing Systems", S. Datta-Barua, J. Lee, S. Pullen, M. Luo, A. Ene, D. Qiu, G. Zhang, P. Enge, Journal Of Aircraft, July–August 2010

[Datta-Barua, "Ionospheric threats to the integrity of airborne GPS users", PhD

2008] dissertation, Stanford University, S. Datta-Barua, June 2008

[DeCleene, 2000] "Defining Pseudorange Integrity. Overbounding", B.DeCleene, ION GPS 2000, Salt Lake City, UT, September 2000

[Diesel, 1995] "PCT: Assured-integrity monitored-extrapolation navigation apparatus WO 95/34850", J. Diesel, LITTON SYSTEMS, December 1995

[Diesel *et al.*, 1995] "GPS/IRS AIME: Calculation of Thresholds and Protection Radius Using Chi-Square Methods", J. Diesel, S. Luu, ION GPS 1995

[ED117, 2003] "Minimum operational performance specification for mode S multilateration systems for use in advanced surface movement guidance and control systems (A-SMGCS) ", EUROCAE, November 2003

[Enge, 2003] "GPS Modernization: Capabilities of the New Civil Signals", P.Enge, Australian international aerospace congress, Brisbane, July-August 2003

[Ercek *et al.*, 2005] "Study of pseudo-range error due to non-line-of-sight-multipath in urban canyons," R.Ercek, P. De Doncker and F. Grenez, ION GNSS 2005

[ESA, 2005] "Galileo Integrity Concept", European Space Agency, May 2005

[Escher, 2003] "PhD dissertation, Study of the contribution of GNSS/INS hybridization to GNSS integrity monitoring for civil aviation applications", A.C. Escher, December 2003

[EUROCAE, 2010] "Minimum Operational Performance Specification for Airborne Open Service Galileo Satellite Receiving Equipment", European Organization for Civil Aviation Equipment, December 2010

[Eurocontrol, 2010] "Study of the impact of solar activity on aviation applications based on GNSS over ECAC", EUROCONTROL funded study, 2010

[EC, 2013] "European Commission website", October 2011

[Evennou *et al.*, 2006] "Advanced Integration of WiFi and Inertial Navigation Systems for Indoor Mobile Positioning", F. Evennou, F. Marx, EURASIP Journal on Applied Signal Processing, 2006

[FAA, 1999] "Criteria for Approval of CAT III weather minima for takeoff, landing and rollout", FAA AC120-28D, 1999

[FAA, 2011] "WAAS reaction to iono activity", FAA WAAS team, presented by B. Wanner, October 2011

[FAA, 2013] "Runway safety report 2011-2012", FAA, 2013

[Farrell *et al.*, 1999] "The global positioning system and inertial navigation", J. A. Farrell, M. Barth, Mc Graw Hill, 1999

[Fernow, 2011] Personal discussion with James. P. Fernow, MITRE corporation, October

2011

[Foucras *et al*., 2013] "An efficient strategy for the acquisition of weak Galileo E1 OS signals", M. Foucras, B. Ekambi, ABBIA GNSS technologies, O. Julien, C. Mababiau, ENC 2013

[ICD, 2010] "European GNSS Galileo Open Service, Signal in Space Interface Control Document", European Union, September 2010

[Gao, 2007] "Ph.D. dissertation: Development of a Precise GPS/INS/On-Board Vehicle Sensors Integrated Vehicular Positioning System", J. Gao, University of Calgary, June 2007

[GEAS, 2010] "Phase II of the GNSS Evolutionary Architecture Study", GEAS, February 2010

[GPS SPS, 2008] "Global positioning System Standard Positioning Service Performance Standard", US Department of Defense, 2008

[GPS Wing, 2008] "Navstar GPS space segment/user segment L1C interfaces, Interface Specification IS-GPS-800", Global Positioning System Wing, Systems engineering and integration, September 2008

[GPS Wing, 2010] "Navstar GPS space segment/user segment L5 interfaces, Interface Specification IS-GPS-705", Global Positioning System Wing, Systems engineering and integration, June 2010

[GPS world, 2013] GPS World website, July 2013

[GPS, 2013] "GPS gov website, http://www.gps.gov/systems/gps/space/#II", October 2013

[Groves *et al*., 2013] "A Portfolio Approach to NLOS and Multipath Mitigation in Dense Urban Areas", P. D. Groves, Z. Jiang, M. Rudi, P. Strode, University College London, United Kingdom 2013, ION GNSS+ 2013, Nashville TN USA, Septembre 2013

[Groves, 2004] "Monitoring Ionospheric scintillation with GPS", K. Groves, Space Weather Center of Excellence, Air Force Research Laboratory, July 2004

[Groves, 2008] "Principles of GNSS, Inertial, and Multisensor Integrated Navigation Systems", P.D. Groves, Arctech House, 2008

[Gruber, 2011] "GPS Modernization and Program Update", B. Gruber, Space and Missile Systems Center, Munich satellite navigation summit, March 2011

[Guilloton *et al*., 2011] "A Methodology to Elaborate Aircraft Localization Requirements for Airport Navigation", A. Guilloton, J.P. Arenthens, C. Macabiau, A.C. Escher, D. Koenig, ION GNSS 2011

[Hegarty *et al*., "Modeling the effects of ionosphere scintillation on GPS/SBAS

2000] availability", R.S. Conker, M.B. El-Arini, C. J. Hegarty, T.Y. Hsiao, MITRE, 2000

[Honeywell, 2010] "Pressure transducers and barometers, product catalog", Honeywell, August 2010

[Humphreys *et al*., 2008] "Assessing the Spoofing Threat: Development of a Portable GPS Civilian Spoofer", T. E. Humphreys, B.M. Ledvina, M. L. Psiaki, B. W. O'hanlon, P. M. Kintner, ION GNSS, September 2008

[Humphreys *et al*., 2009] "GNSS and ionospheric scintillation, how to survive the next solar maximum", P. M. Kintner, T. Humphreys, J. Hinks, Inside GNSS, August 2009

[ICAO, 2001] "Annex 13 to the Convention on International Civil Aviation, Aircraft Accident and Incident Investigation", ICAO, Ninth Edition, July 2001

[ICAO, 2004] "ICAO-Manual on advanced surface movement guidance and control systems (A-SMGCS)", Doc 9830 AN/452-First Edition, 2004

[ICAO, 2005] "Annex 2 to the Convention on International Civil Aviation, Rules of the Air", ICAO, Tenth Edition, July 2005

[ICAO, 2006] "Annex 10 to the Convention on International Civil Aviation, Aeronautical Telecommunications, Volume I Radio Navigation Aids", ICAO, Sixth Edition, July 2006

[ICAO, 2006b] "ICAO NSP, Draft NSP Paper on Ionospheric Effects on GNSS", Working Group (WG1&2) Meeting, Brussels, Belgium, May 2006

[ICAO, 2008] "Doc 9613, Performance-based Navigation (PBN) Manual", ICAO, Third Edition, 2008

[ICAO, 2009] "Annex 14 to the Convention on International Civil Aviation, Aerodromes", ICAO, Fifth Edition, July 2009

[ICAO, 2009b] "ICAO NSP, Standard Threat Model Used in GAST D Ionospheric Monitoring Validation", ICAO, 2009

[ICAO, 2009b] "ICAO NSP, Conceptual Framework for the Proposal for GBAS to Support CAT III Operations", ICAO, 2009

[ICAO, 2010b] "ICAO NSP, Development Baseline SARPs Proposal", T. Murphy and S. Naerlich for ICAO, 2010

[ICAO, 2010] "Annex 6 to the Convention on International Civil Aviation, Operation of Aircraft", ICAO, Ninth Edition, July 2010

[ICAO, 2013] "Strategic objectives of ICAO, ICAO website, http://www.icao.int/icao/en/strategic_objectives.htm", 2013

[ICAO-CAST, 2010] "Phase of flight definitions and usage notes", CAST and ICAO, June 2010

[IGS, 2013] "International GNSS Service website, http://igs.org/mgex/Status_CMP.htm", October 2013

[Intermap, 2012] "NextMap datasheat", Intermap technologies, 2012

[Jahn *et al*., 1996] "Channel characterization for spread spectrum satellite communications", A. Jahn, H.Bischl, G. Heiss, in Proceedings on IEEE Fourth International Symposium on Spread Spectrum Techniques and Applications, 1996

[Jakowski] "Space weather effects in the ionosphere and their impact on positioning", N. Jakowski, A. Wehrenpfennig, S. Heise, S. Schlüter, T. Noack, DLR

[JAXA, 2012] "Quasi-Zenith Satellite System, Office of National Space Policy, Cabinet Office, Government of Japan", 2012, JAXA

[Julien, 2007] "Ph.D. dissertation: Design of Galileo L1F Receiver Tracking Loops", O. Julien, University of Calgary, 2005

[Julien 2010] "Galileo E1 OS/SoL Acquisition, Tracking and Data Demodulation Performances for Civil Aviation", O. Julien, C. Macabiau, L. Ries, NaviTec 2010

[Julien *et al*., 2007] "Two for one, tracking Galileo CBOC signal with TMBOC", O. Julien, C. Macabiau, J-L. Issler, L. Ries, Inside GNSS, Spring 2007

[Kaplan *et al*., 2006] "Understanding GPS Principles and Applications, Second Edition", E.D. Kaplan, C. J. Hegarty, 2006

[Kayton *et al*., 1996] "Avionics navigation Systems Wiley interscience", M. Kayton, W.R. Fried, 2nd edition, 1996

[Kelly, 1997] "Hypothesis testing as applied to GPS receiver autonomousFault Detection and Exclusion (FDE)", R.J.Kelly, lecture notes presented at Ohio University Avionics Engineering Center, November 1997

[Klobuchar, 1987] "Ionospheric time-delay algorithm for single-frequency GPS users", J.A. Klobuchar, IEEE transactions on aerospace and electronic systems, May 1987

[Konno *et al*., 2006] "Evaluation of Two Types of Dual-Frequency Differential GPS Techniques under Anomalous Ionosphere Conditions", H. Konno, S. Pullen, J. Rife, P. Enge, ION NTM, 2006

[Kovach, 2008] "GPS III Integrity Concept", K. Kovach, J. Dobyne, M. Crews, C. Miles, ION GNSS 2008

[Kunysz, 2010]. "Antenna phase center effects and measurements in GNSS ranging applications", W. Kunysz, 14th ANTEM and AMEREM conference, 2010

[Lee *et al*., "Terrain-Based Navigation: Trajectory Recovery from LiDAR Data", C.

2008] Toth, D. A. Grejner-Brzezinska, Y.J Lee, IEEE, 2008

[Lee *et al.*, 2007] "Feasibility Analysis of RAIM to Provide LPV-200 Approaches with Future GPS",Y.C. Lee, M.C. McLaughlin, ION GNSS 2007

[Lee, 1995] "New techniques relating fault detection and exclusion performance to GPS primary means integrity requirements", Y.C. Lee, ION GPS 1995

[Lee, 2004] "Performance of Receiver Autonomous Integrity Monitoring (RAIM) in the Presence of Simultaneous Multiple Satellite Faults", Y.C.Lee, ION GNSS 2004

[Leick, 1995] "GPS Satellite Surveying Wiley-Interscience", A.Leick, 2nd edition, 1995

[Lemmens, 2009] "Airborne LIDAR Sensors, Product survey", M. Lemmens (GIM International), February 2009

[Li, 2009] "Use of Wheel Speed Sensors to Enhance a Reduced IMU Ultra-Tight GNSS Receiver, Master thesis", T. Li, University of Calgary, 2009

[Lo *et al*., 2009] "Assessing the Security of a Navigation System: A Case Study using Enhanced Loran", S. C. Lo, B. B. Peterson, P. K. Enge, European Navigation Conference GNSS, Italy, May 2009

[Lohani] "Airborne Altimetric LIDAR: principle, data collection, processing and applications", (http://home.iitk.ac.in/~blohani/LiDAR_Tutorial/Airborne_AltimetricLidar_Tutorial.htm), B. Lohani

[Macabiau, 1997] "Ph.D. dissertation, Analysis of the Feasibility of Using GPS Carrier Phase Ambiguity Resolution Techniques for Precision Approaches", C. Macabiau, Institut National Polytechnique de Toulouse, September 1997

[Macabiau, 2004] "GPS signals, lecture notes", C. Macabiau, 2004

[Macabiau *et al*., 2006] "GNSS Airborne Multipath Errors Distribution Using the High Resolution Aeronautical Channel Model and Comparison to SARPs Error Curve", C. Macabiau, L. Moriella, M. Raimondi, C. Dupouy, A. Steingass, A. Lehner, PNT ION 2006

[Macabiau *et al*., 2014] "Impact of Nominal Biases Bounding Techniques on Final ARAIM User Performance", C. Macabiau, C. Milner, Q. Tessier, M. Mabilleau, J. Vuillaume, N. Suard, C. Rodriguez, ION ITM, January 2014

[MacGougan *et al*., 2009] "Ultra-wideband ranging precision and Accuracy", G. MacGougan, K. O'Keefe, R. Klukas, IOP Science, July 2009

[Martineau, 2008] "Ph.D. dissertation, Performance of Receiver Autonomous Integrity Monitoring (RAIM) for Vertically Guided Approaches", A. Martineau,

Institut National Polytechnique de Toulouse, November 2008

[Milner *et al.*, 2010] "A fast and efficient integrity computation for non-precision approach performance assessment", C. Milner, W.Y. Ochieng, GPS Solutions, March 2010

[Mitelman *et al.*, 2004] "Signal Deformations On Nominally Healthy GPS Satellites", A.M. Mitelman, R.E. Phelts, D.M. Akos, S.P. Pullen, P.K. Enge, ION NTM 2004

[Motella *et al.*, 2010] "Performance Assessment of Low Cost GPS Receivers Under Civilian Spoofing Attacks", B. Motella, M. Pini, M. Fantino, P. Mulassano, M. Nicola, J. Fortuny-Guasch, M. Wildemeersch, D. Symeonidis, IEEE, 2010

[Murphy *et al.*, 2000] "Validation of the Airframe Multipath Error Allocation for Local Area Differential GPS", J. Booth, T. Murphy, B. Clark, F. Liu, Proceedings of the IAIN World Congress in association with the U.S. ION annual meeting, June 2000

[Murphy *et al.*, 2007] "GPS Antenna Group Delay Variation Induced Errors in a GNSS Based Precision Approach and Landing Systems", T. Murphy, P. Geren, T. Pankaskie, ION GNSS 2007

[Muthuraman, 2010] "Ph.D. dissertation, Tracking Techniques for GNSS Data/Pilot Signals", K. Muthuraman, University of Calgary, January 2010

[PNT, 2010] "National PNT advisory board comments on jamming the GPS – a national security threat: recent events and potential cures", US National PNT advisory board, 2010

[Navipedia, 2013] "Navipedia website, http://www.navipedia.net/index.php/IRNSS", October 2013

[NDEP, 2004] "Guidelines for Digital Elevation Data, V.1", National Digital Elevation Program (NDEP), May 2004

[Néri, 2011] "Ph.D. Dissertation, Use of GNSS signals and their augmentations for civil aviation navigation during approaches with vertical guidance and precision approaches", P. Néri, Université de Toulouse, 2011

[Ober, 2003] "Ph.D. dissertation: Integrity Prediction and Monitoring of Navigation Systems", P.B. Ober, TU Delft, 2003

[Ochieng] "Integrity monitoring for detection of interference", W. Ochieng, Imperial college London

[Ouzeau, 2009] "Ph.D. dissertation, Degraded Modes Resulting From the Multi Constellation Use of GNSS", C. Ouzeau, Université de Toulouse, 2009

[Pagani *et al.*, 2008] "Ultra-wideband radio propagation channels: a practical approach", P. Pagani, F.T. Talom, P. Pajusco, B. Uguen, Wiley, 2008

[Papadimitratos *et al*., 2008] "Protection and Fundamental Vulnerability of GNSS", P. Papadimitratos, A. Jovanovic, IEEE, 2008

[Papoulis, 1991] "Probability, Random Variables and Stochastic Processes", A. Papoulis, McGraw-Hill, 1991

[Park *et al*., 2009] "Indoor localization for autonomous mobile robot based on passive RFID", S. Park, S. Hashimoto, Proceedings of IEEE, International Conference on Robotics and Biomimetics Bangkok, Thailand, February 2009

[Park *et al*., 2010] "A Study of Severe Multipath Errors for the Proposed GBAS Airport Surface Movement Application", Y.S. Park, S. Pullen, P. Enge, ION GNSS 2010

[Parkinson *et al*., 1996] "Global Positioning System: Theory and Applications", B. W. Parkinson, J. J. Spilker, Progress in Astronautics and Aeronautics, 1996

[Pervan, 2011] "Development of EOP threat model for GPS", B. Pervan, Illinois institute of technology, June 2011

[Peyraud *et al*., 2013] "About Non-Line-Of-Sight Satellite Detection and Exclusion in a 3D Map-Aided Localization Algorithm", S. Peyraud, D. Bétaille, S. Renault, M. Ortiz, F. Mougel, D. Meizel, F. Peyret, Sensors, 2013

[Phelts, 2001] "Ph.D. dissertation, Multicorrelator Techniques for Robust Mitigation of Threats to GPS Signal Quality", R.E. Phelts, Stanford University, Stanford, CA

[Proakis, 2001] "Digital Communications, Introduction", J.G. Proakis, McGraw-Hill, 2001

[Pullen *et al*., 2006] "Prior Probability Model Development to Support System Safety Verification in the Presence of Anomalies", S. Pullen, J. Rife, P. Enge, IEEE, 2006

[Pullen *et al*., 2011] "SBAS and GBAS integrity for non-aviation users: moving away from "specific risk"", S. Pullen, T. Walter, P.K. Enge, ION ITM 2011

[Pullen, 2014] Personal discussion with S. Pullen, Stanford University, January 2014

[Raimondi, 2008] "Ph.D. dissertation, Development and Characterization of Pulsed Interference Mitigation Techniques for on-board GNSS Receivers ", M. Raimondi, Université de Toulouse, October 2008

[Rebeyrol, 2007] "Ph.D. dissertation, Galileo signals and payload optimization", E. Rebeyrol, Telecom Paris, October 2007

[RTCA, 1991] "Minimum Operational Performance Standards for airborne supplemental navigation equipment using Global Positioning System (GPS), DO-208", RTCA, SC-159, July 1991

[RTCA, 1999] "The role of the Global Navigation Satellite System (GNSS) in supporting airport surface operations, DO-247", RTCA, January 1999

[RTCA, 2003] "Minimum Aviation System Performance Standards: Required Navigation Performance for Area Navigation, DO-236B", RTCA, SC-181, October 2003

[RTCA, 2004] "Assessment of Radio Frequency Interference Relevant to the GNSS L5/E5a Frequency band, DO-292", RTCA, SC-159, July 2004

[RTCA, 2006] "Minimum Operational Performance Standards for Global Positioning System (GPS) / Wide Area Augmentation System Airborne Equipment, DO-229D", RTCA, SC-159, December 2006

[RTCA, 2008] "Assessment of Radio Frequency Interference Relevant to the GNSS L1 Frequency band, DO-235B", RTCA, SC-159, March 2008

[RTCA, 2008b] "Minimum Operational Performance Standards for Global Positioning System (GPS) / Local Area Augmentation System Airborne Equipment, DO-253C", RTCA, SC-159, December 2008

[RTCA, 2008c] "Minimum Operational Performance Standards for Global Positioning System (GPS) / Ground Based Regional Augmentation System Airborne Equipment, DO-310", RTCA, SC-159, March 2008

[RTCA, 2009] "Minimum Operational Performance Standards for Global Positioning System / Aircraft Based Augmentation System Airborne Equipment, DO-316", RTCA, SC-159, April 2009

[FSA, 2013] "Russian Federal Space Agency website, http://glonass-iac.ru/en/", October 2013

[Salos, 2012] "PhD dissertation, Integrity monitoring applied to the reception of GNSS signals in urban environments", D. Salos, Université de Toulouse, 2012

[Schuster *et al*., 2011] "Airport Surface Movement – Critical Analysis of Navigation System Performance Requirements", W. Schuster, W. Ochieng, The journal of Navigation, 2011

[Shallberg *et al*., 2002] "Considerations for Characterizing Antenna Induced Range Errors" K. Shallberg, J. Grabowski, ION GNSS 2002

[SIA, 2013] "Service de l'Information Aéronautique (SIA) map, Toulouse Blagnac airport", 2013

[Souteyrat, 1997] "Contrôle séquentiel de l'intégrité du GPS, Rapport LTST", L. Souteyrat, Septembre 1997

[Sparks *et al*., 2005] "Extreme ionospheric storms and their impact on WAAS", L. Sparks, A. Komjathy, A. J. Mannucci, E. Altshuler, T. Walter, J. Blanch, M. B. El-

Arini, R. Lejeune, Ionospheric Effects Symposium, 2005

[Sparks *et al*., 2011] "Estimating ionospheric delay using kriging: impact on satellite-based augmentation system availability", L. Sparks, J. Blanch, N. Pandya, Radio Science, 2011

[Steingaß et al., 2004] "The high resolution aeronautical multipath navigation channel", A. Steingaß, A. Lehner, F. Pérez-Fontán, E. Kubista, M.J. Martín, B. Arbesser-Rastburg, IEEE PLANS 2004

[TDC, 2011] "Data Sheet PulsON 400 RCM", Time Domain Corp., July 2011

[Tran *et al*., 2001] "Validation of the feasibility of coexistence of the new civil signal L5 with existing systems", M. Tran, T. Kim, C. Hegarty, J. Devincentis, S. Ericson, MITRE product, 2001

[Van Dierendonck *et al*., 1992] "Theory and Performance of Narrow Correlator Spacing in a GPS Receiver", A.J. Van Dierendonck, P.Fenton, T. Ford, Journal of Institute of Navigation, Fall 1992

[Vézinet, 2013] "Study, analysis and modeling of the different sensors measurements at the input of the fusion filter and their failure modes, Intermediate report for PhD thesis", J. Vézinet, 2013

[Von Hippel, 1961] "Les diélectriques et leurs applications", A. R. Von Hippel, Dunod, 1961

[Walter *et al*., 2000] "Robust detection of ionospheric irregularities", T. Walter, A. Hansen, J. Blanch, P. Enge, T. Mannucci, X. Pi, L. Sparks, B. Iijima, B. El-Arini, R. Lejeune, M. Hagen, E. Altshuler, R. Fries, A. Chu, ION GPS, 2000

[Walter *et al*., 2003] "Integrity lessons from the WAAS Integrity Performance Panel (WIPP)", T. Walter, P.K. Enge, B. DeCleene, ION ITM 2003

[Wang *et al*., 2013] "Urban Positioning on a Smartphone: Real-time Shadow Matching Using GNSS and 3D City Models", L. Wang, P.D. Groves, M.K. Ziebart, University College London, UK, ION GNSS+ 2013, Nashville TN USA

[WG-C ARAIM, 2012] "EU-U.S. Cooperation on Satellite Navigation, Working Group C, ARAIM Technical Subgroup", Interim report, December 2012

[Wilkinson *et al*., 1998] "Functional hazard analysis for highly integrated aerospace systems", P.J. Wilkinson, T.P. Kelly, Certification of Ground/Air Systems Seminar, IEEE, 1998

[Winkel, 2000] "PhD dissertation, Modelling and simulating GNSS signal structures and receivers,", J. O. Winkel, 2000

[Xing, 2010] "Over-bounding Integrated INS/GNSS Output Errors", Z. Xing, University of Minnesota, October 2010

[Xiong, 1998] "A selective model to suppress NLOS signals in angle-of-arrival (AOA)

location estimation", L. Xiong, IEEE, 1998

[Younes, 2000] "Ph.D. dissertation, Sequential theory applied to GNSS Integrity Monitoring and to GNSS/INS Hybridization", A. Younes, Université de Toulouse, November 2000

[Zebra, 2008] "Data sheet Sapphire DART", Multispectral Solutions – Zebra Technologies Company, 2008

ACRONYMS

AAIM	Aircraft Autonomous Integrity Monitoring
ABAS	Aircraft Based Augmentation System
ADS-B	Automatic Dependent Surveillance – Broadcast
AL	Alert Limit
AltBOC	Alternate Binary Offset Carrier
APV	Approach and landing Procedures with Vertical guidance
A-SMGCS	Advanced Surface Movement Guidance and Control System
ATC	Air Traffic Control
ATM	Air Traffic Management
BARO-VNAV	APV Barometric Vertical Navigation
BPSK	Binary Phase Shift Keying
C/A	Coarse/Acquisition
CAST	Commercial Aviation Safety Team
CBOC	Composite Binary Offset Carrier
CDF	Cumulative Density Function
CNS	Communications, Navigation, Surveillance
CW	Carrier Wave
DEM	Digital Elevation Map
DH	Decision height
DLL	Delay Locked Loop
DME	Distance Measuring Equipment
DoA	Direction of Arrival
EKF	Extended Kalman Filter
EM	ElectroMagnetic
EMLP	Early Minus late Power
EUROCAE	European Organization for Civil Aviation Equipment
FAA	Federal Aviation Administration
FHA	Functional Hazard Assessment
FOG	Fiber Optic Gyroscope
FTE	Fight Technical Error
GBAS	Ground Based Augmentation System
GO	Geometrical Optics
GPS	Global Positioning System
HAL	Horizontal Alert Limit
HMI	Hazardous Misleading Information
HPLs	Horizontal Protection Levels
HRG	Hemispherical Resonator

I&D	Integrate and Dump
ICAO	International Civil Aviation Organization
IF	Intermediate Frequency
IFR	Instrument Flight Rules
Ifree	Iono-free
IGS	International GNSS Service
ILS	Instrument Landing System
IMU	Inertial Measurement Unit
INS	Inertial Navigation System
IR	Integrity Risk
IRNSS	Indian Regional Navigation Satellite System
IRS	Inertial Reference System
JTIDS	Joint Tactical Information Distribution System
LAL	Lateral Alert Limit
LIDAR	Light Detection and Ranging
LLA	Latitude Longitude Altitude
LNA	Low Noise Amplifier
LOS	Line Of Sight
LS	Least-Squares
MBOC	Multiplexed Binary Offset Carrier
MEMS	Micro-Electro-Mechanical System
MOPS	Minimum Operational Performance Specification
MOPS	Minimum Operational Performance Standards
NCO	Numerically Controlled Oscillator
NED	North East Down
NLOS	Non Line Of Sight
NPA	Non-Precision Approach
NSE	Navigation System Error
P(Y)	Precise
PA	Precision Approach
PBN	Performance Based Navigation
PDE	Path Definition Error
PDF	Probability Density Function
PDOP	Position Precision Of Dilution
PLs	Protection Levels
PO	Physical Optics
PRN	Pseudo Range Noise
QPSK	Quadrature Phase Shift Keying
QZSS	Quasi Zenith Satellite System
RAIM	Receiver Autonomous Integrity Monitoring
RF	Radio Frequency
RF	Radio-Frequency
RFID	Radio Frequency IDentification
RHCP	Right Hand Circular Polarization
RLG	Ring Laser Gyroscope
RNAV	Area Navigation
RTCA	Radio Technical Commission for Aeronautics

RVR	Runway visual range
SARPs	Standards And Recommended Practices
SBAS	Satellite Based Augmentation System
SIA	Service de l'Information Aéronautique
SISA	Signal In Space Accuracy
SSR	Secondary Surveillance Radar
TACAN	TACtical Air Navigation
TEC	Total Electron Content
TIDs	Travelling Ionosphere Disturbances
TLS	Target Level of Safety
TMBOC	Time Multiplexed Binary Offset Carrier
TSE	Total System Error
TTA	Time-To-Alert
URA	User Range Accuracy
URE	User Ranging Error
UWB	Ultra Wide Band
VAL	Vertical Alert Limit
VFR	Visual Flight Rules
WiMAX	Worldwide Interoperability for Microwave Access
WLS	Weight Least-Squares
WSS	Wheel Speed Sensor

APPENDIX A

GNSS multipath parameters and ranging errors

This appendix:

- provides the analytical expression of the relative code delay and of the relative phase shift related to an echo signal scattered by a single point reflector,
- investigates the relative Doppler frequency shift and the relative phase shift related to an echo signal reflected by the ground over a uniform and rectilinear trajectory,
- derives the analytical expression of the raw code multipath ranging error induced by a single echo signal,
- analyzes the multipath ranging induced by the ground and by aircraft structure,
- develops a GNSS multipath ranging error model induced by the ground and by the aircraft structure during turns and assesses the validity of this model.

A.1. Multipath parameters of an echo signal scattered by a single point reflector

This subsection derives the analytical expression of the relative code delay and of the relative phase shift of an echo signal mentioned by index "2". Echo signal "2" is emitted by a stationary GNSS satellite, scattered on a single static point reflector and reaches the static GNSS receiver antenna. The notations used in this appendix are provided in Table A-1.

	Parameter description
Satellite position	Satellite elevation angle El
	Satellite azimuth angle Az_{sat}
Reflector position	Illuminated facade orientation with respect to the GNSS satellite: Az_{faca} .
	Obstacle height: h_{obs}
GNSS airborne antenna position	On segment [AB] that is parallel to the airport surface considered as a planar and infinite and in the specular direction. Aircraft azimuth angle constant on [AB].
	Antenna height: h_{ant}

Table A-1: Description of the scenario

The GNSS airborne antenna, the obstacle, the direct signal, the echo signal reflected from the obstacle, and the ground are illustrated in Figure A-1.

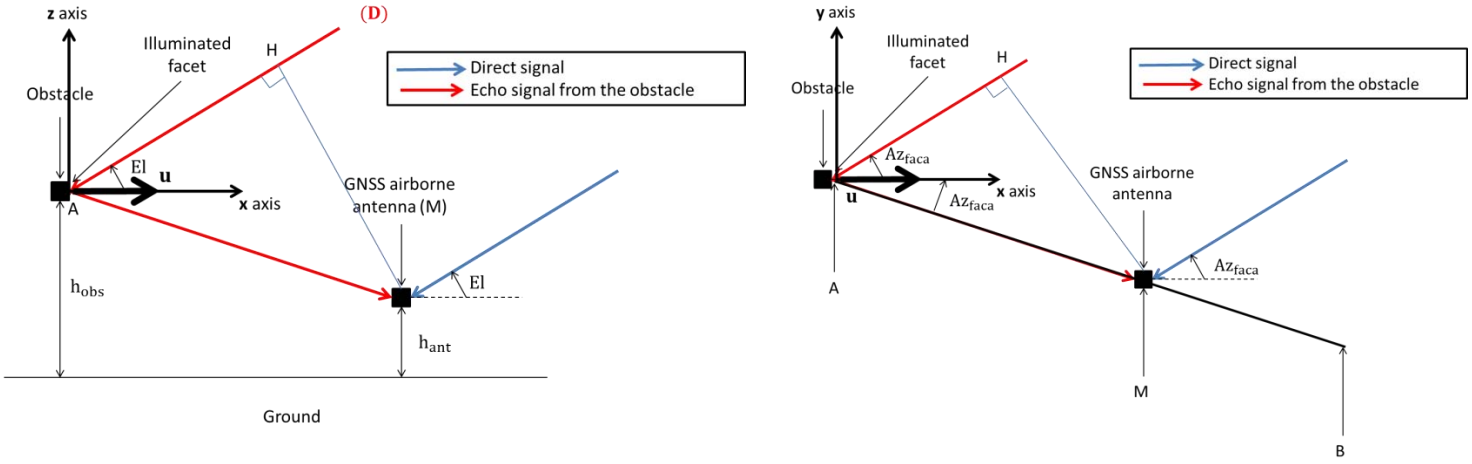

Side view ***Top view***

Figure A-1 : Description of the scenario

A.1.1. Relative code delay

The relative code delay at a point M of segment [AB] is given by:

$$\Delta\tau_2 = \frac{\|\mathbf{HA}\| + \|\mathbf{AM}\|}{c} \qquad \text{Eq - A-1}$$

where:

- H is the orthogonal projection of M on line (D) represented in Figure A-1.
- $\|\mathbf{HA}\|$ and $\|\mathbf{AM}\|$ are the distances between points H and A, and between points A and M, respectively.

Let's consider $(A, \mathbf{x}, \mathbf{y}, \mathbf{z})$ the orthonormal reference frame attached to A. The $\mathbf{x}$ axis is orthogonal to the illuminated façade and is oriented as depicted in Figure 1. The $\mathbf{y}$ axis is parallel to the illuminated façade and the $\mathbf{z}$ axis points up in such a way that $(A, \mathbf{x}, \mathbf{y}, \mathbf{z})$ is a

orthonormal direct reference frame. Let's compute $\|\mathbf{AM}\|$. The coordinates of M in $(A, \mathbf{x}, \mathbf{y}, \mathbf{z})$ are:

$$\mathbf{AM} = \begin{bmatrix} d\cos(Az_{faca}) \\ -d\sin(Az_{faca}) \\ -(h_{obs} - h_{ant}) \end{bmatrix} \quad \text{Eq - A-2}$$

where d is the distance between A and M in $(A, \mathbf{x}, \mathbf{y})$ plane. The norm of vector $\mathbf{AM}$ is:

$$\|\mathbf{AM}\| = \sqrt{d^2 + (h_{obs} - h_{ant})^2} \quad \text{Eq - A-3}$$

Let's compute $\|\mathbf{HA}\|$. Let's state $\mathbf{u}$ the unit vector on line (D) pointing to the satellite. The coordinates of $\mathbf{u}$ in $(A, \mathbf{x}, \mathbf{y}, \mathbf{z})$ are:

$$\mathbf{u} = \begin{bmatrix} \cos(El)\cos(Az_{faca}) \\ \cos(El)\sin(Az_{faca}) \\ \sin(El) \end{bmatrix} \quad \text{Eq - A-4}$$

Denote $\mathbf{AH}$ the coordinates of H in $(A, \mathbf{x}, \mathbf{y}, \mathbf{z})$. Since H is on line (D):

$$\exists t \in \mathbb{R} / \mathbf{AH} = t \begin{bmatrix} \cos(El)\cos(Az_{faca}) \\ \cos(El)\sin(Az_{faca}) \\ \sin(El) \end{bmatrix} \quad \text{Eq - A-5}$$

Moreover, vectors $\mathbf{MH}$ and $\mathbf{u}$ are orthogonal. Hence:

$$\mathbf{MH}.\mathbf{u} = 0 \quad \text{Eq - A-6}$$

Using Eq - A-2, Eq - A-4 and Eq - A-5, and considering the constraint stated in Eq - A-6:

$$t = d\cos(El)\cos(2Az_{faca}) - (h_{obs} - h_{ant})\sin(El) \quad \text{Eq - A-7}$$

Using Eq - A-5 and Eq - A-7:

$$\mathbf{AH} = (d\cos(El)\cos(2Az_{faca}) - (h_{obs} - h_{ant})\sin(El)) \begin{bmatrix} \cos(El)\cos(Az_{faca}) \\ \cos(El)\sin(Az_{faca}) \\ \sin(El) \end{bmatrix} \quad \text{Eq - A-8}$$

The norm of vector $\mathbf{AH}$ is:

$$\|\mathbf{AH}\| = d\cos(El)\cos(2Az_{faca}) - (h_{obs} - h_{ant})\sin(El) \quad \text{Eq - A-9}$$

Eq – 9, Eq – 3 in Eq – 1 lead to:

$$\Delta\tau_2 = \frac{1}{c}\left\{\sqrt{d^2 + (h_{obs} - h_{ant})^2} + d\cos(El)\cos(2Az_{faca}) - (h_{obs} - h_{ant})\sin(El)\right\} \quad \text{Eq - A-10}$$

where d is the horizontal distance beween the obstacle and the airborne antenna. When $d \gg |h_{obs} - h_{ant}|$, it can be considered that $\Delta\tau_2$ increases linearly with respect to d:

$$\Delta\tau_2 \approx \frac{1}{c}\{d(1 + \cos(El)\cos(2Az_{faca}))\} \quad \text{Eq - A-11}$$

The evolution of $\Delta\tau_2$ along [AB] depends on the orientation of the segment [AB] w.r.t. the reflector since it depends on the angle Az_{faca}. It also depends on the satellite elevation angle El.

A.1.2. Relative phase shift

The relative phase shift is given by:

$$\Delta\theta_2 = -2\pi f_L \Delta\tau_2 + \Delta\phi_2 \quad \text{Eq - A-12}$$

where $\Delta\phi_2$ is the phase shift induced by the reflection of the EM wave on the obstacle and by the GNSS antenna phase shift. In the case where the $\Delta\phi_2$ is constant on [AB], and from Eq - A-11 and Eq - A-12, it is deduced that, when $m \gg |h_{obs} - h_{ant}|$, two points on [AB] separated by a distance of $\frac{\lambda_L}{1+\cos(El)\cos(2Az_{faca})}$ have the same modulo 2π relative phase $\Delta\theta_2$. Hence, along segment [AB], the spatial period of $\Delta\theta_2$ is equal to:

$$p = \frac{\lambda_L}{1 + \cos(El)\cos(2Az_{faca})} \quad \text{Eq - A-13}$$

To conclude, the spatial period of $\Delta\theta_2$ along [AB] depends on the orientation of the segment [AB] w.r.t. the reflector (Az_{faca}), on the satellite elevation angle (El), on the GNSS central frequency (λ_L). For a segment [AB] in the specular direction of the reflector, the spatial period p is between λ_L and $\frac{\lambda_L}{2}$.

A.2. Multipath parameters of an echo signal reflected from the ground

A.2.1. Relative Doppler frequency

This subsection shows that, in the dynamic configuration, the Doppler frequency shifts of the direct signal and of the echo signal emitted by the satellite, reflected from the ground and reaching the GNSS receiver antenna are roughly equal and constant throughout a uniform and rectilinear trajectory.

Assuming a stationary satellite, the Doppler frequency shift of the direct signal $f_{D,0,L}$ at time t is:

$$f_{D,0,L}(t) = \frac{f_c}{c}(-\mathbf{v}(t).\mathbf{e}_r(t)) \qquad \text{Eq - A-14}$$

where:

- $\mathbf{v}(t)$ is the GNSS airborne antenna velocity vector at time t,
- $\mathbf{e}_r(t)$ is the unit vector from the GNSS satellite to the GNSS airborne antenna at time t.

Throughout the trajectory, $\mathbf{e}_r(t)$ is roughly constant since the satellite is static and the aircraft has a weak dynamic during surface operations. In addition, $\mathbf{v}(t)$ is constant throughout a constant speed straight line trajectory. Hence, $f_{D,0,L}(t)$ is roughly constant throughout the trajectory. This is validated by the fact that the maximal variation of $f_{D,0,L}(t)$ throughout the trajectory [FG] described in Section 5.5.1.1. is of the order of 10^{-5}Hz.

The Doppler frequency shift of the echo signal $f_{D,1,L}$ reflected from the ground at time t is:

$$f_{D,1,L}(t) = \frac{f_c}{c}\left(-\mathbf{v}(t).\mathbf{e}_{r,gnd}(t)\right) \qquad \text{Eq - A-15}$$

where $\mathbf{e}_{r,gnd}(t)$ is the unit vector from the point P of the ground where the echo signal is reflected to the GNSS airborne antenna at time t.

Let's state:

$$\mathbf{e}_r(t) = \begin{bmatrix} e_{r,sat,x}(t) \\ e_{r,sat,y}(t) \\ e_{r,sat,z}(t) \end{bmatrix} \quad \text{and} \quad \mathbf{e}_{r,gnd}(t) = \begin{bmatrix} e_{r,gnd,x}(t) \\ e_{r,gnd,y}(t) \\ e_{r,gnd,z}(t) \end{bmatrix} \qquad \text{Eq - A-16}$$

From the generalized image theorem detailed in [Chen, 2010], it can be considered that:

$$\begin{bmatrix} e_{r,gnd,x}(t) \\ e_{r,gnd,y}(t) \\ e_{r,gnd,z}(t) \end{bmatrix} \approx \begin{bmatrix} e_{r,sat,x}(t) \\ e_{r,sat,y}(t) \\ -e_{r,sat,z}(t) \end{bmatrix} \qquad \text{Eq - A-17}$$

Since the vertical component of the aircraft velocity vector is null, we can write:

$$\mathbf{v}(t).\mathbf{e}_r(t) \approx \mathbf{v}(t).\mathbf{e}_{r,gnd}(t) \qquad \text{Eq - A-18}$$

It is deduced that:

$$f_{D,0,L}(t) \approx f_{D,1,L}(t) \qquad \text{Eq - A-19}$$

Hence, the Doppler frequency shifts of the direct signal and of the echo signal emitted by the satellite, reflected from the ground and reaching the GNSS receiver antenna are roughly equal and constant throughout a uniform and rectilinear trajectory. As an illustration, the difference between both Doppler frequency shifts on the trajectory [FG] described in Section 5.5.1.1 is of order 10^{-6}Hz.

A.2.2. Relative phase shift

This subsection shows that the relative phase shift of the echo signal emitted by the satellite, reflected over the ground and reaching the GNSS receiver antenna on a segment of the airport is roughly the same in both static and dynamic configurations.

Along the segment, and at time t, the echo signal from the ground is characterized by the following relative phase shift:

$$\Delta\theta_{1,\mathrm{dyn}}(t) = -2\pi\left(f_L + f_{D,1,L}(t)\right)\tau_1(t) + 2\pi\left(f_L + f_{D,0,L}(t)\right)\tau_0(t) + \phi_1(t) - \phi_0(t) \quad \text{Eq - A-20}$$

The relative phase shift of the echo signal from the ground at time t of a static aircraft characterized by the same aircraft orientation on that segment is given by:

$$\Delta\theta_{1,\mathrm{static}}(t) = -2\pi f_L\tau_1(t) + 2\pi f_L\tau_0(t) + \phi_1(t) - \phi_0(t) \quad \text{Eq - A-21}$$

The static aircraft and the dynamic aircraft have the same orientation on the segment. Hence, the phase shift $\phi_1(t) - \phi_0(t)$ induced by the reflection of the signal on the ground and by the airborne antenna is the same in both static and dynamic configurations. By using the following notation: $\tau_1(t) = \tau_0(t) + \Delta\tau_1(t)$, it comes:

$$\Delta\theta_{1,\mathrm{dyn}}(t) = \Delta\theta_{1,\mathrm{static}}(t) + 2\pi\left(f_{D,0,L}(t) - f_{D,1,L}(t)\right)\tau_0(t) - 2\pi f_{D,1,L}(t)\Delta\tau_1(t) \quad \text{Eq - A-22}$$

From Section A.2.1, $f_{D,0,L}(t) - f_{D,1,L}(t)$ is of order 10^{-6}Hz. $\tau_0(t)$ is of order few dozens of milliseconds. Hence, $2\pi\left(f_{D,0,L}(t) - f_{D,1,L}(t)\right)\tau_0(t)$ is of order 10^{-7}rad. Hence, $2\pi\left(f_{D,0,L}(t) - f_{D,1,L}(t)\right)\tau_0(t)$ can be neglecting regarding $\Delta\theta_{1,\mathrm{static}}(t)$:

$$\Delta\theta_{1,\mathrm{dyn}}(t) \approx \Delta\theta_{1,\mathrm{static}}(t) - 2\pi f_{D,1,L}(t)\Delta\tau_1(t) \quad \text{Eq - A-23}$$

From Section 5.4.1.2, the code delay difference between the direct signal and the echo signal reflected from the ground $\Delta\tau_1(t)$ is of the order of 10^{-9}s up to 10^{-8}s. In addition, since aircraft speeds during the taxi operation are in the range $[1\mathrm{m.s^{-1}}; 10\mathrm{m.s^{-1}}]$, $f_{D,1,L}(t)$ does not exceed few Hz. Hence, $2\pi f_{D,1,L}(t)\Delta\tau_1(t)$ is of order 10^{-6}rad. Hence, $2\pi f_{D,1,L}(t)\Delta\tau_1(t)$ can be neglected regarding $\Delta\theta_{1,\mathrm{static}}(t)$. It comes:

$$\Delta\theta_{1,\mathrm{dyn}}(t) \approx \Delta\theta_{1,\mathrm{static}}(t) \quad \text{Eq - A-24}$$

A.3. Multipath code tracking error in the presence of a single multipath

This subsection derives the analytical expression of the multipath code tracking error under the following assumptions:

- The front-end low-pass filter is assumed to be of infinite bandwidth,

- The GNSS signal at the receiver antenna output is modelled as the sum of the direct signal and a single echo signal,
- The DLL uses a BPSK-modulated signal to track the code delay of the resulting GNSS signal,
- The tracking loops perfectly track the phase and the Doppler frequency of the direct signal,
- The satellite, the reflector and the antenna are static, meaning the Doppler frequency of the direct and echo signals are null,
- The DLL discriminator is a EMLP discriminator,
- The code delays and carrier phases of the direct and echo signals are considered to be constant during the integration time.

Under these conditions, from Eq - 4-9, the Early and Late DLL correlator outputs are modelled as:

$$I_E + jQ_E = \sum_{k=0}^{1} \frac{a_k}{2} R_{c,P}\left(\varepsilon_\tau + \Delta\tau_k - \frac{\Delta}{2}\right)\exp(\Delta\theta_k)$$
$$I_L + jQ_L = \sum_{k=0}^{1} \frac{a_k}{2} R_{c,P}\left(\varepsilon_\tau + \Delta\tau_k + \frac{\Delta}{2}\right)\exp(\Delta\theta_k) \qquad \text{Eq - A-25}$$

Let's derive the expressions of the DLL discriminator output:

$$D_{out} = \left(I_E{}^2 + Q_E{}^2\right) - \left(I_L{}^2 + Q_L{}^2\right)$$

$$D_{out} = a_0{}^2\left[R_{c,P}{}^2\left(\varepsilon_\tau + \frac{\Delta}{2}\right) - R_{c,P}{}^2\left(\varepsilon_\tau - \frac{\Delta}{2}\right)\right]$$
$$+a_1{}^2\left[R_{c,P}{}^2\left(\varepsilon_\tau + \frac{\Delta}{2} + \Delta\tau_1\right) - R_{c,P}{}^2\left(\varepsilon_\tau - \frac{\Delta}{2} + \Delta\tau_1\right)\right] \qquad \text{Eq - A-26}$$
$$-2a_0a_1\cos(\Delta\theta_1)\left[R_{c,P}\left(\varepsilon_\tau + \frac{\Delta}{2}\right)R_{c,P}\left(\varepsilon_\tau + \frac{\Delta}{2} + \Delta\tau_1\right) - R_{c,P}\left(\varepsilon_\tau - \frac{\Delta}{2}\right)R_{c,P}\left(\varepsilon_\tau - \frac{\Delta}{2}\right.\right.$$

$R_{c,P}\left(\varepsilon_\tau + \frac{\Delta}{2}\right)$ and $R_{c,P}\left(\varepsilon_\tau + \frac{\Delta}{2}\right)$ are represented in Figure A-2 as a function of ε_τ.

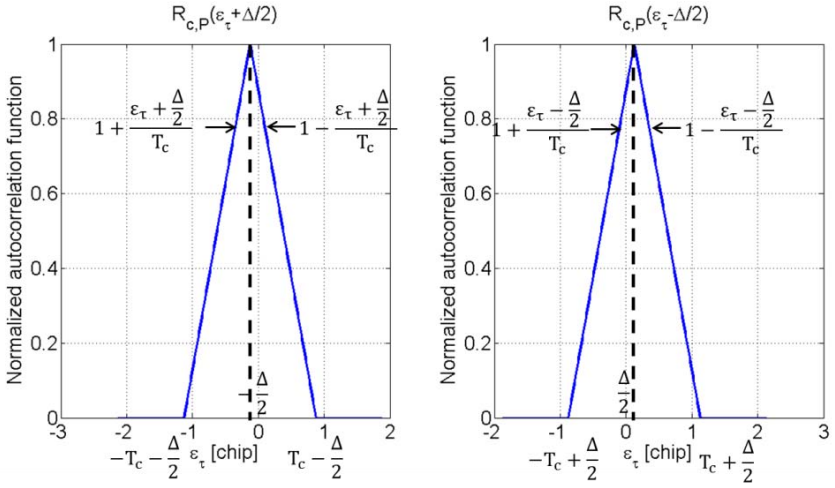

Figure A-2 : Early and Late auto-correlation functions

The analytical expressions of the Early and Late autocorrelation functions are provided in Table A-2 [Macabiau, 2004].

ε_τ	$-T_c-\frac{\Delta}{2}$	$-T_c+\frac{\Delta}{2}$	$-\frac{\Delta}{2}$	$\frac{\Delta}{2}$	$T_c-\frac{\Delta}{2}$	$T_c+\frac{\Delta}{2}$
$R_{c,P}\left(\varepsilon_\tau+\frac{\Delta}{2}\right)$	0	$1+\frac{\varepsilon_\tau+\frac{\Delta}{2}}{T_c}$	$1+\frac{\varepsilon_\tau+\frac{\Delta}{2}}{T_c}$	$1-\frac{\varepsilon_\tau+\frac{\Delta}{2}}{T_c}$	$1-\frac{\varepsilon_\tau+\frac{\Delta}{2}}{T_c}$	0	0
$R_{c,P}\left(\varepsilon_\tau+\frac{\Delta}{2}\right)$	0	0	$1+\frac{\varepsilon_\tau-\frac{\Delta}{2}}{T_c}$	$1+\frac{\varepsilon_\tau-\frac{\Delta}{2}}{T_c}$	$1-\frac{\varepsilon_\tau-\frac{\Delta}{2}}{T_c}$	$1-\frac{\varepsilon_\tau-\frac{\Delta}{2}}{T_c}$	0

Table A-2 : Analytical expressions of the Early and Late auto-correlation functions

$\Delta\tau_1$ can only have a positive value since the echo code delay is always larger than the direct code delay. Let's consider the following example:

$$0 \le \Delta\tau_1 \le \left(1-\frac{a_1}{a_0}\right)\frac{\Delta}{2} \qquad \text{Eq - A-27}$$

From Figure 4-6 we get:

$$0 \le \Delta\tau_1 \le \left(1-\frac{a_1}{a_0}\right)\frac{\Delta}{2} \Rightarrow -\frac{\Delta a_1}{2a_0} \le \varepsilon_\tau \le \frac{\Delta a_1}{2a_0} \qquad \text{Eq - A-28}$$

Hence:

$$-\frac{\Delta a_1}{2a_0} \le \varepsilon_\tau + \Delta\tau_1 \le \frac{\Delta}{2} \qquad \text{Eq - A-29}$$

Since $\frac{a_1}{a_0} \le 1$, we get:

$$-\frac{\Delta}{2} \le \varepsilon_\tau + \Delta\tau_1 \le \frac{\Delta}{2} \text{ and } -\frac{\Delta}{2} \le \varepsilon_\tau \le \frac{\Delta}{2} \qquad \text{Eq - A-30}$$

By taking into account the expressions of the Early and Late autocorrelation functions proposed in Table A-2**,** we get:

$$\begin{aligned} D_{out} = {a_0}^2\left[-4\frac{\varepsilon_\tau}{T_c}+\frac{2\varepsilon_\tau\Delta}{{T_c}^2}\right] + {a_1}^2\left[-4\frac{\varepsilon_\tau+\Delta\tau_1}{T_c}+\frac{2(\varepsilon_\tau+\Delta\tau_1)\Delta}{{T_c}^2}\right] \\ + 2a_0a_1\cos(\Delta\theta_1)\left[-2\frac{\varepsilon_\tau+\Delta\tau_1}{T_c}-2\frac{\varepsilon_\tau}{T_c}+\frac{2\varepsilon_\tau\Delta}{T_c^2}+\frac{\Delta\tau_1\Delta}{{T_c}^2}\right] \end{aligned} \qquad \text{Eq - A-31}$$

A stable lock point is reached when $D_{out} = 0$. In this case, Eq - A-31 becomes:

$$\varepsilon_\tau = -\Delta\tau_1\frac{{a_1}^2+a_0a_1\cos(\Delta\theta_1)}{{a_0}^2+{a_1}^2+2a_0a_1\cos(\Delta\theta_1)} \qquad \text{Eq - A-32}$$

Eq - A-32 provides the analytical expression of the DLL code delay estimate error for $\Delta\tau_1 \in \left[0,\left(1-\frac{a_1}{a_0}\right)\frac{\Delta}{2}\right]$.

A.4. Multipath ranging error induced by the ground and the aircraft structure

This subsection analyzes the multipath ranging error in steady state induced by the airport surface and by the aircraft structure when the satellite has a low elevation angle and is aligned with the fuselage and is forward the aircraft, that is to say when $\mathrm{Az}_{\mathrm{air}} = 0°$.

The GPSL1C+GPSL5 and the GalileoE1+GalileoE5a multipath ranging errors in steady state due to the airport surface and the structure of the assessed aircraft are represented in Figure A-3 for a wide range of pairs $\{\text{satellite elevation El}, \text{aircraft azimuth } \mathrm{Az}_{\mathrm{air}}\}$ and for a planar and infinite ground made of dry tar.

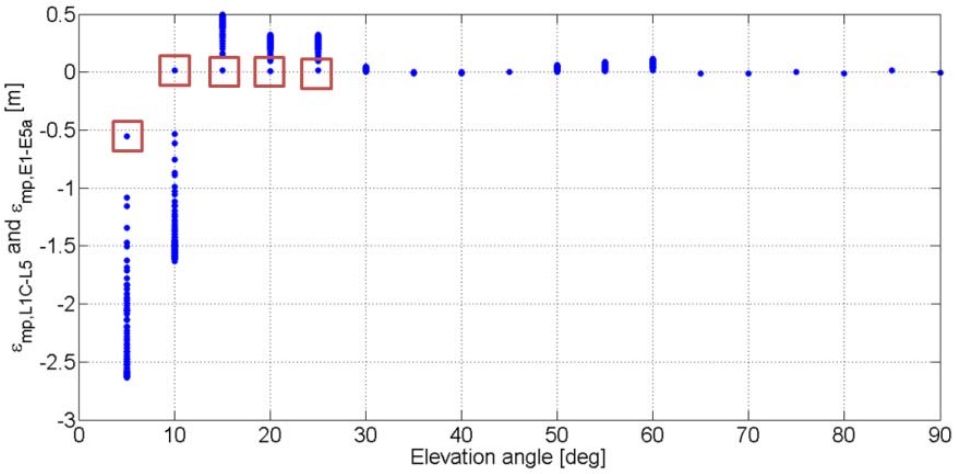

Figure A-3: Dual-frequency raw code multipath ranging error due to the airport surface and the aircraft structure

From Figure A-3, at low elevation angle, the error for an aircraft azimuth angle of $\mathrm{Az}_{\mathrm{air}} = 0°$ is significantly different from the values of the errors for other azimuths. The errors for $\mathrm{Az}_{\mathrm{air}} = 0°$ and for $\mathrm{El} = 5°, \mathrm{El} = 10°, \mathrm{El} = 15°, \mathrm{El} = 20°, \mathrm{El} = 25°$ are indicated by a red square in Figure 3. When $\mathrm{Az}_{\mathrm{air}} = 0°$, the satellite is aligned with the fuselage and is forward the aircraft. This situation is depicted in Figure A-4.

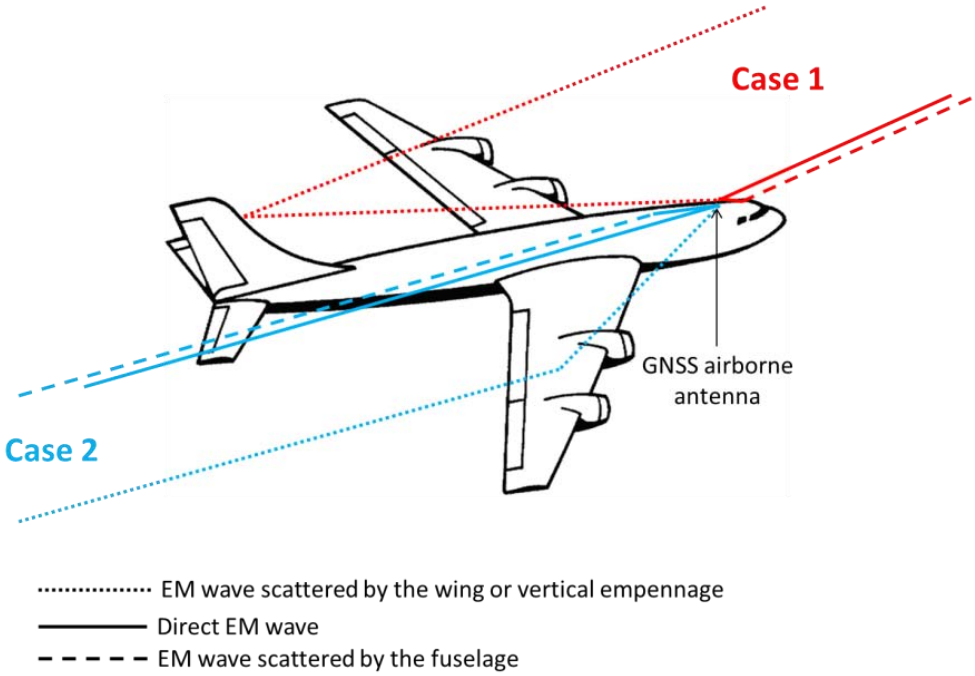

Figure A-4: EM waves scattered by the wing or by the vertical empennage

The echo signals from the aircraft structure are scattered from the fuselage. At low elevation angles, these echo signals can also be scattered from the wings, as shown by Case 2 in Figure A-4. However, in this case, the echo signal scattered by the wings arrive from downwards and are thus strongly rejected by the antenna. When the satellite has a low elevation angle and is aligned with the fuselage and is forward the aircraft, that is to say when $\mathrm{Az}_{\mathrm{air}} = 0°$, the echo signals may be scattered by the fuselage and by the vertical empennage. In this case, the echo signals scattered by the empennage arrive from above the horizon at low elevation angle and are not strongly rejected by the antenna. This explains why the error for an aircraft azimuth angle of $\mathrm{Az}_{\mathrm{air}} = 0°$ is significantly different from the values of the error for other azimuths.

A.5. Dynamic multipath ranging error model induced by the ground and the aircraft structure during turns

This subsection develops a GNSS multipath ranging error model induced by the airport surface and by the aircraft structure during turns and assesses the validity of this model. This section is organized as follows. Firstly, the multipath ranging error model established for straight line trajectories is recalled. This model is extended to curved trajectories and is compared to the multipath ranging errors induced by the airport surface and by the aircraft structure obtained by the deterministic ranging error simulator [Chen, 2010] during turns. Secondly, the position biases induced by multipath from the airport surface and from the aircraft structure are computed by means of the error model extended to curved trajectories and compared to the position biases obtained by means on the GNSS multipath ranging error simulator.

A.5.1. Extended error model to curved line trajectories

It is established in Chapter 5 that the GNSS multipath ranging error induced by the airport surface and by the aircraft structure during a straight line trajectory at time t can be modelled as a constant ranging error:

$$\varepsilon_{mp}(t) = b_{AC+ground}(El, Az_{air}) \quad \text{Eq - A-33}$$

It is proposed to extend the dynamic multipath ranging error adapted to straight line trajectories to non-uniform and curved trajectories as follows:

$$\varepsilon_{mp}(t) = b_{AC+ground}\left(El, Az_{air}(t)\right) \quad \text{Eq - A-34}$$

where $Az_{air}(t)$ is the aircraft azimuth angle at time t throughout the trajectory.

In order to discuss the validity of this model, the following scenario is considered. An aircraft performs a trajectory at Toulouse Blagnac airport along segments 3 and 4 of the LVP procedure path. The aircraft turns between segments 3 and 4. The trajectory is simulated by means of the trajectory simulator presented in Chapter 6. The GNSS multipath ranging errors induced by the airport surface and by the aircraft structure along the simulated trajectory are obtained:

- by the model stated in Eq - A-34,
- by means of the GNSS ranging error simulator [Chen, 2010].

Both errors are plotted in Figure A-5. This figure also represents the evolution of the aircraft azimuth angle Az_{air} along the simulated trajectory. Simulation parameters are recapped in Table A-3.

It is shown in Figure A-5 that the GNSS ranging error predicted by the error model is varying during the turn and becomes constant at time $t_{model} = 58.4s$, that is to say when the aircraft begins the straight line trajectory on segment 4.

In comparison, the GNSS ranging error obtained by the GNSS multipath error simulator is delayed with respect to the error obtained by the model. The simulated error is varying until $t_{simu} = 65.0s$. In other words, the error is still varying when the GNSS airborne antenna has left the turn. This can be explained as follows. The DLL behaves as a first-order low pass filter characterized by a response time of the order of few seconds. The DLL is thus characterized by a response time. The DLL response time is not taken into account in the error model presented in Eq - A-34, while the DLL response time is taken into account in the simulated errors. For this reason, the simulated error is delayed of few seconds with respect to the error obtained by the model.

	Parameter description	Parameter value
Satellite position	Satellite elevation angle El	20°
	Satellite azimuth angle Az_{sat}	0°
GNSS signals		GPSL1C+GPSL5
GNSS airborne antenna position		Along segments 3 and 4 of the LVP procedure
GNSS airborne antenna speed	Aircraft speed v	$2m.s^{-1}$

Table A-3 : Simulation parameters for Figure A-5

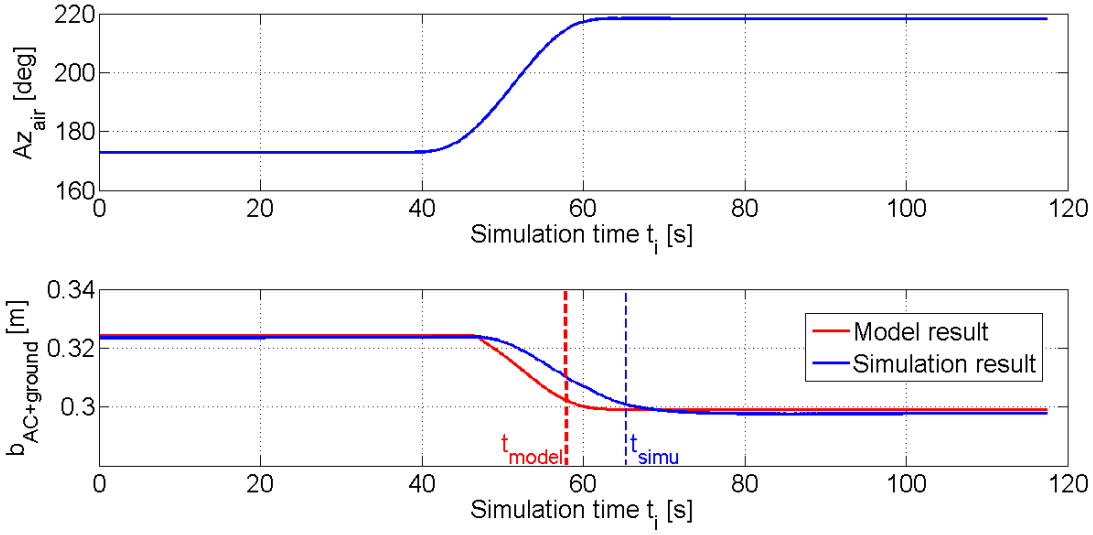

Figure A-5: Aircraft azimuth angle and GNSS multipath ranging error induced by the aircraft structure and by the airport obstacle

For a fixed simulation time t_i, the maximal difference between the error predicted by the model and the error obtained by the simulator is 7 millimeters, which is low regarding the value of the error that is several decimeters. It is concluded that the error model proposed in Eq - A-34 can be used to model the GNSS ranging error model induced by multipath from the airport surface and from the aircraft structure during curved trajectories.

A.5.2. Horizontal position biases obtained by the extended error model

It has been shown in Chapter 7 that multipath ranging errors induced by the airport surface and the aircraft structure induce an horizontal position bias denoted as $\mathbf{b}_p$. This section compares the horizontal position biases $\mathbf{b}_p$ obtained when the GNSS multipath ranging error vector is computed by means of:

- the extended error model developed in Eq - A-34,
- the GNSS multipath ranging error simulator.

In order to compare the position biases obtained by means of the multipath ranging error model and by means of the multipath ranging error simulator, the following scenario is considered. An aircraft performs a trajectory at Toulouse Blagnac airport along segments 3 and 4 of the LVP procedure path. The aircraft turns between segments 3 and 4. The trajectory is simulated by means of the trajectory simulator presented in Chapter 6. The horizontal position biases $\mathbf{b}_p$ are computed along the trajectory based on Eq - 7-15 and are plotted in Figure A-6. Figure A-6 also represents the evolution of the aircraft azimuth angle Az_{air} along the simulated trajectory. Simulation parameters are recapped in Table A-4.

	Parameter description	Parameter value
Satellite constellations	Total number of satellites in the constellation	GPS: 24 Galileo: 27
	Number of satellites in view during the trajectory	GPS: 6 Galileo: 6
	Elevation mask angle	GPS: 15° Galileo: 15°
GNSS signals		Dual frequency GPSL1C+GPSL5 Dual frequency GalileoE1+GalileoE5a
GNSS airborne antenna position		Along segments 3 and 4 of the LVP procedure
GNSS airborne antenna speed	Aircraft speed v	$2\mathrm{m.s}^{-1}$

Table A-4 : Simulation parameters for Figure A-6

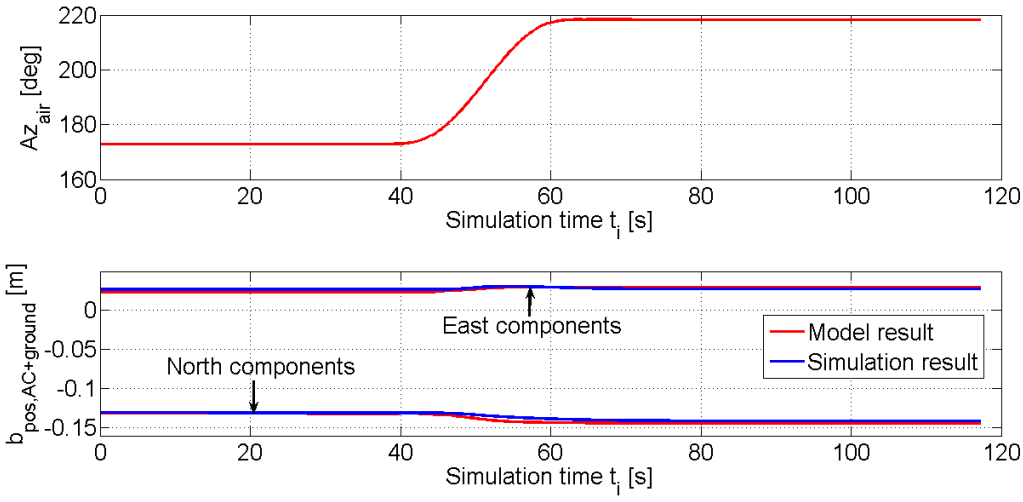

Figure A-6 : Aircraft azimuth angle and GNSS multipath position biases induced by the aircraft structure and by the airport obstacle

It is shown in Figure A-6 that the horizontal position biases $\mathbf{b}_p$ obtained when the GNSS multipath ranging error vector is computed by the error model or by the GNSS multipath ranging error are similar. For the same reason as the one exposed in Section A.5.1, the position bias obtained by the GNSS multipath error simulator is delayed of roughly 5 seconds with respect to the bias obtained by the model. The maximal difference in terms of horizontal position bias between the blue and red curves is 1.9mm in the East direction and 5.6mm in the North direction. It is concluded that the error model proposed in Eq - A-34 can be used to model the horizontal position biases induced by multipath from the airport surface and from the aircraft structure.

APPENDIX B

GNSS stochastic multipath ranging error models

This appendix:

- analyses the validity of the 3D model of Blagnac airport to derive the parameters σ_{static} and σ_{dyn} of the stochastic multipath error models in both static and dynamic configurations,
- presents the convergence test implemented for the derivation of the error model parameter σ_{static},
- shows that the parameters σ_{static} and σ_{dyn} presented in this thesis for the dual-frequency GPSL1C+GPSL5 mode are also valid for the dual-frequency GalileoE1+GalileoE5a mode,
- investigates the PSD functions of the components u_{obs} over two distinct trajectories chosen randomly along a given segment in the impact zone.

B.1. Validity of the 3D model of Toulouse Blagnac airport

As detailed in Section 5.1.2.2.3, five simplifications have been made when designing the 3D model of the terminal buildings and the terminal gates of Toulouse Blagnac airport, France. Among these simplifications there are:

- **Simplification 1**: Details characterized by a size below the wavelength, that is to say centimeter level details, are not represented. Amongst these details there are:
  - Bricks
  - Windows frames
  - Metallic armatures on the glass walls characterized by a width of a few centimeters. Glass facades with such metallic armatures are represented by homogeneous and flawless glass facades.
  - Glass horizontal sticks on metallic walls (such as for the metallic façade of Hall C of Toulouse Blagnac airport) characterized by a width of a few centimeters. Metallic facades with such glass parts are represented by homogeneous and flawless metallic facades.

- **Simplification 2**: Sub-meter level concrete details on concrete walls such as concrete overhangs and recesses on are not represented.

This subsection analyzes the validity of simplifications 1 and 2 for the development of the GNSS stochastic multipath error models induced by multipath from the airport obstacles. In other words, this subsection assesses the validity of these simplifications to estimate the impact zone location and to estimate the statistical parameters σ_{static} and σ_{dyn} that characterize the GNSS stochastic multipath error models induced by multipath from the airport obstacles in the impact zone. The analysis does not aim to assess the validity of the simplifications on the estimation of the GNSS multipath error in the impact zone.

This section is organized as follows. Previous works on the feasibility to simplify the representation of complex facades for the estimation of the GNSS multipath ranging errors are presented in Section B.1.1. Based on this review, the simplification 1 can be justified. Next, the simplification 2 is discussed in Section B.1.2.

B.1.1. Previous work

Among the previous works dealing with the simplification of the representation of complex facades, Ait Ighil in [Ait Ighil, 2013] identifies the required level of details for the estimation of GNSS multipath errors in urban environments and for the satellite navigation application. Using simplified façade representations is essential in urban environments due to the complexity and diversity of the façade architectures. In order to find the required level of details for the application, a given façade is represented with four levels of details:

- In the **null resolution** representation, no details are present. The façade is represented as a homogeneous and flawless wall.
- In the **low resolution** representation, details much larger than the wavelength, that is roughly 20cm in the satellite navigation application, are represented. At this level of details, only windows, recesses and overhangs of roughly one meter are represented.
- In the **medium resolution** representation, details in the range of the wavelength are represented. As an example, metallic armatures on the glass walls characterized by a width of few decimeters are represented.
- In the **high resolution** representation, sub-wavelength details, such as bricks, are considered.

Ait Ighil in [Ait Ighil, 2013] uses the Method of Moment (MoM) to compute the scattered EM field. This method is valid even in the presence of details which size is small regarding the wavelength. The error is estimated by modelling the transmission channel by a narrowband and by a wideband model. Different required levels of details are established regarding the type of model that is used to represent the transmission channel. The GNSS multipath error simulator used in this Ph.D. thesis [Chen, 2010] uses the PO method to compute the scattered EM field. This method is not valid in the presence of details which size is small regarding the wavelength. The wideband transmission channel model is used. Hence, this subsection focuses on the required level of details for the estimation of GNSS multipath errors when this estimation is based on the wideband transmission channel model.

The low resolution model can be used to estimate the GNSS code ranging errors when the error estimation is based on the wideband transmission channel model [Ait Ighil, 2013]. Note that this conclusion is valid under clear LOS conditions, that is to say when the direct signal power is not attenuated by shadowing effects. This is the case in this Ph.D. thesis, as discussed in Sections 5.2 and 6.2.2.

Based on this result, the simplification 1 can be made in this thesis to estimate the GNSS code multipath ranging errors. Hence, simplification 1 can be done to estimate the impact zone location and to estimate the statistical parameters σ_{static} and σ_{dyn} that characterize the GNSS stochastic multipath error models induced by multipath from the airport obstacles in the impact zone.

B.1.2. Representation of facades with meter-level overhangs and recesses

Concrete overhangs and recesses of the order of several decimeters, that is to say much larger than the wavelength, have not been represented on concrete facades in the 3D model of Blagnac airport. This section analyses the validity of this simplification to estimate the impact zone location and to estimate the statistical parameters σ_{static} and σ_{dyn} that characterize the GNSS stochastic multipath error models in the impact zone. For this analysis, the simulation scenario is firstly presented. After that, the power of the scattered EM field is analyzed in the presence of a façade with overhangs, and in the presence of a façade without overhangs. Next, the multipath errors on a given segment and the impact zone location are analyzed in the presence and absence of the concrete overhangs. Finally, the statistical parameters σ_{static} and σ_{dyn} are compared in the presence of a façade with overhangs, and in the presence of a façade without overhangs.

B.1.2.1. Simulation scenario

The airport scene is composed of a single façade which dimensions are detailed in Table B-1. The positions of the façade and of the GNSS airborne antenna are expressed in the direct and orthogonal reference frame $(0, \mathbf{x}, \mathbf{y}, \mathbf{z})$. The horizontal plane $(0, \mathbf{x}, \mathbf{y})$ represents the airport surface. The $\mathbf{z}$ axis is the local vertical vector pointing upwards. The single façade is represented in Figure B-1.

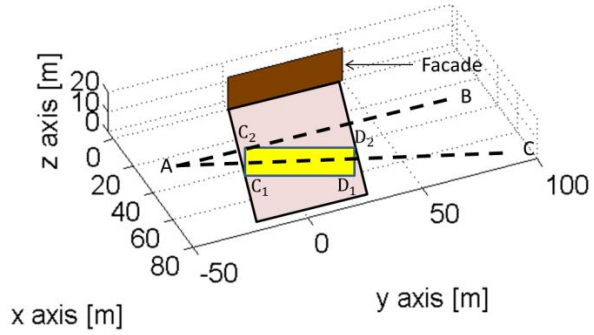

Figure B-1 : Representation of the single façade

The façade is illuminated by a satellite which elevation and azimuth angles are indicated in Table B-1. Other simulation parameters are presented in Table B-1.

	Parameter description	Parameter value
Satellite position	Satellite elevation angle El	20°
	Satellite azimuth angle Az_{sat}	10°
Façade dimensions	Height H	16m
	Length L	50m

Table B-1 : Simulation parameters used for Figure B-3 to Figure B-5 and Table B-2

Two facades have been designed.

- A concrete facade that has 50cm deep overhangs that are evenly distributed over the facade. The overhangs represent 93% of the total surface of the façade. This façade is called "**low resolution concrete facade**" in the following. Note that estimating the multipath errors in the impact zone of the low resolution façade by means of the PO model corresponds to the limit of validity of this PO model. Indeed, this model is not valid in the presence of details characterized by a size in the range or lower than the wavelength (approximately 20 centimeters).
- A flawless and concrete facade. This façade is called "**null resolution concrete facade**" in the following.

The dimensions of both facades are the same and are indicated in Table B-1. The dielectric permittivity and thickness of these concrete facades are indicated in Table 5-1. Both low and null resolution concrete façades are represented in Figure B-2.

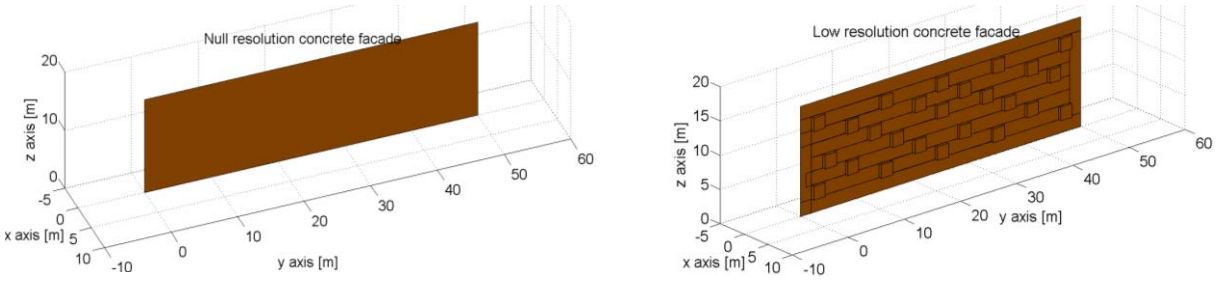

Figure B-2: Representation of the null and low resolution concrete facades

In this section, only concrete overhangs and recesses are simulated on concrete facades. The main limitation of this analysis on the effects of concrete overhangs and recesses on the impact zone location and on the parameters σ_{static} and σ_{dyn} is that the conclusions of this analysis cannot be extended to non-concrete overhangs or recesses on concrete facades. This is explained as follows.

Concrete overhangs on concrete facades influence the phase of the echo signals. The amplitude of the echo signals scattered by the concrete facades with concrete overhangs is comparable with the amplitude of the echo signals scattered by the null resolution concrete façade. If non-concrete overhangs are represented on the concrete facades, both phase and amplitude of the echo signals scattered by the null resolution concrete façade will be different than the phase and amplitude of the echo signals scattered by the concrete façade with non-concrete overhangs. In this situation, the conclusions proposed in this section on the effects of concrete overhangs and recesses on the impact zone location and on the parameters σ_{static} and σ_{dyn} may not be valid.

Note finally that, in Sections B.1.2.3 and B.1.2.4., ground first-order reflections, obstacle first-order interactions, ground/obstacle second-order interactions, obstacle/ground second-order interactions and obstacle/obstacle second-order interactions are taken into account. However, for the analysis of the scattered pattern in Section B.1.2.2, only obstacle first-order interactions and obstacle/obstacle second-order interactions are taken into account. Indeed, this analysis aims to underline the impact of the façade representation on the power of the field scattered by the façade.

B.1.2.2. Analysis of the scattered pattern

Figure B-3 presents the power of the EM field scattered from both null resolution and low resolution concrete facades in the L1 frequency band. The power of the EM field is plotted in the horizontal plane at the height $h_{ant} = 5.88m$ above the ground to represent the height of the GNSS airborne antenna of A319 aircraft. The EM field has not been computed for points characterized by an **x** coordinate smaller than 5m. Indeed, when a facet size of 70cm is adopted to mesh the facade, the EM field computed by the GNSS error simulator is valid at a minimal distance of 4.9m from the façade. This is fully justified in [Chen, 2010].

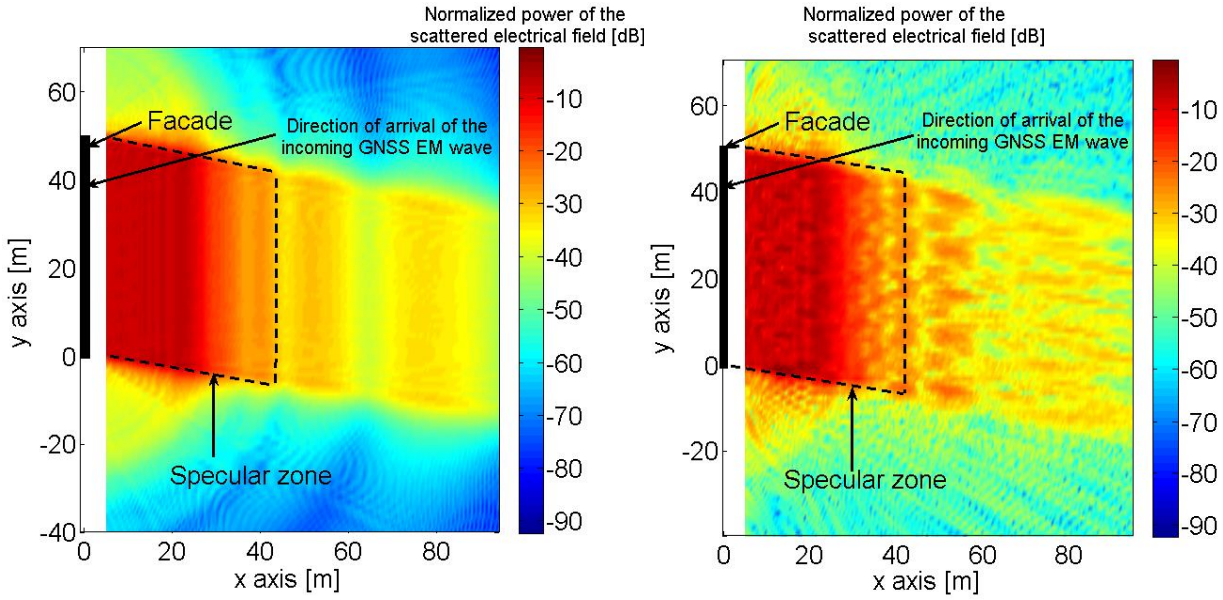

Null resolution concrete facade ***Low resolution concrete facade***

Figure B-3: Power of the EM field scattered on the L1 frequency band

From Figure B-3, the overhangs on the low resolution façade lead to spread the EM field power in the airport surface towards different directions. The EM field scattered by the null resolution facade is more directional and the energy of the scattered field is mainly focused around a single direction, which is the specular direction. The regular interference pattern observed in the specular zone with the null resolution façade is not present for the low resolution façade. The presence of recesses and overhangs has a strong impact on the scattering pattern. Hence, it is required to represent decimeter level overhangs and recesses on a façade for a suitable representation of the power scattered by this façade.

B.1.2.3. Analysis of the GNSS multipath ranging errors and of the impact zone location

Figure B-4 presents the GNSS ranging errors in the static configuration along segments [AB] and [AC] represented in Figure B-1. The coordinates of A, B, C in $(0, \mathbf{x}, \mathbf{y}, \mathbf{z})$ are indicated in Table B-1. [AB] is parallel to the **y** axis and thus to the façade. The angle between [AC] and the **y** axis is 20°.

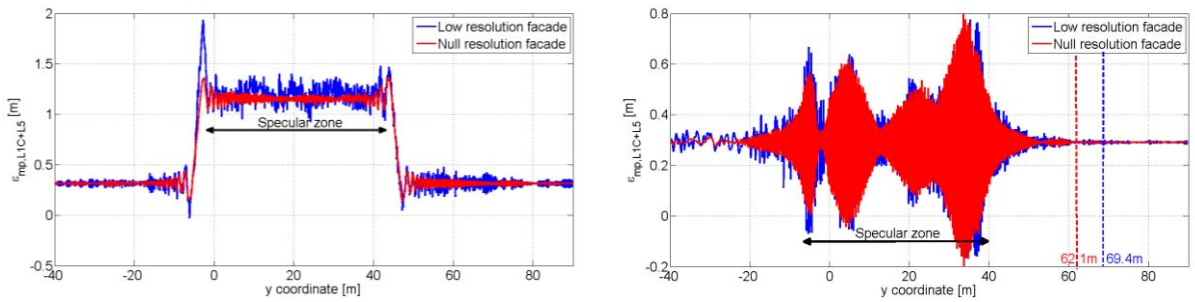

Error along segment [AB] *Error along segment [AC]*

Figure B-4 : GPSL1C+GPSL5 ranging error along segments [AB] and [CD] in the static configuration

Figure B-5 presents the GNSS ranging errors in the dynamic configuration along segments [AB] and [CD].

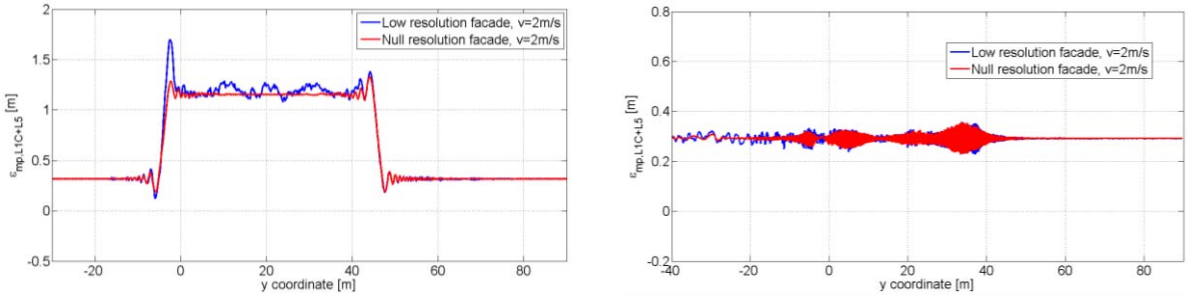

Error along segment [AB] *Error along segment [AC]*

Figure B-5 : GPSL1C+GPSL5 ranging error along segments [AB] and [CD] in the dynamic configuration

From Figure B-4, the variations of the amplitude of the multipath errors along segment [AB] in the specular zone are stronger for the low resolution model than for the null resolution model. This is because the phase of the echo signals along the segment [AB], and thus the amplitude of the EM field along segment [AB], does not present high variations along [AB] in the presence of the null resolution concrete façade. In comparison, the phase of the echo signals along the low resolution façade presents higher variations due to the presence of the concrete overhangs, resulting in variations of the amplitude of the GNSS ranging error along segment [AB]. A similar observation can be made for the dynamic configuration along segment [AB] in Figure B-5.

It can also be observed in Figure B-4 that the amplitude of the multipath errors outside the specular zone is stronger with the low resolution façade than with the low resolution façade along both segments [AB] and [AC]. This is because the EM field scattered by the null resolution façade is more directional than the EM field scattered by the low resolution façade. This results in an extension of the static impact zone for the low resolution façade. As an illustration, it is shown in Figure B-4 that the upper impact zone limit on segment [AC] and along the **y** axis is 62.1m for the null resolution façade and is 69.4m for the low resolution façade. Similarly, for the dynamic configuration, it can be observed in Figure B-5 that the multipath errors outside the specular zone are stronger with the low resolution façade than with the low resolution façade.

To conclude, the presence of decimeter level overhangs has a significant impact on the estimation of the GNSS multipath errors when the aircraft trajectory is parallel to the façade. When it is not the case, the errors in the impact zone of the façade with and without overhangs locally have significant differences. However, in this case, the errors induced by both facades have approximately the same order of magnitude and the same shape over the whole segment. In addition, the presence of concrete overhangs on a concrete façade leads to extend and enlarge the impact zone location of a few meters.

B.1.2.3. Analysis of the GNSS stochastic multipath error models σ_{static} and σ_{dyn}

Derivation of GNSS multipath ranging error models

Table B-2 presents the parameters σ_{static} and σ_{dyn} of the stochastic GNSS ranging error models along segments [AC] and [AB] in the area $C_1C_2D_1D_2$ of the impact zone. The area $C_1C_2D_1D_2$ is presented in Figure 5-16 and is depicted in Figure B-1 along segment [AC]. Simulation parameters are indicated in Table B-1. More details about the derivation of these parameters are provided in Sections 5.4 and 5.5. Note also that, in this Table, the impact zone locations related to the null and low resolution facades have been predetermined based on the methodology presented in Section 5.4.2.1. Next, the statistical parameters σ_{static} and σ_{dyn} have been estimated in both impact zones.

	Facade	σ_{static}	σ_{dyn}
Segment [AB]	Null resolution concrete	51cm	2.77m
	Low resolution concrete	51cm	2.97m
Segment [AC]	Null resolution concrete	22cm	82.2cm
	Low resolution concrete	20cm	79.5cm

Table B-2: Comparison of the static and dynamic model parameters for the null resolution and low resolution concrete facades

From Table B-2, the maximal relative difference between the values of σ_{static} estimated in the presence of the null and low resolution facades is 10%. The maximal relative difference between the values of σ_{dyn} estimated in the presence of the null and low resolution facades is 7.2%.

B.1.2.4. Conclusions

This section has analyzed the impact of the sub-meter concrete overhangs and recesses located on concrete facades on the impact zone location and on the statistical parameters σ_{static} and σ_{dyn} computed along the taxiway in the area $C_1C_2D_1D_2$ of the impact zone. Conclusions provided in this section may not be valid for non-concrete overhangs or recesses on concrete facades.

It has been shown that, along a given segment that is not perfectly parallel to the façade (most frequency scenario), the multipath errors are locally significantly different in the presence and in the absence of overhangs. However, the errors induced by facades with and without overhangs have approximately the same order of magnitude and the same shape over the whole segment. The GNSS stochastic error model parameters σ_{static} and σ_{dyn} are estimated by computing the multipath errors in the area $C_1C_2D_1D_2$ located around the center line if the taxiway. Hence, errors are not computed locally to estimate both statistical parameters σ_{static} and σ_{dyn}. When extracting the statistical parameters σ_{static} and σ_{dyn} in $C_1C_2D_1D_2$, it is acceptable not to represent the decimeter level overhangs and recesses on a façade. Finally,

the presence of concrete overhangs on a concrete façade leads to extend and enlarge the impact zone location of a few meters. This extension is considered to be low regarding the building and impact zone size at Toulouse Blagnac airport that are few hundred of meters.

B.2. Convergence test for the estimation of σ_{static}

This section presents the convergence test implemented for the derivation of the over-bounding Gaussian multipath ranging error model in the static configuration (see Figure 5-15).

Let's note $\sigma_{static}(p)$ the estimated standard deviation of the Gaussian distribution that over-bounds the distribution of the multipath error in the impact zone at iteration p (or computed based on p values of multipath errors in the impact zone). $\sigma_{static}(p)$ is computed based on DeCleene CDF algorithm, as explained in Section 5.4. After p iterations, the standard deviation estimate converges towards the true standard deviation of the Gaussian distribution that over-bound the distribution of the multipath errors in the impact zone. The simulation has converged at iteration p if [Chen, 2010]:

$$\forall j \in [1, N_C], |\sigma_{static}(p) - \sigma_{static}(p-j)| \leq C_\sigma \qquad \text{Eq - B-1}$$

where:

- C_σ is the convergence criteria related to the standard deviation of the multipath errors. C_σ is set to 1cm in the thesis.
- N_C is the number of previous iterations used in the convergence test. N_C is set to 500 in the thesis.

At each iteration $p > N_C$, the convergence test is performed and the simulation is stopped at the first iteration for which the convergence test is passed, that is for $p = N$. As an illustration, Figure B-6 shows the evolution of $\sigma_{static}(p)$ for the simulation scenario described in Section 5.4.2.4.1.

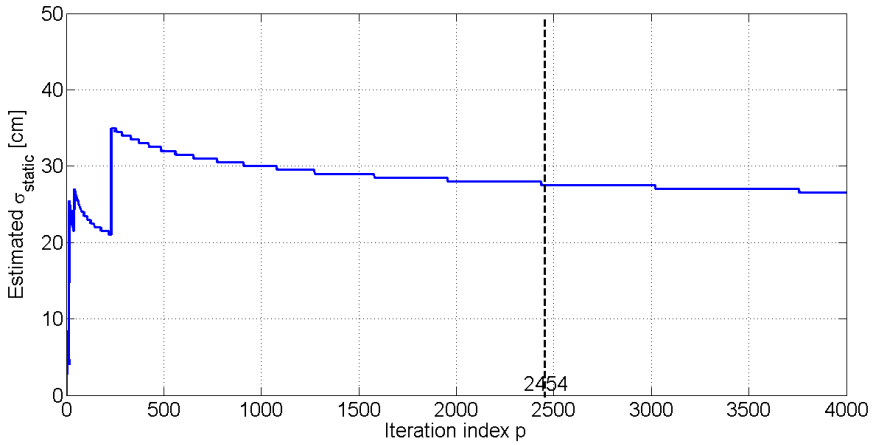

Figure B-6: Estimated standard deviation of the Gaussian distribution that over-bounds b_{obs} over the impact zone on segment 4

Based on these parameters, the first iteration for which the convergence test is passed is $p = 2454$ under the simulation scenario described in Section 5.4.2.4.1.

B.3. Impact of the GNSS signal on the estimation of σ_{static} and σ_{dyn}

This section shows that the modulation difference between GPSL1C and GalileoE1 signals does not significantly impact the values of the parameters σ_{static} and σ_{dyn} in the dual-frequency mode. Hence this appendix shows that the model parameters σ_{static} and σ_{dyn} presented in this thesis for the dual-frequency GPSL1C+GPSL5 mode are also valid for the dual-frequency GalileoE1+GalileoE5a mode.

Figure 4-7 shows that the GPSL1C steady-state raw code multipath ranging error induced by a single echo signal may be slightly different from the GalileoE1 error induced by the same echo signal, especially when the relative code delay of the echo signal is above $\frac{T_c}{2}$, where T_c represents the chip period of the GPSL1C and GalileoE1 pilot spreading codes in this Appendix. For this reason, the over bounding Gaussian model parameters are analyzed in two scenarios:

- In scenario 1, the model parameters are derived in zone 1 of the impact zone located closed to the obstacles, in a way that some echo signals reaching the GNSSS receiver antenna in this region are characterized by relative code delays in the interval $\left[0; \frac{T_c}{2}\right]$,
- In scenario 2, the model parameters are derived in zone 2 of the impact zone located far from the obstacles, in a way that the echo signals reaching the GNSSS receiver antenna in this region are mainly characterized by relative code delays longer than $\frac{T_c}{2}$.

Figure B-7 shows that several multipath parameters are characterized by a relative code delay shorter than $\frac{T_c}{2}$ under scenario 1 while all echo signals have a relative code delay longer than $\frac{T_c}{2}$ under scenario 2, except the echo signal emitted by the satellite, reflected by the ground, and reaching the GNSS receiver antenna. These relative code delays have been obtained by simulating the multipath parameters over 100 true receiver antenna positions equally distributed in an inner grid in zones 1 and 2. Simulation parameters are provided in Table B-3.

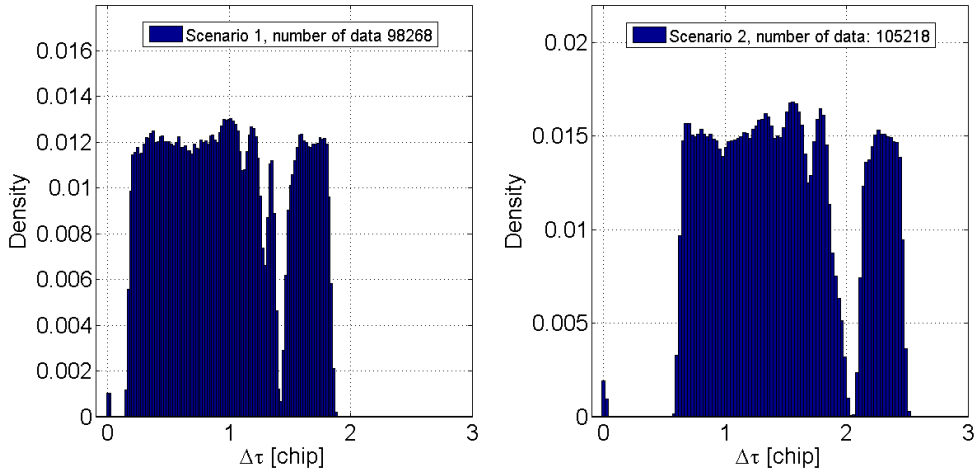

Figure B-7: Histograms of the L1 relative code delays of the direct and echo signals

The dual-frequency GPSL1C+GPSL5 and GalileoE1+GalileoE5a over-bounding Gaussian model parameters obtained in zones 1 and 2 are compared in Table B-4. The simulation parameters used for these simulations are recapped in Table B-3.

	Parameter description	Parameter value
Satellite position	Satellite elevation angle El	20°
	Satellite azimuth angle Az_{sat}	0°
GNSS airborne antenna positions	Scenario 1: antenna positions in zone 1 (closed to the airport buildings)	x range: $[30.0; 40.0]$ y range: $[140.0; 160.0]$ $z = 5.88$
	Scenario 2: antenna positions in zone 2 (far from the airport buildings)	x range: $[150.0; 160.0]$ y range: $[140.0; 160.0]$ $z = 5.88$

Table B-3: Simulation parameters used for Figure B-7 and Table B-4

	σ_{static}	σ_{dyn}
Scenario 1	GPSL1C+GPSL5:36cm GalileoE1+GalileoE5a: 37cm	GPSL1C+GPSL5: 39.1cm GalileoE1+GalileoE5a: 39.5cm
Scenario 2	GPSL1C+GPSL5: 1.00cm GalileoE1+GalileoE5a: 1.00cm	GPSL1C+GPSL5: 4.8cm GalileoE1+GalileoE5a: 4.1cm

Table B-4: Comparison of σ_{static} between GPSL1C+GPSL5 and GalileoE1+GalileoE5a

Regardless of the scenario, the deviation between the GPSL1C+GPSL5 model parameters and the GalileoE1+GalileoE5a model parameters is less than 14% of the value of the parameters. This deviation is considered as insignificant in the application. The values of σ_{static} and σ_{dyn} presented in this thesis for the dual-frequency GPSL1C+GPSL5 mode are considered to be valid for the dual-frequency GalileoE1+GalileoE5a mode. Note finally that this conclusion has been obtained by using the same DLL integration time, the same early-late spacing, the same loop bandwidth, and the same front-end filter bandwidth (see Table 4-1) for GPSL5 and GalileoE5a and for GPSL1C and GalileoE1C. Further analysis are needed to investigate the difference between the GPSL1C+GPSL5 error model parameters (σ_{static} and σ_{dyn}) and the GalileoE1+GalileoE5a error model parameters when different receiver and DLL settings are used for both L1 signals and both L5 signals.

B.4. Comparison of the PSD of u_{obs} along two distinct trajectories

This subsection shows that the PSD functions of the components u_{obs} over two distinct trajectories chosen randomly along a given segment in the impact zone are almost the same.

Figure B-8 plots the PSD obtained along two trajectories chosen randomly along segment 4. Both trajectories are called trajectory 1 and trajectory 2. The angle between both trajectories is 0.49°. The aircraft speed is $v = 1 m.s^{-1}$. The satellite elevation and azimuth angles are $El = 20°$ and $Az_{sat} = 0°$, respectively.

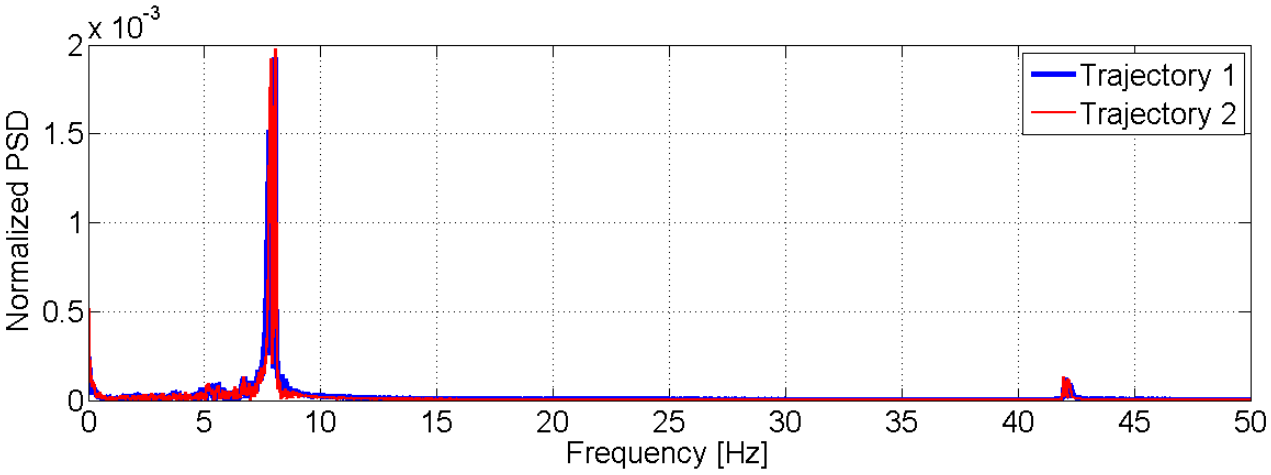

Figure B-8 : Estimated PSD of u_{obs} in the impact zone on segment 4

Two reasons explain why the PSD functions over two distinct trajectories are almost the same. Firstly, the maximal distance between two segments chosen randomly is relatively low regarding the spatial period of the oscillations of the amplitude of the echo signals in the scene that is described in Section 5.4.2.2. This maximal distance is $6\sigma_{FTE}$, that is 2.8m for the *taxi on taxi lane* sub-phase (segment 4), 3.7m for the *taxi on apron taxiway* sub-phase (segment 3) and 6.06m for the *taxi on taxiway* sub-phase. Hence, the amplitude of the variations of the errors u_{obs} is similar along two distinct segments. Secondly, two distinct trajectories chosen randomly in the impact zone have roughly the same orientation in the scene. As an example, over segment 4, it can be easily demonstrated that the maximal angular difference between the orientations of two trajectories is 1.38°. Hence, the time period of the errors u_{obs} is similar along two distinct segments. Both reasons explain why the errors over two distinct trajectories along a given segment have approximately the same spectral characteristics.

APPENDIX C

Navigation sensor review

This Appendix presents the main advantages and drawbacks of several sensors and signals of opportunity that can be hybridized with GNSS pseudo range measurements.

Sensor or signal of opportunity	Advantage(s)	Drawback(s)
Distance Measure-ment Equipment (DME)	- Onboard equipment installed in Airbus aircraft	- Usable in the coverage of a DME ground equipment - Low accuracy: few hundreds of meters (DME/N) to few dozens of meters (DME/P) at 95% [ICAO, 2006]
Instrument Landing System (ILS)	- Onboard equipment installed in Airbus aircraft	- Usable in the coverage of ILS: on the runway only
Secondary surveillance radar	- Usable in the coverage of the equipped airport	- Low accuracy: few meters (7.5m) at 95% on taxiways and apron taxiways and few dozens of meters (20m) at 95% of a parked aircraft at the gate [ED117, 2003]
Wheel Speed Sensor (WSS) and odometer	- Usable anywhere in the airport - Wholly self-contained within the aircraft	- Onboard equipment installed in Airbus aircraft on the main landing gear - Requires equipment installation on the nose landing gear

Sensor or signal of opportunity	Advantage(s)	Drawback(s)
Wi-Fi or Worldwide Interoperability for Microwave Access (WiMAX)	- Airport surface wireless communication networks are under development [Byrne, 2013] - Techniques based on existing network infrastructure	- Low accuracy: few dozens of meters in the positioning domain for Wi-Fi cell identification methods [Evennou *et al*., 2006] - And /or sensitive to topologic changes for fingerprinting methods [Bahl *et al*., 2000]
Ultra Wide Band (UWB)	- Accuracy on the ranging measurement: few decimeters up to few centimeters [TDC, 2011] [Zebra, 2008] [MacGougan *et al*., 2009]	- Requires requester and responder installation - Not adapted to large scale environments (maximal distance receptor/transmitter: few dozens of meters)
Light Detection and Ranging (LIDAR)	- Accuracy on the ranging measurement: few centimeters at 95% [Lemmens, 2009]	- Sensitive to weather conditions, such as fog, rain, temperature [Clipp, 2006], [Campbell *et al*., 2003] - LIDAR-based PVT algorithms require high-resolution/expensive terrain data base (decimeter resolution) [Lemmens, 2009] [Lohani] [Campbell *et al*, 2003] [Lee *et al*., 2008]
Radio-Frequency Identifi-cation (RFID)		- Requires tag installation on the airport surface with a small scale spacing (decimeter level) [Park *et al*., 2009] - Requires reader installation onboard - Technology not mature for large-scale environments - Accuracy relatively unknown
Ultrasound sensors and infrared sensors		- Accuracy level not available - Sensitive to weather conditions such as temperature, fog, rain - Sensitive to luminosity for infrared sensors
Video camera		- Sensitive to weather conditions such as fog, rain - Accuracy / failure modes not available

Figure C-1 : Advantages and drawbacks of navigation sensors and signals of opportunity

APPENDIX D

GPS and Galileo link budget

The C/N0 ratio [dB-Hz] at the output of the GNSS receiver antenna is computed as follows:

$$C/N0 = P_S + G_S + G_R - L_S - L_A - L_{FS} - N_0 \qquad \text{Eq - D-1}$$

where:

- P_S is the power of the signal at the amplifier output of the satellite [dBW],
- G_S is the satellite antenna gain [dBi],
- G_R is the receiver antenna gain [dBi],
- L_S is the total loss introduced by the satellite filters and by the payload components imperfections [dB],
- L_A represents the atmospheric and polarization losses [dB],
- L_{FS} represents the free-space losses [dB],
- $N_0 = -201.2\text{dBW} - \text{Hz}$ is the constant noise power spectral density of the thermal noise.

D.1. Satellite component losses L_S

Table D-1 provides the assumed values of the total loss introduced by the satellite filters and by the payload components imperfections.

	GalileoE1	GalileoE5a	GPSL1C	GPSL5
Loss due to payload filters and component imperfections L_S [dB]	0.6 [ICD, 2010]	0.6 [ICD, 2010]	0.2 [GPS Wing, 2008]	0.6 [GPS Wing, 2010]

Table D-1 : Power losses introduced by the satellite filters and by the payload components imperfections

D.2. Atmospheric and polarization losses L_A

Table D-2 provides the assumed values of the atmospheric and polarization losses.

	GalileoE1	GalileoE5a	GPSL1C	GPSL5
Atmospheric loss [dB]	0.3 [Parkinson *et al*., 1996]	0.3 [Parkinson *et al*., 1996]	0.5 [GPS Wing, 2008]	0.3 [Parkinson *et al*., 1996]
Polarization loss [dB] [Parkinson *et al*., 1996]	1	1	1	1
Atmospheric and polarization losses L_A [dB]	1.3	1.3	1.5	1.3

Table D-2: Atmospheric and polarization losses

D.3. Satellite amplifier output power P_S

The complete methodology to compute P_S is provided in [Rebeyrol, 2007]. P_S is evaluated as follows:

$$P_S = P_{R,min} + L_S + L_A + L_{FS,a} - G_{S,a} - G_{R,a} \quad \text{Eq - D-2}$$

where:

- $P_{R,min}$ [dBW] is the minimum power of the received signal at the receiver input assuming a receiver antenna gain of $G_{R,a}$ dBi,
- $G_{S,a}$ is the satellite antenna gain [dBi] assumed in the computation of P_S,
- $G_{R,a}$ is the receiver antenna gain [dBi] assumed in the computation of P_S,
- $L_{FS,a}$ represents the free-space losses [dB] assumed in the computation of P_S. The free-space losses calculation is fully developed in [Rebeyrol, 2007] and depends on the satellite elevation angle. In this document, the worst case satellite elevation angle are considered in the computation of $L_{FS,a}$ (5° elevation angle for GPS and 10° elevation angle for Galileo).

Table D-3 provides the values of $P_{R,min}$, $L_{FS,a}$, $G_{S,a}$, and $G_{R,a}$ used for the computation of P_S.

	GalileoE1	GalileoE5a	GPSL1C	GPSL5
Total received minimum power $P_{R,min}$ [dBW]	GalileoE1: -157 [ICD, 2010]	GalileoE5a: -155 [ICD, 2010]	GPSL1C: -157 [GPS Wing, 2008]	GPSL5: -154 assuming the GPS block III [GPS Wing, 2010]
	GalileoE1C: -157dBW-3dB= -160 (50/50% E1B/E1C power sharing)	GalileoE5a/Q: -155dBW-3dB= -158 (50/50% I/Q power sharing)	GPSL1C/Pilot: -158.25 (75%/25% Pilot/Data power sharing)	GPSL5/Pilot: -157 (50%/50% Pilot/Data power sharing)
Receiver antenna gain $G_{R,a}$ (dBi)	0 [ICD, 2010]	0 [ICD, 2010]	3 [GPS Wing, 2008]	3 [GPS Wing, 2010]
Free-space loss $L_{FS,a}$ [dB]	185.4	182.87	184.4	181.9
Satellite antenna gain $G_{S,a}$ [dBi] [Czopek *et al.*, 1993]	15	15	15	15
Power at the amplifier output P_S [dBW]	15.30 for E1	14.77 for E5a	11.1 for L1C	11.88 for L5
	12.30 for E1C	11.77 for E5a/Q	9.85 for L1C/Q	8.88 for L5/Q

Table D-3: Computation of the minimum power of the signal at the satellite amplifier output

D.4. Satellite antenna gain G_S

The satellite antenna gains are computed based on the relative positions of the satellite and of the receiver antenna and based on the RHCP satellite antenna gains of a GPS block II satellite on the L1 frequency band. It is recommended as future work to use antenna gains on the L5 frequency band for GPSL5 and GalileoE5a signals.

D.5. Free space losses L_{FS}

The free-space loss is computed as follows:

$$L_{FS} = 10\log_{10}\left[\left(\frac{4\pi d}{\lambda_L}\right)^2\right] \qquad \text{Eq - D-3}$$

where d is the distance between the center of the satellite antenna to the center of the receiver antenna [m].

D.6. Receiver antenna gain G_R

The RHCP receiver antenna gains are described in Section 5.1.2.3.

APPENDIX E

Impact of multipath on the GNSS-based position error

E.1. Impact of multipath on the Kalman filter state vector estimate error

This paragraph analyses the theoretical impact of multipath on the state vector estimate error at time t_i, $\mathbf{dx}(t_i) - d\hat{\mathbf{x}}^+(t_i)$. Let's state the following hypotheses (*):

- At any time t_i, the GNSS measurement error vectors $\mathbf{z}(t_i), \mathbf{b}(t_i) + \mathbf{u}(t_i)$ and the process noise vector $\mathbf{w_s}(t_i)$ are independent each other. This assumption is considered to be valid. Indeed, the process noise and the GNSS measurement errors can be considered as independent since they are due to error sources that are independent.
- The initial prediction of the state vector $d\hat{\mathbf{x}}^+(t_0)$ is independent on the multipath ranging error vectors $\mathbf{b}(t_i) + \mathbf{u}(t_i)$.
- The initial prediction of the covariance matrix $\mathbf{P}^+(t_0)$ of the state vector $d\hat{\mathbf{x}}^+(t_0)$ is independent on the multipath ranging error vectors $\mathbf{b}(t_i) + \mathbf{u}(t_i)$.
- The state vector $d\mathbf{x}$ is estimated by a linearized Kalman filter, meaning that the Kalman filter matrices $\mathbf{H}, \mathbf{F}$ are independent of the GNSS measurements. In addition, it is assumed that the Kalman filter contains the exact models of the transition state matrix **F** and of the design matrix **H**. The potential non-linearities in the propagation model (matrix **F**) are not accounted for.
- The Kalman filter matrice **R** is independent of the GNSS multipath measurement errors.

Let's demonstrate that, under the hypotheses (*) stated above, the error in the state vector estimated in the presence of multipath $d\mathbf{x}(t_i) - d\hat{\mathbf{x}}^+(t_i)$ and the error in the state vector that would have been estimated in the absence of multipath $\left(d\mathbf{x}(t_i) - d\hat{\mathbf{x}}^+{}_{w/o\ mp}(t_i)\right)$ can be related by:

$$d\mathbf{x}(t_i) - d\hat{\mathbf{x}}^+(t_i) = \left(d\mathbf{x}(t_i) - d\hat{\mathbf{x}}^+{}_{w/o\ mp}(t_i)\right) + \boldsymbol{\phi}(t_i) \qquad \text{Eq - E-1}$$

where:

- $d\mathbf{x}(t_i)$, $d\hat{\mathbf{x}}^+_{w/o\ mp}(t_i)$, $d\hat{\mathbf{x}}^+(t_i)$ are defined in Chapter 7,
- $\boldsymbol{\phi}(t_i)$ represents the impact of the multipath on the error in the state vector estimate at time t_i and can be expressed as:

$$\boldsymbol{\phi}(t_i) = \big(I - \mathbf{K}(t_i)\mathbf{H}(t_i)\big)\big(\mathbf{F}(t_{i-1})\boldsymbol{\phi}(t_{i-1})\big) - \mathbf{K}(t_i)\big(\mathbf{b}(t_i) + \mathbf{u}(t_i)\big) \qquad \text{Eq - E-2}$$

where:

- $\boldsymbol{\phi}(t_0) = \mathbf{0}$.

Proof:

The state vector at time t_i is given by the state propagation equation:

$$d\mathbf{x}(t_i) = \mathbf{F}(t_{i-1})d\mathbf{x}(t_{i-1}) + \mathbf{w_s}(t_{i-1}) \qquad \text{Eq - E-3}$$

The updated state vector is obtained in the Kalman filter as follows:

$$d\hat{\mathbf{x}}^+(t_i) = d\hat{\mathbf{x}}^-(t_i) + \mathbf{K}(t_i)\big(d\mathbf{y}(t_i) - \mathbf{H}(t_i)d\hat{\mathbf{x}}^-(t_i)\big) \qquad \text{Eq - E-4}$$

The measurement vector at time t_i is given by the observation model:

$$d\mathbf{y}(t_i) = \mathbf{H}(t_i)d\mathbf{x}(t_i) + \mathbf{w_o}(t_i) \qquad \text{Eq - E-5}$$

Note that, since it is assumed that the Kalman filter contains the exact models of the transition state matrix **F** and of the design matrix **H**, the matrices **H** and **F** used in Eq - E-4 are the same as the matrices used in Eq - E-3 and Eq - E-5. The a priori state vector $d\hat{\mathbf{x}}^-(t_i)$ estimated by the Kalman filter at time t_l is obtained in the Kalman filter as:

$$d\hat{\mathbf{x}}^-(t_i) = \mathbf{F}(t_{i-1})d\hat{\mathbf{x}}^+(t_{i-1}) \qquad \text{Eq - E-6}$$

Subtracting Eq - E-3 to Eq - E-4 leads to:

$$\begin{aligned} d\mathbf{x}(t_i) - d\hat{\mathbf{x}}^+(t_i) &= \mathbf{F}(t_{i-1})d\mathbf{x}(t_i) + \mathbf{w_s}(t_{i-1}) - d\hat{\mathbf{x}}^-(t_i) \\ &\quad - \mathbf{K}(t_i)\big(d\mathbf{y}(t_i) - \mathbf{H}(t_i)d\hat{\mathbf{x}}^-(t_i)\big) \end{aligned} \qquad \text{Eq - E-7}$$

Eq - E-6 in Eq - E-7 leads to:

$$\begin{aligned} d\mathbf{x}(t_i) - d\hat{\mathbf{x}}^+(t_i) &= \mathbf{F}(t_{i-1})d\mathbf{x}(t_i) + \mathbf{w_s}(t_{i-1}) - \mathbf{F}(t_{i-1})d\hat{\mathbf{x}}^+(t_{i-1}) \\ &\quad - \mathbf{K}(t_i)\big(d\mathbf{y}(t_i) - \mathbf{H}(t_i)\mathbf{F}(t_{i-1})d\hat{\mathbf{x}}^+(t_{i-1})\big) \end{aligned} \qquad \text{Eq - E-8}$$

Eq - E-5 in Eq - E-8 leads to:

$$\begin{aligned} d\mathbf{x}(t_i) - d\hat{\mathbf{x}}^+(t_i) &= \mathbf{F}(t_{i-1})d\mathbf{x}(t_{i-1}) + \mathbf{w_s}(t_{i-1}) - \mathbf{F}(t_{i-1})d\hat{\mathbf{x}}^+(t_{i-1}) \\ &\quad - \mathbf{K}(t_i)\big(\mathbf{H}(t_i)d\mathbf{x}(t_i) + \mathbf{w_o}(t_i) - \mathbf{H}(t_i)\mathbf{F}(t_{i-1})d\hat{\mathbf{x}}^+(t_{i-1})\big) \end{aligned} \qquad \text{Eq - E-9}$$

Eq - E-3 in Eq - E-9 leads to:

$$\begin{aligned} &d\mathbf{x}(t_i) - d\hat{\mathbf{x}}^+(t_i) \\ &\quad = \mathbf{F}(t_{i-1})d\mathbf{x}(t_{i-1}) + \mathbf{w_s}(t_{i-1}) - \mathbf{F}(t_{i-1})d\hat{\mathbf{x}}^+(t_{i-1}) \\ &\quad - \mathbf{K}(t_i)\big(\mathbf{H}(t_i)\mathbf{F}(t_{i-1})d\mathbf{x}(t_{i-1}) + \mathbf{H}(t_i)\mathbf{w_s}(t_{i-1}) + \mathbf{w_o}(t_i) \\ &\quad - \mathbf{H}(t_i)\mathbf{F}(t_{i-1})d\hat{\mathbf{x}}^+(t_{i-1})\big) \end{aligned} \qquad \text{Eq - E-10}$$

Rearranging Eq - E-10 leads to:

$$\begin{aligned} &d\mathbf{x}(t_i) - d\hat{\mathbf{x}}^+(t_i) \\ &\quad = \big(\mathbf{I} - \mathbf{K}(t_i)\mathbf{H}(t_i)\big)\Big(\mathbf{F}(t_{i-1})\big(d\mathbf{x}(t_{i-1}) - d\hat{\mathbf{x}}^+(t_{i-1})\big) \\ &\quad + \mathbf{w_s}(t_{i-1})\Big) - \mathbf{K}(t_i)\mathbf{w_o}(t_i) \end{aligned} \qquad \text{Eq - E-11}$$

From the hypotheses (*) stated above, $\mathbf{H}(t_i)$ and $\mathbf{F}(t_i)$ do not depend on the presence of multipath in the GNSS pseudo-range measurement error vector. In addition, $\mathbf{R}(t_i)$ does not depend on the presence of multipath in the GNSS pseudo-range measurement error vector. Finally, $\mathbf{P}^+(t_0) = \mathbf{P}^+{}_{\text{w/o mp}}(t_0)$ since the initial prediction of the covariance matrix of the state vector is independent on the multipath ranging errors. Hence, $\mathbf{K}(t_i)$ does not depend on the presence of multipath in the GNSS pseudo-range measurement error vector. Hence, the state vector estimate error that would have been estimated by the Kalman filter if the GNSS pseudo-range measurement vector at time t_i were not affected by multipath is:

$$\begin{aligned} &d\mathbf{x}(t_i) - d\hat{\mathbf{x}}^+{}_{\text{w/o mp}}(t_i) \\ &\quad = \big(\mathbf{I} - \mathbf{K}(t_i)\mathbf{H}(t_i)\big)\Big(\mathbf{F}(t_{i-1})\Big(d\mathbf{x}(t_{i-1}) - d\hat{\mathbf{x}}^+{}_{\text{w/o mp}}(t_{i-1})\Big) \\ &\quad + \mathbf{w_s}(t_{i-1})\Big) - \mathbf{K}(t_i)\mathbf{w}_{\text{o,w/o mp}}(t_i) \end{aligned} \qquad \text{Eq - E-12}$$

Subtracting Eq - E-12 to Eq - E-11 leads to:

$$\begin{aligned} &d\hat{\mathbf{x}}^+(t_i) - d\hat{\mathbf{x}}^+{}_{\text{w/o mp}}(t_i) \\ &\quad = \big(\mathbf{I} - \mathbf{K}(t_i)\mathbf{H}(t_i)\big)\Big(\mathbf{F}(t_{i-1})\Big(d\hat{\mathbf{x}}^+(t_{i-1}) - d\hat{\mathbf{x}}^+{}_{\text{w/o mp}}(t_{i-1})\Big)\Big) \\ &\quad + \mathbf{K}(t_i)\Big(\mathbf{w}(t_i) - \mathbf{w}_{\text{o,w/o mp}}(t_k)\Big) \end{aligned} \qquad \text{Eq - E-13}$$

Equivalently:

$$\begin{aligned} &d\hat{\mathbf{x}}^+(t_i) - d\hat{\mathbf{x}}^+{}_{\text{w/o mp}}(t_i) \\ &\quad = \big(\mathbf{I} - \mathbf{K}(t_i)\mathbf{H}(t_i)\big)\Big(\mathbf{F}(t_{i-1})\Big(d\hat{\mathbf{x}}^+(t_{i-1}) - d\hat{\mathbf{x}}^+{}_{\text{w/o mp}}(t_{i-1})\Big)\Big) \\ &\quad + \mathbf{K}(t_i)\big(\mathbf{b}(t_i) + \mathbf{u}(t_i)\big) \end{aligned} \qquad \text{Eq - E-14}$$

The error in the state vector estimated in the presence of multipath can be expressed as:

$$d\mathbf{x}(t_i) - d\hat{\mathbf{x}}^+(t_i) = \Big(d\mathbf{x}(t_i) - d\hat{\mathbf{x}}^+{}_{\text{w/o mp}}(t_i)\Big) + \Big(d\hat{\mathbf{x}}^+{}_{\text{w/o mp}}(t_i) - d\hat{\mathbf{x}}^+(t_i)\Big) \qquad \text{Eq - E-15}$$

Using Eq - E-14, Eq - E-15 can be written as:

$$d\mathbf{x}(t_i) - d\hat{\mathbf{x}}^+(t_i) = \left(d\mathbf{x}(t_i) - d\hat{\mathbf{x}}^+{}_{w/o\ mp}(t_i)\right) + \boldsymbol{\phi}(t_i) \quad \text{Eq - E-16}$$

where:

$$\boldsymbol{\phi}(t_i) = \left(\mathbf{I} - \mathbf{K}(t_i)\mathbf{H}(t_i)\right)\left(\mathbf{F}(t_{i-1})\left(d\hat{\mathbf{x}}^+{}_{w/o\ mp}(t_{i-1}) - d\hat{\mathbf{x}}^+(t_{i-1})\right)\right) - \mathbf{K}(t_i)\left(\mathbf{b}(t_i) + \mathbf{u}(t_i)\right) \quad \text{Eq - E-17}$$

Hence:

$$\boldsymbol{\phi}(t_i) = \left(\mathbf{I} - \mathbf{K}(t_i)\mathbf{H}(t_i)\right)\left(\mathbf{F}(t_{i-1})\boldsymbol{\phi}(t_{i-1})\right) - \mathbf{K}(t_i)\left(\mathbf{b}(t_i) + \mathbf{u}(t_i)\right) \quad \text{Eq - E-18}$$

where:

- $\boldsymbol{\phi}(t_0) = d\hat{\mathbf{x}}^+{}_{w/o\ mp}(t_0) - d\hat{\mathbf{x}}^+(t_0)$. From the hypotheses (*) stated above, the initial predictions of the state vectors $d\hat{\mathbf{x}}^+(t_0)$ is independent on the multipath ranging error vectors $\mathbf{b}(t_i)$ and $\mathbf{u}(t_i)$. Hence, $d\hat{\mathbf{x}}^+{}_{w/o\ mp}(t_0) = d\hat{\mathbf{x}}^+(t_0)$. Hence, $\boldsymbol{\phi}(t_0) = 0$.

E.2. Expectation of the horizontal position error

Let's derive the expectation of the horizontal position error under the following hypothesis. The GNSS measurement error vectors $\mathbf{z}(t_i), \mathbf{u}(t_i)$ and the process noise vector $\mathbf{w_s}(t_i)$ are zero-mean stochastic error vectors.

The horizontal position error at the output of Kalman filter and at time t_i can be expressed as:

$$\boldsymbol{\varepsilon}_p(t_i) = [d\mathbf{x}(t_i) - d\hat{\mathbf{x}}^+(t_i)]_{\mathbf{1:2}} \quad \text{Eq - E-19}$$

From Eq - E-16, we get:

$$\boldsymbol{\varepsilon}_p(t_i) = \left[d\mathbf{x}(t_i) - d\hat{\mathbf{x}}^+{}_{w/o\ mp}(t_i) + \boldsymbol{\phi}(t_i)\right]_{\mathbf{1:2}} \quad \text{Eq - E-20}$$

Hence:

$$E\left[\boldsymbol{\varepsilon}_p(t_i)\right] = \left[E\left[d\mathbf{x}(t_i) - d\hat{\mathbf{x}}^+{}_{w/o\ mp}(t_i)\right] + E[\boldsymbol{\phi}(t_i)]\right]_{1:2} \quad \text{Eq - E-21}$$

From Eq - E-12, we get

$$E\left[d\mathbf{x}(t_i) - d\hat{\mathbf{x}}^+{}_{w/o\ mp}(t_i)\right] = E\left[\left(\mathbf{I} - \mathbf{K}(t_i)\mathbf{H}(t_i)\right)\left(\mathbf{F}(t_{i-1})\left(d\mathbf{x}(t_{i-1}) - d\hat{\mathbf{x}}^+{}_{w/o\ mp}(t_{i-1})\right) + \mathbf{w_s}(t_{i-1})\right) - \mathbf{K}(t_i)\mathbf{w}_{o,w/o\ mp}(t_k)\right] \quad \text{Eq - E-22}$$

Assuming that the process noise vector $\mathbf{w_s}(t_k)$ is unbiased and the GNSS pseudo-range measurement vector $\mathbf{w}_{o,w/o\ mp}(t_k) = \mathbf{z}(t_k)$ is a zero-mean stochastic vector:

$$E\left[d\mathbf{x}(t_i) - d\hat{\mathbf{x}}^+{}_{w/o\ mp}(t_i)\right] = \mathbf{0} \quad \text{Eq - E-23}$$

Hence:

$$\mathrm{E}\left[\boldsymbol{\varepsilon}_{\mathrm{p}}(\mathrm{t_i})\right] = \left[\mathrm{E}[\boldsymbol{\phi}(\mathrm{t_i})]\right]_{1:2} \quad \text{Eq - E-24}$$

Assuming that the GNSS pseudo-range measurement vector $\mathbf{u}(\mathrm{t_k})$ is a zero-mean stochastic vector, and from Eq - E-18, we get:

$$\mathrm{E}\left[\boldsymbol{\varepsilon}_{\mathrm{p}}(\mathrm{t_i})\right] = \left[\left(\mathrm{I} - \mathbf{K}(\mathrm{t_i})\mathbf{H}(\mathrm{t_i})\right)\mathbf{F}(\mathrm{t_{i-1}})\mathrm{E}[\boldsymbol{\phi}(\mathrm{t_{i-1}})] - \mathbf{K}(\mathrm{t_i})\mathbf{b}(\mathrm{t_i})\right]_{1:2} \quad \text{Eq - E-25}$$

where $\mathrm{E}[\boldsymbol{\phi}(\mathrm{t_0})] = \mathrm{E}[\mathbf{0}] = \mathbf{0}$.

E.3. Covariance matrix of the horizontal position error

Let's derive the covariance of the horizontal position error under the following hypothesis. The correlated multipath error process $\mathbf{u}$ can be modeled as zero-mean first-order Gauss-Markov process. The horizontal position error at the output of Kalman filter and at time $\mathrm{t_i}$ can be expressed as:

$$\boldsymbol{\varepsilon}_{\mathrm{p}}(\mathrm{t_i}) = [\mathrm{d}\mathbf{x}(\mathrm{t_i}) - \mathrm{d}\hat{\mathbf{x}}^{+}(\mathrm{t_i})]_{\mathbf{1:2}} \quad \text{Eq - E-26}$$

Let's compute $\mathrm{cov}\left[\mathrm{d}\mathbf{x}(\mathrm{t_i}) - \mathrm{d}\hat{\mathbf{x}}^{+}{}_{\mathrm{w/o\ mp}}(\mathrm{t_i}) + \boldsymbol{\phi}(\mathrm{t_i})\right]$.

Assuming that the multipath error vector $\mathbf{u}(\mathrm{t_k}) + \mathbf{b}(\mathrm{t_k})$ is independent of the process noise vector $\mathbf{w_s}(\mathrm{t_k})$ and of the GNSS pseudo-range measurement vector $\mathbf{z}(\mathrm{t_k})$, we get:

$$\begin{aligned}\mathrm{cov}&\left[\mathrm{d}\mathbf{x}(\mathrm{t_i}) - \mathrm{d}\hat{\mathbf{x}}^{+}{}_{\mathrm{w/o\ mp}}(\mathrm{t_i}) + \boldsymbol{\phi}(\mathrm{t_i})\right] \\ &= \mathrm{cov}\left[\mathrm{d}\mathbf{x}(\mathrm{t_i}) - \mathrm{d}\hat{\mathbf{x}}^{+}{}_{\mathrm{w/o\ mp}}(\mathrm{t_i})\right] + \mathrm{cov}[\boldsymbol{\phi}(\mathrm{t_i})]\end{aligned} \quad \text{Eq - E-27}$$

where: $\mathrm{cov}\left[\mathrm{d}\mathbf{x}(\mathrm{t_i}) - \mathrm{d}\hat{\mathbf{x}}^{+}{}_{\mathrm{w/o\ mp}}(\mathrm{t_i})\right]_{\mathbf{1:2},\mathbf{1:2}}$ is denoted as $\mathrm{C}_{\mathrm{p,w/o\ mp}}(\mathrm{t_i})$ and is analyzed in Section E.4 of this appendix.

Computation of $\mathrm{cov}[\boldsymbol{\phi}(\mathrm{t_i})]$:

$$\mathrm{cov}[\boldsymbol{\phi}(\mathrm{t_i})] = \mathrm{E}[(\boldsymbol{\phi}(\mathrm{t_i}) - \mathrm{E}[\boldsymbol{\phi}(\mathrm{t_i})])(\boldsymbol{\phi}(\mathrm{t_i}) - \mathrm{E}[\boldsymbol{\phi}(\mathrm{t_i})])^{\mathrm{T}}] \quad \text{Eq - E-28}$$

Let's compute $\boldsymbol{\phi}(\mathrm{t_i}) - \mathrm{E}[\boldsymbol{\phi}(\mathrm{t_i})]$. Using Eq - E-18 and Eq - E-25, we get:

$$\begin{aligned}\boldsymbol{\phi}(\mathrm{t_i}) - \mathrm{E}&[\boldsymbol{\phi}(\mathrm{t_i})] \\ &= \left(\mathbf{I} - \mathbf{K}(\mathrm{t_i})\mathbf{H}(\mathrm{t_i})\right)\mathbf{F}(\mathrm{t_{i-1}})\boldsymbol{\phi}(\mathrm{t_{i-1}}) - \mathbf{K}(\mathrm{t_i})\left(\mathbf{b}(\mathrm{t_i}) + \mathbf{u}(\mathrm{t_i})\right) \\ &- \left(\mathbf{I} - \mathbf{K}(\mathrm{t_i})\mathbf{H}(\mathrm{t_i})\right)\mathbf{F}(\mathrm{t_{i-1}})\mathrm{E}[\boldsymbol{\phi}(\mathrm{t_{i-1}})] + \mathbf{K}(\mathrm{t_i})\mathbf{b}(\mathrm{t_i})\end{aligned} \quad \text{Eq - E-29}$$

By rearranging Eq – 29, we get:

$$\boldsymbol{\phi}(\mathrm{t_i}) - \mathrm{E}[\boldsymbol{\phi}(\mathrm{t_i})] = \left(\mathbf{I} - \mathbf{K}(\mathrm{t_i})\mathbf{H}(\mathrm{t_i})\right)\mathbf{F}(\mathrm{t_{i-1}})(\boldsymbol{\phi}(\mathrm{t_{i-1}}) - \mathrm{E}[\boldsymbol{\phi}(\mathrm{t_{i-1}})]) - \mathbf{K}(\mathrm{t_i})\mathbf{u}(\mathrm{t_i}) \quad \text{Eq - E-30}$$

Let's note:

$$\mathbf{A}(t_i) = \left(\mathbf{I} - \mathbf{K}(t_i)\mathbf{H}(t_i)\right)\mathbf{F}(t_{i-1}) \qquad \text{Eq - E-31}$$

Using this notation, Eq - E-30 is equivalent to:

$$\boldsymbol{\phi}(t_i) - \mathrm{E}[\boldsymbol{\phi}(t_i)] = \mathbf{A}(t_i)(\boldsymbol{\phi}(t_{i-1}) - \mathrm{E}[\boldsymbol{\phi}(t_{i-1})]) - \mathbf{K}(t_i)\mathbf{u}(t_i) \qquad \text{Eq - E-32}$$

Hence, Eq - E-28 can be written as:

$$\begin{aligned}\mathrm{cov}[\boldsymbol{\phi}(t_i)] = \mathrm{E}\Big[&\left(\mathbf{A}(t_i)(\boldsymbol{\phi}(t_{i-1}) - \mathrm{E}[\boldsymbol{\phi}(t_{i-1})]\right) \\ &- \mathbf{K}(t_i)\mathbf{u}(t_i)\Big)\left(\mathbf{A}(t_i)(\boldsymbol{\phi}(t_{i-1}) - \mathrm{E}[\boldsymbol{\phi}(t_{i-1})]) - \mathbf{K}(t_i)\mathbf{u}(t_i)\right)^{\mathrm{T}}\Big]\end{aligned} \qquad \text{Eq - E-33}$$

Rearranging Eq - E-33 leads to:

$$\mathrm{cov}[\boldsymbol{\phi}(t_i)] = \mathrm{E}\begin{bmatrix}\mathbf{A}(t_i)(\boldsymbol{\phi}(t_{i-1}) - \mathrm{E}[\boldsymbol{\phi}(t_{i-1})])(\boldsymbol{\phi}(t_{i-1}) - \mathrm{E}[\boldsymbol{\phi}(t_{i-1})])^{\mathrm{T}}\mathbf{A}^{\mathrm{T}}(t_i) \\ +\mathbf{K}(t_i)\mathbf{u}(t_i)\mathbf{u}^{\mathrm{T}}(t_i)\mathbf{K}^{\mathrm{T}}(t_i) \\ -\mathbf{A}(t_i)(\boldsymbol{\phi}(t_{i-1}) - \mathrm{E}[\boldsymbol{\phi}(t_{i-1})])\mathbf{u}^{\mathrm{T}}(t_i)\mathbf{K}^{\mathrm{T}}(t_i) \\ -\mathbf{K}(t_i)\mathbf{u}(t_i)(\boldsymbol{\phi}(t_{i-1}) - \mathrm{E}[\boldsymbol{\phi}(t_{i-1})])^{\mathrm{T}}\mathbf{A}^{\mathrm{T}}(t_i)\end{bmatrix} \qquad \text{Eq - E-34}$$

Let's remark that:

$$\begin{aligned}&\mathbf{A}(t_i)\mathrm{E}[(\boldsymbol{\phi}(t_{i-1}) - \mathrm{E}[\boldsymbol{\phi}(t_{i-1})])(\boldsymbol{\phi}(t_{i-1}) - \mathrm{E}[\boldsymbol{\phi}(t_{i-1})])^{\mathbf{T}}]\mathbf{A}^{\mathrm{T}}(t_i) \\ &\quad = \mathbf{A}(t_i)\mathrm{cov}[\boldsymbol{\phi}(t_{i-1})]\mathrm{A}^{\mathrm{T}}(t_i)\end{aligned} \qquad \text{Eq - E-35}$$

$$\mathbf{K}(t_i)\mathrm{E}[\mathbf{u}(t_i)\mathbf{u}^{\mathbf{T}}(t_i)]\mathbf{K}^{\mathrm{T}}(t_i) = \mathbf{K}(t_i)\mathbf{R}_{\mathrm{mp}}(t_i)\mathbf{K}^{\mathrm{T}}(t_i)$$

In Eq - E-35, the covariance matrix of $\mathbf{u}(t_i)$ is denoted as $\mathbf{R}_{\mathrm{mp}}(t_i)$:

$$\mathbf{R}_{\mathrm{mp}}(t_i) = \begin{bmatrix}\sigma_{\mathrm{dyn}\,1}(t_i)^2 & 0 & 0 \\ 0 & \ddots & 0 \\ 0 & 0 & \sigma_{\mathrm{dyn}\,N}(t_i)^2\end{bmatrix} \qquad \text{Eq - E-36}$$

By using Eq - E-35, Eq - E-34 is equivalent to:

$$\begin{aligned}\mathrm{cov}[\boldsymbol{\phi}(t_i)] = \; &\mathbf{A}(t_i)\mathrm{cov}[\boldsymbol{\phi}(t_{i-1})]\mathbf{A}^{\mathrm{T}}(t_i) \\ &+\mathbf{K}(t_i)\mathbf{R}_{\mathrm{mp}}(t_i)\mathbf{K}^{\mathrm{T}}(t_i) \\ &-\mathbf{A}(t_i)\mathrm{E}[(\boldsymbol{\phi}(t_{i-1}) - \mathrm{E}[\boldsymbol{\phi}(t_{i-1})])\mathbf{u}^{\mathrm{T}}(t_i)]\mathbf{K}^{\mathrm{T}}(t_i) \\ &-\left(\mathbf{A}(t_i)\mathrm{E}[(\boldsymbol{\phi}(t_{i-1}) - \mathrm{E}[\boldsymbol{\phi}(t_{i-1})])\mathbf{u}^{\mathrm{T}}(t_i)]\mathbf{K}^{\mathrm{T}}(t_i)\right)^{\mathrm{T}}\end{aligned} \qquad \text{Eq - E-37}$$

Computation of $\mathbf{E}[(\boldsymbol{\phi}(t_{i-1}) - \mathbf{E}[\boldsymbol{\phi}(t_{i-1})])\mathbf{u}^{\mathbf{T}}(t_i)]$:

Let's compute $\mathrm{E}[(\boldsymbol{\phi}(t_{i-1}) - \mathrm{E}[\boldsymbol{\phi}(t_{i-1})])\mathbf{u}^{\mathrm{T}}(t_i)]$**:**

$$\mathrm{E}[(\boldsymbol{\phi}(t_{i-1}) - \mathrm{E}[\boldsymbol{\phi}(t_{i-1})])\mathbf{u}^{\mathrm{T}}(t_i)] = \mathrm{E}[\boldsymbol{\phi}(t_{i-1})\mathbf{u}^{\mathrm{T}}(t_i)] - \mathrm{E}[\mathrm{E}[\boldsymbol{\phi}(t_{i-1})]\mathbf{u}^{\mathrm{T}}(t_i)] \qquad \text{Eq - E-38}$$

Since $\mathbf{u}(t_i)$ is assumed to be a zero-mean stochastic error vector, we get:

$$E[E[\boldsymbol{\phi}(t_{i-1})]\mathbf{u}^T(t_i)] = E[\boldsymbol{\phi}(t_{i-1})]E[\mathbf{u}^T(t_i)] = \mathbf{0} \quad \text{Eq - E-39}$$

Let's compute $E[\boldsymbol{\phi}(t_{i-1})\mathbf{u}^T(t_i)]$**.** Since the stochastic multipath ranging error vector $\mathbf{u}$ is modelled as a zero-mean, first order Gauss-Markov process vector, $\mathbf{u}(t_i)$ can be written as:

$$\mathbf{u}(t_i) = \mathbf{C}(t_i)\mathbf{u}(t_{i-1}) + \boldsymbol{\eta}(t_i) \quad \text{Eq - E-40}$$

where:

- The vector $\boldsymbol{\eta}(t_i)$ and the matrix $\mathbf{C}(t_i)$ are detailed as follows:

$$\mathbf{u}(t_i) = \begin{bmatrix} u_{obs\,1}(t_i) \\ \vdots \\ u_{obs\,N}(t_i) \end{bmatrix} = \underbrace{\begin{bmatrix} e^{-\frac{T_e}{\tau_{dyn\,1}(t_i)}} & 0 & 0 \\ 0 & \ddots & 0 \\ 0 & 0 & e^{-\frac{T_e}{\tau_{dynN}(t_i)}} \end{bmatrix}}_{\mathbf{C}(t_i)} \underbrace{\begin{bmatrix} u_{obs\,1}(t_{i-1}) \\ \vdots \\ u_{obs\,N}(t_{i-1}) \end{bmatrix}}_{\mathbf{u}(t_{i-1})} + \underbrace{\begin{bmatrix} \eta_1(t_i) \\ \vdots \\ \eta_N(t_i) \end{bmatrix}}_{\boldsymbol{\eta}(t_i)}$$

- The vector $\boldsymbol{\eta}(t_i)$ is a zero-mean white-noise Gauss process.

Hence:

$$E[\boldsymbol{\phi}(t_{i-1})\mathbf{u}^T(t_i)] = E\left[\boldsymbol{\phi}(t_{i-1})\left(\mathbf{u}^T(t_{i-1})\mathbf{C}^T(t_i) + \boldsymbol{\eta}^T(t_i)\right)\right] \quad \text{Eq - E-41}$$

$$E[\boldsymbol{\phi}(t_{i-1})\mathbf{u}^T(t_i)] = E[\boldsymbol{\phi}(t_{i-1})\mathbf{u}^T(t_{i-1})]\mathbf{C}^T(t_i) + E[\boldsymbol{\phi}(t_{i-1})\boldsymbol{\eta}^T(t_i)]$$

Since $\boldsymbol{\eta}(t_i)$ is independent of $\boldsymbol{\phi}(t_{i-1})$ and is a zero-mean stochastic error vector, we get:

$$E[\boldsymbol{\phi}(t_{i-1})\mathbf{u}^T(t_i)] = E[\boldsymbol{\phi}(t_{i-1})\mathbf{u}^T(t_{i-1})]\mathbf{C}^T(t_i) \quad \text{Eq - E-42}$$

Let's compute $E[\boldsymbol{\phi}(t_{i-1})\mathbf{u}^T(t_{i-1})]$**.** From Eq - E-18 and Eq - E-40:

$$\begin{aligned} \boldsymbol{\phi}(t_{i-1})\mathbf{u}(t_{i-1})^T &= \mathbf{A}(t_{i-1})\boldsymbol{\phi}(t_{i-2})(\mathbf{u}(t_{i-2})^T\mathbf{C}(t_{i-1})^T + \boldsymbol{\eta}(t_{i-1})^T) \\ &\quad - \mathbf{K}(t_{i-1})\left(\mathbf{b}(t_{i-1}) + \mathbf{u}(t_{i-1})\right)\mathbf{u}(t_{i-1})^T \end{aligned} \quad \text{Eq - E-43}$$

Since $\mathbf{b}(t_{i-1})$ and $\mathbf{u}(t_{i-1})$ are assumed to be independent and since $\mathbf{u}(t_{i-1})$ is assumed to be a zero-mean stochastic error vector, we get:

$$\begin{aligned} E[\boldsymbol{\phi}(t_{i-1})\mathbf{u}(t_{i-1})^T] &= \mathbf{A}(t_{i-1})E[\boldsymbol{\phi}(t_{i-2})\mathbf{u}(t_{i-2})^T]\mathbf{C}(t_{i-1})^T \\ &\quad - \mathbf{K}(t_{i-1})E[\mathbf{u}(t_{i-1})\mathbf{u}(t_{i-1})^T] \end{aligned} \quad \text{Eq - E-44}$$

Using Eq - E-35, we get:

$$E[\boldsymbol{\phi}(t_{i-1})\mathbf{u}(t_{i-1})^T] = \mathbf{A}(t_{i-1})E[\boldsymbol{\phi}(t_{i-2})\mathbf{u}(t_{i-2})^T]\mathbf{C}(t_{i-1})^T - \mathbf{K}(t_{i-1})\mathbf{R}_{mp}(t_{i-1}) \quad \text{Eq - E-45}$$

Hence, $E[\boldsymbol{\phi}(t_{i-1})\mathbf{u}(t_{i-1})^T]$ can be computed by recurrence. Let's compute the initial condition:

$$\mathrm{E}[\boldsymbol{\phi}(t_0)\mathbf{u}(t_0)^{\mathbf{T}}] = \mathrm{E}[\boldsymbol{\phi}(t_0)\boldsymbol{\eta}(t_0)^{\mathbf{T}}] \quad \text{Eq - E-46}$$

Since $\boldsymbol{\eta}(t_0)$ is considered to be a white Gaussian noise that is independent of $\boldsymbol{\phi}(t_0)$, we get:

$$\mathrm{E}[\boldsymbol{\phi}(t_0)\mathbf{u}(t_0)^{\mathbf{T}}] = \mathrm{E}[\boldsymbol{\phi}(t_0)]\mathrm{E}[\boldsymbol{\eta}(t_0)^{\mathbf{T}}] = \mathbf{0} \quad \text{Eq - E-47}$$

Hence, $\mathrm{E}[\boldsymbol{\phi}(t_{i-1})\mathbf{u}(t_{i-1})^{\mathbf{T}}]$ can be computed by recurrence:

$$\mathrm{E}[\boldsymbol{\phi}(t_{i-1})\mathbf{u}(t_{i-1})^{\mathbf{T}}] = \mathbf{A}(t_{i-1})\mathrm{E}[\boldsymbol{\phi}(t_{i-2})\mathbf{u}(t_{i-2})^{\mathbf{T}}]\mathbf{C}(t_{i-1})^{\mathrm{T}} - \mathbf{K}(t_{i-1})\mathbf{R}_{\mathrm{mp}}(t_{i-1}) \quad \text{Eq - E-48}$$

where $\mathrm{E}[\boldsymbol{\phi}(t_0)\mathbf{u}(t_0)^{\mathbf{T}}] = \mathbf{0}$.

Conclusion:

$$\mathrm{cov}\left[\boldsymbol{\varepsilon}_{\mathrm{p}}(t_i)\right] = \left[\mathrm{cov}\left[d\mathbf{x}(t_i) - d\hat{\mathbf{x}}^{+}{}_{\mathrm{w/o\ mp}}(t_i) + \boldsymbol{\phi}(t_i)\right]\right]_{1:2,1:2} \quad \text{Eq - E-49}$$

$\mathrm{cov}\left[d\mathbf{x}(t_i) - d\hat{\mathbf{x}}^{+}{}_{\mathrm{w/o\ mp}}(t_i) + \boldsymbol{\phi}(t_i)\right]$ can be decomposed as follows:

$$\mathrm{cov}\left[d\mathbf{x}(t_i) - d\hat{\mathbf{x}}^{+}{}_{\mathrm{w/o\ mp}}(t_i) + \boldsymbol{\phi}(t_i)\right] = \mathrm{cov}\left[d\mathbf{x}(t_i) - d\hat{\mathbf{x}}^{+}{}_{\mathrm{w/o\ mp}}(t_i)\right] + \mathrm{cov}[\boldsymbol{\phi}(t_i)] \quad \text{Eq - E-50}$$

where:

- $\mathrm{cov}\left[d\mathbf{x}(t_i) - d\hat{\mathbf{x}}^{+}{}_{\mathrm{w/o\ mp}}(t_i)\right]$ represents the covariance matrix of the state vector estimate error at time t_i that would have been obtained if no multipath would affect the GNSS pseudo-range measurements,
- $\mathrm{cov}[\boldsymbol{\phi}(t_i)]$ represents the covariance term due to multipath.

$\mathrm{cov}[\boldsymbol{\phi}(t_i)]$ is given by:

$$\begin{aligned}\mathrm{cov}[\boldsymbol{\phi}(t_i)] = {} & \mathbf{A}(t_i)\mathrm{cov}[\boldsymbol{\phi}(t_{i-1})]\mathbf{A}(t_i)^{\mathrm{T}} \\ & + \mathbf{K}(t_i)\mathbf{R}_{\mathrm{mp}}(t_i)\mathbf{K}(t_i)^{\mathrm{T}} \\ & - \mathbf{A}(t_i)\mathrm{E}[\boldsymbol{\phi}(t_{i-1})\mathbf{u}^{\mathbf{T}}(t_{i-1})]\mathbf{C}^{\mathrm{T}}(t_i)\mathbf{K}^{\mathrm{T}}(t_i) \\ & - \left(\mathbf{A}(t_i)\mathrm{E}[\boldsymbol{\phi}(t_{i-1})\mathbf{u}^{\mathbf{T}}(t_{i-1})]\mathbf{C}^{\mathrm{T}}(t_i)\mathbf{K}^{\mathrm{T}}(t_i)\right)^{\mathrm{T}}\end{aligned} \quad \text{Eq - E-51}$$

$\mathrm{E}[\boldsymbol{\phi}(t_{i-1})\mathbf{u}(t_{i-1})^{\mathbf{T}}]$ can be computed by recurrence:

$$\mathrm{E}[\boldsymbol{\phi}(t_{i-1})\mathbf{u}(t_{i-1})^{\mathbf{T}}] = \mathbf{A}(t_{i-1})\mathrm{E}[\boldsymbol{\phi}(t_{i-2})\mathbf{u}(t_{i-2})^{\mathbf{T}}]\mathbf{C}(t_{i-1})^{\mathrm{T}} - \mathbf{K}(t_{i-1})\mathbf{R}_{\mathrm{mp}}(t_{i-1}) \quad \text{Eq - E-52}$$

E.4. Analysis of $\mathbf{C_{p,w/o\ mp}}$

This subsection presents the technique that has been used to estimate the covariance matrix $\mathrm{C_{p,w/o\ mp}}$ of the GNSS/IRS horizontal position error along a given segment in a specific airport. This subsection is organized as follows. Firstly, the methodology to evaluate $\mathrm{C_{p,w/o\ mp}}$ is presented and the reasons of this choice of methodology are detailed. This technique requires estimating the correlation times of the position errors in the East and North

components. Secondly, the methodology used to quantify these correlation times is presented and these correlation times are evaluated by simulations.

E.4.1. Evaluation of the covariance matrix $\mathbf{C_{p,w/o\ mp}}$

E.4.1.1. Technique based on the predicted covariance matrix

The state vector covariance matrix denoted as $\mathbf{P}^{+}(t_i)$ in Section 6.2.5.3 is an estimator of the covariance of the error made in the estimation of the state vector $d\mathbf{x}(t_i)$ at time t_i. $\mathbf{P}^{+}{}_{1:2,1:2}(t_i)$ consists of the first two lines and of the first two columns of $\mathbf{P}^{+}(t_i)$. $\mathbf{P}^{+}{}_{1:2,1:2}(t_i)$ is an estimator of the covariance of the horizontal position error at the output of the Kalman filter at time epoch t_i. It can be easily proven that $\mathbf{P}^{+}{}_{1:2,1:2}(t_i)$ is the true covariance of the horizontal position error at time t_i if the following constraints are met:

- The implemented Kalman filter is an optimal Kalman filter, meaning that :
  - The filter contains the exact models of the system dynamics and of the GNSS measurement process,
  - The filter contains the exact model of the covariance matrix of the process noise and of the measurement errors,
  - The filter contains the exact initial estimate of covariance of the state vector error.
- The implemented Kalman gain is the gain expressed in Section 6.2.5.3.
- The process noise vector and the measurement noise vector are zero-mean Gaussian white noise processes, meaning that their components are not correlated in the time domain.

In this thesis, the implemented Kalman filter is not an optimal Kalman filter. This is due to the fact that the predicted the covariance matrix of the process noise and of the measurement errors are not the exact process noise and measurement noise covariance matrices, as explained in Section 6.2.5. In addition, the measurement errors are time correlated. Even if the long term ranging errors induced by the satellite clock and ephemeris inaccuracies are partially removed from the innovation vector (see Section 6.2.5.2), other ranging errors, such as the troposphere errors, are time correlated and still affect the innovation vector. Since the Kalman filter is suboptimal and since the ranging errors are time correlated, $\mathbf{P}^{+}{}_{1:2,1:2}(t_i)$ is not an accurate estimator the covariance of the horizontal position error. As an illustration, under the simulation scenario fully described in Section 7.2.1.1., a Monte Carl simulation has shown that the standard deviations of the North and East error components over the LVP procedure path are roughly constant throughout the trajectory and are equal to 21.7cm and 19.2cm respectively. In comparison, the estimated standard deviations of the North and East components from $\mathbf{P}^{+}{}_{1:2,1:2}(t_i)$ are 54.4cm and 48.3cm, respectively, when the Kalman filter has converged. To conclude, in the application, the covariance matrix of the GNSS/IRS position error cannot be estimated by means of the predicted covariance matrix $\mathbf{P}^{+}{}_{1:2,1:2}$.

E.4.1.2. Technique based on Monte Carlo simulations

The covariance matrix $C_{p,w/o\ mp}$ over a segment of a procedure path in a given airport has been estimated by means of Monte Carlo simulations. This section details the simulation scenario that has been used to estimate the covariance matrix $C_{p,w/o\ mp}$ over a segment of the LVP procedure path at Toulouse Blagnac airport, France and given a specific satellite geometry. The satellite geometry is indicated by the index t_0 in the rest of this section.

Let's firstly recall that, from Section 7.3.2.3, the covariance matrix $C_{p,w/o\ mp}(t_0)$ of the GNSS/IRS/DEM horizontal position error given the satellite geometry t_0 can be considered as

constant in the (NED) reference frame over the whole LVP procedure path. The procedure path consists of four segments. $C_{p,w/o\ mp}(t_0)$ is considered to be independent of the segment. Based on this remark, the covariance matrix $C_{pos,w/o\ mp}(t_0)$ throughout the LVP procedure path for the satellite geometry t_0 has been obtained using the methodology sketched in Figure E-1.

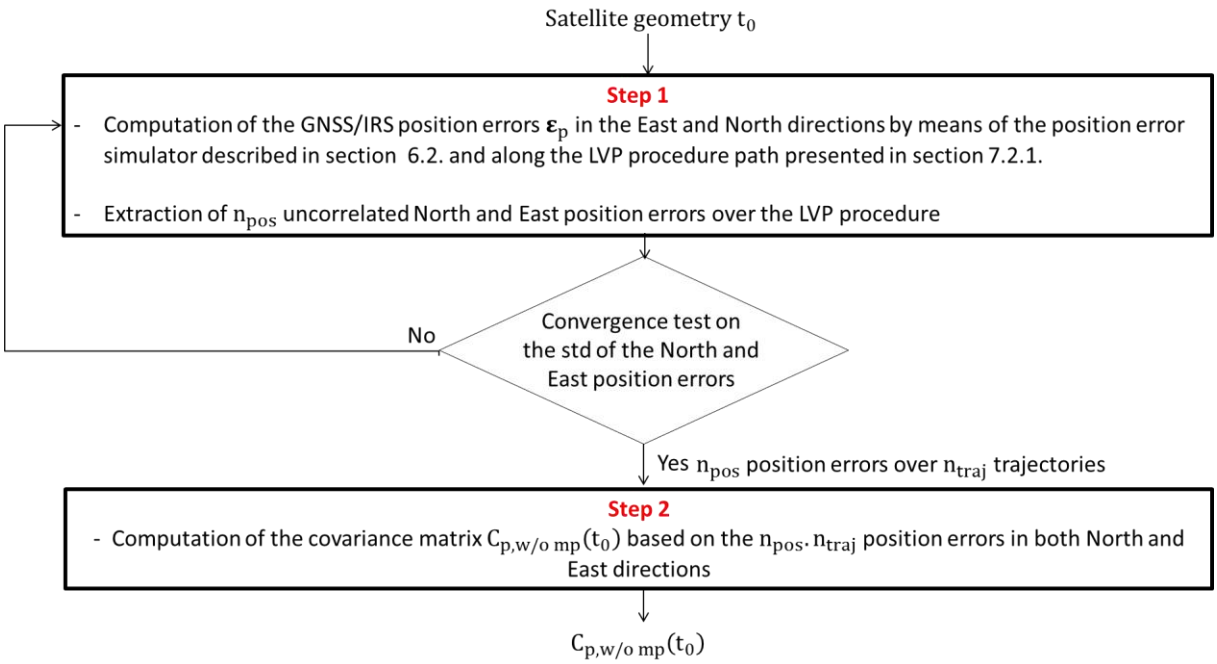

Figure E-1: Methodology to estimate the covariance matrix $C_{p,w/o\ mp}$

As described in Figure E-1, only North and East position errors that are uncorrelated in the time domain are used to estimate the covariance matrix throughout the LVP procedure. Indeed, the North and East position errors are correlated in the time domain. There are two reasons for this. The GNSS measurements are affected by errors that are modelled in the time domain by first order Gauss-Markov processes characterized by relatively long correlation times (few hundred of seconds for the troposphere error). In addition, the Kalman filter itself induces a temporal correlation on the GNSS/IRS/DEM position errors.

The convergence test described in Appendix B, Section B.2, is performed on the standard deviation of the uncorrelated position errors in both North and East direction. The simulation is stopped when the convergence tests on both North and East errors are passed. It is shown in the next section that a correlation time of $T_{corr} = 200s$ can be used to extract uncorrelated data over the trajectory. Table E-1 provides the number of position errors used to estimate $C_{p,w/o\ mp}(t_k)$.

Number of trajectories	$n_{traj} = 16$
Number of position errors per trajectory	5247
Upper bound of the correlation time	$T_{corr} = 200s$
Number of uncorrelated position errors per trajectory	$n_{pos} = 5$
Number of position errors to estimate $C_{p,w/o\ mp}(t_k)$	$n_{pos}.n_{traj} = 80$

Table E-1: Number of GNSS/IRS position errors used in the estimation of $C_{pow/o\ mp}$

E.4.2. Correlation time of the GNSS/IRS/DEM position errors

For this analysis, let's consider the following simulation scenario. An aircraft performs a uniform and rectilinear trajectory at Blagnac, France, for a given constellation configuration. The elevation mask angle is set to 15° for both GPS and Galileo constellations. The trajectory length is 6 kilometers. The minimal trajectory duration is obtained for an aircraft speed of 10m/s and is 10 minutes. Note that this simulation scenario is relatively long compared to the exposure times related to taxi operations that are few hundred of seconds [Schuster *et al.*, 2011]. However, in this simulation, the exposure time has been artificially increased in order to analyze the autocorrelation of the GNSS/IRS position errors over a wide time interval. The position error simulator presented in Chapter 6 has been used to compute the GNSS/IRS horizontal position $\boldsymbol{\varepsilon}_p$. The GNSS pseudo-range measurements are affected by the nominal errors induced by the troposphere, the ionosphere, the satellite clock and ephemeris inaccuracies, and the receiver noise. The autocorrelations of the North and East position errors are depicted in Figure E-2 for a constant aircraft speed throughout the trajectory of 1m/s.

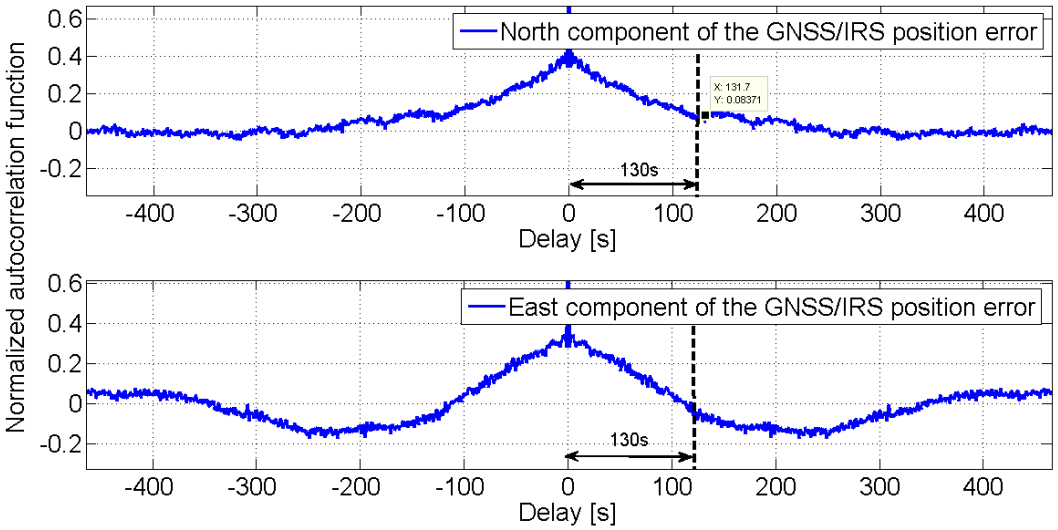

Figure E-2: Normalized autocorrelation functions of the GNSS/IRS horizontal position errors

Simulation results from Figure E-2 show that the correlation time of the position errors in the North and East directions is several dozens of seconds. Correlation times of roughly 130 seconds have been obtained in the North and East directions. This simulation has been reiterated for different aircraft speeds. Indeed, the dynamic of the aircraft is expected to modify the correlation time of the position error since it will modify the Kalman gain. Table E-2 presents the estimated correlation times obtained for different aircraft speeds throughout the trajectory. in this thesis, it is considered that an upper bound of the correlation time of $T_{corr} = 200s$ can be adopted.

Aircraft speed	Estimated correlation time	
	North	East
1m/s	130s	130s
5m/s	205s	205s
10m/s	170s	210s

Table E-2: Estimated correlation times of the GNSS/IRS position errors

APPENDIX F

Reference frames

F.1. Inertial reference frame – (I)

It is a reference frame for which its orientation is fixed relative to stars. Its origin is at the Earth's center of mass(O). It consists in 3 axes $(\mathbf{X_I}, \mathbf{Y_I}, \mathbf{Z_I})$. $\mathbf{Z}$ axis is along the earth's spin axis. At a given initial time (t=0), $\mathbf{X_I}$ axis is perpendicular to $\mathbf{Z_I}$ in the Equator plane in the direction of Greenwich meridian. $\mathbf{Y_I}$ axis is defined to complete the right-handed coordinate system such as $(\mathbf{X_I}, \mathbf{Y_I}, \mathbf{Z_I})$ is an orthogonal coordinate system.

F.2. Earth-Centered Earth-Fixed (ECEF) reference frame

Its origin is fixed at the center of the Earth. It is deduced from inertial frame by rotation of $\Omega_E t$ radians about the earth's spin axis during interval $[0, t]$. Ω_E is the Earth's angular rate detailed in [Groves, 2008]. The ECEF refrence frame consists in 3 axes $(\mathbf{X_E}, \mathbf{Y_E}, \mathbf{Z_E})$. $\mathbf{X_E}$ axis is in the Greenwich meridian plane. Earth's shape and gravity models are defined by geodetic datum. The datum that is globally most used is the World Geodetic System 84.

F.3. NED Navigation reference frame – (NED)

It is the North, East, Down rectangular coordinate frame whose origin is at the position of the central IMU of the aircraft. North $(\mathbf{e_N})$ and East $(\mathbf{e_E})$ axes point to true North and East respectively, such as $(\mathbf{e_N}, \mathbf{e_E})$ plane is tangent to the surface of the earth on the position of the central IMU of the aircraft. $\mathbf{e_D}$ is normal to the plane $(\mathbf{e_N}, \mathbf{e_E})$ and down-oriented.

F.4. Wander Azimuth Navigation reference frame – (w)

It is a coordinate frame whose origin is at the position of the central IMU of the aircraft. $\mathbf{e_{x,w}}$ and $\mathbf{e_{y,w}}$ axes are located in the $(\mathbf{e_N}, \mathbf{e_E})$ plane that is tangent to the surface of the earth on the position of the central IMU of the aircraft. They deviate from the North and East directions of an angle (the azimuth angle α_w detailed in [Diesel, 1995]). $\mathbf{e_{z,w}}$ is normal to the plane $(\mathbf{e_{x,w}}, \mathbf{e_{y,w}})$ and down-oriented. The (NED), (w) and ECEF reference frames are represented in Figure F-1. In this figure, P represents the the position of the central IMU of the aircraft. Transformation matrices from the (NED) reference frame to the (w) reference frame are provided in [Diesel, 1995].

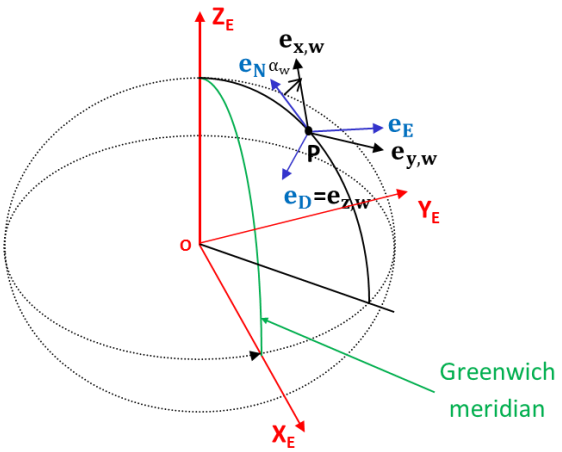

Figure F-1 : ECEF and NED and wander azimuth reference frames

F.5. Aircraft body reference frame – (b)

The aircraft body frame is rigidly attached to the central IMU of the aircraft. $\mathbf{e_{x,b}}$ axis is pointing in the forward direction, $\mathbf{e_{z,b}}$ axis is pointing to the bottom of the mobile. The $\mathbf{e_{y,b}}$ axis is defined to complete the right-handed coordinate system such as ($\mathbf{e_{x,b}}$, $\mathbf{e_{y,b}}$, $\mathbf{e_{z,b}}$) is an orthogonal coordinate system. $\mathbf{e_{x,b}}$, $\mathbf{e_{y,b}}$, $\mathbf{e_{z,b}}$ axes are depicted in Figure F-2.

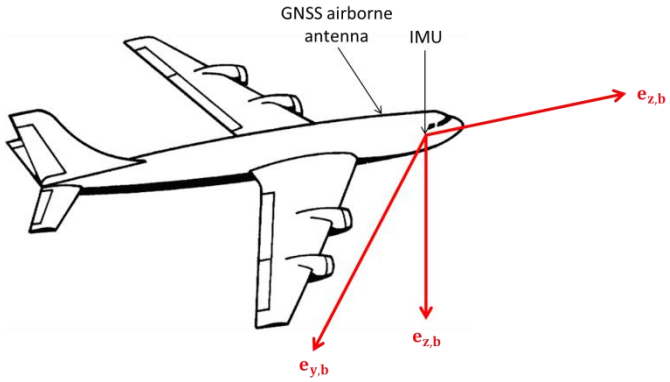

Figure F-2 : Aircraft body reference frame

(b) - frame is deduced from (NED) - frame with rotations α about $\mathbf{e_N}$, β about $\mathbf{e_E}$ and ϕ about $\mathbf{e_D}$ where α, β, ϕ are roll, pitch, yaw angles, respectively. Assuming that both roll and pitch angles are null during the taxi operations, the transformation matrix from the navigation reference frame (NED) to the aircraft body reference frame (b) $\mathbf{M}_{\mathrm{ned2b}}(t_i)$ at time t_i is given by:

$$M_{ned2b}(t_i) = \begin{bmatrix} c_\phi & s_\phi & 0 \\ -s_\phi & c_\phi & 0 \\ 0 & 0 & 1 \end{bmatrix} \qquad \text{Eq - F-1}$$

where c_ϕ is the cosine of the yaw angle and s_ϕ is the sine of the yaw angle at time t_i.

APPENDIX G

GNSS/IRS/DEM/WSS positioning algorithm

The goals of this Appendix are:

- To propose a GNSS/IRS/DEM/WSS hybridization positioning algorithm for airport surface operations.
- To present the GNSS/IRS/DEM/WSS position error simulator that has been implemented to assess the accuracy performance of the proposed GNSS/IRS/DEM/WSS algorithm.
- To assess the accuracy performance of this algorithm in the absence of multipath from airport buildings and airport gates and during the *taxi on apron taxiway* and the *taxi on taxi lane* sub-phases along the LVP procedure path at Toulouse Blagnac airport. The LVP procedure path is presented in Section 7.2.1.1.
- To compare these performances to the performances obtained with the GNSS/IRS/DEM hybridization positioning algorithm presented in Chapter 6.

The WSS is a device used for reading the speed of the aircraft wheel rotation rate which can be used to calculate the wheel speed. More details about the operation of WSS are provided in [Gao, 2007] [Li, 2009]. The main landing gear of an A319 aircraft consists of four wheels. Each wheel of the main landing gear is equipped with a WSS.

G.1. GNSS/IRS/WSS positioning error computation

In this Appendix, a GNSS/IRS/DEM/WSS tight coupling hybridization positioning algorithm is presented. The choice of this hybridization algorithm is further detailed in Chapter 6. Note that more details about the use of WSS in ultra-tight coupling and in loose coupling algorithms are provided in [Gao, 2007] [Li, 2009].

G.1.1. GNSS/IRS/DEM/WSS positioning error simulator architecture

The general architecture of the software that computes the positioning error at the output of the GNSS/IRS/DEM/WSS coupling algorithm is provided in Figure G-1.

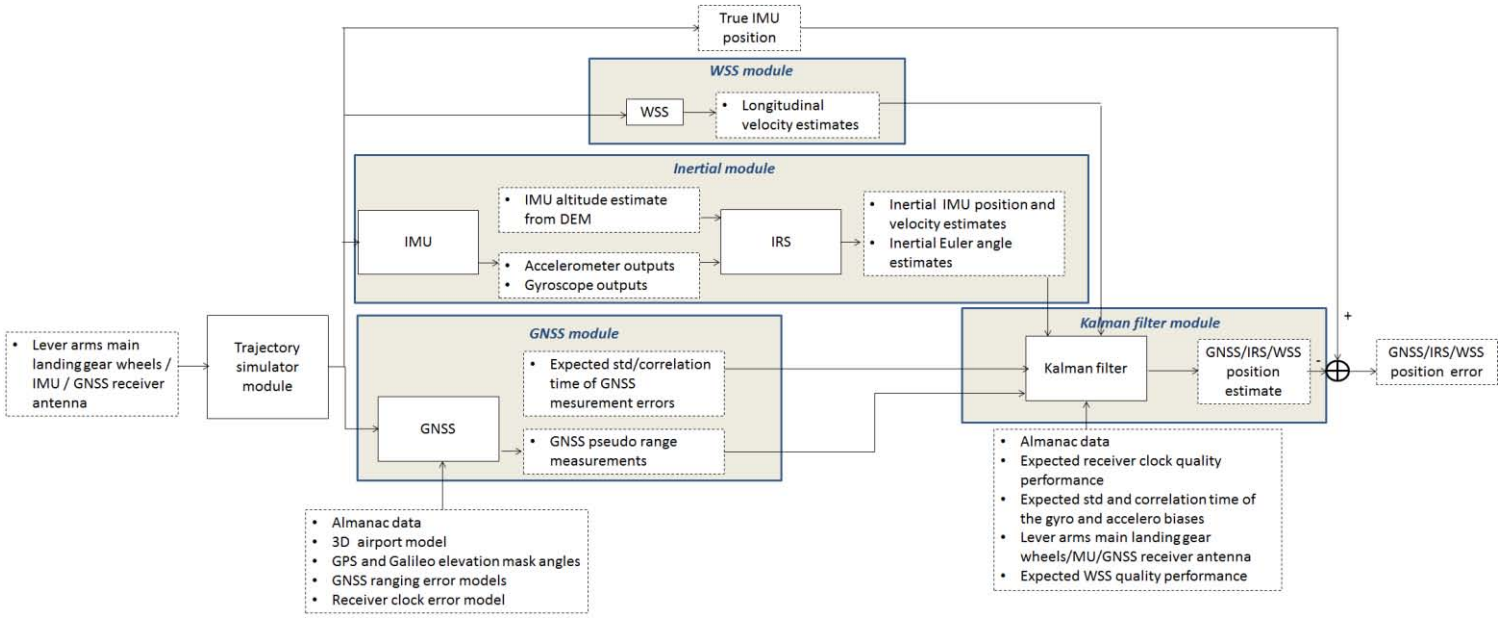

Figure G-1 : Architecture of the GNSS/IRS/DEM/WSS positioning error simulator

As depicted in the last Figure, five main modules are implemented in the software, namely the trajectory simulator module, the GNSS module, the inertial module, the WSS module and the Kalman filter module. The GNSS module and the inertial module are presented in Chapter 6. The trajectory module, the WSS module and the Kalman filter modules are briefly presented below.

G.1.2. Trajectory simulator module

A trajectory simulator is implemented so as to compute:

- The true IMU position and the true IMU velocity vector in (NED),
- The true aircraft attitude angles,
- The true GNSS receiver antenna position in LLA,
- The true longitudinal velocity at the center of each wheel of the main landing gear.

Further details concerning the computation of the true IMU positions and velocity vectors, of the true aircraft attitude angles, and of the true GNSS antenna positions throughout the trajectory are provided in Chapter 6. The main landing gear of A319 aircraft consists of four wheels. In this thesis, it is assumed that the angular velocity of each wheel of the main landing gear is measured by a WSS. By denoting $\mathbf{v}_{\mathrm{IMU}}^{\mathrm{n}}(\mathrm{t_i})$ the true IMU velocity vector in NED at time $\mathrm{t_i}$, the true velocity vector of the aircraft at the center of the wheel $\mathrm{w_j}$ expressed in the body reference frame (b) can be calculated as [Farrell *et al.*, 1999]:

$$\mathbf{v}_{\mathrm{w_j}}^{\mathrm{b}}(\mathrm{t}_i) = \mathbf{M}_{\mathrm{n2b}}(\mathrm{t_i})\mathbf{v}_{\mathrm{IMU}}^{\mathrm{n}}(\mathrm{t_i}) + \mathbf{\Omega}_{\mathrm{nb}}^{\mathrm{b}}(\mathrm{t_i})\mathbf{r}_{\mathrm{IMU2w_j}}^{\mathrm{b}} \qquad \text{Eq - G-1}$$

where:

- $\mathbf{M}_{n2b}(t_i)$ is the transformation matrix from the navigation reference frame (NED) to the aircraft body reference frame (b). Note that both reference frames are defined in Appendix F.
- $\mathbf{\Omega}_{nb}^{b}(t_i)$ is the skew-symmetric matrix of the angular rate vector $\boldsymbol{\omega}_{nb}^{b}(t_i)$ at time t_i. $\boldsymbol{\omega}_{n2b}^{b}(t_i)$ is the rate of rotation of the (b) frame axes with respect to the (NED) frame axes resolved about the (b) frame axes.
- $\mathbf{r}_{IMU2w_j}^{b}$ is the lever arm between the center of the IMU and the center of the of the wheel w_j expressed in the aircraft body reference frame (b). The lever arms IMU/landing gear wheels cannot be published in the context of this thesis.

From the definition of the aircraft body reference frame provided in Appendix F, the true longitudinal velocity at the center of the wheel w_j can be computed as follows:

$$v_{w_j}^{longi}(t_i) = \left[\mathbf{v}_{w_j}^{b}(t_i)\right]_{1:1} \qquad \text{Eq - G-2}$$

The true IMU and GNSS receiver antenna positions, the true IMU velocity vector, the true yaw angle and the longitudinal velocities at the center of each wheel w_j are computed with a sampling frequency of 5Hz, that is a typical sampling frequency used in the GNSS/IRS tight coupling Kalman filters in commercial aircraft.

G.1.3. WSS module

A WSS module is implemented so as to compute the longitudinal velocity measurements at the center of the four wheels of the main landing gear. Note that a WSS measures the rotation rate of each wheel and converts the measured angular velocities in longitudinal velocity measurements. The Kalman filter presented in this Appendix only uses the longitudinal velocity measurements as additional aiding information. For this reason, only longitudinal velocity measurements are generated in this module.

The final longitudinal velocity measurements are affected by two sources of errors. Firstly there are the errors in the estimation of the rotation rates of the wheels by the WSS. These errors essentially come from the acquisition, quantification and digitalization processes used by the WSS and described in [Li, 2009]. Secondly, there are the errors on the model of the tire radius used to convert the estimated rotation rates in longitudinal velocity measurements.

The angular velocity measurement of the rotation of the wheel w_j can be expressed as follows:

$$\hat{\omega}_{w_j}(t_i) = \omega_{w_j}(t_i) + \eta_{w_j}(t_i) \qquad \text{Eq - G-3}$$

where:

- $\omega_{w_j}(t_i)$ represents the true rotation rate of the wheel w_j at time t_i,
- $\eta_{w_j}(t_i)$ is modelled as a zero-mean Gaussian white noise [Li, 2009] characterized by a standard deviation σ_{wss}. In this thesis, σ_ω is considered to be independent of the wheel. σ_ω depends on the characteristics of the WSS mounted on the wheels of the aircraft. The value of σ_{wss} for A319 aircraft cannot be publically published in the context of this PhD thesis.

The longitudinal velocity obtained from a WSS can be represented as:

$$\hat{v}_{w_j}^{longi}(t_i) = R_{w_j}\left(\omega_{w_j}(t_i) + \eta_{w_j}(t_i)\right) \quad \text{Eq - G-4}$$

where: R_{w_j} is the nominal tire radius that is used by the WSS to convert the measured rotation rate of the wheel to the longitudinal velocity at the center of the wheel. It is assumed that no measurement unit is used to estimate the value of the tire radius throughout the trajectory in real-time. R_{w_j} is set to a constant value of 57cm. This value corresponds to the mean radius of the wheels of an A319 aircraft.

Let's note $R_{w_j,true}(t_i)$ the true tire radius w_j at time t_i. The tire radius is changing over a given trajectory due to variations in the taxiway conditions and due to the variations in the tire pressure [Gao, 2007]. $R_{w_j,true}(t_i)$ is given as:

$$R_{w_j,true}(t_i) = R_{w_j} + \delta R_{w_j}(t_i) \quad \text{Eq - G-5}$$

where: $\delta R_{w_j}(t_i)$ represents the variations of the tire radius with respect to the nominal tire radius R_{w_j} throughout the trajectory. An analysis detailed in [Vézinet, 2013] shows that the term $\delta R_{w_j}(t_i)$ depends on the true longitudinal velocity at the center of the wheel w_j at time t_i. More specifically, it is shown in this publication that, in the context of airport surface operations, $\delta R_{w_j}(t_i)$ can be modelled as:

$$\delta R_{w_j}(t_i) = \alpha + \beta v_{w_j,true}^{longi}(t_i) \quad \text{Eq - G-6}$$

where : α and β have been obtained in an empirical way and cannot be published in the context of this PhD thesis. Eq - G-4 and Eq - G-5 lead to:

$$\hat{v}_{w_j}^{longi}(t_i) = \left(1 - S_{w_j}(t_i)\right) R_{w_j,true}(t_i)\omega_{w_j}(t_i) + R_{w_j}\eta_{w_j}(t_i) \quad \text{Eq - G-7}$$

where: $S_{w_j}(t_i) = \frac{\delta R_{w_j}(t_i)}{R_{w_j} + \delta R_{w_j}(t_i)}$. The true longitudinal velocity at the center of the wheel w_j at time t_i is as follows:

$$v_{w_j}^{longi}(t_i) = R_{w_j,true}(t_i)\omega_{w_j}(t_i) \quad \text{Eq - G-8}$$

From Eq - G-7 and Eq - G-8, the measured longitudinal velocities can be generated as follows [Li, 2009]:

$$\hat{v}_{w_j}^{longi}(t_i) = \left(1 - S_{w_j}(t_i)\right) v_{w_j}^{longi}(t) + w_{o,w_j}(t_i) \quad \text{Eq - G-9}$$

where $w_{w_{o,j}}(t_i) = R_{w_j}\eta_{w_j}(t_i)$ is a zero-mean white noise Gaussian error characterized by a standard deviation $\sigma_{wss} = R_{w_j}\sigma_\omega$.

G.1.4. Kalman filter module

A Kalman filter module is implemented so as to estimate the slowly varying inertial estimation errors. The GNSS raw code pseudo range measurements and the WSS longitudinal velocity measurements are used to estimate the inertial estimation errors. The coupling technique is a tight coupling, wherein INS outputs are integrated with GNSS measurements

and the WSS measurements in a linearized Kalman filter. This section presents the Kalman filter architecture used to estimate the inertial estimation errors. Remark also that other tight coupling GNSS/IRS/WSS implementations exist in the literature. Particularly, one methodology consists in using the lateral and vertical velocities at the center of each wheel as extra measurements to aid the estimation of the state vector. These velocities are set to 0m/s. This is generally true since, most of the time, the vehicle does not jump and does not slide during the trajectory. This technique is known as the "3D velocity update technique" or "non-holonomic technique" in the literature [Gao, 2007]. However, such techniques have not been tested in the context of this PhD thesis. It is also assumed in this thesis that the noise terms that affect the WSS measurements is a white Gaussian noise and that the WSS measurement noises on the four wheels are independent each other. The identification of the WSS correlation modes in the time domain and between the wheels have not been investigated. This analysis can be done based on real data and remains a future work.

The state vector used in the GNSS/IRS/DEM/WSS implementation is detailed in Section 6.2.5 and is unchanged compared to the state vector used for the GNSS/IRS/DEM hybridization algorithm. Hence, the state transition matrix and the predicted state noise covariance matrix are the same for both GNSS/IRS/DEM and GNSS/IRS/DEM/WSS implementations.

Design matrix

The linearized measurement model can be written as follows:

$$\begin{bmatrix} d\mathbf{y}_{GNSS}(t_i) \\ d\mathbf{y}_{WSS}(t_i) \end{bmatrix} = \begin{bmatrix} \mathbf{H}_{GNSS}(t_i) \\ \mathbf{H}_{WSS}(t_i) \end{bmatrix} d\mathbf{x}(t_i) + \begin{bmatrix} \mathbf{w}_{o,GNSS}(t_i) \\ \mathbf{w}_{o,WSS}(t_i) \end{bmatrix} \quad \text{Eq - G-10}$$

where:

- $d\mathbf{y}_{GNSS}(t_i)$ is the GNSS observation vector defined as the difference between the GNSS pseudo-range measurements and ranges calculated between the reference trajectory position and the tracked satellites position**.**
- $d\mathbf{y}_{WSS}(t_i)$ is the WSS observation vector defined as the difference between the WSS longitudinal velocity measurements and longitudinal velocities calculated from the velocity of the IMU estimated by the inertial module**.** $d\mathbf{y}_{WSS}(t_i)$ is presented below.
- $\mathbf{w}_{o,GNSS}(t_i)$ is the GNSS observation noise vector.
- $\mathbf{w}_{o,WSS}(t_i)$ is the WSS observation noise vector.
- $d\mathbf{x}(t_i)$ is the state vector.
- $\mathbf{H}_{GNSS}(t_i)$ is the GNSS design matrix.
- $\mathbf{H}_{WSS}(t_i)$ is the WSS design matrix presented below.

The linearized WSS measurement model can be written as:

$$d\mathbf{y}_{WSS}(t_i) = \mathbf{H}_{WSS}(t_i)d\mathbf{x}(t_i) + \mathbf{w}_{o,WSS}(t_i) \quad \text{Eq - G-11}$$

Since four WSS are installed onboard to measure the rotation rates of the four wheels of the main landing gear, Eq - G-11 can be developed as:

$$\begin{bmatrix} \hat{v}_{w_1}^{longi}(t_i) - \hat{v}_{IRS,w_1}^{longi}(t) \\ \hat{v}_{w_2}^{longi}(t_i) - \hat{v}_{IRS,w_2}^{longi}(t) \\ \hat{v}_{w_3}^{longi}(t_i) - \hat{v}_{IRS,w_3}^{longi}(t) \\ \hat{v}_{w_4}^{longi}(t_i) - \hat{v}_{IRS,w_4}^{longi}(t) \end{bmatrix} = \begin{bmatrix} \mathbf{H}_{WSS,w_1}(t_i) \\ \mathbf{H}_{WSS,w_2}(t_i) \\ \mathbf{H}_{WSS,w_3}(t_i) \\ \mathbf{H}_{WSS,w_4}(t_i) \end{bmatrix} d\mathbf{x}(t_i) + \begin{bmatrix} w_{o,w_1}(t_i) \\ w_{o,w_2}(t_i) \\ w_{o,w_3}(t_i) \\ w_{o,w_4}(t_i) \end{bmatrix} \quad \text{Eq - G-12}$$

where:

- $\hat{v}_{w_j}^{longi}(t_i)$ is the WSS longitudinal velocity measurement on the wheel w_j at time t_i,
- $\hat{v}_{IRS,w_j}^{longi}(t)$ is the longitudinal velocity at the center of the wheel w_j calculated from the inertial estimate of the IMU velocity vector at time t_i.

In order to compute the linearized design matrix $\mathbf{H}_{WSS,w_j}$, let's state the WSS measurement model. Based on Eq - G-1 and on Eq - G-9, the WSS longitudinal velocity measurement $\hat{v}_{w_j}^{longi}(t_i)$ on the wheel w_j and the true IMU velocity vector $\mathbf{v}_{IMU}^{w}(t_i)$ expressed in the wander azimuth reference frame at time t_i are linked by the following equation:

$$\hat{v}_{w_j}^{longi}(t_i) = \left(1 - S_{w_j}(t_i)\right)\left([\mathbf{M}_{w2b}(t_i)]_{1,1:3}\mathbf{v}_{IMU}^{w}(t_i) + \left[\mathbf{\Omega}_{nb}^{b}(t_i)\right]_{1,1:3}\mathbf{r}_{IMU2w_j}^{b}\right) + w_{o,w_j}(t_i) \quad \text{Eq - G-13}$$

Where:

- $\mathbf{M}_{w2b}(t_i)$ is the transformation matrix from the wander azimuth navigation reference frame (w) to the aircraft body reference frame (b). Note that both reference frames are defined in Appendix F.
- $\mathbf{\Omega}_{nb}^{b}(t_i)$ is the skew-symmetric matrix of the angular rate vector $\boldsymbol{\omega}_{nb}^{b}(t_i)$ at time t_i. $\boldsymbol{\omega}_{nb}^{b}(t_i)$ is the rate of rotation of the (b) frame axes with respect to the (w) frame axes resolved about the (b) frame axes.

Eq - G-13 can be rewritten as:

$$\hat{v}_{w_j}^{longi}(t_i) = h_{WSS,w_j}(\mathbf{v}_{IMU}^{w}(t_i)) + w_{o,w_j}(t_i) \quad \text{Eq - G-14}$$

From Chapter 6, the linearized design matrix $\mathbf{H}_{WSS,w_j}(t_i)$ can be written as:

$$\mathbf{H}_{WSS,w_j}(t_i) = \left.\frac{\partial h_{WSS,w_j}}{\partial \mathbf{x}}\right|_{\mathbf{x}(t_i)=\bar{\mathbf{x}}(t_i)} \quad \text{Eq - G-15}$$

where $\bar{\mathbf{x}}$ is the reference trajectory around which the design matrix is linearized. As explained in Chapter 6, the design matrix is linearized around the IMU position, the IMU velocity vector and the aircraft attitude angles estimated by the inertial module. By differentiating the right hand side of Eq - G-14 and by neglecting the second-order differential terms, we get:

$$\left.\frac{\partial h_{WSS,w_j}}{\partial \mathbf{x}}\right|_{\mathbf{x}(t_i)=\bar{\mathbf{x}}(t_i)} d\mathbf{x}(t_i) \qquad \text{Eq - G-16}$$
$$= \left(1 - S_{w_j}(t_i)\right)\left(\begin{array}{c}\boldsymbol{\delta}\left([\mathbf{M}_{w2b}(t_i)]_{1,1:3}\right)\hat{\mathbf{v}}^{w}_{IRS,IMU}(t_i) + \\ \left[\widehat{\mathbf{M}}_{w2b}(t_i)\right]_{1,1:3}\boldsymbol{\delta}\left(\mathbf{v}^{w}_{IMU}(t_i)\right) + \boldsymbol{\delta}\left(\left[\boldsymbol{\Omega}^{b}_{nb}(t_i)\right]_{1,1:3}\right)\mathbf{r}^{b}_{IMU2w_j}\end{array}\right)$$

where:

- $\widehat{M}_{w2b}(t_i)$ is calculated based on the and aircraft attitude angles estimated by the inertial module.
- $\hat{\mathbf{v}}^{w}_{IRS,IMU}(t_i)$ is the IMU velocity vector the wander azimuth reference frame (w) estimated by the inertial module.

The perturbations of the terms $[\mathbf{M}_{w2b}(t_i)]_{1,1:3}$ and $\left[\boldsymbol{\Omega}^{b}_{nb}(t_i)\right]_{1,1:3}$ can be calculated as follows [Farrell *et al*., 1999]:

$$\begin{array}{c}\boldsymbol{\delta}\left([\mathbf{M}_{w2b}(t_i)]_{1,1:3}\right)\hat{\mathbf{v}}^{w}_{IRS,IMU}(t_i) = -\left[\hat{\mathbf{V}}^{w}_{IRS,IMU}(t_i)\right]_{1,1:3} d\boldsymbol{\Phi}(t_i) \\ \boldsymbol{\delta}\left(\left[\boldsymbol{\Omega}^{b}_{nb}(t_i)\right]_{1,1:3}\right)\mathbf{r}^{b}_{IMU2w_j} = -\left[\mathbf{R}^{b}_{IMU2w_j}\right]_{1,1:3}\mathbf{b_g}(t_i)\end{array} \qquad \text{Eq - G-17}$$

where:

- $\hat{\mathbf{V}}^{w}_{IRS,IMU}(t_i)$ is the skew-symmetric matrix of $\widehat{\mathbf{M}}_{w2b}(t_i)\hat{\mathbf{v}}^{w}_{IRS,IMU}(t_i)$.
- $\mathbf{R}^{b}_{IMU2w_j}$ is the skew-symmetric matrix of $\mathbf{r}^{b}_{IMU2w_j}$.

By neglecting the second-order differential terms (such as $S_{w_j}(t_i)\left[\hat{\mathbf{V}}^{w}_{IRS,IMU}(t_i)\right]_{1,1:3} d\boldsymbol{\Phi}(t_i)$), and since the vertical velocity error is not part of the state vector, Eq - G-16 can be written as:

$$\left.\frac{\partial h_{WSS,w_j}}{\partial \mathbf{x}}\right|_{\mathbf{x}(t_i)=\bar{\mathbf{x}}(t_i)} d\mathbf{x}(t_i)$$
$$\approx \left(-\left[\hat{\mathbf{V}}^{w}_{IRS,IMU}(t_i)\right]_{1,1:3} d\boldsymbol{\Phi}(t_i) + \left[\widehat{\mathbf{M}}_{w2b}(t_i)\right]_{1,1:2} d\mathbf{v}(t) - \left[\mathbf{R}^{b}_{IMU2w_j}\right]_{1,1:3}\mathbf{b_g}(t_i)\right) \qquad \text{Eq - G-18}$$

Hence, we get:

$$H_{WSS,w_j}(t_i)$$
$$= \left[0_{1\times 2} \quad \left[\widehat{\mathbf{M}}_{w2b}(t_i)\right]_{1,1:2} \quad -\left[\hat{\mathbf{V}}^{w}_{IRS,IMU}(t_i)\right]_{1,1:3} \quad -\left[\mathbf{R}^{b}_{IMU2w_j}\right]_{1,1:3} \quad 0_{1\times 3} \quad 0 \quad 0 \quad 0_{1\times N}\right] \qquad \text{Eq - G-19}$$

where N is the number of GNSS measurements used in the Kalman filter at time t_i.

Measurement noise covariance matrix

The measurement noise covariance matrix at time t_i is implemented by assuming that GNSS and WSS measurement noises are independent each other at time t_i:

$$\mathbf{R}(t_i) = \begin{bmatrix} \mathbf{R}_{GNSS}(t_i) & 0 & 0 & 0 & 0 \\ 0 & {\sigma_{wss}}^2 & 0 & 0 & 0 \\ 0 & 0 & {\sigma_{wss}}^2 & 0 & 0 \\ 0 & 0 & 0 & {\sigma_{wss}}^2 & 0 \\ 0 & 0 & 0 & 0 & {\sigma_{wss}}^2 \end{bmatrix} \qquad \text{Eq - G-20}$$

where:

- σ_{wss} is the standard deviation of WSS longitudinal velocity measurement noise error. It is assumed that the Kalman filter perfectly knows the standard deviation of the noise errors affecting the WSS longitudinal velocity measurement.
- $\mathbf{R}_{GNSS}(t_i)$ is the GNSS measurement noise covariance matrix at time t_i.

G.2. Analysis of the GNSS/IRS/DEM/WSS positioning error

This section analyses the GNSS/IRS/WSS positioning error over a given trajectory and compares the positioning error to the GNSS/IRS positioning error. In this section, the GNSS/IRS/DEM/WSS positioning errors are obtained by means of the simulator presented in Section G.2 of this Appendix. The GNSS/IRS/DEM positioning errors are obtained by means of the simulator presented in Chapter 6.

G.2.1. Simulation scenario

Both GNSS/IRS/DEM and GNSS/IRS/DEM/WSS position errors have been calculated following the simulation scenario indicated in Table G-1.

Trajectory description	The procedure path is depicted by a red line in Figure G-2. Aircraft speed on the runway 14R: 10m/s Aircraft speed on the taxiways M2 and N2 : 5m/s	
Number of satellites in the constellation	GPS	24 satellites
	Galileo	27 satellites
Elevation mask angle	GPS	15°
	Galileo	15°
GNSS signals	GPS	Dual frequency GPSL1C+GPSL5
	Galileo	Dual frequency GalileoE1+GalileoE5a
GNSS receiver settings	As described in Section 4.2.4	
GNSS measurement error models	**Error source**	**Error model**
	• troposphere • ionosphere • satellite clock and ephemeris inaccuracies • receiver thermal noise	Stochastic error models described in Chapter 3
Inertial sensor error models	Stochastic error models described in Section 6.2.3	
WSS error models	Error models described in Section G.2 of this Appendix	

Table G-1 : Simulation settings for Figure 3

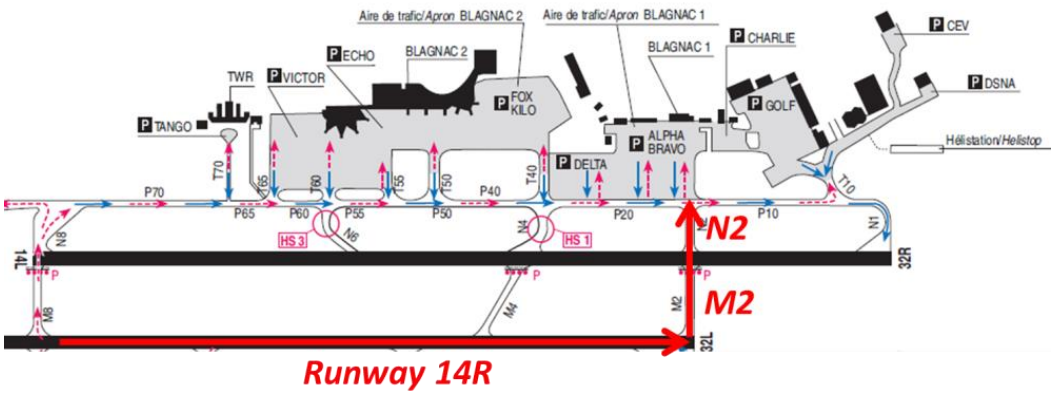

Figure G-2: Representation of the procedure path for Figure G-3

G.2.2. Simulation results

The GNSS/IRS and GNSS/IRS/WSS position errors throughout the trajectory described in the previous section are plotted in Figure G-3 as a function of time in the aircraft body (b) reference frame (left side) and in the (NED) reference frame (right side).

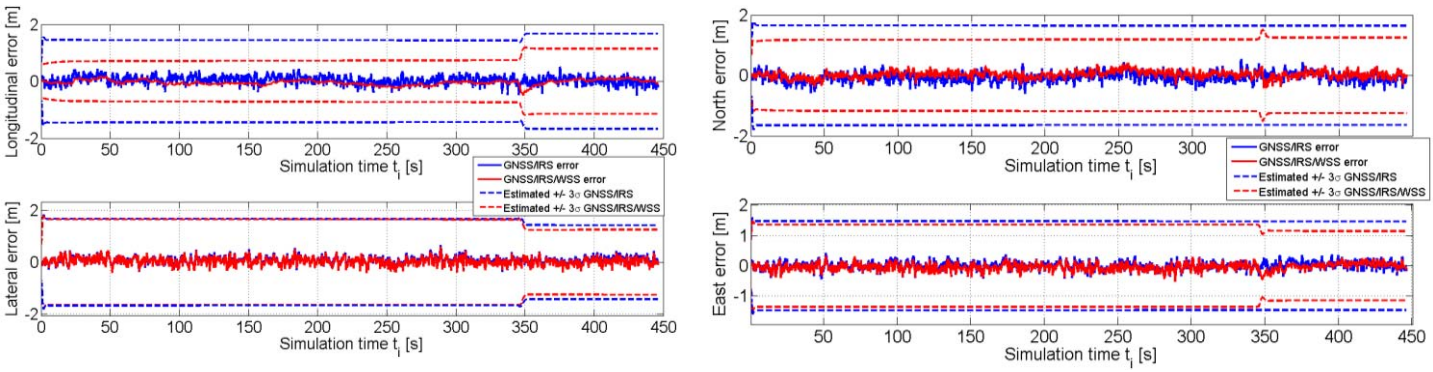

Longitudinal and lateral error components ***North and East error components***

Figure G-3: Horizontal position errors with and without WSS aiding

It can be observed in Figure G-3, left part, that the WSS longitudinal velocity measurements used in the Kalman filter allows reducing the standard deviation of the longitudinal position error throughout the trajectory. The standard deviation of the longitudinal error predicted by the state vector covariance matrix $\mathbf{P}^+$ is roughly two times lower with the GNSS/IRS/WSS implementation than with the GNSS/IRS implementation. The lateral position error is not strongly reduced by the use of WSS. The standard deviations of the lateral error predicted by the state vector covariance matrix $\mathbf{P}^+$ are roughly the same in both GNSS/IRS and GNSS/IRS/WSS implementations.

It can be observed in Figure G-3, right part, that the predicted covariance matrix of the horizontal position errors in the North-East reference frame is constant throughout the trajectory with the GNSS/IRS implementation. An interpretation of this observation is provided in Section 7.3. However, since the WSS aids only the longitudinal position error, the covariance matrix of the horizontal position errors in the North-East reference frame is varying with the route of the aircraft in the GNSS/IRS/WSS implementation. The predicted standard deviations of the North and East errors are different along the runway (when the

simulation time is below 350s) and along the taxiway (when the simulation time is above 350s).

G.3. Accuracy assessment

The objective of this section is to evaluate the accuracy of the horizontal position estimated by the tight coupling GNSS/IRS/DEM/WSS Kalman filter during the *taxi on taxiway* (segment 1), *taxi on apron taxiway*, and *taxi on taxi lane* sub-phases related to the LVP procedure path at Toulouse Blagnac airport, France. The methodology used to estimate the accuracy performance of the algorithm along each sub-phase is fully described in Section 7.3 and is re-used in this section. Since the covariance of the GNSS/IRS/DEM/WSS position error depends on the segment route, the position error covariance matrices $\mathbf{C_{p,w/o\ mp}}$ have been estimated by simulating position errors on each segment. Since the covariance matrix $\mathbf{C_{p,w/o\ mp}}$ is not constant over the LVP trajectory, the GNSS/IRS/DEM/WSS position errors simulated on different segments cannot be merged to estimate the matrix $\mathbf{C_{p,w/o\ mp}}$ on each segment of the LVP trajectory.

The percentage of satellite geometries for which $P_{|\varepsilon_p|<Acc_{95\%}} > 0.95$ with the GNSS/IRS/DEM/WSS algorithm is quantified in Table G-2. Table G-2 also presents the mean $P_{|\varepsilon_p|<Acc_{95\%}}$ computed over the $N_{const} = 433$ satellite geometries simulated over three days. Finally, this Table compares these results with the results obtained with the GNSS/IRS/DEM tight coupling algorithm.

	$\mathbf{Acc_{95\%}}$	**Percentage of satellite geometries for which $P_{\lvert\varepsilon_p\rvert<Acc_{95\%}} > 0.95$**		**Mean probability $P_{\lvert\varepsilon_p\rvert<Acc_{95\%}}$ calculated over three days**	
		GNSS/IRS/ DEM	**GNSS/IRS/ DEM/WSS**	**GNSS/IRS/ DEM**	**GNSS/IRS/ DEM/WSS**
Taxi on taxiway (segment 1)	1.9m	100%	100%	100%	100%
Taxi on apron taxiway	1.0m	95.85%	95.85%	98.41%	98.74%
Taxi on taxi lane	0.50m	0%	0%	67.40%	70.13%

Table G-2 : Accuracy performance of the GNSS/IRS/DEM/WSS algorithm and of the GNSS/IRS/DEM algorithm – Elevation mask angle 15° for GPS and Galileo

The availability of the accuracy function remains constant in the absence or in the presence of the WSS measurement aid. The use of the WSS measurements in the positioning algorithm leads to improve the mean probability that the horizontal position error exceeds the 95% accuracy confidence bounds computed over three days. However, this improvement is not significant for the *apron* sub-phase. Concerning the *taxi on taxi lane* sub-phase, the mean probability is of the order of 70.13% with the WSS aid. The accuracy requirement is not met with the WSS measurements and along the *taxi on taxi lane* sub-phase, regardless of the satellite geometry. It is concluded that the use of WSS measurements does not significantly improve the accuracy of the horizontal position error during the apron sub-phase and does not allow meeting the accuracy performance requirement during the *taxi on taxi lane* sub-phase.

Résumé
Les systèmes GNSS sont actuellement utilisés en aviation civile pour estimer la position et la vitesse de l'avion pendant les phases de route jusqu'aux approches de précision. Etendre l'utilisation de GNSS aux opérations de surface en environnement aéroportuaire et sous de faibles conditions de visibilité reste un challenge pour la communauté aviation civile. En effet, durant ces opérations, les mesures GNSS peuvent être affectées par des évènements singuliers tels que les multi-trajet ou les anomalies ionosphériques. Ces évènements peuvent engendrer des erreurs de position jugées inacceptables en termes de précision et d'intégrité pour assurer le guidage de l'avion. Les algorithmes de surveillance d'intégrité GNSS actuellement utilisés ne sont pas conçus pour prendre totalement en compte les effets de tels évènements. Il est essentiel de développer des algorithmes de surveillance conçus pour protéger les utilisateurs des effets de tels évènements afin de pouvoir utiliser GNSS pour le guidage de l'avion en milieu aéroportuaire et sous de faibles conditions de visibilité.
Afin de concevoir de tels algorithmes de surveillance d'intégrité, il est nécessaire de développer des modèles d'erreurs de mesures GNSS et des modèles de pannes GNSS. La thèse a été principalement orientée vers la conception de modèles d'erreurs de mesures GNSS dues aux multi-trajets et vers le développement de modèles de pannes GNSS dues aux multi-trajets.
Pour ce faire, un modèle d'erreurs multi-trajets GNSS sur les mesures bi-fréquence GPSL1C+GPSL5 et GalileoE1+GalileoE5a a d'abord été proposé. Ensuite, l'impact des multi-trajets sur l'erreur de position a été étudié. Pour cette étude, un algorithme de couplage serré GPS+Galileo/IRS a été considéré. Cet algorithme est basé sur un filtre de Kalman linéarisé. Une analyse théorique et quantitative a été conduite pour étudier l'impact des erreurs de mesures GNSS dues aux multi-trajets sur le biais et sur la matrice de covariance de l'erreur de position horizontale en sortie de l'algorithme de positionnement considéré. Finalement, un modèle de pannes GNSS dues aux multi-trajets a été proposé. Ce modèle décrit la signature des pannes multi-trajets, les facteurs influençant cette signature, le modèle d'occurrence des pannes multi-trajets ainsi que les conditions d'occurrence de telles pannes.
Mots-clés: GNSS, multitrajet, aviation civile, intégrité

Abstract
GNSSs are currently used in civil aviation to provide aircraft with position and velocity estimates from en-route to precision approach operations. Extending the use of GNSS to the guidance function during airport surface operations and under zero-visibility conditions remains a challenge. Indeed, during these operations, GNSS measurements may be affected by GNSS singular events, such as multipath or ionosphere anomalies. GNSS singular events may lead to unacceptable position errors in terms of accuracy and integrity for the zero-visibility guidance function. Current GNSS integrity monitoring systems are not designed to totally account for the GNSS singular event effects. The development of GNSS integrity monitoring systems designed to properly protect users from the singular event effects is essential to use GNSS for the guidance function under zero-visibility conditions.
GNSS measurement error and integrity failure models are key inputs in the design of GNSS integrity monitoring systems. In this thesis, work has been mainly focused on the development of GNSS multipath measurement errors, on the assessment of the multipath impact on the GNSS-based position error, and on the development of GNSS multipath integrity failure models.
For this matter, the dual frequency GPSL1C+GPSL5 and GalileoE1+GalileoE5a multipath pseudo-range error model adapted to airport navigation has been firstly proposed. Next, the impact of multipath on the GNSS-based position error has been assessed. To do so, a double constellation GPS+Galileo/IRS tight coupling algorithm based on a linearized Kalman filter has been selected. The theoretical and quantitative analysis of the impact of the GNSS multipath ranging errors on the horizontal position bias and on the covariance matrix of the horizontal position error have been proposed. Finally, a GNSS multipath integrity failure model has been proposed. The model describes the signature of the GNSS single multipath ranging failures, the factors influencing the signature as well as the occurrence model of these failures and their conditions of occurrence.
Keywords: GNSS, multipath, civil aviation, integrity